

CAMBRIDGE TEXTS
IN APPLIED
MATHEMATICS

Hydrodynamic Instabilities



FRANÇOIS CHARRU

CAMBRIDGE

CAMBRIDGE

more information – www.cambridge.org/9780521769266

This page intentionally left blank

HYDRODYNAMIC INSTABILITIES

The instability of fluid flows is a key topic in classical fluid mechanics because it has huge repercussions for applied disciplines such as chemical engineering, hydraulics, aeronautics, and geophysics. This modern introduction is written for any student, researcher, or practitioner working in the area, for whom an understanding of hydrodynamic instabilities is essential.

Based on a decade's experience of teaching postgraduate students in fluid dynamics, this book brings the subject to life by emphasizing the physical mechanisms involved. The theory of dynamical systems provides the basic structure of the exposition, together with asymptotic methods. Wherever possible, Charru discusses the phenomena in terms of characteristic scales and dimensional analysis. The book includes numerous experimental studies, with references to videos and multimedia material, as well as over 150 exercises which introduce the reader to new problems.

FRANÇOIS CHARRU is a Professor of Mechanics at the University of Toulouse, France, and a researcher at the Institut de Mécanique des Fluides de Toulouse.

Cambridge Texts in Applied Mathematics

All titles listed below can be obtained from good booksellers or from Cambridge University Press. For a complete series listing, visit www.cambridge.org/mathematics

Nonlinear Dispersive Waves
MARK J. ABLOWITZ

Complex Variables: Introduction and Applications (2nd Edition)
MARK J. ABLOWITZ & ATHANASSIOS S. FOKAS

Scaling
G. I. R. BARENBLATT

Introduction to Symmetry Analysis
BRIAN J. CANTWELL

A First Course in Continuum Mechanics
OSCAR GONZALEZ & ANDREW M. STUART

Theory of Vortex Sound
M. S. HOWE

Applied Solid Mechanics
PETER HOWELL, GREGORY KOZYREFF & JOHN OCKENDON

Practical Applied Mathematics: Modelling, Analysis, Approximation
SAM HOWISON

A First Course in the Numerical Analysis of Differential Equations (2nd Edition)
ARIEH ISERLES

A First Course in Combinatorial Optimization
JON LEE

An Introduction to Parallel and Vector Scientific Computation
RONALD W. SHONKWILER & LEW LEFTON

HYDRODYNAMIC INSTABILITIES

FRANÇOIS CHARRU

University of Toulouse

Translated by

PATRICIA DE FORCRAND-MILLARD



CAMBRIDGE UNIVERSITY PRESS
Cambridge, New York, Melbourne, Madrid, Cape Town,
Singapore, São Paulo, Delhi, Tokyo, Mexico City
Cambridge University Press
The Edinburgh Building, Cambridge CB2 8RU, UK

Published in the United States of America by Cambridge University Press, New York

www.cambridge.org
Information on this title: www.cambridge.org/9780521769266

Originally published in French as *Instabilités Hydrodynamiques* by EDP Sciences in 2007
© 2007, EDP Sciences, 17, avenue du Hoggar, BP 112, Parc d'activités de
Courtabeuf, 91944 Les Ulis Cedex A
et
CNRS ÉDITIONS, 15, rue Malebranche, 75005 Paris

First published in English by Cambridge University Press 2011
English translation © Cambridge University Press 2011
Foreword © P. Huerre 2011

Cover photo: manifestation of the Kelvin–Helmholtz instability between two atmospheric layers with different velocity, above Laramie, Wyoming, USA. © Brooks Martner, NOAA, Environmental Technology Laboratory.

Ouvrage publié avec le concours du Ministère français chargé de la culture – Centre national du livre.
Published with the assistance of the French Ministry of Culture – Centre national du livre.

This publication is in copyright. Subject to statutory exception
and to the provisions of relevant collective licensing agreements,
no reproduction of any part may take place without the written
permission of Cambridge University Press.

First published 2011

Printed in the United Kingdom at the University Press, Cambridge

A catalogue record for this publication is available from the British Library

Library of Congress Cataloging in Publication data
Charru, François. [Instabilités hydrodynamiques. English]
Hydrodynamic instabilities / François Charru;
translated by Patricia de Forcrand-Millard.
p. cm.—(Cambridge texts in applied mathematics; 37)
Includes bibliographical references and index.
ISBN 978-0-521-76926-6 (hardback) — ISBN 978-0-521-14351-6 (pbk.)
1. Unsteady flow (Fluid dynamics) I. Title.
TA357.5.U57C4813 2011
620.1'064—dc22 2011000388

ISBN 978-0-521-76926-6 Hardback
ISBN 978-0-521-14351-6 Paperback

Cambridge University Press has no responsibility for the persistence or
accuracy of URLs for external or third-party internet websites referred to
in this publication, and does not guarantee that any content on such
websites is, or will remain, accurate or appropriate.

To my father

Contents

	<i>page</i>
<i>Foreword</i>	x
<i>Preface</i>	xiii
<i>Video resources</i>	xvi
1 Introduction	1
1.1 Phase space, phase portrait	1
1.2 Stability of a fixed point	2
1.3 Bifurcations	6
1.4 Examples from hydrodynamics	12
1.5 Non-normality of the linearized operator	30
1.6 Exercises	36
2 Instabilities of fluids at rest	43
2.1 Introduction	43
2.2 The Jeans gravitational instability	44
2.3 The Rayleigh–Taylor interface instability	53
2.4 The Rayleigh–Plateau capillary instability	64
2.5 The Rayleigh–Bénard thermal instability	68
2.6 The Bénard–Marangoni thermocapillary instability	76
2.7 Discussion	79
2.8 Exercises	80
3 Stability of open flows: basic ideas	88
3.1 Introduction	88
3.2 A criterion for linear stability	96
3.3 Convective and absolute instabilities	98
3.4 Exercises	102

4 Inviscid instability of parallel flows	104
4.1 Introduction	104
4.2 General results	107
4.3 Instability of a mixing layer	116
4.4 The Couette–Taylor centrifugal instability	126
4.5 Exercises	134
5 Viscous instability of parallel flows	139
5.1 Introduction	139
5.2 General results	145
5.3 Plane Poiseuille flow	154
5.4 Poiseuille flow in a pipe	162
5.5 Boundary layer on a flat surface	162
5.6 Exercises	169
6 Instabilities at low Reynolds number	171
6.1 Introduction	171
6.2 Films falling down an inclined plane	174
6.3 Sheared liquid films	193
6.4 Exercises	199
7 Avalanches, ripples, and dunes	201
7.1 Introduction	201
7.2 Avalanches	202
7.3 Sediment transport by a flow	208
7.4 Ripples and dunes: a preliminary dimensional analysis	218
7.5 Subaqueous ripples under a continuous flow	220
7.6 Subaqueous ripples in oscillating flow	230
7.7 Subaqueous dunes	238
7.8 Exercises	244
8 Nonlinear dynamics of systems with few degrees of freedom	246
8.1 Introduction	246
8.2 Nonlinear oscillators	249
8.3 Systems with few degrees of freedom	260
8.4 Illustration: instability of a sheared interface	264
8.5 Exercises	268
9 Nonlinear dispersive waves	274
9.1 Introduction	274
9.2 Instability of gravity waves	275
9.3 Instability due to resonant interactions	279

9.4	Instability to modulations	287
9.5	Resonances revisited	294
9.6	Exercises	295
10	Nonlinear dynamics of dissipative systems	299
10.1	Introduction	299
10.2	Weakly nonlinear dynamics	300
10.3	Saturation of the primary instability	305
10.4	The Eckhaus secondary instability	305
10.5	Instability of a traveling wave	311
10.6	Coupling to a field at large scales	317
10.7	Exercises	323
11	Dynamical systems and bifurcations	326
11.1	Introduction	326
11.2	Phase space and attractors	327
11.3	Linear stability	334
11.4	Invariant manifolds and normal forms	338
11.5	Structural stability and genericity	345
11.6	Bifurcations	351
11.7	Exercises	365
paragraphMultimedia Fluid Mechanics.xv	paragraphAIP Gallery of Fluid Motion. xvii	
Appendix A: The Saint-Venant equations	369	
A.1	Outflow from a slice of fluid	369
A.2	Mass conservation	370
A.3	Momentum conservation	371
A.4	Modeling the wall friction	372
A.5	Consistent depth-averaged equations	373
<i>References</i>	375	
<i>Index</i>	387	

Foreword

Hydrodynamic instabilities occupy a special position in fluid mechanics. Since the time of Osborne Reynolds and G. I. Taylor, it has been known that the transition from laminar flow to turbulence is due to the instability of the laminar state to certain classes of perturbations, both infinitesimal and of finite amplitude. This paradigm was first displayed in a masterful way in the studies of G. I. Taylor on the instability of Couette flow generated by the differential rotation of two coaxial cylinders. From then on, the theory of hydrodynamical instability has formed a part of the arsenal of techniques available to the researcher in fluid mechanics for studying transitions in a wide variety of flows in mechanical engineering, chemical engineering, aerodynamics, and in natural phenomena (climatology, meteorology, and geophysics).

The literature on this subject is so vast that very few researchers have attempted to write a pedagogical text which describes the major developments in the field. Owing to the enormity of the task, there is a temptation to cover a large number of physical situations at the risk of repetition and of wearying the reader with just a series of methodological approaches. François Charru has managed to avoid this hazard and has risen to the challenge. With this book he fills the gap between the classical texts of Chandrasekhar and Drazin and Reid, and the more recent book of Schmid and Henningson.

Classical instability theory essentially deals with quasi-parallel or parallel shear flows such as mixing layers, jets, wakes, Poiseuille flow in a channel, boundary-layer flow, and so on. Such configurations are the focus of the books by Drazin and Reid and by Schmid and Henningson, and they are of particular interest to researchers of a “mechanical” bent. François Charru has chosen to follow an approach which synthesizes these classical situations, while carefully avoiding the treatment of the critical layer in all these states (*cf.* Drazin and Reid), known to be a source of difficulties. He opens perspectives on the most recent developments in the study of transition in shear flows, for example, the

phenomena of nonmodal growth, “by-pass” transition, and convective or absolute instabilities.

During the last 25 years, our understanding of instabilities has evolved significantly under the combined influence of physicists and mathematicians specializing in nonlinear phenomena and the theory of dynamical systems. In particular, the influx of physicists studying macroscopic phenomena into the ideal playing field of fluid mechanics has led to a profound renewal of our discipline. It is therefore important to introduce the student to the essential concepts without getting mired in technical details. Here also François Charru has succeeded in attractively presenting the most important ideas which have become standard tools of any specialist in instabilities. The fundamentals of the spatio-temporal dynamics of dissipative structures are also introduced in such a way that they can be further pursued using the works by Manneville and by Godrèche and Manneville. By now, many authors have shown that the study of model amplitude equations of the Ginzburg–Landau or the nonlinear Schrödinger type can reveal the nature of the weakly nonlinear dynamics near the instability threshold. It is also known that these toy models remain relevant far from threshold, in a regime which is essentially supercritical, for extracting the generic characteristics of instabilities such as the Benjamin–Feir or the Eckhaus instability, and for testing methodological tools such as the phase dynamics of dissipative textures.

Finally, I would like to draw the attention of the reader to the two chapters at the heart of this book devoted to the surface instabilities of films and the instabilities governing the formation of ripples and dunes. The author has in his own research contributed very significantly in these two areas, and he discusses these topics from his own point of view. Here it should be emphasized that the law governing the behavior of granular media has not yet been set in stone. Experimental observation of the instabilities occurring in such complex media will make it possible to confirm or reject any particular behavior postulated in the theoretical models. In his discussion of the trends in current research, the author helps the student appreciate the vitality and current relevance of this field.

The resolutely “physical” approach adopted by the author is an essential characteristic of this work. For each instability class François Charru presents, by means of dimensional analysis and elegant physical arguments, the mechanism responsible for amplifying the perturbations. This type of reasoning and evaluation of orders of magnitude is carried out before any systematic mathematical treatment is undertaken. The author also makes a special effort to present examples of laboratory experiments which allow confirmation of the theoretical results. This type of exposition familiarizes the student with both the theoretical and the experimental aspects of the research process.

The reader is therefore encouraged to adopt the concepts and methods presented in this book, and to become immersed in the author's approach in which an important role is played by intuition and physical understanding of the phenomena. He or she will then have an ideal jumping-off point for the discovery of more beautiful hydrodynamic instabilities.

Patrick Huerre

Preface

La raison a tant de formes, que nous ne savons à laquelle nous prendre ;

l'expérience n'en a pas moins.

Montaigne, *Essais*, Livre 3, 13.

*Reason has so many forms that we know not to which to take;
experience has no fewer.*

Montaigne, *Essays*, XXI. *Of Experience*, tr. Charles Cotton.

For over a century now, the field of hydrodynamic instabilities has been constantly and abundantly renewed, and enriched by a fruitful dialogue with other fields of physics: phase transitions, nonlinear optics and chemistry, plasma physics, astrophysics and geophysics. Observation and analysis have been stimulated by new experimental techniques and numerical simulations, as well as by the development and adaptation of new concepts, in particular, those related to asymptotic analysis and the theory of nonlinear dynamical systems. Ever since the observations of Osborne Reynolds in 1883, there has been unflagging interest in the fundamental problem of the transition to turbulence. This topic has been given new life by concepts such as convective instabilities, transient growth, and by the recognized importance of unstable nonlinear solutions. New problems have emerged, such as flows involving fluid–structure interactions, granular flows, and flows of complex fluids – non-Newtonian and biological fluids, suspensions of particles, bubbly flows – where constitutive laws play an essential role.

This book has been written over the course of 10 years of teaching postgraduate students in fluid dynamics at the University of Toulouse. It is intended for any student, researcher, or engineer already conversant with basic hydrodynamics, and interested in the questions listed above. As far as possible, the phenomena are discussed in terms of characteristic scales and dimensional analysis in order to elucidate the underlying physical mechanisms or, in Feynman's words, the “qualitative

content of the equations.”¹ This approach blends well with the theory of dynamical systems, bifurcations, and symmetry breaking, which provides the basic structure for our exposition. Asymptotic methods also play an important role. Their power and success, sometimes well beyond the region where they should apply, are always amazing. Numerous experimental studies are discussed in detail in order to confirm the theoretical developments or, conversely, to display their shortcomings.

The first part of the book (Chapters 1 to 7) is essentially devoted to linear stability, while the second part (Chapters 8 to 11) deals with nonlinear aspects. The first chapter presents an introduction to the theory of dynamical systems, including numerous examples of “simple” hydrodynamical problems; there we also introduce the idea of transient growth. In the second chapter we present the general methodology of a stability analysis: perturbation of a base state, linearization, normal modes, and the dispersion relation; we illustrate these techniques by the classical problems of thermal, capillary, and gravitational instabilities.

Chapters 3 to 5 give the classical analyses of instabilities in open flows (the instability criterion, convective and absolute instabilities, temporal and spatial growth) and then instabilities of parallel flows: inviscid instabilities are discussed in Chapter 4 (the Rayleigh inflection-point theorem, the Kelvin–Helmholtz instability) and viscous ones in Chapter 5 (the Orr–Sommerfeld equations, Tollmien–Schlichting waves in boundary layers and Poiseuille flow).

In Chapters 6 and 7 we discuss problems that are barely touched on in the classical textbooks: (i) instabilities at small Reynolds number, which arise, in particular, in the presence of deformable interfaces (liquid films falling down an inclined plane or sheared by another fluid, flows of superposed layers), and (ii) the instabilities of granular beds flowing down a slope (avalanches) or eroded by a flow, which give rise to the growth of surface waves, ripples, and dunes. Chapter 7 also presents a (very sketchy) introduction to the physics of granular media, and illustrates how stability is strongly affected by the modeling, in particular, by the introduction of relaxation phenomena.

Chapters 8 to 10 present an introduction to weakly nonlinear dynamics, where the method of multiple scales plays an essential role. In Chapter 8 we discuss nonlinear oscillators and the “canonical” nonlinear effects such as amplitude saturation and frequency correction (the Landau equation), and frequency locking for forced oscillators. Next, the analysis of systems that are governed by partial differential equations but which are spatially confined reveals how the dynamics near the instability threshold is controlled by the weakly unstable “master mode.” Chapter 9 is devoted to dispersive nonlinear waves, the canonical model of which is the Stokes gravity wave, and to the Benjamin–Feir instability. The latter is analyzed from two

¹ *The Feynman Lectures on Physics*, Volume 2. Electromagnetism, §41.6, Addison Wesley Longman, 1970.

viewpoints: in terms of resonances with side-band wave numbers (described by amplitude equations), and in terms of modulations of the envelope of the wave packet (described by the nonlinear Schrödinger equation). Chapter 10 presents the dynamics of dissipative systems in the supercritical and subcritical cases, typically Rayleigh–Bénard convection or Couette–Taylor flow for the former, and Poiseuille and boundary-layer flow for the latter. Then for the supercritical case we analyze the secondary instabilities of the Eckhaus type, or the Benjamin–Feir–Eckhaus type in the case of waves. Finally, we study the situation where, owing to a particular invariance (Galilean, or an invariance associated with a conservation law), the mode of zero wave number is marginal, leading to a nontrivial coupling of two nearly neutral phase modes.

The final chapter is devoted to a more mathematical exposition of bifurcation theory (the central manifold theorem, normal forms, bifurcations of codimension greater than unity), providing a systematic treatment of the ideas introduced in the earlier chapters. Finally, in the Appendix we derive the depth-averaged Saint-Venant equations, which offer a simple framework for analyzing problems where the gradients in the flow direction are small.

A list of videos and multimedia material that illustrate the phenomena covered by this book is given below. At the end of each chapter we suggest some exercises which often serve as introductions to new problems. Finally, dispersed throughout the text are 11 short biographies of some of the most important figures in the study of instabilities: Bagnold, Chandrasekhar, Helmholtz, Kapitza, Kelvin, Landau, Poincaré, Rayleigh, Reynolds, Stokes, and Taylor.

This work does not pretend to be exhaustive: choices had to be made from among the enormous diversity of advances in the subject. Important topics like wakes and vortices, and ideas like transient growth and global modes, are only briefly addressed or completely omitted, but some general bibliographical information is provided.*

The author would like to thank his colleagues and friends who, in numerous conversations, have contributed to enriching this work, in particular, B. Andreotti, A. Bottaro, G. Casalis, G. Iooss, E. J. Hinch, P. Luchini, P. Brancher, and J. Magnaudet.

Finally, I would like to warmly thank Bud Homsy for his kind and fruitful help. His thorough reading of the initial translation of the French book, the fine questions he raised, the detailed modifications he proposed, and his contribution to the final writing significantly improved this book.

**Note from the Editor:* Every effort has been made to secure the necessary permissions to reproduce copyright material in this work, but in some cases it has proved impossible to trace the copyright holders. If any omissions are brought to our notice, we will be happy to include the appropriate acknowledgments on reprinting.

Video resources

There are increasing numbers of videos and multimedia material available that illustrate various instability phenomena covered in this book. Below is a list of resources that were available at the time this book went to press. It is easily anticipated that the number of resources will only increase, so the reader is encouraged to search the popular websites: efluids.com, YouTube.com, etc.

The NSF/NCFMF Series. Between the years 1961–1969, the US National Science Foundation supported the production of a series of movies by the National Committee for Fluid Mechanics Films under the leadership of the late Asher Schapiro. These can be accessed at the MIT website: <http://web.mit.edu/hml/ncfmf.html> as part of MIT’s iFluids program, requiring only the use of RealPlayer software. Of particular interest are the films on *Flow Instabilities*, *Turbulence*, and *Boundary Layers*, although others will also contain material related to hydrodynamic instabilities.

Multimedia Fluid Mechanics. Between the years 1998–2008 the US National Science Foundation supported the production of the DVD, *Multimedia Fluid Mechanics* (G. M. Homsy *et al.*, Cambridge University Press, 2007). It is available from the publisher at reasonable cost and contains over 800 movies and animations illustrating fluid phenomena. These media pieces are displayed on explanatory pages and also collected in a “Video Library.” Below we list those relevant to hydrodynamic stability by their number in the Video Library. Links from there will take the interested viewer to the page where further explanation may be found.

- 4, 702, Steady and spiral Couette–Taylor instabilities
- 84, Boundary layer flow showing both laminar and turbulent boundary layers
- 172, 173, 174, 180, 455, 643, 645, Pipe Flow – a series of experiments on transition in pipe flow conducted on Osborne Reynolds’ original apparatus
- 392, 393, In- and out-of-phase vortex shedding from pairs of aligned cylinders
- 636, Wake instabilities and vortex shedding from a cylinder

- 484, 638, Tollmien–Schlichting waves, spanwise instabilities and turbulent spots in a boundary layer
- 3489, 3490, Plateau–Rayleigh instability of a water jet
- 3487, Instability of a soap film
- 3489, Viscous Rayleigh–Taylor instability of a thin liquid film
- 3584, Gravity–capillary waves
- 3587, 4305, Plateau–Rayleigh instability of an annular film on a wire
- 3518, 4053, Formation and instability of a soap film catenoid
- 3599, Famous film by Breidenthal showing the instability and “mixing transition” in a free shear layer
- 3600, Turbulent streaks in a boundary layer
- 3696, 3697, 3698, 3699, 3703, 3704, Taylor vortices in Couette–Taylor flow exhibiting turbulent bursts, drifting, and intermittency
- 3805, Famous film by Brown and Roshko showing instability of the free shear layer
- 3832, 3838, The rivulet instability in climbing Marangoni films
- 3915, Hexagonal Marangoni–Bénard convection cells
- 3936, Onset of Rayleigh–Bénard convection
- 3976, 3978, Simulation of turbulent Rayleigh–Taylor instability
- 4013, 4015, Dewetting instability of thin films of nonwetting liquids
- 4412, Simulation of thermal convection in the Sun
- 4548, 4818, Kelvin–Helmholtz instability of a jet
- 5396, Turbulent mixing in Rayleigh–Taylor instability
- 5104, Axial instability of a vortex pair

efluids Media Gallery. There are many static images and movies of fluid phenomena posted in the Media Gallery at www.efluids.com (then link to “galleries”). Of particular interest are:

1. Breakup of a liquid jet:
<http://media.efluids.com/galleries/all?medium=717>
2. Viscous fingering of an elastic liquid:
<http://web.mit.edu/nmf/people/jbico/exp89.mov>
3. Fractal viscous fingering:
<http://media.efluids.com/galleries/all?medium=581>
4. von Kármán vortex street:
<http://media.efluids.com/galleries/all?medium=578>
5. Piano waves in a vibrated granular media:
<http://media.efluids.com/galleries/all?medium=507>
6. Shear layer instabilities:
<http://media.efluids.com/galleries/youtube?medium=579>

7. Flow around a cylinder:
<http://media.efluids.com/galleries/instability?medium=417>
8. Wake of a low aspect ratio pitching plate:
<http://media.efluids.com/galleries/instability?medium=332>
9. Helical instability in a compressible jet:
<http://media.efluids.com/galleries/instability?medium=424>
10. Ferrofluid instability:
<http://media.efluids.com/galleries/instability?medium=3>
11. Collapse of a soap bubble:
<http://media.efluids.com/galleries/all?medium=723>
12. Richtmeyer–Meshkov instability:
<http://media.efluids.com/galleries/all?medium=707>

AIP Gallery of Fluid Motion. The Division of Fluid Dynamics of the American Physical Society (APS/DFD) chooses winners of the annual Gallery of Fluid Motion. The winning images and videos are available at: <http://scitation.aip.org/pof/gallery/archives.jsp>. Of particular interest are:

1. Viscous fingering in microgravity:
<http://scitation.aip.org/pof/gallery/video/2001/915109phfVFFilm.mov>
2. Faraday jets and sand:
<http://scitation.aip.org/pof/gallery/2003-sandtke.jsp#video>
3. Turbulent Rayleigh–Taylor instability:
<http://scitation.aip.org/pof/gallery/video/2005/908509phfenhanced.mov>
4. Rayleigh–Taylor instability of an evaporating liquid:
<http://scitation.aip.org/pof/gallery/2009-Dehaeck.jsp#video>
5. Helical instability of a rotating jet:
<http://scitation.aip.org/pof/gallery/2008-Weidman.jsp#video>
6. Water bell and sheet instabilities:
<http://scitation.aip.org/pof/gallery/2006-Bush.jsp#video>
7. Breakdown modes of swirling jets:
<http://scitation.aip.org/pof/gallery/2002-ruith.jsp#video>

1

Introduction

1.1 Phase space, phase portrait

In this first chapter we give an introduction to the stability of discrete systems and bifurcations from the geometrical viewpoint of the theory of dynamical systems in phase space. In the first part, which is more mathematical than physical, we define the fundamental ideas. These ideas are then illustrated by examples borrowed from hydrodynamics and the physics of liquids. We close the chapter with a brief presentation of the idea of transient growth, which is related to nonorthogonality of the eigenvectors of a linear system.

The time evolution of a discrete (noncontinuous) physical system is generally governed by differential equations following from physical conservation principles and the laws describing the phenomenological behavior. These equations can often be written as a system of first-order *ordinary differential equations* (ODEs) of the form (see, e.g., Glendinning (1994)):

$$\frac{dx_i}{dt} = X_i(x_1, \dots, x_n, t), \quad i = 1, \dots, n. \quad (1.1)$$

The remainder of this chapter will consider only *autonomous* systems, in which time does not appear explicitly on the right-hand side. The variables x_i are called the *degrees of freedom of the system*.¹ As an example, let us consider a simple damped nonlinear pendulum whose vertical position is specified by the angle θ . Its equation of motion

$$\frac{d^2\theta}{dt^2} + \mu \frac{d\theta}{dt} + \omega_0^2 \sin \theta = 0 \quad (1.2)$$

¹ The degrees of freedom in question are the dynamical degrees of freedom (here, the position and velocity), which are different from the kinematical degrees of freedom in physical space (the positions).

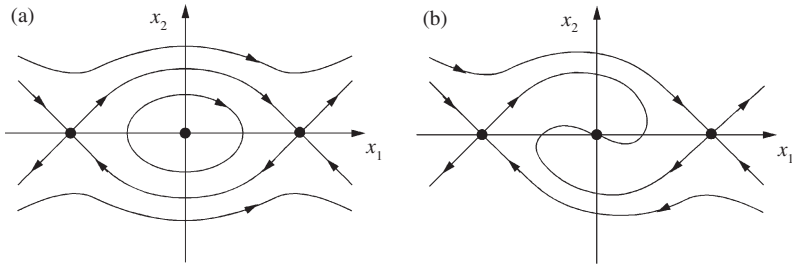


Figure 1.1 Phase portraits of the oscillator (1.3) for (a) $\mu = 0$; (b) $\mu > 0$.

can be written equivalently as a system of two ODEs by setting $x_1 = \theta$, $x_2 = d\theta/dt$:

$$\frac{dx_1}{dt} = x_2, \quad \frac{dx_2}{dt} = -\mu x_2 - \omega_0^2 \sin x_1. \quad (1.3)$$

Any solution of a system of ODEs for a given initial condition can be represented by a curve in the space of the degrees of freedom, called the *phase space*. For the system (1.3) the phase space is the (x_1, x_2) plane. Figure 1.1 shows typical trajectories corresponding to given initial conditions for $\mu = 0$ and $\mu > 0$. The case $\mu = 0$ corresponds to a nondissipative oscillator (i.e., where the mechanical energy remains constant), and the case $\mu > 0$ corresponds to a dissipative oscillator (where the mechanical energy decreases over time). A representation of this type which depicts the essential features of the solutions of a system of ODEs is called the *phase portrait*, which allows the trajectory to be plotted qualitatively for any given initial condition. We use the term *dynamical system* to refer to any system of ODEs studied from the viewpoint of obtaining the phase portrait of the system.

The phase portrait can be guessed easily for a system as elementary as the pendulum (1.3). For more complicated systems the first step is to determine the fixed points and study their stability. When there are several fixed points the second important step is to determine to which fixed point the system evolves for various initial conditions. The ensemble of initial conditions resulting in motion to a particular fixed point is called the *basin of attraction* of that fixed point.

1.2 Stability of a fixed point

1.2.1 Fixed points

The *equilibrium states* of a physical system correspond to the stationary solutions of the system of ODEs, defined as

$$\frac{dx_i}{dt} = 0, \quad i = 1, \dots, n.$$

These solutions are represented in phase space by points called *fixed points*. The fixed points are determined by solving the nonlinear system

$$X_i(x_1, \dots, x_n) = 0, \quad i = 1, \dots, n.$$

The fixed points of the system (1.3) are $(x_1, x_2) = (0, 0)$ and $(x_1, x_2) = (\pi, 0)$ (modulo 2π). In the case of a system where the forces acting can be derived from a potential $V(x_1, \dots, x_n)$, or are proportional to velocities (viscous or friction forces), the equilibrium states correspond to the extrema of the potential (Landau and Lifshitz, 1976).

1.2.2 Linear stability of a fixed point

Once the fixed points are determined, the question of their stability (i.e., the stability of the corresponding equilibrium states) arises. When these equilibrium states are the extrema of a potential, the states of stable and unstable equilibrium correspond respectively to the minima and maxima of the potential (Landau and Lifshitz, 1976), and knowledge of the potential is sufficient for sketching the phase portrait. For example, the phase portrait of the system (1.3) for $\mu = 0$ can easily be drawn by noticing that the only force involved in the equation of motion, the weight, can be derived from the potential $V(\theta) = -mg \cos \theta$. When there is no such potential, a general method based on linear algebra can be used to study the stability of a fixed point with respect to small perturbations. Accordingly, let us consider the system (1.1) written in vector form

$$\frac{dx}{dt} = \mathbf{X}(x), \quad \text{where} \quad x = (x_1, \dots, x_n),$$

which has a fixed point at $x = \mathbf{a}$. The idea is that for small perturbations from equilibrium of amplitude $\epsilon \ll 1$, the smooth function \mathbf{X} can be expanded about the fixed point in a Taylor series, and all products of perturbations can be neglected because they are of order ϵ^2 or smaller. Setting $y = x - \mathbf{a}$, the resulting linearized system is written as

$$\frac{dy}{dt} = \mathbf{L}(\mathbf{a})y, \quad (1.4)$$

where $\mathbf{L}(\mathbf{a})$ is the Jacobian matrix of $\mathbf{X}(x)$ calculated at the point \mathbf{a} , the elements of which are $L_{ij} = \partial X_i / \partial x_j(\mathbf{a})$. When, as in the present case of autonomous systems, the elements L_{ij} are independent of time, the system (1.4) is linear with constant coefficients and its solutions are exponentials $\exp(st)$. The problem then becomes an algebraic eigenvalue problem $\mathbf{L}(\mathbf{a})y = sy$, which has a nontrivial solution only if the determinant of $\mathbf{L} - s\mathbf{I}$ vanishes, where \mathbf{I} is the unit matrix. This determinant

is a polynomial in s , called the *characteristic polynomial*, and its roots are the *eigenvalues*. If the real parts of the eigenvalues are all negative, the solution is a sum of decaying exponentials, and any perturbation from equilibrium dies out at large times: the fixed point is asymptotically stable. However, if at least one of the eigenvalues has positive real part, the fixed point is unstable. To study the *linear stability* of a fixed point we therefore need to (i) find the eigenvalues of the linearized problem, (ii) find the eigenvectors or eigendirections in the phase space, and (iii) plot the phase portrait in the neighborhood of the fixed point.

In two dimensions the classification of types of fixed point is simple. The characteristic polynomial $\det(\mathbf{L} - sI)$ depends only on the trace $\text{tr}(\mathbf{L})$ and the determinant $\det(\mathbf{L})$ of the matrix \mathbf{L} :

$$\det(\mathbf{L} - sI) = s^2 - \text{tr}(\mathbf{L})s + \det(\mathbf{L}). \quad (1.5)$$

The various cases, illustrated in Figure 1.2, are the following:

- $\det(\mathbf{L}) < 0$: s_1 and s_2 are real and have opposite signs; the trajectories are hyperbolas whose asymptotes are the eigendirections, and the fixed point is called a *saddle* (Figure 1.2a).
- $\det(\mathbf{L}) > 0$ and $4\det(\mathbf{L}) \leq \text{tr}^2(\mathbf{L})$ (positive or zero discriminant): s_1 and s_2 are real and have the same sign as $\text{tr}(\mathbf{L})$; the fixed point is called a *node*, and is attractive (stable) if $\text{tr}(\mathbf{L}) < 0$ or repulsive (unstable) if $\text{tr}(\mathbf{L}) > 0$ (Figure 1.2b). If the discriminant is zero, s is a double root and two cases can be distinguished: either \mathbf{L} is a multiple of the identity \mathbf{I} , in which case the trajectories are straight lines and the node is called a *star*, or \mathbf{L} is nondiagonalizable and the node is

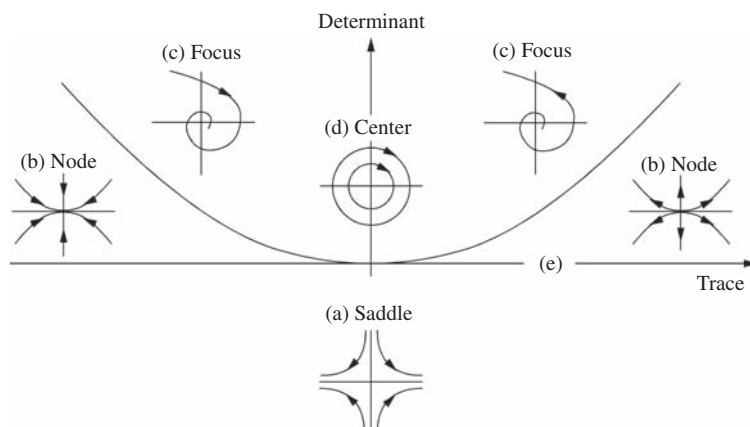


Figure 1.2 Types of fixed point in \mathbb{R}^2 . The parabola corresponds to $\text{tr}^2\mathbf{L} - 4\det\mathbf{L} = 0$ (discriminant of the characteristic polynomial equal to zero).

termed *improper*. In the latter case \mathbf{L} can at best be written as a Jordan block:

$$\mathbf{L} = \begin{pmatrix} s & 1 \\ 0 & s \end{pmatrix}.$$

- $\det(\mathbf{L}) > 0$ and $4\det(\mathbf{L}) > \text{tr}^2(\mathbf{L})$ (negative discriminant): $s_1 = s_2^*$ are complex conjugates with real part $\text{tr}(\mathbf{L})/2$ and nonzero imaginary part; the trajectories are spirals and the fixed point is a *focus*, attractive (stable) if $\text{tr}(\mathbf{L}) < 0$ or repulsive (unstable) if $\text{tr}(\mathbf{L}) > 0$ (Figure 1.2c).
- $\det(\mathbf{L}) > 0$ and $\text{tr}(\mathbf{L}) = 0$: $s_1 = s_2^*$ are purely imaginary; the trajectories are ellipses and the fixed point is a *center* (Figure 1.2d). A perturbation neither grows nor decays, and the stability is termed neutral.
- $\det(\mathbf{L}) = 0$: \mathbf{L} is not invertible (Figure 1.2e). If $\text{tr}(\mathbf{L}) \neq 0$, zero is a simple eigenvalue, whereas if $\text{tr}(\mathbf{L}) = 0$, zero is a double eigenvalue. In the latter case, if the proper subspace has dimension 2, \mathbf{L} is diagonalizable ($\mathbf{L} = \mathbf{0}$); otherwise \mathbf{L} is a Jordan block of the form

$$\mathbf{L} = \begin{pmatrix} 0 & 1 \\ 0 & 0 \end{pmatrix}.$$

In the first three cases the real part of each of the two eigenvalues is *nonzero* and the fixed point is termed *hyperbolic*. In the last two cases the real parts are zero and the fixed point is termed *nonhyperbolic*.

As an example, let us consider the stability of the fixed point $(0, 0)$ of the system (1.3). The linearized system is written as

$$\frac{dx_1}{dt} = x_2, \quad \frac{dx_2}{dt} = -\mu x_2 - \omega_0^2 x_1. \quad (1.6)$$

The trace and the determinant of the matrix of this system are respectively $-\mu$ and ω_0^2 . The eigenvalues are $s_{\pm} = \frac{1}{2}(-\mu \pm \sqrt{\mu^2 - 4\omega_0^2})$. For $\mu < -2\omega_0$ or $\mu > 2\omega_0$ the discriminant is positive and the eigenvalues are real and of the same sign, that of $-\mu$; the fixed point is a node and determination of the eigenvectors permits the local phase portrait to be sketched. For $-2\omega_0 < \mu < 2\omega_0$ the eigenvalues are complex conjugates of each other, and the fixed point is a focus or a center for $\mu = 0$. In the end, $(0, 0)$ is attractive (stable) for $\mu > 0$ and repulsive (unstable) for $\mu < 0$. A similar analysis can be performed for the other fixed point $(\pi, 0)$, for which the trace and the determinant of the matrix \mathbf{L} are respectively $-\mu$ and $-\omega_0^2$. The eigenvalues are real and of opposite signs, and so the fixed point is a saddle.

1.2.3 Stability of a nonhyperbolic fixed point

A special situation occurs when all the eigenvalues have negative real part except for one (or several) which have *zero* real part. The fixed point is then *nonhyperbolic*, and we can learn nothing about its stability from the linear stability analysis. Its stability is therefore determined by the nonlinear terms, whose effect can be stabilizing or destabilizing. Let us take as an example the oscillator described by the system (1.3) in the nondissipative case ($\mu = 0$) with an additional force $\beta(d\theta/dt)^3$. The system linearized about the fixed point $(0, 0)$ possesses two purely imaginary eigenvalues $\pm i\omega_0$, and so the linear stability analysis tells us nothing. However, in this particular case it can be shown simply, without linearization, that the fixed point is stable for $\beta > 0$ and unstable for $\beta < 0$. We multiply the first equation in (1.3) by x_1 and the second by x_2 and then add them. Introducing the distance to the fixed point $r = \sqrt{x_1^2 + x_2^2}$, we obtain

$$r \frac{dr}{dt} = -\beta x_2^4. \quad (1.7)$$

The distance r therefore varies monotonically with time, decreasing for $\beta > 0$ and increasing for $\beta < 0$, thus proving the result.

1.3 Bifurcations

1.3.1 Definition

The behavior of a physical system depends in general on a certain number of parameters, for example, the damping constant μ of the oscillator (1.3). An important question is the following: how does the system behave when one of these parameters is varied? The answer is that nothing much happens except when the parameter passes through certain values where the qualitative behavior of the system changes. Let us take the oscillator (1.3) as an example. As μ varies without changing sign, the oscillator remains unstable when μ is negative, and stable when μ is positive. However, when μ passes through the critical value $\mu_c = 0$, the stability of the equilibrium position changes. It is said that the oscillator undergoes a *bifurcation* at $\mu = \mu_c$. The general definition of a bifurcation of a fixed point is the following.

Definition 1.1 Let a dynamical system depend on a parameter μ and possess a fixed point $\mathbf{a}(\mu)$. This system undergoes a *bifurcation* of the fixed point for $\mu = \mu_c$ if for this value of the parameter the system linearized at the fixed point \mathbf{a} admits an eigenvalue with zero real part, i.e., if the fixed point is nonhyperbolic.

The rest of this section is devoted to the study of three important bifurcations.

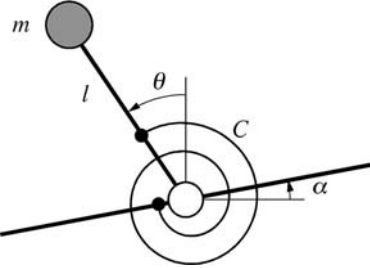


Figure 1.3 Schematic representation of the oscillator described by (1.10).

1.3.2 Saddle-node bifurcation

Let us consider the mechanical system represented in Figure 1.3. An arm of length l is attached to a pivot at its lower end and holds a mass m at its other end; its angular position is given by the angle θ . One end of a helical torsion spring with spring constant C is attached to the arm, while the other end of the spring is attached to a plane inclined at an angle α with respect to the horizontal. The spring tends to restore the arm to the direction perpendicular to the attached plane. We also include a moment of viscous friction $-mgl\tau^*\frac{d\theta}{dt}$ about the pivot, where τ^* is a relaxation time.

Denoting the mass, length, and time scales as m , l , and $\sqrt{l/g}$, the oscillator potential energy in the gravitational field can be written as

$$V(\omega^2, \alpha, \theta) = \frac{\omega^2}{2}(\theta - \alpha)^2 + \cos \theta - 1, \quad (1.8)$$

where the characteristic frequency ω is defined as

$$\omega^2 = \frac{C}{mgl}. \quad (1.9)$$

In terms of these scales the friction moment takes the form $-\tau \frac{d\theta}{dt}$, where $\tau = \tau^*/\sqrt{l/g}$ is the dimensionless relaxation time. The equation of motion is then

$$\frac{d^2\theta}{dt^2} + \tau \frac{d\theta}{dt} = -\frac{\partial V}{\partial \theta}. \quad (1.10)$$

This equation can be rewritten as a dynamical system of two ODEs in the phase space $(\theta, d\theta/dt)$. The fixed points (equilibrium states) are defined by $d\theta/dt = 0$, and θ is the root of the equation for the potential extrema:

$$0 = \frac{\partial V}{\partial \theta} = \omega^2(\theta - \alpha) - \sin \theta. \quad (1.11)$$

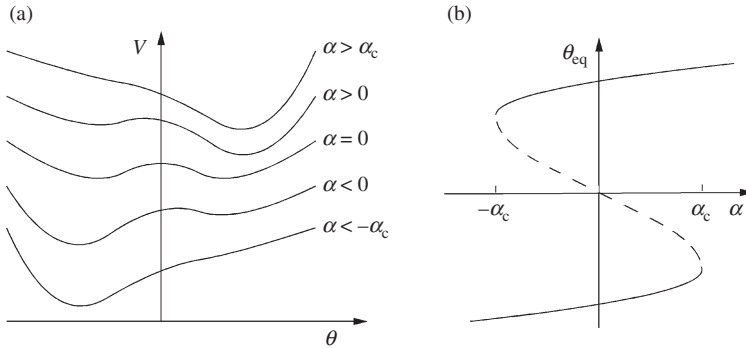


Figure 1.4 (a) The potential $V(\theta)$ for various inclinations α (the relative vertical positions of the various curves are arbitrary). (b) The bifurcation diagram: (—) stable states, (- -) unstable states.

The dependence of the equilibrium states on the two parameters ω^2 and α can be determined graphically or, for $|\alpha|$ small and ω^2 near unity, by a Taylor series expansion about $\theta = 0$. For $\alpha = 0$ the potentials at the equilibrium points θ_- and θ_+ are the same (Figure 1.4a). For $|\alpha|$ small and $\omega^2 < 1$ the system possesses an unstable equilibrium state θ_0 near $\theta = 0$ (the corresponding fixed point is a saddle) and two stable equilibrium states on either side, $\theta_- < 0$ and $\theta_+ > 0$ (whose corresponding fixed points are nodes). For $\alpha < 0$ the state $\theta_- < 0$ has the lowest potential and is therefore the most stable state, while the state $\theta_+ > 0$ is only metastable. The situation is reversed for $\alpha > 0$.

Let us consider the system in the state θ_- with α positive and small (Figure 1.4b). As α increases, the metastable equilibrium state θ_- and the unstable equilibrium state θ_0 approach each other, and there exists a critical inclination α_c for which the two equilibrium states merge. For $\alpha > \alpha_c$, the system jumps to the stable branch θ_+ . For $\alpha = \alpha_c$, the phase portrait of the system therefore undergoes a qualitative change when the stable node $(\theta_-, 0)$ and the unstable saddle $(\theta_0, 0)$ coalesce. This qualitative change corresponds to a bifurcation: for $\alpha = \alpha_c$, an eigenvalue of the system linearized about each of the fixed points $(\theta_0, 0)$ and $(\theta_-, 0)$ crosses the imaginary axis (the proof is left as an exercise). The corresponding bifurcation is called a *saddle-node bifurcation*. A similar bifurcation occurs for decreasing α when α reaches the value $-\alpha_c$. Figure 1.4b, which shows the fixed points as a function of the parameter α , is called the *bifurcation diagram*. At each bifurcation the system jumps from one branch to another, and the critical value of the bifurcation parameter α is different depending on whether it is increasing or decreasing: the system displays hysteresis.

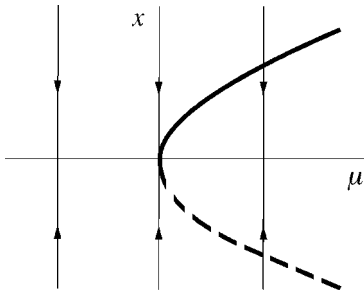


Figure 1.5 The saddle-node bifurcation diagram: (—) stable states, (---) unstable states.

This example² displays a bifurcation corresponding to the coalescence of two fixed points, called a saddle-node bifurcation. The general definition of such a bifurcation is the following.

Definition 1.2 A dynamical system possessing a stable fixed point \mathbf{a} undergoes a *saddle-node bifurcation* at $\mu = \mu_c$ if a real eigenvalue of the system linearized about \mathbf{a} crosses the imaginary axis for $\mu = \mu_c$. For μ in the neighborhood of μ_c , the behavior of the system is then governed, maybe after an appropriate change of variables, by the following equation, called the normal form of a saddle-node bifurcation:

$$\frac{dx}{dt} = \mu - x^2. \quad (1.12)$$

Figure 1.5 shows the corresponding bifurcation diagram.

1.3.3 Pitchfork bifurcation

Let us return to the oscillator of Figure 1.3, and now consider what happens when we allow ω^2 to vary for fixed $\alpha = 0$. As ω^2 increases, the potential barrier between the two minima flattens, and the three equilibrium points coalesce for $\omega_{c0}^2 = 1$ (Figure 1.6a). For $\omega^2 > \omega_{c0}^2$, only the stable equilibrium state $\theta = 0$ exists. This qualitative change of the phase portrait again corresponds to a bifurcation: for $\omega^2 = \omega_{c0}^2$, an eigenvalue of the system linearized about $(0, 0)$ crosses the imaginary axis (the proof is left as an exercise). The corresponding bifurcation is called a *supercritical pitchfork bifurcation* and the bifurcation diagram is shown in Figure 1.6b. The term supercritical means that in passing through the bifurcation a *stable* branch of equilibrium positions varies continuously, without any discontinuity.

² An extension of the analysis to the case of a chain of coupled oscillators can be found in Charru (1997).

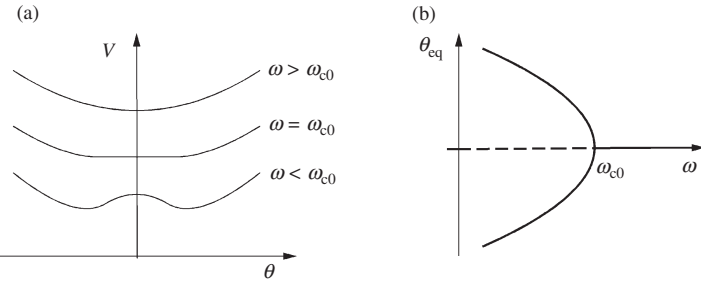


Figure 1.6 (a) The potential for various ω and $\alpha=0$ (the relative vertical positions of the various curves are arbitrary). (b) Bifurcation diagram: (—) stable states, (---) unstable states.

The existence of the pitchfork bifurcation displayed in this example is related in a crucial way to the symmetry of the problem about $\theta=0$, i.e., to the invariance of the equation for the transformation of θ into $-\theta$, which is referred to as reflection invariance. A pitchfork bifurcation is defined more generally as follows.

Definition 1.3 A dynamical system which is invariant under reflection, i.e., invariant under the transformation $x \rightarrow -x$ (associated with a symmetry of the physical system), and which possesses a stable fixed point \mathbf{a} undergoes a *pitchfork bifurcation* at $\mu = \mu_c$ if a real eigenvalue of the system linearized about \mathbf{a} crosses the imaginary axis for $\mu = \mu_c$. For μ in the neighborhood of μ_c , the behavior of the system is then governed, perhaps after an appropriate change of variables, by the following equation, called the normal form of a pitchfork bifurcation:

$$\frac{dx}{dt} = \mu x - \delta x^3, \quad \delta = \pm 1. \quad (1.13)$$

The case $\delta = 1$ is termed *supercritical* and the case $\delta = -1$ is termed *subcritical*.

Figure 1.7 shows the corresponding bifurcation diagrams. In the supercritical case the equilibrium state $x = 0$ is stable for $\mu < 0$ and unstable for $\mu > 0$; in the latter case any perturbation of this equilibrium state makes the system jump to one of the stable branches $\pm\sqrt{\mu}$. In the subcritical case and for $\mu < 0$, $x = 0$ is always stable with respect to infinitesimal amplitude perturbations, but an amplitude perturbation larger than $\pm\sqrt{-\mu}$, i.e., a *perturbation of finite amplitude*, can destabilize it: for $\mu > 0$, any perturbation of the state $x = 0$ causes the system to jump discontinuously to a state that the normal form (1.13) is incapable of describing; higher-order terms (of degree five or higher) must be taken into account.

What happens in a system when the reflection symmetry $x \rightarrow -x$ is broken by an imperfection? We return to the oscillator of Figure 1.3 but now for small, nonzero angle α , which breaks the $\theta \rightarrow -\theta$ invariance, and we consider the effect

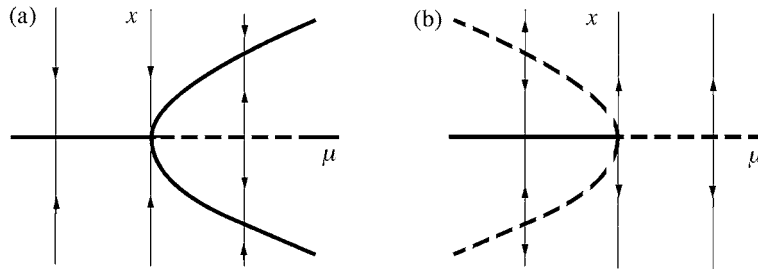


Figure 1.7 Pitchfork bifurcation diagrams: (a) supercritical ($\delta = +1$), (b) subcritical ($\delta = -1$); (—) stable states, (---) unstable states.

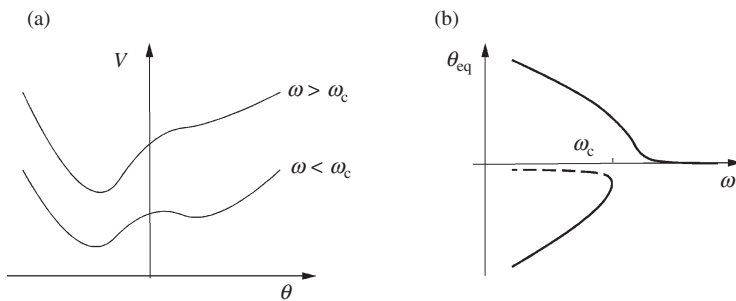


Figure 1.8 (a) The potential for $\omega < \omega_c$ and $\omega > \omega_c$, for $\alpha \neq 0$. (b) Bifurcation diagram: (—) stable states, (---) unstable states. A saddle-node bifurcation survives for $\omega = \omega_c$.

of varying ω . For ω small there are still two stable equilibria on either side of an unstable equilibrium, but the positions of stable equilibria are no longer symmetric about $\theta = 0$, and the position of the unstable equilibrium is no longer located at $\theta = 0$ (Figure 1.8a). As α increases, the two stable branches approach each other as for $\alpha = 0$, but they do not coalesce: the lower branch merges with the unstable branch for $\omega_c^2(\alpha) < \omega_{c0}^2$ (Figure 1.8b), and we again arrive at a saddle-node bifurcation. This example shows that the pitchfork bifurcation is a special case corresponding to a system which is invariant under the change of variable $\theta \rightarrow -\theta$, i.e., a system which possesses symmetry under reflection. The breaking of this symmetry causes pitchfork bifurcation to be replaced by saddle-node bifurcation. The latter is termed *generic*, as it is robust with respect to additional terms in (1.13) describing imperfections of the physical system in question.

Another type of perturbation of a pitchfork bifurcation can occur; its bifurcation diagram is shown in Figure 1.9. This other type of symmetry breaking, which has the effect of moving the parabolic branches off-center, restores the saddle-node bifurcation for $\mu < 0$, but another bifurcation survives at $\mu = 0$. This other type of

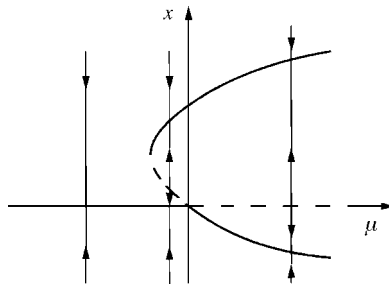


Figure 1.9 Transcritical bifurcation generated by breaking the symmetry of a pitchfork bifurcation: (—) stable states, (--) unstable states.

bifurcation, termed *transcritical*, corresponds to exchange of the stability of two branches of fixed points. An illustration is given in Chapter 11.

1.3.4 Hopf bifurcation

We have just seen that a saddle-node bifurcation for $\mu = \mu_c$ corresponds to a *real* eigenvalue s crossing the imaginary axis: $s(\mu_c) = 0$. A Hopf bifurcation (Hopf, 1942) corresponds to the crossing of the imaginary axis by a pair of *complex conjugate* eigenvalues $s = \sigma \pm i\omega$, with $\sigma(\mu_c) = 0$. For example, the oscillator (1.3) undergoes a Hopf bifurcation for $\mu = 0$, as seen from the eigenvalues of the linearized system (1.6). A Hopf bifurcation is often manifested by the appearance of oscillatory behavior corresponding to a *limit cycle* in phase space. In polar coordinates the normal form of this bifurcation is

$$\frac{dr}{dt} = \mu r - \delta r^3, \quad \delta = \pm 1, \quad (1.14)$$

$$\frac{d\phi}{dt} = \omega. \quad (1.15)$$

The case $\delta = 1$ is termed supercritical, and the case $\delta = -1$ subcritical. Figure 1.10 shows the diagram corresponding to the first case. This type of bifurcation will be studied in more detail in Chapter 8.

1.4 Examples from hydrodynamics

1.4.1 Stability of a soap film

Imagine that we dip two rings of radius a in soapy water and then remove them, resulting in the formation of a soap film between the rings (Figure 1.11). When we increase the distance $2d$ between the rings the film breaks and vanishes when $d/a \approx 0.66$ (Taylor and Michael, 1973). Why does the film break?

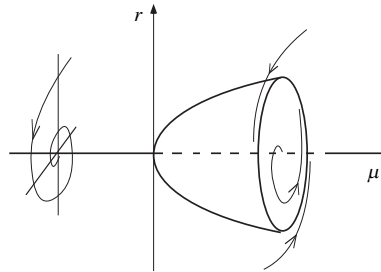


Figure 1.10 Diagram of supercritical Hopf bifurcation.

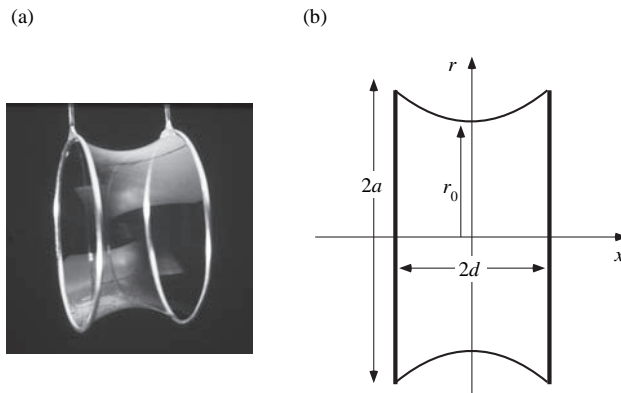


Figure 1.11 (a) Soap film between two circular rings, © Palais de la découverte; (b) diameter section of the catenoid.

Equilibrium shapes

The shape of the interface is determined by the Laplace–Young law (1805), according to which the difference of the pressures on the two sides of an interface is equal to the product of the surface tension γ and the film curvature (Guyon *et al.*, 2001):

$$P_2 - P_1 = \gamma \left(\frac{1}{R'} + \frac{1}{R''} \right), \quad (1.16)$$

where R' and R'' are the radii of curvature in two perpendicular planes (the sum of the curvatures $1/R'$ and $1/R''$ is an invariant independent of the particular choice of these planes).

In the case of a soap film the pressures on the two sides are equal, and so the curvature must vanish at all points. The surface which satisfies this condition is a catenoid, which is expressed in cylindrical coordinates (r, x) as

$$\frac{r}{r_0} = \cosh \frac{x}{r_0}, \quad (1.17)$$

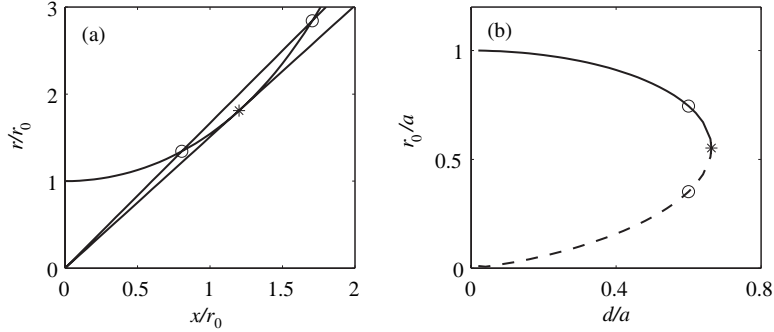


Figure 1.12 (a) (\circ) solutions d/r_0 satisfying (1.18) for $d/a = 0.6$, $(*)$ the same for $d/a = 0.6627$ (the critical point); (b) saddle-node bifurcation diagram showing the stable (—) and unstable (--) branches. Note the similarity between this diagram and that of the normal form (Figure 1.5).

where r_0 is the radius of the catenoid at the saddle (Figure 1.11b). This radius is defined by the catenoid-matching condition on the two circular rings, which is written as

$$\frac{a}{r_0} = \cosh \frac{d}{r_0}, \quad \text{or} \quad \frac{a}{d} \frac{d}{r_0} = \cosh \frac{d}{r_0}. \quad (1.18)$$

The last expression allows d/r_0 to be determined graphically for a given a/d as the intersection of the straight line of slope a/d and the hyperbolic cosine (Figure 1.12a). We see that there exists a critical value of the slope a/d for which the straight line is tangent to the hyperbolic cosine; this critical value, defined as $d/r_0 = \coth(d/r_0) = 1.200$, corresponds to the ring separation $d = 0.663a$. For $d/a < 0.663$ there exist two solutions for d/r_0 located on either side of the critical value 1.200. For $d/a > 0.663$ there is no solution, and so the soap film cannot exist. The existence condition $d/a < 0.663$ is well verified experimentally, but only a single catenoid corresponding to the largest radius r_0 has been observed. Why isn't the other one ever seen?

Stability of the catenoids

Let us now study the stability of these two catenoids by finding how the restoring force exerted by the film on the rings varies as their separation is varied by an amount δd (Taylor and Michael, 1973). This force can be calculated by projecting the tension exerted by the film on the ring onto the axis of revolution:

$$F = 4\pi a\gamma / \cosh(d/r_0).$$

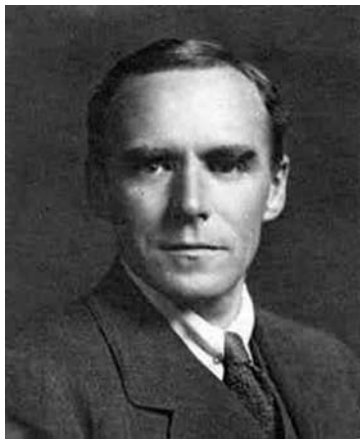
For a distance variation δd the variation δF of the force is $\delta F = F'(d)\delta d$, where F' is the derivative of F with respect to d . If $F'(d) < 0$, δF is a restoring force and

the film is stable, while in the opposite case the film is unstable. Using (1.18) and differentiating to calculate $r'_0(d)$, we find

$$F'(d) = \frac{4\pi\gamma}{d/r_0 - \coth(d/r_0)}. \quad (1.19)$$

$F'(d)$ is therefore negative for the smaller of the two solutions d/r_0 of (1.18), and the film of larger radius r_0 is stable. The other solution of (1.18) corresponds to an unstable film.³ Figure 1.12b shows the variation of the radius at the saddle, r_0/a , with distance d/a for the two solutions. We see that the critical value corresponds to coalescence of the stable and unstable branches, and therefore to a saddle-node bifurcation.

Geoffrey Ingram Taylor (1886–1975)



G. I. Taylor was born in London, England, where his father was a painter and interior decorator of ocean liners, and his mother a daughter of George Boole (of Boolean algebra). As a child, he displayed a precocious interest in science and met William Thomson (Lord Kelvin). He studied at Trinity College, Cambridge. His earliest research work included a theoretical study of shock waves (for which he won the Smith Prize) and an experimental study inspired by J. J. Thomson to test quantum theory. After appointment to the post of Reader in Dynamical Meteorology at Trinity College, he worked on turbulence. After the sinking of the *Titanic* in 1912 he worked as meteorologist on the ship the *Scotia* assigned to iceberg surveillance in the North Atlantic, where his measurements of temperature,

³ The more complete stability calculation of Taylor and Michael (1973) uses the calculus of variations. The shorter calculation presented here does not require calculation of the second derivative of the area of the catenoid

$$A = 2\pi r_0^2 \left(\frac{d}{r_0} + \frac{1}{2} \sinh \frac{2d}{r_0} \right).$$

We note that the force variation δF can also be written as $\delta F = -E_p''(d)\delta d$, where $E_p = \gamma A$ is the potential energy of the film (the free energy). The stability condition is therefore just the condition of convexity of the potential energy ($E_p''(d) > 0$). Finally, it should be observed that the equilibrium does not correspond to an extremum of the film energy with respect to variations of d : $E_p'(d) = -F \neq 0$ (see the exercise in Section 1.6.6 below).

pressure, and humidity helped him develop a model of turbulent mixing of air. During World War I he participated in the design and operation of airplanes at the Royal Aircraft Factory at Farnborough, where he studied the stress on propellor shafts and learned to fly airplanes and make parachute jumps. After returning to Trinity College he worked on turbulent flow as applied to oceanography and on the problem of bodies passing through a rotating fluid. In 1923 he was appointed Research Professor by the Royal Society of London, which allowed him to give up teaching. (*He was not a natural lecturer and not much interested in teaching...* wrote G. K. Batchelor.^a) He carried out many important studies, in particular on the deformation of crystalline materials, and introduced a new statistical approach to velocity fluctuations in turbulence. Batchelor again: *His investigations in the mechanics of fluids and solids covered an extraordinary wide range, and most of them exhibited the originality and insight for which he was now becoming famous... The nature of his thinking was like that of Stokes, Kelvin and Rayleigh, although he got more from experiments than any one of these three.* During World War II he worked on the propagation of blast waves and continued his research at Cambridge until 1972, twenty years after his retirement. His name is associated with several concepts in turbulence and hydrodynamical phenomena, as well as three fundamental instabilities: Couette–Taylor, Rayleigh–Taylor, and Saffman–Taylor. He was elected a Fellow of the Royal Society in 1919, and awarded the Royal Medal (1933), the Copley Medal (1944), and more than twenty other prizes. He was knighted and appointed to the Order of Merit, and elected to membership in academic societies in many countries, including the USSR and the USA. He published over 250 papers in applied mathematics, mathematical physics, and mechanical and chemical engineering. He was keenly interested in botany, traveling, and sailing, and made numerous voyages with his wife in their boat.^b

^a G. K. Batchelor (1976), *Geoffrey Ingram Taylor*, Biographical Memoirs of Fellows of the Royal Society of London **22**, 565–633.

^b This biographical note, like others in this book, has been adapted from the excellent site *The MacTutor History of Mathematics* of J.J. O’Connor and E.F. Robertson, St. Andrews University, Scotland: <http://www-history.mcs.st-andrews.ac.uk/>. The photograph also comes from this site. For a historical perspective, see also Darrigol (2005).

1.4.2 Stability of a bubble

Let us consider a bubble of radius r in a liquid at pressure p and temperature T (Figure 1.13). The bubble contains a mixture of vapor of the liquid and an incondensable gas (air, for example). How do the radius and stability of the bubble vary as the pressure or temperature of the surrounding liquid varies?

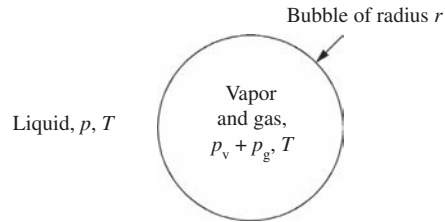


Figure 1.13 A bubble of vapor and incondensable gas in a liquid.

Equilibrium radii

Assuming that the mixture is ideal, the pressure in the bubble is the sum of the pressure p_g of the incondensable gas and the pressure $p_v(T)$ of the vapor in equilibrium with the liquid (the saturation vapor pressure).⁴ The Laplace–Young law and the isothermal evolution of the gas (assumed perfect) give the relation between the pressure and the radius:

$$p(r) = p_v(T) + p_g - \frac{2\gamma}{r}, \quad p_g = p_{g0} \frac{r_0^3}{r^3}, \quad (1.20)$$

where the subscript 0 denotes a reference state of the bubble. For r sufficiently small the $1/r^3$ term dominates and the pressure $p(r)$ decreases with r . For r sufficiently large it is the other term, proportional to $-1/r$, that dominates, and the pressure $p(r)$ is an increasing function of r . The curve $p = p(r)$ therefore has a minimum corresponding to a radius r_c and pressure p_c in the liquid given by

$$r_c = \left(\frac{3p_{g0}r_0^3}{2\gamma} \right)^{1/2}, \quad p_c = p_v - \frac{4\gamma}{3r_c}.$$

Choosing r_c and γ/r_c as the length and pressure scales, the relation between pressure and radius becomes

$$\frac{p - p_v(T)}{\gamma/r_c} = \frac{2}{3} \left(\frac{r_c}{r} \right)^3 - 2 \frac{r_c}{r},$$

as illustrated in Figure 1.14. We note that for $r/r_c > 0.6$ the pressure p is lower than the saturation pressure $p_v(T)$ (and possibly negative), and from the viewpoint of thermodynamics the liquid is in metastable equilibrium.

⁴ Here we ignore the shift of the liquid–vapor equilibrium curve $p_v(T)$ induced by the surface tension, which is important only for bubbles less than a micron in diameter.

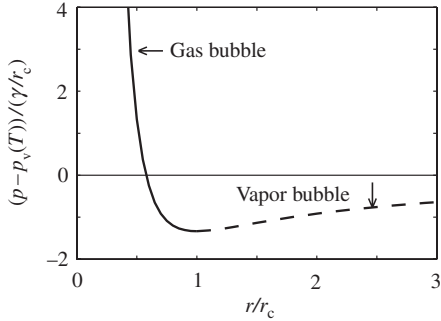


Figure 1.14 Variation of the pressure $(p - p_v(T)) / (\gamma/r_c)$ with the equilibrium radius r/r_c of a bubble; (—) stable bubbles of incondensable gas, (- -) unstable bubbles of vapor. The minimum corresponds to a saddle-node bifurcation.

Stability from the mechanical point of view

The stability of the equilibrium states can be studied by evaluating the net force acting on a half-bubble perturbed from its equilibrium radius r . A perturbation δr of this radius is associated with a perturbation δp_g of the pressure $p_g + p_v(T)$ of the bubble (the saturation vapor pressure p_v depends only on temperature and therefore is not changed in a slow perturbation). The net force on the half-bubble directed toward the outside is then

$$((p_v(T) + p_g + \delta p_g) - p) \pi(r + \delta r)^2 - \gamma 2\pi(r + \delta r).$$

Linearizing about the equilibrium radius, this becomes

$$2\pi\gamma\delta r + \pi r^2\delta p_g. \quad (1.21)$$

For $r \ll r_c$ the pressure inside the bubble is dominated by the pressure p_g , as the vapor pressure is negligible. The bubble behaves like a bubble of incondensable gas for which the pressure varies with radius as $\delta p_g/p_g + 3\delta r/r = 0$ for isothermal evolution. The linearized net force then becomes

$$(2\pi\gamma - 3\pi r p_g)\delta r = -(2p_g + p)\pi r\delta r.$$

This force, of opposite sign to δr , is therefore a restoring force and the bubble is *stable* (the same result is obtained in the case of isentropic evolution).

For $r \gg r_c$ the pressure inside the bubble is now dominated by the vapor pressure p_v and the gas pressure is negligible. This bubble behaves like a vapor bubble whose pressure is determined by the temperature. The net force (1.21) acting on

a half-bubble then reduces to the term $2\pi\gamma\delta r$. This force, which has the same sign as δr , therefore tends to amplify the initial perturbation, and so the bubble is *unstable*.

Stability from the thermodynamic point of view

From the thermodynamic point of view, the first thing to note is that the slope of the curve $p(r)$ is related to the isothermal compressibility of the bubble as

$$\kappa_T = -\frac{1}{V} \frac{\partial V}{\partial p} = -3 \frac{1}{r} \frac{\partial r}{\partial p}.$$

This compressibility is positive on the decreasing branch of Figure 1.14, diverges at the minimum, and then is negative on the growing branch. According to a general result of thermodynamic stability (Callen, 1985), the decreasing branch corresponds to stable equilibrium states and the increasing branch to unstable ones. We therefore recover the result of the mechanical analysis performed above.

The general result of thermodynamic stability for the sign of the compressibility follows from the second law of thermodynamics regarding the increase of the entropy of an isolated system. This result can be rederived for the particular case studied here by considering not the entropy (the bubble is not an isolated system), but rather the free energy F of the system consisting of the bubble and a thin liquid film of condensed vapor.⁵ Let us consider the simple case of a vapor bubble. This bubble is in contact with a heat bath which determines its temperature (but not its pressure, owing to the surface tension). Under a variation dV of its volume, the variation dF of its free energy is then equal to the work $\delta W_{\text{rev}} = -pdV$ done by the external forces. We therefore find $d(F + pV) = 0$, i.e., the function $F + pV$ is an extremum. This function can be expressed as a function of the bubble radius as

$$F + pV = -p_v V + \gamma A + F_0 + pV = -(p_v - p) \frac{4\pi r^3}{3} + \gamma 4\pi r^2 + F_0,$$

where A is the bubble area and F_0 is a reference free energy which involves the chemical potential but not the bubble radius. The equilibrium condition

$$\frac{\partial(F + pV)}{\partial r} = 0$$

⁵ Consideration of the film of condensed vapor makes it possible to assume that the bubble has constant mass. We could also use the fact that the liquid imposes a chemical potential μ and then work with the grand potential $\Omega = F - \mu N$.

again gives the Laplace–Young law. The bubble potential $F + pV$ then grows as r^2 for radii smaller than the equilibrium radius, and as $-r^3$ for radii larger than it. The potential extremum is a maximum, and so the equilibrium of the vapor bubble is unstable.

In conclusion, the minimum of the curve $p(r)$ in Figure 1.14 corresponds to the merging of two branches of equilibrium states, one stable and the other unstable. This minimum therefore corresponds to a saddle–node bifurcation.

A numerical illustration

As a numerical illustration, let us consider a bubble of radius $r_0 = 1 \mu\text{m}$ in water at atmospheric pressure $p_0 = 101.3 \text{ kPa}$ and temperature $T_0 = 20^\circ\text{C}$. At this temperature the saturation vapor pressure is $p_v(T_0) = 2.3 \text{ kPa}$, and for $\gamma = 0.070 \text{ N/m}$ the pressure of the gas inside the bubble is $p_{g0} = 239 \text{ kPa}$. The minimum of the curve $p(r)$ corresponds to $r_c = 2.3 \mu\text{m}$ and $p_c = -38.9 \text{ kPa}$. The radius r_0 is therefore smaller than r_c and the bubble is stable. Let us see how this equilibrium is affected by variation of the pressure or temperature.

- When the pressure is decreased at constant temperature, the bubble becomes unstable when the liquid pressure reaches the value $p_c = -38.9 \text{ kPa}$, where the negative pressure corresponds to a metastable state. If a larger bubble is present in the water, i.e., a bubble of radius r_0 initially larger than $1 \mu\text{m}$, it will become unstable for a liquid pressure either less negative or positive, but always less than the saturation pressure $p_v(T_0)$ owing to the surface tension.
- When the temperature is raised at constant pressure p_0 , the bubble becomes unstable when the saturation vapor pressure reaches $p_v(T) = p_c + 4\gamma/3r_c = 142 \text{ kPa}$ with $p_c = p_0$, or $T = 110^\circ\text{C}$. This temperature (which is slightly changed when the temperature dependence of γ is taken into account) is clearly higher than the equilibrium temperature $T = 100^\circ\text{C}$ of a planar interface. A bubble initially larger ($r_0 > 1 \mu\text{m}$) would become unstable at a temperature below 110°C (but always higher than 100°C owing to the surface tension).

1.4.3 Stability of a colloidal suspension

Many fluids which appear homogeneous to the naked eye actually contain micron-sized particles suspended in a liquid; such fluids are called colloids or colloidal suspensions. Some examples are mud (clay particles in water), inks, paint (white zinc oxide particles in water, for example), fruit juices, and emulsions (water droplets in oil or the opposite, such as milk). These suspensions are in general unstable: the particles tend to regroup themselves to form aggregates called flocs,

and small droplets coalesce to form larger ones. This instability originates in the attractive van der Waals forces between the particles. The range of these forces is very small, on the order of a micron, but thermal agitation or motion of the liquid can make the particles approach each other to distances small enough that these forces become dominant and cause the particles to stick together. Colloids can be stabilized by introducing additives such as polymer molecules or surfactants. Conversely, flocculation can be encouraged, as is done, for example, in water treatment plants to separate particles from the liquid.

Here we shall consider the effect of a dissolved salt on the stability of a suspension, a phenomenon originally studied by Faraday (1791–1867). Faraday observed that a colloid of gold, prepared by rubbing together two gold electrodes immersed in water and connected to an electric battery, is stable.⁶ Even though they are subject to van der Waals attraction, the particles in this colloid remain separated. The reason is that the gold particles spontaneously carry negative charges on their surfaces which keep the particles far apart owing to electrostatic repulsion (Figure 1.15a). Faraday attempted to confirm this explanation by dissolving sodium chloride in the water. The color of the colloid changed from red to blue: the suspension had become unstable and the particles had formed aggregates. Why had this happened? The sodium chloride had dissolved, and the Na^+ ions, attracted by the negatively charged gold particles, stuck to them, thus screening the electrostatic interaction created by these charges (Figure 1.15b). The repulsive force thereby being neutralized, the van der Waals force became dominant, and the suspension flocculated.

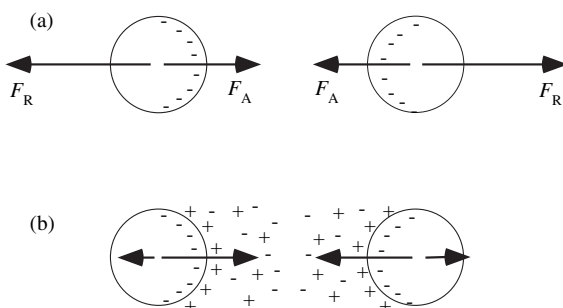


Figure 1.15 Forces between two charged spheres: (a) electrostatic repulsion dominates van der Waals attraction and the suspension is stable; (b) the positive ions of a dissolved salt screen the electrostatic force and the attractive force dominates, making the suspension unstable.

⁶ Our description of the experiment follows that of de Gennes and Badoz (1994).

A variation of the Faraday experiment is to observe the effect of adding salt to a suspension of clay particles in water. Like gold particles, clay particles carry negative charge on their surface and the suspension is stable. The particles are heavier than water and gradually undergo sedimentation. The addition of salt makes the suspension unstable and causes the particles to flocculate. The sedimentation rate varies as the square of the particle size (Guyon *et al.*, 2001), and this instability is manifested as a marked increase in the sedimentation rate of the particles. Try the experiment yourself!

Let us now perform a more quantitative analysis. For two spheres of radius a whose surfaces are separated by a distance $d \ll a$, calculation of the van der Waals attractive interaction potential V_A gives

$$V_A = -\frac{Aa}{12d}, \quad (1.22)$$

where $A = 10^{-19}$ J is a typical value for the Hamaker constant (Probstein, 2003). The repulsive electrostatic potential V_R generated by the double layer of negative and positive charges decreases very rapidly – exponentially – with distance. In the vicinity of a particle, i.e., up to a distance of the order of the particle radius, this potential is given by

$$V_R = 2\pi a \epsilon \phi_w^2 e^{-d/\lambda_D}, \quad \lambda_D = \left(\frac{\epsilon k_B T}{2z^2 e^2 N_A C} \right)^{1/2}, \quad (1.23)$$

where ϕ_w is the potential at the particle surface and λ_D is the Debye wavelength, which corresponds to the range of the electrostatic force of the double layer.⁷ This range is smaller the larger the ion concentration C ; for an aqueous solution of monovalent ions it is about 1 nm for a concentration of 10^2 mol·m⁻³ and 10 nm for one of 1 mol·m⁻³.

Figure 1.16 shows the shape of the attractive and repulsive potentials V_A and V_R for three different concentrations, along with the net potential $V_A + V_R$ in the three cases. We see that the potential barrier keeping the particles separate decreases as the concentration increases. The critical concentration above which the suspension is unstable corresponds to the vanishing of the barrier when the maximum and minimum coalesce (the minimum, which lies to the right of the maximum, is very flat). In terms of dynamical systems, this fusion of two

⁷ ϵ is the electrical permittivity of the electrolyte (7.1×10^{10} C V⁻¹ m⁻¹ for water), $k_B = 1.38 \times 10^{-23}$ J K⁻¹ is the Boltzmann constant, z is the valence of the ions (1 for Na⁺ and Cl⁻), $e = 1.60 \times 10^{-19}$ C is the elementary electric charge, and $N_A = 6.02 \times 10^{23}$ mol⁻¹ is Avogadro's number.

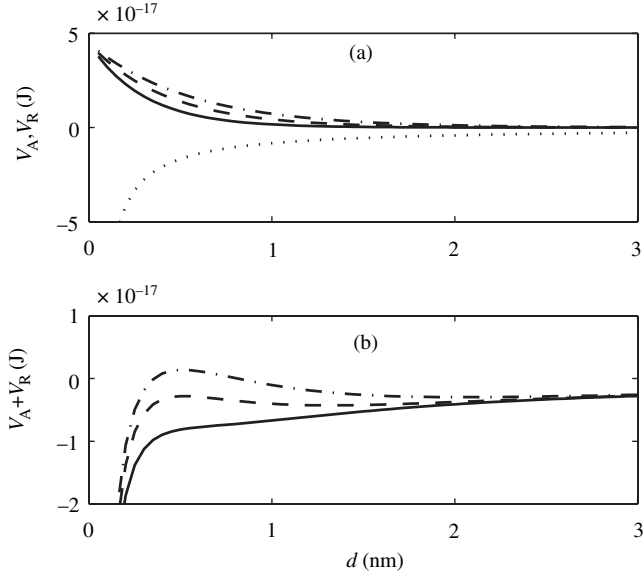


Figure 1.16 (a) Negative van der Waals potential V_A (...) and positive electrostatic potential V_R for monovalent ions of concentration $C = 300 \text{ mol}\cdot\text{m}^{-3}$ (− · −), $C = 500 \text{ mol}\cdot\text{m}^{-3}$ (− −), and $C = 1000 \text{ mol}\cdot\text{m}^{-3}$ (—); $\phi_w = 0.1 \text{ V}$. (b) Resultant potential $V_A + V_R$; at the highest concentration the potential barrier has vanished.

equilibrium states, one stable and the other unstable, corresponds to a saddle–node bifurcation.

1.4.4 Convection in a ring

Thermal convection can be modeled very schematically by a system of three ODEs, as shown by Lorenz (1963). This system displays a pitchfork bifurcation, which represents a transition between the regime of the fluid at rest, where thermal transfer occurs via diffusion, and the regime of convection cells. This system can be obtained in the following simple way (Welander, 1967). We consider a toroidal ring of radius a filled with a fluid of density ρ (Figure 1.17) which is immersed in a vertical temperature gradient:

$$\bar{T} = T_0 - T_1 \frac{z}{a} = T_0 + T_1 \cos \phi. \quad (1.24)$$

We are interested in the stationary states of the fluid in the interior of the ring and their stability.

Let $U(t, \phi)$ be the average speed of the fluid in a cross-section of the ring and $T(t, \phi)$ be the average temperature. The equation for momentum conservation

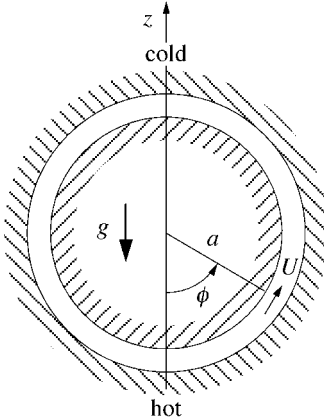


Figure 1.17 A ring of fluid immersed in a vertical temperature gradient.

integrated over the cross-section of the ring is then written as

$$\frac{\partial U}{\partial t} = -\frac{1}{\rho a} \frac{\partial p}{\partial \phi} + \alpha g(T - \bar{T}) \sin \phi - \gamma U. \quad (1.25)$$

This equation is obtained using the Boussinesq approximation, i.e., neglecting density variations except in the gravity term. The advective acceleration does not enter into the problem because incompressibility imposes the condition $\partial_\phi U = 0$. The pressure p here is the departure from the hydrostatic distribution $\bar{p}(z)$, the solution of the equation $0 = \partial_z \bar{p} - \bar{\rho}(z)g$. The next term corresponds to the buoyancy, where the expansion coefficient α enters via the equation of state

$$\frac{d\rho}{\rho} = -\alpha dT + \kappa_T dP,$$

which, neglecting the compressibility κ_T and taking the expansion coefficient to be constant, can be integrated to give

$$\rho - \bar{\rho} = -\alpha \bar{\rho}(T - \bar{T}).$$

The last term in Eq. (1.25) corresponds to viscous damping with coefficient γ , equal to ν/a^2 up to a numerical constant.

We seek a solution for the temperature of the form

$$T(t, \phi) = \bar{T} + T_A(t) \sin \phi - T_B(t) \cos \phi, \quad (1.26)$$

where $T_A(t)$ and $T_B(t)$ are two amplitudes. The pressure can be eliminated from the problem by integrating (1.25) from $\phi = 0$ to $\phi = 2\pi$. We then obtain

$$\frac{dU}{dt} = \frac{\alpha g}{2} T_A - \gamma U. \quad (1.27)$$

This equation shows that the temperature difference $2T_A$ between the left and right branches acts as a destabilizing forcing term.

The equation for energy conservation is written in simplified form as

$$\frac{\partial T}{\partial t} + \frac{U}{a} \frac{\partial T}{\partial \phi} = k(T - \bar{T}). \quad (1.28)$$

The left-hand side represents the material derivative of the temperature, and the right-hand side corresponds to heat transfer to the surroundings. Viscous dissipation is neglected, as is the coefficient affecting the advection term (the average of a nonlinear term is not equal to a product of averages). Taking into account (1.26) and the fact that (1.28) must be satisfied for all ϕ , we obtain the two differential equations governing T_A and T_B :

$$\frac{dT_A}{dt} = -\frac{U}{a}(T_B - T_1) - kT_A, \quad (1.29a)$$

$$\frac{dT_B}{dt} = \frac{U}{a}T_A - kT_B. \quad (1.29b)$$

The differential equations (1.27) and (1.29) form a dynamical system with three degrees of freedom, U , T_A , and T_B , which is nonlinear (the nonlinearities arise from the advection of the temperature by the flow). After a change of scale

$$X = \frac{1}{ka}U, \quad Y = \frac{\alpha g}{2\gamma ka}T_A, \quad Z = \frac{\alpha g}{2\gamma ka}T_B, \quad \tau = kt, \quad (1.30)$$

this system becomes

$$\frac{dX}{d\tau} = -PX + PY, \quad (1.31a)$$

$$\frac{dY}{d\tau} = -Y - XZ + RX, \quad (1.31b)$$

$$\frac{dZ}{d\tau} = -Z + XY, \quad (1.31c)$$

where the parameters P and R , defined as

$$P = \frac{k}{\gamma}, \quad R = \frac{\alpha g T_1}{2\gamma ka},$$

are analogs of the Prandtl and Rayleigh numbers. The system (1.31) is identical to that obtained by Lorenz (1963) for describing atmospheric motions in a simplified manner. His landmark study showed that a system with three degrees of freedom can display disordered, “unpredictable” behavior, and played an important role in understanding deterministic chaos (Lighthill, 1986; Bergé *et al.*, 1987; Schuster and Wolfram, 2005).

The fixed points of the dynamical system (1.31) are $(X, Y, Z) = (0, 0, 0)$, corresponding to the fluid at rest, and, for $r = R - 1$ positive, $(X, Y, Z) = (\pm\sqrt{r}, \pm\sqrt{r}, r)$, corresponding to steady rotation of the fluid in one or the other direction.

Let us study the linear stability of the fixed point corresponding to the fluid at rest. Linearizing (1.31) about $(0, 0, 0)$, we obtain a linear system with a constant-coefficient matrix \mathbf{L} which has solutions of the type $\exp(s\tau)$. The resulting system of equations has a nontrivial solution only if the determinant of $\mathbf{L} - s\mathbf{I}$ vanishes, leading to

$$(s + 1) \left(s^2 + (P + 1)s - rP \right) = 0. \quad (1.32)$$

It is easy to verify that the roots of the second-degree polynomial are real and both negative for $r < 0$ ($R < 1$), or of opposite signs for $r > 0$ ($R > 1$). We therefore conclude that the rest state is stable for $r < 0$ and unstable for $r > 0$.

The stability of the other two branches of fixed points is studied in the same manner. The characteristic polynomial, which is the same for the two branches, is

$$s^3 + (P + 2)s^2 + (P + 1 + r)s + 2rP = 0. \quad (1.33)$$

Near the threshold $r = 0$ of instability of the fluid at rest we can seek solutions in the form of a series in powers of r , $s = s^{(0)} + rs^{(1)} + \dots$, which leads to

$$s_1 = -\frac{2rP}{P + 1} + \mathcal{O}(r^2), \quad (1.34a)$$

$$s_2 = -1 + \mathcal{O}(r), \quad (1.34b)$$

$$s_3 = -(P + 1) + \mathcal{O}(r). \quad (1.34c)$$

These three roots are negative, the branches $(X, Y, Z) = (\pm\sqrt{r}, \pm\sqrt{r}, r)$ are therefore stable, and the bifurcation at $r = 0$ is a supercritical pitchfork bifurcation.

We can go further by noting that the characteristic polynomial (1.33), which has the form $s^3 + As^2 + Bs + C = 0$, has positive real coefficients. A real root can only be negative, and so an instability necessarily corresponds to a complex root $s = s_r + is_i$. The instability threshold of the branches $(X, Y, Z) = (\pm\sqrt{r}, \pm\sqrt{r}, r)$ therefore corresponds to $s_r = 0$. We thereby demonstrate that for $P < 2$ the branches $(X, Y, Z) = (\pm\sqrt{r}, \pm\sqrt{r}, r)$ are stable for all R , and for $P > 2$ they become unstable for $R = P(P + 4)/(P - 2)$ via a Hopf bifurcation (Glendinning, 1994).

1.4.5 Double diffusion of heat and matter

The presence of a concentration gradient of dissolved salt together with a temperature gradient leads to remarkable instability phenomena such as the development of salt fingers. This particular phenomenon, which is illustrated in Figure 1.18, occurs in a fluid with stabilizing (positive) temperature gradient when the salt concentration is higher on the top than on the bottom. Since salt water is denser than fresh water, this distribution of the salt concentration is unstable, thus leading to the observed fingers.

Here we consider the different situation of a *statically stable* mixture of salt and water, i.e., a mixture with a concentration profile $C(z)$ such that the density decreases with height, and investigate the effect of a temperature gradient that can be either positive or negative. The density is given by the equation of state $\rho = \rho(P, T, C)$ which, neglecting compressibility, can be written in differential form as

$$\frac{d\rho}{\rho} = -\alpha dT + \beta dC, \quad (1.35)$$

where $\alpha > 0$ is the thermal expansion coefficient and $\beta > 0$ is an analogous coefficient describing the variation of the density with the salt concentration. Near any reference height z_0 the concentration profile is

$$\bar{C}(z) = C_0 + C'_0(z - z_0),$$

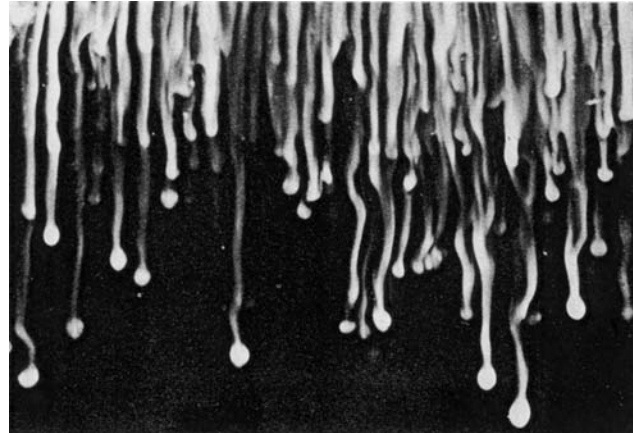


Figure 1.18 Descending fingers of salt water, formed by pouring a salt water solution into fresh water possessing a stabilizing (positive) temperature gradient. The fingers are rendered visible by adding fluorescein to the salt water and illuminating it from below through a slit (Huppert and Turner, 1981).

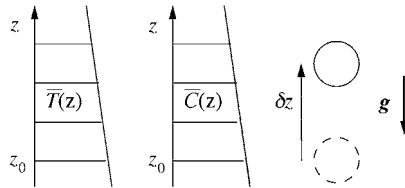


Figure 1.19 A fluid particle displaced in a concentration gradient and a temperature gradient (here both negative).

where C_0 and C'_0 are the concentration and its gradient at height z_0 . A stable stratification, which corresponds to density $\bar{\rho}(z)$ decreasing with height, is achieved for negative C'_0 (since $\beta > 0$). Similarly, the temperature distribution near the reference height is

$$\bar{T}(z) = T_0 + T'_0(z - z_0)$$

using the same notation as for the concentration profile.

Let us consider a fluid particle displaced vertically from its equilibrium position z_0 (Figure 1.19), and study its subsequent motion. We make the following hypotheses:

- the particle moves under the effect of its weight and the Archimedes force, the other forces can be neglected;
- since the thermal diffusivity of water is one hundred times greater than the molecular diffusivity of salt, the particle preserves its initial concentration C_0 throughout its motion;
- in the inertia term of the momentum equation, the particle density ρ can be taken to be the unperturbed density $\bar{\rho}$ (the Boussinesq approximation);
- the variation rate of the particle temperature $T(z, t)$ is proportional to the difference between $T(z, t)$ and the temperature $\bar{T}(z)$ of the surrounding fluid (a simplification of the energy conservation equation), that is,

$$\frac{dT}{dt} = -k(T - \bar{T}), \quad (1.36)$$

where k is a constant.

Let us first consider the case of zero temperature gradient. A particle displaced from its equilibrium position z_0 to the position $z_0 + \delta z$ is acted on by its weight $-\bar{\rho}(z_0)V_0g\mathbf{e}_z$ and by the Archimedes force $\bar{\rho}(z_0 + \delta z)V_0g\mathbf{e}_z$, where V_0 is the

constant volume of the particle. Its equation of motion is then

$$\frac{d^2}{dt^2}\delta z = g\beta C'_0 \delta z.$$

For $C'_0 < 0$ the net vertical force is a restoring force which gives rise to neutral oscillations of the particle with frequency $N = \sqrt{-g\beta C'_0}$, called the Brunt–Väisälä frequency.

Let us now assume a nonzero temperature gradient T'_0 . A particle displaced a distance δz is subject to its weight $-\bar{\rho}(z_0)V_0g\mathbf{e}_z$, as before, and the Archimedes force $\bar{\rho}(z_0 + \delta z)(V_0 + \delta V)g\mathbf{e}_z$, where $\delta V = V_0\alpha\delta T$ is the variation of the particle volume associated with the temperature variation $\delta T = T - T_0$. The equation of motion becomes

$$\frac{d^2}{dt^2}\delta z = \alpha g\delta T + \beta C'_0 g\delta z. \quad (1.37)$$

Introducing the temperature variation δT into the energy conservation equation (1.36), the latter becomes

$$\frac{d}{dt}\delta T = -k\delta T + kT'_0\delta z. \quad (1.38)$$

The system (1.37)–(1.38) is a system of linear differential equations with constant coefficients, and has nonzero exponential solutions of the form $\exp(st)$ when the eigenvalue s is a solution of the characteristic polynomial

$$(s+k)(s^2 + N^2) - \alpha g k T'_0 = 0. \quad (1.39)$$

For a weak temperature gradient T'_0 we can seek the eigenvalues as perturbations s' of the eigenvalues $\pm iN$ corresponding to zero temperature gradient, that is, $s = \pm iN + s'$. We then find

$$s'_{\pm} = \frac{-N \pm ik}{2N(N^2 + k^2)} \alpha g k T'_0. \quad (1.40)$$

The imaginary part of these eigenvalues corresponds to a shift of the Brunt–Väisälä frequency. The real part provides the answer for the stability: for positive temperature gradient T'_0 , the real part is negative and the oscillation decays; conversely, for negative temperature gradient T'_0 , the oscillation amplifies and the stratification is unstable. For $T'_0 = 0$ the pair of complex-conjugate eigenvalues crosses the imaginary axis at $\pm N$, which is none other than a Hopf bifurcation. This result can be interpreted physically by noting that for $T'_0 < 0$ the particle is subject not only to

the restoring force due to the concentration gradient which produces an oscillation at frequency N , but also to an additional destabilizing force associated with the temperature gradient. Accordingly, as the particle passes through its equilibrium position z_0 , say, from below, it is hotter and lighter than the surrounding fluid. It is then pulled upwards by the buoyancy force and overshoots the previous maximum, so that the oscillation amplitude increases.

1.5 Non-normality of the linearized operator

1.5.1 Algebraic transient growth

Strictly speaking, any study of linear stability is incomplete if it deals only with the asymptotic stability of an equilibrium state under “infinitesimal” amplitude perturbations. In the real world, perturbations (various types of fluctuation, vibrations, etc.) have a finite amplitude. Fortunately, it has been proved that for many physical systems the predictions of linear stability analysis are well confirmed experimentally for amplitudes (normalized by a scale characteristic of the problem) of order 10^{-2} or even 10^{-1} , for which nonlinear effects remain negligible. However, the domain of validity of the linear analysis is sometimes limited to amplitude perturbations which are extremely small, perhaps of order 10^{-3} , smaller than the ordinary ambient “noise,” and so, except in experiments where noise effects are really under control, the predictions may not agree with observation.

Noise effects are particularly important in the neighborhood of a subcritical bifurcation. Let us consider the simple case of a subcritical pitchfork bifurcation whose normal form is given by Eq. (1.13) with $\delta = -1$. As seen from the bifurcation diagram, for $\mu < 0$ the equilibrium state $x = 0$ is stable with respect to infinitesimal perturbations but unstable if the initial amplitude is larger than $\sqrt{-\mu}$. Therefore, if the system is subject to noise of characteristic amplitude ϵ , the bifurcation for μ increasing will occur for $\mu \approx -\epsilon^2$, not for $\mu = 0$. Experimentally, a spread in the measured bifurcation thresholds associated with the random nature of the noise is observed.

The phenomenon described above becomes dramatic for systems in which certain perturbations, even though they decay exponentially at long times, can display transient growth. Such *transient growth* can amplify the initial energy of the perturbation by extremely large factors of 10^2 or 10^3 or more. Nonlinear effects may then become significant and can eventually destabilize the system. This phenomenon is related to non-normality of the linearized operator, i.e., to the nonorthogonal nature of the eigenvectors (for a more complete introduction to this problem, see Trefethen *et al.* (1993) and Schmid and Henningson (2001, §4)).

In order to illustrate the above ideas, let us consider the linear dynamical system

$$\frac{d\mathbf{x}}{dt} = \mathbf{Ax}, \quad \mathbf{A} = \begin{pmatrix} 0 & 1 \\ 0 & 0 \end{pmatrix}, \quad (1.41)$$

where \mathbf{A} is a Jordan block. This system possesses a double-zero eigenvalue associated with the unique eigenvector $\mathbf{e} = (1, 0)$. The solution of this system for the initial condition (x_{10}, x_{20}) is

$$x_1 = x_{20}t + x_{10}, \quad x_2 = x_{20}.$$

The solution therefore grows with time not exponentially, but *algebraically*.

Let us now consider the “perturbed” system

$$\frac{d\mathbf{x}}{dt} = \mathbf{Ax}, \quad \mathbf{A} = \begin{pmatrix} -\epsilon & 1 \\ 0 & -2\epsilon \end{pmatrix}, \quad 0 < \epsilon \ll 1. \quad (1.42)$$

The origin $(0, 0)$ is the only fixed point of this system and it is stable: the eigenvalues are $-\epsilon$ and -2ϵ , with eigenvectors $\mathbf{e}_1 = (1, 0)$ and $\mathbf{e}_2 = (1, -\epsilon)$, respectively. We note that the angle between these two vectors is small, of order ϵ . The solution of this system for the initial condition (x_{10}, x_{20}) is

$$\mathbf{x} = y_{10} e^{-\epsilon t} \mathbf{e}_1 + y_{20} e^{-2\epsilon t} \mathbf{e}_2, \quad y_{10} = x_{10} + \frac{x_{20}}{\epsilon}, \quad y_{20} = -\frac{x_{20}}{\epsilon}, \quad (1.43)$$

where y_{10} and y_{20} are the initial conditions in the basis of the eigenvectors. The phase portrait is shown in Figure 1.20: since the eigenvalues are nonorthogonal, the trajectories are initially parallel to the more stable eigendirection \mathbf{e}_2 ; they then converge toward the fixed point following the less stable eigendirection \mathbf{e}_1 .

How, for ϵ tending to zero, does the exponential decay match up with the algebraic growth at $\epsilon = 0$? In order to answer this question, let us study how the energy $E(t) = \mathbf{x}(t) \cdot \mathbf{x}(t)$ of the perturbation varies with time. At long times, i.e., for $\epsilon t \gg 1$, the behavior of the solution (1.43) is no surprise: the component in the most stable direction \mathbf{e}_2 is exponentially small, and the solution becomes

$$\mathbf{x} \sim y_{10} e^{-\epsilon t} \mathbf{e}_1,$$

for which the energy decreases exponentially.⁸ At short times ($\epsilon t \ll 1$), a Taylor series expansion of the energy gives

$$E(t) = (y_{10} + y_{20})^2 + (\epsilon y_{20})^2 - (2y_{10}^2 + 4(1 + \epsilon^2)y_{20}^2 + 6y_{10}y_{20})\epsilon t + \mathcal{O}(\epsilon^2 t^2). \quad (1.44)$$

⁸ Here the symbol \sim is used in the sense of asymptotic equivalence (Hinch, 1991).

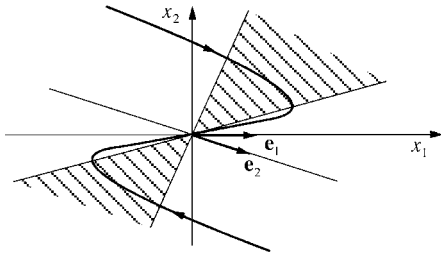


Figure 1.20 Phase portrait of the dynamical system (1.42), with a stable fixed point at the origin. Initial conditions in the hatched region lead to transient growth.

This expansion shows that the energy can grow if the coefficient of ϵt is negative, which can happen for particular initial conditions to be determined. Since the dynamical system is linear, there is no loss of generality if we take y_{10} to be strictly positive and set $y_{20} = -ay_{10}$ (the special case $y_{10} = 0$ corresponds to trivial decay along the most stable eigendirection). Analysis of the sign of the coefficient of ϵt then shows that a necessary condition for growth at short times is $\epsilon^2 < 1/8$, and that the initial conditions for which the energy is amplified are such that

$$a_- < a < a_+, \quad \text{with} \quad a_{\pm} = \frac{3 \pm \sqrt{1 - 8\epsilon^2}}{4(1 + \epsilon^2)}. \quad (1.45)$$

Therefore, in the phase space, all initial conditions located in the sector delimited by the straight lines of slope $-a_-$ and $-a_+$ in the eigenvector basis (i.e., for small ϵ , the lines $x_{20} \sim \epsilon x_{10}$ and $x_{20} \sim (1/2\epsilon)x_{10}$) give rise to transient growth of the energy.

The phase portrait shown in Figure 1.20 explains the situation geometrically. Initial conditions “downstream” of the hatched region lead to exponential decay to the origin (the norm of the vector \mathbf{x} , and therefore of the energy $\mathbf{x} \cdot \mathbf{x}$, decreases monotonically). Initial conditions within the hatched region lead first to transient growth, and then, as the point exits the hatched region, to exponential decay. Finally, for initial conditions “upstream” of the hatched region, the energy first decays then grows, and eventually decays. We emphasize the fact that this growth at short times can only be transient, and that at long times the exponential decay will eventually prevail.

We can next ask which of the above initial conditions corresponds to the largest transient growth. This particular initial condition, called the “optimal perturbation” in control theory, is obtained in two steps. The first is to find the time at which the energy $E(t)$ associated with a given initial condition passes through a maximum;

by differentiation we find that this time t_{\max} is

$$\epsilon t_{\max} = \ln \frac{a}{a_-}, \quad a_- \leq a \leq a_+.$$

The relation between the maximum $E(t_{\max})$ and the initial energy E_0 , referred to as the “gain,” is then

$$\frac{E(t_{\max})}{E_0} = \frac{a_-^2}{a^2} \frac{(1+\epsilon^2)a_-^2 - 2a_- + 1}{(1+\epsilon^2)a^2 - 2a + 1}. \quad (1.46)$$

The second step is to find the initial condition which maximizes this gain. We find, again by differentiation, that this optimal condition corresponds to

$$a_{\text{opt}} = a_+, \quad \text{or} \quad x_{20} \sim \frac{x_{10}}{2\epsilon}.$$

In Figure 1.20, this line corresponds to the edge with highest slope of the hatched region, with a clear geometrical interpretation. It should be noted that the optimal perturbation is located on a direction close to the normal to the eigendirections; we shall return to this later. Then the maximal gain is

$$\max_a \left(\frac{E(t_{\max})}{E_0} \right) = \frac{(3a_- - 1)(1 - a_-)}{(3a_+ - 1)(1 - a_+)}. \quad (1.47)$$

It can be verified that the optimal perturbation, giving the maximum gain, corresponds to zero initial growth rate, i.e., $dx^2/dt = 0$ at time $t = 0$. This maximum gain depends only on ϵ and is larger the smaller ϵ is. For example, it reaches 625 for $\epsilon = 10^{-2}$ and 62,500 for $\epsilon = 10^{-3}$. Figure 1.21 shows the time evolution of the energy for $\epsilon = 0.1$, normalized by the initial energy, for two initial conditions. One, for $y_{20} = -a_- y_{10}$, leads to monotonic decrease of the energy, while the other, for $y_{20} = -a_{\text{opt}} y_{10}$, corresponds to the optimal condition maximizing the gain.

In conclusion, certain perturbations of an asymptotically stable equilibrium state can be strongly amplified in a transient manner by a *purely linear* effect. This transient growth is essentially related to the nonorthogonal nature of the eigenvectors of the system linearized at the fixed point. The optimal perturbation is oriented in a direction normal to the neighboring eigendirections.

1.5.2 Optimal excitation of an unstable mode

The above discussion of the possibility of transient growth concerns an equilibrium state which is linearly *stable*. In the case of an unstable equilibrium state, i.e., for a system with an eigenvalue which has positive real part, a related question is that of the “optimal excitation” of the unstable mode (Farrell, 1988). This optimal excitation corresponds to the initial perturbation which allows, at a given instant, the

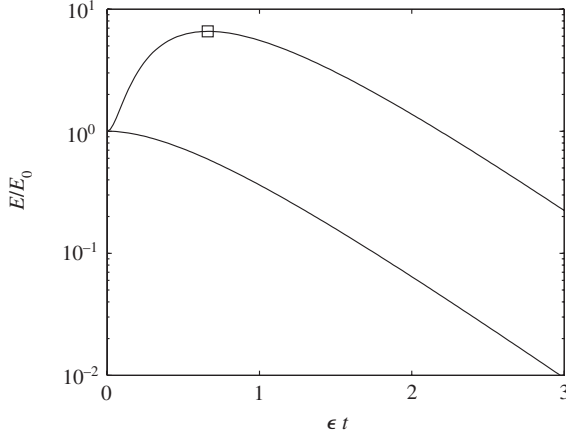


Figure 1.21 Time evolution of the energy of the system (1.42) for $\epsilon = 0.1$, normalized by the initial energy, for two initial conditions. One leads to monotonic decrease of the energy ($y_{20} = -a - y_{10}$), and the other corresponds to the optimal condition ($y_{20} = -a_{\text{opt}}y_{10}$) maximizing the gain at the position of the open square (\square).

maximum energy to be obtained for a given initial energy. When the eigenvectors are orthogonal, this perturbation is located on the proper subspace associated with the most unstable eigenvalue. However, when the eigenvectors are not orthogonal, part of the initial energy will in general be distributed among the stable modes.

As an illustration, we consider the dynamical system

$$\frac{d\mathbf{x}}{dt} = \mathbf{A}\mathbf{x}, \quad \mathbf{A} = \begin{pmatrix} \epsilon_1 & 1 \\ 0 & -\epsilon_2 \end{pmatrix}, \quad (1.48)$$

where ϵ_1 and ϵ_2 are two small positive parameters. The eigenvalues of the system are ϵ_1 and $-\epsilon_2$, and are respectively associated with the unit eigenvectors

$$\mathbf{e}_1 = \begin{pmatrix} 1 \\ 0 \end{pmatrix}, \quad \mathbf{e}_2 = \frac{1}{\sqrt{1+(\epsilon_1+\epsilon_2)^2}} \begin{pmatrix} 1 \\ -(\epsilon_1+\epsilon_2) \end{pmatrix}. \quad (1.49)$$

The evolution of an initial condition $\mathbf{x}_0 = y_{10}\mathbf{e}_1 + y_{20}\mathbf{e}_2$ is given by

$$\mathbf{x}(t) = y_{10} e^{\epsilon_1 t} \mathbf{e}_1 + y_{20} e^{-\epsilon_2 t} \mathbf{e}_2. \quad (1.50)$$

The calculation of the optimal excitation for this system is discussed in detail in Exercise 1.6.8. One finds that, for initial energy $E_0 = \mathbf{x}_0 \cdot \mathbf{x}_0 = 1$, the initial condition

$$y_{10,\text{opt}} = -\frac{1}{\epsilon_1 + \epsilon_2} + \mathcal{O}(1), \quad y_{20,\text{opt}} = \frac{1}{\epsilon_1 + \epsilon_2} + \mathcal{O}(1) \quad (1.51)$$

or vice versa, corresponds to the optimal excitation, i.e., at a given t these maximize the energy $E(t) = \mathbf{x}(t) \cdot \mathbf{x}(t)$. (Owing to the linear nature of the problem, taking the initial energy to be unity does not lead to loss of generality of the result.)

We define the “optimal gain” G_{opt} at a given time as the energy of the optimal excitation, divided by the energy the system would have at the same time for initial condition of the single unstable mode ($y_{10} = 1, y_{20} = 0$):

$$G_{\text{opt}} = \frac{\max_{y_{20}}(E)}{E_{y_{20}=0}}. \quad (1.52)$$

At long times ($\epsilon_1, \epsilon_2 t \gg 1$) this gain can be written simply as

$$G_{\text{opt}} \sim \frac{1}{(\epsilon_1 + \epsilon_2)^2} \sim \frac{1}{2(1 - \mathbf{e}_1 \cdot \mathbf{e}_2)}. \quad (1.53)$$

We see that the smaller the angle between the eigenvectors, the closer the scalar product is to unity, and the larger the gain. Figure 1.22 compares, for $\epsilon_1 = \epsilon_2 = 0.1$, the growth of the energy of the single unstable mode (a straight line in semi-logarithmic coordinates) to that of the optimal excitation. It is clear that the energy of the optimal excitation grows more quickly than that of the single unstable mode. At long times the component of the optimal excitation on the stable subspace vanishes exponentially, and the two time evolutions then become parallel, corresponding to constant gain (1.53).

Finally, we note that a powerful mathematical concept for dealing with the ideas of transient growth and optimal excitation is that of the adjoint operator. For the scalar product $\langle \mathbf{x}, \mathbf{y} \rangle = \mathbf{x} \cdot \mathbf{y}$, the adjoint operator \mathbf{A}^\dagger associated with an operator \mathbf{A}

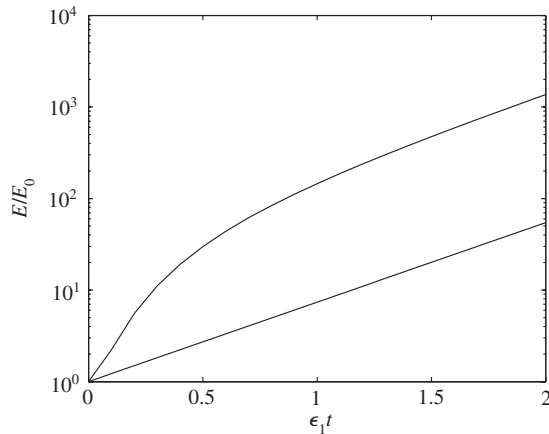


Figure 1.22 Growth of the energy for $\epsilon_1 = \epsilon_2 = 0.1$ for the single unstable mode ($y_{10} = 1, y_{20} = 0$, lower curve) and for the optimal excitation (1.51) (upper curve).

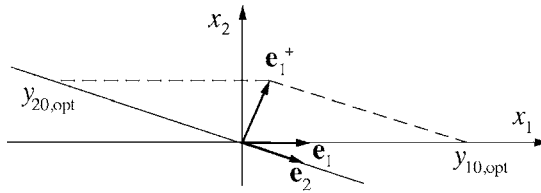


Figure 1.23 Eigenvectors \mathbf{e}_1 and \mathbf{e}_2 of the matrix \mathbf{A} , eigenvector \mathbf{e}_1^+ of the adjoint matrix \mathbf{A}^\dagger associated with the eigenvalue ϵ_1 , and the optimal excitation $(y_{10,\text{opt}}, y_{20,\text{opt}})$.

is defined by the relation

$$\langle \mathbf{x}, \mathbf{A}^\dagger \mathbf{y} \rangle = \langle \mathbf{A}\mathbf{x}, \mathbf{y} \rangle$$

for any pair (\mathbf{x}, \mathbf{y}) . When \mathbf{A} is a matrix operator, the adjoint \mathbf{A}^\dagger corresponds to the complex conjugate transpose matrix, $\mathbf{A}^\dagger = \mathbf{A}^{t*}$, and when the matrix \mathbf{A} and its eigenvalues are real, as is the case here, the eigenvalues of \mathbf{A}^\dagger are identical to those of \mathbf{A} . It can be shown that the optimal excitation at long times corresponds to the eigenvector of the adjoint operator associated with the most unstable eigenvalue (Farrell, 1988). Then, at long times, the optimal excitation of unit energy is the unitary eigenvector of \mathbf{A}^\dagger associated with ϵ_1 . For the example at hand,

$$\mathbf{e}_1^\dagger = \frac{1}{\sqrt{1 + (\epsilon_1 + \epsilon_2)^2}} \begin{pmatrix} \epsilon_1 + \epsilon_2 \\ 1 \end{pmatrix}. \quad (1.54)$$

This eigenvector is orthogonal to \mathbf{e}_2 , as shown in Figure 1.23 (we note that the optimal excitation (1.51) and that shown on this figure have opposite components but equal energy).

1.6 Exercises

1.6.1 The forced harmonic oscillator

Consider a harmonic oscillator of characteristic frequency ω_0 and damping coefficient 2μ . The oscillator, initially at rest, is subject for $t > 0$ to a sinusoidal forcing of frequency ω_f and amplitude ϵ . The oscillator motion is then described by the differential equation

$$\frac{d^2u}{dt^2} + 2\mu \frac{du}{dt} + \omega_0^2 u = \epsilon \cos \omega_f t. \quad (1.55)$$

- What is the phase space of the system? The above equation depends explicitly on time via the forcing term (it is nonautonomous). It can be made artificially

autonomous by introducing a third degree of freedom $w = t$. Write down the system of ODEs in this enlarged phase space.

2. We begin by considering the nondissipative case $\mu = 0$. Show that when the forcing is nonresonant ($\omega_f \neq \omega_0$), the oscillator response is a superposition of two sinusoidal motions of frequencies ω_f and ω_0 :

$$u(t) = \frac{\epsilon}{\omega_f^2 - \omega_0^2} (\cos \omega_0 t - \cos \omega_f t). \quad (1.56)$$

Under what condition is the motion periodic? Quasi-periodic (i.e., not strictly periodic)? What is the response of the oscillator when the forcing and the oscillator are in resonance? Why is this response not physically admissible at long times?

3. Introducing the half-difference $\Omega = \frac{1}{2}(\omega_f - \omega_0)$ between ω_f and ω_0 , show that the nondissipative response can be written as

$$u(t) = \frac{\epsilon}{2\Omega(\omega_0 + \Omega)} \sin \Omega t \sin(\omega_0 + \Omega)t. \quad (1.57)$$

What does the above response represent for a forcing term of small amplitude close to resonance ($\epsilon \ll 1$ and $\Omega/\omega_0 = \mathcal{O}(\epsilon)$)? Graph the behavior of the oscillator response (for example, for $\omega_0 = 1 \text{ s}^{-1}$, $\epsilon = \Omega/\omega_0 = 0.1$).

4. Generalize the analysis for arbitrary initial conditions. Show that, as before, the response of the harmonic oscillator is the superposition of its characteristic response and the forced response.
5. What is the asymptotic behavior of the system at large times ($t \gg 1/\omega_0$) in the dissipative case ($\mu \geq 0$)?

1.6.2 Particle in a double-well potential

Consider a particle of unit mass and a single degree of freedom x subject to a force $F = -V'(x)$ derived from the potential

$$V(x) = -\frac{x^2}{2} + \frac{x^4}{4}. \quad (1.58)$$

1. Give an example of a mechanical realization of such a system. Write the equation of motion as a system of first-order differential equations. For arbitrary mass m , what is the change of scale needed to transform the problem to unit mass? What is the dimension of the phase space? Is this system dissipative?
2. Determine the fixed points of the system as well as their type. Sketch the phase portrait. Show that for each trajectory there exists an invariant $H(x, \dot{x})$. What

does this invariant represent physically? Derive the equation for the trajectories and complete the phase portrait. Interpret these trajectories in terms of the particle motion.

3. Without any calculation, but instead imagining a ball in a double-well potential, show how a friction force $-\mu\dot{x}$ ($\mu > 0$) modifies the type of fixed point. Sketch the phase portrait.
4. Answer the above questions for the potential $W(x) = -V(x)$. For additional discussion, see Guckenheimer and Holmes (1983, §2.2).

1.6.3 Avalanches in a sand pile

Consider the nonlinear oscillator

$$\ddot{\psi} - \gamma \dot{\psi}^2 + k\psi = 0, \quad \gamma \geq 0, \quad k \text{ real}, \quad (1.59)$$

which can be interpreted as an oscillator with a friction term $\Gamma(\dot{\psi})\dot{\psi}$ involving a nonconstant friction coefficient $\Gamma(\dot{\psi}) = -\gamma\dot{\psi}$. This oscillator is a rudimentary model of avalanches in a sand pile, with ψ representing the deviation of the slope of the sand pile from the equilibrium slope; see Linz (1995). An avalanche corresponds to $\dot{\psi} < 0$, and $\dot{\psi} = 0$ corresponds to the stopping of the avalanche.

1. Write Eq. (1.59) as a system of two first-order ODEs, and study the linear stability of the fixed point as a function of the value of k . What can we conclude?
2. Equation (1.59) can be written as

$$\frac{d}{dt} (\dot{\psi} e^{-\gamma\psi}) = F(\psi), \quad F(\psi) = -k\psi e^{-\gamma\psi}, \quad (1.60)$$

which can be interpreted as the equation of motion of a mass $e^{-\gamma\psi}$ depending on the position ψ and subject to a force $F(\psi)$. We then define the kinetic energy E_k and the potential V of the system as

$$E_k = \frac{1}{2} e^{-2\gamma\psi} \dot{\psi}^2, \quad V = -\frac{k}{4\gamma^2} (1 + 2\gamma\psi) e^{-2\gamma\psi}. \quad (1.61)$$

Show that the extrema of V are the equilibrium positions ($F = 0$), the minima and maxima respectively corresponding to stable and unstable equilibrium states. Verify that the energy $E_k + V$ of the system remains constant throughout the motion.

3. Study the variations of the potential V in the cases $k < 0$ and $k > 0$. Sketch the behavior of the potential V as a function of $\gamma\psi$ for $k = -4\gamma^2$ and $k = 4\gamma^2$. Find the equilibrium positions of the system and their stability. Compare these results with those of the first question.

4. For what values of k and the energy does the system (1.59) possess periodic solutions?
5. Sketch the phase portrait of the system (1.59) for $k < 0$ and $k > 0$ with reference to the behavior of the potential V .

1.6.4 A second-order phase transition

Consider a pure material near a phase transition. The thermodynamic state of the material is described by an “order parameter” $A(t)$ assumed to be uniform in space (since the material is homogeneous). This order parameter might be the molar volume of a fluid, the magnetization of a ferromagnetic material, the orientation of liquid crystals, and so on. The order parameter obeys the real equation

$$\frac{dA}{dt} = -V'(A), \quad V(A) = \mu \frac{A^2}{2} - \alpha \frac{A^4}{4} - \frac{A^6}{6}, \quad (1.62)$$

where $V'(A)$ is the derivative of the thermodynamic potential $V(A)$. This equation expresses the fact that the rate of variation of the order parameter is proportional to the slope of the thermodynamic potential $V(A)$. Here, μ is the control parameter of the transition proportional to the difference from the transition temperature. In this exercise we take $\alpha = 1$.

1. Show that the stable and unstable fixed points respectively correspond to the minima and maxima of $V(A)$. Justify the term thermodynamic potential for the function $V(A)$.
2. Sketch the behavior of the potential as a function of the control parameter μ and find the bifurcation diagram as a function of μ . Specify the nature of the bifurcation.

1.6.5 A first-order phase transition

For the same situation as in the preceding exercise we now take $\alpha = -1$ in the expression for the potential (1.62). The order parameter can take only positive or zero values. To make the ideas more precise, suppose that $A = 0$ represents a liquid phase and $A > 0$ a solid phase of the pure material.

1. Show that outside an interval $[\mu_1, \mu_2]$, to be determined, the potential has a single minimum, while inside this interval it has two minima which are equal for a value μ_0 to be calculated. Graph the potential in the two cases.
2. Sketch the bifurcation diagram as a function of the control parameter μ . Specify the nature of the displayed bifurcations in $\mu = \mu_1$ for μ decreasing from $\mu \gg 0$, and in $\mu = \mu_2$ for μ increasing from $\mu \ll 0$. Are μ_1 and μ_2 equal? What is

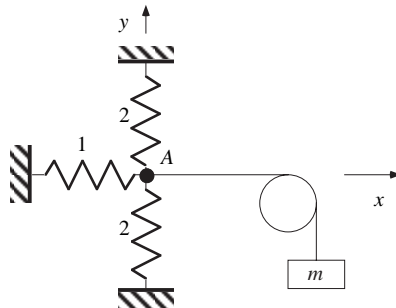


Figure 1.24 Schematic diagram of a model of soap-film instability.

this phenomenon called? Why does the case $\alpha = -1$ correspond to a first-order phase transition?

3. A phase is termed metastable when it is stable but its potential is higher than that of the other stable phase. Sketch the bifurcation diagram again, this time showing the stable phases by a continuous line, the unstable phases by a broken line, and the metastable phases by a dot-dash line (the solution to this problem is given in Chapter 8).

1.6.6 A model of soap-film instability

Consider the system described in Figure 1.24. The horizontal spring 1 and the two identical vertical springs 2 have spring constants k_j and stretches $l_j - l_{j0}$, $j = 1, 2$, where l_{j0} are their rest lengths. The mass $m = k_1(l_1 - l_{10})/g$ ensures that the node A is at equilibrium at $x = 0$.

1. Before doing any calculations, give a qualitative discussion of the equilibrium of the node A based on the direction of the variation of the force exerted by the springs in a displacement $(\delta x, \delta y)$. Show, in particular, that A is stable under any displacement δy .
2. Show that for a small displacement δx of the node A the variation of the force exerted by the springs is given by

$$\delta F = -(k_1 + 2k_2(1 - l_{20}/l_2)) \delta x.$$

Derive the stability condition.

3. Expand the potential energy and the work performed by the spring force in Taylor series about $x = 0$ for a displacement δx of the node A. Show by identification that the restoring force is $F = -E'_p(0)$ and that the variation of this

force is $\delta F = -E_p''(0)\delta x$. Derive the stability condition in terms of the convexity of the potential energy of the springs. What is the potential (different than the potential energy E_p) whose extrema correspond to the equilibrium states?

1.6.7 Transient growth and optimal perturbation

Derive the results (1.43) to (1.47) for the system (1.42).

1.6.8 Optimal excitation of an unstable mode

Consider the dynamical system (1.48),

$$\frac{d\mathbf{x}}{dt} = \mathbf{A}\mathbf{x}, \quad \mathbf{A} = \begin{pmatrix} \epsilon_1 & 1 \\ 0 & -\epsilon_2 \end{pmatrix},$$

where ϵ_1 and ϵ_2 are two small positive parameters associated with the initial condition $\mathbf{x}_0 = (x_{10}, x_{20})$.

1. Show that the eigenvalues of the system are ϵ_1 and $-\epsilon_2$, respectively associated with the unitary eigenvectors (1.49).
2. We define the energy of the system at time t as $E(t) = \mathbf{x}(t) \cdot \mathbf{x}(t)$. Owing to the linear nature of the problem, without loss of generality we can consider the case of unit initial energy $E_0 = \mathbf{x}(0) \cdot \mathbf{x}(0) = 1$, with $\mathbf{x}(0) = y_{10}\mathbf{e}_1 + y_{20}\mathbf{e}_2$. Show that the energy $E(t)$ can be written as

$$\frac{E(t)/e^{2\epsilon_1 t} - 1}{1 - \alpha} = (2p^2 - 1 - \alpha)y_{20}^2 \pm 2p y_{20} \sqrt{1 - (1 - p^2)y_{20}^2},$$

where $\alpha = e^{-(\epsilon_1 + \epsilon_2)t}$ and $p = \mathbf{e}_1 \cdot \mathbf{e}_2$.

3. Show that the initial conditions y_{20} which make the energy E an extremum at time t are the roots of the biquadratic equation

$$(1 - p^2)y_{20}^4 - y_{20}^2 + \frac{p^2}{4p^2(1 - p^2) + (1 - \alpha - 2(1 - p^2))^2} = 0.$$

4. Using the linearity of the system of differential equations, without loss of generality we can seek only the positive roots. Show that for $\epsilon_1 \ll 1$ and $\epsilon_2 \ll 1$ and using $1 - p^2 \sim (\epsilon_1 + \epsilon_2)^2$, the positive roots of the above equation are

$$y_{20}^{(1)} = \frac{1}{1 - \alpha} + \mathcal{O}(\epsilon_1 + \epsilon_2), \quad y_{20}^{(2)} = \frac{1}{\epsilon_1 + \epsilon_2} + \mathcal{O}(1).$$

Find the corresponding initial conditions $y_{10}^{(1)}$ and $y_{10}^{(2)}$.

5. Show that the optimal gain (1.52) corresponds to the initial condition $y_{20}^{(2)}$, and that at long times ($\epsilon_1 t \gg 1$ and $\epsilon_2 t \gg 1$) this gain is given by (1.53). Qualitatively sketch $\ln(E(t)/E_0)$ as a function of time for initial condition corresponding to (a) the energy at the single unstable mode, and (b) the energy at the optimal excitation. What do you conclude?
6. Discuss the meaning of the initial condition $y_{20}^{(1)}$.

1.6.9 Subcritical bifurcation via a transient growth

Construct a nonlinear dynamical system with two degrees of freedom which has a fixed point displaying subcritical pitchfork bifurcation for a critical value μ_c of a parameter μ , and such that for $\mu < \mu_c$ there exist unstable initial conditions owing to a transient growth. It may be helpful to consult Trefethen *et al.* (1993).

2

Instabilities of fluids at rest

2.1 Introduction

In this chapter we discuss how various gravitational, capillary, and thermal phenomena can initiate an instability in a fluid initially at rest. In such a motionless fluid, advection of momentum plays a negligible role in the small amplitude theory, unlike the situations that will be studied in later chapters. We also present the basic techniques for studying linear stability: derivation of the equations for small perturbations of a base state, linearization, and determination of the normal modes and the dispersion relation.

An important part of this chapter is devoted to the analysis of problems in terms of ratios of *characteristic scales*. The approach we take is to simplify the problem by evaluating the *order of magnitude* of the involved phenomena before embarking on long analytic or numerical calculations. This allows us to retain only the most important effects and to elucidate mechanisms. This dimensional analysis, which is essential in both fundamental and applied research, is often sufficient for determining the scaling laws governing the problem. It allows the choice of a set of suitable reference scales to recast the problem in dimensionless form, or, in other words, to recast the problem in a system of units composed of scales that are *intrinsic* to the problem. This modeling approach then guides the later calculations, for example, by revealing a small parameter which suggests an asymptotic expansion. It also serves to justify or reject *a posteriori* certain hypotheses, and leads to a better understanding of the physics of the problem.

This chapter is organized as follows. First we present the basic technique for studying stability using the example of the gravitational instability of a cloud of interstellar gas (Section 2.2). We then study some classical instabilities related to gravity, surface tension, and temperature gradients (Sections 2.3–2.6). From these examples we can abstract (Section 2.7) some common and fundamental features of broader generality introduced in the preceding chapter, such as the concepts

of *control parameter* of an instability, *bifurcation*, *symmetry breaking*, and the mechanism of *structure selection*.

2.2 The Jeans gravitational instability

The instability of a distribution of masses interacting gravitationally – an instability which should cause the Universe to collapse toward its center – did not escape the notice of Isaac Newton. After speculating with the theologian Richard Bentley about what he considered to be an unacceptable collapse, Newton concluded in 1692 that our Universe must be infinite, as then it has no center, and therefore no collapse: “...providence had designed a Universe of infinite extent in which uniformly distributed stars stand poised in unstable equilibrium like needles on their points” (Edward Harrison; quoted by Longair, 2006). In 1902 the British physicist Sir James Jeans made a major advance in solving this problem by determining a length scale above which a mass of uniformly distributed gas is effectively unstable. The problems that this study raised led to much later research, which continues today, to better understand the formation and evolution of stars, galaxies, and the Universe. Here we give an elementary introduction to the subject. First we discuss the effect of terrestrial gravity on classical acoustic waves, which allows us to introduce the fundamental ideas of normal modes and a dispersion relation. We then turn to the case of a nonuniform gravitational field within the framework of the Jeans approximation. Finally, we briefly discuss this approximation in the light of some recent developments.

2.2.1 Acoustic waves

Base state, perturbations, and linearization

Let us consider a fluid – a liquid or a gas – at rest in the Earth’s gravitational field \mathbf{g} . The velocity, density, and pressure fields are defined as

$$\bar{\mathbf{U}} = \mathbf{0}, \quad \bar{\rho} = \rho_0, \quad \bar{P} = P_0 - \rho_0 g z, \quad (2.1)$$

where ρ_0 and P_0 are the density and pressure at a reference altitude $z = 0$. These quantities define a *base state* satisfying the laws of mass and momentum conservation (at least on a height scale for which the density variation associated with fluid compressibility can be neglected. As an example, for a height variation of one hundred meters, the density variation of the Earth’s atmosphere is 1.7% and that of the ocean, 0.04%).

Under a small perturbation of this base state, the velocity, density, and pressure fields become

$$\mathbf{U} = \bar{\mathbf{U}} + \mathbf{u}, \quad \rho = \bar{\rho} + \rho', \quad P = \bar{P} + p.$$

The evolution of these fields must satisfy the laws of mass and momentum conservation:

$$\partial_t \rho + \operatorname{div}(\rho \mathbf{U}) = 0, \quad (2.2a)$$

$$\rho(\partial_t \mathbf{U} + (\mathbf{U} \cdot \operatorname{grad}) \mathbf{U}) = -\operatorname{grad} P + \rho \mathbf{g}. \quad (2.2b)$$

It can be verified *a posteriori* that the viscosity effects omitted above are negligible; we have, however, included gravity, which is essential to our discussion. A fifth equation is necessary to account for the thermodynamic behavior of the fluid and to close the system of equations. Assuming the evolution of the perturbations to be isentropic (adiabatic and reversible), the variations of the density and pressure perturbations are related via the equation of state:

$$d\rho = \frac{\partial \rho}{\partial P} \Big|_s dP = \rho \kappa_s dP, \quad (2.3)$$

where κ_s is the isentropic compressibility (Callen, 1985). Taking into account the equation of hydrostatic equilibrium satisfied by the base state,

$$\mathbf{0} = -\operatorname{grad} \bar{P} + \bar{\rho} \mathbf{g},$$

and linearizing the above equations about this base state neglecting products of perturbations, we obtain

$$\partial_t \rho' + \rho_0 \operatorname{div} \mathbf{u} = 0, \quad (2.4a)$$

$$\rho_0 \partial_t \mathbf{u} = -\operatorname{grad} p + \rho' \mathbf{g}, \quad (2.4b)$$

$$\rho' = \rho_0 \kappa_s p. \quad (2.4c)$$

Taking the divergence of (2.4b) and substituting Eqs (2.4a) and (2.4c) results in an equation involving only the pressure:

$$\partial_t^2 p - c_s^2 \Delta p + \mathbf{g} \cdot \operatorname{grad} p = 0, \quad (2.5)$$

where we have introduced the speed c_s defined as

$$c_s = \frac{1}{\sqrt{\rho_0 \kappa_s}}. \quad (2.6)$$

We note that for $\mathbf{g} = 0$ we recover the classical equation for acoustic waves (Lighthill, 1978; Billingham and King, 2000).

Normal modes and the dispersion relation

Equation (2.5) above is linear with constant coefficients (a reflection of the translation invariance of the problem), and therefore for unbounded domains admits

solutions that are exponentials in time and in space. These solutions can be written as

$$p = \frac{1}{2} \hat{p} e^{i(\mathbf{k} \cdot \mathbf{r} - \omega t)} + \text{c.c.}, \quad (2.7)$$

where c.c. stands for complex conjugate, corresponding to plane waves of wave vector \mathbf{k} and angular frequency ω , with amplitude \hat{p} . This amplitude, which is *a priori* complex, can be written as $|\hat{p}|e^{i\theta}$ where $|\hat{p}|$ and θ are its modulus and phase.¹ For \mathbf{k} real and $\omega = \omega_r + i\omega_i$ complex, the perturbation can be written as

$$p = |\hat{p}| e^{\omega_i t} \cos(\mathbf{k} \cdot \mathbf{r} - \omega_r t + \theta)$$

(in the next chapter we shall consider the more general situation of complex wave number). The real part of the angular frequency ω_r therefore corresponds to propagation of the perturbation at speed $c = \omega_r/k$, where $k = |\mathbf{k}|$. The imaginary part ω_i is the temporal growth rate: $\omega_i < 0$ corresponds to a damped perturbation, $\omega_i = 0$ to a neutral perturbation, and $\omega_i > 0$ to an amplified perturbation. Any perturbation, like a localized excitation, can be treated as a superposition of perturbations of the form (2.7) which, in a linearized problem, evolve independently of each other. Such perturbations are called the *normal modes* (owing to the orthogonality of the exponential functions). Thus, when studying linear stability, we can in general consider only the evolution of a single generic normal mode of the form (2.7); this statement will be made more precise in the next chapter.

With (2.7) the wave equation (2.5) becomes

$$-\omega^2 \hat{p} + c_s^2 k^2 \hat{p} + i \mathbf{g} \cdot \mathbf{k} \hat{p} = 0.$$

This equation has a nonzero solution only if the coefficient of \hat{p} is zero, i.e.

$$\omega^2 = c_s^2 k^2 + i \mathbf{g} \cdot \mathbf{k}. \quad (2.8)$$

This is the *dispersion relation* for small perturbations; it shows that the frequency and the wave vector of a normal mode, or eigenmode, are not independent, but are related in a specific way. The dispersion relation does not involve the amplitude of the perturbation, which remains undetermined owing to the linear and homogeneous nature of Eq. (2.5). Here we have managed to solve the system (2.4) simply by substitution; as we shall see in the following section, the introduction of normal modes leads more generally to a homogeneous algebraic system for the amplitudes of the perturbations, which has a nonzero solution only if its determinant vanishes; it is this more general condition that gives the dispersion relation.

¹ The coefficient 1/2 in (2.7) may be omitted since the problem to be solved is linear and homogeneous; however, it is introduced for consistency with the nonlinear analyses of later chapters.

Temporarily ignoring the last term $i\mathbf{g}\cdot\mathbf{k}$ in the dispersion relation, we see that the frequency of a wave with real wave vector is $\omega = \pm c_s k$; it is real, which corresponds to a wave which propagates without amplification or attenuation. The phase velocity of this wave, also called the wave speed, is

$$c = \frac{\omega}{k} = \pm c_s, \quad (2.9)$$

which explains the physical meaning of the speed c_s . We note that this speed, the “speed of sound,” is independent of the wave number, i.e., acoustic waves are not dispersive. In air (assumed to be an ideal gas), we find² $c_s = \sqrt{\gamma r T_0} = 340 \text{ m s}^{-1}$ for $T_0 = 288 \text{ K}$; therefore, a typical acoustic wave of frequency $\omega/2\pi = 1000 \text{ Hz}$ has wavelength $\lambda = 2\pi/(\omega/c_s) = 0.34 \text{ m}$. In water, which has compressibility $\kappa_s \approx 0.47 \times 10^{-9} \text{ Pa}^{-1}$, the speed of sound is $c_s \approx 1460 \text{ m s}^{-1}$, and the wavelength at the same frequency is $\lambda = 1.46 \text{ m}$. Let us now consider the effect of gravity, which corresponds to the term $i\mathbf{g}\cdot\mathbf{k}$. The first thing to note is that this effect arises only when the wave vector has a vertical component. For audible acoustic waves of wavelength about a meter, the order of magnitude of the gravity term compared to ω^2 is 10^{-5} , so that the effect of gravity is completely negligible. But gravity does become important for waves of frequency below 1 Hz, whose wavelength is about a kilometer. However, for such long waves the assumption of uniform gravitational field must be revised. This is the subject of the following section.

2.2.2 The effect of gravity at large scales

Dimensional analysis

As shown in the preceding section, the propagation of an acoustic wave with speed c_s is essentially a consequence of a balance between the fluid inertia and an elastic restoring force due to the fluid compressibility. Gravity plays a role only at length scales above c_s^2/g , which is about 10 km for the Earth’s atmosphere and 200 km for the ocean. Thus the role of gravity is essential at the scale of astrophysical phenomena. In particular, it gives rise to an instability of an interstellar gas cloud which causes the cloud to collapse on itself, leading to star formation. This instability can be analyzed qualitatively as follows.

First we recall that a mass m produces a gravitational field $\mathcal{G} = Gm/r^2$ at a distance r , where $G = 6.67 \times 10^{-11} \text{ m}^3/\text{kg s}^2$ is the gravitational constant, and

² The isentropic compressibility of an ideal gas is $\kappa_s = \gamma/P$, where $\gamma = c_p/c_v$ is the adiabatic index (the ratio of the heat capacity at constant pressure to the heat capacity at constant volume). Taking into account the Boyle–Mariotte law $P/\rho = rT$, where $r = R/M$ is the ratio of the ideal gas constant $R = 8.314 \text{ J K}^{-1} \text{ mol}^{-1}$ and the molar mass M , one obtains $c_s^2 = \gamma r T_0$. For air, $\gamma = 1.4$ and $M = 29.0 \text{ g mol}^{-1}$.

that this gravitational field exerts on a mass m' an attractive force $m'\mathcal{G}$. Now let us take a large mass of gas at rest, for example, an interstellar gas cloud, and perturb its equilibrium by density and pressure nonuniformities $\delta\rho$ and δP on a spatial scale L . This leads to a nonuniformity of the gravitational field of order $\delta\mathcal{G} \sim G\delta\rho L^3/L^2 = G\delta\rho L$. A fluid particle of typical size a is then subject to two competing forces, an elastic force and a gravitational force. The elastic force, which is related to the compressibility of the fluid, points from compressed regions to neighboring rarefied regions, and its order of magnitude is

$$F_a \sim (\delta P/L)a^3 \sim \delta\rho c_s^2 a^3/L.$$

The net gravitational force is directed toward the compressed region containing a mass excess of order $\delta\rho L^3$, and its order of magnitude is

$$F_g \sim \rho a^3 \delta\mathcal{G} \sim \rho a^3 G \delta\rho L.$$

The ratio of these two forces is then $F_g/F_a = \rho GL^2/c_s^2$. Thus, if the spatial scale of the nonuniformities is such that $L \ll c_s/\sqrt{\rho G}$, the elastic force dominates and the perturbation propagates as an acoustic wave, without amplification. Conversely, if $L \gg c_s/\sqrt{\rho G}$, the gravitational force dominates and the gas moves from rarefied regions to compressed ones, which enhances the initial density difference. Thus, the effect amplifies the cause, and an instability develops which destroys the initial uniformity of the cloud and causes it to collapse.³

The dimensional analysis carried out above therefore indicates a length scale

$$L_c = \frac{c_s}{\sqrt{\rho G}} \quad (2.10)$$

above which a mass of gas is susceptible to collapsing on itself. This length corresponds (up to a numerical factor) to the length discovered by Jeans in 1902. For the Earth's atmosphere this length is about 36,000 km, which is much larger than the Earth's radius: gravity does not enter into the propagation of sound waves, and so the Earth's atmosphere is not at risk of collapse! For a low-density cloud of interstellar gas, where the parameters are typically $c_s = 200 \text{ m s}^{-1}$ and $\rho = 2 \times 10^{-17} \text{ kg m}^{-3}$, the length L_c is about $5 \times 10^{12} \text{ km}$, that is, about a thousand times the size of the Solar System, or half a light-year.⁴

³ The analogy with a liquid–vapor phase transition should be noted: the liquid results from “collapse” of the gas. However, in this case it is not the gravitational interaction which is responsible for the instability, but rather interactions of the van der Waals type.

⁴ This analysis is incorrect for astrophysical objects which are very dense such as white dwarfs, whose density is of order $5 \times 10^6 \text{ g/cm}^3$. For such objects it is a pressure of quantum rather than thermal origin which opposes the gravitational attraction and ensures equilibrium.

The base state, perturbations, and linearization

We now make the above dimensional analysis quantitative by considering solutions to the linearized equations. Consider a large cloud of interstellar gas of density ρ , pressure P , and temperature T , assumed to be an ideal gas (Chandrasekhar, 1961, §119). The stability of this cloud can be studied from the thermodynamic point of view by seeking the extrema of a suitable thermodynamic potential (the entropy for an isolated system described by the microcanonical formalism, or the free energy for a system held at constant temperature and described by the canonical formalism (Chavanis, 2002)). Equivalently, this stability can be studied using the mechanics of continuous media. It is this latter approach that we follow here. The conservation equations are then identical to Eqs (2.2) governing acoustic waves, with the gravitational acceleration \mathbf{g} replaced by the gravitational field $\mathcal{G} = -\mathbf{grad}\Phi$, where Φ is the gravitational potential:

$$\partial_t \rho + \text{div} \rho \mathbf{U} = 0, \quad (2.11a)$$

$$\rho(\partial_t \mathbf{U} + (\mathbf{U} \cdot \mathbf{grad}) \mathbf{U}) = -\mathbf{grad} P - \rho \mathbf{grad} \Phi. \quad (2.11b)$$

The gravitational potential is related to the density distribution by the Poisson equation:

$$\Delta \Phi = 4\pi G \rho. \quad (2.12)$$

Finally, as before, we assume that the perturbations evolve isentropically, with the entropy given by the equation of state (Callen, 1985):

$$s - s_0 = c_v \ln \frac{P}{P_0} - c_p \ln \frac{\rho}{\rho_0}, \quad (2.13)$$

where c_v and c_p are the heat capacities at constant volume and pressure, and the subscript 0 refers to a reference equilibrium state.

We note first of all that equations (2.11)–(2.12) do not admit a solution with uniform P and ρ : for such a solution, the potential Φ would have to be uniform according to (2.11b), and the Poisson equation (2.12) would then imply $\rho = 0$. A nonuniform hydrostatic equilibrium can be found for a spherical mass distribution, corresponding to a uniform temperature and a density which varies as $1/r^2$, where r is the distance to the center of the distribution (Binney and Tremaine, 1988). However, this distribution corresponds to infinite total mass (the mass $\int \rho(r) 4\pi r^2 dr$ in a sphere of radius R diverges as R). This difficulty can be overcome by artificially confining the gas inside a sphere of radius R (Chavanis, 2002). A full treatment of this problem lies outside the scope of the present book, and so here we shall consider the simplified version studied by Jeans in 1902. The simplification is to study the stability of a *uniform* base state, although this base state

does not satisfy the Poisson equation (2.12). In spite of this simplification, known as the “Jeans swindle” (Binney and Tremaine, 1988), the calculation merits reproduction owing to its historical importance and the fact that in the end it gives a stability condition close to that obtained in the solution of the full problem.⁵

Let us consider a stationary and uniform base state defined as

$$\bar{\mathbf{U}} = \mathbf{0}, \quad \bar{\rho} = \rho_0, \quad \bar{s} = s_0, \quad \bar{\Phi} = \Phi_0, \quad \bar{P} = P_0, \quad (2.14)$$

and a small isentropic perturbation of this base state, \mathbf{u} , ρ' , ϕ , and p . The equations governing the evolution of these perturbations are then, according to (2.11)–(2.13),

$$\partial_t(\rho_0 + \rho') + \operatorname{div}((\rho_0 + \rho')\mathbf{u}) = 0, \quad (2.15a)$$

$$(\rho_0 + \rho')(\partial_t \mathbf{u} + (\mathbf{u} \cdot \mathbf{grad})\mathbf{u}) = -\mathbf{grad}(P_0 + p) - (\rho_0 + \rho')\mathbf{grad}(\Phi_0 + \phi), \quad (2.15b)$$

$$\Delta\phi = 4\pi G\rho', \quad (2.15c)$$

$$\ln(1 + \frac{p}{P_0}) - \gamma \ln(1 + \frac{\rho'}{\rho_0}) = 0. \quad (2.15d)$$

We note that, although the base state does not satisfy the Poisson equation, the perturbations do. For small perturbations we can linearize the equations about the base state neglecting products of perturbations. The linearized equations are then

$$\partial_t \rho' + \rho_0 \operatorname{div} \mathbf{u} = 0, \quad (2.16a)$$

$$\rho_0 \partial_t \mathbf{u} = -\mathbf{grad}p - \rho_0 \mathbf{grad}\phi, \quad (2.16b)$$

$$\Delta\phi = 4\pi G\rho', \quad (2.16c)$$

$$p = c_s^2 \rho'. \quad (2.16d)$$

Normal modes and the dispersion relation

Like the problem of acoustic waves treated above, the problem (2.16) is linear with constant coefficients, again a reflection of its translation invariance. It therefore has solutions which are exponentials in time and space and can be written as plane waves of wave vector \mathbf{k} and frequency ω :

$$u = \frac{1}{2} \hat{u} e^{i(\mathbf{k} \cdot \mathbf{r} - \omega t)} + \text{c.c.}, \quad (2.17)$$

with similar expressions for the other velocity components v and w , as well as for ρ' , p , and ϕ .

⁵ The “Jeans swindle” in fact becomes legitimate in cosmology when the expansion of the Universe is taken into account, in which case the Poisson equation is involved only for the perturbations.

Taking the divergence of (2.16b), by substitution we obtain an equation involving only the pressure perturbation p :

$$\partial_t^2 p - c_s^2 \Delta p - 4\pi \rho_0 G p = 0. \quad (2.18)$$

For a normal mode of the form (2.17) this equation becomes

$$\omega^2 \hat{p} = c_s^2 k^2 \hat{p} - 4\pi G \rho_0 \hat{p}, \quad (2.19)$$

where $k = |\mathbf{k}|$. This equation has a nonzero solution only when the coefficient of \hat{p} vanishes, from which we find the dispersion relation:

$$\omega^2 = c_s^2 k^2 - 4\pi G \rho_0. \quad (2.20)$$

Note that this is the dispersion relation (2.8) for acoustic waves with the corrected gravitational term $4\pi G \rho_0$.

2.2.3 Discussion

Let us now study the dispersion relation (2.20) by considering a plane wave with real wave vector \mathbf{k} whose temporal stability is to be determined. Since the dispersion relation is quadratic in ω , there exist two eigenmodes with frequency

$$\omega_{\pm}(k) = \pm \sqrt{c_s^2 k^2 - 4\pi G \rho_0}.$$

This indicates the existence of a critical wave number

$$k_J = \frac{\sqrt{4\pi G \rho_0}}{c_s} \quad (2.21)$$

for which the expression in the square root vanishes. Any perturbation with wave number above k_J has real frequency, and therefore corresponds to a wave which propagates without growth or decay with velocity

$$c_{\pm} = \omega_{\pm}/k = \pm c_s \sqrt{1 - k_J^2/k^2} \quad (k > k_J),$$

which is close to c_s for short wavelengths ($k \gg k_J$) and vanishes at $k = k_J$. On the other hand, any perturbation with wave number below k_J has purely imaginary frequency. The mode corresponding to $\omega_+ = +i\omega_i$ grows exponentially at a rate

$$\omega_i = c_s \sqrt{k_J^2 - k^2} \quad (k < k_J),$$

while the other mode of frequency $\omega_- = -i\omega_i$ decreases exponentially. The phase velocity of these modes, $c = \omega_r/k$, is zero.

We conclude that in a gas cloud of size smaller than the Jeans length $L_J = 2\pi/k_J$, any perturbation propagates without amplification, and so the cloud is linearly stable. On the other hand, if the cloud is larger than the Jeans length, it is unstable with respect to perturbations of large wavelength. We note that L_J corresponds, up to a numerical factor $\sqrt{\pi}$, to the critical length (2.10) obtained in our earlier dimensional analysis.

Subrahmanyan Chandrasekhar (1910–1995)



Subrahmanyan Chandrasekhar was born in Lahore, India (now Pakistan) into a well-off, cultivated Brahmin family. One of his uncles, Sir Chandrasekhara Venkata Raman, was awarded the Nobel Prize in Physics in 1930 for his discovery of the optical effect bearing his name. He did his secondary and undergraduate studies in Madras, at which time he published his first article in the *Proceedings of the Royal Society*. Following the example of his uncle, he left India in 1930 to study at Trinity College, Cambridge, England, where he obtained his doctorate in 1933. He

got married in India in 1936, and then moved to the University of Chicago where he remained for the rest of his life. During World War II he worked on shock waves and detonation. He was elected a Fellow of the Royal Society of London in 1944. He and his wife became American citizens in 1953. He contributed to many fields in physics, including white dwarfs, stellar dynamics, radiation, hydrodynamic and hydromagnetic stability, general relativity, black holes, and gravitational waves. In particular, he showed that a star of mass less than 1.44 solar masses evolves at the end of its life into a white dwarf, while a star of mass greater than this limit collapses violently into an object of enormous density, a neutron star or a black hole. He won the Nobel Prize in 1983 for his work on stellar structure and evolution. He published about 400 papers and many important books, in particular, *Hydrodynamic and Hydromagnetic Stability* (1961). He received many honors, including the Royal Medal (1962) and the Copley Medal (1984) of the Royal Society of London. He was editor in chief of the *Astrophysical Journal* for 19 years, and raised its stature enormously. He was interested in the connections between art and science, and later in life wrote the books *Truth and Beauty: Aesthetics and Motivations in Science* (1987) and *Newton's Principia for the Common Reader* (1995), and

gave thought-provoking lectures such as *Shakespeare, Newton and Beethoven or patterns of creativity* and one on comparison of Newton's *Principia* and Michelangelo's frescoes in the Sistine Chapel.

Let us now return to the “Jeans swindle” for the case of a uniform base state. This swindle can be considered acceptable on a length scale over which the gravitational potential is nearly constant, i.e. the scale given by the Poisson equation. Actually, since the equilibrium condition imposes $\rho\Phi/L \sim P/L$ with $P/\rho = c_s^2/\gamma \approx c_s^2$, the Poisson equation gives

$$\frac{c_s^2}{L^2} \sim \frac{\Phi}{L^2} \sim 4\pi G\rho.$$

The length scale L that appears is again none other than the critical length (2.10) (up to a numerical factor of order unity)! Therefore, the conclusion that a cloud of uniform density and size smaller than L_J is stable appears completely reasonable for a realistic cloud of nonuniform density satisfying the Poisson equation. The appearance of an instability for a cloud of size of order L_J suggested by the dimensional analysis also seems quite plausible. On the other hand, the result of maximal growth rate for $k = 0$ is not reasonable. Recent studies on this subject confirm these conclusions (Chavanis, 2002). Interestingly, a study of the *nonlinear* evolution of the instability suggests a fractal organization of the mass distribution at the time of its collapse (de Vega *et al.*, 1996).

2.3 The Rayleigh–Taylor interface instability

2.3.1 Dimensional analysis

We consider two infinitely deep superposed fluid layers subject to constant gravity and separated by a horizontal interface. We shall first neglect viscosity and assume that the walls bounding the fluid are far enough from the interface to be ignored (the effect of walls and of viscous forces is studied in Exercises 2.8.1 and 2.8.2). The only physical variables then are the two densities ρ_1 and ρ_2 , the surface tension γ , and gravity g . These four dimensional variables bring in the three fundamental dimensions of mass, length, and time, and so the problem depends on only a single dimensionless parameter, namely, the density contrast or the Atwood number,

$$\text{At} = \frac{\rho_1 - \rho_2}{\rho_1 + \rho_2}. \quad (2.22)$$

This key parameter is negative if the denser fluid is on top, and positive in the opposite case. It is equal to 1.0 if the upper fluid has negligible density, as for the case of a gas on top of a liquid, and equal to -1.0 in the opposite case of liquid over gas.

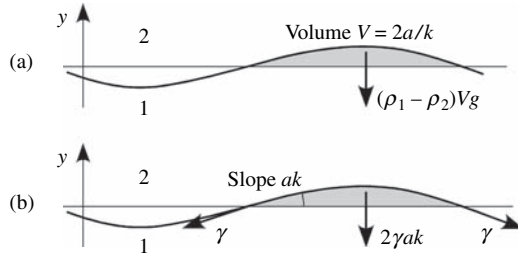


Figure 2.1 Forces acting on a half-wave of a perturbation of wave number k and amplitude a . (a) Net gravitational force $(2a/k)(\rho_2 - \rho_1)g$; (b) surface tension γ and the resultant $2\gamma ak$.

We consider a perturbation of the interface in a vertical plane (x, y) of amplitude a and wave number $k = 2\pi/\lambda$ (Figure 2.1), and analyze the forces exerted on a ‘bulge’ of fluid 1 between the plane $y = 0$ (the interface at rest) and the deformed interface. This bulge is therefore a half wavelength in horizontal extent. The net force due to gravity, or the buoyancy force (the algebraic sum of the weight and the Archimedes force) is

$$(2a/k)(\rho_2 - \rho_1)g$$

per unit width. This force is stabilizing if $\rho_1 > \rho_2$ (since it is negative and tends to pull the bulge back down) and destabilizing otherwise, and it is larger the smaller the wave number. Surface tension exerts a force on the left and right edges of the bulge equal to γ per unit length; the resultant force is vertical and equal to

$$-2\gamma ak.$$

This is always a stabilizing, restoring force, and the larger the wave number the stronger the force.

We see that for $\rho_1 > \rho_2$ the two forces tend to restore the interface to the horizontal, and behave like a spring of stiffness $K = F/a$ with $F = 2\gamma ak + 2(\rho_1 - \rho_2)ga/k$ (the net force per unit width). This restoring force sets in motion a volume of order $1/k^2$ per unit width on each side of the interface, corresponding to a mass M of order $(1/k^2)(\rho_2 + \rho_1)$. This results in oscillations with frequency given by the classical relation for an oscillator of stiffness K and mass M :

$$\omega^2 = \frac{K}{M} \sim 2 \frac{\gamma k^3 + (\rho_1 - \rho_2)gk}{(\rho_2 + \rho_1)}.$$

We have therefore found the dispersion relation for gravity–capillary waves between two fluids by dimensional analysis and simple ideas about oscillators. Of course, the numerical coefficient is not exact owing to the fact that we have

estimated the amount of mass in motion. Comparison with the exact dispersion relation given below in (2.40) shows that the effective mass is equal to twice the mass estimated here.

For $\rho_1 < \rho_2$, gravity is destabilizing, and its action overcomes that of the surface tension if

$$2(\rho_2 - \rho_1)ag/k - 2\gamma ak > 0.$$

We deduce that the interface is unstable to perturbations of wave number lower than a cutoff k_c defined as

$$k_c = \frac{1}{l_c}, \quad \text{with} \quad l_c = \sqrt{\frac{\gamma}{g|\rho_2 - \rho_1|}}, \quad (2.23)$$

where l_c is the *capillary length* (Guyon *et al.*, 2001). For a water–air interface ($\gamma = 70 \times 10^{-3}$ N/m) the capillary length is $l_c = 2.7$ mm. In the absence of surface tension (two miscible liquids or two gases, for example, cold air above a layer of warm air) all wave numbers are unstable.

Therefore, with or without surface tension, the configuration of a heavy fluid on top of a light one is always unstable to long wavelength perturbations. However, if an interface is confined to a length scale smaller than the capillary length, it is stable. This explains why a narrow vertical tube can hold a column of liquid without emptying.

The time for the instability to grow, i.e., the time over which the amplitude of the perturbation changes significantly, is on the order of the only time scale in the problem, the capillary time:

$$\tau_c = \sqrt{\frac{l_c}{g}} = \left(\frac{\gamma}{|\rho_1 - \rho_2| g^3} \right)^{1/4}. \quad (2.24)$$

The assumption of negligible viscosity and infinite vertical extent of the liquids can now be made more precise. The length scale of the problem being the capillary length l_c , the walls limiting the vertical extent of the fluids do not play a role if the thickness of the layers is large compared to l_c . Additionally, viscous effects can be neglected if during the characteristic time for the instability to grow, τ_c , the momentum has not diffused appreciably, i.e., it has diffused only a small distance compared to l_c . This condition can be written as

$$\sqrt{\nu \tau_c} \ll l_c.$$

In other words, viscosity effects are negligible if the capillary Reynolds number $Re_{cap} = l_c^2 / \tau_c \nu$ is large compared to unity. This condition is satisfied for a water–air interface for which $Re_{cap} = 15$. Let us now carry out a quantitative analysis of the problem.

2.3.2 Perturbation equations

The base state and nature of the perturbations

Here the base state corresponds to the fluid at rest, a planar interface $\eta(x, z, t)$, and a hydrostatic pressure distribution:

$$\bar{\mathbf{U}}_j = \mathbf{0}, \quad \bar{\eta} = 0, \quad \bar{P}_j(y) - P_0 = -\rho_j gy, \quad j = 1, 2, \quad (2.25)$$

where P_0 is a reference pressure at the interface. This state satisfies the conservation equations and the boundary conditions, as we shall verify later on. Perturbing this base state, the velocity, pressure, and interface position are written

$$\begin{aligned} \mathbf{U}_j &= \bar{\mathbf{U}}_j + \mathbf{u}_j, \\ P_j &= \bar{P}_j + p_j, \\ \eta &= \bar{\eta} + \eta. \end{aligned}$$

The stability problem can be solved without loss of generality by considering an *irrotational* perturbation, for which

$$\mathbf{u}_j = \mathbf{grad} \phi_j$$

where ϕ_j is the velocity potential. As justification, let us consider the Helmholtz equation for the vorticity perturbations ω , linearized about the rest state of the fluid:

$$\partial_t \omega = v \Delta \omega.$$

In the absence of viscous diffusion, this equation reduces to $\partial_t \omega = 0$ (Batchelor, 1967). The velocity field associated with an initial vorticity distribution can therefore be only a *time-independent* field, which cannot participate in the growth of an instability.

The conservation equations

In order to simplify the algebra, we consider perturbations which are two-dimensional in a vertical plane (x, y). The incompressibility equation can then be written as

$$\partial_{xx} \phi_j + \partial_{yy} \phi_j = 0, \quad j = 1, 2. \quad (2.27)$$

The momentum conservation is given by the Bernoulli equation (the first integral of the Euler equations):

$$\rho_j \partial_t \phi_j + \frac{1}{2} \rho_j (\mathbf{grad} \phi_j)^2 + (\bar{P}_j + p_j) + \rho_j gy = P_0, \quad j = 1, 2,$$

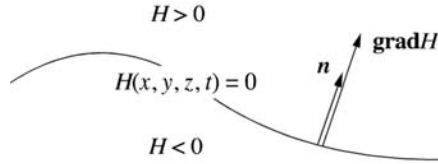


Figure 2.2 The normal to a surface $H(x, y, z, t) = 0$ is parallel to its gradient.

where the integration constant P_0 is determined by the requirement that the equation be satisfied by the unperturbed flow (2.25). Subtracting the unperturbed flow, we find the equation for the perturbations:

$$\rho_j \partial_t \phi_j + \frac{1}{2} \rho_j (\mathbf{grad} \phi_j)^2 + p_j = 0, \quad j = 1, 2. \quad (2.28)$$

The boundary conditions

Searching for perturbations that fall off at infinity, the potential must satisfy

$$\phi_1 \rightarrow 0 \quad \text{for } y \rightarrow -\infty, \quad (2.29a)$$

$$\phi_2 \rightarrow 0 \quad \text{for } y \rightarrow +\infty. \quad (2.29b)$$

Before specifying the interface conditions, let us recall some properties regarding the kinematics of a surface given by $H(x, y, z, t) = 0$ (Figure 2.2). The unit normal \mathbf{n} to this surface is obtained from the fact that the differential of H vanishes for a displacement $d\mathbf{x}$ at fixed t along a line on this surface: $dH = \mathbf{grad} H \cdot d\mathbf{x} = 0$. The normal is then parallel to $\mathbf{grad} H$, which gives

$$\mathbf{n} = \frac{\mathbf{grad} H}{|\mathbf{grad} H|}. \quad (2.30)$$

The differential of $H(x, y, z, t) = 0$ is

$$dH = \partial_t H dt + \mathbf{grad} H \cdot d\mathbf{x} = 0.$$

With $d\mathbf{x} = \mathbf{w} dt$, where \mathbf{w} is the velocity of a point of the surface, we find the normal component of the velocity:

$$\mathbf{w} \cdot \mathbf{n} = \frac{-\partial_t H}{|\mathbf{grad} H|}. \quad (2.31)$$

(Note that the tangential velocity of a geometrical surface is undetermined.)

For the two-dimensional problem under consideration here, the interface is defined geometrically as

$$H(x, y, t) = y - \eta(x, t) = 0.$$

The normal and the normal velocity of the interface are then

$$\mathbf{n} = \frac{(-\partial_x \eta, 1)}{\sqrt{1 + \partial_x^2 \eta}}, \quad \mathbf{w} \cdot \mathbf{n} = \frac{\partial_t \eta}{\sqrt{1 + \partial_x^2 \eta}},$$

where $\partial_x \eta$ is the interface slope.

There are two types of boundary condition at the interface: a “kinematic” condition which expresses the impermeability of the interface, and a “dynamical” condition on the stresses. The kinematic condition states that in each fluid the normal velocity at the interface $\mathbf{U}_j \cdot \mathbf{n}$ must be equal to the normal velocity $\mathbf{w} \cdot \mathbf{n}$ of the interface:

$$\mathbf{U}_j \cdot \mathbf{n} = \mathbf{w} \cdot \mathbf{n} \quad \text{at } y = \eta(x, t), \quad j = 1, 2,$$

or

$$\partial_x \phi_1 (-\partial_x \eta) + \partial_y \phi_1 = \partial_t \eta \quad \text{at } y = \eta, \quad (2.32a)$$

$$\partial_x \phi_2 (-\partial_x \eta) + \partial_y \phi_2 = \partial_t \eta \quad \text{at } y = \eta. \quad (2.32b)$$

Now let us turn to the matching condition of the stresses. Here, since we have neglected viscous effects, the stress is purely normal to the interface and equal to $-P_1 \mathbf{n}$ in the lower fluid and $-P_2(-\mathbf{n})$ in the upper one (Figure 2.3). The matching condition expresses the balance of normal forces and is given by the Laplace–Young relation:

$$P_1 - P_2 = \frac{\gamma}{R} \quad \text{at } y = \eta, \quad (2.33)$$

where γ is the surface tension and $R^{-1} = \operatorname{div} \mathbf{n}$ is the interface curvature, here equal to

$$\frac{1}{R} = \operatorname{div} \mathbf{n} = \frac{-\partial_{xx} \eta}{(1 + \partial_x^2 \eta)^{3/2}}.$$

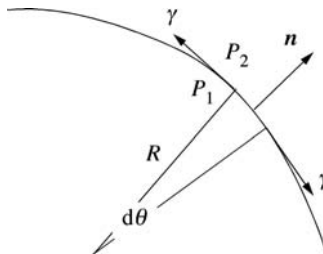


Figure 2.3 For a cylindrical interface the equilibrium condition $(P_1 - P_2)Rd\theta = 2\gamma d\theta/2$ gives the Laplace–Young law $P_1 - P_2 = \gamma/R$.

An interface which is concave downward (the case of Figure 2.3) corresponds to positive curvature and thus to $P_1 > P_2$ according to (2.33), as expected.

2.3.3 Linearization, normal modes, and the dispersion relation

Linearizing the perturbation equations (2.27) and (2.28) and the boundary conditions (2.29), (2.32), and (2.33), we obtain a system with constant coefficients independent of x and t . The dependence of the solutions on x and t is therefore exponential, and the perturbations can be sought in the form of normal modes:

$$(\phi_j, p_j, \eta) = \frac{1}{2} (\hat{\phi}_j(y), \hat{p}_j(y), \hat{\eta}) e^{i(kx - \omega t)} + \text{c.c.}, \quad j = 1, 2, \quad (2.34)$$

with k real for the translational invariance to be satisfied. We note that in contrast to the case of gravitational instability in a gas of infinite extent, here the y dependence of ϕ_j and p_j is *a priori* unknown. This is because the problem is not invariant under translations in y (which pass from one fluid to the other). The system of linearized perturbation equations becomes

$$(\partial_{yy} - k^2)\hat{\phi}_j = 0, \quad j = 1, 2, \quad (2.35a)$$

$$-i\omega\rho_j\hat{\phi}_j + \hat{p}_j = 0, \quad j = 1, 2, \quad (2.35b)$$

with the boundary conditions far from the interface

$$\hat{\phi}_1 \rightarrow 0 \quad \text{for } y \rightarrow -\infty, \quad (2.36a)$$

$$\hat{\phi}_2 \rightarrow 0 \quad \text{for } y \rightarrow +\infty, \quad (2.36b)$$

and the boundary conditions at the interface

$$\partial_y \hat{\phi}_1 = -i\omega\hat{\eta} \quad \text{at } y = 0, \quad (2.37a)$$

$$\partial_y \hat{\phi}_2 = -i\omega\hat{\eta} \quad \text{at } y = 0, \quad (2.37b)$$

$$(\hat{p}_1 - \rho_1 g \hat{\eta}) - (\hat{p}_2 - \rho_2 g \hat{\eta}) = k^2 \gamma \hat{\eta} \quad \text{at } y = 0. \quad (2.37c)$$

The last equation is obtained by using a Taylor series expansion of the pressure near $y = 0$:

$$P(\eta) = \bar{P}(\eta) + p(\eta) = \bar{P}(0) + \eta \partial_y \bar{P}(0) + p(0) + \mathcal{O}(\eta^2).$$

We note that the linearization results in the application of boundary conditions at the unperturbed interface location, i.e., at $y = 0$.

The general solution of (2.35a) is written as

$$\hat{\phi}_j = A_j e^{-ky} + B_j e^{ky}, \quad j = 1, 2. \quad (2.38)$$

Taking into account the conditions (2.36) of decay at infinity and setting $k > 0$ without loss of generality, we find $A_1 = 0$ and $B_2 = 0$ (the case $k < 0$ can be included in the analysis by writing $|k|$ instead of k in the argument of the exponentials). We note that the eigenfunction then decreases exponentially on either side of the interface, which implies that a perturbation of wave number k penetrates to a depth of order $k^{-1} = \lambda/2\pi$. Using (2.38) and (2.35b), the interface conditions (2.37) can be rewritten as

$$i\omega\hat{\eta} + kB_1 = 0, \quad (2.39a)$$

$$i\omega\hat{\eta} - kA_2 = 0, \quad (2.39b)$$

$$-i\rho_1\omega B_1 + i\rho_2\omega A_2 + (\rho_1 - \rho_2)g\hat{\eta} = -k^2\gamma\hat{\eta}. \quad (2.39c)$$

This homogeneous algebraic system has a nonzero solution for B_1 , A_2 , $\hat{\eta}$ only if its determinant vanishes, which after some algebra results in (Rayleigh, 1883a)

$$(\rho_1 + \rho_2)\omega^2 - ((\rho_1 - \rho_2)gk + k^3\gamma) = 0. \quad (2.40)$$

This is the dispersion relation for small perturbations.⁶ It contains complete information about the linear stability of the two superposed fluid layers.

2.3.4 Discussion

Since the dispersion relation (2.40) is quadratic in ω , it has two real or complex-conjugate roots ω_{\pm} . For $\rho_1 > \rho_2$ (the heavier fluid on the bottom, Atwood number $At > 0$), the roots are real for any wave number. Introducing the capillary length (2.23) and the capillary time (2.24), these can be written as

$$\tau_c \omega_{\pm} = \pm \sqrt{Atkl_c(1 + k^2l_c^2)}. \quad (2.41)$$

The eigenmodes then correspond to two waves of constant amplitude propagating in opposite directions with speed $c_{\pm} = \pm\omega/k$. In particular, for $\rho_2 = 0$ ($At = 1$) we recognize the classical dispersion relation for gravity–capillary waves in deep water (Lighthill, 1978; Billingham and King, 2000). The existence of these two modes is a consequence of the invariance of the problem under the transformation $x \rightarrow -x$ corresponding to spatial reflection symmetry.

For $\rho_1 < \rho_2$ (the heavier fluid on top, $At < 0$), the eigenmodes with wave number such that $kl_c > 1$ correspond to waves of neutral stability (real roots of opposite

⁶ The dispersion relation including the case $k < 0$ is

$$(\rho_1 + \rho_2)\omega^2 - |k|((\rho_1 - \rho_2)g + k^2\gamma) = 0.$$

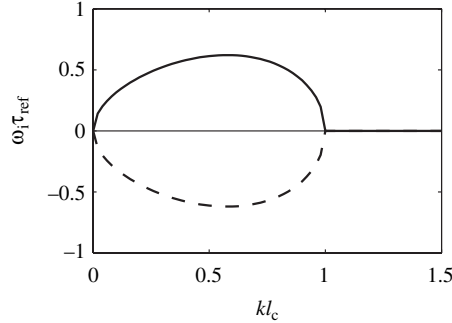


Figure 2.4 Growth rates of the two Rayleigh–Taylor modes when the heavier fluid is on top ($\text{At} < 0$), normalized to $\tau_{\text{ref}} = \tau_c(-\text{At})^{-1/2}$, as a function of the normalized wave number kl_c ; (—) stable mode, (—) unstable mode.

sign). However, for $kl_c < 1$, i.e., long waves, the roots of the dispersion relation are purely imaginary:

$$\tau_c \omega_{\pm} = \pm i \sqrt{(-\text{At}) kl_c (1 - k^2 l_c^2)}. \quad (2.42)$$

The mode corresponding to ω_- is such that $e^{-i\omega_- t}$ decreases with time, i.e., it is stable; the other mode ω_+ is unstable. The existence of these two modes of opposite stability is a consequence of the invariance of the problem under the transformation $t \rightarrow -t$ and $\mathbf{u} \rightarrow -\mathbf{u}$. This invariance under time reflection is related to the nondissipative nature of the flow and disappears when viscous effects are taken into account.

The results of the dimensional analysis are thus confirmed and made specific: when the heavy fluid is on top, the wave number satisfying $kl_c = 1$ is a cutoff above which the perturbations are neutral and below which they grow. This is the Rayleigh–Taylor instability. Figure 2.4 shows the growth rate of the two modes as a function of the wave number. The more amplified mode with the faster growth is the one for which $kl_c \approx 0.6$. If the initial perturbation contains a broad spectrum of wave numbers, it is this mode that will eventually dominate, at least as long as its amplitude remains sufficiently small that nonlinear effects remain unimportant. An instability for which the band of unstable wave numbers extends from $k = 0$ to a finite cutoff k_{off} is referred to as a *long wave instability*.

2.3.5 The effects of horizontal walls and viscosity

The preceding study shows that the amplitude of the eigenfunctions (2.38) decreases exponentially on each side of the interface with a penetration depth of k^{-1} . It can therefore be expected that the presence of horizontal boundaries has

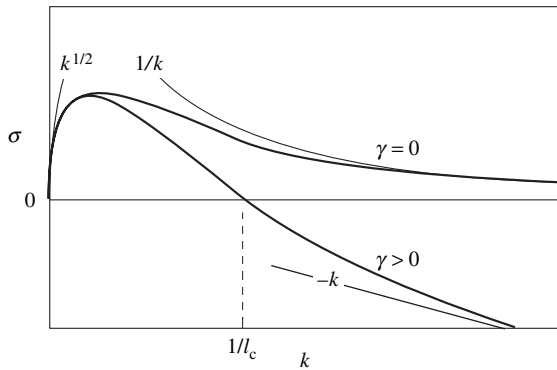


Figure 2.5 Growth rate when viscosity effects cannot be neglected, with and without surface tension γ , and asymptotic behavior for small and large wave numbers.

a non-negligible effect if the thickness of the layers is of the same order of magnitude or smaller than the penetration depth, and calculations show that this is effectively the case; see Exercise 2.8.1. Only the growth rate of small wave numbers is changed significantly: it varies as k rather than as \sqrt{k} . The cutoff wave number is not changed.

The effect of the viscosity is manifested at large wave numbers for which the velocity gradients are large – viscosity dissipates energy at short wavelengths. For vanishing surface tension (as in the case of miscible fluids), short wavelengths remain unstable with growth rate decreasing as $1/k$ (Figure 2.5). For nonzero surface tension, short wavelengths are stable, and their growth rate varies as $-k$. A remarkable result is that the cutoff wave number $kl_c = 1$ is independent of the viscosities (Chandrasekhar, 1961, §94).

An interesting case is that of a thin viscous layer suspended above a lighter fluid, for example, a film of paint spread on a ceiling (Fermigier *et al.*, 1992). The growth of long-wavelength perturbations (with wavelengths longer than the film thickness) is slowed by viscosity, and the growth rate varies as k^2 rather than as k ; see Exercise 2.8.1. The structure of the interface resulting from this instability is illustrated in Figure 2.6: it is a periodic array of stable, hanging drops. The array can be hexagonal, square, or any array that fills the space. Much work has been devoted to the problem of pattern selection: if we restrict our attention to linear theory, the shape of the boundaries, especially in small aspect-ratio containers, can dictate the pattern. However, weak nonlinear effects and imperfections can compete with the effect of boundaries, especially if these are far away.

The Rayleigh–Taylor instability is also manifested in the case of a strongly accelerated interface (Taylor, 1950). Here gravity plays a minor role and it is

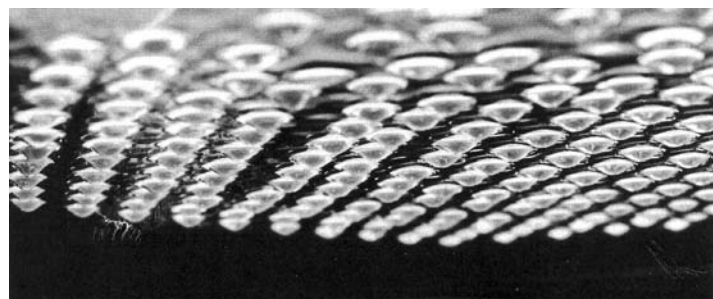


Figure 2.6 A thin film of oil spread on a planar surface which is then turned over. The oil film is unstable, and the instability is manifested in the appearance of hanging drops arranged in an array which here is hexagonal. Reprinted with permission from Fermigier *et al.* (1990). ©1969, American Institute of Physics.



Figure 2.7 Impact of a drop on a liquid surface. The crown of filaments is the result of a Rayleigh–Taylor instability. Reprinted with permission from Andrew Davidhazy, Rochester Institute of Technology, New York.

the acceleration in the reference frame of the interface which must be taken into account. If the relative acceleration points toward the less dense fluid, the interface is unstable. This phenomenon may occur, for example, in the impact of a drop on a thin liquid film, as illustrated in Figure 2.7. The impact of the drop creates a cylindrical liquid film (via a mechanism which we do not discuss here) whose upper rim is pulled down owing to the effect of the surface tension. This rim, being strongly accelerated downward, is unstable and gives rise to the formation of fingers or

filaments which in turn break up into droplets (via a mechanism described in the following section). The order of magnitude of the acceleration g' of the upper rim can be obtained by assuming that the rim is a torus of radius r and thickness e , for which the momentum conservation equation is written as

$$\rho 2\pi r \pi (e/2)^2 g' \approx 2\gamma 2\pi r.$$

Using $e = 0.2$ mm and $\gamma = 0.07$ Pa·m, we obtain $g' \approx 5000$ m/s², an acceleration which is very large compared to gravity. The characteristic time for growth of the instability can be estimated from the capillary time (2.24) substituting g' for g , which gives $\tau_c \approx 0.2$ ms. Owing to this very short time a fast shutter speed is needed to photograph the phenomenon.

2.4 The Rayleigh–Plateau capillary instability

2.4.1 Description

Anyone who has noticed a faucet left open a bit so that a thin jet of water runs out has observed a capillary instability: the breakup of the jet into droplets. It is possible to control the frequency of the droplets, and therefore their spacing and size, by exciting the liquid jet by acoustic waves from a loudspeaker placed nearby. Figure 2.8 shows the formation of such forced droplets; the higher the excitation frequency, the higher the droplet frequency and the more closely spaced the droplets. The size of the droplets can also be controlled by acoustic vibrations in the liquid supply pipe generated by a piezoelectric element. This technique is widely used in inkjet printers, where it is desired that the droplets sent to the paper are as small and well calibrated as possible. The volume of the drops produced and controlled in this fashion can be as small as the order of a few picoliters.

The first observations of the breakup of a fluid jet into droplets were made by Félix Savart (1833), but he did not recognize surface tension as the source of the instability even though surface tension had been demonstrated in 1805 by Pierre-Simon de Laplace and Thomas Young. It was the Belgian physicist Joseph Plateau (1857) who recognized the role played by surface tension. Plateau forced the frequency of the drops using a cello, and his numerous observations are described in his book of 1873; he showed in particular that higher viscosity tends to increase the wavelength of the perturbations and therefore the volume of the drops. It was Rayleigh who performed the first stability study (1879), and his calculation neglecting viscosity correctly identified the inertia of the liquid as the phenomenon retarding the destabilizing effect of the surface tension. Rayleigh

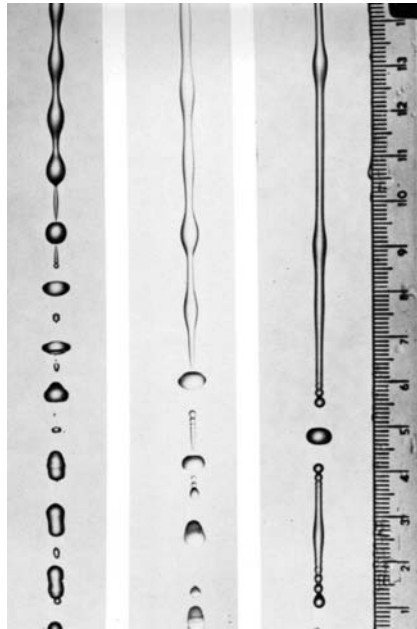


Figure 2.8 A thin jet of water flowing out of a tube 4 mm in diameter is perturbed at various frequencies by a loudspeaker. The “wavelengths” of the strings of droplets are 4.6, 12.5, and 42 diameters. Photograph by Rutland and Jameson (1971), taken from van Dyke (1982).

gives the following value for the most amplified wave number k_{\max} ,

$$k_{\max}a = 0.697,$$

where a is the radius of the jet. This corresponds to a wavelength $\lambda_{\max} = 9.01a$ which agrees with the observations of Savart to within 3%! Rayleigh later considered the viscous case (Rayleigh, 1892), and his calculations were extended to finite Reynolds numbers by Chandrasekhar (1961). A series expansion of the Chandrasekhar result for small wave numbers ($ka \ll 1$) gives the following for the most amplified wave number:

$$(k_{\max}a)^2 = \frac{1}{2 + \sqrt{18/\text{Re}}},$$

where $\text{Re} = Ua/\nu$ is the Reynolds number constructed using the capillary velocity $U = \sqrt{\gamma/\rho a}$. This relation has been confirmed as a very good approximation for all wavelengths and viscosities. A review of recent developments beyond the linear analysis is given by Eggers (1997). Below, we shall perform a dimensional analysis of the linear problem neglecting viscosity.

2.4.2 Dimensional analysis

As discussed above, surface tension stabilizes the *planar* interface between two layers of superposed fluids subject to gravity. The reason for this is that any perturbation of a planar interface increases its area A and therefore also the interface energy γA . In the present case of a cylindrical column the surface tension is, on the contrary, destabilizing, and is responsible for the instability. Indeed, for a given fixed volume of fluid, the interface area is smaller for an ensemble of spherical drops of radius r than for a cylinder of radius a ; more precisely, the ratio of the areas of the drops formed from a cylinder of radius a is (Figure 2.9a)

$$\frac{\text{area of drops}}{\text{area of cylinder}} = \frac{3}{2} \frac{a}{r}.$$

Therefore, the ratio of the areas is smaller the larger the droplets: minimization of the interface area must lead to the largest possible drops. The instability therefore corresponds to the transition to a state of smaller interface energy. However, the formation of large drops involves large displacements of fluid particles, displacements which are opposed by the fluid inertia (Figure 2.9). The droplet diameter that results is therefore a compromise between a destabilizing factor, the surface tension, and a stabilizing – or at least retarding – factor, the fluid inertia.

The droplet formation time can be estimated by dimensional analysis omitting viscous effects. We assume that the liquid column moves with constant velocity, and we consider the perturbed flow in the reference frame attached to the unperturbed cylindrical column. The variables on which the problem depends are then the density ρ , the radius a of the column, and the surface tension γ . Thus the only

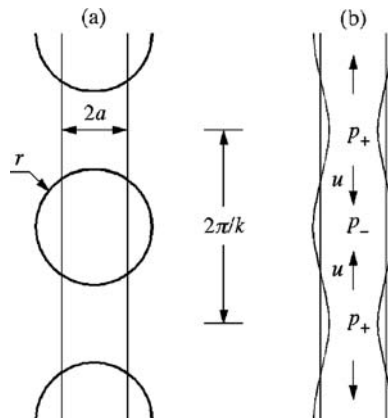


Figure 2.9 Capillary instability of a column of water: a perturbation of the interface is amplified owing to a capillary pressure gradient, thereby leading to droplet formation.

length and time scales are the radius a and the capillary time

$$\tau_c = \sqrt{\rho a^3 / \gamma}. \quad (2.43)$$

We can then suppose that these scales give the orders of magnitude of the droplet diameter and formation time. This droplet formation time grows with the droplet mass ρa^3 and decreases with the surface tension, which seems reasonable. For a 1 mm diameter water column, the time scale τ_c is a few milliseconds.

To make our discussion more precise, let us consider an axisymmetric perturbation of wavelength $2\pi/k$ and amplitude η of the cylindrical interface, as shown schematically in Figure 2.9b (this perturbation preserves the volume up to terms of order $(\eta/a)^2$, which are negligible for small perturbations). If this wavelength is small compared to the radius a , the perturbation “sees” a planar interface and so we have the case of a neutral capillary wave (zero growth rate). If, on the other hand, the wavelength is large, the perturbation induces a difference of the radii of curvature: it is close to $a - \eta$ at the necks and $a + \eta$ at the bulges of the column. The difference of the curvatures, which can be written as

$$\frac{1}{a - \eta} - \frac{1}{a + \eta} \approx \frac{2\eta}{a^2}$$

for small η/a , then leads to a pressure difference, according to the Laplace–Young law, of $p_+ - p_- \approx 2\gamma\eta/a^2$ and therefore to an average pressure gradient $(k/\pi)(p_+ - p_-) \approx 2k\gamma\eta/\pi a^2$. This gradient induces an acceleration of the fluid toward the bulges where the pressure is lower, which, from a one-dimensional momentum balance, is of order

$$\frac{du}{dt} \sim \frac{k(p_+ - p_-)}{\rho} \sim \frac{ak\eta}{\tau_c^2},$$

where we have introduced the capillary time (2.43). Mass conservation gives another equation relating velocity to displacement amplitude: the volume of fluid leaving a pinch during a time dt is of order $ua^2 dt$; this decrease corresponds to a volume variation of order $(a/k)d\eta$, where $d\eta$ is the variation of η during the time dt . We then deduce that $ua^2 dt \sim (a/k)d\eta$, or

$$\frac{d\eta}{dt} \sim kau.$$

Differentiating the first equation with respect to time and taking into account the second, we obtain

$$\frac{d^2 u}{dt^2} = \sigma^2 u, \quad \sigma \sim \frac{ka}{\tau_c}. \quad (2.44)$$

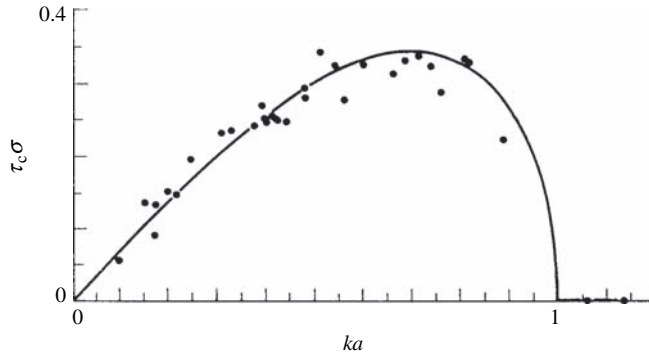


Figure 2.10 Growth rate $\tau_c\sigma$, with $\tau_c=\sqrt{\rho a^3/\gamma}$, of the instability of a low viscosity liquid column, along with the experimental points of Donnelly and Glaberson (1966).

The solution of this differential equation is the sum of two exponentials, the one with positive growth rate $+\sigma$ corresponding to the instability in question.

The full stability calculation without viscosity was performed by Rayleigh (1879); this calculation, which involves Bessel functions as the eigenfunctions (Drazin and Reid, 2004), leads to the growth rate shown in Figure 2.10 (solid line): linear increase with wave number for $ka \ll 1$, a maximum for $ka \approx 0.70$ (or $\lambda/a \approx 9.0$), a cutoff wave number at $ka = 1$, and neutral waves thereafter. Note that this picture is essentially the same as that provided by the above dimensional analysis. The measurements by Donnelly and Glaberson (1966) for a low-viscosity liquid, also displayed in Figure 2.10, show good agreement with the inviscid theory.

The droplets formed from this instability are observed to oscillate, with the oscillations damping out after several periods due to viscosity, which dissipates the liberated surface energy. The order of magnitude of the oscillation period (of the mode of lowest frequency) can be found by arguments similar to that above, assuming that a droplet behaves like an oscillator of mass of order ρa^3 and stiffness of order γ . We find that the period is of the order of the capillary time τ_c , as expected because τ_c is the only time scale in problems involving only surface tension and fluid inertia.

2.5 The Rayleigh–Bénard thermal instability

2.5.1 Description

The thermal instability of a fluid layer heated from below is the source of the convection motion observed on a huge range of spatial scales, from millimeters in cooling devices located inside electronics housings, up to planetary or even

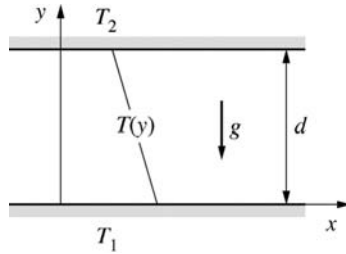


Figure 2.11 Schematic view of an experiment displaying the Rayleigh–Bénard instability.

stellar scales. An experiment used to study this instability is shown schematically in Figure 2.11. A fluid is held between two parallel, horizontal plates separated by a distance d . These plates are kept at temperatures T_1 and $T_2 < T_1$, which are maintained as uniform as possible.

When the temperature difference is sufficiently small, the heat transfer occurs by diffusion (i.e., conduction) from the bottom to the top. The fluid is at rest, and the vertical temperature profile, which is the solution of the energy conservation equation, is linear. A key element of the mechanism is the expansion of the fluid when heated: the fluid near the bottom is less dense than that near the top. When the temperature difference reaches a critical threshold this situation becomes unstable due to the density stratification, and fluid motion arises in the form of convection cells. This is the Rayleigh–Bénard instability.⁷ Two adjacent cells turn in opposite directions like gear wheels. Under some circumstances, their geometry depends on the conditions imposed at the plate edges: in a rectangular box the cells are parallel and rectilinear (Figure 2.12), while in a circular box they are concentric (Figure 2.13). Once convection cells have appeared, the heat transfer no longer occurs only by diffusion because convection of energy by the flowing fluid contributes to the transport. Heat transfer by convection is more efficient than purely diffusive transfer: its variation with temperature difference $T_1 - T_2$ is no longer linear but instead quadratic (Drazin and Reid, 2004).

A further increase of the temperature difference tends to destabilize the convection cells that appeared originally, causing them to “zigzag” or oscillate periodically; see Figure 10.4 in Chapter 10. As the temperature difference increases further, the behavior becomes more and more disordered and difficult to analyze. This behavior was studied in great detail in the 1980s as a manifestation of chaos with a small number of degrees of freedom (Lighthill, 1986; Bergé *et al.*, 1987;

⁷ Here we consider the case of a fluid whose isobaric thermal expansion coefficient is positive, the most common situation; in the opposite case (water between 0 and 4°C, for example), the instability occurs when the upper plate is heated.

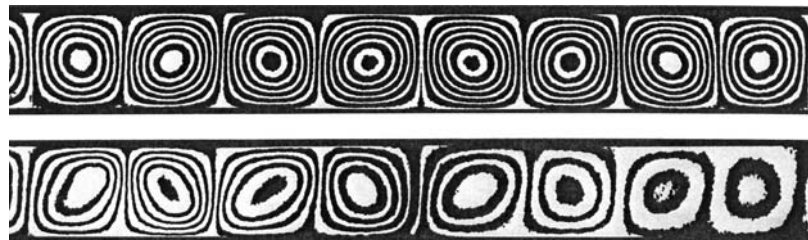


Figure 2.12 Thermal convection cells in silicone oil. The flow lines are visualized by interferograms. The relative dimensions of the box are 10:4:1. Top: regular cells oriented parallel to the short side for uniform temperature gradient. Bottom: the temperature difference and consequently the intensity of the cells decreases from left to right. Photograph by Oertel and Kirchartz (1979), taken from van Dyke (1982). With kind permission of Springer Science + Business Media.

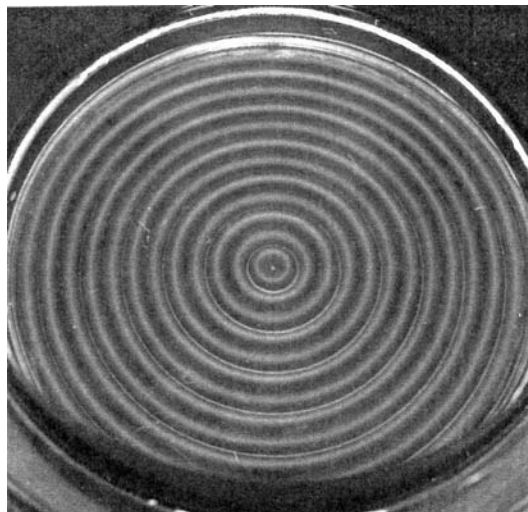


Figure 2.13 Top view through a transparent Plexiglas plate of thermal convection cells in silicone oil, visualized by means of aluminum powder. The circular boundary induces circular cells. $\text{Ra} = 2.9 \text{ Ra}_c$. Photograph by Koschmieder (1974), taken from van Dyke (1982).

Schuster and Wolfram, 2005). These are nonlinear effects that are outside the scope of the present discussion; a good reference describing these phenomena is Koschmieder (1993).

The temperature difference is not the only parameter whose variation leads to an instability. It is possible, for example, to move the walls closer together while holding the temperatures constant, thereby increasing the vertical temperature gradient. The onset of the instability is in fact governed by a dimensionless number

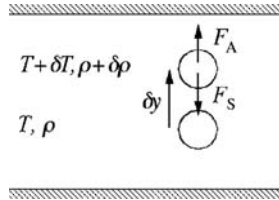


Figure 2.14 A fluid particle perturbed vertically in a temperature gradient.

called the Rayleigh number Ra which is the control parameter of the instability. This number, defined below, represents the net effect of two phenomena, one destabilizing (the buoyancy force) and the other stabilizing (thermal diffusion).

2.5.2 The instability mechanism ($\text{Pr} \gg 1$)

Let us consider a small fluid particle of radius $a \ll d$, temperature T , and density ρ , which, owing to fluctuations, is displaced upward a distance δy (Figure 2.14). The particle therefore finds itself surrounded by colder, denser fluid of temperature $T + \delta T$ and density $\rho + \delta \rho$ such that

$$\begin{aligned}\delta T &= \frac{T_2 - T_1}{d} \delta y < 0, \\ \delta \rho &= -\alpha_p \rho \delta T > 0,\end{aligned}$$

where α_p is the isobaric thermal expansion coefficient of the fluid.⁸ The particle is then subject to an upward-directed buoyancy force (the sum of its weight and the Archimedes force) equal to

$$F_A = \frac{4}{3} \pi a^3 \delta \rho g.$$

However, the resulting rising motion is counteracted by the viscous resistance. Let us consider the case of a fluid with high Prandtl number $\text{Pr} = v/\kappa$, where κ is the thermal diffusivity. Then the relaxation time of the particle motion, of order a^2/v , is much shorter than the time during which the temperature difference is maintained, which is of order a^2/κ . The particle therefore reaches its equilibrium speed v without the temperature having varied significantly. This equilibrium

⁸ The general equation of state is written as

$$\frac{\delta \rho}{\rho} = -\alpha_p \delta T + \kappa_T \delta P,$$

where α_p is the isobaric thermal expansion coefficient and κ_T is the isothermal compressibility, but here compressibility effects are negligible.

speed corresponds to equilibrium between the Archimedes force and the Stokes drag force:

$$F_S + F_A = 0, \quad \text{with} \quad F_S \propto \mu a v.$$

The equilibrium speed is therefore

$$v \propto \frac{\alpha_p g a^2 \delta T}{\nu}. \quad (2.46)$$

According to this equation, the speed v of the particle adapts very quickly to the temperature difference δT , to which it is “enslaved.”

Two phenomena compete in the rising motion: thermal diffusion, which tends to eliminate the temperature difference δT and therefore to stop the motion, and advection at speed v toward the colder fluid which restores the temperature difference and tends to amplify the motion. Marginal stability must correspond to these two phenomena being in equilibrium, which is equivalent to the equality of their characteristic times. The time for thermal diffusion of the temperature difference is a^2/κ , while that for restoration of this difference is $\delta y/v$, with $\delta y/d = \delta T/(T_1 - T_2)$ and the velocity v given by (2.46). Thus, equal characteristic times corresponds to

$$\frac{a^2}{\kappa} \propto \frac{v d}{\alpha_p g a^2 (T_1 - T_2)}. \quad (2.47)$$

This condition for marginal stability appears to depend on the particle radius a . The destabilizing force F_A varies as a^3 and the drag force F_S as a and so the largest particles are the first to be destabilized. For those with radius $d/2$ corresponding to the size of the observed convection cells, the marginal stability condition (2.47) can be written as $\text{Ra} = \text{Ra}_c$, where

$$\text{Ra} = \frac{\alpha_p g (T_1 - T_2) d^3}{\nu \kappa} \quad (2.48)$$

is known as the Rayleigh number, and Ra_c is a number corresponding to the critical value of the Rayleigh number at the instability threshold. The actual numerical value of Ra_c cannot be obtained by dimensional analysis: the full calculation gives $\text{Ra}_c = 1708$ for rigid no-slip boundaries, a value independent of the Prandtl number. The important thing here is not the numerical value of the threshold, but the fact that we have found, by reasoning in terms of characteristic scales, a dimensionless number controlling the onset of the instability. This key parameter has the physical interpretation of the ratio of destabilizing to stabilizing forces. For $\text{Ra} < \text{Ra}_c$ thermal diffusion prevails over advection and any perturbation is dissipated, while for $\text{Ra} > \text{Ra}_c$ the motion is amplified.

2.5.3 Study of stability within the Boussinesq approximation

The problem involves mass, momentum, and energy conservation. Since the thermodynamic and diffusion coefficients depend on the temperature and pressure, the main difficulty is to formulate hypotheses which allow the problem to be recast in a tractable form. The classic model is based on the Boussinesq approximation:

1. Density variations are neglected, except in the buoyancy term of the Navier–Stokes equation. Actually, these variations are typically of order 10^{-2} or 10^{-3} , and can be considered as second-order corrections in the equations describing perturbations of the base state, except for the gravity term, where they are a first-order correction.
2. In the energy conservation equation the viscous dissipation is negligible, as is the pressure dependence of the internal energy.
3. The thermophysical properties are assumed to be constant (which is valid if the temperature difference is not too large, say, less than 10 K). Moreover, the density variations arise only from temperature variations, i.e., compressibility effects are negligible.

The complete linear stability calculation was carried out by Rayleigh (1916a) for free boundary conditions (stress-free rather than no-slip at the walls), which led to a critical Rayleigh number of $Ra_c = 27\pi^4/4 \approx 657$. This calculation, along with others corresponding to various types of boundary conditions, is described in many texts (Manneville, 1990; Koschmieder, 1993; Drazin and Reid, 2004). The main result of interest here is the marginal stability curve in the wave number–Rayleigh number plane, which is shown in Figure 2.15 for rigid boundary conditions. This curve reveals, in particular, the critical Rayleigh number $Ra_c = 1708$, independent of the Prandtl number, and the first wave number to be destabilized, $k_cd = 3.117$, which corresponds to a wavelength very close to $2d$. Beyond Ra_c ,

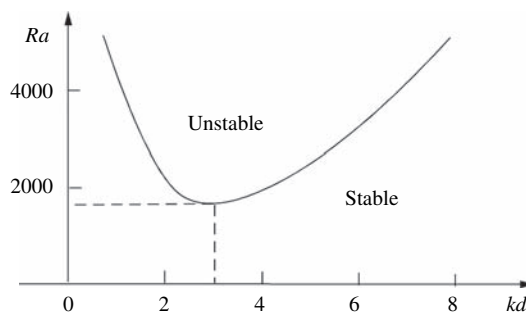


Figure 2.15 Marginal stability curve of the Rayleigh–Bénard instability.

the width δk of the unstable band is centered at k_c and grows as $\sqrt{\text{Ra} - \text{Ra}_c}$. This result is in good agreement with experiments, which must be performed very carefully to ensure, in particular, that the thermal conditions are uniform over the plates.

Let us conclude by returning to the question of the instability mechanism. We write down the two equations for vertical momentum conservation and energy conservation. Linearized about the base state, these two equations become

$$\frac{\partial v}{\partial t} = -\frac{\partial_y p}{\rho} + v \Delta v + \alpha_p g \delta T, \quad (2.49a)$$

$$\frac{\partial \delta T}{\partial t} = \kappa \Delta \delta T + v \frac{T_1 - T_2}{d}. \quad (2.49b)$$

In the first equation the first two terms on the right-hand side correspond to the retarding force induced by pressure and viscous drag,⁹ and the third corresponds to the buoyancy force. For $\text{Pr} \gg 1$, where the velocity is quasi-statically slaved to the temperature disturbance, the equilibrium between these two forces corresponds to the dimensional equation (2.46) with $\Delta \sim -1/a^2$. The second equation (2.49b) shows that the instability depends on the relative importance of the stabilizing thermal diffusion and the destabilizing advection. The equilibrium of these two terms corresponds to the marginal stability condition given by the dimensional equation (2.47), again with $\Delta \sim -1/a^2$. Using the estimate (2.46) for the velocity, from (2.49b) we find an estimate for the growth rate at large Prandtl number:

$$\sigma \sim \frac{\kappa}{d^2} \frac{\text{Ra} - \text{Ra}_c}{\text{Ra}_c}. \quad (2.50)$$

We note that this growth rate, the scale of which is the thermal diffusion time d^2/κ , is proportional to the distance from threshold $\text{Ra} - \text{Ra}_c$.

Rayleigh (1916a) thought that his calculation would explain the observations made by Bénard (1900) of convection cells on thin layers of a liquid heated from below and open to air at the top. It was later realized that the instability which Rayleigh had found did not correspond to the situation studied by Bénard, because the liquid layer was too thin and the dynamics involved surface tension. In those experiments the instability is due not to the Archimedes force but to the surface tension gradients generated by temperature nonuniformities of the free surface. This instability is discussed in the following section.

⁹ Here we note that the pressure gradient has the same scaling as the viscous force, as in all low Reynolds number Stokes flows. A well-known example is the force on a sphere in Stokes flow, where the two contributions are exactly equal to $3\pi\mu av$.

John William Strutt, Lord Rayleigh (1842–1919)

John William Strutt, son of the second Baron Rayleigh of Terling Place, Witham, was born in Langford Grove, Essex, England. He studied at Cambridge under the mathematician Edward Routh, and was strongly influenced by George G. Stokes. His first paper was inspired by Maxwell's 1865 paper on electromagnetic theory. He was elected a Fellow of Trinity College, Cambridge in 1866. In 1871 he published his theory of light scattering, which was the first correct explanation of why the sky is blue.

After a serious illness, he traveled to Egypt in 1872 with his wife and spent several months sailing down the Nile, during which time he began writing a major text, *The Theory of Sound*, later published in 1877 (Volume 1) and 1878 (Volume 2). He became the third Baron Rayleigh after the death of his father in 1873 and set up his laboratory in the family home. In 1873 he was elected a Fellow of the Royal Society, and in 1879 he succeeded Maxwell as Cavendish professor of experimental physics at Cambridge. One of his important pieces of experimental work was the standardization of the ohm. In 1884 he resigned his Chair at Cambridge and returned to his research on his own estate at Terling. He received honors from many learned societies, and served as scientific advisor to various maritime and aeronautical associations. He became chancellor of Cambridge University in 1908. He corresponded widely with many of the leading scientists of the time. His scientific output was large: 446 publications on physics and applied mathematics, sometimes on unusual subjects such as *Insects and the colour of flowers* (1874), *On the irregular flight of a tennis ball* (1877), *The soaring of birds* (1883), and *The problem of the Whispering Gallery* (1910). Note should also be made of his 1879 paper on traveling waves, which later developed into the theory of solitons, and his 1885 paper on waves propagating along the plane surface of an elastic solid, which play a major role in seismology. He made important contributions to hydrodynamics, especially to similarity and stability of flows. In 1895, while performing experiments to measure the density of nitrogen, he discovered argon (the name was taken from the Greek word for inactive): two measurement methods had led to a tiny difference (one part in a thousand!), which Rayleigh could not ignore (*It is a good rule in experimental work to seek to magnify a discrepancy when it first appears rather than to follow the natural instinct of trying to get rid of it. What was the difference between the two kinds of nitrogen?*) This work earned him a Nobel Prize in 1904. He donated the proceeds of his Prize to the University of Cambridge.

2.6 The Bénard–Marangoni thermocapillary instability

2.6.1 Description

When a thin layer of liquid open to the air is heated by the plate on which it rests, an instability arises in the form of convection cells, which are generally hexagonal as shown in Figures 2.16 and 2.17. It should be observed in Figure 2.16 how the hexagonal cells adapt themselves to a circular boundary, and also how a flower-like imperfection is formed, at the right center, owing to a tiny perturbation on the lower copper plate. This convection phenomenon, discovered and studied by Bénard (1900), resembles the Rayleigh–Bénard instability described above in that it occurs in a heated liquid, but its physical origin is different: it originates not with the buoyant force, but from gradients of the surface tension due to temperature nonuniformities. Thus the presence of a free surface is essential. This thermocapillary instability is now associated with the name of the Italian physicist Carlo Marangoni (1871), who noticed that a surface tension gradient induced by a temperature gradient or a concentration gradient in an aqueous solution can generate fluid motion, a phenomenon now known as the Marangoni effect (Probstein, 2003). The correct interpretation of the Bénard experiments is due to Pearson (1958).

Since the mechanism of this thermocapillary instability is associated with the variation of the surface tension with temperature, we need to describe this variation. For a liquid in equilibrium with its vapor or with air, the following approximate equation of state is well satisfied over a large temperature range (Rocard, 1967):

$$\gamma = \gamma_0 \left(1 - \frac{1.03 T}{T_c} \right), \quad (2.51)$$

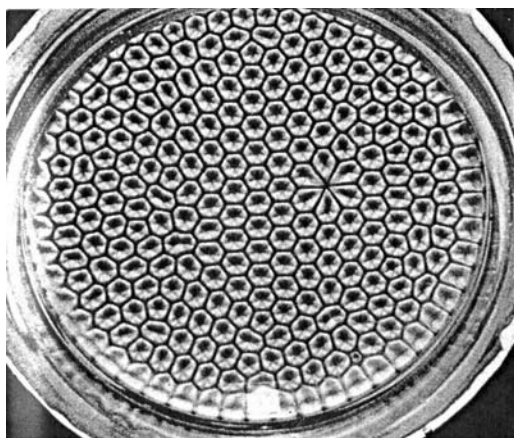


Figure 2.16 Thermocapillary convection cells in a thin layer of silicone oil of viscosity $0.5 \text{ cm}^2/\text{s}$. Photograph by Koschmieder (1974), taken from van Dyke (1982).

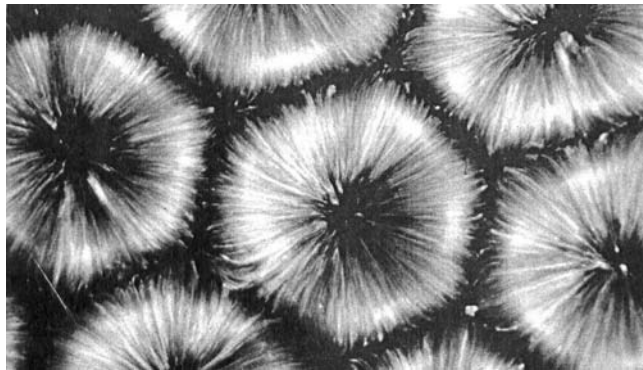


Figure 2.17 View from above of thermocapillary convection cells in a layer of silicone oil 1 mm thick with air on top of it. The light reflected by the aluminum particles shows the fluid climbing in the center of the hexagonal cell and descending at its edges. The exposure time is 10 seconds, and the fluid crosses the cell from the center to the edge in 2 seconds. The cell dimension is 3.6 mm. Photograph by Velarde *et al.*, taken from van Dyke (1982).

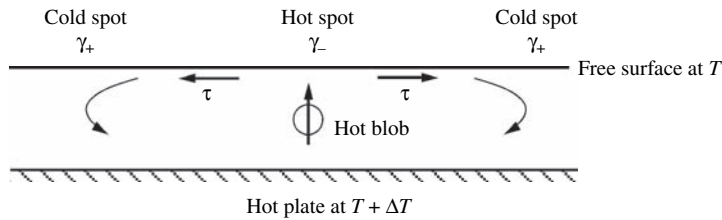


Figure 2.18 Fluid motion induced in a liquid film by a surface tension gradient.

where T_c is the critical temperature of the fluid and γ_0 is a surface tension determined from a known value of γ at a given temperature. This law therefore indicates that the surface tension decreases linearly with temperature, which holds down to very close to the critical point (at which the surface tension vanishes). Thus, temperature nonuniformities on an interface give rise to surface tension gradients. A fluid particle located on the interface is pulled more strongly in the direction where the tension (temperature) is higher (lower), and this results in a surface current of warm points moving toward cold points (Figure 2.18). Some of the warmer fluid then rises to replace the fluid which has flowed away, so that the effect amplifies the cause, hence causing the instability.

2.6.2 Dimensional analysis

We can obtain the dimensionless number that governs the problem using arguments similar to those we made for the Rayleigh–Bénard instability. The situation is depicted in Figure 2.18: a fluid layer of thickness d , viscosity μ , and thermal

diffusivity κ is subject to a temperature difference $\Delta T > 0$ between the lower plate and the free surface. Now consider a fluctuation in the form of a fluid upwelling that brings a patch of hot fluid to the surface. This will raise the temperature there by an amount on the order of ΔT relative to the undisturbed surface temperature. The warmer fluid will have a lower interfacial tension relative to the colder point on the surface (where the fluid must down-well in order to conserve mass). The scaling estimates that follow can be developed with the wavelength of the convection, λ , different from the depth, d , but for simplicity we take these length scales to be the same order of magnitude.

The temperature gradient results in a horizontal Marangoni shearing stress,

$$\tau \sim \frac{d\gamma}{dx} \sim \gamma' \frac{\Delta T}{d}.$$

The tangential force (per unit length in the direction perpendicular to the plane) due to the applied Marangoni stress is therefore

$$F_\gamma \sim \gamma' \Delta T.$$

The question is now whether the viscous drag on the blob and diffusion of temperature are both small enough to allow a sustained circulation driven by the Marangoni stress produced by the initial upwelling. The viscous drag per unit length is

$$F_\mu \sim \mu |\nabla^2 \mathbf{u}| d^2 \sim \mu u.$$

If the convection is to be self-sustaining the convection of energy must compete with thermal diffusion, i.e.

$$\mathbf{u} \cdot \nabla T \sim \kappa \nabla^2 T,$$

from which we determine the velocity scale as

$$u \sim \kappa/d.$$

Eliminating the velocity, the ratio of the driving force to the retarding force becomes

$$\frac{F_\gamma}{F_\mu} \sim \frac{\gamma' \Delta T d}{\kappa \mu} = \text{Ma}. \quad (2.52)$$

This dimensionless number is known as the Marangoni number, and governs a variety of thermocapillary flows. The review of Schatz and Neitzel (2001) can be consulted for a more complete analysis of this and other thermocapillary instabilities.

2.7 Discussion

2.7.1 Characteristic scales and mode selection

Our discussion of various instabilities has demonstrated the importance of the characteristic scales in a problem. We have shown that the size of the structure or *pattern* selected by the instability often corresponds to the characteristic length scale. In the same way, the growth rate of the instability is often given by a characteristic time in the problem. Dimensional analysis is therefore an essential component of any stability study. However, when a problem presents several different characteristic length or time scales, it becomes difficult to tell which of them is important for the instability, and simple arguments must be replaced by detailed calculations based on the governing equations. Dimensional analysis can again become useful in the limit where one scale is much smaller than another, so that certain variables play a passive role (as in the discussion above on the velocity being slaved to temperature in Rayleigh–Bénard instability at large Prandtl number).

An important element in the structure selection is the size of the region in which the instability can develop. For example, for the Rayleigh–Bénard instability the size of the cells is determined by the spacing of the horizontal surfaces, but it can also be influenced by the side walls if they are sufficiently close, say two or three cell sizes away. Conversely, if the side walls are very far away they will have little effect on the cell size; then nonuniformities in the structure, such as modulations or defects, can arise; these will be studied in Chapters 9 and 10.

2.7.2 General characteristics of a threshold instability

Many of the instabilities encountered in this chapter, like the thermal and thermo-capillary instabilities, are *threshold instabilities* governed by a *control parameter* denoted generally as R . The critical value of this parameter R_c marking the destabilization of a marginal wave number k_c reflects the inversion of the relative strengths of a stabilizing phenomenon and a destabilizing one. Some general properties of a threshold instability can be derived by means of a Taylor series expansion of the instability growth rate near the critical point (k_c, R_c) (assuming that the dispersion relation is analytic in the neighborhood of this point, which is generally the case). Truncating the series after the first few terms, we find

$$\sigma(k, R) = \frac{\partial \sigma}{\partial R}(k_c, R_c)(R - R_c) + \frac{1}{2} \frac{\partial^2 \sigma}{\partial k^2}(k_c, R_c)(k - k_c)^2, \quad (2.53)$$

where we have taken into account the fact that at marginal stability the curve $\sigma(k)$ is tangent to the axis $\sigma = 0$ (Figure 2.19a), which implies that $\sigma(k_c, R_c) = 0$ and

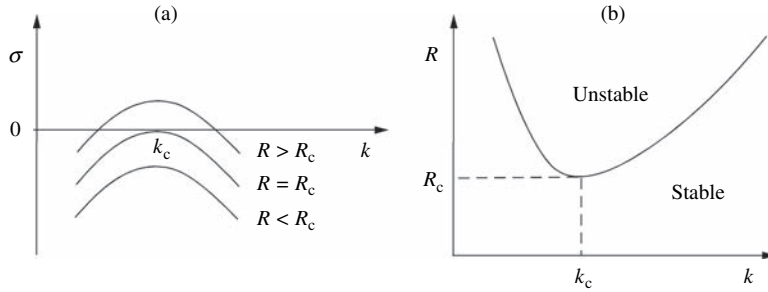


Figure 2.19 (a) Growth rate $\sigma(k)$ for $R < R_c$, $R = R_c$, and $R > R_c$; (b) parabolic shape of the marginal stability curve $\sigma(k, R) = 0$ near threshold (k_c, R_c) .

$\partial_k \sigma(k_c, R_c) = 0$. We have also used the fact that the omitted second derivatives are negligible because $R - R_c \sim (k - k_c)^2$, as we shall see below.

From the expression (2.53) we can find the form of the growth rate $\sigma(k)$ in the three cases of stable flow ($R < R_c$), marginal flow ($R = R_c$), and unstable flow ($R > R_c$) (Figure 2.19a). Equation (2.53) can also be used to show that the shape of the marginal stability curve $\sigma(k, R) = 0$ near threshold is parabolic (Figure 2.19b):

$$R - R_c = -\frac{1}{2} \frac{\partial_{kk} \sigma(k_c, R_c)}{\partial_R \sigma(k_c, R_c)} (k - k_c)^2.$$

Equation (2.53) shows that the growth time τ of an unstable wave number near k_c , which we define as the inverse growth rate σ , diverges as $1/(R - R_c)$ near threshold. Therefore, the closer to threshold, the longer it takes for the instability to manifest itself. Finally, we note that the experimental study of a threshold instability requires that the control parameter R vary sufficiently slowly – in a quasi-static fashion – so that the flow can at any instant be considered to be in equilibrium. More precisely, the characteristic time for variation of the control parameter should be larger than the relaxation time of the flow (which is, for example, of order d^2/κ for a thermal diffusion problem). This time must also be short compared to the growth time, otherwise the instability would develop on a nonstationary flow.

2.8 Exercises

2.8.1 Rayleigh–Taylor instability between walls

Consider two fluids of density ρ_1 and ρ_2 at rest in the gravity field, separated by a horizontal flat interface with surface tension γ . We want to solve the inviscid stability problem for two-dimensional disturbances in the vertical plane, using the stream function ψ defined from the velocity perturbations as $u = \partial_y \psi$, $v = -\partial_x \psi$.

1. Show that in the case of unbounded layers (infinite depths), the dispersion relation is given by (2.40).
2. For bounded layers of thicknesses h_1 and h_2 , show that the dispersion relation is

$$c^2(\rho_1 \coth kh_1 + \rho_2 \coth kh_2) - [(\rho_1 - \rho_2)g/k + \gamma k] = 0.$$

3. Compare the cases of finite and infinite depths: is the band of unstable wave numbers different? How does the growth rate vary for k small? The solution can be found in Milne-Thompson (1968).

2.8.2 Instability of a suspended thin film

Consider a thin liquid film of thickness h , viscosity μ , and density ρ , applied to the underside of a horizontal wall in the gravity field $\mathbf{g} = -g\mathbf{e}_y$. We shall study the stability of this film to two-dimensional perturbations in the vertical plane (x, y) . The free surface of the unperturbed film is defined by $y = 0$ (the surface to which the film is applied is therefore at $y = h$), and so the pressure is $\bar{P} = P_0 - \rho gy$, where P_0 is the air pressure under the film.

We study perturbations of wavelength large compared to the film thickness ($kh \ll 1$) ($\partial_x u + \partial_y v = 0$ implies that $v \sim (kh)u \ll u$, so that the flow is quasi-parallel), and we also assume that the flow is quasi-static, that is, it adapts very rapidly to the boundary conditions: time enters only through the condition at the deformed free surface $\eta(x, t) = \hat{\eta} e^{i(kx - \omega t)} + \text{c.c.}$

1. Show that the linearized equations for perturbations of the base state are

$$0 = -\partial_x p + \mu \partial_{yy} u, \quad 0 = -\partial_y p.$$

2. We recall that the components of the stress tensor of a Newtonian fluid are given by $\sigma_{ij} = -P\delta_{ij} + \mu(\partial_{x_j} U_i + \partial_{x_i} U_j)$. Assuming that the air under the film imposes only its pressure P_0 (the free surface condition), show that, after linearization about $y = 0$, the boundary conditions tangential and normal to the free surface $y = \eta(x, t)$ can be written as

$$\partial_y u = 0, \quad p - \rho g \eta = \gamma \partial_{xx} \eta.$$

3. Using the boundary conditions at $y = h$ and at the free surface, find the speed u as a function of the pressure gradient $\partial_x p$.
4. Determine the speed v as a function of the pressure gradient $\partial_x p$.

5. Using the kinematic condition at the interface, derive the following expression for the growth rate of the perturbations:

$$\omega_i = \frac{1}{\tau} (kh)^2 (1 - (kl_c)^2), \quad \tau = \frac{3\mu}{\rho gh}, \quad l_c = \sqrt{\frac{\gamma}{\rho g}}.$$

Comment on the result.

2.8.3 Rayleigh–Plateau instability on a wire

An annular thin fluid layer deposited on a wire is unstable and leads to the formation of isolated drops (Figure 2.20a). The droplets that can be seen on spider webs (see Figure 2.20b) result from this instability, where the initial water layer arises from vapor condensation. This instability is due to surface tension, in a manner analogous to the instability of a cylindrical column studied in Section 2.4 (Quéré, 1999).

We consider here the quasi-static problem of a thin viscous film of thickness $h + \eta$, where h is the thickness of the undisturbed annular film and $\eta(x, t)$ an axisymmetric disturbance, on a wire of radius a .

1. Show in the limit of small thickness ($h \ll a$) and ignoring gravity that the equations governing the evolution of the velocity and pressure perturbations of the film are given by

$$-\frac{\partial p}{\partial x} + \mu \frac{\partial^2 u}{\partial r^2} = 0, \quad p = p(x), \quad v = \int_0^r u \, dr.$$

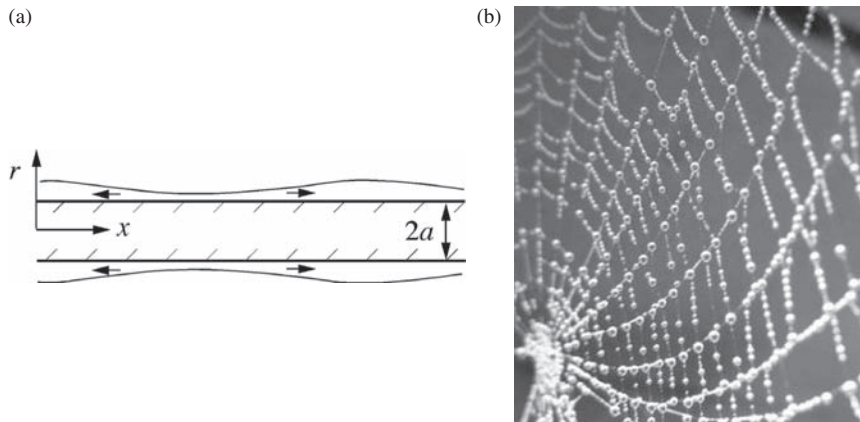


Figure 2.20 (a) Sketch of the Rayleigh–Plateau instability on a wire of diameter $2a$; (b) water drops on a spider web (photograph M. Charru).

Also show that the relevant boundary conditions are no-slip, $u = v = 0$, on the wire at $r = a$, and the following linearized conditions at the free surface at $r = a + h$:

$$\mu \frac{\partial u}{\partial r} = 0, \quad p = \gamma \left(-\frac{\eta}{a^2} - \frac{\partial^2 \eta}{\partial x^2} \right).$$

2. Introducing time-independent normal modes except for η (which is the same quasi-static approximation as in the previous exercise), show that the growth rate of the disturbances is

$$\sigma = \frac{1}{\tau} \left(\frac{h}{a} \right)^3 (ka)^2 (1 - (ka)^2), \quad \tau = \frac{3\mu a}{\gamma}.$$

3. Discuss the stability, and in particular determine the most amplified and the cutoff wave numbers.

2.8.4 Stability of a planar front between two fluids in a porous medium

When a viscous fluid 2 is pushed by another less viscous fluid 1 in a porous medium or in a Hele–Shaw cell (Figure 2.21), the initially rectilinear front is unstable to the growth of fingers, as shown in Figure 2.22. This phenomenon is known as “viscous fingering” (Homsy, 1987). We want to determine the linear stability condition of the horizontal front between the two fluids (Saffman and Taylor, 1958). The motion of each fluid is governed by the Darcy equation

$$\mathbf{U}_j = -\frac{K}{\mu_j} \mathbf{grad}(P_j + \rho_j gy), \quad j = 1, 2, \quad (2.54)$$

where ρ_j and μ_j are the density and viscosity of fluid j , and K is the permeability, assumed uniform, of the porous medium. The thickness of the front is assumed to be negligible compared to the other characteristic lengths of the problem. Viscous

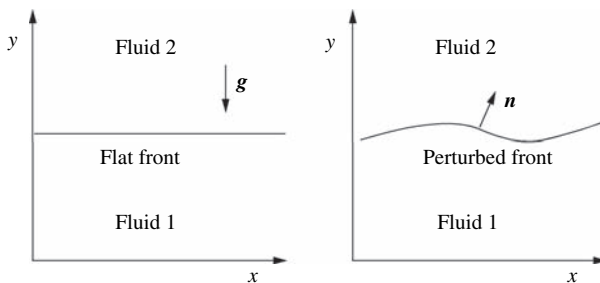


Figure 2.21 Front between two viscous fluids in a porous medium or a Hele–Shaw cell.

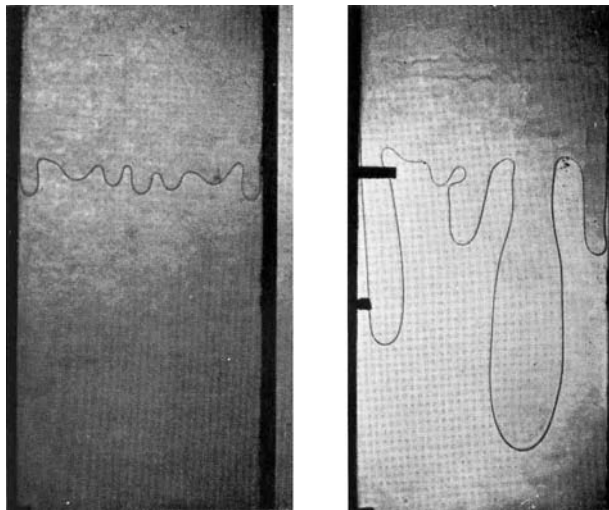


Figure 2.22 Two different stages of the growth of the Saffman–Taylor instability in a vertical Hele–Shaw cell, at the interface between glycerin pushed down by air above. The cell cross-section is $0.9\text{ mm} \times 120\text{ mm}$ and the descending speed of the front is $V \approx 1\text{ mm/s}$ (Saffman and Taylor, 1958).

stresses are negligible compared to pressure, and we also neglect surface tension, leaving only a pressure continuity condition at the front between the fluids.

1. Using the Darcy equation, show that there exists a velocity potential Φ_j and find the equation it satisfies.
2. Show that the problem has the basic solution

$$\overline{\Phi}_j = Vz, \quad \overline{P}_j = -\left(\frac{\mu_j V}{K} + \rho_j g\right)z + P_0(t), \quad (2.55)$$

where V is the uniform velocity of ascension of the fluids, $z = y - Vt$ is the distance to the unperturbed front, and $P_0(t)$ is a reference pressure on the front.

3. Determine the linearized equations for small perturbations of the potential, $\phi_j(x, z, t)$, pressure, $p_j(x, z, t)$, and front position, $h(x, t)$, i.e., the mass conservation and Darcy equations and the boundary conditions (i) at $z = \pm\infty$ and (ii) on the front (continuity of the normal velocity and the pressure, and impermeability of the front).
4. Introduce perturbations proportional to $\exp(ikx + \sigma t)$ with k real. Justify the chosen form, state the meaning of k and σ , and write down the system of equations satisfied by the amplitudes of the perturbations. Solve this system

and derive the dispersion relation

$$\sigma = k \frac{K}{\mu_1 + \mu_2} \left(\frac{\mu_2 - \mu_1}{K} V + (\rho_2 - \rho_1) g \right). \quad (2.56)$$

5. Sketch the possible shapes of $\sigma(k)$ for $\rho_1 = \rho_2$, and then for $\rho_1 \neq \rho_2$. Comment on this. Is the divergence of $\sigma(k)$ at large k physical? Beyond what order of magnitude of wave number is the model no longer valid?
6. We want to extract oil ($\rho_2 = 900 \text{ kg/m}^3$, $\mu_2 = 0.1 \text{ Pa}\cdot\text{s}$) from a porous medium of permeability $K = 10 \text{ Darcys}$ ($1 \text{ Darcy} = 10^{-12} \text{ m}^2$) by injecting water to the bottom of a well ($\rho_1 = 1000 \text{ kg/m}^3$, $\mu_1 = 10^{-3} \text{ Pa}\cdot\text{s}$). Beyond what speed is the flow unstable? For a speed of 1 cm/s, how long does it take for the amplitude of a perturbation of wave number $k = 1 \text{ cm}^{-1}$ to be multiplied by 10?

We finally note that a similar analysis is possible for the “printer’s instability.” Consider counter-rotating horizontal cylinders immersed in a bath of viscous liquid. The rotation of the cylinders entrains thin films of fluid which cover the cylinders. The film with uniform thickness appears to be unstable, showing periodic variations of its thickness along the cylinder axes (Rabaud *et al.*, 1990; Couder, 2000). This instability can be interpreted as a Saffman–Taylor instability in a wedge (Ruschak, 1985).

2.8.5 The Darrieus–Landau instability of a flame front

The front of the flame separating premixed, gaseous reactants, from burnt gas can be unstable. This instability has been studied theoretically by Darrieus (1938) and later by Landau (1944), and has been displayed in a well-controlled experiment by Clanet and Searby (1998). On the left of Figure 2.23 is the experimental setup. An air–propane mixture is injected into the bottom of a vertical tube, and the burnt gas escapes from the top. The planar flame front is excited by an acoustic wave generated by a loudspeaker, and its position is recorded by a fast camera. The amplification with time of the front perturbation selected by the excitation is seen in the photographs shown on the right.

The situation is shown schematically in Figure 2.24. The equations governing the problem admit a stationary solution in a reference frame attached to the planar front, with uniform velocities \bar{U}_1 at the upstream end and \bar{U}_2 at the downstream end. We make the following assumptions about the perturbed flow (Landau and Lifshitz, 1987, §128; Joulin and Vidal, 1998):

- the flow is incompressible on each side of the front, and viscous effects can be neglected;
- the density of each gas remains uniform, with $\rho_1 > \rho_2$;

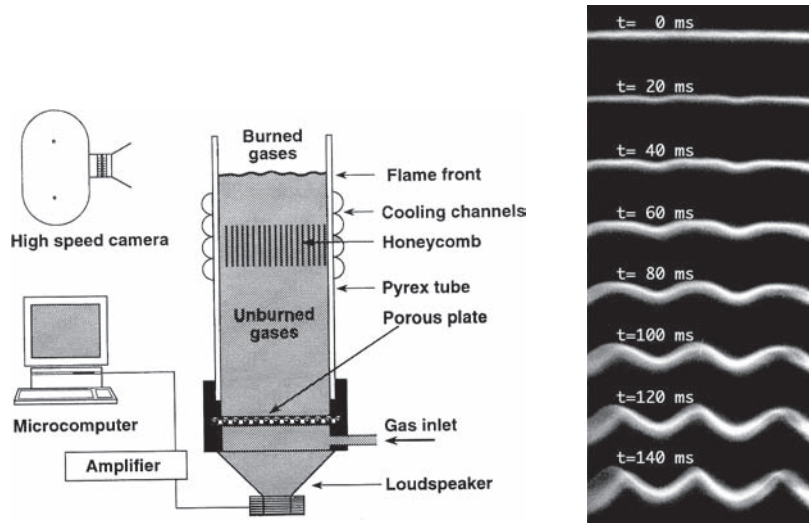


Figure 2.23 Experimental demonstration of the Darrieus–Landau instability. Figure reprinted with permission from Clanet and Searby (1998). ©1998 by the American Physical Society. Left: schematic view of the setup. Right: growth with time of the eigenmode selected by the excitation.

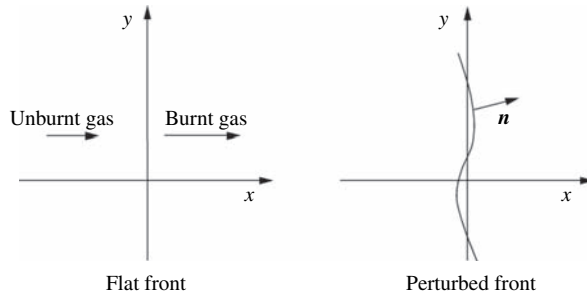


Figure 2.24 Flow through a planar flame front and a perturbed flame front.

- the relative local speed U_L of the flame front relative to the incoming reactants (a few meters per second) is constant;
- the thickness of the flame front (less than one millimeter) is very small compared to the wavelength of the perturbations.

The equations governing the problem are therefore the Euler equations:

$$\operatorname{div} \mathbf{U}_j = 0, \quad (2.57a)$$

$$\rho_j (\partial_t \mathbf{U}_j + (\mathbf{U}_j \cdot \mathbf{grad}) \mathbf{U}_j) = -\mathbf{grad} P_j, \quad j = 1, 2. \quad (2.57b)$$

The boundary conditions are decay of the perturbations at infinity both upstream and downstream, along with the following jump conditions at the flame front $x = \eta(y, t)$:

$$\rho_1(\mathbf{U}_1 - \mathbf{w}) \cdot \mathbf{n} = \rho_2(\mathbf{U}_2 - \mathbf{w}) \cdot \mathbf{n}, \quad (2.58a)$$

$$P_1 + \rho_1((\mathbf{U}_1 - \mathbf{w}) \cdot \mathbf{n})^2 = P_2 + \rho_2((\mathbf{U}_2 - \mathbf{w}) \cdot \mathbf{n})^2, \quad (2.58b)$$

$$\mathbf{U}_1 \times \mathbf{n} = \mathbf{U}_2 \times \mathbf{n}, \quad (2.58c)$$

$$(\mathbf{U}_1 - \mathbf{w}) \cdot \mathbf{n} = U_L. \quad (2.58d)$$

Defining the position of the front as $H(x, y, t) = x - \eta(y, t) = 0$, the normal \mathbf{n} and the normal velocity $\mathbf{w} \cdot \mathbf{n}$ at the front are obtained from (2.30) and (2.31).

1. State the physical meaning of the four jump conditions listed above. Sketch a streamline which crosses the front obliquely. By analogy with geometrical optics, what should this phenomenon be called?
2. Show that the base flow given by

$$\bar{U}_1 = U_L,$$

$$\bar{U}_2 = \frac{\rho_1}{\rho_2} U_L,$$

$$\bar{P}_2 = \bar{P}_1 + \rho_1 \bar{U}_1^2 - \rho_2 \bar{U}_2^2,$$

satisfies the conservation equations and jump conditions.

3. Write down the linearized equations for small perturbations of the base flow.
4. Introduce perturbations in the form of normal modes proportional to $\exp(iky + \sigma t)$ with k real. Justify the choice of this form, give the meaning of k and σ , and write down the system of equations satisfied by the amplitudes of the normal modes.
5. Find the general solution for the amplitudes of the normal modes, taking into consideration their decay at infinity upstream and downstream (in anticipation choose $\sigma > 0$, a hypothesis to be verified at the end of the calculation).
6. Write the system of four algebraic equations corresponding to the jump conditions at the flame front, and show that the dispersion relation can be written as

$$(1+r)\sigma^2 + 2rkU_L\sigma + r(1-r)k^2U_L^2 = 0 \quad (2.60)$$

where $r = \rho_1/\rho_2$.

7. Discuss the type of the eigenvalues and sketch the shape of $\sigma(k)$. Is the divergence of $\sigma(k)$ at large k physical? What is the length scale, not taken into account in the above model, below which the model is no longer valid?

3

Stability of open flows: basic ideas

3.1 Introduction

In this chapter we begin our study of the stability of flows. We start by making our discussion of linear stability introduced in Chapter 2 more precise (Section 3.1). The approach for deciding whether a flow is stable or unstable on the basis of temporal normal modes is justified by studying the spatio-temporal evolution of an arbitrary perturbation (Section 3.2). In the case of open flows, where a perturbation never passes the same point more than once (in contrast to closed flow such as Couette flow between two cylinders), we distinguish two types of instability: convective and absolute (Section 3.3). The ideas introduced in a rather abstract way in this chapter will be illustrated more concretely in the following chapters.

3.1.1 Linear dynamics of a wave packet

We have seen that in many cases, normal mode analysis admits the possibility of stable or unstable propagating waves. Here we shall derive some classical results on the propagation of a packet of dispersive waves for the special case of a Gaussian packet. A more general discussion can be found in, for example, Lighthill (1978, §3.7). We consider a wave represented by the integral of its spatial Fourier components

$$u(x, t) = \frac{1}{2} \int_{-\infty}^{+\infty} \hat{u}(k) e^{i(kx - \omega(k)t)} dk, \quad (3.1)$$

where the wave number k and frequency $\omega(k)$ are real and $\hat{u}(k)$ is the spectrum of the wave packet.¹ Assuming that the waves propagate at positive speed $c = \omega/k$, we choose the corresponding branch of the dispersion relation, namely, the one for

¹ This spectrum does not correspond exactly to the Fourier transform of $u(x)$ owing to the factor of $1/\pi$ which for convenience we have omitted from (3.1).

which $\omega(k)$ has the same sign as k . Then, using the relation $\hat{u}(-k) = \hat{u}^*(k)$, the above integral can be rewritten as

$$u(x, t) = \frac{1}{2} \int_0^{+\infty} \hat{u}(k) e^{i(kx - \omega(k)t)} dk + \text{c.c.} \quad (3.2)$$

For x large and x/t fixed, this integral can be evaluated using the method of stationary phase.² It can also be evaluated directly in the case of a Gaussian spectrum of width σ^{-1} centered on a wave number k_0 (Figure 3.1a), i.e.

$$\hat{u}(k) = \hat{u}_0 e^{-\sigma^2(k-k_0)^2}, \quad k > 0. \quad (3.3)$$

A Gaussian spectrum is typical of many experimental situations and leads to simple calculations of the wave evolution: in particular, the Fourier transform of a Gaussian is also a Gaussian. The wave (3.2) can also be written as a traveling wave of wave number k_0 and frequency $\omega_0 = \omega(k_0)$:

$$u(x, t) = \frac{1}{2} A(x, t) e^{i(k_0 x - \omega_0 t)} + \text{c.c.} \quad (3.4)$$

where $A(x, t)$ is the envelope of the wave packet, defined as

$$A(x, t) = \int_0^{\infty} \hat{u}(k) e^{i(k-k_0)x - i(\omega-\omega_0)t} dk. \quad (3.5)$$

This envelope depends on space and time, and so it differs from the amplitude of a Fourier mode, which can depend on time but is spatially uniform.

The wave envelope at the initial time

Setting $v = \sigma(k - k_0 - ix/2\sigma^2)$, the argument of the exponential inside the integral (3.5) can be written at the initial time $t = 0$ as

$$-\sigma^2(k - k_0)^2 + i(k - k_0)x = -v^2 - \frac{x^2}{4\sigma^2}. \quad (3.6)$$

² We consider the integral $I(x) = \int_{k_1}^{k_2} f(k) e^{ix\psi(k)} dk$. When there exists a number k_0 inside the integration range such that $\psi^{(p)}(k_0) \neq 0$ but $\psi'(k_0) = \dots = \psi^{(p-1)}(k_0) = 0$ with $f(k_0) \neq 0$, then for x large (Bender and Orszag, 1978, §6.5)

$$I(x) \sim 2f(k_0) \exp(ix\psi(k_0) \pm i\pi/2p) \left(\frac{p}{x|\psi^{(p)}(k_0)|} \right)^{1/p} \frac{\Gamma(1/p)}{p},$$

where we use the factor $e^{i\pi/2p}$ if $\psi^{(p)}(k_0) > 0$, or the factor $e^{-i\pi/2p}$ if $\psi^{(p)}(k_0) < 0$. The usual case corresponds to $p = 2$, for which $\Gamma(1/2) = \sqrt{\pi}$.

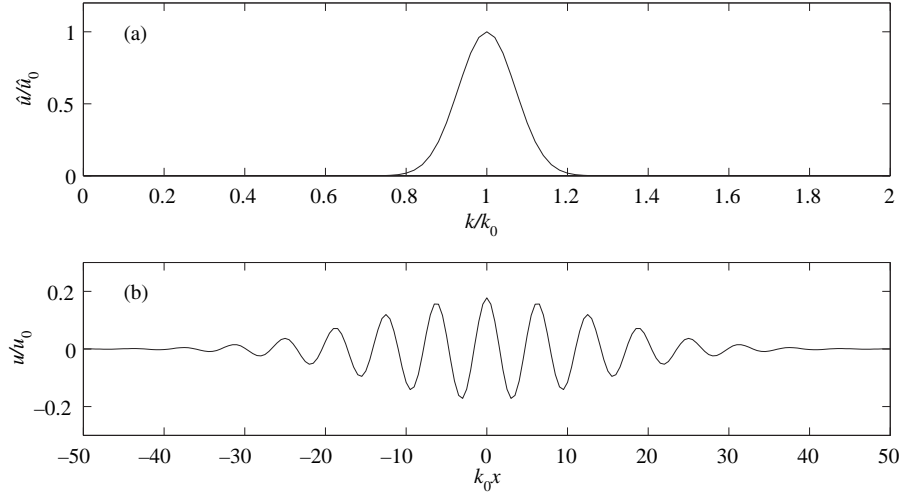


Figure 3.1 (a) Gaussian spectrum of width $\sigma^{-1} = 0.1k_0$; (b) the corresponding wave.

We then find the expression for the envelope $A(x, t)$ at $t = 0$:

$$A(x, 0) = \frac{\hat{u}_0}{\sigma} e^{-\frac{x^2}{4\sigma^2}} \int_0^\infty e^{-v^2} dv = \frac{\hat{u}_0 \sqrt{\pi}}{2\sigma} e^{-\frac{x^2}{4\sigma^2}}, \quad (3.7)$$

where we have used the classical result

$$\int_{-\infty}^\infty e^{-v^2} dv = \sqrt{\pi}.$$

The envelope of a Gaussian wave packet is therefore a Gaussian whose width is larger the narrower the peak of the spectrum, and we recover the classical result for the Fourier transform (Figure 3.1b). In particular, a spectrum which is infinitesimally narrow (a Dirac delta-function) corresponds to a sine wave.

Propagation of the wave packet

In the case of a quasi-monochromatic wave packet, i.e., a narrow spectrum centered at k_0 , the dispersion relation $\omega = \omega(k)$ can be expanded in a Taylor series about k_0 , which is then truncated after the first order:

$$\omega - \omega_0 = c_g(k - k_0), \quad c_g = \frac{\partial \omega}{\partial k}(k_0), \quad (3.8)$$

where c_g is the *group velocity* of the wave packet, which represents the speed of propagation of the wave number k_0 or the speed at which the energy of the packet propagates (Lighthill, 1978, §3.6). By a calculation identical to that which gave

(3.7), but with x replaced by $x - c_g t$, we find

$$A(x, t) = \frac{\hat{u}_0 \sqrt{\pi}}{2\sigma} e^{-\frac{(x-c_g t)^2}{4\sigma^2}}. \quad (3.9)$$

Therefore, to the leading order (3.8) of the Taylor expansion of the dispersion relation, the envelope of a quasi-monochromatic wave propagates at the group velocity without distortion.

Dispersion of the wave packet

We can go farther in our description of the evolution of a wave packet by expanding the dispersion relation $\omega = \omega(k)$ through second order:

$$\omega - \omega_0 = c_g(k - k_0) + \frac{\omega''_0}{2}(k - k_0)^2, \quad (3.10a)$$

$$c_g = \frac{\partial \omega}{\partial k}(k_0), \quad \omega''_0 = \frac{\partial^2 \omega}{\partial k^2}(k_0). \quad (3.10b)$$

By a calculation identical to that which gave (3.9), but with σ^2 replaced by $\sigma^2 + i\omega''_0 t/2$, we find

$$A(x, t) = \frac{\hat{u}_0}{2} \sqrt{\frac{\pi}{\sigma^2 + \frac{1}{2}i\omega''_0 t}} \exp\left(-\frac{(x-c_g t)^2}{4(\sigma^2 + \frac{1}{2}i\omega''_0 t)}\right). \quad (3.11)$$

This expression for the envelope (which is now complex) shows that at short times, i.e., times $t \ll \sigma^2/\omega''_0$, the wave packet propagates without significant dispersion (i.e., without flattening or spreading out), consistent with the previous result (3.9) obtained at the leading order. Dispersion is manifested after a time of order σ^2/ω''_0 , when the wave packet has traveled a distance of order $\sigma^2 c_g / \omega''_0$. Then, the width of the packet grows linearly with time, and its amplitude decreases as $1/\sqrt{t}$, as illustrated in Figure 3.2. The wave energy, which is proportional to the product of the squared amplitude and the width of the packet, therefore remains constant, consistent with the fact that we have neglected any dissipative phenomena. The spreading of the packet corresponds to the dispersion of the Fourier components of the packet: the wave numbers with higher speeds outrun the slower ones (see Exercise 3.4.1).

The above results remain valid for non-Gaussian spectra, provided the width $\delta k \sim 1/\sigma$ is small, or $\delta k/k_0 \ll 1$. In particular, the characteristic dispersion time and the distance traveled by the wave packet in that time can easily be obtained by considering the propagation of two adjacent wave numbers k_0 and $k_0 + \delta k$. Since the group velocity corresponds to the propagation speed of the wave number, the

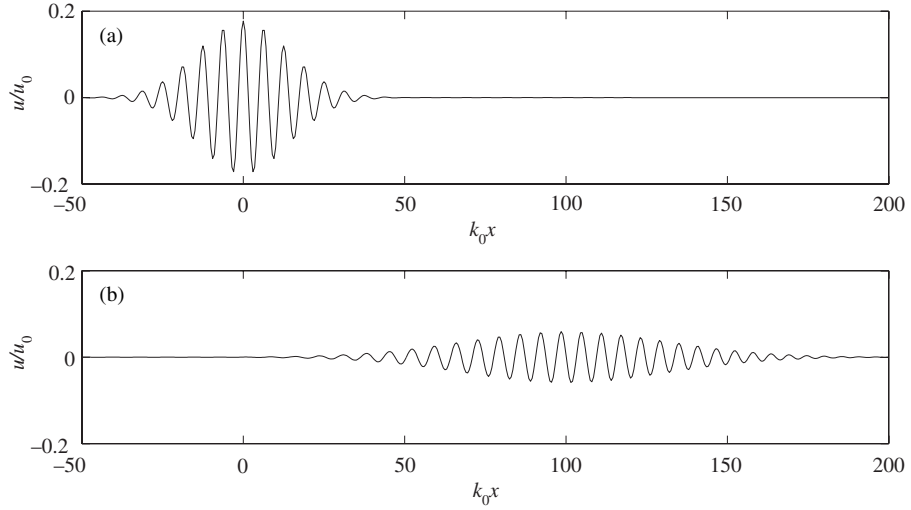


Figure 3.2 The wave corresponding to the envelope (3.11) for $\sigma^{-1}k_0 = 0.1$ and $\omega_0'' = 4c_g/k_0$ at (a) the initial time $t = 0$ and (b) $c_g t = 100/k_0$.

difference of the propagation speeds of these two wave numbers is $\delta c_g = \omega_0''(k_0)\delta k$. Defining the dispersion time as that needed for the separation between the two wave numbers to be $1/\delta k$, this time is $(1/\delta k)/\delta c_g = 1/\omega_0''\delta k^2$. This dispersion time is of the same order as that of the Gaussian spectrum, $\sigma^2 c_g / \omega_0''$. This type of analysis of the characteristic scales forms the basis for nonlinear analyses in Chapters 9 and 10.

3.1.2 Stability in the Lyapunov sense, asymptotic stability

Here we give a precise definition of the stability of a flow or “base state” $U_0(x, t)$ satisfying the equations governing the problem. This base state is termed *Lyapunov stable* if a small perturbation remains small as time progresses, that is if the perturbed state $U(x, t)$ remains close to the base state. The formal definition is the following.

Definition 3.1 A base state $U_0(x, t)$ is termed *Lyapunov stable* if for all positive ϵ there exists $\delta(\epsilon)$ such that if $\|U(x, 0) - U_0(x, 0)\| \leq \delta$, then $\|U(x, t) - U_0(x, t)\| \leq \epsilon$ for all $t \geq 0$, where the norm $\|\dots\|$ in the physical space E is defined as

$$\|U(x, t) - U_0(x, t)\| = \max |U(x, t) - U_0(x, t)|, x \in E. \quad (3.12)$$

If, in addition, a Lyapunov stable system decays to its base state, the system is termed *asymptotically stable*, as defined below.

Definition 3.2 A base state $U_0(x, t)$ which is Lyapunov stable is termed *asymptotically stable* if there exists a δ such that if $\|U(x, 0) - U_0(x, 0)\| \leq \delta$, then

$$\lim_{t \rightarrow \infty} \|U(x, t) - U_0(x, t)\| = 0. \quad (3.13)$$

The simplest example is the harmonic oscillator: without damping, it is Lyapunov stable, but not asymptotically stable; with damping, it is asymptotically stable. However, except for elementary examples such as the harmonic oscillator, it is not possible to determine the stability of a particular base state by directly verifying the above definitions! It is therefore essential to find stability criteria that are easier to verify, and that is the goal of this chapter. The first step is to study the linear stability, that is, the evolution of a perturbation given by the equations linearized about the base state. The linearization procedure allows us to determine whether the state is stable or unstable, provided the parameter values do not correspond to a bifurcation, as discussed in Chapter 1. Strictly speaking, the results of a linear stability analysis are valid only for perturbations of infinitesimal amplitude. In practice, the predictions of a linear stability analysis are generally valid for perturbations of relative amplitude from 1% to 10%. Therefore, a linearly stable base state is expected to be also Lyapunov stable.

A third stability definition, namely, that of *global* stability, is useful in the case where the flow returns to its base state for any perturbation amplitude, i.e., without regard for the magnitude of δ .

Definition 3.3 A base state $U_0(x, t)$ is globally stable if it is asymptotically stable for arbitrary δ . In other words, the basin of attraction of the base flow coincides with the entire phase space.

3.1.3 Linear stability and instability

We shall illustrate the ideas introduced in this chapter using the Ginzburg–Landau equation with real coefficients:

$$\partial_t u + V \partial_x u = Ru + \partial_{xx} u - |u|^2 u, \quad (3.14)$$

where $u(x, t)$ is a complex scalar field and R and V are two parameters. This equation models the behavior of many physical systems (Cross and Hohenberg, 1993). Here we need only note that the left-hand side of the equation has the structure of a total derivative, implying an advection speed V , and that the right-hand side contains a linear term involving the control parameter R , a diffusion term, and a nonlinear term. This equation has a base solution $u_0 = 0$ which is invariant under translations in x and t , as is the complete equation (3.14).

Linearizing (3.14) about the base state $u_0 = 0$ (which here amounts simply to neglecting the nonlinear term $|u|^2 u$), we obtain the evolution equation for the perturbation which is written in operator form as

$$Lu(x, t) = 0 \quad \text{with} \quad L = \partial_t + V \partial_x - R - \partial_{xx}. \quad (3.15)$$

If the base state is perturbed by a given forcing function $S(x, t)$, the perturbation evolves according to the equation

$$Lu(x, t) = S(x, t). \quad (3.16)$$

Three elementary forcing functions are of special importance:

$$S(x, t) = F(x)\delta(t), \quad (3.17a)$$

$$S(x, t) = \delta(x)\delta(t), \quad (3.17b)$$

$$S(x, t) = \delta(x)H(t)e^{-i\omega t}, \quad (3.17c)$$

where δ and H are the Dirac and Heaviside functions, respectively. The first corresponds to a forcing with some spatial distribution applied at the instant $t = 0$, and the problem then becomes an initial-value problem. The second corresponds to an impulse localized at $x = 0$ and $t = 0$; the solution is the “impulse response,” i.e., the Green function $G(x, t)$ associated with the linear operator L . The third forcing function corresponds to periodic forcing beginning at $t = 0$ and localized at $x = 0$. This type of forcing is often used in experiments, for example, when a small ribbon is made to vibrate at some point in a flow; examples are given in Chapters 5 and 6. Under typical experimental conditions the forcing can be modeled by a superposition of two of the elementary forcing functions (3.17b) and (3.17c), or (3.17a) and (3.17c), with the initial forcing (3.17a) or (3.17b) corresponding to the start of the experiment.

The definition of linear stability is based on the response to an impulse perturbation (3.17b). This perturbation can give rise to three types of behavior, which are illustrated in Figure 3.3. The perturbation advected by the flow can decay to zero (Figure 3.3a). The Green function then satisfies

$$\lim_{t \rightarrow \infty} G(x, t) = 0 \quad \text{along any ray } x/t = \text{constant.} \quad (3.18)$$

The base state $u_0 = 0$ is then termed *linearly stable*. Otherwise, it is termed *linearly unstable*, i.e.,

$$\lim_{t \rightarrow \infty} G(x, t) = \infty \quad \text{along at least one ray } x/t = \text{constant.} \quad (3.19)$$

In the latter case two types of instability can be distinguished. The first, termed *convective*, corresponds to a perturbation which, in addition to being amplified,

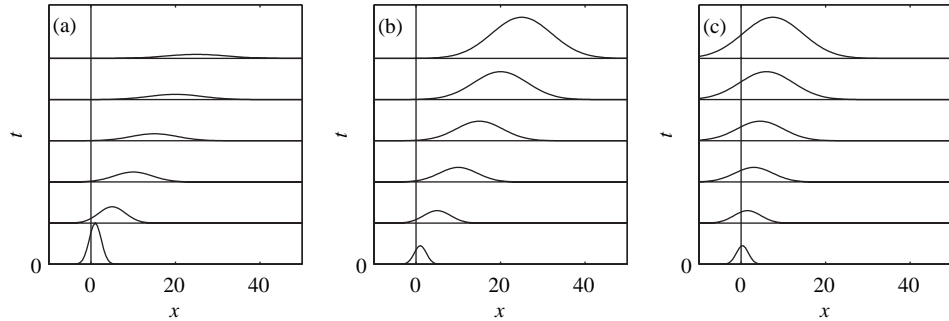


Figure 3.3 Evolution in the (x, t) plane of a perturbation localized near $x = 0$ at time $t = 0$, for a base state which is (a) stable; (b) convectively unstable; (c) absolutely unstable. These cases correspond to the solutions of the linearized equation (3.14) with the impulse response $G(x, t) = \frac{1}{2\sqrt{\pi t}} \exp(Rt - (x - Vt)^2/4t)$: (a) $V = 1, R = -0.03$; (b) $V = 1, R = 0.1$; (c) $V = 0.3, R = 0.1$.

is advected and moves far from the point at which it was initiated (Figure 3.3b), such that

$$\lim_{t \rightarrow \infty} G(x, t) = 0 \quad \text{along the ray } x/t = 0. \quad (3.20)$$

The other type of instability, termed *absolute* (Figure 3.3c), corresponds to growth at the location of the impulse, i.e.,

$$\lim_{t \rightarrow \infty} G(x, t) = \infty \quad \text{along the ray } x/t = 0. \quad (3.21)$$

The distinction between convective and absolute instability, introduced into hydrodynamics by Huerre and Monkewitz (1985), leads to the idea of a global instability mode (Huerre and Monkewitz, 1990; Schmid and Henningson, 2001; Chomaz, 2005).

We note that the distinction between convective and absolute makes sense only if the reference frame in which the problem is formulated has something special about it which distinguishes it from other reference frames in uniform translation with respect to it. This reference frame could be that of an obstacle placed in the flow, or that of the walls bounding the flow, or that of a source of perturbation such as a vibrator. In other words, the distinction between convective and absolute instability makes sense only if the Galilean invariance of the problem (invariance under the transformation $x \rightarrow x + Ut$, $V \rightarrow V + U$) is broken by the boundary conditions. There is another case for which the distinction between convective and absolute is irrelevant, namely, the case of flow which returns back on itself, like the Couette flow between two cylinders, or the flow between two spheres (a type of problem encountered in astrophysics (Chandrasekhar, 1961)). In such flows, an

unstable perturbation in the convective sense periodically passes the same point, and therefore essentially becomes equivalent to an absolute instability.

We must now find a simple criterion that allows us to determine (i) whether a base state is linearly stable or unstable, and (ii) if it is unstable, whether it is convectively or absolutely unstable.

3.2 A criterion for linear stability

The condition for stability used in the preceding chapter is that the growth rate of any “temporal” normal mode, i.e., a mode with real wave number k and complex frequency ω , be negative. Here we shall justify this criterion, and show that it is necessary and sufficient for linear stability in the sense defined in the preceding section.

3.2.1 Spatio-temporal evolution of a general perturbation

We want to solve the initial-value problem for the evolution of a perturbation written in the general form of a Fourier integral:

$$u(x, t) = \frac{1}{(2\pi)^2} \int_{F_k} \int_{L_\omega} \hat{u}(k, \omega) e^{i(kx - \omega t)} d\omega dk, \quad (3.22)$$

where F_k and L_ω are the integration contours in the complex planes (k_r, k_i) and (ω_r, ω_i) , respectively (Huerre and Rossi, 1998, §3). These contours must be chosen so as to ensure the convergence of the integrals, and they must satisfy the causality principle. According to this principle, an effect cannot precede its cause, and so the result must satisfy $u(x, t) = 0$ for all $t < 0$ for a forcing which begins at time $t = 0$. It can be shown that, for this condition to be fulfilled, it is sufficient to take the real axis for F_k and the line $i\gamma$ for L_ω , where γ is an upper limit on the growth rates $\omega_{ji}(k)$ of the temporal modes (Figure 3.4). The subscript j labels the different branches of the temporal modes (for example, the Rayleigh–Taylor instability has two branches of temporal modes; cf. Chapter 2).

Then in the Fourier space the problem (3.16) becomes

$$D(k, \omega) \hat{u}(k, \omega) = \hat{S}(k, \omega),$$

where $D(k, \omega)$ is the Fourier transform of the linear operator L corresponding to replacing ∂_t and ∂_x by $-i\omega$ and ik , respectively. As a result, $D(k, \omega) = 0$ is the dispersion relation. Then the solution of the problem in the Fourier space is

$$\hat{u}(k, \omega) = \frac{\hat{S}(k, \omega)}{D(k, \omega)}.$$

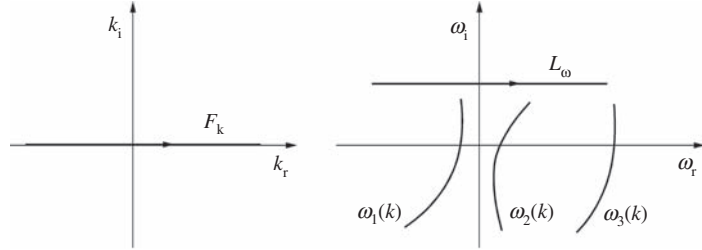


Figure 3.4 Integration contours F_k and L_ω in the (k_r, k_i) and (ω_r, ω_i) planes assuring the convergence of the integral (3.22) as well as the causality principle. The $\omega_j(k)$ are the temporal branches.

Insertion of this result into (3.22) formally solves the problem in physical space:

$$u(x, t) = \frac{1}{(2\pi)^2} \int_{F_k} \int_{L_\omega} \frac{\hat{S}(k, \omega)}{D(k, \omega)} e^{i(kx - \omega t)} d\omega dk. \quad (3.23)$$

This integral is dominated by the poles of the integrand, that is, the zeros of $D(k, \omega)$. Since the integration contour F_k is the real axis, these zeros correspond to the temporal modes $\omega_j(k)$. If the poles are simple, the residue theorem³ can be used to write the solution as

$$u(x, t) = -\frac{i}{2\pi} \sum_j \int_{-\infty}^{\infty} \frac{\hat{S}(k, \omega_j(k))}{\partial_\omega D(k, \omega_j(k))} e^{i(kx - \omega_j(k)t)} dk. \quad (3.24)$$

Therefore, the response to the forcing $S(x, t)$ is, in the end, a sum of temporal normal modes. A necessary and sufficient condition for stability then is that the growth rates, that is, the imaginary parts of the $\omega_j(k)$, are negative for all j and any wave number k . In conclusion, the stability criterion defined at the beginning of the present chapter and based on the response to a localized perturbation is identical to the criterion used in the preceding chapter based only on the temporal modes.

³ We recall that a function $f(z)$ of a complex variable z is holomorphic in a domain \mathcal{D} if it is uniform (single-valued) and differentiable at any point of \mathcal{D} . A pole a is a point where $f(z)$, being uniform, is neither bounded nor holomorphic, but where $\frac{1}{f(z)}$ is holomorphic (an example is $\frac{1}{z-a}$). The residue associated with a pole a is the coefficient A_{-1} of the term $\frac{1}{z-a}$ of the expansion of $f(z)$ in negative or positive powers of $(z-a)$ (a Laurent series). Let L be an integration contour in the complex plane for a function $f(z)$ which is holomorphic inside L , except at n poles with residues $A_{-1}^{(j)}$, $j = 1, n$. Then

$$\int_L f(z) dz = 2i\pi \sum_j A_{-1}^{(j)}.$$

This is the residue theorem. (The theorem remains valid if $1/f(z)$ is not holomorphic at the points a_j , i.e., for essential singularities.)

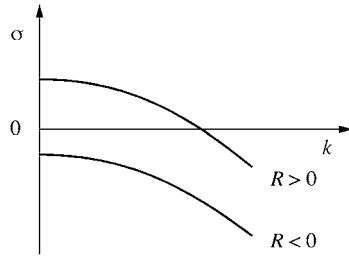


Figure 3.5 Temporal growth rate (3.27) of a temporal mode for the Ginzburg–Landau equation.

3.2.2 An illustration

For the Ginzburg–Landau equation (3.14), the linear stability of the base state $u_0 = 0$ is determined by seeking solutions in the form of normal modes:

$$u(x, t) = \hat{u} e^{i(kx - \omega t)}. \quad (3.25)$$

Inserting this solution into the linearized version of (3.14) gives the dispersion relation:

$$i(\omega - kV) + R - k^2 = 0. \quad (3.26)$$

Let us consider the time evolution of a temporal mode (k real). The complex frequency $\omega = \omega_r + i\omega_i$ is given by the temporal branches

$$\omega_i = R - k^2, \quad c = \omega_r/k = V. \quad (3.27)$$

For $R < 0$, $\omega_i(k)$ is negative for all k , and so the base state is stable; for $R > 0$, the base state is unstable to perturbations of wave number smaller than \sqrt{R} (Figure 3.5). The marginal stability curve ($\omega_i = 0$) in the (k, R) plane is the parabola $R = k^2$.

3.3 Convective and absolute instabilities

3.3.1 The criterion for absolute instability

For a wave packet centered on a wave number k_0 and propagating without decaying or growing (both k and ω are real), the envelope of the packet propagates, as discussed above, at the real group velocity

$$c_g(k_0) = \frac{\partial \omega}{\partial k}(k_0). \quad (3.28)$$

Let us now see what happens in the neighborhood of an instability threshold (with k and ω complex) for a value of the bifurcation parameter R close to the critical value R_c (Huerre and Rossi, 1998, §3). At the threshold $R = R_c$ the curve describing the growth rate $\omega_i(k_r)$ of the temporal normal modes is tangent to the axis k_r at real critical wave number k_c , and so $\partial\omega_i/\partial k_r$ is necessarily zero. The group velocity of a wave packet centered on the critical wave number k_c ,

$$c_g(k_c) = \frac{\partial\omega}{\partial k}(k_c, R_c) = \frac{\partial\omega_r}{\partial k_r} = \frac{\partial\omega_i}{\partial k_i}, \quad (3.29)$$

is indeed real.⁴

Above the threshold, if there exists a wave number k_0 for which the group velocity $c_g(k_0)$ is zero and the temporal growth rate (i.e., the imaginary part of $\omega_0 = \omega(k_0)$) is positive, then the packet grows in place (Figure 3.3c). This result is obtained by calculating the impulse response $G(x, t)$ along the ray $x/t = 0$, given by (3.24) with $\hat{S}(k, \omega) = 1$ inside the integral. The integral is calculated by generalizing the stationary-phase method to the case where the argument of the exponential is not purely imaginary, but contains a real part (Bender and Orszag, 1978, §6.6). The resulting asymptotic response at long times is given by

$$G(x, t) \sim \frac{1}{\sqrt{2\pi\omega''(k_0)t}} \frac{e^{i\pi/4}}{\partial_\omega D(k_0, \omega_0)} e^{i(k_0x - \omega_0t)}, \quad (3.30)$$

where k_0 and ω_0 are defined through

$$\frac{\partial\omega}{\partial k}(k_0) = 0, \quad \omega_0 = \omega(k_0). \quad (3.31)$$

It follows that the instability criterion is simply that the imaginary part of ω_0 , referred to as the *absolute growth rate*, be positive.

From this discussion we can deduce an essential characteristic of convective and absolute instabilities. A convective instability amplifies any unstable perturbation, and advects it downstream. If the perturbations are viewed as “noise,” an unstable convective system then behaves as a noise amplifier. On the other hand, a system which is absolutely unstable responds selectively to perturbations: its response is

⁴ For a function $Z = X + iY$ of a complex variable $z = x + iy$ to be differentiable at the point z_0 , it is necessary and sufficient that $X(x, y)$ and $Y(x, y)$ be differentiable at (x_0, y_0) and that at this point (the Cauchy conditions)

$$\frac{\partial X}{\partial x} = \frac{\partial Y}{\partial y}, \quad \frac{\partial X}{\partial y} = -\frac{\partial Y}{\partial x}.$$

The derivative Z' is then given by

$$\text{Re}(Z') = \frac{\partial X}{\partial x} = \frac{\partial Y}{\partial y}, \quad \text{Im}(Z') = -\frac{\partial X}{\partial y} = \frac{\partial Y}{\partial x}.$$

dominated by the mode with zero group velocity, which grows in place, while the other modes are “swept away” by the flow. Since this mode is selected by the dispersion relation, which is intrinsic to the system, an absolutely unstable system behaves like an oscillator with its own natural frequency.

3.3.2 The spatial branches of a convective instability

Let us consider the situation shown in Figure 3.3b of a perturbation with given frequency advected by a flow. We want to determine the spatial growth rate of this perturbation. This problem makes sense only in the case of a convective instability, because for an absolute instability the perturbation field is dominated by the mode with zero group velocity, which grows in place. The spatial growth rate is obtained by using the dispersion relation $D(k, \omega) = 0$ to find the spatial branches, that is, the complex wave number(s) $k_r + ik_i$ corresponding to a real frequency ω . The spatial growth rate is then $-k_i$ and the speed of the wave is ω/k_r .

3.3.3 Illustrations

As a simple example, let us consider the Ginzburg–Landau equation, for which the dispersion relation is (3.26). The (complex) group velocity of a wave number k is then

$$c_g = \frac{\partial \omega}{\partial k} = V - 2ik, \quad (3.32)$$

which vanishes for wave number $k_0 = V/2i$. Inserting this wave number into the dispersion relation (3.26), we find the corresponding frequency $\omega_0 = i(R - V^2/4)$. We conclude that for $0 < R < V^2/4$ the base state $u_0 = 0$ is convectively unstable (Figure 3.3b), and that for $R > V^2/4$ it is absolutely unstable (Figure 3.3c).

When the instability is convective, i.e., $R < V^2/4$, the two spatial branches (or spatial modes) are obtained from (3.26):

$$k_{\pm}(\omega) = \frac{1}{2} \left(-iV \pm \sqrt{4(R + i\omega) - V^2} \right), \quad (3.33)$$

from which we easily obtain the spatial growth rate $-k_{\pm,i}$. We stress the fact that the spatial branches can be determined only when we are sure that the instability is convective.

We briefly mention some hydrodynamical illustrations which will be treated in more detail later on. The mixing layer between two concurrent and parallel flows with different velocities is a typical example of a flow which is convectively unstable. The Poiseuille flow between flat plates or in a pipe, as well as the boundary

layer on a flat plate, are two other important examples. In such flows, any perturbation which is forced at an upstream location is amplified downstream; the instability does not have its own dynamics. On the other hand, the wake downstream from a solid obstacle is absolutely unstable beyond a critical Reynolds number of a few tens. For example, $\text{Re}_c = U_\infty d / \nu = 48.5$ for a cylinder of diameter d in a flow of unperturbed velocity U_∞ . At this critical Reynolds number the flow bifurcates from a stationary state to an oscillatory state characterized physically by the appearance of a Kármán vortex street (Williamson, 1996; Huerre and Rossi, 1998, §6). The oscillation frequency f corresponds to a well-defined value of the Strouhal number fd/U_∞ , which is quite insensitive to perturbations of the flow ($\text{St} = 0.19$ for the cylinder at moderate Reynolds numbers). In terms of dynamical systems, the appearance of this oscillation corresponds to a Hopf bifurcation.

3.3.4 The Gaster relation

The Gaster relation (1962) is an expression allowing the temporal growth rate to be related to the spatial growth rate in the vicinity of marginal stability. Let us consider a marginal normal mode (k_c, ω_c) such that $\omega_{ci} = 0$ and $k_{ci} = 0$. Expanding the dispersion relation $\omega(k)$ in a Taylor series in the neighborhood of the marginal stability, to first order we have

$$\omega - \omega_c = \frac{\partial \omega}{\partial k}(k_c, R)(k - k_c),$$

from which, taking the imaginary part, we find

$$\omega_i = \frac{\partial \omega_i}{\partial k_r}(k_c, R)(k_r - k_c) + \frac{\partial \omega_r}{\partial k_r}(k_c, R)k_i. \quad (3.34)$$

For a temporal mode, k_i is zero and the above relation gives the temporal growth rate $\omega_i^{(T)}$:

$$\omega_i^{(T)} = \frac{\partial \omega_i}{\partial k_r}(k_c, R)(k_r - k_c).$$

For a spatial mode, ω_i is zero and (3.34) gives the spatial growth rate $-k_i^{(S)}$:

$$0 = \frac{\partial \omega_i}{\partial k_r}(k_c, R)(k_r - k_c) + \frac{\partial \omega_r}{\partial k_r}(k_c, R)k_i^{(S)}.$$

Subtracting these two equations from each other and using $c_g = \partial \omega_r / \partial k_r$, we find

$$\omega_i^{(T)} = -c_g k_i^{(S)}. \quad (3.35)$$

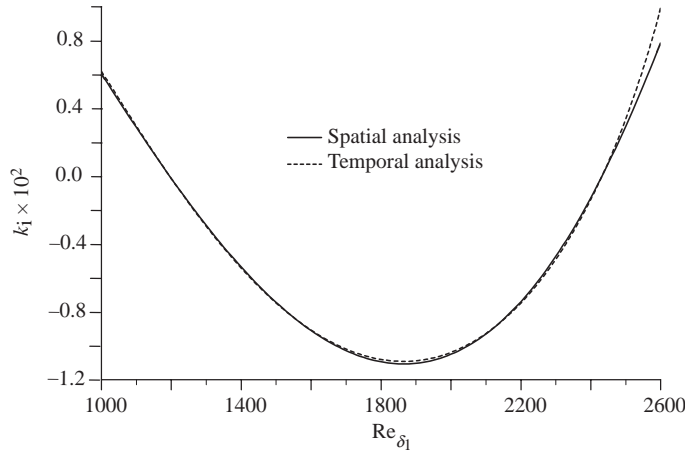


Figure 3.6 Spatial growth rate (m^{-1}) of the eigenmode with frequency $\omega v/U_\infty^2 = 0.4 \times 10^{-4}$ in a boundary layer as a function of the Reynolds number Re_{δ_1} obtained by (—) spatial analysis and (---) temporal analysis and the Gaster relation (3.35) (calculation by G. Casalis, ONERA).

The above Gaster relation shows that in the limit of weak departures from marginal conditions, the temporal growth rate $\omega_i^{(T)}$ and the spatial growth rate $k_i^{(S)}$ are related by the group velocity. In other words, for a spatially advected wave packet which is observed in the reference frame of the group velocity, it is the temporal growth rate which is measured.

The usefulness of the Gaster relation is illustrated in Figure 3.6, which displays the spatial growth rate of the instability of the Blasius boundary layer on a flat plate, as a function of the Reynolds number Re_{δ_1} (cf. Chapter 5). Two different calculations are compared: the spatial growth rate obtained from the spatial stability analysis (real frequency), and that inferred from the temporal stability analysis (real wave number) and the Gaster relation (3.35). We observe that the curves coincide exactly for $k_i = 0$, corresponding to marginal stability, and remain very close to each other even far from marginal stability.

3.4 Exercises

3.4.1 Dispersion of a wave packet

Consider a wave packet $u(x, t)$ with Gaussian spectrum

$$\hat{u}(k) = \hat{u}_0 e^{-\sigma^2(k-k_0)^2}, \quad k > 0.$$

1. Show that $u(x, t)$ is given at long times ($\Omega t \gg 1$ with $\Omega = \omega_0''/2\sigma^2$) by

$$u(x, t) \sim \frac{\hat{u}_0 \sqrt{\pi}}{2\sigma} \frac{1}{\sqrt{\Omega t}} e^{-\frac{(x - c_g t)^2}{(2\sigma \Omega t)^2}} \cos [k_0 x - \omega_0 t + \phi(x, t)],$$

where the phase $\phi(x, t)$ is defined as

$$\phi(x, t) = -\frac{\theta}{2} + \frac{(x - c_g t)^2}{4\sigma^2 \Omega t}, \quad \tan \theta = \Omega t.$$

2. Show that the local wave number (the gradient of the phase) varies spatially as

$$\partial_x \phi(x, t) = \frac{x - c_g t}{\omega_0'' t}.$$

Interpret this variation.

3. For gravity waves in deep water and $\delta k = 0.1 k_0$, at what distance from the amplitude maximum are the wave numbers $k_0 \pm \delta k$ found?

3.4.2 Spatial branches of a convective instability

Determine the spatial growth rate (3.33) of perturbations of the solution $u(x, t) = 0$ of the Ginzburg–Landau equation (3.14) when the instability is convective ($R < V^2/4$).

4

Inviscid instability of parallel flows

4.1 Introduction

An instability typical of a parallel flow was demonstrated in an experiment performed by Osborne Reynolds (1883) and repeated by Thorpe (1969). A horizontal long tube is filled carefully with a layer of water lying on top of a layer of heavier colored brine (salt water), as sketched in Figure 4.1a. The tube is suddenly tipped several degrees: the brine falls and the water rises, creating a shear flow which displays an inflection point near the interface (Figure 4.1b). In a few seconds a wave of sinusoidal shape develops at the interface of the two fluids, and leads to regular co-rotating vortices, as shown in Figure 4.2. These vortices are a manifestation of the Kelvin–Helmholtz instability. This instability owes its origin to the inertia of the fluids; viscosity plays only a minor role, tending to attenuate the growth of the wave only slightly by momentum diffusion.

Another manifestation of the Kelvin–Helmholtz instability on a much larger atmospheric scale is illustrated in Figure 4.3. An upper air layer flows over a lower layer moving more slowly, with different humidity and temperature. The thin layer of clouds formed at the interface displays billows which are the exact analogs of those in Figure 4.1. Figure 4.4 shows another example, in a mixing layer formed between a flow of water on the left and a flow of water and air bubbles on the right.

The parallel flow of two fluid layers moving at different speeds, as in the above examples, is a typical situation manifesting the Kelvin–Helmholtz instability. A jet is a situation of the same type, as shown in Figure 4.5. This figure shows carbon dioxide jetting into air as observed by shadowgraphy. The laminar jet emerging from the nozzle is convectively unstable. The instability grows spatially and becomes apparent at a distance of the order of a diameter, where it develops annular vortices. These vortices in turn become unstable at a distance of the order of two wavelengths. This *secondary instability* leads to intense turbulent mixing between the jet and the surrounding air.

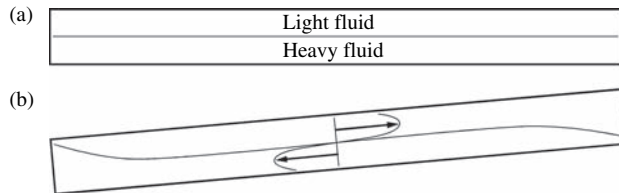


Figure 4.1 (a) Two superposed fluid layers in a horizontal tube. (b) Shape of the velocity profile as the tube is inclined.

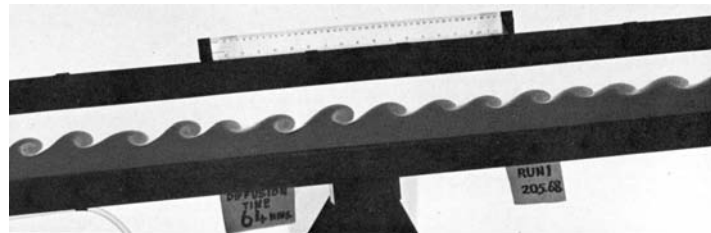


Figure 4.2 Kelvin–Helmholtz instability at the shear interface between two liquids in a tube of rectangular cross-section. Photograph by Thorpe (1971), taken from van Dyke (1982).

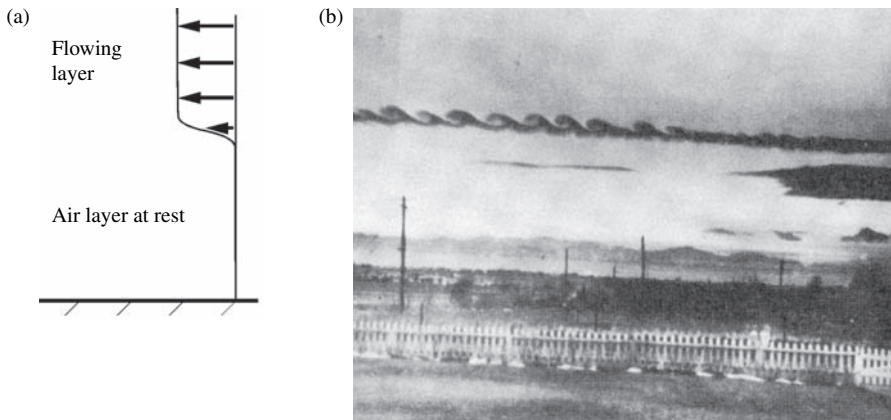


Figure 4.3 Kelvin–Helmholtz instability between two layers of air on a geophysical scale. (a) Sketch of the mean velocity profile; (b) photograph taken by P. E. Branstine in 1954, near Denver, Colorado (Drazin and Reid, 2004).

Along with mixing layers and jets, wakes at large Reynolds number represent a third type of flow susceptible to the Kelvin–Helmholtz instability, the result of which is shown in Figure 4.6. The structure of a wake is nearly independent of the Reynolds number for Reynolds numbers greater than about 100, which suggests that the structure is essentially governed by inertial effects and not by viscosity.

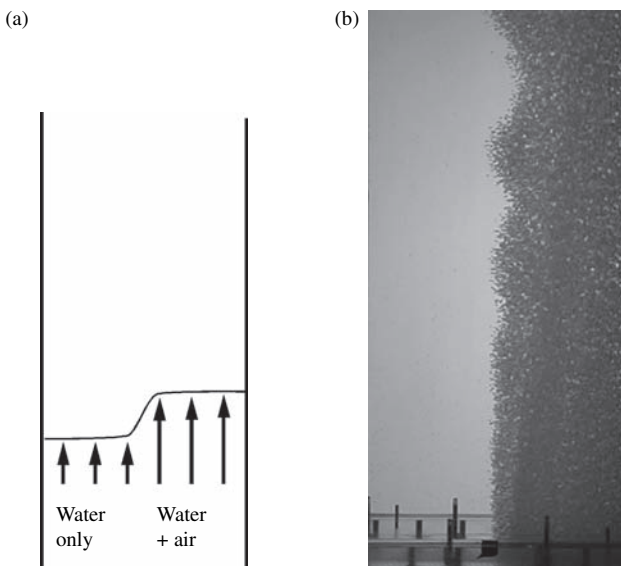


Figure 4.4 Rising mixing layer in a vertical channel between a water flow (at the left, $U = 0.35 \text{ m s}^{-1}$) and an air-bubble–water flow (at the right, $U = 0.72 \text{ m s}^{-1}$, air volume fraction of 9%). (a) Sketch of the experiment and the mean velocity profile; (b) development of the Kelvin–Helmholtz instability. The width and depth of the channel are $0.3 \times 0.15 \text{ m}^2$ (V. Roig and A. Larue de Tournemine, 2001, IMFT, reprinted with permission).

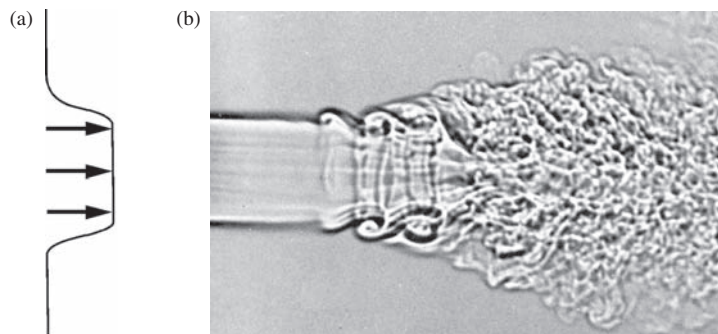


Figure 4.5 Kelvin–Helmholtz instability of a jet of carbon dioxide 6 mm in diameter issuing into air at a speed of 40 m s^{-1} ($\text{Re} = 30,000$). (a) Sketch of the mean velocity profile; (b) photograph taken by F. Landis and A. H. Shapiro (van Dyke, 1982).

The importance of inflection points of the mean velocity profiles, as sketched in the figures, will appear in the next section.

The present chapter is devoted to the analysis of inertial instabilities of free shear flows far from a wall such as mixing layers, jets, and wakes at large Reynolds

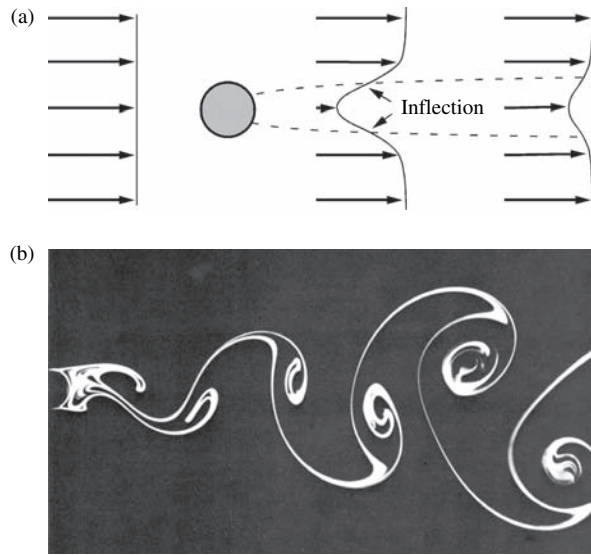


Figure 4.6 Wake of a cylinder. (a) Sketch of mean velocity profiles and their inflection points. (b) Kármán vortex street resulting from the Kelvin–Helmholtz instability. The water is flowing at a speed of 1.4 cm s^{-1} and the cylinder diameter is 1 cm ($\text{Re} = 140$). The emission lines are obtained by electrolytic precipitation of colloidal particles visualized by means of a light sheet. Photograph taken by S. Taneda in 1956 (van Dyke, 1982).

number (Sections 4.2 and 4.3). We shall also describe another type of inertial instability due to centrifugal force (Section 4.4). In all these situations viscosity only attenuates the instability via diffusion, and plays a smaller role the higher the Reynolds number.

4.2 General results

4.2.1 Linearized equations for small perturbations

Ignoring viscous effects compared to inertial ones, we choose the characteristic scales L , V and ρV^2 of the flow as our length, speed, and pressure units. The incompressibility and momentum conservation equations (the Euler equations) then become

$$\operatorname{div} \mathbf{U} = 0, \quad (4.1a)$$

$$\partial_t \mathbf{U} + (\mathbf{U} \cdot \mathbf{grad}) \mathbf{U} = -\mathbf{grad} P. \quad (4.1b)$$

These equations have the family of base solutions

$$\bar{\mathbf{U}}(\mathbf{x}, t) = \bar{U}(y) \mathbf{e}_x, \quad \bar{P}(\mathbf{x}, t) = \bar{P}, \quad (4.2)$$

corresponding to a parallel flow in the x -direction specified by the unit vector \mathbf{e}_x , invariant in the spanwise z -direction. Let us consider the perturbed base flow $\bar{\mathbf{U}} + \mathbf{u}$, $\bar{P} + p$; the linearized perturbation equations are written as

$$\operatorname{div} \mathbf{u} = 0, \quad (4.3a)$$

$$(\partial_t + \bar{U} \partial_x) \mathbf{u} + v \partial_y \bar{U} \mathbf{e}_x = -\mathbf{grad} p. \quad (4.3b)$$

Since the problem is translationally invariant in time and in the spatial directions x and z , the solution can be sought in the form of normal modes of wave vector $\mathbf{k} = k_x \mathbf{e}_x + k_z \mathbf{e}_z$ and frequency ω . For the longitudinal velocity perturbation a normal mode is written as

$$u(\mathbf{x}, t) = \frac{1}{2} \hat{u}(y) e^{i(k_x x + k_z z - \omega t)} + \text{c.c.}, \quad (4.4)$$

with similar expressions for v , w and p . Substituting these into (4.3), we obtain the system of homogeneous differential equations satisfied by the amplitudes $\hat{u}(y)$, $\hat{v}(y)$, $\hat{w}(y)$, and $\hat{p}(y)$:

$$ik_x \hat{u} + \partial_y \hat{v} + ik_z \hat{w} = 0, \quad (4.5a)$$

$$i(k_x \bar{U} - \omega) \hat{u} + \partial_y \bar{U} \hat{v} = -ik_x \hat{p}, \quad (4.5b)$$

$$i(k_x \bar{U} - \omega) \hat{v} = -\partial_y \hat{p}, \quad (4.5c)$$

$$i(k_x \bar{U} - \omega) \hat{w} = -ik_z \hat{p}. \quad (4.5d)$$

In addition to the equations (4.5), we impose the conditions that the perturbations fall off for $y \rightarrow \pm\infty$:

$$\hat{u}, \hat{v}, \hat{w} \rightarrow 0 \quad \text{for} \quad y \rightarrow \pm\infty, \quad (4.6)$$

or, for bounded domains, that walls located at $y = y_1$ and $y = y_2$ are impermeable, i.e.

$$\hat{v}(y_1) = 0, \quad \hat{v}(y_2) = 0. \quad (4.7)$$

The system (4.5)–(4.6) or (4.5)–(4.7) can formally be written as

$$L\phi = \omega M\phi,$$

where $\phi = (\hat{u}, \hat{v}, \hat{w}, \hat{p})$ and L and M are linear differential operators.

We recognize this as a generalized eigenvalue problem which has a nonzero solution ϕ only if the operator $L - \omega M$ is noninvertible, i.e., if for a given wave number the frequency ω is an eigenvalue. This condition can be written formally as

$$D(\mathbf{k}, \omega) = 0, \quad (4.8)$$

which is the dispersion relation of perturbations of infinitesimal amplitude. Obtaining the explicit dispersion relation for a specific base flow is the essential component of a linear stability study. The rest of this chapter is devoted to the description of some general results on inviscid shear flows.

4.2.2 The Squire theorem

Using a change of variable and a theorem due to Squire (1933), the three-dimensional problem (4.5)–(4.6) or (4.5)–(4.7) can be reduced to an equivalent two-dimensional one. The Squire transformation consists of introducing the variables

$$\tilde{k}^2 = k_x^2 + k_z^2, \quad (4.9a)$$

$$\tilde{\omega} = (\tilde{k}/k_x)\omega, \quad (4.9b)$$

$$\tilde{k}\tilde{u} = k_x\hat{u} + k_z\hat{w}, \quad (4.9c)$$

$$\tilde{v} = \hat{v}, \quad (4.9d)$$

$$\tilde{p} = (\tilde{k}/k_x)\hat{p}. \quad (4.9e)$$

The system (4.5) then becomes

$$i\tilde{k}\tilde{u} + \partial_y \tilde{v} = 0, \quad (4.10a)$$

$$i\tilde{k}(\bar{U} - \tilde{c})\tilde{u} + \partial_y \bar{U}\tilde{v} = -i\tilde{k}\tilde{p}, \quad (4.10b)$$

$$i\tilde{k}(\bar{U} - \tilde{c})\tilde{v} = -\partial_y \tilde{p}, \quad (4.10c)$$

where $\tilde{c} = c = \omega/k_x$ is the phase velocity of the perturbation in the direction x , with the boundary conditions

$$\tilde{v}(y) \rightarrow 0 \quad \text{for} \quad y \rightarrow \pm\infty, \quad \text{or} \quad \tilde{v}(y_1) = \tilde{v}(y_2) = 0. \quad (4.11)$$

The resulting system of equations (4.10)–(4.11) is formally identical to the original system (4.5)–(4.6) or (4.5)–(4.7) with $\hat{w} = k_z = 0$; in other words, the system obtained after the Squire transformation is identical to that corresponding to two-dimensional perturbations. This system of two-dimensional perturbations has a nonzero solution only if the dispersion relation

$$\tilde{D}(\tilde{k}, \tilde{\omega}) = 0 \quad (4.12)$$

is satisfied. If this relation is known, i.e., if we have managed to solve the stability problem for two-dimensional perturbations, the dispersion relation (4.8) for three-dimensional perturbations can be obtained without further calculation by means of

the Squire transformation:

$$D(\mathbf{k}, \omega) = \tilde{D} \left(\sqrt{k_x^2 + k_z^2}, \frac{\sqrt{k_x^2 + k_z^2}}{k_x} \omega \right) = 0. \quad (4.13)$$

This leads us to Squire's theorem.

Theorem 4.1 *For any three-dimensional unstable mode (\mathbf{k}, ω) of temporal growth rate ω_i there is an associated two-dimensional mode $(\tilde{k}, \tilde{\omega})$ of temporal growth rate $\tilde{\omega}_i = \omega_i \sqrt{k_x^2 + k_z^2} / k_x$, which is more unstable since $\tilde{\omega}_i > \omega_i$.*

Therefore, when the problem is to determine an instability condition, it is sufficient to consider only two-dimensional perturbations.

4.2.3 The Rayleigh equation of two-dimensional perturbations

With Squire's theorem in mind, we shall henceforth consider only two-dimensional perturbations. Then we can introduce the stream function ψ of the velocity perturbation, defined as $u = \partial_y \psi$ and $v = -\partial_y \psi$. Eliminating the pressure by cross-differentiation of the Euler equations, we obtain

$$(\partial_t + \bar{U} \partial_x) \Delta \psi - \partial_{yy} \bar{U} \partial_x \psi = 0. \quad (4.14)$$

(It may be noted that this equation is simply the linearized transport equation for the vorticity $\boldsymbol{\omega} = -\Delta \psi \mathbf{e}_z$ in the absence of diffusion.) Seeking the solution in the form of normal modes

$$\psi(\mathbf{x}, t) = \frac{1}{2} \hat{\psi}(y) e^{i(kx - \omega t)} + \text{c.c.}$$

of wave vector $\mathbf{k} = k \mathbf{e}_x$ and frequency ω , we obtain the *Rayleigh equation*

$$(\bar{U} - c)(\partial_{yy} \hat{\psi} - k^2 \hat{\psi}) - \partial_{yy} \bar{U} \hat{\psi} = 0 \quad (4.15)$$

with the boundary conditions

$$\hat{\psi} \rightarrow 0 \quad \text{for } y \rightarrow \pm\infty, \quad \text{or} \quad \hat{\psi}(y_1) = \hat{\psi}(y_2) = 0. \quad (4.16)$$

In light of the results obtained in the preceding chapter, to determine the stability of a flow it is sufficient to consider modes with real wave number. For such a mode, if $\hat{\psi}$ is an eigenfunction associated with an eigenvalue c , then, if we consider the complex conjugate version of the Rayleigh equation, we see that $\hat{\psi}^*$ is also an eigenfunction associated with the eigenvalue c^* . The eigenvalues associated with the Rayleigh equation must therefore be either real or complex conjugates of each

other. If the eigenvalues are real for any wave number, the perturbations are waves which propagate without amplification, and the flow is neutrally stable. If there exists a wave number for which the two eigenvalues are complex conjugates of each other, one of the modes decays and the other is amplified, and so the flow is unstable.

A result which will prove useful for what follows is that if the flow is stable with respect to a normal mode ($c_i = 0$), then the corresponding perturbations u and v are exactly out of phase. Here the Rayleigh equation has real coefficients, and the real and imaginary parts of $\hat{\psi}$ satisfy the same linear equation: they are proportional, and so their ratio is independent of y . The phase ϕ of $\hat{\psi}(y) = A(y)e^{i\phi(y)}$ is therefore independent of y , and the perturbations u and v may be written as

$$u = A'(y) \cos(kx - \omega t + \phi), \quad v = kA(y) \sin(kx - \omega t + \phi),$$

which proves that they are out of phase.

The critical layer

A complication can arise in solving the Rayleigh equation if there exists a layer in the flow, at some location $y = y_c$, where the speed c of an eigenmode is equal to the fluid velocity $\bar{U}(y_c)$: the coefficient of the highest-order differential in the Rayleigh equation (4.15) vanishes. The eigenfunction therefore must have a singularity at $y = y_c$ (at least, it is not differentiable there). Such a layer is called a *critical layer*. Since the speed $c = \bar{U}(y_c)$ is real, the stability of such a mode must be neutral.

It may be remarked in general that the factor $\bar{U}(y) - c$ can vanish for a *complex* value of the variable y , as the associated eigenvalue is no longer real. Such a situation may seem to have no physical consequence because the spatial variable y is real, but in fact it can have an important effect on the structure of the eigenfunctions. For a deeper discussion of this point see in particular the studies of Lin (1955), Bender and Orszag (1978, §3.1–3.3), Drazin and Reid (2004, §22), Huerre and Rossi (1998), or Schmid and Henningson (2001, §2.2).

The continuous spectrum

If, for a given wave number, there exists a mode associated with a critical layer at $y = y_c$ near which the velocity $\bar{U}(y)$ is continuous, one might think that there must exist other neutral eigenmodes with speed $c = \bar{U}(y)$ in a range about $y = y_c$; the eigenvalue spectrum associated with these modes is then *continuous*. The case of Couette flow discussed below offers a simple illustration of this type of spectrum. We note that the continuity we are discussing here concerns an ensemble of modes of *the same wave number*; it is different than that of a Fourier spectrum where the wave number is continuous.

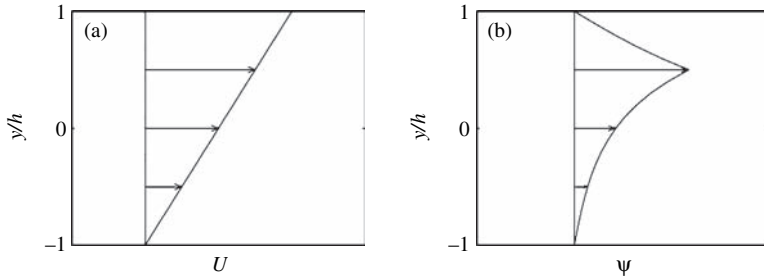


Figure 4.7 (a) Couette flow between two walls at $y = \pm h$; (b) an eigenfunction $\hat{\psi}(y)$ such that $c = \bar{U}(h/2)$.

The existence of a critical layer is not necessary for the existence of a continuous spectrum; such a spectrum is encountered also in flows which are not bounded in the transverse direction, a typical example being the boundary layer flow above a wall (Mack, 1976).

Stability of Couette flow

Let us consider inviscid Couette flow $\bar{U} = U_0(y/h + 1)$ between two planes at $y = -h$ and $y = +h$ (Figure 4.7a). Since the second derivative $\partial_{yy}\bar{U}$ in the Rayleigh equation vanishes, the latter possesses, for nonzero $\bar{U} - c$, the general solution

$$\hat{\psi}(y) = A \sinh(ky + \phi),$$

where A and ϕ are two integration constants. Taking into account the impermeability of the walls $\hat{\psi}(-h) = \hat{\psi}(+h) = 0$ then implies that $A = 0$: there is no eigenmode satisfying the boundary conditions! In fact there are eigenmodes, but they are not smooth at a certain level y_c corresponding to a critical layer. These modes can be found by solving the Rayleigh equation on each side of the critical layer and then matching the two solutions. In this way, we find the following solution satisfying the conditions at the walls:

$$\hat{\psi}_-(y) = A_- \sinh k(y + h) \quad \text{for } y < y_c, \quad (4.17a)$$

$$\hat{\psi}_+(y) = A_+ \sinh k(y - h) \quad \text{for } y > y_c. \quad (4.17b)$$

The continuity of the fluid across the critical layer implies continuity of the normal velocity $v = -\partial_x \psi$, from which we find $\hat{\psi}_-(y_c) = \hat{\psi}_+(y_c)$, or

$$A_- \sinh k(y_c + h) = A_+ \sinh k(y_c - h).$$

This equation determines a continuous family of eigenfunctions, parametrized by y_c in the interval $[y_1, y_2]$ (up to a multiplicative constant, since as usual, the problem is linear and homogeneous). The eigenfunction with $y_c = h/2$ associated with the eigenvalue $c = \bar{U}(h/2)$ is shown in Figure 4.7b: it is continuous at $y = y_c$ but not differentiable. Physically, the discontinuity of the derivative corresponds to a discontinuity of the longitudinal velocity $u = \partial_y \psi$, which is entirely admissible for inviscid flow.

Therefore, for inviscid Couette flow, any normal mode of wave number k and speed $c = \omega/k$ in the range between $\bar{U}(-h) = 0$ and $\bar{U}(+h) = 2U_0$ is an eigenmode. The dispersion relation can then be written as

$$k\bar{U}(-h) < \omega < k\bar{U}(+h).$$

In other words, for any wave number k the eigenvalue spectrum $\omega(k)$ is *continuous*. It can be concluded that the discrete spectrum of inviscid Couette flow is empty, but there exists a continuous spectrum associated with the neutral modes. This flow is therefore linearly stable (Case, 1960). As will be shown in the following chapter, the inclusion of viscous effects does not modify this result: as a consequence, Couette flow is linearly stable for any Reynolds number (Romanov, 1973).

4.2.4 The Rayleigh inflection point theorem

Inviscid modes of instability are governed by the Rayleigh equation (4.15). It is of some interest to establish general properties of solutions to this equation without actually solving it for specific velocity profiles. The Rayleigh theorem (1880) is one such general result, which establishes conditions of far-reaching consequence.

The Rayleigh theorem. The existence of an inflection point in the velocity profile of a parallel flow is a necessary (but not sufficient) condition for instability.

Let us prove this theorem. According to the results of the preceding chapter, it is sufficient to study the temporal stability for determining the stability of a given flow, i.e., it is sufficient to consider modes with real wave number and complex frequency. Let us assume that the flow is unstable. Then $c_i \neq 0$ and $\bar{U} - c \neq 0$ for real y . We divide the Rayleigh equation (4.15) by $(\bar{U} - c)$, multiply by $\hat{\psi}^*$, and integrate between the walls at y_1 and y_2 . After integrating by parts taking into account the conditions $\hat{\psi}(y_1) = \hat{\psi}(y_2) = 0$, the imaginary part of the result is written as

$$c_i \int_{y_1}^{y_2} \frac{\partial_{yy} \bar{U}}{|\bar{U} - c|^2} |\hat{\psi}|^2 dy = 0. \quad (4.18)$$

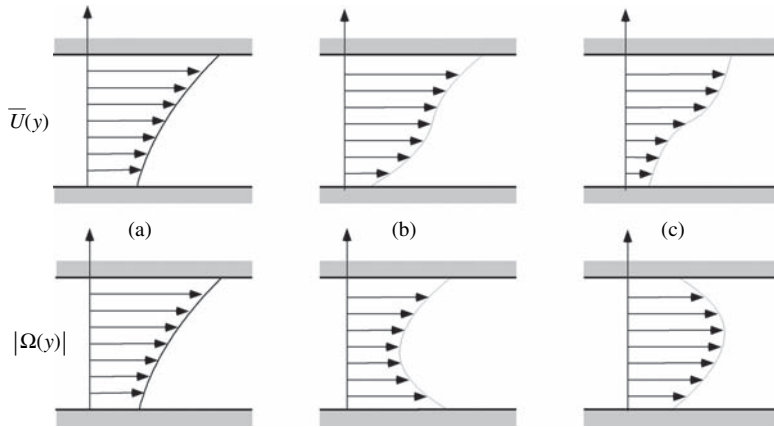


Figure 4.8 Top: velocity profiles; bottom: the corresponding vorticity profiles. According to the Rayleigh theorem, profile (a) is stable. According to the Fjørtoft theorem, profiles (a) and (b) are stable.

Since $c_i \neq 0$ by assumption, the integral must vanish and so $\partial_{yy}\bar{U}$ must change sign, i.e., the velocity profile must have an inflection point. This proves the Rayleigh theorem.

Figure 4.8 shows three examples of velocity profiles. Application of the Rayleigh theorem allows us to state that profile (a) is stable because it has no inflection point. However, it does not allow us to predict the stability of profiles (b) and (c). An illustration of the fact that the presence of an inflection point is only a necessary but not a sufficient condition for instability is provided by the flow $\bar{U} = \sin y$ between two walls at y_1 and y_2 . As shown by Tollmien, this flow is stable for $y_2 - y_1 < \pi$ even if there exists an inflection point in the interval (Drazin and Reid, 2004, §22; Drazin, 2002, §8.2).

The Rayleigh theorem leads to the conclusion that two fundamental flows, plane Poiseuille flow and the Blasius boundary layer on a flat plate, neither of which has an inflection point in the velocity profile, are linearly stable as long as the effects of viscosity on the perturbations are ignored. However, experiment indicates that these flows are unstable, which suggests that viscosity plays an important role even if the Reynolds number is large. This question will be the topic of the following chapter.

The Rayleigh criterion was extended by a theorem due to Fjørtoft (1950); see, for example, Huerre and Rossi (1998). This theorem states that for a monotonic velocity profile, a necessary (but still not sufficient) condition for instability is that the inflection point corresponds to a vorticity maximum. Therefore, in Figure 4.8 profiles (a) and (b) are stable, and only (c) might be unstable.

Another general result pertaining to inviscid instability is the Howard semicircle theorem (Howard, 1961), according to which the eigenvalues c in the complex plane (c_r, c_i) are located in the interior of a circle of center $(U_{\min} + U_{\max})/2$ and radius $(U_{\max} - U_{\min})/2$.

4.2.5 Jump conditions between two layers of uniform vorticity

An important simplification of the problem of determining the stability of a parallel flow occurs when the curvature of the velocity profile vanishes (i.e., flows with uniform vorticity). The Rayleigh equation then has constant coefficients and is easily solved. This suggests that as a first step in obtaining analytical results and insight, we approximate any profile by a piecewise-linear profile. The eigenfunctions of the perturbations are then exponentials in the interior of each layer, and it is only necessary to match them at the discontinuity using the conditions of continuity of the normal velocity and the normal force balance.

Accordingly, let us take a piecewise-linear flow whose velocity $\bar{U}(y)$ or gradient $\partial_y \bar{U}(y)$ is discontinuous at $y = y_0$. Let $y = y_0 + \eta(x, t)$ be the perturbed position of this discontinuity, and \mathbf{n} be the normal. At this interface the normal velocity of the fluid must be continuous and equal to the normal velocity $\mathbf{w} \cdot \mathbf{n}$ of the interface. Denoting the velocities and pressures on either side of the interface by a subscript $-$ or $+$, this continuity condition can be written as

$$(\mathbf{U}_+ \cdot \mathbf{n})(y_0 + \eta) = (\mathbf{U}_- \cdot \mathbf{n})(y_0 + \eta) = \mathbf{w} \cdot \mathbf{n}. \quad (4.19)$$

Referring these quantities to the unperturbed interface by means of a Taylor series, the components U_{\pm} and V_{\pm} can be written as follows, keeping only first-order terms:

$$\begin{aligned} \bar{U}_{\pm}(y_0 + \eta) &= \bar{U}_{\pm}(y_0) + \eta \partial_y \bar{U}_{\pm}(y_0) + \partial_y \psi_{\pm}(y_0), \\ \bar{V}_{\pm}(y_0 + \eta) &= -\partial_x \psi_{\pm}(y_0). \end{aligned}$$

Then, the linearized normal is $\mathbf{n} = (-\partial_x \eta, 1)$ and the normal velocity of the linearized interface is $\mathbf{w} \cdot \mathbf{n} = -\partial_t \eta$ (Chapter 2). The continuity of the normal velocity (4.19) results in the following condition applied at $y = y_0$:

$$-\bar{U}_+ \partial_x \eta - \partial_x \psi_+ = -\bar{U}_- \partial_x \eta - \partial_x \psi_- = -\partial_t \eta.$$

Introducing normal modes of the form $\eta = \frac{1}{2} \hat{\eta} e^{ik(x-ct)} + \text{c.c.}$, these relations become

$$\hat{\psi}_{\pm} = -(\bar{U}_{\pm} - c)\hat{\eta}.$$

Eliminating $\hat{\eta}$ from the above two equations, continuity of the normal velocity can finally be written as

$$\Delta \left(\frac{\hat{\psi}}{\bar{U} - c} \right) = 0, \quad (4.21)$$

where $\Delta[X] = X_+(y_0) - X_-(y_0)$ represents the jump in any quantity X at the discontinuity.

The continuity of normal forces reduces to continuity of the pressure, which is written as

$$\begin{aligned} 0 &= \Delta[P(y_0 + \eta)] \\ &= \Delta[\bar{P}(y_0) + \eta \partial_y \bar{P}(y_0) + p(y_0) + \mathcal{O}(\eta^2)] \\ &= \Delta[p(y_0) + \mathcal{O}(\eta^2)]. \end{aligned}$$

The last equation corresponds to the fact that since the transverse distribution of $\bar{P}(y)$ is uniform or hydrostatic, the jump of \bar{P} and of its derivatives is zero. Taking into account the longitudinal Euler equation (4.3), this condition becomes

$$\Delta[(\bar{U} - c) \partial_y \hat{\psi} - \partial_y \bar{U} \hat{\psi}] = 0. \quad (4.22)$$

The continuity conditions (4.21) and (4.22), together with the conditions of decay at infinity or the impermeability of solid walls, allow the complete determination of the eigenfunctions of a piecewise-linear flow.

4.3 Instability of a mixing layer

Here we consider the instability of a fundamental flow, some illustrations of which were given at the beginning of this chapter, namely, the instability of a mixing layer. This problem was studied theoretically by Helmholtz (1868) and later by Kelvin (1871) for the purpose of explaining, in particular, the formation of ocean waves by the wind (Darrigol, 2005, §4.6). The modeling performed by Kelvin and Helmholtz is too simplistic to give a good description of wind-generated waves, as discussed in particular by T. B. Benjamin and J. W. Miles in a series of famous papers, see e.g. (Miles, 1957; Benjamin, 1959). However, the instability they discovered proved to be a generic instability of shear flows at large Reynolds number.

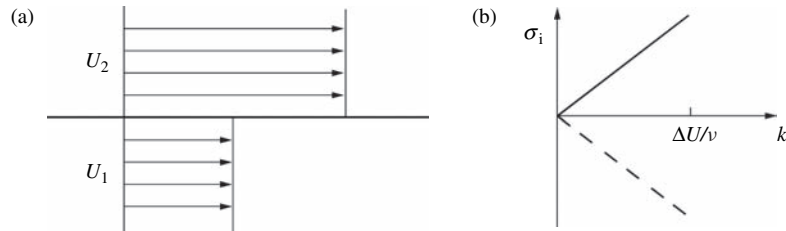


Figure 4.9 (a) The flow of two superposed layers of uniform velocity. (b) Growth rate of the stable and unstable modes of the Kelvin–Helmholtz instability, with the wave number $\Delta U/\nu$ beyond which the inviscid analysis breaks down.

4.3.1 Kelvin–Helmholtz instability of a vortex sheet

The simplest flow demonstrating the Kelvin–Helmholtz instability is that of two unbounded fluids¹ with uniform velocities U_1 for $y < 0$ and U_2 for $y > 0$ (Figure 4.9a). The interface is therefore the site of a velocity jump. Here we consider the case of two fluids of the same density ρ without surface tension. The more general case including buoyancy and surface tension is simply the superposition of the case studied here and the Rayleigh–Taylor instability studied in Chapter 2, see Exercise 4.5.1.

The solution of the Rayleigh equation (4.15) is written as

$$\hat{\psi}_j = A_j e^{-ky} + B_j e^{ky}, \quad j = 1, 2.$$

Taking into account the conditions that the perturbations fall off at infinity leads to $A_1 = 0$ and $B_2 = 0$ (for k positive). We see immediately that the eigenfunction therefore decreases exponentially on either side of the interface; physically, this means that the perturbations induced by a wave of wave number k penetrate to a depth of order k^{-1} . Taking into account the jump conditions at the interface (4.21) and (4.22), we obtain the homogeneous algebraic system of equations

$$(U_1 - c)A_2 - (U_2 - c)B_1 = 0, \\ (U_2 - c)A_2 + (U_1 - c)B_1 = 0,$$

which has a nontrivial solution only when the determinant vanishes, or

$$(U_1 - c)^2 + (U_2 - c)^2 = 0. \quad (4.23)$$

¹ For the case of a flow bounded between two walls, see Exercise 4.5.2.

This is the desired dispersion relation, which shows that there exist two modes corresponding to two complex-conjugate eigenvalues

$$c = \frac{\omega}{k} = U_{\text{av}} \pm i\Delta U, \quad (4.24)$$

where we have introduced the average speed $U_{\text{av}} = (U_1 + U_2)/2$ and the half-difference of the speeds $\Delta U = (U_1 - U_2)/2$. From the viewpoint of the temporal stability of a perturbation of real wave number, the speed c_r and the temporal growth rate $\omega_i = kc_i$ of these modes are

$$c_r = U_{\text{av}}, \quad \omega_i = \pm k \Delta U. \quad (4.25)$$

Therefore, both modes propagate at the same speed equal to the average speed U_{av} (waves are not dispersive), and because of the mode with positive growth rate the flow is unstable for any velocity difference, no matter how small. Moreover, it is unstable to any perturbation, no matter what its wave number k , with growth rate increasing linearly with k (Figure 4.9b).

The unphysical conclusion that the growth rate is unbounded at large wave numbers (small wavelengths) is a consequence of the fact that all effects of viscous diffusion have been ignored. In fact, inertial effects dominate viscous effects for wave numbers such that $\rho k \Delta U^2 \gg \mu k^2 \Delta U$, i.e., $k \ll \Delta U/\nu$, but they cannot be ignored for $k \gtrsim \Delta U/\nu$. The quantity $\Delta U/\nu$ therefore determines the wave number scale beyond which the above analysis is no longer valid (Figure 4.9b). A more realistic model that avoids the divergence of the growth rate at large wave numbers while retaining the inviscid approximation will be discussed later on.

The Kelvin–Helmholtz instability mechanism can be explained as a sort of “Bernoulli effect.” Let us consider the flow in a reference frame moving at the average speed (Figure 4.10), in which the speeds of the fluids are $U_1 = -\Delta U$ and $U_2 = \Delta U$ and the speed of the perturbations vanishes according to (4.25). Above a perturbation $\eta > 0$ of the shear layer the fluid is accelerated owing to the fact that the cross-sectional area perpendicular to the flow is decreased. This perturbation plays a role to a depth of order k^{-1} , the only length scale in the problem, on either side of the interface. The order of magnitude of the velocity perturbation is therefore such that $\eta \Delta U \sim u/k$ owing to the incompressibility of the fluid. This velocity excess above a crest leads to a pressure decrease of order $p \sim -\rho \Delta U u$ according to the linearized Bernoulli theorem, so that the pressure difference across the interface amplifies the perturbation. We then obtain the growth rate from a one-dimensional momentum balance as

$$\sigma = \frac{1}{u} \frac{du}{dt} = -\frac{1}{\rho u} \frac{\partial p}{\partial x} \sim -\frac{kp}{\rho u} \sim k \Delta U.$$

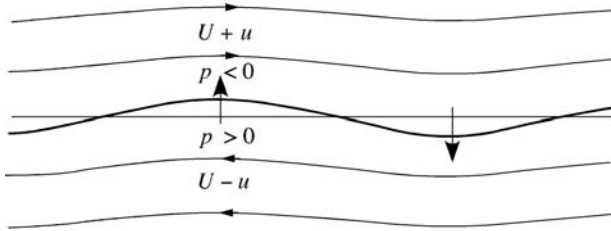


Figure 4.10 The Kelvin–Helmholtz instability mechanism, observed in a reference frame moving at the average speed of the fluids.

This mechanistic analysis is in good agreement with the full theory. We note that the same scaling law for σ can also be obtained via strictly dimensional arguments: since the only scales in the problem are the velocity ΔU and the wave number k , the only time scale is $1/k\Delta U$, and the growth rate must therefore vary as $k\Delta U$. Another interpretation of the instability mechanism is given by Batchelor (1967) in terms of vorticity.

We conclude by remarking that the normal modes

$$\psi_j = \frac{1}{2} \left(A_j e^{-ky} + B_j e^{ky} \right) e^{i(kx - \omega t)} + \text{c.c.}, \quad j = 1, 2,$$

correspond to irrotational perturbations; their vorticity

$$\boldsymbol{\omega} = -\Delta \psi \mathbf{e}_z$$

is zero. And so, what happens to a rotational perturbation? In the absence of diffusion by the viscosity, the vorticity field associated with such a perturbation is transported according to the linearized Helmholtz equation (Batchelor, 1967, §5.2)

$$(\partial_t + \bar{U} \partial_x) \boldsymbol{\omega} = \mathbf{0},$$

the solution of which is $\boldsymbol{\omega}(x, y, t) = \boldsymbol{\omega}(x - \bar{U}t, y)$. Therefore, the rotational component of the perturbation is simply advected by the base flow – it is neutral: only its irrotational component can amplify. This result remains valid for a piecewise-linear base flow, where the vorticity is uniform in each layer. We note that the neutral nature of vorticity perturbations has already been encountered in the study of the inviscid Rayleigh–Taylor instability, where the base state corresponds to a fluid at rest (Chapter 2).

William Thomson, Lord Kelvin (1824–1907)

Born in Belfast, Ireland, William Thomson was raised by his mathematician father in a strict Presbyterian fashion. At age 15 he received a gold medal from the University of Glasgow for his *Essay on the Figure of the Earth*. Between 1838 and 1841, encouraged by his professors, he discovered and read the works of the French mathematicians Lagrange, Laplace, Legendre, Fresnel, and Fourier. He entered Cambridge University in 1841 and in the same year published his first article *Fourier's expansions of functions in trigonometrical series*. In 1845 he moved to

Paris and studied in the physical laboratory of Henri-Victor Regnault at the Collège de France. At the request of Liouville, he embarked on unifying the ideas of Faraday, Coulomb, and Poisson on electrical theory. In 1846 he was appointed Professor of Natural Philosophy (Physics) at the University of Glasgow. Over many years he maintained a correspondence with G. G. Stokes which comprises several hundred letters. His studies of thermodynamics led him to propose an absolute scale of temperature in 1848. In 1852 he observed what is now called the Joule–Thomson effect of the cooling of a gas upon expansion. Based on the work of Joule he understood the dynamical nature of heat as molecular motion, and, inspired by this idea, developed a dynamical theory of electricity and magnetism (1856), on which James Clerk Maxwell relied heavily in his development of his own theory. The second part of Thomson's career is notable for his unfortunate biases against the existence of atoms, Darwin's theory of evolution, and Rutherford's radioactivity. With Peter Guthrie Tait he undertook an ambitious project for the comprehensive description of physics, the *Treatise on Natural Philosophy*, the two published volumes of which, on kinematics and dynamics, remained the definitive reference text for several generations. During the 1850s he joined a group of industrialists in a project to lay a telegraph cable under the Atlantic Ocean. His ideas, in particular those related to his invention of the mirror-galvanometer, proved superior to those of his competitor Whitehouse, and his patents and consulting activities brought him great celebrity and a large personal fortune. In 1866 he was knighted by Queen Victoria, and then raised to the rank of Baron Kelvin of Largs in 1892. He was elected a member of the Royal Society in 1851, and served as its president from

1890 to 1895. He was also president of the Royal Society of Edinburgh for more than twenty years until his death. Thomson published over 600 papers. He is buried at Westminster Abbey in London.

Hermann Ludwig Ferdinand von Helmholtz (1821–1894)



Helmholtz was born in Potsdam, Germany, into a modest family. Despite his interest in physics, he undertook university studies in medicine in Berlin in order to obtain a scholarship, studying mathematics and philosophy on his own. He wrote his first paper in 1841 on muscular activity, where he proposed that physiology be based not on the idea of unphysical “vital forces,” but rather on the principles of physics and chemistry. He later showed that the notion of vital force implies the existence of perpetual motion. In 1847 he published *Über die Erhaltung der Kraft*, an

article which laid the foundation of the principle of conservation of energy based on earlier work of Sadi Carnot, Clapeyron, Mayer, and Joule, among others. He understood that when energy appears to have been lost, it has actually been converted into kinetic or potential energy at the atomic scale (at a time when the existence of atoms was far from being accepted). His arguments were based on physical principles as well as philosophical convictions, an attitude characteristic of Helmholtz. His convictions, drawn from Kant, were based on a general requirement that Nature be intelligible and on the postulate of a fundamental invariance underlying natural transformations. The publication of this article permitted him to give up his work as a military doctor and accept a chair in physiology at Königsberg. During a visit to England in 1853 he became a friend of William Thomson (Lord Kelvin). In 1855 he left Königsberg for a chair in anatomy and physiology in Bonn, and then in 1858 he moved to Heidelberg. In 1858 in *Crelle's Journal* he published what Lord Kelvin referred to as “the splendid discovery of the dynamical laws governing the rotational motion” of a perfect fluid, where he defined vorticity and established his famous theorems governing its dynamics. His experimental and theoretical work in optics and acoustics formed the basis of the physiology of sensory functions, from which he rapidly gained an international reputation. In 1856 and 1866 he published the two-volume *Handbuch der physiologischen Optik*, where he

developed, in particular, a theory of color vision. In 1862 he published a major study on musical theory and sound perception, where he promoted the use of the new technique of Fourier series. Beginning in 1866 he distanced himself from physiology and moved toward physics and mathematics. He did research on non-Euclidean geometry, on the foundations of geometry and the role experiment could play, in connection with a critique of the philosophy of Kant. In 1871 he was appointed to the chair of physics at Berlin, and took over as director of a new institute. He made important contributions to electrodynamics, the discovery of the electron, electrochemical batteries, and electric double layers. He was the advisor of H. Hertz. He attempted to provide a mechanical foundation for thermodynamics and tried to derive the Maxwell equations from the principle of least action. His activities and personality dominated German and European science of the nineteenth century. He had a universal spirit which, in the tradition of Leibniz, embraced all the sciences as well as philosophy and the fine arts.

4.3.2 The case of nonzero vorticity thickness

Owing to diffusion by viscosity, a velocity discontinuity – which can be thought of as a singular distribution of vorticity – cannot be maintained. A more realistic model of the base flow must include a shear layer which connects the two uniform flows in a continuous manner. A simple model solved analytically by Rayleigh (1880) is the piecewise-linear profile shown in Figure 4.11:

$$\bar{U} = U_1, \quad y < -\delta, \quad (4.26a)$$

$$\bar{U} = U_{av} + \Delta U y/\delta, \quad -\delta < y < \delta, \quad (4.26b)$$

$$\bar{U} = U_2, \quad \delta < y, \quad (4.26c)$$

where δ is the half-thickness of the shear layer. This thickness actually grows with time by diffusion, but we shall assume that this growth is slow compared to the growth of the instability, i.e., that δ can be considered constant, an assumption which we will discuss *a posteriori*.

The dispersion relation

The Rayleigh equation (4.15) and the condition of decay of the perturbations at infinity gives the general form of the perturbations:

$$\hat{\psi}_1 = B_1 e^{ky}, \quad y < -\delta, \quad (4.27a)$$

$$\hat{\psi}_0 = A_0 e^{-ky} + B_0 e^{ky}, \quad -\delta < y < \delta, \quad (4.27b)$$

$$\hat{\psi}_2 = A_2 e^{-ky}, \quad \delta < y. \quad (4.27c)$$

The jump relations (4.21) and (4.22) for the two interfaces lead to a homogeneous algebraic system of equations for the four integration constants. This has a solution only when the determinant vanishes, leading to the dispersion relation

$$4(k\delta)^2(c - U_{av})^2 - \Delta U^2 \left((2k\delta - 1)^2 - e^{-4k\delta} \right) = 0. \quad (4.28)$$

Temporal stability

We consider a temporal mode of real wave number k . For $(2k\delta - 1)^2 > e^{-4k\delta}$, i.e., $k\delta > k_c\delta = 0.6392$, the dispersion relation possesses two real roots c_{\pm} , and the perturbation is neither amplified nor attenuated, but is neutral. For $k\delta < k_c\delta$ the eigenvalues c_{\pm} are complex conjugates of each other, and one of the eigenmodes is attenuated and the other amplified. The flow is therefore unstable to perturbations of small wave number. Figure 4.11 shows the speed $c_{\pm r}$ and the temporal growth rate $\omega_{\pm i} = kc_{\pm i}$ as functions of the wave number. The maximal growth rate is

$$\omega_{i,\max} \approx 0.2 \Delta U / \delta,$$

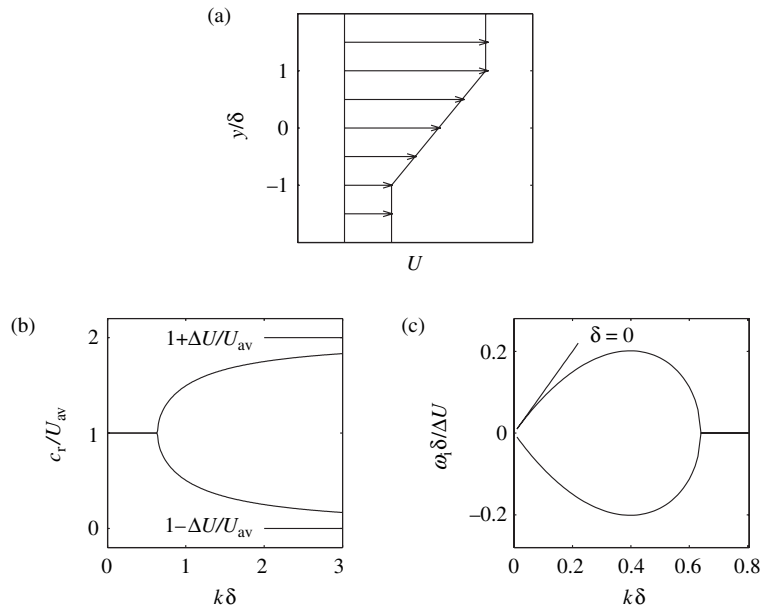


Figure 4.11 (a) Mixing layer of thickness 2δ ; (b) speed; and (c) temporal growth rate of the stable and unstable modes.

and corresponds to $k_{\max}\delta \approx 0.4$. For $k\delta \ll 1$, i.e., perturbations of wavelength large compared to the vorticity thickness, we recover the dimensional growth rate $\omega_{\pm i} = \pm k\Delta U$ for a vorticity sheet of zero thickness, as we would expect.

A better model of the base flow which is more regular than the piecewise-linear flow is that described by the hyperbolic tangent function:

$$\bar{U} = U_{\text{av}} + \Delta U \tanh(y/\delta). \quad (4.29)$$

Numerical solution of the Rayleigh equation leads to a stability curve very close to that of Figure 4.11 (Michalke, 1964). The cutoff wave number is $k_{\text{off}}\delta = 1$, and the maximum temporal growth rate $\omega_{i,\max}\delta/U_{\infty} \approx 0.2$ occurs at $k_{\max}\delta \approx 0.44$, values which are very close to those of the piecewise-linear flow.

Finally, the Kelvin–Helmholtz instability is manifested in the growth of perturbations with wavelength large compared to the thickness δ over an advective time of order $\delta/\Delta U$. This result is obtained more generally for any shear flow at large Reynolds number when the velocity profile has an inflection point, including jets and wakes.

Spatial stability and the convective–absolute transition

Since a study of spatial stability is meaningful only if the instability is convective and not absolute, the first step is to determine the condition for convective instability as discussed in the preceding chapter. The convective–absolute transition corresponds to the vanishing of the group velocity for a wave number k_0 to be determined. Differentiating the dispersion relation and setting $\partial\omega/\partial k = 0$, we find

$$\frac{\omega_0\delta}{U_{\text{av}}} = k_0\delta - \frac{1}{2} \left(\frac{\Delta U}{U_{\text{av}}} \right)^2 (2k_0\delta - 1 + e^{-4k_0\delta}). \quad (4.30)$$

Substituting this expression into the dispersion relation (4.28), we see that k_0 is the solution of the equation

$$(2k_0\delta - 1 + e^{-4k_0\delta})^2 \left(\frac{\Delta U}{U_{\text{av}}} \right)^2 - [(2k_0\delta - 1)^2 - e^{-4k_0\delta}] = 0. \quad (4.31)$$

Numerical solution of this equation allows the determination of the complex wave number $k_0\Delta U/U_{\text{av}}$ at which the group velocity vanishes, and then the corresponding complex frequency $\omega_0\Delta U/U_{\text{av}}$ can be obtained. It turns out that the absolute growth rate ω_{0i} is negative for $|\Delta U/U_{\text{av}}| < 1$ and becomes positive for $|\Delta U/U_{\text{av}}| > 1$ (Huerre and Rossi, 1998). For $|\Delta U/U_{\text{av}}| < 1$, that is, when the two fluids flow together, the instability is convective, and the mixing layer behaves as a noise amplifier. For $|\Delta U/U_{\text{av}}| > 1$, when the two fluids flow in opposite directions, the instability is absolute and the mixing layer behaves like an oscillator

with growth rate ω_{0i} . We note that this analysis makes sense only if there exists a privileged reference frame in which to measure the velocities, such as a reference frame attached to the spot where the two streams come into contact.

4.3.3 Viscous effects

This chapter is primarily about inviscid instabilities, i.e., instabilities that do not rely on the presence or absence of viscosity to explain their physical origin. However, it is natural to enquire how viscous effects, which inevitably are present in real fluids, modify the results obtained from an inviscid analysis. Here we focus on the mixing layer. Viscosity thickens the vorticity layer and therefore modifies the base flow while also affecting the instability. Let us begin by dealing with the first of these effects from the viewpoint of temporal stability. The vorticity thickness δ , which so far we have treated as constant, actually grows on a time scale δ^2/ν , while the characteristic time for the growth of the instability is $\delta/\Delta U$. The assumption of a stationary base flow is correct if the characteristic time of the instability is short compared to the time for variation of the base flow, or $\delta/\Delta U \ll \delta^2/\nu$: in other words, the Reynolds number $Re = \Delta U \delta/\nu$ should be large compared to unity.

Regarding the effect of viscosity on the instability itself, viscous diffusion is found to reduce the growth rate as well as the cutoff wave number k_c , as shown schematically in Figure 4.12, with $k_c\delta \sim Re/4\sqrt{2}$ for $Re \rightarrow 0$ (Betchov and Szewczyk, 1963). The instability remains fundamentally an inertial instability of long wavelength, with weak viscous effects corresponding to a *regular* perturbation (in contrast to the situations studied in the following chapter, where the perturbation will be *singular* due to the presence of a wall). Analysis of the competition between the growth of the instability and the spreading due to viscosity leads to the following estimate for the growth rate:

$$\omega_{i,\max} \frac{\delta}{\Delta U} \approx \sqrt{\frac{0.2}{1 + a/0.2Re}}, \quad (4.32)$$

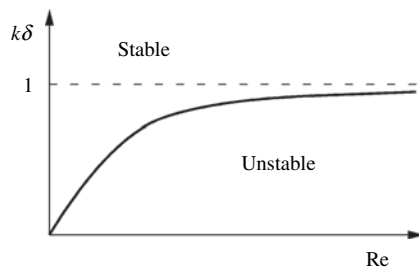


Figure 4.12 Schematic of the marginal stability curve for the mixing layer described by the hyperbolic tangent in the $Re - k\delta$ plane.

where a is a constant close to unity (Villermaux, 1998). This simple prediction is in fairly good agreement with the analytic and numerical calculations of Betchov and Szewczyk (1963).

Regarding the effect of viscosity on the base state, the vorticity layer (which can be very thin at the spot where the two streams come into contact) becomes thicker downstream, and so the flow is no longer strictly parallel. However, $d\delta/dx$ is small, so that the streamwise inhomogeneities of the basic flow are characterized by a length scale $L = \delta/(d\delta/dx)$ which is large compared to δ . The most amplified wavelength being itself of the same order of magnitude as δ , the basic flow is then locally parallel at the scale of the wavelength. Owing to this separation of scales, a *weakly nonparallel* analysis can be conducted using a WKB-type perturbation method where the small parameter is $\epsilon = \delta/L$ (Huerre and Rossi, 1998, §5.2). Since viscosity is taken into account only through the spreading of the base flow, the stability analysis remains inviscid. For a hyperbolic-tangent base flow, this analysis leads to a good prediction for the spatial development of the amplitude of forced perturbations (Gaster *et al.*, 1985).

4.4 The Couette–Taylor centrifugal instability

4.4.1 Introduction

The purely azimuthal flow between two coaxial cylinders (Figure 4.13a) is found to be unstable when the speed of the inner cylinder exceeds a critical value. The instability is manifested by the appearance of vortices aligned in the flow direction (Figure 4.13b). This so-called Couette–Taylor instability is fundamental for at least two reasons. The first is that this instability, of centrifugal origin, is *generic*, i.e., it can appear in any flow which is deflected by a curved wall. Examples are the boundary-layer flow on a concave wall, which produces *Görtler*

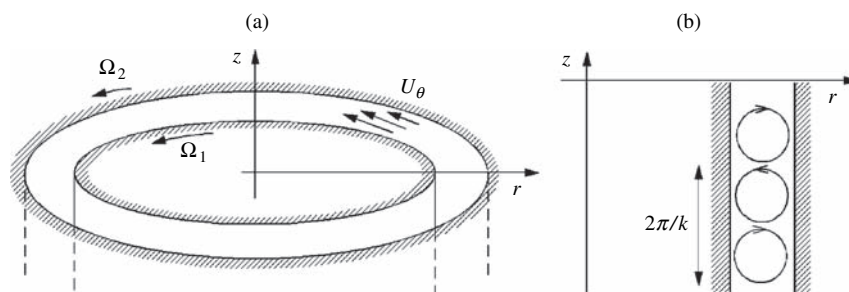


Figure 4.13 Couette–Taylor flow: (a) geometry and azimuthal velocity profile; (b) cutaway view of counter-rotating vortices generated in the primary bifurcation.

vortices, and Poiseuille flow in a curved pipe or channel, which exhibits very similar *Dean vortices* (Floryan, 1991). The second reason for the importance of the Couette–Taylor instability is that after the first bifurcation, a series of very rich bifurcations gives rise to flows which are more and more complex, finally leading to turbulence. This “route to chaos” has many features in common with that of Rayleigh–Bénard thermal convection; it has since the 1970s been the subject of a large number of experimental, numerical, and theoretical studies that have led to important advances in the understanding of the nonlinear dynamics of flows.

The Couette–Taylor instability is discussed in detail in many texts, in particular, by Chandrasekhar (1961) and Drazin and Reid (2004). The nonlinear aspects are the subject of the more specialized studies of Chossat and Iooss (1994) and Koschmieder (1993). Here we shall limit ourselves to the essential features of the problem and stress the physical mechanisms. We begin by ignoring viscous effects, and take them into account later on.

4.4.2 The steady flow and its instability

We consider purely azimuthal flow $V(r)$ of a fluid in the annular space between two coaxial cylinders of radii r_1 and r_2 rotating with angular velocities Ω_1 and Ω_2 (Figure 4.13a). This important flow was first studied by Maurice Couette (1890), and the first definitive study of the instability was made in a landmark paper by Geoffrey Taylor (1923): hence the appellation Couette–Taylor flow. The curvature of the trajectory of a fluid particle corresponds to a centripetal acceleration $-V(r)^2/r$ created by a radial pressure force per unit mass $-\partial_r P$:

$$-\frac{V(r)^2}{r} = -\frac{\partial P}{\partial r}. \quad (4.33)$$

This equation shows that the pressure must necessarily increase toward the outside, following a law which depends on the velocity profile $V(r)$. For inviscid flow, momentum conservation in the azimuthal direction or, equivalently, the condition of constant angular momentum for a fluid cylinder of thin thickness, is satisfied for any profile $V(r)$. For viscous flow this condition means that the azimuthal shear $\tau(r)$ must be such that the torque per unit length $2\pi r^2 \tau(r)$ is independent of the radius. This condition selects the unique velocity profile (Guyon *et al.*, 2001)

$$U_\theta = Ar + B/r, \quad (4.34)$$

where the constants A and B are imposed by the no-slip conditions on the cylinders:

$$A = \frac{\Omega_2 r_2^2 - \Omega_1 r_1^2}{r_2^2 - r_1^2}, \quad B = \frac{\Omega_1 - \Omega_2}{r_1^{-2} - r_2^{-2}}.$$

The first experiments on this type of flow were performed by Maurice Couette (1890) with the goal of determining the fluid viscosity. His apparatus allowed only the *outer* cylinder to rotate, and the torque was measured on the inner cylinder. These experiments showed that over a large range of velocity Ω_2 the torque varies linearly with this velocity, consistent with the velocity profile (4.34). These experiments also showed that beyond a certain velocity Ω_2 which is difficult to define precisely, the torque increases strongly, an observation that Couette correctly attributed to an instability of the flow (4.34) and the appearance of turbulent motion.

These experiments were repeated by Geoffrey I. Taylor (1923) using an apparatus which permitted the *inner* cylinder to also be turned. The large axial length of the cylinders, 90 cm or one hundred times the annular spacing $r_2 - r_1$, made it possible to largely avoid end effects at the top and bottom boundaries. The main observation of Taylor was that if only the inner cylinder is turned, an instability is manifested beyond a certain velocity Ω_1 as the appearance of a new flow which is not turbulent but instead stationary with a particular spatial structure; this structure corresponds to pairs of counter-rotating toroidal vortices that are periodic in the axial direction with wave number k such that $2\pi/k \approx 2(r_2 - r_1)$ (Figures 4.13b and 4.14a). This instability is also observed for nonzero Ω_2 : Figure 4.15 shows the instability threshold in the plane of Reynolds numbers formed using the cylinder velocities and spacing:

$$\text{Re}_1 = \frac{\Omega_1 r_1 (r_2 - r_1)}{\nu}, \quad \text{Re}_2 = \frac{\Omega_2 r_2 (r_2 - r_1)}{\nu}. \quad (4.35)$$

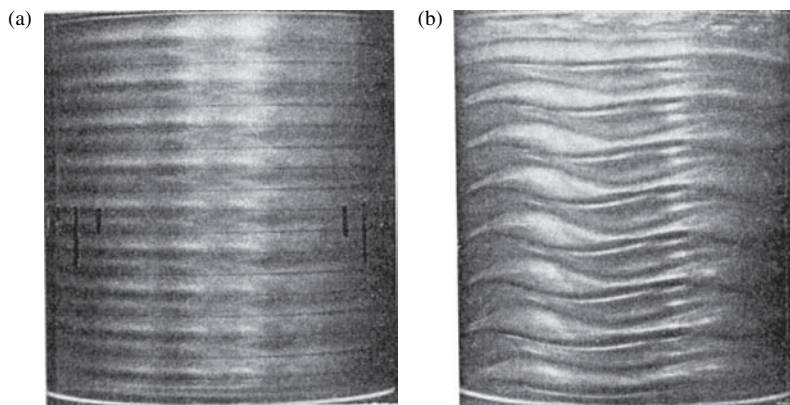


Figure 4.14 The annular vortices of Taylor. (a) $\text{Ta}/\text{Ta}_c = 1.1$; (b) $\text{Ta}/\text{Ta}_c = 6.0$, and the vortices now display waves after a second instability has appeared ($\lambda = 2\pi R/4$) (Fenstermacher *et al.*, 1979).

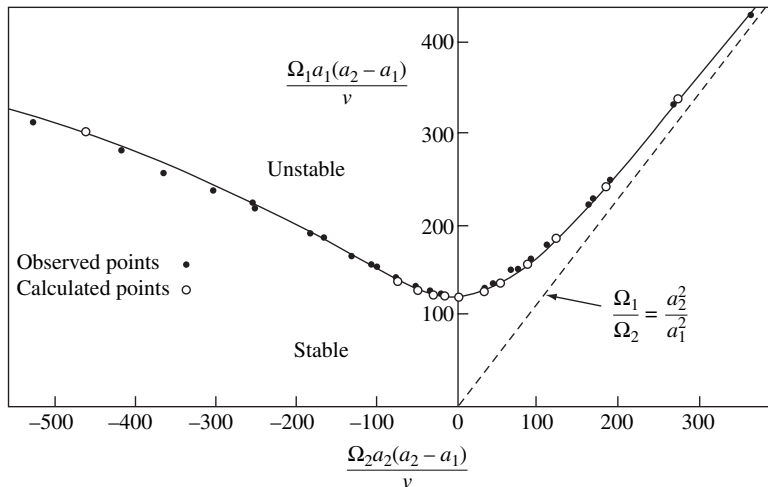


Figure 4.15 Marginal stability of Couette flow in the Reynolds number plane. The points were observed and calculated by Taylor (1923) for cylinder radii $a_1 = 3.55$ cm and $a_2 = 4.035$ cm, and the dashed line corresponds to the inviscid criterion of Rayleigh (1916b). Taken from Tritton (1988, figure 17.11).

(Note that the problem involves a third dimensionless parameter, the dimensionless spacing $R = (r_2 - r_1)/r_1$ which is equal to 0.14 in Figure 4.15.) White circles correspond to the marginal stability of the azimuthal flow obtained by the linear stability calculation, and the black points correspond to the experimental appearance of vortices. These results, which will be discussed in more detail below, marked a major stage in the development of hydrodynamic stability, as it was the first time quantitative agreement was obtained between experimental observations and the predictions of a stability analysis.

Taylor also showed that beyond a second critical velocity the vortex structure becomes unstable and complicated: the vortices become helical or, as shown in Figure 4.14b, display waves which propagate in the direction of the flow. The perimeter is filled by an integer number m of wavelengths, and the flow remains stationary in a reference frame rotating with these waves. As noted by Taylor, the observed structure depends not only on the parameter values, but on the path taken to reach these values; in other words, the flow corresponding to a given set of parameters is not unique, but depends on the history of the flow. In the language of the theory of dynamical systems, the first bifurcation is a supercritical pitchfork bifurcation which breaks the translational invariance along the z -axis of the cylinders, while the second breaks the rotational invariance. The multiplicity of observed flows for a given set of parameters indicates that these flows are metastable: the initial conditions

leading to each of these attractors correspond to a basin of attraction of finite extent.

The situation regarding the stability of *inviscid* flow can be phrased in very simple terms: if the pressure distribution $P(r)$ is such that a fluid particle perturbed from its circular equilibrium trajectory is subject to a restoring force, the azimuthal flow is stable, otherwise, it is unstable. For viscous flow this instability condition is necessary but not sufficient: the instability requires that the destabilizing force be larger than the viscous retarding force. We shall make these instability criteria more precise below.

4.4.3 The instability criterion for inviscid flow

Since the instability of Couette flow results from an inertial mechanism, an instability criterion and insight into the mechanism can be obtained by initially neglecting viscous effects. Following von Kármán (1934), we consider a fluid ring of radius r and velocity V for which the angular momentum per unit mass is $J = rV$ and the circulation² is $2\pi J$. From (4.33) the centripetal pressure gradient exerted on this ring is then $V^2/r = J^2/r^3$. According to the Kelvin theorem, a deformation of this ring into a ring of radius $r + dr$ must conserve the circulation $2\pi J$ (Batchelor, 1967, §5.3), i.e., it must conserve its angular momentum J . The pressure gradient necessary to just keep the ring in its new position is therefore $J(r)^2/(r + dr)^3$. If the existing pressure gradient $J(r + dr)^2/(r + dr)^3$ is larger than $J(r)^2/(r + dr)^3$, the ring is subject to a force tending to restore it to its initial position; otherwise, this gradient tends to amplify the deformation. We then deduce that a necessary and sufficient condition for instability to *axisymmetric* perturbations is $J(r + dr)^2 < J(r)^2$. This instability condition is therefore the condition that the squared angular momentum decrease:

$$\frac{dJ^2}{dr} < 0, \quad \text{where} \quad J = rV. \quad (4.36)$$

In other words, the flow is unstable if the increase of the pressure with radius is too slow, with the result that $r^3 \partial_r P(r)$ decreases with increasing r . The criterion (4.36) was originally obtained by Rayleigh (1916b), using a clever argument involving the analogy with the instability of a fluid at rest under gravity with an unstable density stratification. This criterion was confirmed by a complete linear stability

² The circulation of the velocity field $\mathbf{u}(x)$ round a closed curve C is defined as (Batchelor, 1967, §2.6)

$$\int_C \mathbf{u} \cdot d\mathbf{x}.$$

calculation for non-axisymmetric perturbations proportional to $e^{i(kz+m\theta-\omega t)}$: non-axisymmetric perturbations ($m \neq 0$) are found to be more stable than axisymmetric ones ($m = 0$), the latter being unstable if and only if the Rayleigh criterion is satisfied. The determination of the criterion for axisymmetric perturbations is left as an exercise (Exercise 4.5.4).

For Couette flow (4.34), the Rayleigh stability criterion (4.36) becomes

$$\frac{d}{dr}(Ar^2 + B)^2 = 4Ar^2 U_\theta < 0,$$

i.e., $A < 0$, or

$$\Omega_2 r_2^2 < \Omega_1 r_1^2. \quad (4.37)$$

Inviscid Couette flow is therefore stable to axisymmetric perturbations if the circulation of the outer cylinder $2\pi\Omega_2 r_2^2$ is smaller than that of the inner cylinder $2\pi\Omega_1 r_1^2$.

As already mentioned, Rayleigh (1916b) pointed out that the centrifugal instability described above is very similar to the instability of a density-stratified fluid in the gravity field (Rayleigh–Taylor instability): the radial pressure gradient (4.33) here plays a role analogous to the buoyancy force. More precisely, the instability condition (4.36) that the angular momentum decrease toward the outside is analogous to the condition that the density increase toward the top. Putting it another way, the unstable stratification of centrifugal force is analogous to the unstable stratification of density.

4.4.4 The effect of viscosity: the Taylor number

According to the Rayleigh criterion, even the slightest rotation Ω_1 of the inner cylinder when the outer cylinder is fixed ($\Omega_2 = 0$) allows the possibility of an instability. In reality, the appearance of the instability is postponed by viscous diffusion, and it occurs only beyond a nonzero Ω_1 . Figure 4.15 shows the marginal stability curve obtained by Taylor (1923) in the plane of the rotation velocities Ω_1 and Ω_2 normalized by $v/r_1(r_2 - r_1)$. This curve is an interpolation between the experimental points and the points obtained from the detailed stability calculation described below. We see that the agreement between experiment and calculation is excellent, and that the Rayleigh criterion, which ignores the stabilizing effect of the viscosity, gives the correct asymptotic behavior for large velocities of the same sign, the conditions under which viscous effects are effectively small compared to inertial ones.

We now show how the Taylor number controlling the instability arises, how this problem is related to the Rayleigh–Bénard problem, and how the Taylor number is related to the Rayleigh number. We consider an axisymmetric perturbation

(corresponding to the observed vortices). For such a perturbation we can write the linearized equations for the perturbations of the radial and azimuthal velocities u_r and u_θ as (Drazin and Reid, 2004, §17; Chandrasekhar, 1961, chapter 7)

$$\frac{\partial u_r}{\partial t} = -\frac{1}{\rho} \frac{\partial p}{\partial r} + \nu \Delta_* u_r + \frac{2\bar{U}_\theta u_\theta}{r}, \quad (4.38a)$$

$$\frac{\partial u_\theta}{\partial t} = \nu \Delta_* u_\theta - (D_* \bar{U}_\theta) u_r, \quad (4.38b)$$

where the starred operators are defined as

$$D_* = \frac{\partial}{\partial r} + \frac{1}{r}, \quad \Delta_* = \frac{\partial^2}{\partial r^2} + \frac{1}{r} \frac{\partial}{\partial r} - \frac{1}{r^2} + \frac{\partial^2}{\partial z^2}.$$

In each of these equations the first terms on the right-hand side correspond to viscous retardation, and the last term is an inertial term. In the first equation the inertial term arises from the rotation of the vector \mathbf{e}_θ in the frame of a fluid particle, and in the second the inertial term is the sum of the advection by u_r of the radial gradient $\partial_r \bar{U}_\theta$ of the base flow and the term $u_r \bar{U}_\theta / r$ from the rotation of the vector \mathbf{e}_r . The complete analysis of this set of linearized equations is outside the scope of this text. However, insight into the physical mechanism of the instability is gained by discussing the analogy between this problem and the Rayleigh–Bénard problem.³

These two equations are quite similar to the equations (2.49) of the Rayleigh–Bénard problem (Chapter 2). The radial speed u_r generated by the radial inertial force corresponds to the vertical speed v due to the buoyancy force, and the azimuthal speed u_θ corresponds to the temperature difference δT . To make the analogy between the two problems clearer, we artificially distinguish a radial viscosity ν_r and an azimuthal viscosity ν_θ , and analyze the case $\nu_r/\nu_\theta \gg 1$ in the same way as for the Rayleigh–Bénard problem at large Prandtl number $\text{Pr} = \nu/\kappa$. For a fluid particle displaced from its equilibrium position, the radial motion relaxes much more quickly to equilibrium than the azimuthal motion. In addition, like

³ The acceleration is the Lagrangian derivative of the velocity:

$$\mathbf{a} = \frac{d}{dt} (U_r \mathbf{e}_r + U_\theta \mathbf{e}_\theta) = \frac{dU_r}{dt} \mathbf{e}_r + U_r \frac{d\mathbf{e}_r}{dt} + \frac{dU_\theta}{dt} \mathbf{e}_\theta + U_\theta \frac{d\mathbf{e}_\theta}{dt}.$$

Decomposing the velocity into the sum of a base flow $\bar{U}_\theta \mathbf{e}_\theta$ and perturbations $u_r \mathbf{e}_r + u_\theta \mathbf{e}_\theta$, we obtain

$$a_r = \frac{du_r}{dt} - \frac{(\bar{U}_\theta + u_\theta)^2}{r},$$

$$a_\theta = \frac{du_\theta}{dt} + \frac{\bar{U}_\theta u_r}{r}.$$

The linearization of these equations with $d/dt = \partial_t + \mathbf{U} \cdot \mathbf{grad} = \partial_t + U_r \partial_r + (U_\theta/r) \partial_\theta + U_z \partial_z$ leads to (4.38).

Taylor, we shall assume that only the inner cylinder turns ($\Omega_2 = 0$, $\text{Re}_2 = 0$) and that the spacing of the cylinders $r_2 - r_1$ is small compared to r_1 ($R \ll 1$). With the following estimates for the viscous and inertial forces

$$F_{\text{visc},r} \sim -\frac{\nu_r}{(r_2 - r_1)^2} u_r, \quad F_{\text{in},r} \sim 2\Omega_1 u_r,$$

the radial equilibrium (4.38a) is then written as

$$u_r \sim 2 \frac{\Omega_1 (r_2 - r_1)^2}{\nu_r} u_\theta. \quad (4.40)$$

This relation can be interpreted as indicating that the radial speed is “slaved” to the azimuthal speed. Estimating the azimuthal forces in the same way,

$$F_{\text{visc},\theta} \sim -\frac{\nu_\theta}{(r_2 - r_1)^2} u_\theta, \quad F_{\text{in},\theta} \sim \frac{\Omega_1 r_1}{r_2 - r_1} u_r,$$

Eq. (4.38b) can be written as

$$\frac{\partial u_\theta}{\partial t} \sim \frac{\nu_\theta}{(r_2 - r_1)^2} \left(\frac{\text{Ta}}{\text{Ta}_c} - 1 \right) u_\theta, \quad (4.41)$$

where we have introduced the *Taylor number* (a tentative definition taking into account the (temporary) statement that $\nu_r \neq \nu_\theta$):

$$\text{Ta} = \frac{\Omega_1^2 r_1 (r_2 - r_1)^3}{\nu_r \nu_\theta},$$

and where Ta_c is a number of order unity. Equation (4.41) shows that for $\text{Ta} < \text{Ta}_c$ the azimuthal inertial force is dominated by the viscous force, and the perturbation dies out. For $\text{Ta} > \text{Ta}_c$ this inertial force is strong enough that the difference of the azimuthal velocity is maintained, and the perturbation grows exponentially at a rate

$$\sigma \sim \frac{\nu_\theta}{(r_2 - r_1)^2} \frac{\text{Ta} - \text{Ta}_c}{\text{Ta}_c}, \quad (4.42)$$

proportional to the distance from the threshold $\text{Ta} - \text{Ta}_c$ with the scaling $\nu_\theta / (r_2 - r_1)^2$.

Just as the marginal stability in the Rayleigh–Bénard problem is defined by only the Rayleigh number independently of the Prandtl number, we can assume that the results of the above analysis remain valid in the only physically relevant case $\nu_r = \nu_\theta$. The Taylor number governing the appearance of the instability is then written as

$$\text{Ta} = \frac{\Omega_1^2 r_1 (r_2 - r_1)^3}{\nu^2} = \text{Re}_1^2 R. \quad (4.43)$$

The complete viscous stability calculation including not only the equations (4.38) but also axial momentum conservation, the incompressibility condition, and the no-slip conditions on the cylinders confirms this analogy. In particular, it shows that the flow is completely stable when the inviscid Rayleigh criterion regarding the growth of $r\bar{U}_\theta(r)$ is satisfied. For fixed outer cylinder ($\Omega_2 = 0$), the critical Taylor number is found to be $T_{\text{c}} = 1695$. For nonzero Ω_2 the relevant Taylor number T appears to be

$$T = \frac{4(-A)\Omega_1(r_2 - r_1)^4}{v^2} = 4\text{Ta} \frac{1 - \Omega_2/\Omega_1(r_2/r_1)^2}{r_2/r_1 + 1}, \quad (4.44)$$

which reduces to 2Ta for $\Omega_2 = 0$ and $r_2 - r_1 \ll r_1$. In the limit of nearly equal rotational speeds and $(r_2 - r_1) \ll r_1$, the Couette–Taylor problem reduces exactly to the Rayleigh–Bénard problem with the same critical values of the control parameter and the wave number: $T_{\text{c}} = 1708$ and $k_{\text{c}}(r_2 - r_1) = 3.12$ (Jeffreys, 1928).

4.5 Exercises

4.5.1 The Kelvin–Helmholtz instability with gravity and capillarity

Consider two superposed fluid layers with densities ρ_1 and ρ_2 separated by a horizontal interface with surface tension γ in the gravitational field \mathbf{g} acting in the vertical. These layers move at uniform velocities $-U$ and U .

1. Show that the dispersion relation (4.23) becomes

$$\rho_1(U + c)^2 + \rho_2(U - c)^2 - ((\rho_1 - \rho_2)g/k + \gamma k) = 0. \quad (4.45)$$

2. Choosing as the scales the capillary length $l_{\text{cap}} = \sqrt{\gamma/g(\rho_1 - \rho_2)}$ and the speed V_{cap} such that $V_{\text{cap}}^2 = \frac{1}{2}gl_{\text{cap}}(\rho_1/\rho_2 - \rho_2/\rho_1)$, show that the instability condition can be written as

$$\frac{U^2}{V_{\text{cap}}^2} > \frac{1}{kl_{\text{cap}}} + kl_{\text{cap}}. \quad (4.46)$$

3. Sketch the marginal stability curve in the $[kl_{\text{cap}}, (U/V_{\text{cap}})^2]$ plane, as well as the marginal stability curves in the limits $g = 0$ and $\gamma = 0$, and determine the critical point.
4. Show that there exists a wave number k for which the speed is equal to that of its harmonic $2k$, and that these two wave numbers become unstable at the same speed U .

4.5.2 The effect of walls on the Kelvin–Helmholtz instability

Show that for a flow between two walls located at $y = -h_1$ and $y = h_2$ on either side of the velocity discontinuity, the dispersion relation (4.45) becomes (Rayleigh, 1880; Drazin and Reid, 2004, §23.2)

$$\rho_1(U_1 - c)^2 \coth kh_1 + \rho_2(U_2 - c)^2 \coth kh_2 - ((\rho_1 - \rho_2)g/k + \gamma k) = 0. \quad (4.47)$$

4.5.3 Internal waves in a density-stratified shear flow

Consider an inviscid shear flow $U(y)$ with a stable density profile $\rho(y)$, i.e., $\rho'(y) < 0$ with y vertical upwards. It can be shown that small two-dimensional perturbations are governed by a “generalized Rayleigh equation”

$$\hat{v}'' + \frac{\rho'}{\rho} \hat{v}' + \left(\frac{N^2}{(c-U)^2} + \frac{U''}{c-U} + \frac{\rho'}{\rho} \frac{U'}{c-U} - k^2 \right) \hat{v} = 0, \quad (4.48)$$

where \hat{v} is the amplitude of the transverse component $v = \frac{1}{2}\hat{v}(y)e^{i(kx-\omega t)} + \text{c.c.}$ of the velocity perturbation, $c = \omega/k$, and N is the Brunt–Väisälä frequency. This frequency, defined as

$$N^2 = -g \frac{\rho'}{\rho}, \quad (4.49)$$

is the angular frequency of vertical oscillations of a fluid particle displaced from its equilibrium position and restored by the Archimedes force.

1. Show that

- in the case of uniform density, Eq. (4.48) leads back to the Rayleigh equation (4.15);
- when the density gradient is small compared to the velocity gradient, the above equation reduces to the following so-called Taylor–Goldstein equation:

$$\hat{v}'' + \left(\frac{N^2}{(c-U)^2} + \frac{U''}{c-U} - k^2 \right) \hat{v} = 0. \quad (4.50)$$

2. The flow is bounded by two rigid planes at $y = \pm L$, and so the velocity perturbation must satisfy $\hat{v}(\pm L) = 0$. Make the change of variable $\hat{v} = (U - c)^n q$, where n is a free parameter, and rewrite (4.50) in terms of the function q . Use the same techniques as used in proving the Rayleigh theorem to show that

$$\begin{aligned} \int_{-L}^L (U - c)^{2n} (|q'|^2 + k^2 |q|^2) dy = \\ \int_{-L}^L ((N^2 + n(n-1)U'^2)(U - c)^{2n-2} + (n-1)U''(U - c)^{2n-1}) |q|^2 dy. \end{aligned} \quad (4.51)$$

3. Set $c = c_r + c_i$ and show that, for a suitable choice of n , the flow is stable if

$$U'^2 < 4N^2 \quad (4.52)$$

in the range $-L \leq y \leq L$. Comment on this result taking into account the assumptions made.

4. For a different choice of n , show that if the flow is unstable the speed c of any unstable mode is located between the smallest and the largest value of U in the range $-L \leq y \leq L$. The solution can be found in Acheson (1990).
5. In the case of a stationary fluid ($U(y) = 0$) and for perturbations of wavelength small compared to the scale $(\rho'/\rho)^{-1}$ of the density variations, show that we can explicitly obtain the dispersion relation for the internal waves

$$\omega^2 = N^2 \frac{k^2}{k^2 + l^2}, \quad (4.53)$$

where l is the transverse component of the wave vector $\mathbf{k} = (k, l)$ (Acheson, 1990, §3.8; Tritton, 1988, §15).

4.5.4 Instability of inviscid Couette–Taylor flow

We wish to determine the Rayleigh criterion for the instability of inviscid azimuthal flow between two cylinders of radii r_1 and r_2 aligned along the z -axis. The Euler and the incompressibility equations are written in cylindrical coordinates (r, θ, z) as

$$\frac{\partial U_r}{\partial t} + (\mathbf{U} \cdot \mathbf{grad}) U_r - \frac{U_\theta^2}{r} = -\frac{1}{\rho} \frac{\partial P}{\partial r}, \quad (4.54a)$$

$$\frac{\partial U_\theta}{\partial t} + (\mathbf{U} \cdot \mathbf{grad}) U_\theta + \frac{U_\theta U_r}{r} = -\frac{1}{\rho r} \frac{\partial P}{\partial \theta}, \quad (4.54b)$$

$$\frac{\partial U_z}{\partial t} + (\mathbf{U} \cdot \mathbf{grad}) U_z = -\frac{1}{\rho} \frac{\partial P}{\partial z}, \quad (4.54c)$$

$$\frac{1}{r} \frac{\partial}{\partial r} (r U_r) + \frac{1}{r} \frac{\partial U_\theta}{\partial \theta} + \frac{\partial U_z}{\partial z} = 0, \quad (4.54d)$$

with $\mathbf{U} \cdot \mathbf{grad} = U_r \frac{\partial}{\partial r} + \frac{U_\theta}{r} \frac{\partial}{\partial \theta} + U_z \frac{\partial}{\partial z}$.

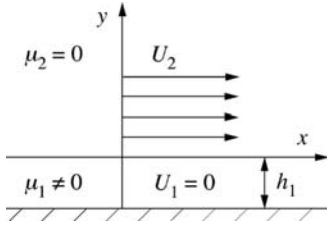


Figure 4.16 A viscous film sheared by an inviscid flow.

1. Determine the system of linearized equations of small perturbations of the base flow $\mathbf{U} = U_\theta(r)\mathbf{e}_\theta$, where \mathbf{e}_θ is an azimuthal unit vector.
2. Consider perturbations of the form $u_r = \hat{u}_r(r)e^{ikz+st}$. Discuss the nature of these normal modes, i.e., what type of flow do they describe? Show by elimination that the stability is governed by the equation

$$(r\hat{u}'_r)' - \left(\frac{k^2}{s^2 r^3} (r^2 U_\theta^2)' + k^2 + \frac{1}{r^2} \right) r\hat{u}_r = 0. \quad (4.55)$$

3. Follow the procedure used to prove the Rayleigh inflection-point theorem (multiplication of the above equation by \hat{u}_r^* , complex conjugation of \hat{u}_r , and integration by parts between r_1 and r_2) to show that the flow is
 - stable if $(r^2 U_\theta^2)' > 0$ in the range $r_1 \leq r \leq r_2$,
 - unstable if $(r^2 U_\theta^2)' < 0$ in the range $r_1 \leq r \leq r_2$.

(It is possible to do better: the flow is unstable if there exists a subrange in the interval $r_1 \leq r \leq r_2$ in which $(r^2 U_\theta^2)'$ is negative (Drazin and Reid, 2004, §15).)

4.5.5 Instability of a viscous film

We consider a very viscous liquid film at rest on a flat surface ($U_1 = 0$), covered by the inertial flow of a different fluid of uniform velocity U_2 (viscous effects negligible), as shown schematically in Figure 4.16. See Benjamin (1959) and Miles (1960) for a discussion of the relevance of this situation. We make the following additional assumptions.

- The growth rate and the speed of the perturbations are small enough that the perturbed flow can be considered to be stationary (the quasi-static boundary condition). Thus time enters only via the condition of impermeability of the interface $\eta(x, t)$ (the kinematic condition), which makes it possible to determine the growth rate. Then, for example, a normal mode is written as $u_1 = \hat{u}_1 e^{ikx} + \text{c.c.}$, except at the interface, where it is written as $\eta = \hat{\eta} e^{i(kx - \omega t)} + \text{c.c.}$

- The perturbations in the inviscid fluid are irrotational.
- The perturbations in the film are governed by the lubrication equations

$$0 = -\partial_x p_1 + \mu_1 \partial_{yy} u_1, \quad 0 = -\partial_y p_1. \quad (4.56)$$

- Surface tension and gravity can be neglected, except in the last question.

1. Determine the perturbation ϕ_2 of the velocity potential and the perturbation p_2 of the pressure in the inviscid fluid, up to a multiplicative constant A .
2. Determine the flow u_1 in the film as a function of p_1 (after linearization at the unperturbed interface $y=0$ of the condition of zero tangential stress at the interface). Next, use the incompressibility condition to determine the speed v_1 in the film as a function of p_1 .
3. Write down the linearized conditions for matching the normal velocities and the normal forces at the interface (it will be shown that the normal forces reduce to pressures). Find the velocity and pressure fields (up to a constant, since we are solving a linear homogeneous problem).
4. Write down the kinematic condition at the interface (this equation is the only one which involves the time). Deduce the dispersion relation

$$\omega\tau = \frac{\alpha^3}{\alpha^2 R - 3i} \quad (4.57)$$

where $\alpha = kh_1$ is a dimensionless wave number, $R = \rho_2 U_2 h_1 / \mu_1$, and $\tau = \mu_1 / \rho_2 U_2^2$ is seen to be the characteristic time of the instability. Sketch the speed and the growth rate as functions of α . Discuss.

5. Include gravity g and surface tension γ in the analysis of a horizontal interface (the corresponding pressure field of the base is $\bar{P}_1 = P_0 - \rho_1 gy$, $\bar{P}_2 = P_0 - \rho_2 gy$, where P_0 is the pressure at the interface). The study of the Rayleigh–Taylor instability can be used as a guide. Sketch the speed and the growth rate as functions of α . Discuss.

5

Viscous instability of parallel flows

5.1 Introduction

The inertial instability of parallel flows described in the preceding chapter is associated with the existence of an inflection point in the velocity profile. This is the principal instability of parallel or quasi-parallel shear flows at large Reynolds number and far from walls or interfaces, such as mixing layers, jets, and wakes. We have seen that the order of magnitude of the growth rate is U/δ , where U is the difference of the speeds on either side of the vorticity layer of thickness δ , and that viscosity plays only a diffusive role tending to attenuate the growth rate. The instability of flow profiles without inflection points is profoundly different. Let us consider two fundamental flows: plane Poiseuille flow and boundary layer flow. Observation shows that plane Poiseuille flow is unstable beyond a certain Reynolds number. Similarly, a boundary layer on a surface becomes unstable at some distance from the leading edge. However, these two flows do not possess an inflection point, and so, ignoring viscosity, they are stable according to the Rayleigh theorem. On the other hand, the growth rate of the observed instabilities is much smaller than would be expected for an inertial instability. It is therefore clearly important to investigate the role played by viscosity, which is the goal of the present chapter. We shall see that viscosity has two effects: the expected stabilizing dissipative effect, and also a *destabilizing* effect. The latter, which unfortunately admits no simple explanation, is due to a subtle coupling between inertia, viscous effects near critical layers, and the no-slip condition.

We begin this chapter by presenting the two canonical situations where a viscous instability is manifested: plane Poiseuille flow and boundary layer flow on a flat surface (Section 5.1). We then display some general results (Section 5.2) before returning to a more detailed study of Poiseuille flow (plane flow in Section 5.3 and pipe flow in Section 5.4) and boundary layer flows (Section 5.5). We also briefly discuss the phenomenon of the transient growth of particular

combinations of eigenmodes, which is important for understanding the transition to turbulence.

5.1.1 Instability of Poiseuille flow in a tube

The celebrated experiment of Osborne Reynolds (1883) on the instability of laminar flow in a tube, shown in Figure 5.1, can be considered the “foundational” experiment in the study of hydrodynamic instabilities. The apparatus is a glass tube submerged in a tank with one end of the tube (on the left in the figure) open in the tank, and the other initially closed by a valve (bottom right). When the valve is opened, liquid in the tank drains through the tube. The trumpet-shaped mouth of the tube should be noted; this is designed to gradually accelerate the fluid without producing flow separation. Dye from a small reservoir (upper left) can be injected at the tube entrance in order to visualize the flow structure.

Reynolds’s observations are illustrated in Figure 5.2, which shows the behavior of a thin stream of dye injected at the tube entrance for three speeds, increasing from top to bottom. In the first photograph the dye stream remains rectilinear without any noticeable distortion. The flow is laminar, and remains so when

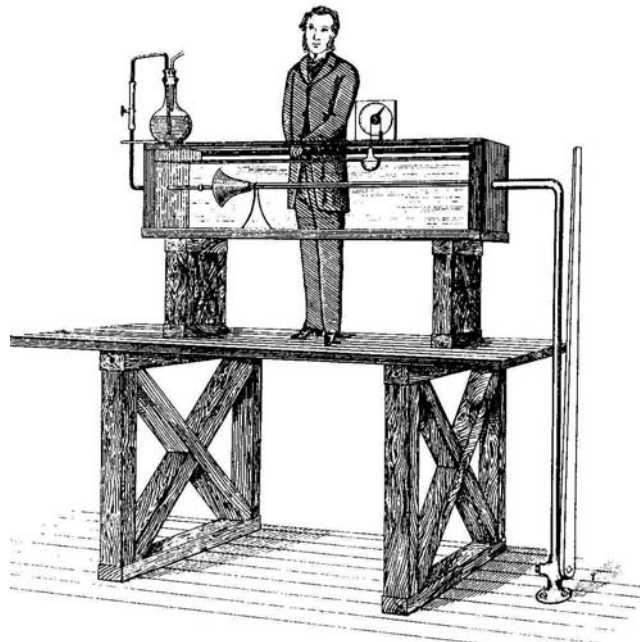


Figure 5.1 Osborne Reynolds in 1883 standing behind his experiment in Manchester. From Reynolds (1883, figure 13)



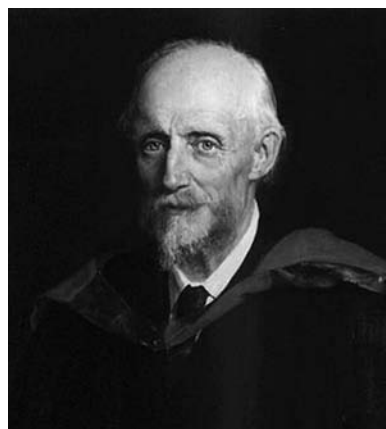
Figure 5.2 The Reynolds experiment, repeated a century later using the original apparatus preserved at the University of Manchester. The speed increases from top to bottom. Photograph taken by Johannessen and Lowe (van Dyke, 1982).

subjected to small perturbations (lightly tapping the tube, for example). In the second photograph the stream undulates, indicating the presence of vortices: the laminar flow has become unstable, but the dye remains quite distinct. In the last photograph the whirling agitation mixes the fluid and disperses the colored stream, so that the dye spreads throughout the tube: the flow is turbulent. Reynolds reproduced this sequence many times while varying the average flow velocity U , the diameter d of the tube, and the viscosity ν of the fluid. His analysis revealed a fundamental rule: the instability appears at a critical value of a dimensionless ratio of scales – what is now known as the Reynolds number Ud/ν .

Reynolds's landmark paper is important on a number of grounds. While the regimes of laminar and turbulent flows were known to exist, there was little understanding of the criteria for the occurrence of one or the other. In addition, Reynolds introduced the first and arguably the most important dimensionless number into hydrodynamics, the famous *Reynolds number*. This opened the door to the analysis of other fluid mechanical phenomena in terms of characteristic scales and the discovery of scaling and universal behavior. Reynolds understood well that difficult and profound questions were hidden beneath the seeming simplicity of the instability criterion. Some of these questions remain unanswered at the present time (Kerswell, 2005). First of all, there is no simple physical interpretation for

this instability, in contrast to, for example, the Couette–Taylor centrifugal instability or the Kelvin–Helmholtz instability. In fact, a linear stability analysis shows that Poiseuille flow in a tube should be stable for any Reynolds number, no matter how large! Second, the experiment, which has been repeated many times, shows that the critical value is not “universal,” but depends on the intensity and nature of the velocity fluctuations present upstream of the flow or those induced by the roughness of the tube or by vibrations of the apparatus. When no special care is taken, the critical value is near 2000; Reynolds reported a value of 13,000 for extremely weak fluctuations at the entrance of the tube. Even larger values have been obtained since then. Finally, this instability is the first stage in the transition to turbulence, a phenomenon which is still poorly understood.

Osborne Reynolds (1842–1912)



Osborne Reynolds was born in Belfast, Ireland, where his father was an Anglican priest, headmaster of a school, and a lover of mechanics. After his secondary education, in 1861 he took an apprenticeship with an engineering firm. He later studied mathematics at Cambridge University with Rayleigh. After graduating in 1867 he again worked as a civil engineer. In 1868 he became a professor at Owens College (later to become the University of Manchester), occupying a newly created chair of engineering, the second one in England. He

remained at this post until his retirement in 1905. His early work was on magnetism and electricity, and on the electromagnetic properties of the Sun and of comets. After 1873 he concentrated on hydraulics and hydrodynamics. He became a Fellow of the Royal Society in 1877. He inaugurated a high-level course in Applied Mathematics designed for engineers. His article of 1883, *An experimental investigation of the circumstances which determine whether the motion of water in parallel channels shall be direct or sinuous and of the law of resistance in parallel channels*, introduced the famous dimensionless number later called the Reynolds number, and established the theory of hydrodynamical stability. In 1886 he formulated a theory of lubrication. His physical and mental health declined in the early 1900s.

5.1.2 Instability of a boundary layer

A configuration similar to the flow in a tube or between two walls is that of flow near a single wall, a situation typically encountered in open flows, on transport vehicles for example. Let us consider the simplest situation of a flat plate placed at zero incidence in a flow of uniform velocity U_∞ (Figure 5.3). A boundary layer develops which is the result of competition between the vertical diffusion of the vorticity produced at the wall and the advection downstream of this vorticity. The thickness $\delta(x)$ of the boundary layer grows as the square root of the distance from the leading edge (Batchelor, 1967). Transitional and intermittent structures occur farther downstream (most notably in the form of waves), leading ultimately to fully developed turbulence. Figure 5.4 illustrates the appearance and development of the instability for three increasing speeds. In photograph (a) corresponding to the lowest speed the flow lines are clearly rectilinear and the instability is not seen because it develops downstream of the field of the photograph. Photograph (b), taken at a higher speed, displays oscillations on the right-hand side which are a manifestation of the instability. Photograph (c), taken at even higher speed, shows that the waves develop closer to the leading edge and then become unstable to spanwise perturbations, presenting a typical peak–valley form. Still farther downstream the boundary layer becomes turbulent.

Therefore, the higher the flow velocity, the closer to the leading edge the instability is manifested. The parameter which controls the onset of the instability is the Reynolds number Re_δ constructed using the thickness $\delta(x)$ of the boundary layer as the length scale:

$$Re_\delta(x) = \frac{U_\infty \delta(x)}{\nu}.$$

More precisely, choosing $\delta(x)$ to be the distance the streamlines of the potential flow exterior to the boundary layer are displaced, i.e., $\delta = 1.73\sqrt{\nu x / U_\infty}$ for the

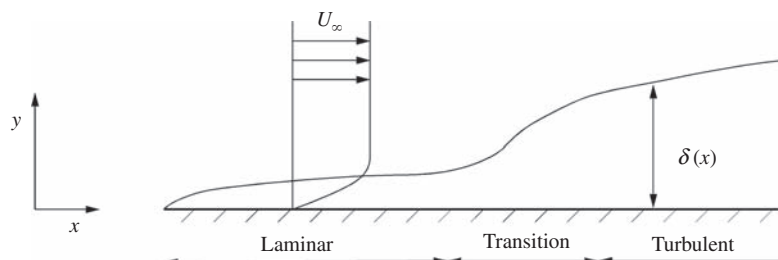


Figure 5.3 Development of a boundary layer on a flat surface at zero incidence.

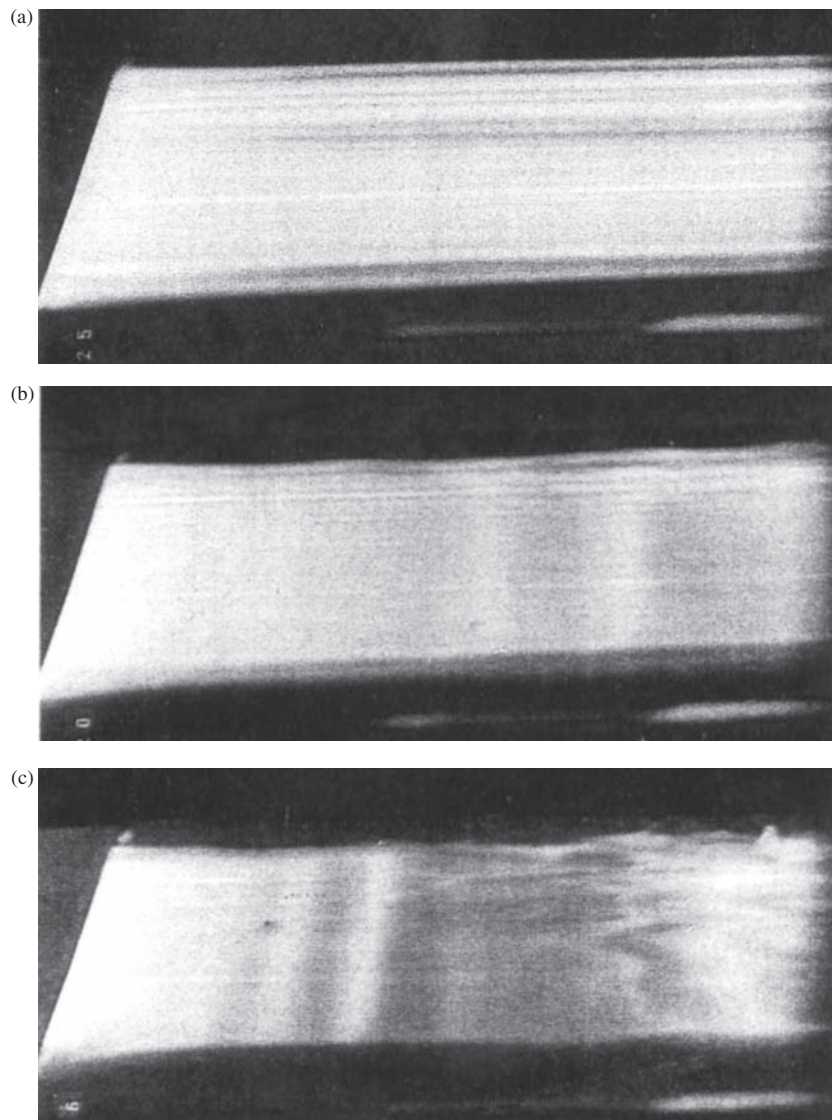


Figure 5.4 Flow lines on a boundary layer starting from the leading edge on the left. The velocity increases in going from the top to the bottom photograph. (a) The instability is not visible; (b) Tollmien–Schlichting waves are seen; (c) the waves now appear closer to the leading edge and then themselves become unstable (from Werlé (1980), courtesy of ONERA).

Blasius boundary layer, the instability appears for $\text{Re}_{\delta,c} = 520$ (or $\text{Re}_x = U_\infty x / \nu \approx 90,000$).

After the work by Prandtl (1921), who was the first to develop the idea of a viscous instability mechanism, these oscillations were predicted by Tollmien (1929)

and Schlichting (1933), and since then have been known as *Tollmien–Schlichting waves*. The first experimental demonstration of the phenomenon was obtained much later by Schubauer and Skramstad (1947). Since then, many studies have been devoted to this problem in connection with transportation engineering in particular. Since turbulent friction is much higher than laminar friction, the overall frictional drag force is weaker the farther downstream from the leading edge the instability develops. Owing to the industrial and ecological requirements of reducing friction (in order to reduce energy consumption and combustion gas emission), it is clearly important to have a good understanding of this instability. Unfortunately, its physical mechanism cannot be understood using dimensional analysis, as for Poiseuille flow.

5.2 General results

In this section we present some general results on the stability of viscous parallel flows. These include the basic linearized equations of the subject and the role of numerical analysis in their solution, an extension of the Squire theorem to include viscous effects, and a discussion of the mechanism of viscous instability.

5.2.1 The linearized perturbation equations

We choose two characteristic scales L and V as our units of length and velocity, and ρV^2 as our unit of pressure. Defining the Reynolds number as $\text{Re} = UL/\nu$, the incompressibility and Navier–Stokes equations can be written as

$$\text{div}\mathbf{U} = 0, \quad (5.1)$$

$$\partial_t \mathbf{U} + (\mathbf{U} \cdot \mathbf{grad}) \mathbf{U} = -\mathbf{grad} P + \frac{1}{\text{Re}} \Delta \mathbf{U}. \quad (5.2)$$

Let $\bar{U}(y)\mathbf{e}_x$ and \bar{P} be a parallel stationary solution of these equations, which define the base flow. For example, for plane Poiseuille flow the base flow is $\bar{U}(y) = 1 - y^2$, taking as the length scale the half-distance between the walls and as the velocity scale the maximum velocity. For the boundary layer on a flat plate the base flow $\bar{U}(y)$ is typically the Blasius solution of the boundary-layer equations (of course $\bar{U}(y)$ is only an approximate quasi-parallel flow solution of the full Navier–Stokes equations; this point will be discussed later on).

We consider the perturbed flow $(\bar{\mathbf{U}} + \mathbf{u}, \bar{P} + p)$ and linearize the equations for the perturbations. This gives

$$\operatorname{div} \mathbf{u} = 0, \quad (5.3)$$

$$(\partial_t + \bar{U} \partial_x) \mathbf{u} + v \partial_y \bar{U} \mathbf{e}_x = -\mathbf{grad} p + \frac{1}{Re} \Delta \mathbf{u}. \quad (5.4)$$

Since they are invariant under translations in x , z , and t (but not in y), these equations have a solution corresponding to normal modes proportional to $e^{i(k_x x + k_z z - \omega t)}$, with wave vector $\mathbf{k} = k_x \mathbf{e}_x + k_z \mathbf{e}_z$ and frequency ω , as in the preceding chapter. Therefore, these equations reduce to a system of homogeneous differential equations for the amplitudes $\hat{\mathbf{u}}(y)$ and $\hat{p}(y)$:

$$ik_x \hat{u} + \partial_y \hat{v} + ik_z \hat{w} = 0, \quad (5.5a)$$

$$ik_x (\bar{U} - c) \hat{u} + \partial_y \bar{U} \hat{v} = -ik_x \hat{p} + \frac{1}{Re} (\partial_{yy} - k_x^2 - k_z^2) \hat{u}, \quad (5.5b)$$

$$ik_x (\bar{U} - c) \hat{v} = -\partial_y \hat{p} + \frac{1}{Re} (\partial_{yy} - k_x^2 - k_z^2) \hat{v}, \quad (5.5c)$$

$$ik_x (\bar{U} - c) \hat{w} = -ik_z \hat{p} + \frac{1}{Re} (\partial_{yy} - k_x^2 - k_z^2) \hat{w}, \quad (5.5d)$$

where $c = \omega/k_x$ is the phase velocity of the perturbation in the direction x . The boundary conditions correspond to no-slip on the walls for Poiseuille flow, and to no-slip on the wall at $y = 0$ and decay of the perturbations for $y \rightarrow \infty$ for boundary-layer flow. The system (5.5) together with these conditions constitutes a generalized eigenvalue problem which has nonzero solution only when the operator is singular, that is, when the frequency ω and the wave vector \mathbf{k} satisfy a dispersion relation

$$D(\mathbf{k}, \omega, Re) = 0. \quad (5.6)$$

5.2.2 The Squire theorem

As for the inviscid flows of the preceding chapter, use of a transformation of variables and a theorem due to Squire (1933) allows the three-dimensional problem to be reduced to an equivalent two-dimensional one. The Squire transformation consists of introducing the same transformations defined in the preceding chapter:

$$\tilde{k}^2 = k_x^2 + k_z^2, \quad (5.7a)$$

$$\tilde{\omega} = (\tilde{k}/k_x) \omega, \quad (5.7b)$$

$$\tilde{k} \tilde{u} = k_x \hat{u} + k_z \hat{w}, \quad (5.7c)$$

$$\tilde{v} = \hat{v}, \quad (5.7d)$$

$$\tilde{p} = (\tilde{k}/k_x) \hat{p}, \quad (5.7e)$$

as well as an additional one:

$$\tilde{k}\widetilde{\text{Re}} = k_x \text{Re}. \quad (5.8)$$

The system of four equations (5.5) is then replaced by the following system of three equations, with $\tilde{c} = \tilde{\omega}/\tilde{k} = \omega/k_x = c$:

$$i\tilde{k}\tilde{u} + \partial_y \tilde{v} = 0, \quad (5.9a)$$

$$i\tilde{k}(\overline{U} - \tilde{c})\tilde{u} + \partial_y \overline{U}\tilde{v} = -i\tilde{k}\tilde{p} + \frac{1}{\text{Re}}(\partial_{yy} - \tilde{k}^2)\tilde{u}, \quad (5.9b)$$

$$i\tilde{k}(\overline{U} - \tilde{c})\tilde{v} = -\partial_y \tilde{p} + \frac{1}{\text{Re}}(\partial_{yy} - \tilde{k}^2)\tilde{v}. \quad (5.9c)$$

Associated with this system are the boundary conditions of decay at infinity, $\tilde{u}, \tilde{v} \rightarrow 0$ for $y \rightarrow \infty$, or no-slip at a solid surface, $\tilde{u}(y_1) = \tilde{v}(y_1) = 0$, $\tilde{u}(y_2) = \tilde{v}(y_2) = 0$. This homogeneous system of two-dimensional perturbations has nonzero solution only if the following dispersion relation is satisfied:

$$\tilde{D}(\tilde{k}, \tilde{\omega}, \widetilde{\text{Re}}) = 0. \quad (5.10)$$

Once this relation is known, the three-dimensional dispersion relation can be obtained without further calculation by means of the Squire transformation:

$$D(\mathbf{k}, \omega; \text{Re}) = \tilde{D} \left(\sqrt{k_x^2 + k_z^2}, \frac{\sqrt{k_x^2 + k_z^2}}{k_x} \omega; \frac{k_x}{\sqrt{k_x^2 + k_z^2}} \text{Re} \right) = 0. \quad (5.11)$$

From this expression we deduce the Squire theorem.

Theorem 5.1 *With any unstable oblique mode (\mathbf{k}, ω) of temporal growth rate ω_i for Reynolds number Re it is possible to associate a two-dimensional mode $(\tilde{k}, \tilde{\omega})$ of temporal growth rate $\tilde{\omega}_i = \omega_i \sqrt{k_x^2 + k_z^2} / k_x$, higher than ω_i , at a Reynolds number $\widetilde{\text{Re}} = \text{Re} k_x / \sqrt{k_x^2 + k_z^2}$, lower than Re .*

Corollary 5.2 *If there exists a Reynolds number Re_c above which a flow is unstable, the normal mode which destabilizes the flow for $\text{Re} = \text{Re}_c$ is two-dimensional. Indeed, if this were not the case, it would be possible to find an unstable two-dimensional mode for $\text{Re} < \text{Re}_c$ which contradicts the definition of Re_c .*

If the problem is to determine an instability condition (typically, a critical Reynolds number), the Squire theorem states that it is sufficient to consider two-dimensional perturbations. However, beyond the critical Reynolds number

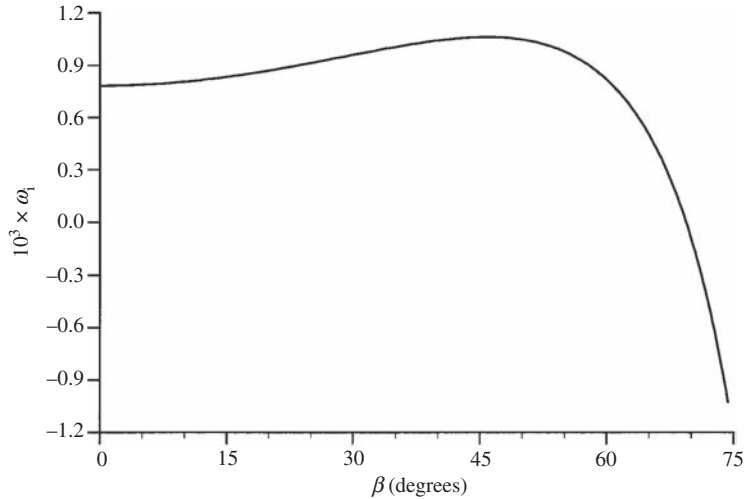


Figure 5.5 Temporal growth rate (s^{-1}) of a boundary layer instability as a function of the angle β of the perturbation relative to the direction of the base flow. $Re_\delta = 1500$, $\omega v / U_\infty^2 = 0.3 \times 10^{-4}$ (calculation by G. Casalis, ONERA).

($Re > Re_c$) the most unstable perturbation is not necessarily two-dimensional, but may be oblique ($k_z \neq 0$). This is illustrated in Figure 5.5, which shows the growth rate of a perturbation of the Blasius boundary layer as a function of the angle β between the wave vector \mathbf{k} and the direction of the base flow. For the Reynolds number $Re_\delta = 1500$ above the critical value $Re_{\delta,c} = 520$ we see that the most unstable perturbation is not two-dimensional (angle β equal to zero), but corresponds to an angle of about 50° .

The Squire theorem was obtained above for rigid walls. It has been generalized to the case of two or more fluid layers separated by a deformable interface, where velocity continuity and stress balance conditions must be satisfied (Hesla *et al.*, 1986).

5.2.3 The Orr–Sommerfeld equation

Bearing in mind the Squire theorem, from now on we shall consider two-dimensional perturbations, and introduce the stream function ψ of the velocity perturbation defined as $u = \partial_y \psi$ and $v = -\partial_x \psi$. Eliminating the pressure by cross-differentiating the equations (5.4), we obtain

$$(\partial_t + \bar{U} \partial_x) \Delta \psi - \partial_{yy} \bar{U} \partial_x \psi = \frac{1}{Re} \Delta^2 \psi. \quad (5.12)$$

This can also be recognized as the linearized transport equation for the vorticity perturbation $\omega = -\Delta \psi$. Seeking the solution in the form of normal modes

$$\psi(\mathbf{x}, t) = \frac{1}{2} \hat{\psi}(y) e^{i(kx - \omega t)} + \text{c.c.}$$

of wave number k , frequency ω , and speed $c = \omega/k$, we find the *Orr–Sommerfeld equation* (Orr, 1907; Sommerfeld, 1908):

$$(\bar{U} - c)(\partial_{yy} - k^2)\hat{\psi} - \partial_{yy}\bar{U}\hat{\psi} = \frac{1}{ik\text{Re}}(\partial_{yy} - k^2)^2\hat{\psi}. \quad (5.13)$$

The only difference between this equation and the Rayleigh equation (*cf.* Chapter 4) is the term on the right-hand side due to the viscous forces, which raises the equation from second to fourth order (with the corresponding increase in the number of boundary conditions).

The associated boundary conditions are no-slip at the walls at $y = y_1$ and $y = y_2$,

$$\partial_y \hat{\psi}(y_1) = \hat{\psi}(y_1) = 0, \quad (5.14a)$$

$$\partial_y \hat{\psi}(y_2) = \hat{\psi}(y_2) = 0, \quad (5.14b)$$

or, in the case of a boundary layer on a wall at $y = 0$, the conditions of no-slip at the wall and decay at large distances:

$$\partial_y \hat{\psi} = \hat{\psi} = 0 \quad \text{at } y = 0, \quad (5.15a)$$

$$\partial_y \hat{\psi}, \hat{\psi} \rightarrow 0 \quad \text{for } y \rightarrow \infty, \quad (5.15b)$$

or, finally, the conditions of velocity continuity and stress balance on a deformable interface (in which case the speed also enters into the boundary conditions; *cf.* Chapter 6).

Writing the Orr–Sommerfeld equation as

$$L_A \hat{\psi} = c L_B \hat{\psi},$$

where the differential operators L_A and L_B are defined as

$$L_A = (\partial_{yy} - k^2)^2 - ik\text{Re}(\bar{U}(\partial_{yy} - k^2) - \partial_{yy}\bar{U}),$$

$$L_B = -ik\text{Re}(\partial_{yy} - k^2),$$

the problem becomes a generalized eigenvalue problem which has a nontrivial solution only if the speed c satisfies a dispersion relation.

When temporal stability is studied, the problem is solved by imposing the condition that k is real, and then the complex speed is calculated; on the other hand, when spatial stability is studied, the condition of real frequency ω is imposed and the wave numbers are calculated. For a given value of k or ω there exist in general several modes with different growth rates. Since the speed enters linearly into

the problem (except possibly in the boundary conditions at a deformable interface) while the wave number enters quadratically, it is much easier to study temporal stability than spatial stability, and generally it is the former that is considered when seeking marginal stability conditions.

The Orr–Sommerfeld equation (5.13) is a fourth-order linear differential equation with nonconstant coefficients. Exact solutions are known only in certain very special cases, notably when $\partial_{yy}\bar{U} = 0$ (i.e., piecewise-linear velocity profiles): the vorticity then satisfies an Airy equation, and the speed is expressed as integrals of Airy functions (Exercise 5.6.3). For finite wave number and Reynolds number the coefficient of the highest-order term $(ik\text{Re})^{-1}$ does not vanish, and the problem of degeneracy of the Rayleigh equation for $\bar{U} = c$ (existence of a critical layer) does not arise. However, when the instability appears at large Reynolds number, which is the case in, for example, Poiseuille flow, the problem becomes difficult to solve: the viscous term on the right-hand side, even though it has a small coefficient, can become of the same order as the inertial terms in regions where the eigenfunction or its derivatives have large gradients. This happens, in particular, near a wall and within the critical layer of the associated inviscid problem, where the thickness of the region affected by viscosity is of order $(kh\text{Re})^{-1/2}$ and $(kh\text{Re})^{-1/3}$, respectively. Some imaginative and ingenious mathematical techniques have been developed, in particular, by Heisenberg (1924), Tollmien (1929), Schlichting (1933), and Lin (1955), to find solutions approached by asymptotic series, or at least to determine an approximate marginal stability curve in the (k, Re) plane; see Drazin and Reid (2004, chapters 4 and 5). At small Reynolds number or small wave number the asymptotic series are in general regular; an example is given in Chapter 6 for a liquid film flowing on an inclined plane.

Nowadays the Orr–Sommerfeld equation can be solved numerically without much difficulty. The numerical methods used most frequently are either shooting or spectral methods (Canuto *et al.*, 1988; Schmid and Henningson, 2001, appendix A). The former consists of spatially integrating the equation starting from a guess for the solution on one of the boundaries, integrating up to the other boundary, and then correcting the “trajectory” iteratively in order to satisfy the conditions on this other boundary. This method is easy to implement, but not very stable due to the large spatial gradients alluded to above. Spectral methods consist of projecting the amplitude $\hat{\psi}$ of the eigenfunction onto a basis of suitable functions $\phi_k(y)$:

$$\hat{\psi}(y) = \sum_{k=0}^n a_k \phi_k(y), \quad (5.17)$$

and solving for the coefficients a_k in a manner consistent with the Orr–Sommerfeld equation. Choosing the functions $\phi_k(y)$ such that their derivatives are expressed as

linear combinations of the functions themselves (like the trigonometric functions), the Orr–Sommerfeld equation and boundary conditions can be transformed into a system of linear equations. The Chebyshev polynomials $T_k(y)$ are a particularly appropriate basis¹ because the collocation points cluster near the walls or the interface, where the gradients of the eigenfunctions are in general large (Orszag, 1971). Spectral (or pseudo-spectral, there are several variants) methods have the advantage of being very precise and of giving approximations of the entire eigenvalue spectrum (up to the order of the discretization), as well as of the associated eigenfunctions.

We note that even though high-performance numerical methods are now readily accessible, asymptotic methods may still be needed for analyzing the behavior of the solution near a singularity. Asymptotic methods are also very helpful in understanding the role played by the various parameters, as well as for gaining a deeper insight into the problem.

5.2.4 The viscous instability mechanism

As mentioned in Section 5.1, the viscous instability mechanism of a shear flow near a solid boundary or a deformable interface is not simple to describe. However, some understanding can be obtained from the equation for the kinetic energy of the perturbation, $e_k = \frac{1}{2}(u^2 + v^2 + w^2)$ per unit mass. Performing scalar multiplication of the Navier–Stokes equation by the velocity perturbation vector and rearranging it using $\operatorname{div} \mathbf{u} = 0$, we find

$$(\partial_t + \overline{U}\partial_x)e_k + \operatorname{div}((p + e_k)\mathbf{u}) = -\partial_y \overline{U}(\overline{U} + u)v + \frac{1}{Re} (\operatorname{div}(\mathbf{u} \times \boldsymbol{\omega}) - \boldsymbol{\omega} \cdot \boldsymbol{\omega}), \quad (5.18)$$

where $\boldsymbol{\omega} = \operatorname{rot}(\mathbf{u})$ is the vorticity perturbation. Let us take a spatially periodic perturbation with wavelength $2\pi/k_x$ and $2\pi/k_z$ in the x - and z -directions. Defining the spatial average of a quantity $q(x, y, z, t)$ as

$$\langle q \rangle(y, t) = \frac{k_x}{2\pi} \frac{k_z}{2\pi} \int_0^{2\pi/k_x} \int_0^{2\pi/k_z} q(x, y, z, t) dx dz \quad (5.19)$$

¹ The Chebyshev polynomials, defined as $T_n(y) = \cos(n \cos^{-1}(y))$, form a basis on the interval $[-1, 1]$, to which a more general integration range $[y_1, y_2]$ or $[0, \infty]$ may be transformed by means of a change of variable. These polynomials are related by the recursion relation $T_0 = 1$, $T_1 = y$, $T_{n+1} = 2yT_n - T_{n-1}$. Other recursion relations permit the derivative of a polynomial to be expressed as a function of other polynomials, so that a differential system can be transformed into an algebraic system.

and noting that because of the boundary and periodicity conditions, $\langle \partial_x q \rangle = \langle \partial_z q \rangle = 0$ and $\langle v \rangle = 0$, the average of Eq. (5.18) can be written as

$$\partial_t \langle e_k \rangle + \partial_y (\langle p v \rangle + \langle e_k v \rangle) = \partial_y \bar{U} \tau_{xy} + \frac{1}{Re} \partial_y \langle \omega_x w - \omega_z u \rangle - \frac{1}{Re} \langle \omega \cdot \omega \rangle, \quad (5.20)$$

where $\tau_{xy} = -\langle uv \rangle$ is a Reynolds stress (Tritton, 1988, §19.3). Integrating this equation between two walls at y_1 and y_2 and taking into account the no-slip conditions, we finally obtain the *exact* equation that holds for perturbations of arbitrary amplitude as

$$\frac{d}{dt} \int_{y_1}^{y_2} \langle e_k \rangle dy = \int_{y_1}^{y_2} \partial_y \bar{U} \tau_{xy} dy - \frac{1}{Re} \int_{y_1}^{y_2} \langle \omega \cdot \omega \rangle dy. \quad (5.21)$$

This is a special version of the Reynolds–Orr equation (Lin, 1955; Drazin and Reid, 2004, §53). The left-hand side represents the growth rate of the average kinetic energy of the perturbation. If it is negative the base flow is stable, otherwise it is unstable. The second term on the right-hand side corresponds to viscous dissipation. It is always positive, and always tends to attenuate the perturbation. Therefore, only the first term can cause the perturbation to grow and will do so if it dominates the dissipative term: this term corresponds to energy being “pumped” from the base flow into the perturbations.

We can also find an equation for the kinetic energy of an eigenmode starting from the linearized equations. We then obtain an equation *identical* to (5.21), because the contribution of the nonlinear advective term is in fact zero after integration and application of the boundary and periodicity conditions. Let us therefore consider Eq. (5.21) for eigenmodes of the form

$$u = \frac{1}{2} \hat{u}(y) e^{i(kx - \omega t)} + \text{c.c.}, \quad \hat{u}(y) = |\hat{u}(y)| e^{i\phi_u(y)}.$$

The Reynolds stress involved in the kinetic energy production term then becomes

$$\tau_{xy}(y) = -\frac{1}{2} |\hat{u}| |\hat{v}| \cos(\phi_u - \phi_v) e^{2\omega_i t}. \quad (5.22)$$

We note that this expression involves only the phase difference between u and v ; it is only this difference which is physically meaningful, as the phases themselves are associated with the arbitrary choice of origin (fixed, if needed, by a normalization condition for the eigenfunctions).

Let us neglect viscous dissipation for the time being. Since according to the Rayleigh theorem a velocity profile without an inflection point is stable, the

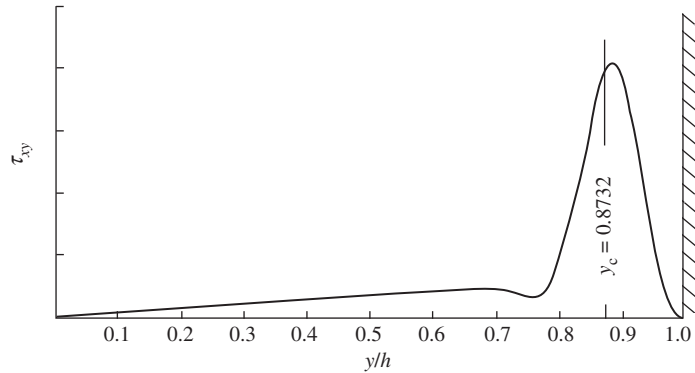


Figure 5.6 Transverse distribution of the Reynolds stress τ_{xy} (5.22) for plane Poiseuille flow (the vertical scale, which is related to the normalization condition, is arbitrary). y_c is the location of the critical layer where $c_r = \bar{U}(y_c)$. $Re = 10^4$, $kh = 1$, and $c = 0.24 + 0.0037i$. Taken from Stuart (1963).

eigenmodes are necessarily neutral, and the rate of variation of the kinetic energy is zero. On the other hand, for a *neutral* perturbation of an inviscid flow the components u and v of the velocity are exactly out of phase (Section 4.2.3), and so the Reynolds stress (5.22) is zero. The kinetic energy production term is therefore zero, and Eq. (5.21) is satisfied trivially.

Let us now consider the effect of viscosity. Figure 5.6 shows a typical profile of the Reynolds stress $\tau_{xy}(y)$, corresponding to the unstable eigenmode of plane Poiseuille flow (since this stress is antisymmetric [$\tau_{xy}(-y) = -\tau_{xy}(y)$], we show it only in the half-plane). $\tau_{xy}(y)$ has the same sign as the gradient $\partial_y \bar{U}$, and the kinetic energy production term is therefore positive. We see that the Reynolds stress vanishes at the symmetry plane ($y/h = 0$), remains very weak up to $y/h \approx 0.8$, has a sharp peak at $y/h \approx 0.9$ located near the critical layer (where the speed of the eigenmode is equal to the flow speed), and then vanishes at the wall. Its higher value near the wall corresponds to a viscously-induced *phase shift* between u and v , which is related to a combination of viscous effects near the critical layer and those near the wall due to the no-slip condition (see also Figures 5.8 and 5.10 below).

Therefore, at small Reynolds number the production of kinetic energy is smaller than the dissipation, and the flow is stable. However, at large Reynolds number dissipation becomes negligible (measured on the characteristic scales of the flow h and $\bar{U}(0)$), and production dominates, making the flow unstable. Viscous diffusion therefore has two effects: a stabilizing effect via the dissipation term, and a destabilizing effect related to the no-slip condition which distorts the phase angle between u and v . A similar situation can arise near a deformable interface. This discussion does not really explain the instability, but it does nevertheless shed some light on

the subtle and delicate role played by viscosity near a wall. Note finally that a mechanism has been proposed by Baines *et al.* (1996) for the growth of Tollmien–Schlichting waves, based on a linear resonance between an inviscid mode and a viscous mode; see Exercise 5.6.4.

5.3 Plane Poiseuille flow

5.3.1 Marginal stability, eigenmodes

Plane Poiseuille flow is typical of a parallel flow being unstable beyond a critical Reynolds number, when the production of kinetic energy of small perturbations, associated with the Reynolds stress τ_{xy} , exceeds the viscous dissipation. The control parameter of this instability is the Reynolds number

$$\text{Re} = \frac{Uh}{\nu}, \quad (5.23)$$

where U is the speed in the center of the channel, h is the half-height of the channel, and ν is the kinematic viscosity. Figure 5.7 shows the marginal stability curve obtained by solving the Orr–Sommerfeld equation. For $\text{Re}_c = 5772$ the flow becomes unstable to a perturbation of wave number $k_c h = 1.02$. Near threshold the curve is parabolic and the width of the band of unstable wave numbers grows as $\sqrt{\text{Re} - \text{Re}_c}$. At large Reynolds number this unstable band shifts toward zero (long wavelengths) and becomes narrower. It can be shown that the upper branch behaves as $\text{Re} \sim (kh)^{-11}$, and that the two regions affected by the viscosity,

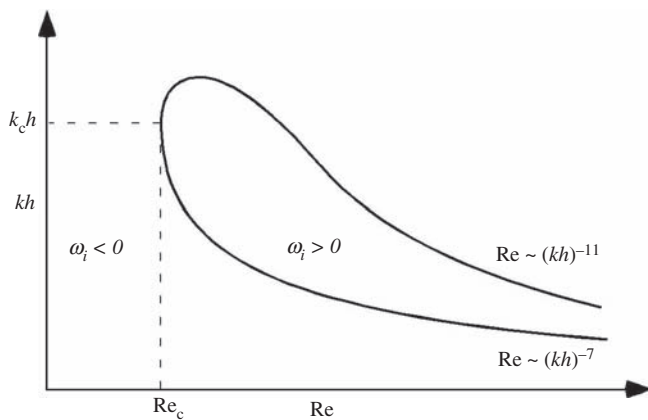


Figure 5.7 Shape of the marginal stability curve in the $\text{Re}-kh$ plane for plane Poiseuille flow.

near the wall and the critical layer, are disconnected. The lower branch behaves as $\text{Re} \sim (kh)^{-7}$ and there the two regions affected by viscosity overlap. The upper and lower branches must merge at infinite Reynolds number since the flow is inviscidly stable (Drazin and Reid, 2004). The growth rate in the unstable region is never large and is a maximum at $\text{Re} = 48,000$. As an illustration of the magnitude of the maximum growth rate, it takes a time of approximately $300h/U$ for a small perturbation to grow by a factor of ten, during which time a fluid particle at the center of the channel has traveled a distance equal to 150 times the channel height.

For a given wave number there is only a single unstable mode corresponding to the longitudinal velocity disturbance being odd, i.e., $u(-y) = -u(y)$, and the transverse velocity is even, i.e., $v(-y) = v(y)$. Figure 5.8 shows the amplitude $\hat{\psi}(y)$ of the stream function of the unstable mode for $\text{Re} = 10^4$, normalized to unity at the center of the channel (this eigenfunction is even, like v). The imaginary part is much smaller than the real part (note the difference of the scales). Thus, the transverse velocity $|\hat{v}| = |-ik\hat{\psi}|$ is maximal at the center of the channel, while the longitudinal velocity $|\hat{u}| = |\partial_y \hat{\psi}|$ is zero at the center and maximal near the walls. The numerical calculation reveals the existence, for the same pair (kh, Re) , of other eigenmodes, all of which are stable and of positive speed, with discrete eigenvalues arranged along well-defined branches in the (c_r, c_i) plane (Orszag, 1971; Schmid and Henningson, 2001, §3; Drazin and Reid, 2004, §31.3). In particular, the modes with parity opposite to that of the unstable mode are very strongly attenuated. Beyond the critical Reynolds number the instability remains convective over a large range of Reynolds number (Huerre and Rossi, 1998, §8).

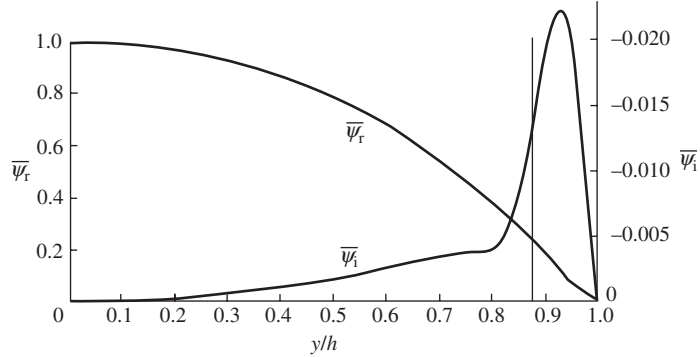


Figure 5.8 The unstable eigenfunction (normalized to unity at the channel center) of plane Poiseuille flow corresponding to $c = 0.23 + 0.0037i$, for $\text{Re} = 10^4$ and $kh = 1$. From a numerical calculation by Thomas (1953), quoted in Drazin and Reid (2004).

5.3.2 Experimental study for small perturbations

The instability of this flow has been studied in great detail experimentally by Nishioka *et al.* (1975). The experimental setup is shown in Figure 5.9. Air flows through a channel of rectangular cross-section of height $2h = 1.46$ cm and exits into the atmosphere. A large width-to-height ratio of 27.4 makes it possible to obtain two-dimensional flow in the central region of the channel. Air is injected very carefully so that the level of residual turbulence is extremely small, less than 0.05% of the mean flow. This level is so low that without any artificial excitation the instability is not detected at the channel exit up to $\text{Re} \approx 8000$, a value well above the prediction $\text{Re}_c = 5772$. A perturbation of controlled frequency f is generated by the vibration of a metal ribbon close to the lower wall; the vibration is excited by an alternating current in the ribbon placed in the field of a magnet. The perturbation so produced is advected downstream by the flow in the form of a Tollmien–Schlichting wave which is attenuated or amplified depending on the Reynolds number. The other modes naturally present in the residual noise have amplitude too small to be detected, even if they are unstable. A hot-wire probe mounted on a traversing mechanism is used to measure the perturbation amplitude at various points in the channel.

Figure 5.10 shows the variation of the phase and amplitude of the longitudinal velocity perturbation u under various conditions of driving frequency and Reynolds number. These variations correspond closely to the eigenmodes

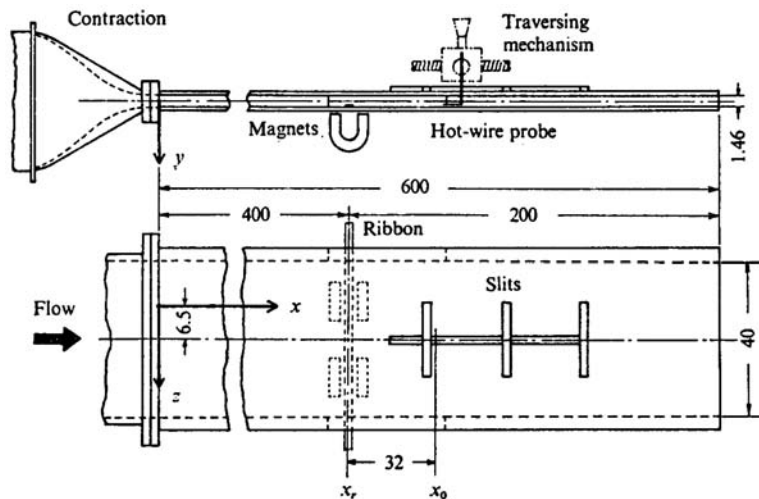


Figure 5.9 Experimental setup for the study of plane Poiseuille flow (from Nishioka *et al.* (1975), © Cambridge University Press, reproduced with permission). The dimensions are in centimeters.

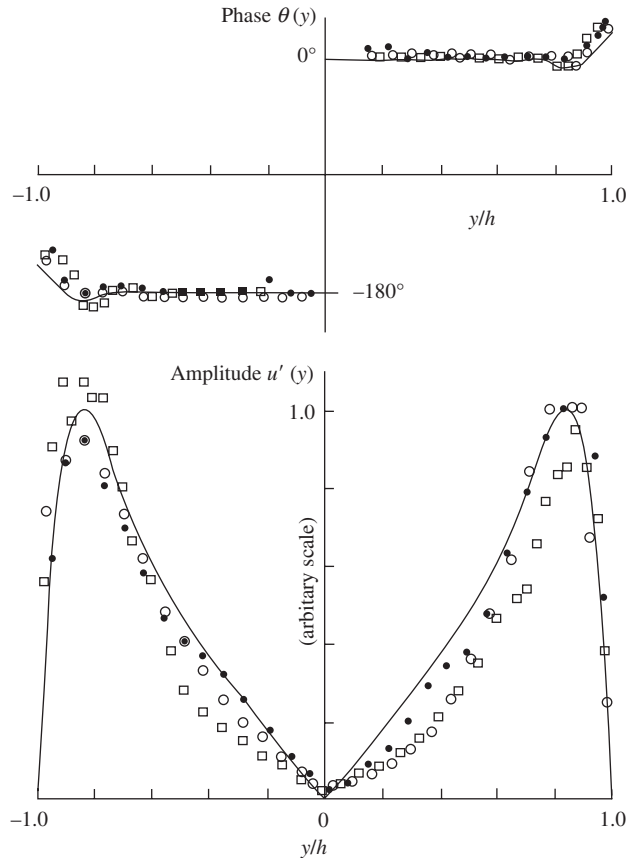


Figure 5.10 Amplitude and phase of the longitudinal velocity perturbation: (●) $Re = 3000$, $\omega = 2\pi f U/h = 0.36$; (○) $Re = 4000$, $\omega = 0.27$; (□) $Re = 6000$, $\omega = 0.32$. (—) Eigenmode calculated for $Re = 4000$, $\omega = 0.27$. (From Nishioka *et al.* (1975), © Cambridge University Press, reproduced with permission.)

calculated theoretically (even ones for $\hat{\psi}$, odd ones for \hat{u}). The phase jump of 180° at the channel center should be noted; it corresponds to a change of sign of u . For the frequency and Reynolds number ranges explored, $f = 40–100$ Hz and $Re = 3000–8000$, the wavelength lies between $4h$ and $8h$ and the wave speed between $0.2U$ and $0.3U$.

Figure 5.11 shows the downstream evolution of the perturbation amplitude; the vertical scale is logarithmic, so that the expected exponential growth corresponds to a straight line. This exponential growth is clearly manifested over a distance of about 10–15 cm for cases for which the mode is damped (negative slope), nearly neutral (slope almost zero), or amplified (positive slope). Note that the growth rate increases monotonically with the Reynolds number (Figure 5.11a), whereas

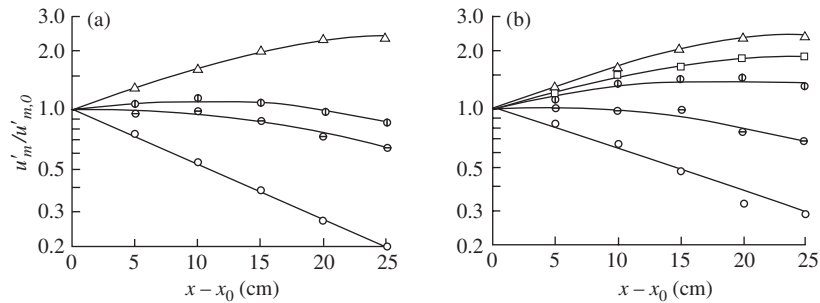


Figure 5.11 Downstream evolution of the perturbation amplitude: (a) $f = 72$ Hz and $\text{Re} = 4000$ (○), 5300 (⊖), 6400 (⊕), 7000 (△); (b) $\text{Re} = 7000$ and $f = 50$ (⊕), 60 (□), 72 (△), 82 (⊖), and 92 (○) Hz. (From Nishioka *et al.* (1975), © Cambridge University Press, reproduced with permission.)

it first increases and then decreases with increasing frequency (Figure 5.11b). Beyond this region of exponential growth the amplitude of the perturbation, which is of order $0.025 U$, suggests a saturation, but in fact, downstream from the measurement region shown here, the amplitude grows catastrophically and the flow becomes turbulent. This evolution is related to the subcritical nature of the instability, demonstrated by Stewartson and Stuart (1971) using a weakly nonlinear analysis: the dominant nonlinear effects do not saturate the instability as they do in Rayleigh–Bénard convection or Couette–Taylor flow, but rather further amplify it. We shall return to this point in Chapter 9.

Figure 5.12 shows the spatial growth rate derived from the amplitude measurements as a function of the excitation frequency, for four Reynolds numbers below and above threshold. The measured values are in good agreement with the values calculated earlier, which are shown by the solid curves. Finally, Figure 5.13 shows the measurement points in the $\text{Re} - kh$ plane corresponding to stable and unstable flows. We see that these points are distributed on either side of the calculated marginal stability curve and are in general agreement with the theory.

5.3.3 Transient growth

The observations of Nishioka *et al.* (1975) described above correspond to the case where the perturbations at the channel entrance are well controlled and of very small amplitude, typically of order 1% of the speed at the channel center. In the more common situation where these perturbations are not controlled, they generally have much larger amplitude. The instability arises below the critical Reynolds number $\text{Re}_c = 5772$, and the structure of the perturbations is not that of the most amplified Tollmien–Schlichting mode. The current explanation for this is that the

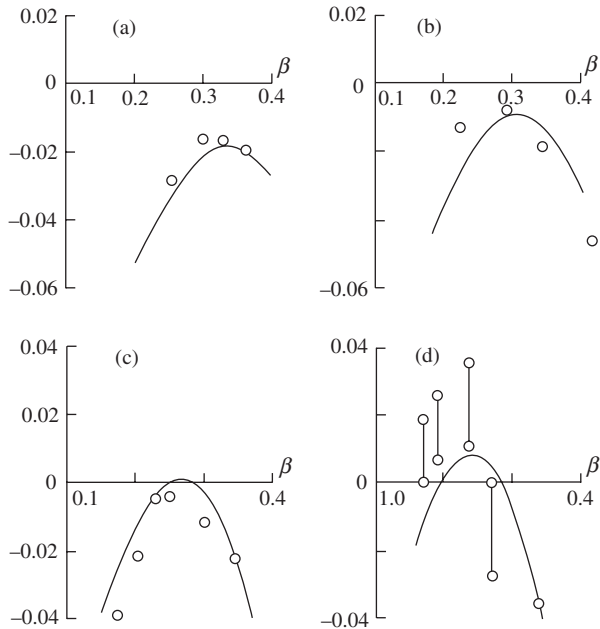


Figure 5.12 Spatial growth rate $-\alpha_i = -k_i h$ as a function of the frequency $\beta = 2\pi f U / h$: (○) measurements, (—) calculation (Itoh, 1974). (a) $Re = 3000$, (b) $Re = 4000$, (c) $Re = 5700$ (calculation: $Re = 6000$), (d) $Re = 7000$ (calculation: $Re = 8000$). (From Nishioka *et al.* (1975), © Cambridge University Press, reproduced with permission.)

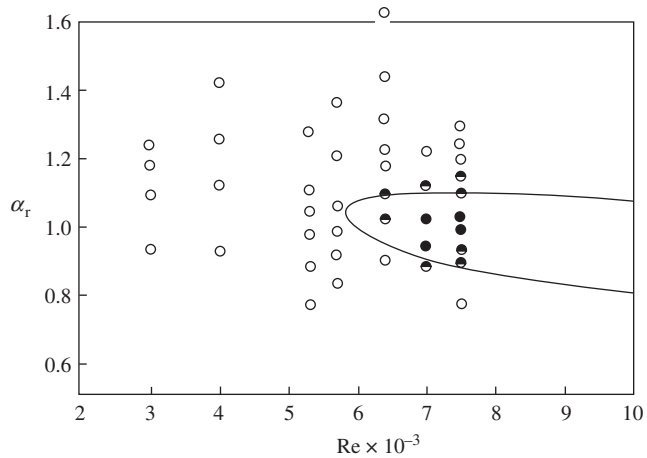


Figure 5.13 Map in the $Re - \alpha_r$ plane ($\alpha_r = k_r h$) of stable measurement points (○), almost neutral points (half-filled circles), and unstable points (●), along with the calculated marginal stability curve. (From Nishioka *et al.* (1975), © Cambridge University Press, reproduced with permission.)

observed structure originates in the transient growth of very special combinations of linearly *stable* eigenmodes; these perturbations can then grow by several orders of magnitude, reaching amplitudes large enough that nonlinear mechanisms – poorly understood – induce the transition to turbulence. These phenomena, introduced in hydrodynamics in the late 1970s (Ellingsen and Palm, 1975; Landahl, 1980), are discussed in detail by Schmid and Henningson (2001), and so we make only a few remarks here.

The phenomenon of transient growth was introduced in Chapter 1 for the case of a simple dynamical system with two degrees of freedom. Near a *stable* fixed point where the eigenvectors are not orthogonal, the “energy” of the system, in a suitable norm, can, for certain initial conditions, grow algebraically before the exponential decay appears. This transient growth, measured by a “gain” defined as the ratio of the maximum energy attained and the initial energy, is the more significant the smaller the angle between the eigenvectors. The Orr–Sommerfeld operator possesses a similar property, due to the fact that its eigenfunctions are not orthogonal: it is said to be *non-normal* (or non-self-adjoint). The phenomenon is even more marked for *three-dimensional* perturbations possessing a spatial structure in the transverse z -direction, and can be understood in a simple way as follows.

Consider the particular perturbation corresponding to vortices aligned in the x -direction of the flow and invariant in this direction, as sketched on the left of Figure 5.14. Neglecting viscous effects (which are unimportant in the present context), the linearized Navier–Stokes equations (5.3)–(5.4) for such a perturbation reduce to

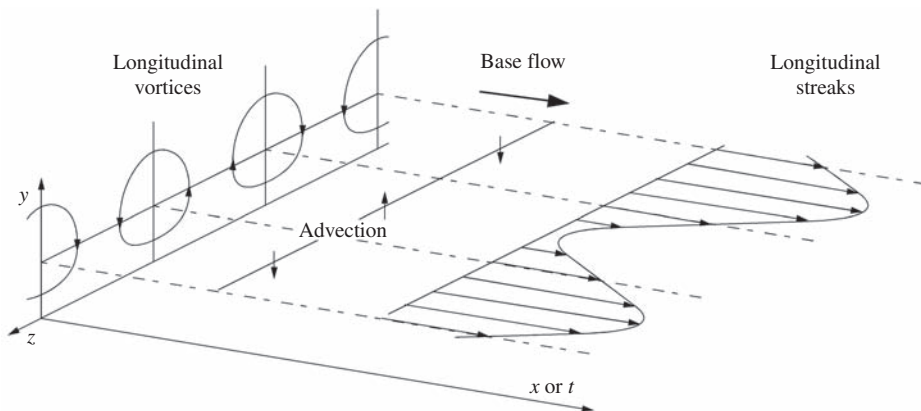


Figure 5.14 Left: the longitudinal vortex structure of the optimal perturbation. Right: streaks of transverse modulation of the longitudinal velocity resulting from the advection of the base flow by the vertical velocity perturbation.

$$\partial_y v + \partial_z w = 0, \quad (5.24a)$$

$$\partial_t u + v \partial_y \bar{U} = -\partial_x p, \quad (5.24b)$$

$$\partial_t v = -\partial_y p, \quad (5.24c)$$

$$\partial_t w = -\partial_z p. \quad (5.24d)$$

This system admits a constant solution for p , v , and w , with the following solution for the longitudinal velocity:

$$u = -v \partial_y \bar{U} t + u_0, \quad (5.25)$$

where u_0 is the initial velocity. Therefore, the longitudinal velocity perturbation u grows not exponentially, but linearly in time. For $\partial_y \bar{U} > 0$ the velocity grows in the regions of descending fluid between two vortices ($v < 0$) and decreases in the regions of ascending fluid ($v > 0$). At a given distance from the wall this results in a transverse modulation of the velocity u corresponding to bands or streaks of alternating slow and fast fluid, as shown on the right-hand side of Figure 5.14. A slow band corresponds to slow fluid advected upwards from near the wall, and a fast band corresponds to fast fluid advected downwards. Clearly, such growing streaks do not correspond to the most amplified Tollmien–Schlichting wave.

A complete analysis of transient growth was performed by Butler and Farrell (1992) for Couette flow, plane Poiseuille flow, and the Blasius boundary layer. Among all the possible initial perturbations, the one with the greatest transient amplification, referred to as the *optimal perturbation* as in control theory, can be sought using one of several optimization techniques. It has been confirmed that this optimal perturbation corresponds to the longitudinal vortices shown in Figure 5.14, which are periodic in the z -direction and essentially localized near the wall. The transverse wavelength $2\pi/k_z$ is of the order of the thickness of the viscous layer, i.e., of order $h\text{Re}^{-1/2}$, and the longitudinal wavelength $2\pi/k_x$ is infinite. These characteristics are opposite those of the most amplified Tollmien–Schlichting wave, for which $2\pi/k_x$ is finite and $2\pi/k_z$ infinite.

In terms of a modal analysis, the optimal perturbation corresponds to a superposition of three-dimensional eigenmodes which initially have large amplitude, but which interfere destructively such that the amplitude of the superposition is small. The disappearance of the most strongly attenuated modes reveals the less attenuated ones, whose amplitude remains relatively large, hence the growth of the perturbation. For a linearly stable flow this growth is transient because the intensity of the vortices decreases owing to viscous diffusion over time (or downstream), as does that of the streaks. The lifetime of the streaks is, however, much larger than that of the vortices, so that in a stochastically perturbed flow, where the optimal perturbation can be present, the streaks can actually be observed. This

has been confirmed by numerical simulations (Luchini, 2000). We finally note that according to the Squire theorem, any three-dimensional perturbation must decrease below the instability threshold of two-dimensional perturbations in the sense of *asymptotic* stability. The result that a three-dimensional perturbation grows in a *transient* manner faster than a two-dimensional perturbation does not contradict this theorem.

5.4 Poiseuille flow in a pipe

Poiseuille flow in a circular pipe is linearly stable for any Reynolds number, in contrast with plane Poiseuille flow. This surprising result, arrived at gradually between the 1920s and the 1960s when numerical computation came into use, seems to contradict the observations of Reynolds described at the beginning of this chapter, namely, destabilization at Reynolds numbers near 2000. This paradox still has not been fully understood (Kerswell, 2005), but several recently identified phenomena may help resolve it, i.e., (i) the phenomenon of advection normal to the wall of the longitudinal momentum by longitudinal vortices, as in planar flow, and (ii) nonlinear effects corresponding to a subcritical bifurcation which amplify the perturbations when their amplitude becomes sufficiently large. The transition to turbulence in plane Couette flow, which is also linearly stable for any Reynolds number even though a transition to turbulence is observed for $\text{Re}_c \approx 350$, may involve the same phenomena. We shall return to this subject in Chapter 9.

5.5 Boundary layer on a flat surface

5.5.1 Experimental demonstration

The instability of a laminar boundary layer is a convective instability with a mechanism very similar to that of plane Poiseuille flow. However, there is a difference in that the former develops from an inhomogeneous (translationally noninvariant) flow in the flow direction. The spatial development of the instability is shown in Figure 5.15, which shows time recordings of a Tollmien–Schlichting wave forced upstream by the vibration of a ribbon at various distances from the leading edge (Schubauer and Skramstad, 1947). The rate of residual turbulence of the incident flow, below 0.05%, is extremely small, as in the experiments of Nishioka *et al.* (1975) on plane Poiseuille flow. The forcing frequency f is such that the dimensionless number

$$F = \frac{\omega v}{U_\infty^2}, \quad \omega = 2\pi f \quad (5.26)$$

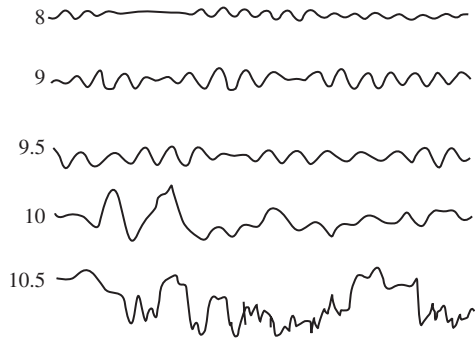


Figure 5.15 Velocity fluctuations in a boundary layer of a forced Tollmien–Schlichting wave, measured at different positions (in feet) downstream from the leading edge, for an upstream velocity $U_\infty = 36.6 \text{ m s}^{-1}$ (Schubauer and Skramstad, 1947²).

is of order 10^{-4} . The velocity fluctuations are measured by hot-wire anemometry. We see that the wave is nearly linear (sinusoidal) in the first three recordings, up to a long-wavelength modulation, and then it rapidly becomes disordered owing to nonlinear effects preceding turbulence. The wavelength is of order $10^4 v/U_\infty$, i.e., a centimeter in air.

5.5.2 Local analysis

Theoretical study of boundary layer instability is complicated by the fact that since the boundary layer gets thicker downstream, the flow is not strictly parallel, especially near the leading edge where the Reynolds number is not very high (Section 5.1.2). This problem can be evaded by assuming that the x -gradient of the base flow is sufficiently small compared to the wave number of the perturbation, and that the characteristics of this perturbation (its amplitude, wave number, growth rate) adapt rapidly to the new local conditions encountered as a result of its advection downstream. This hypothesis of rapid relaxation or “fully developed perturbation” makes it possible to use a *local* stability analysis, where the x -gradients of the base flow are assumed to be zero. The problem then becomes that of the Orr–Sommerfeld equation for the parallel velocity profile $U(x, y)$, where the x -coordinate is treated as a parameter. The growth rates, wavelengths, and eigenfunctions calculated in this way are then parametric functions of x .

The spatial evolution of the amplitude of an eigenmode of a given frequency is affected by the nonuniformity of the base velocity profile in the flow direction.

² Official contribution of the National Institute of Standards and Technology; not subject to copyright in the United States.

Using the “fully developed perturbation” hypothesis, this amplitude is obtained by integrating the local growth rate $-k_i(x)$ starting from the amplitude a_0 at the point x_0 :

$$a(x) = a_0 \exp\left(-\int_{x_0}^x k_i(\xi) d\xi\right). \quad (5.27)$$

Since the local growth rate $-k_i(x)$ is not spatially uniform, this amplitude does not vary exponentially with downstream distance, in contrast with a strictly parallel flow.

5.5.3 Eigenmodes, marginal stability, and nonparallel effects

Figure 5.16 shows the Blasius velocity profile of the base flow, both measured and calculated, as well as an eigenmode of the velocity perturbation u measured and calculated using the local analysis. This particular eigenmode was isolated by the vibration of a ribbon close to the wall in a flow with very low noise.

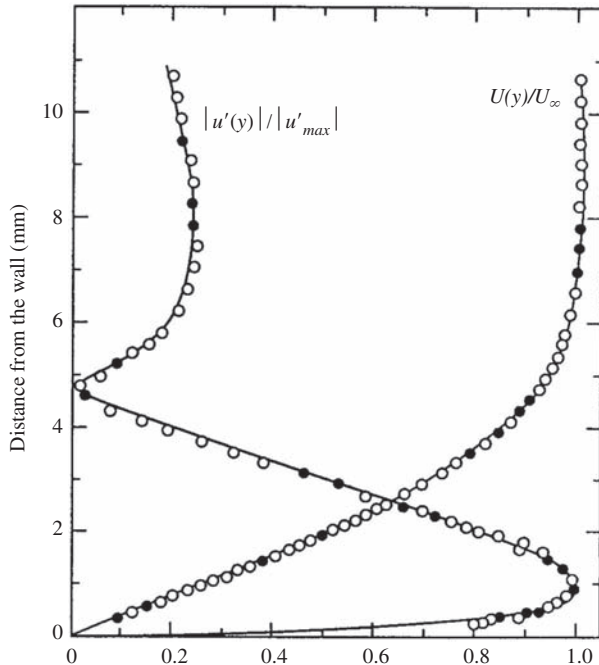


Figure 5.16 Base flow and eigenfunction $u'(y) = |\hat{u}(y)|$ of the Blasius boundary layer: (—) calculation, (○, ●) measurements. Used with permission of Annual Reviews, Inc., from Reed *et al.* (1996); permission conveyed through Copyright Clearance Center, Inc.

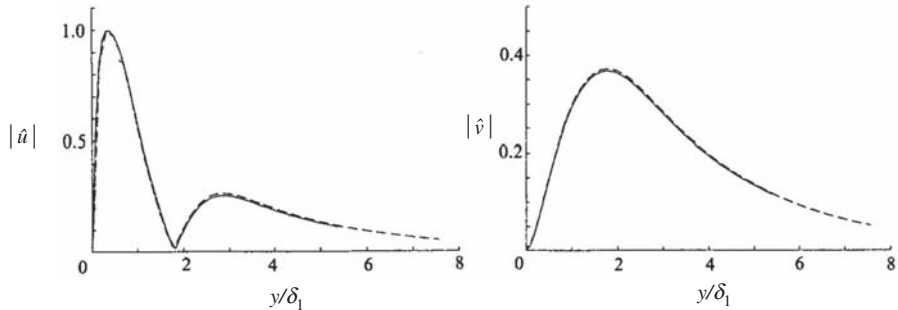


Figure 5.17 Eigenfunctions of the Blasius boundary layer: (---) the parallel theory, (—) direct numerical simulation (Fasel and Konzelmann, 1990). $\text{Re}_\delta = 1000$, $F = 140 \times 10^{-6}$.

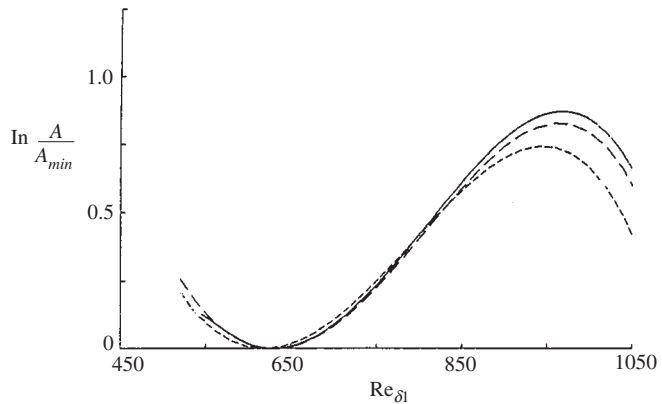


Figure 5.18 Variation of the maximum of the amplitude $|\hat{u}(y)|$ with Reynolds number $\text{Re}_\delta \sim x^{1/2}$, calculated by three methods: (---) the parallel theory (5.27), (—) the Gaster nonparallel theory (1974), (—) direct numerical simulation (Fasel and Konzelmann, 1990). $F = 140 \times 10^{-6}$.

We see that the agreement is excellent. Figure 5.17 compares the eigenfunction obtained from the stability calculation with the result of a direct numerical simulation of the Navier–Stokes equations (Fasel and Konzelmann, 1990). The agreement is again remarkable. Since the direct simulation is free of the local parallel flow assumption, we see that nonparallel effects on the eigenfunctions are very small.

Figure 5.18 shows the spatial evolution of the amplitude of a perturbation imposed upstream, with the evolution calculated by three methods: by the local analysis (5.27), by a nonparallel theory (Gaster, 1974), and by direct numerical simulation (Fasel and Konzelmann, 1990). We see that the amplitude first decreases, then increases, and finally decreases again. The boundary layer is

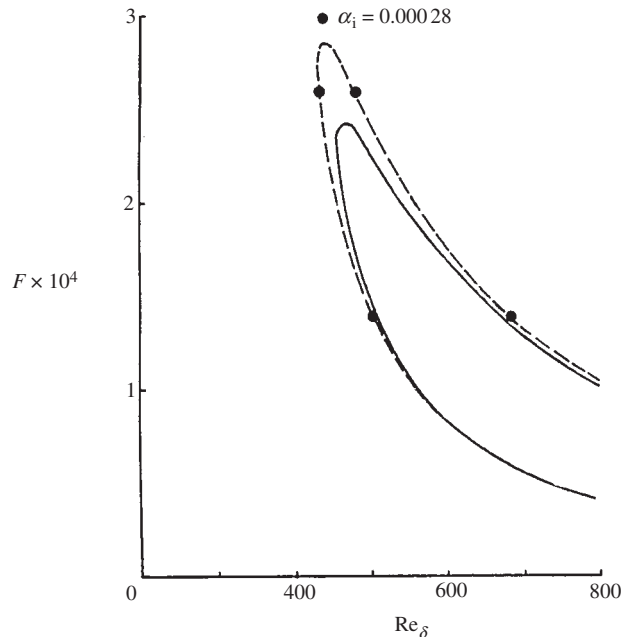


Figure 5.19 Marginal stability of the boundary layer on a flat surface: (—) the parallel theory, (---) the nonparallel theory of Gaster (1974), (●) direct numerical simulations of Fasel and Konzelmann (1990).

therefore first stable, then unstable, and then again stable. The band of unstable Reynolds numbers lies between the minimum and maximum amplitude. Measurements display a similar evolution (Ross *et al.*, 1970), as long as nonlinear or three-dimensional effects remain negligible even when the perturbation reaches its maximum amplitude.

The marginal stability curve in the $\text{Re}_\delta - F$ plane can be obtained from the spatial evolution of a perturbation for various frequencies. This is shown in Figure 5.19, for the three different approaches. The ‘‘half-banana’’ shape corresponds to the restabilization of a wave packet of a given frequency. Such a packet is represented by a point which moves to the right on a line $F = \text{constant}$. The packet is at first stable until it reaches the left-hand branch (called I) of the marginal curve, then unstable until it reaches the right-hand branch (II), after which it is again stable. Theoretical and numerical results are compared with the measurements of Ross *et al.* (1970) in Figure 5.20. We see from these figures that the parallel theory gives good results for $\text{Re}_\delta > 600$, but that significant nonparallel effects are manifested for $\text{Re}_\delta < 600$.

The first calculation of a marginal stability curve (not shown in Figure 5.19) was done by Tollmien (1929) well before the first measurements of Schubauer

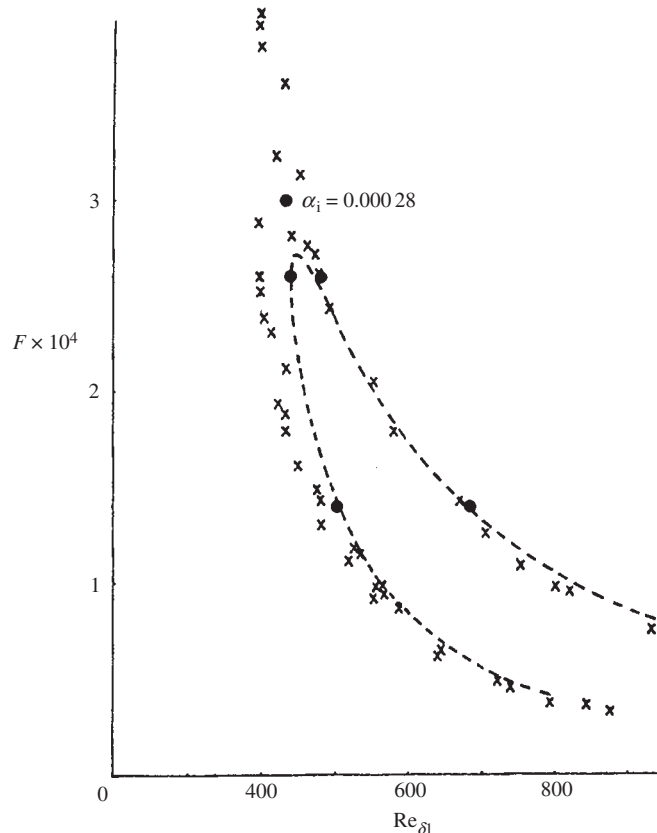


Figure 5.20 Marginal stability of the boundary layer on a flat surface: (—) the nonparallel theory, (×) measurements, (●) simulations of Fasel and Konzelmann (1990).

and Skramstad (1947). Tollmien's solution, obtained well before the widespread use of numerical methods, approximated the base velocity profile by two straight lines connected by an arc of a parabola (Drazin and Reid, 2004, §31.5). The first numerical calculation with the Blasius velocity profile is due to Jordinson (1970), who found $\text{Re}_{\delta,c} = 520$ for the critical Reynolds number, in good agreement with the observations.

In the end, nonparallel effects appear to be of little importance for the situations considered above of two-dimensional waves and negligible pressure gradient. This conclusion is no longer valid when the pressure gradient is significant (as occurs, for example, for nonzero incidence or a curved surface), or when the leading edge of the aerofoil is not perpendicular to the flow (as for swept or triangular wings). In the latter case, the oblique waves are strongly amplified, with the wave vector

making an angle of nearly 90° to the flow (Arnal, 1994; Reed *et al.*, 1996; Schmid and Hennigson, 2001).

5.5.4 Transient growth

Certain perturbations of the boundary layer can grow in a transient fashion for values of the Reynolds number below the critical value and induce transition to turbulence. As for plane Poiseuille flow, this transient growth is maximal for perturbations with a longitudinal vortex structure, and gives rise to the same longitudinal streaks near the wall (Butler and Farrel, 1992). Figure 5.21a shows the amplitudes of the velocities v and w corresponding to the optimal perturbation, and Figure 5.21b gives the corresponding streamwise perturbation u . The frequency of this perturbation is zero ($\omega = 0$) and its transverse wave number is $k_z\delta = 0.45$. Here the calculation takes into account the spatial evolution of the flow in the x -direction by integrating the boundary layer equations, which are parabolic in x (Luchini, 2000).

The amplitude of the transverse modulation of the velocity corresponding to the streaks is higher by a factor of order $\sqrt{\text{Re}}$ than that of the initial vortices (we note that as we are referring to a *linear* problem, the perturbation amplitude is defined only up to a multiplicative constant). These streaks can therefore be strong enough to significantly modify the base flow and in the end inhibit the growth of Tollmien–Schlichting waves. Note that Tollmien–Schlichting waves can nevertheless be observed if the upstream perturbations are small, especially in boundary layers (see Figure 5.4) where they are more amplified than in plane Poiseuille flow (owing to the stabilizing effect of a negative pressure gradient).

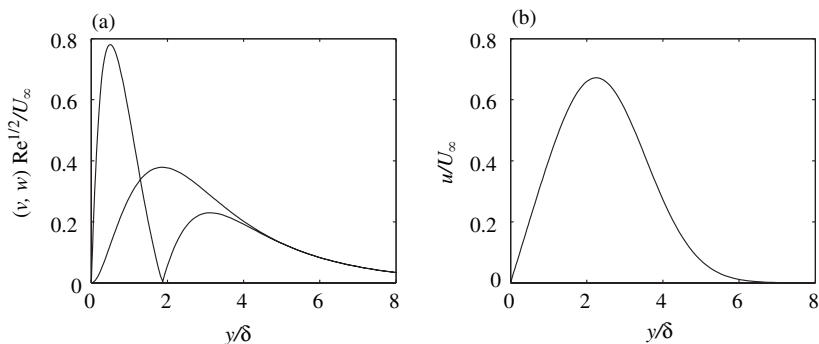


Figure 5.21 (a) Normalized amplitude profiles of v and w corresponding to the optimal perturbation (v is maximal and w is zero at the level of the vortex axis $y/\delta \approx 2$); (b) amplitude profile of u . From Luchini (2000).

We conclude by noting that for the boundary layer on a *flat* wall below the critical Reynolds number, the optimal perturbation is dissipated along with the streaks, as in plane Poiseuille flow. On a *concave* wall the situation is different because the longitudinal vortices are maintained by the centrifugal instability (Luchini and Bottaro, 1998, Bottaro and Luchini, 1999). This situation corresponds to the Görtler and Dean vortices mentioned in the preceding chapter in connection with the Couette–Taylor instability.

5.6 Exercises

5.6.1 A marginal curve

Suppose that for some “toy problem” depending on a control parameter R , the dispersion relation of normal modes proportional to $e^{i(kx-\omega t)}$ is $\mathcal{D}(k, \omega, R) = 0$, where

$$\mathcal{D}(k, \omega, R) = -i\omega R + (k^8 R^2 - k^3 R + 1) + ikR.$$

Sketch the marginal curve in the $(R-k)$ -plane. Determine in particular the points with zero and infinite slope, and the asymptotic behavior of the branches at large R . Deduce that all disturbances are damped for $R < R_c$ with $R_c = \frac{2^{12}}{15^2} \left(\frac{3}{5}\right)^{1/2}$.

5.6.2 Solution of the Orr–Sommerfeld equation for plug flow

Show that for the base flow with uniform velocity \bar{U} , the general solution of the Orr–Sommerfeld equation is

$$\hat{\psi} = a_1 e^{ky} + a_2 e^{-ky} + a_3 e^{\gamma y} + a_4 e^{-\gamma y},$$

where a_1, a_2, a_3 , and a_4 are arbitrary constants and $\gamma^2 = k^2 + ik\text{Re}(\bar{U} - c)$.

5.6.3 Solution of the Orr–Sommerfeld equation for Couette flow

Consider the base flow with dimensional velocity $\bar{U} = \dot{\gamma}y$, where $\dot{\gamma}$ is the shear rate.

- Choosing $\dot{\gamma}^{-1}$ for the time scale and the inverse wave number of the disturbance, k^{-1} , for the length scale, show that the Orr–Sommerfeld equation takes the form

$$(y - c)\hat{\omega} = i\beta^3(\hat{\omega} - \partial_{yy}\hat{\omega}),$$

where $\hat{\omega} = \hat{\psi} - \partial_{yy}\hat{\psi}$ is the amplitude of the vorticity disturbance and $\beta^3 = \nu k^2 / \dot{\gamma}$.

2. Show that the vorticity equation can be put in the form of the standard Airy equation

$$\partial_{zz}\hat{\omega} - z\hat{\omega} = 0$$

by the transformation $z = e^{i\pi/6}(y - c - i\beta^3)/\beta$, with the general solution

$$\hat{\omega} = a_1 \text{Ai}(z) + a_2 \text{Bi}(z),$$

where $\text{Ai}(z)$ and $\text{Bi}(z)$ are the Airy functions (Abramowitz and Stegun, 1964).

3. Show that the amplitude of the stream function is given by

$$\hat{\psi}(y) = \frac{1}{2} \left(e^{-y} \int_{y_1}^y e^Y \hat{\omega}(Y) dY + e^y \int_y^{y_2} e^{-Y} \hat{\omega}(Y) dY \right) + a_3 e^{-y} + a_4 e^y,$$

where y_1 and y_2 are the locations of the linearized boundary conditions (rigid wall or deformable interface), and the constants a_1 , a_2 , a_3 , and a_4 can be determined from the boundary conditions on $\hat{u} = \partial_y \hat{\psi}$ and $\hat{v} = -i\hat{\psi}'$.

4. Write the dispersion relation for the Couette flow between two flat plates, i.e., the determinant of the system of the four no-slip boundary conditions.

5.6.4 Instability due to linear resonance

Consider the linear differential system

$$\frac{dx}{dt} = Ax, \quad A = \begin{pmatrix} -i\omega_1 & \epsilon p_1 \\ \epsilon p_2 & -i\omega_2 \end{pmatrix},$$

where $\omega_2 = \omega_1 + b\epsilon$. Show that this system admits solutions proportional to $\exp(-i\omega t)$ where the frequency satisfies the dispersion relation

$$\omega = \omega_1 + \frac{1}{2}b\epsilon \pm (b^2 - 4p_1 p_2)^{1/2}.$$

Deduce that the fixed point $(0, 0)$ is stable if $\epsilon = 0$ (no coupling), but unstable for small ϵ when $b^2 < 4p_1 p_2$ (coupling with near-resonance). (This system mimicks the resonance mechanism between an inviscid mode and a viscous mode proposed by Baines *et al.* (1996) to understand the growth of Tollmien–Schlichting waves.)

6

Instabilities at low Reynolds number

6.1 Introduction

When a viscous flow has a deformable interface, small inertial effects can give rise to an instability which is manifested as interfacial waves. The principal types of such flows are illustrated in Figure 6.1: liquid films falling down an inclined plane, flows induced by a pressure gradient, and shear flows.

Falling films composed of a single layer (Figure 6.1a) or of several layers (Figure 6.1b) are often encountered in coating processes. Examples are coating of paints and varnishes, printing inks, magnetic tape and disks, photographic film, and so on. Flows set in motion by a pressure gradient (Figure 6.1c) are encountered in extrusion of polymers in planar or annular geometries. The third type of flow, shear flow, typically corresponds to a liquid film sheared by a gas (Figure 6.1d), a situation encountered in chemical reactors or heat exchangers, or by Marangoni stresses. In these applications it is often required that the films have uniform thickness, and so it is essential to avoid instabilities. On the other hand, instabilities may actually be desirable because they typically augment rates of heat and mass transfer.

Figure 6.2 illustrates an instability observed in the oil industry in the transport of oil of very high viscosity on the order of a million times that of water. Water, which is injected into the pipe in order to reduce the viscous friction, migrates to the wall where it forms a lubricating film (Joseph *et al.*, 1997). The resulting annular flow is in general unstable; depending on the flow rates of the water and the oil, the interface takes various shapes, as shown in Figure 6.2. In particular, the sinuous form of the oil core in the middle illustration and the “bamboo” shape in the bottom one should be noted. In situations involving oil transport it is important to avoid breakage of the water film, but the presence of waves at the interface can be tolerated.

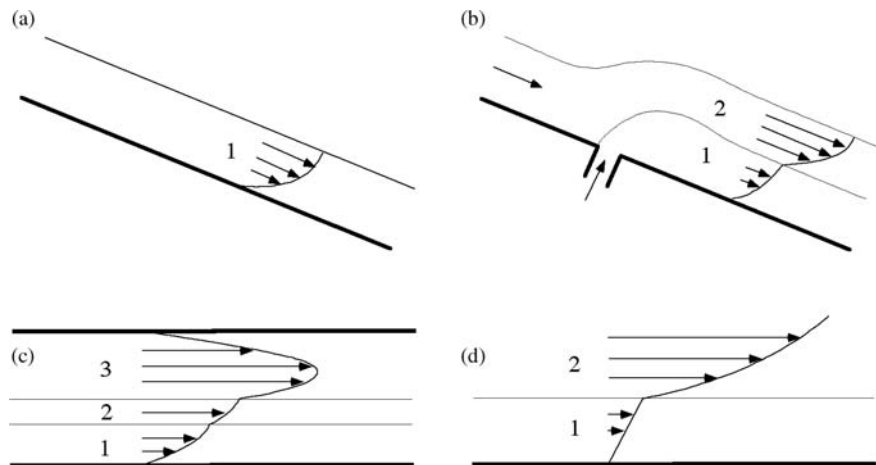


Figure 6.1 Flows of liquid films subject to an instability at small Reynolds number: (a) a liquid film falling down an inclined plane, (b) a two-layer flow subject to gravity, (c) a multi-layer flow subject to a pressure gradient, and (d) a liquid film sheared by a gas.

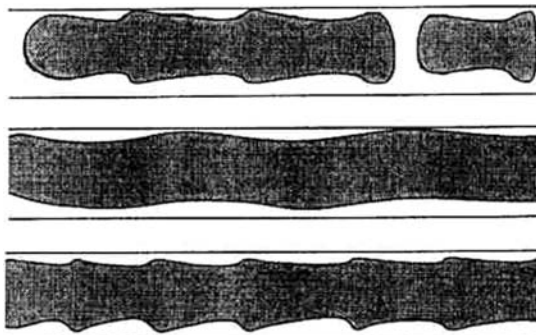


Figure 6.2 Three types of instability structure in the flow of a highly viscous oil through a pipe lubricated by a water film. Republished with permission of Annual Reviews, Inc., from Joseph *et al.* (1997); permission conveyed through Copyright Clearance Center, Inc.

Figure 6.3 presents another illustration of an instability of a sheared film. A tube is initially filled with a certain fluid: a second fluid of a different viscosity is injected in order to displace the first one (a situation encountered, in particular, when drilling oil wells). In general, the displacing fluid leaves a film of the displaced fluid on the wall of the tube. The cylindrical interface between the two fluids is unstable, leading to the development of axisymmetric bulges, as clearly seen in the photograph. Such axisymmetric instabilities are termed “varicose,” in

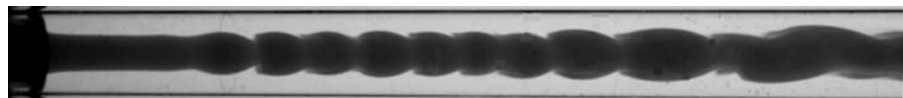


Figure 6.3 Instability arising when water (darker fluid at the center) is injected into a more viscous fluid of the same density. The radius of the tube is exactly one centimeter. Photograph taken by M. d'Olce, J. Martin, N. Rakotomalala, D. Salin, and L. Talon, FAST, Orsay (2006), reprinted with permission.

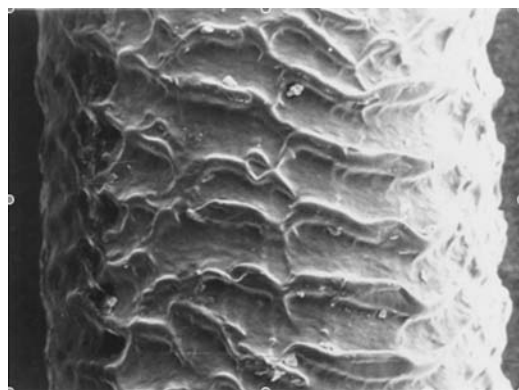


Figure 6.4 A sharkskin-like surface on extruded polyethylene. Used with permission of Annual Reviews, Inc., from Denn (2001); permission conveyed through Copyright Clearance Center, Inc.

contrast to the “sinuous” instability seen in the middle panel of Figure 6.2. Since the two fluids are miscible and have the same density, neither surface tension nor gravity is involved, and the inertia of the fluids is low (the Reynolds number is of order ten). This strongly implies that the viscosity difference plays a key role, as we shall see.

Instability mechanisms other than inertia can also give rise to highly irregular interfaces. For example, in polymer coextrusion an instability can arise from the difference in the elasticities of two adjacent layers (Hinch *et al.*, 1992), or from too rapid a relaxation of the stresses at the exit of an extrusion die (Denn, 2001). This latter instability causes the development of a sharkskin-like surface composed of scales several millimeters long, as illustrated in Figure 6.4.

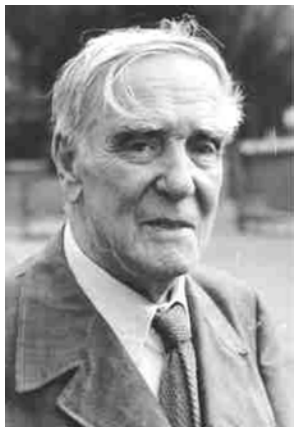
Instabilities at low Reynolds number can therefore arise in a variety of situations. In this chapter we shall study two of these situations in some detail owing to their generic nature: films falling down an inclined plane under the effect of gravity (Section 6.2), and sheared films (Section 6.3). In both cases we are dealing with parallel flows whose stability is governed by one or two Orr–Sommerfeld equations with the associated boundary conditions on a deformable interface.

Since these instabilities arise at small Reynolds number, regular asymptotic series can be used to determine the dispersion relation analytically.

6.2 Films falling down an inclined plane

The first careful experimental and theoretical studies of the hydrodynamics of films falling down a vertical wall were carried out by P. L. Kapitza (1948, 1949). The observed waves were recognized as the result of a long-wave instability at small Reynolds number by T. B. Benjamin (1957) and later by C. S. Yih (1963). Many subsequent studies were performed, revealing, in particular, the presence of Tollmien–Schlichting waves for Reynolds number on the order of a thousand (Floryan *et al.*, 1987). The nonlinear phenomena associated with advection and the deformability of the interface were first analyzed by Benney (1966) and Skhadov (1967); they lead to the formation of large-amplitude solitary waves (Chang, 1994) that we shall discuss later in Chapter 9.

Pyotr Leonidovich Kapitza (1894–1984)



Born near Saint Petersburg, Pyotr Leonidovich Kapitza graduated from the Petrograd Polytechnical Institute in 1919. After the death of his wife and two children from the Spanish influenza, he moved to Cambridge, England in 1921. There he wrote his thesis under the direction of Ernest Rutherford at the Cavendish Laboratory in which he developed techniques for creating ultra-strong magnetic fields. He was elected a Fellow of the Royal Society in 1929. Using a donation from a patron, the Royal Society created the Royal Society Mond Laboratory for him, where he developed a procedure for liquefying large amounts of helium to aid his work in low-temperature physics, thus acquiring a world-wide reputation. In 1934, while on a routine professional visit to the USSR, he was prevented by Stalin from returning to Cambridge. From then on he was forced to live in the USSR, where he continued to carry out exceptional research. With help from Rutherford, he founded and directed the Institute for Physical Problems of the Academy of Sciences in Moscow. He discovered the superfluidity of helium II in 1937, and invented a new method for liquefying air at low pressure by means of a high-efficiency expansion turbine which is used to this day. In 1939 he was elected to the Academy of Sciences in Moscow. During WWII he organized and

directed the Department of Oxygen Industry affiliated with the government. In 1945 he refused to work on nuclear weapons development under Beria, and consequently was dismissed from his posts and sent to live in his house in the countryside. There he worked on high-power electronics until the death of Stalin and the arrest of Beria in 1953. In 1955 he returned to his position as director of the Institute and continued his research on high-power electronics and plasmas. He was a great moral figure, brave and clever, and managed to free several colleagues from Stalin's prisons, including Lev Landau, who had been arrested by the NKVD on the pretext of spying. He later defended Andrei Sakharov (A. Sakharov, *Memoirs*, Knopf, 1990). As a public figure he spoke out on various issues such as economics, ecology, and the organization of science. He was awarded the Nobel Prize in Physics in 1978 for his work in low-temperature physics.

6.2.1 Base flow and characteristic scales

We consider a film of incompressible liquid of thickness h , viscosity μ , and density ρ , falling down a plane inclined at an angle θ with respect to the horizontal (Figure 6.5). The interface at the ambient gas of pressure P_0 has surface tension γ .

The Navier–Stokes equations, subject to the boundary conditions of no-slip on the lower surface and constant pressure P_0 at the free surface, have a steady parallel flow solution corresponding to a planar interface and a parabolic velocity profile:

$$\bar{U}(y) = U_0(1 - y^2/h^2), \quad (6.1a)$$

$$\bar{V}(y) = 0, \quad (6.1b)$$

$$\bar{P}(y) - P_0 = -\rho gy \cos \theta, \quad (6.1c)$$

where the velocity U_0 of the interface is defined as

$$U_0 = \frac{\rho gh^2 \sin \theta}{2\mu}. \quad (6.2)$$

This solution displays the natural scales of the problem: the thickness h of the film, the fluid density ρ , and the speed U_0 of the fluid at the interface.

The importance of inertia relative to viscosity, gravity, and surface tension is measured respectively by the Reynolds, Froude, and Weber numbers, defined as

$$\text{Re} = \frac{\rho U_0 h}{\mu}, \quad \text{Fr} = \frac{U_0^2}{gh \cos \theta} = \frac{\text{Re} \tan \theta}{2}, \quad \text{We} = \frac{\rho U_0^2 h}{\gamma}. \quad (6.3)$$

We note that the Froude number is defined using the gravity component $g \cos \theta$ normal to the flow. To get an idea of the magnitudes of these parameters, for a slope

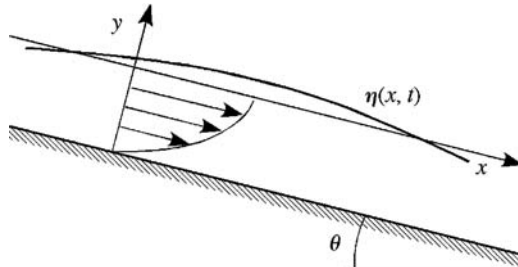


Figure 6.5 Film falling down an inclined plane showing the parabolic velocity profile for a planar interface, and the perturbed interfacial position, $\eta(x, t)$.

of $\theta = 30^\circ$ and a water film 0.1 mm thick, $U_0 = 50$ mm/s, and these three numbers are $\text{Re} = 5$, $\text{Fr} = 1.4$, and $\text{We} = 0.003$. For a film of oil of viscosity ten times higher and for the same film thickness and inclination angle, we have $U_0 = 5$ mm/s, $\text{Re} = 0.05$, $\text{Fr} = 0.014$, and $\text{We} = 0.00008$.

When the interface is perturbed ($\eta(x, t) \neq 0$ as in Figure 6.5), the velocity profile is no longer exactly parabolic. This, together with inertia, leads to the instability studied below.

6.2.2 Formulation of the stability problem

Conservation equations and boundary conditions

Squire's theorem, according to which the instability arises at the threshold for a two-dimensional perturbation (Chapter 5), remains valid for a flow with an interface (Hesla *et al.*, 1986). Therefore, for finding critical conditions it is sufficient to consider the planar problem defined by the two-dimensional Navier–Stokes equations in the longitudinal and transverse directions x and y , and by the boundary conditions at the wall and at the gas–liquid interface. Let us discuss these boundary conditions. The conditions at the wall are the classic no-slip conditions:

$$U = 0, \quad V = 0 \quad \text{at } y = -h. \quad (6.4)$$

At the interface there are two types of condition; kinematic ones reflecting the impermeability of the interface, and dynamic ones on the stresses. These conditions, which are described in detail in Chapter 2 for the Rayleigh–Taylor instability, involve the unit vectors normal and tangent to the interface, defined as

$$\mathbf{n} = \frac{(-\partial_x \eta, 1)}{\sqrt{1 + \partial_x \eta^2}}, \quad \mathbf{t} = \frac{(1, \partial_x \eta)}{\sqrt{1 + \partial_x \eta^2}}, \quad (6.5)$$

where $\eta(x, t)$ is the position of the interface.

- The kinematic condition is that the normal velocity $\mathbf{U} \cdot \mathbf{n}$ of the fluid at the interface must be equal to the normal velocity of the interface $\mathbf{w} \cdot \mathbf{n} = \partial_t \eta / \sqrt{1 + \partial_x \eta^2}$, or

$$U(-\partial_x \eta) + V = \partial_t \eta \quad \text{at } y = \eta. \quad (6.6)$$

- The dynamic conditions pertain to (i) the continuity of the tangential stress and (ii) the jump in the normal stress due to surface tension. Since the stress in the fluid is $\Sigma \cdot \mathbf{n}$, where Σ is the stress tensor, and the effect of the air reduces to a purely normal stress $-P_0 \mathbf{n}$, the dynamic condition is written as

$$\mathbf{t} \cdot (\Sigma \cdot \mathbf{n}) = 0 \quad \text{at } y = \eta, \quad (6.7a)$$

$$\mathbf{n} \cdot (\Sigma \cdot \mathbf{n}) - \mathbf{n} \cdot (-P_0 \mathbf{n}) = \frac{\gamma}{R} \quad \text{at } y = \eta, \quad (6.7b)$$

where $R^{-1} = -\operatorname{div} \mathbf{n} = \partial_{xx} \eta / (1 + \partial_x \eta^2)^{3/2}$ is the curvature of the interface.

For a Newtonian fluid these two equations become

$$\frac{-2\mu \partial_x \eta}{1 + \partial_x \eta^2} (\partial_x U - \partial_y V) + \mu \frac{1 - \partial_x \eta^2}{1 + \partial_x \eta^2} (\partial_y U + \partial_x V) = 0 \quad \text{at } y = \eta, \quad (6.8a)$$

$$-P + \frac{2\mu}{1 + \partial_x \eta^2} [\partial_x \eta^2 \partial_x U + \partial_y V - \partial_x \eta (\partial_y U + \partial_x V)] + P_0 = \frac{\gamma}{R} \quad \text{at } y = \eta. \quad (6.8b)$$

It can be verified that the base flow (6.1) is indeed a solution of the full Navier–Stokes equations with the boundary conditions (6.4), (6.7), and (6.8).

Perturbed flow, linearization, and normal modes

We choose the thickness h as the length scale and h/U_0 as the time scale and introduce the stream function ψ of the perturbations via¹

$$U = \bar{U} + \partial_y \psi, \quad V = \bar{V} - \partial_x \psi = -\partial_x \psi. \quad (6.9)$$

Eliminating the pressure from the Navier–Stokes equations by cross-differentiation and considering perturbations in the form of the normal modes

$$\psi(x, y, t) = \hat{\psi}(y) e^{i\alpha(x-ct)}, \quad \eta(x, t) = \hat{\eta} e^{i\alpha(x-ct)}, \quad \alpha = kh, \quad (6.10)$$

the Navier–Stokes equations lead to the Orr–Sommerfeld equation (Chapter 5):

$$(D^2 - \alpha^2)^2 \hat{\psi} = i\alpha \operatorname{Re} \left[(\bar{U} - c)(D^2 - \alpha^2) - D^2 \bar{U} \right] \hat{\psi}, \quad (6.11)$$

¹ This is how the problem was solved by Yih (1963); it is of course also possible to choose to retain the velocities and pressure as dependent variables (Smith, 1990).

where D is the derivative operator d/dy .

The conditions (6.4) of no-slip on the wall become

$$D\hat{\psi}(-1)=0, \quad (6.12a)$$

$$\hat{\psi}(-1)=0. \quad (6.12b)$$

The kinematic condition at the interface (6.6) linearized about $y=0$ is written as

$$\hat{\psi}(0)-(c-1)\hat{\eta}=0. \quad (6.13)$$

The dynamic condition (6.8b) at the interface involves the pressure, which can be eliminated in two steps by: (i) differentiating (6.8b) along the interface ($\partial P/\partial s=\nabla P \cdot \mathbf{t}$, where s is the curvilinear abscissa at the interface), and then (ii) eliminating the gradients $\partial_x P$ and $\partial_y P$ using the Navier–Stokes equations. The conditions (6.8) linearized about $y=0$ then become

$$D^2\hat{\psi}(0)+\alpha^2\hat{\psi}(0)+\hat{\eta}D^2\bar{U}(0)=0, \quad (6.14a)$$

$$-D^3\hat{\psi}(0)+\left[3\alpha^2-i\alpha\text{Re}(c-1)\right]D\hat{\psi}(0)+i\alpha\text{Re}\left(\frac{1}{\text{Fr}}+\frac{\alpha^2}{\text{We}}\right)\hat{\eta}=0. \quad (6.14b)$$

6.2.3 A long-wave interfacial instability

The Orr–Sommerfeld equation (6.11) together with the boundary conditions (6.12), (6.13), and (6.14) are a generalized eigenvalue problem with the speed c as the eigenvalue. We note that, in contrast to flow between rigid walls, the eigenvalue appears not only in the equations but also in one of the boundary conditions, namely, Eq. (6.13) at the interface. Here we shall study the temporal stability of the base flow to a perturbation of real fixed wave number α and complex unknown speed c . As usual, the real part c_r corresponds to the wave speed (in units of U_0), and $\sigma=\alpha c_i$ is the growth rate (in units of U_0/h).

Asymptotic solution

Experiments show that on a film about a millimeter thick the instability is manifested as the growth of waves of wavelength on the order of several centimeters, which corresponds to a dimensionless wave number of $\alpha=kh\approx 0.1$. On the other hand, since the Reynolds number is typically less than ten, inertial effects, which according to the Orr–Sommerfeld equation (6.11) are of order αRe , are small. Finally, as we have seen, the Weber number is typically small as well. We therefore consider situations satisfying the following conditions:

$$\alpha \ll 1, \quad \text{Re} = \mathcal{O}(1), \quad \text{We}/\alpha^2 = \mathcal{O}(1). \quad (6.15)$$

For these long-wave perturbations the wave number α can be treated as a small parameter, and the form of the equations suggests that the speed c and amplitude $\hat{\psi}$ of the eigenfunction can be sought as a series in powers of α as follows:

$$\hat{\psi}(y) = \hat{\psi}^{(0)}(y) + \alpha \hat{\psi}^{(1)}(y) + \dots, \quad (6.16a)$$

$$c = c^{(0)} + \alpha c^{(1)} + \dots \quad (6.16b)$$

Since we are solving a linear problem, where the solution can be determined only up to a multiplicative constant, the interface perturbation $\hat{\eta}$ can be treated as a normalization constant of the eigenfunctions, and there is no need to expand it in a series.

At lowest order the Orr–Sommerfeld equation reduces to

$$D^4 \hat{\psi}^{(0)}(y) = 0, \quad (6.17)$$

with boundary conditions at the wall ($y = -1$) and at the interface ($y = 0$)

$$\hat{\psi}^{(0)}(-1) = 0, \quad (6.18a)$$

$$D\hat{\psi}^{(0)}(-1) = 0, \quad (6.18b)$$

$$D^3\hat{\psi}^{(0)}(0) = 0, \quad (6.18c)$$

$$D^2\hat{\psi}^{(0)}(0) - 2\frac{\hat{\psi}^{(0)}(0)}{c^{(0)} - 1} = 0. \quad (6.18d)$$

Here we have used $D^2\bar{U}(0) = -2$, $U_0 = 1$, and have eliminated $\hat{\eta}$. The solution of this Stokes (purely viscous) problem is written as

$$\hat{\psi}^{(0)}(y) = \hat{\eta}(y+1)^2, \quad c^{(0)} = 2, \quad (6.19)$$

where $\hat{\eta}$ is the amplitude of the deformation of the interface. The eigenvalue $c^{(0)}$ is real and independent of the wave number, so that the perturbations all propagate at the same dimensional speed $2U_0$, independently of the wave number, that is, without dispersion. Since the imaginary part of $c^{(0)}$ is zero, the growth rate is zero and therefore there is no instability to the lowest order. In addition, since the ratio of the amplitudes $\hat{\eta}$ and $\hat{\psi}^{(0)}$ is real, the interface η and the stream function ψ are in phase. The velocity perturbations $u = \partial_y \psi$ and $v = -\partial_x \psi$ are therefore respectively in and out of phase with the interface, as illustrated in Figure 6.7b below. Therefore, at the lowest order the flow does not manifest any instability to long-wavelength perturbations.

At first order the Orr–Sommerfeld equation becomes

$$D^4 \hat{\psi}^{(1)}(y) = i \operatorname{Re} \left[(\bar{U} - c^{(0)}) D^2 - D^2 \bar{U} \right] \hat{\psi}^{(0)}.$$

This is an inhomogeneous differential equation whose homogeneous part is identical to the zeroth-order equation. The right-hand side is a known function of $\hat{\psi}^{(0)}(y)$ and its derivatives (inertial terms), and behaves as a forcing term associated with weak fluid inertia. The boundary conditions, which we shall not write out explicitly, are obtained in the same way. Skipping considerable but straightforward algebra, the solution of the problem gives the correction $c^{(1)}$ to the eigenvalue:

$$c^{(1)} = i\text{Re} \frac{8}{15} \left[1 - \frac{5}{8} \left(\frac{1}{\text{Fr}} + \frac{\alpha^2}{\text{We}} \right) \right]. \quad (6.20)$$

This correction is purely imaginary; it does not contribute to the wave speed, but affects the growth rate $\sigma = \alpha c_i = \alpha^2 c_i^{(1)}$ in a significant way.

To this order in the expansion the growth rate is

$$\sigma = \frac{\text{Re}}{3} \left(\frac{1}{\text{Fr}_c} - \frac{1}{\text{Fr}} \right) \alpha^2 - \frac{\text{Re}}{3\text{We}} \alpha^4 \quad \text{with} \quad \text{Fr}_c = \frac{5}{8}. \quad (6.21)$$

For $\text{Fr} < \text{Fr}_c$, σ is negative for all α , and the flow of a planar film is linearly stable. For $\text{Fr} > \text{Fr}_c$, perturbations of wave number below the cutoff α_c are amplified, where α_c is defined by

$$\alpha_c^2 = \text{We} \left(\frac{1}{\text{Fr}_c} - \frac{1}{\text{Fr}} \right). \quad (6.22)$$

Perturbations of wave number $\alpha > \alpha_c$ are attenuated owing to the combined effect of the surface tension and the viscosity. The number $\text{Fr}_c = 5/8$ is therefore the critical Froude number above which the film is unstable. Figure 6.6a shows the behavior of the growth rate $\sigma(\alpha)$. We note that the most amplified wave number is given by $\alpha_m = \alpha_c/\sqrt{2}$, and that the mode with wave number $\alpha = 0$ is neutral. Figure 6.6b shows the stability diagram with the marginal stability curve ($\sigma = 0$) separating the stable and unstable domains. This diagram shows that the width of the unstable band tends to zero at the threshold $\text{Fr} = \text{Fr}_c$, and so the most amplified wavelength diverges. Of course, observation of this divergence is limited by the finite axial length of the flow in any real experiment, and also by the duration of the observation, because the characteristic time for the instability to appear, which is $O(\sigma^{-1})$, also diverges at threshold.

Finally, this asymptotic study shows that long waves propagate at a speed equal to twice the speed U_0 of the interface and are not dispersive.² The group velocity,

² Performing the calculations through second order, one finds (Benney, 1966)

$$c^{(2)} = -2 - \frac{32}{63} \text{Re}^2 \left[1 - \frac{5}{8} \left(\frac{1}{\text{Fr}} + \frac{\alpha^2}{\text{We}} \right) \right].$$

This correction is real and so it only affects the wave speed. Therefore, at second order, long wavelengths are weakly dispersive.

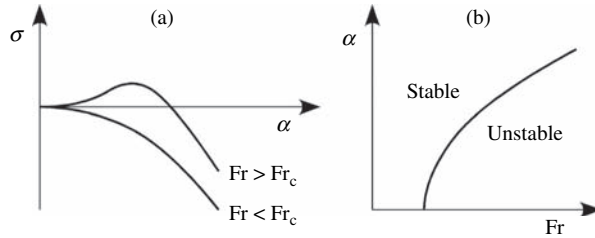


Figure 6.6 (a) Behavior of the growth rate $\sigma(\alpha)$ for $Fr < Fr_c$ and $Fr > Fr_c$; (b) stability diagram.

which is equal to the speed at the order we are considering, is therefore strictly positive, which implies that the instability can only be convective. Beyond the critical Froude number the destabilizing inertia dominates the stabilizing normal component of gravity, and long waves are unstable. The growth rate is proportional to the Reynolds number ($\sigma \propto \alpha^2 Re$), which demonstrates the inertial nature of the instability (the dimensional growth rate $\sigma U_0/h$ is proportional to U_0^2). This instability, where all wave numbers in the band $0 < \alpha < \alpha_c$ are unstable, is called a *long-wave instability*. Its mechanism is discussed in more detail in the following section.

The conclusions reached above are valid for long-wavelength perturbations for which $\alpha = kh \ll 1$. As far as short-wavelength perturbations are concerned, an asymptotic series for $\alpha \gg 1$ obtained by Yih (1963) shows that these waves are stable as a result of damping due to surface tension and viscous dissipation, as expected.

Numerical solution

The problem defined by Eqs (6.11)–(6.14) with the restriction to long waves lifted can be solved numerically. The Chebyshev polynomials $T_j(y) = \cos(n \cos^{-1}(y))$, which were mentioned in Chapter 5, form a suitable basis on which to seek the amplitude of the unknown eigenfunction in the form

$$\hat{\psi}(y) = \sum_{j=0}^n a_j T_j(y). \quad (6.23)$$

Using recursion relations expressing the derivative of a polynomial as a linear combination of other polynomials, the Orr–Sommerfeld equation and the boundary conditions can then be used to transform the problem into an algebraic one where the unknowns are the coefficients a_j . The number of polynomials necessary for the

Table 6.1. Comparison of the asymptotic speeds and growth rate (Benjamin, 1957; Yih, 1963; Benney, 1966) with the corresponding numerical results (obtained by the author using 16 Chebyshev polynomials). $\theta = 60^\circ$, $\alpha = 0.01$

	$\alpha^2/\text{We} = 0$			$\alpha^2/\text{We} = 1$	
	Re = 0.01	Re = 1	Re = 100	Re = 0.01	Re = 1
c_r numerical	1.999800	1.999786	1.77	1.999804	1.999818
c_r asymptotic	1.999800	1.999786	1.50	1.999804	1.999818
σ/α^2 numerical	-0.379500	0.14820	29.7	-0.364853	-0.185036
σ/α^2 asymptotic	-0.379567	0.14843	53	-0.364900	-0.184900

series (6.23) to converge depends on the Reynolds number and the wave number α , and on the required precision; typically 20 or 30 terms are needed.

The numerical solution confirms that at small Reynolds number the only instability is a long-wave instability (waves with α on the order of unity are stable), and allows the region of validity of the asymptotic solution to be determined. Table 6.1 compares the results obtained by the asymptotic calculation with the corresponding numerical results for $\alpha = 10^{-2}$ and three Reynolds numbers, with and without surface tension. Up to $\text{Re} = 1$ the differences are less than 0.1%; noticeable differences appear only for $\text{Re} > 1$, first for the growth rate, and then for the speed. The differences become important for $\text{Re} = 100$, which corresponds to $\alpha\text{Re} = 1$.

It can therefore be stated that the asymptotic solution gives excellent quantitative results up to $\alpha\text{Re} \approx 0.1$, and it has an advantage over the numerical solution in that it provides the explicit dispersion relation.

Solution using depth-averaged equations

For flow varying slowly in the longitudinal direction, depth-averaged equations, also known as *Saint-Venant equations*, are a useful set of simplified equations for the thickness h and average speed U . However, in the course of their derivation, the shape of the velocity profile has to be specified, see the Appendix. With the usual assumption of a parabolic profile, these equations become

$$\frac{\partial h}{\partial t} + \frac{\partial(hU)}{\partial x} = 0, \quad (6.24)$$

$$\frac{\partial(Uh)}{\partial t} + \frac{6}{5} \frac{\partial(U^2h)}{\partial x} = -gh \cos\theta \frac{\partial h}{\partial x} - \frac{\tau}{\rho} + gh \sin\theta, \quad (6.25)$$

where $\tau = 3\mu U/h$ is the shear stress exerted by the parabolic flow on the inclined surface.

These equations have a base solution corresponding to flow at the average speed $\bar{U} = \rho g \bar{h}^2 \sin \theta / 3\mu$, which agrees with the interface speed (6.2). Continuing with a linear stability analysis, it appears that Eqs (6.24)–(6.25) describe well the two major competing effects of stabilizing gravity and destabilizing inertia. However, this analysis does not give the correct critical Froude number. This is because the velocity profile of the perturbed flow is not strictly parabolic, and so the effects of inertia and friction at the wall are not computed precisely. Various attempts have been made to remedy the situation by relaxing the overly strong hypothesis of parabolic flow, and these have led to an interesting description of the weakly nonlinear dynamics; see, in particular, Ruyer-Quil and Manneville (2000).

The failure of the above equations in accurately describing the long-wave instability is due to the fact that they are not a consistent approximation of the Navier–Stokes equations, in the sense that they do not account correctly for first-order corrections in the small parameter kh . A consistent set of depth-averaged equations can however be derived (Luchini and Charru, 2010a), based not on the momentum equation (6.25) but on the kinetic-energy equation

$$\frac{6}{5} \frac{\partial}{\partial t} \left(\frac{hU^2}{2} \right) + \frac{54}{35} \frac{\partial}{\partial x} \left(\frac{hU^3}{2} \right) = -ghU \cos \theta \frac{\partial h}{\partial x} - \frac{3\mu U^2}{\rho h} + ghU \sin \theta. \quad (6.26)$$

Using this equation together with the mass conservation equation (6.24) yields the correct growth rate (6.21) and critical Froude number; see Exercise 6.4.4.

6.2.4 The instability mechanism

The physical mechanism of the long-wave instability can be understood following Smith (1990). For the time being we ignore fluid inertia. On the deformed interface the base flow has a gradient $\bar{U}'(\eta) = \bar{U}'' \eta$, as shown in Figure 6.7a, with $\bar{U}'' = -2U_0/h^2$. This nonzero gradient does not satisfy the condition of zero shear, which leads to a velocity perturbation $u^{(0)}(x, y, t)$ such that $u'^{(0)}(y=0) = -\bar{U}'' \eta$. This condition in conjunction with the no-slip condition and the absence of a pressure gradient gives the linear shear flow³

$$u^{(0)} = -\bar{U}''(y+h) \hat{\eta} \cos(kx - \omega t). \quad (6.27)$$

³ The convention adopted here for superscripts is different from that used in the previous section, in which it corresponded to the order of the expansion in wave number. Here we write $u = u^{(0)} + u^{(1)}$ and $v = v^{(0)} + v^{(1)}$ where the superscript (0) corresponds to the Stokes flow for both u and v , and the superscript (1) corresponds to the inertial correction.

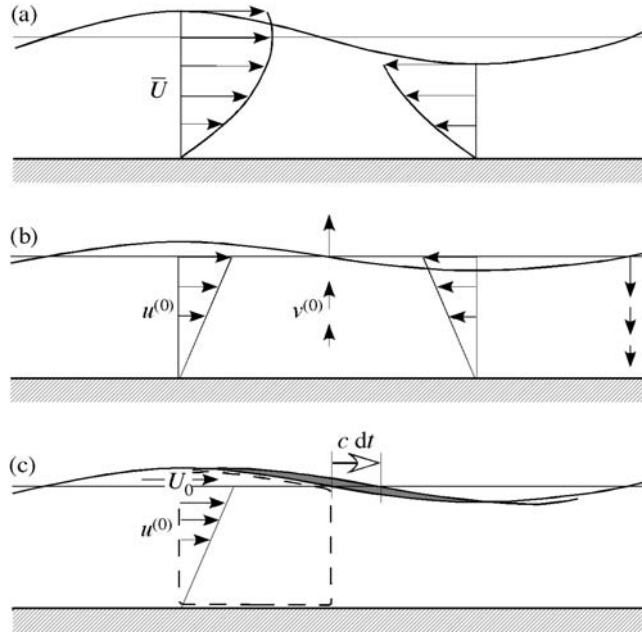


Figure 6.7 (a) Base flow, (b) zeroth-order velocity perturbations, (c) (—) control volume showing the speed c .

The corresponding transverse velocity is obtained from the incompressibility condition $\partial_x u + \partial_y v = 0$, with the result

$$v^{(0)} = \bar{U}'' \int_{-h}^y (y + h) dy k \hat{\eta} \sin(kx - \omega t). \quad (6.28)$$

These velocity fields are shown in Figure 6.7b. The velocity field $\bar{U} + u^{(0)}$ imposes a translation of the interface at speed c that can be determined as follows. Let us consider the volume of fluid, of unit width, entering the control volume defined in Figure 6.7c during a time dt . This volume is the sum of three contributions: (i) the incoming volume $\hat{\eta} U_0 dt$ associated with the base flow, (ii) the incoming volume associated with the velocity perturbations

$$dt \int_{-h}^0 u^{(0)}(y, 0, 0) dy = -\frac{1}{2} \bar{U}'' h^2 \hat{\eta} dt = \hat{\eta} U_0 dt,$$

and (iii) the outgoing volume $\hat{\eta} c dt$ associated with the translation of the interface at speed c . Since the net incoming volume must be zero owing to incompressibility, we see that the speed c must in fact be equal to twice the speed U_0 of the interface. This result agrees well with that of the earlier analysis; see Eq. (6.19).

To exhibit and understand the instability it is necessary to calculate the inertial correction to the Stokes flow (6.27)–(6.28). This correction can be estimated using dimensional arguments. In order to consider a stationary problem, we work in a reference frame attached to the wave of speed $c = 2U_0$, so that the velocity profile of the base solution has the shape shown in Figure 6.8a. Two phenomena compete to first order: gravity, which has a stabilizing effect, and fluid inertia, which is destabilizing. Let us first consider gravity (Figure 6.8b). The pressure p^+ under a peak is higher than the pressure p^- under a trough owing to the hydrostatic effect. This pressure difference gives rise to Poiseuille flow out of phase with the interface deformation, where the average speed $u^{(1g)}$ is such that

$$\mu \frac{u^{(1g)}}{h^2} \sim k(p^+ - p^-) \sim \rho g \cos \theta k \hat{\eta} \quad (6.29)$$

or $u^{(1g)} \sim k \eta U_0$. This flow drains the fluid from the peaks toward the troughs and tends to make the interface planar again; we note that this effect vanishes for a vertical film. The second phenomenon, related to the inertia, is the sum of two contributions: the advection of the perturbation $u^{(0)}$ by the base flow $\bar{U} - c$, and the advection of the transverse gradients \bar{U}' by the perturbation $v^{(0)}$. The first of these two contributions, shown in Figure 6.8c, creates a flow $u^{(1a)}$ out of phase with the interface such that

$$\mu \frac{u^{(1a)}}{h^2} \sim \rho U_0 k u^{(0)} \sim \rho \frac{U_0^2}{h} k \hat{\eta}. \quad (6.30)$$

The other contribution due to advection is expressed in the same way because $\rho U_0 k u^{(0)} \sim \rho v^{(0)} \bar{U}'$ owing to the incompressibility. This inertial flow is directed from the troughs to the peaks and therefore tends to amplify the perturbation. Each of the two flows, gravitational and inertial, produces a vertical velocity $v^{(1)} \sim k h u^{(1)}$ in phase with the interface and contributes to the growth rate σ via a term of the form

$$\sigma \sim \frac{v^{(1)}}{\eta} \sim kh \frac{u^{(1)}}{\eta}. \quad (6.31)$$

When the inertial flow (6.30) is small compared to the gravitational flow (6.29), or

$$\rho \frac{U_0^2}{h} k \hat{\eta} \ll \rho g \cos \theta k \hat{\eta}, \quad (6.32)$$

or equivalently $\text{Fr} \ll 1$, the stabilizing flow due to gravity dominates, and the planar film is stable. In the opposite case $\text{Fr} \gg 1$ the film is unstable. The marginal stability condition corresponds to the two phenomena being in equilibrium, that is, $\text{Fr}_c \sim 1$, and we obtain, up to a numerical factor of 5/8, the stability criterion in terms of the Froude number given by the exact calculation.

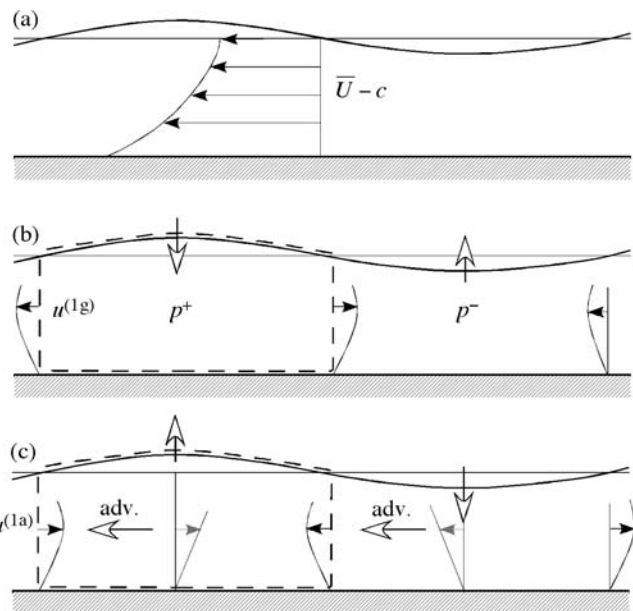


Figure 6.8 (a) Base flow in the reference frame attached to the wave of speed $2U_0$, (b) velocity perturbations associated with the stabilizing hydrostatic pressure gradient, and (c) velocity perturbations associated with the destabilizing advection.

6.2.5 Experimental study

Numerous experimental studies of the stability of falling films have been performed since the time of Kapitza (1948, 1949). The definitive study comparing experimental results with the Benjamin (1957) and Yih theory (1963) is that of Liu *et al.* (1993). Here we shall discuss the part of that work pertaining to linear stability, i.e., the wave growth rate and speed, and the marginal stability curve.

The experimental apparatus

The experimental setup, shown schematically in Figure 6.9, consists of an inclined plane 2 m long and 0.5 m wide on which a water/glycerine mixture flows. Small perturbations of the driving pressure of controlled amplitude and frequency can be imposed on the flow at the entrance plane.

The local slope of the interface is measured at two points by the refraction of a laser beam crossing the film. The resolution of the slope measurement is 5×10^{-5} , which makes it possible to detect an amplitude of $0.4 \mu\text{m}$ of a sinusoidal wave of 5 cm wavelength. The entire wave field can be visualized by a camera: the flow is uniformly illuminated by an ultraviolet light source, which causes fluorescence of

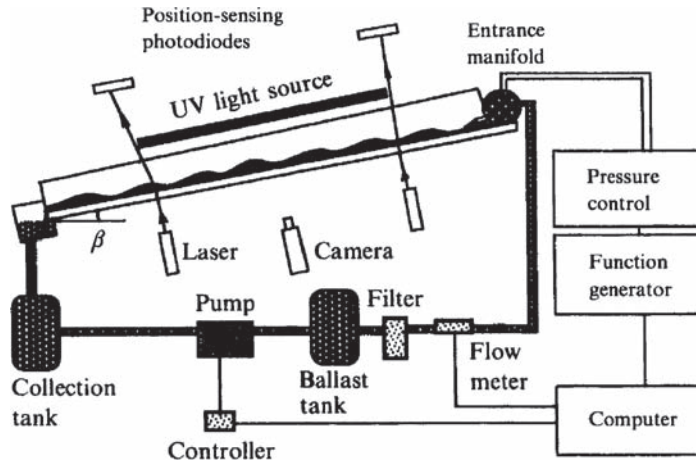


Figure 6.9 Schematic view of the experimental setup of Liu *et al.* (1993), showing in particular the ballast tank designed to reduce pressure fluctuations, the method of periodic forcing of the flow at the entrance plane, and the measurement technique (two local optical measurements of the interface slope and visualization of the wave field by fluorescence).

a small amount of fluorescein added to the fluid. The intensity of the light emitted is proportional to the film thickness $h(x, y, t)$, and the position of the interface can be determined by measuring this intensity with a camera and subsequent image processing. The relative variations of the film thickness measured in this manner are of order 1%.

Figure 6.10 shows images of the wave field obtained by fluorescence and the corresponding surface profiles. Figure 6.10a shows a periodic wave of frequency 5 Hz whose amplitude appears to be constant (a “saturated” wave), while Figure 6.10b shows a train of more widely spaced waves of lower frequency called “solitary” waves, with secondary oscillations ahead of the front of the principal peak. These two figures correspond to forced waves of initially given frequency and amplitude. Figure 6.10c shows a natural (unforced) wave with its characteristic nonperiodic shape.

Determination of the critical Reynolds number

It is difficult to measure the critical Reynolds number Re_c owing to the fact that the first unstable wave number is $k = 0$, i.e., an infinitely long wave. It is therefore necessary to determine Re_c by finding the marginal stability curve for $k \neq 0$ and then extrapolating it to $k = 0$. This curve is obtained as follows. Since the inclination angle and the Reynolds number are fixed, the total power of the perturbation, obtained by integrating the power spectrum about the forcing frequency, is

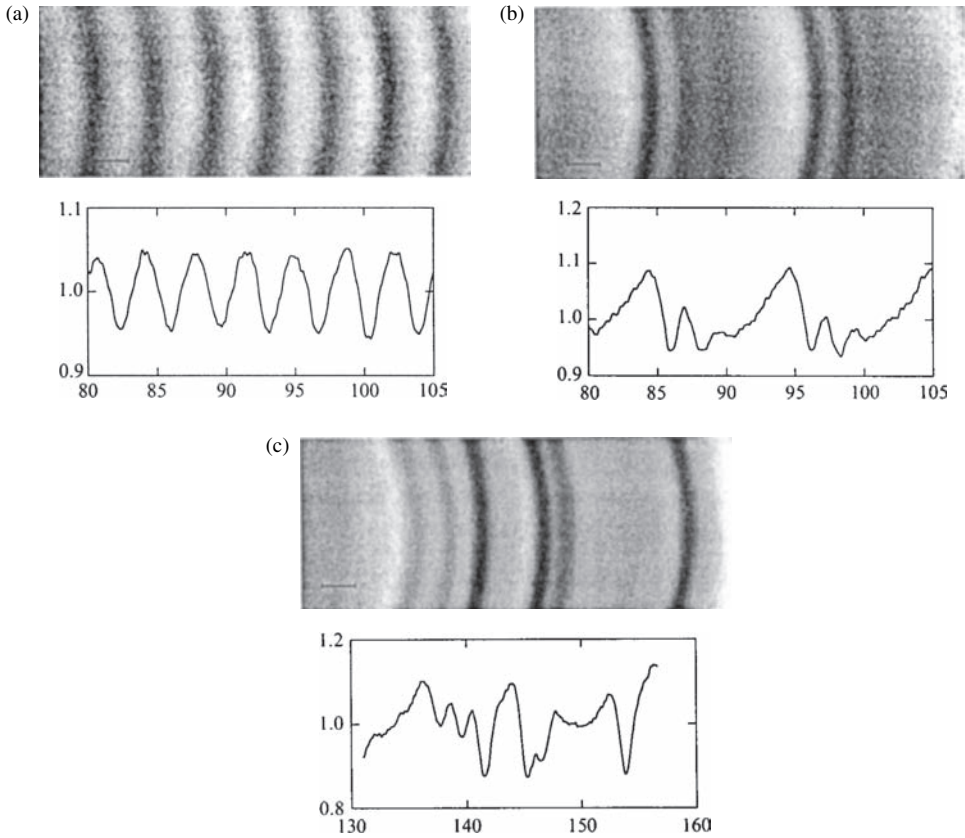


Figure 6.10 Wave images obtained by fluorescence and the corresponding thickness profiles $h(x)$ normalized by the average thickness h_0 . The film flows from left to right on a plane inclined at an angle $\theta = 4.6^\circ$. (a) Nearly sinusoidal waves forced at 5.5 Hz, $Re = 25$; (b) nonlinear waves forced at 2 Hz, $Re = 25$; (c) natural, unforced waves far downstream, $Re = 57$ (from Liu *et al.* (1993), © Cambridge University Press, reproduced with permission).

computed for various excitation frequencies (Figure 6.11). At frequencies below a cutoff f_c the wave is spatially amplified and the signal given by the downstream probe (\square) is stronger than the upstream signal (\circ). At frequencies higher than the cutoff the wave decays. The cutoff frequency is then determined by the intersection of the two curves, which corresponds to a wave which neither grows nor decays, i.e., to a marginally stable wave. The accuracy of this measurement is of order 0.2 Hz.

The procedure for determining the cutoff frequency f_c is repeated for several Reynolds numbers near the instability threshold. Using the fact that the frequency f is linearly related to the wave number k for nondispersive waves ($f = \omega/2\pi =$

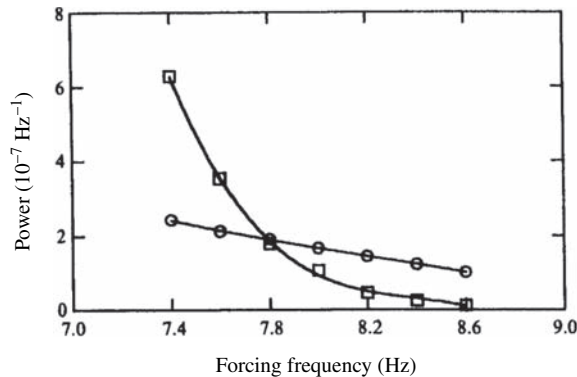


Figure 6.11 Determination of the cutoff frequency f_c from the strength of the slope signal as a function of the forcing frequency at the two abscissas $x = 43$ cm (○) and $x = 134$ cm (□), for $\theta = 5.6^\circ$ and $Re = 20.7$ (from Liu *et al.* (1993), © Cambridge University Press, reproduced with permission).

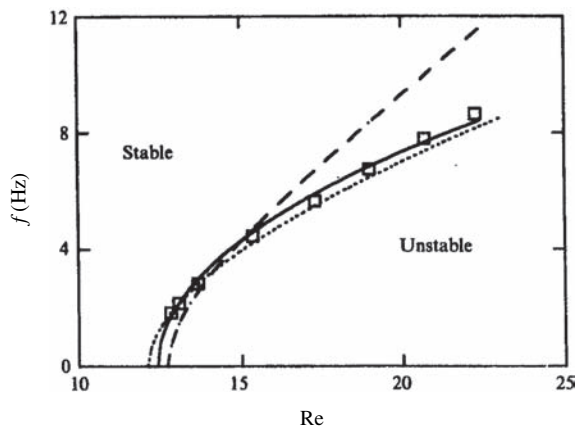


Figure 6.12 Marginal stability curves for $\theta = 5.6^\circ$: (—) smoothed (Eq. (6.33)) experimental points giving $Re_c = 12.4 \pm 0.1$, (- - -) asymptotic solution (6.21) giving $Re_c = 12.7$, (...) approximate solution of Anshus and Goren (1966) (from Liu *et al.* (1993), © Cambridge University Press, reproduced with permission).

$kc/2\pi \approx kU_0/\pi$) and taking into account (6.21) for the temporal growth rate, near the instability threshold we expect to find a relation of the type

$$f_c \sim \sqrt{Re - Re_c}. \quad (6.33)$$

(The control parameter chosen in this study is the Reynolds number, which is related to the Froude number as $Fr = \frac{1}{2}Re \tan \theta$.) Then Re_c is determined by finding

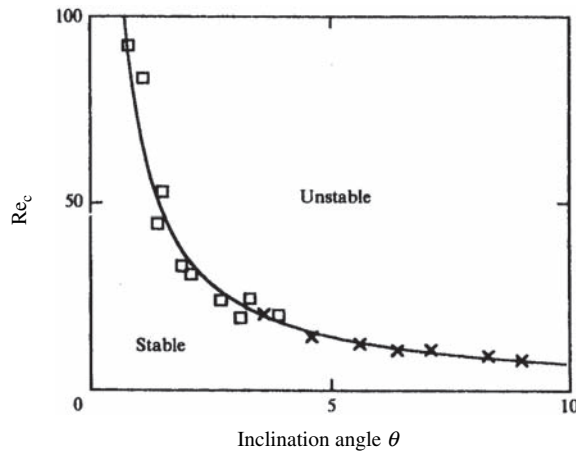


Figure 6.13 Critical Reynolds number Re_c as a function of the angle θ . Results obtained for water (\square) and for a water-glycerin solution (\times). The curve corresponds to the result of the asymptotic theory, $Re_c = 5/(4\tan\theta)$ (from Liu *et al.* (1993), © Cambridge University Press, reproduced with permission).

the parabola that most closely fits the experimental measurements of $f_c(Re)$, as shown in Figure 6.12. This figure also compares the measurements to the long-wave asymptotic theory: the curvature given by the latter is seen to differ from the experimental marginal stability curve. This difference arises from the fact that, owing to the overly strong hypothesis $(kh)^2/\text{We} = \mathcal{O}(1)$, the theory attributes the stabilization of short wavelengths exclusively to the surface tension.

Since the critical Reynolds number is obtained for a particular inclination angle, the procedure is then repeated for other angles. Figure 6.13 compares the experimental results to the marginal stability criterion given by the asymptotic analysis, $Fr_c = 5/8$ or $Re_c = \frac{5}{4}\cot\theta$. The difference between the experimental and theoretical results is of order 10%, which in view of the complexity of the experimental procedure, is considered quite satisfactory.

The spatial growth rate and the phase velocity

The spatial growth rate can be determined from the visualization at a given instant of the wave field resulting from a sinusoidal perturbation at the upstream end of the flow. This visualization gives a thickness profile which, after averaging over several runs in order to decrease the noise, can be approximated by a sinusoidal function of exponentially growing amplitude. The spatial growth rate and the wave number are determined in this manner. Knowing the frequency ω and the wave number k , it is then possible to determine the speed $c = \omega/k$. The temporal growth

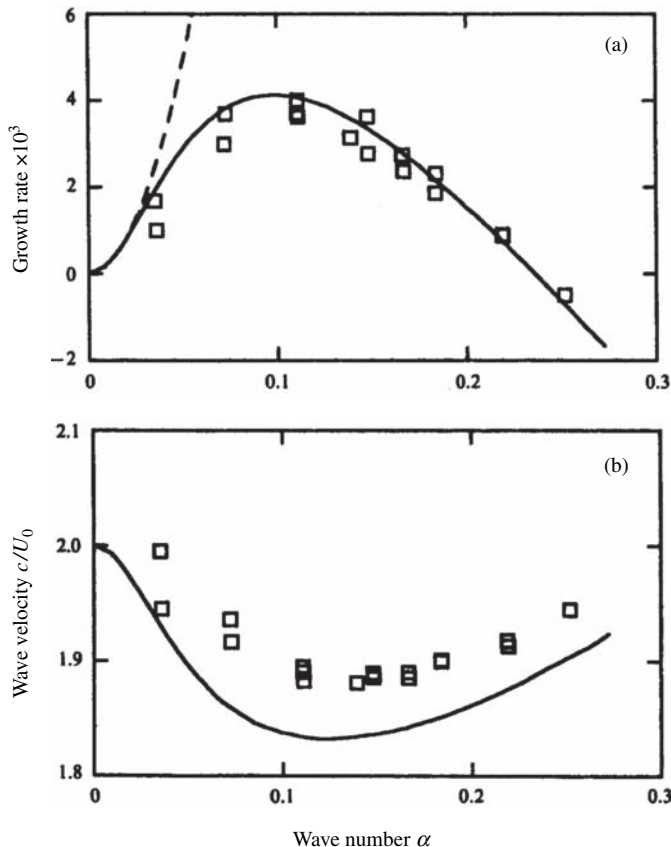


Figure 6.14 (a) Spatial growth rate and (b) speed as a function of the wave number. $\theta = 4.6^\circ$, $Re = 23$, and $We = 0.19$. (□) Observations; (—) Anshus and Goren (1966); (---) long-wave calculation (from Liu *et al.* (1993), © Cambridge University Press, reproduced with permission).

rate can be determined near threshold using the Gaster relation (Chapter 3), where here the group velocity is $c_g \approx 2U_0$.

Figure 6.14 presents the spatial growth rate and the wave speed determined in this manner for a typical case. These results are compared to the long-wave asymptotic solution and to the approximate solution of the Orr–Sommerfeld equation developed by Anshus and Goren (1966) (not discussed here). We see that the long-wave solution gives good results as long as $kh \lesssim 0.03$, or $khRe \lesssim 0.7$. The approximate solution of Anshus and Goren (1966) gives good results for the growth rate as well as for the speed; in particular, a good prediction is obtained for the most amplified wave number.

Convective nature of the instability

The analysis of Yih (1963) shows that perturbations of wavelength large compared to the film thickness are only weakly dispersive and propagate downstream at a speed equal to twice that of the interface U_0 . A “wave packet” is therefore carried by the flow at a group velocity roughly equal to $2U_0$. Therefore, no perturbation can move in the direction opposite to the flow or remain at a given distance from the entrance; this corresponds to a convective instability (see Chapter 3).

The convective nature of the instability can be studied experimentally by following the response to an impulse perturbation generated upstream. Figure 6.15 shows that such a perturbation propagates downstream and is amplified as it spreads out. At a given distance from the entrance of the flow the film returns to its unperturbed initial state after the wave packet has passed. In this fashion, the convective nature of the instability is thereby confirmed experimentally.

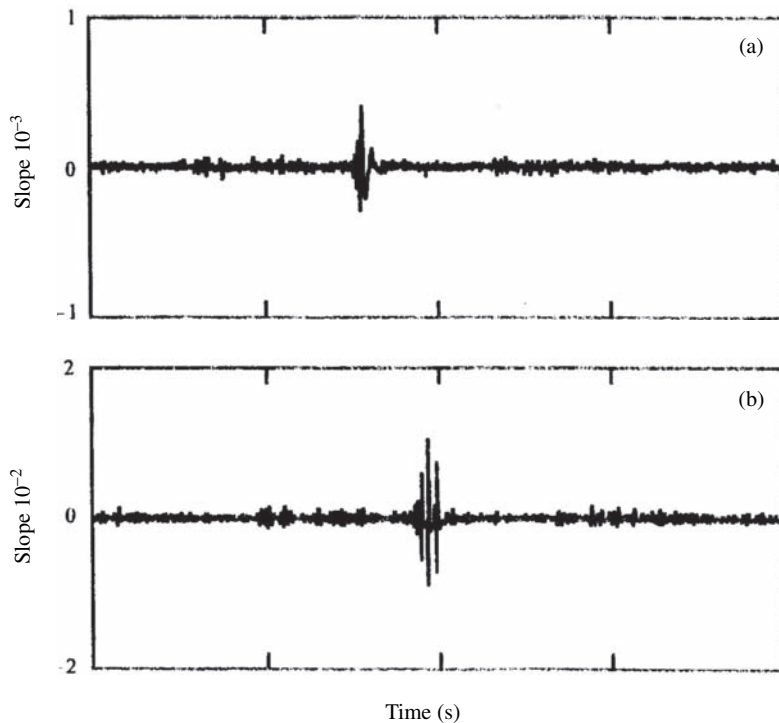


Figure 6.15 A perturbation generated at the entrance is observed (a) at $x = 44$ cm and (b) at $x = 97$ cm ($\theta = 2.5^\circ$, $Re = 150$). The perturbation is amplified as it is convected downstream by the flow. Note that the vertical scales of the two graphs are different (From Liu *et al.* (1993), © Cambridge University Press, reproduced with permission).

6.2.6 Instability of the wall mode at small slope

For a small slope θ , the critical Reynolds number $\text{Re}_c = \frac{5}{4} \cot \theta$ of the interfacial mode becomes very large. An instability is then manifested which is associated with the growth of Tollmien–Schlichting waves near the wall, via a mechanism identical to that of the boundary-layer instability or Poiseuille flow. This instability, which has been calculated by Floryan *et al.* (1987), is characterized by the fact that the maximum of the eigenfunctions is localized near the wall, and no longer near the interface as for the interfacial mode. This instability makes the flow evolve rapidly toward turbulence.

6.3 Sheared liquid films

6.3.1 Introduction

Several of the physical situations listed in the introduction to this chapter involve two or more superposed fluid layers produced by a pressure gradient (Poiseuille flow) or by a shear (Couette flow). Analysis of the stability of this type of flow leads to an Orr–Sommerfeld equation for each layer, coupled by four conditions on the velocities and the stresses at the interfaces. A good introduction to the problem of a liquid film sheared by a (turbulent) air flow is provided by the review of Hanratty (1983). In the simplest case of the *viscous* flow of two liquids, the stability to long-wavelength perturbations, i.e., perturbations with $kh \ll 1$, has been solved by Yih (1967). Short-wavelength perturbations have been considered by Hooper and Boyd (1983) and Hinch (1984), and Tollmien–Schlichting waves by Hooper and Boyd (1987). Situations not amenable to solution by asymptotic series, typically where $kh \sim 1$ and $\text{Re} \geq 1$, have been analyzed numerically (Renardy, 1985). The study of annular flows, begun by Hickox (1971), has been reviewed by Joseph *et al.* (1997).

The analysis of Yih (1967) reveals a simple criterion for instability to long-wavelength perturbations: it is sufficient that the thinnest layer is the most viscous one. Here we shall describe the mechanism of this instability and obtain this result by dimensional arguments (Charru and Hinch, 2000).

We consider a film of thickness h_1 sufficiently thin compared to the characteristic thickness h_2 of the other fluid, so that the flow near the film can be considered a planar shear flow, as shown in Figure 6.16a. In the case of Couette flow or for a solid wall which imposes a speed U_0 on fluid 2 of thickness h_2 , the unperturbed flow is given exactly by

$$\overline{U}_1 = U_I \frac{y}{h_1}, \quad \overline{U}_2 = U_I + (U_0 - U_I) \frac{y - h_1}{h_2}, \quad (6.34)$$

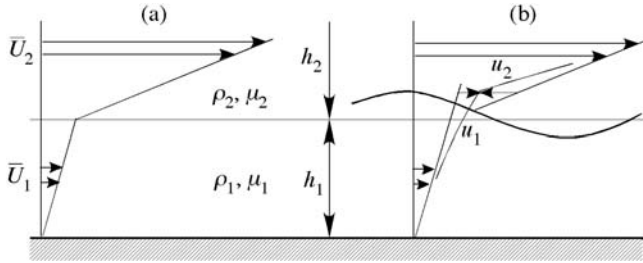


Figure 6.16 Flow near a sheared thin film in the case $\mu_2 < \mu_1$: (a) base flow, (b) mechanism initiating the instability: near a peak the velocity continuity imposes an acceleration of film 1 and a deceleration of film 2.

where the interface speed U_I is defined by the continuity of the tangential stress τ_i at the interface:

$$\tau_i = \mu_1 \frac{U_I}{h_1} = \mu_2 \frac{U_0 - U_I}{h_2}. \quad (6.35)$$

In the case of planar or cylindrical Poiseuille flow due to a pressure gradient $-G$, the expression for the velocity field is a bit more complicated, but for thin films, Eqs (6.34) and (6.35) remain a good approximation near the interface when correction terms of order h_1/h_2 are neglected. For example, for annular flow in a tube of radius R with h_2 defined as the central radius of the flow, $h_2 = R - h_1$, the speed U_0 corresponds to twice the speed at the axis, i.e., $U_0 = 2Gh_2^2/4\mu_2$, and the interface shear is $\tau_i = GR/2$ (up to corrections of order h_1/h_2). Therefore, for Couette or Poiseuille flow the speeds U_2 in fluid 2 are of order U_0 , while the speeds U_1 in the film are of order $U_I \sim (\mu_2 h_1 / \mu_1 h_2) U_0$, i.e., they are smaller by a factor of h_1/h_2 .

6.3.2 The long-wave instability mechanism

We consider a perturbation $\eta = \eta_0 \cos kx$ of the interface (Figure 6.16b). For long wavelengths the longitudinal gradients, which are of order k , are small compared to the transverse gradients of order $1/h_1$ and $1/h_2$. Incompressibility ($\nabla \cdot \mathbf{u} = 0$) then implies that the amplitudes of the transverse velocity perturbations are small compared to the longitudinal amplitudes:

$$v_1 \sim kh_1 u_1 \ll u_1, \quad v_2 \sim kh_2 u_2 \ll u_2. \quad (6.36)$$

Let us estimate the ratio of the inertial and viscous effects associated with the perturbations. For a particle of fluid 2 the inertial force is $O(\rho_2 U_2(ku_2))$ and the viscous forces are $O(\mu_2 u_2/h_2^2)$ per unit volume. The ratio of these two forces

defines an “effective Reynolds number”

$$\text{Re}_{2,\text{eff}} = kh_2 \text{Re}_2, \quad \text{where} \quad \text{Re}_2 = \frac{\rho_2 U_0 h_2}{\mu_2}. \quad (6.37)$$

Similar estimates for the film lead to the effective Reynolds number

$$\text{Re}_{1,\text{eff}} = kh_1 \text{Re}_1, \quad \text{where} \quad \text{Re}_1 = \frac{\rho_1 U_1 h_1}{\mu_1}. \quad (6.38)$$

Using the estimate $U_1/U_0 \sim \mu_2 h_1/\mu_1 h_2$ found above, we obtain, for densities and viscosities of the same order of magnitude,

$$\text{Re}_{1,\text{eff}} \sim \frac{h_1^3}{h_2^3} \text{Re}_{2,\text{eff}} \ll \text{Re}_{2,\text{eff}}. \quad (6.39)$$

Therefore, the inertial effects in the film are much smaller than those in fluid 2.

Let us consider the case where the inertial effects in fluid 2 (and *a fortiori* in the film) are small. At the dominant order the perturbed flow is a purely viscous flow (Stokes flow), which can be estimated as follows. Continuity of the longitudinal velocity at the interface, linearized about $y=0$ on the unperturbed interface, requires that⁴

$$\bar{U}_1 + \eta \bar{U}'_1 + u_1^{(0)} = \bar{U}_2 + \eta \bar{U}'_2 + u_2^{(0)}.$$

Taking into account the continuity of the velocity and shear stress for the base flow, $\bar{U}_1 = \bar{U}_2$ and $\mu_1 \bar{U}'_1 = \mu_2 \bar{U}'_2$, the above equation leads to

$$u_2^{(0)} - u_1^{(0)} \sim U_I \left(1 - \frac{\mu_1}{\mu_2} \right) \frac{\eta}{h_1}. \quad (6.40)$$

On the other hand, the continuity of the perturbation shear stress at the interface, using $v \ll u$, gives

$$\mu_1 (\bar{U}'_1 + \partial_y u_1^{(0)}) = \mu_2 (\bar{U}'_2 + \partial_y u_2^{(0)}),$$

from which we obtain

$$\frac{\mu_1 u_1^{(0)}}{h_1} \sim - \frac{\mu_2 u_2^{(0)}}{h_2}. \quad (6.41)$$

(The minus sign arises from the fact that the perturbations necessarily have the opposite sign; for example, if $\mu_2 < \mu_1$ the situation corresponds to that in

⁴ The convention adopted for superscripts is the same as in Section 6.2.4: see footnote 3.

Figure 6.16, where the film is accelerated ($u_1^{(0)} > 0$) and fluid 2 is decelerated ($u_2^{(0)} < 0$).) Combining (6.40) and (6.41) we obtain the velocity perturbations:

$$u_1^{(0)} \sim \frac{\eta}{h_2} \frac{\mu_1 - \mu_2}{\mu_2} U_I, \quad u_2^{(0)} \sim -\frac{\mu_1 h_2}{\mu_2 h_1} u_1^{(0)}. \quad (6.42)$$

Using the approximation of Stokes flow, these velocity perturbations, shown in Figure 6.17a, are therefore in phase with the deformation η of the interface. From the kinematic condition $\partial_t \eta = v_1^{(0)} - U_I \partial_x \eta$ at the interface we find that the perturbations propagate without growing or decaying at the speed

$$c \sim U_I. \quad (6.43)$$

In order to obtain an instability it is necessary, as for the falling film studied in the preceding section, to include weak inertial corrections to the Stokes flow (6.42). Since according to (6.39) the inertial effects in the film are negligible, only the inertia of fluid 2 needs to be taken into account. We present the argument in terms of vorticity perturbations ω_2 , the transport equation for which does not

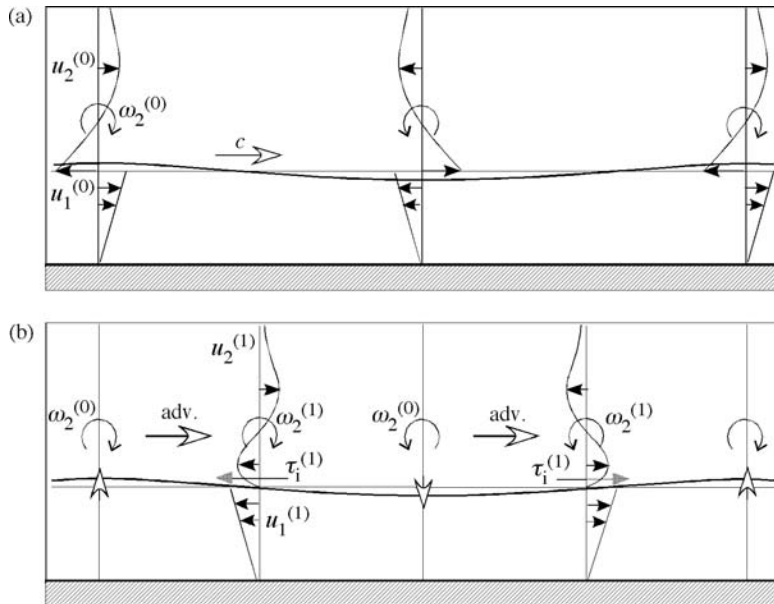


Figure 6.17 Longitudinal velocity perturbations induced by a sinusoidal deformation $\eta(x)$ of the bed and the associated vorticity: (a) Stokes flow in phase with $\eta(x)$, (b) out-of-phase inertial correction.

involve the pressure and is written as

$$\rho_2 \frac{d\omega_2}{dt} = \mu_2 \Delta\omega_2. \quad (6.44)$$

For long-wave perturbations ($kh_2 \ll 1$), to leading order this equation reduces to $\Delta\omega_2^{(0)} = 0$ corresponding to the Stokes flow estimated above and shown in Figure 6.17a. At the next order the inertial correction $\omega_2^{(1)}$ is found from dimensional arguments to be

$$\mu_2 \frac{\omega_2^{(1)}}{h_2^2} \sim \rho_2 k U_0 \omega_2^{(0)},$$

or $\omega_2^{(1)} \sim kh_2 \text{Re}_2 \omega_2^{(0)}$. This correction due to advection is out of phase with $\omega_2^{(0)}$, as illustrated in Figure 6.17b (the $\pi/2$ phase lag can be derived by studying the equation for the complex amplitude $\hat{\omega}_2^{(1)}$ of a normal mode, which involves a factor ik coming from the derivative with respect to x in the advective term). The vorticity $\omega_2^{(1)}$ gives rise to a longitudinal flow of order $u_2^{(1)} \sim \omega_2^{(1)} h_2$, which at the interface must match the flow in the film. Therefore, $u_2^{(1)}$ must vanish at the interface, and so the correction $u_2^{(1)}$ must have the form shown in Figure 6.17b. This correction gives rise to a shearing $\tau_i^{(1)} \sim \mu_2 \omega_2^{(1)}$ of the film, which then responds with a flow satisfying $\mu_1 u_1^{(1)}/h_1 \sim \tau_i^{(1)}$. Putting all these estimates together, we find

$$u_1^{(1)} \sim kh_2 \text{Re}_2 \frac{\mu_1 - \mu_2}{\mu_2} \frac{\eta}{h_2} U_I, \quad \text{with} \quad U_I \sim \frac{\mu_2 h_1}{\mu_1 h_2} U_0. \quad (6.45)$$

For $\mu_2 < \mu_1$ the flow is directed from the troughs to the peaks, and therefore amplifies the initial perturbation. We then obtain the growth rate $\sigma \sim v_1^{(1)}/\eta \sim kh_1 u_1^{(1)} \eta$, or

$$\sigma \sim (kh_1)^2 \text{Re}_2 \frac{\mu_1 - \mu_2}{\mu_1} \frac{U_0}{h_2}. \quad (6.46)$$

Therefore, by dimensional analysis we have recovered the major results of the complete stability analysis, i.e., (i) when fluid 1 is less viscous than fluid 2, the growth rate is negative and so the flow is stable, while in the opposite case the flow is unstable, and (ii) the mechanism involves both weak inertia and viscosity stratification.

6.3.3 Waves of shorter wavelength

The above dimensional analysis is valid as long as the transverse gradients in fluid 2 are of order $1/h_2$, a hypothesis which is always true for waves of sufficiently long

wavelength, but which may not hold for waves of shorter wavelength. By “waves of shorter wavelength” we mean waves for which the penetration depth δ of the vorticity perturbations governed by (6.44) becomes smaller than the transverse scale h_2 . The relevant transverse scale is then no longer h_2 but rather δ . This depth δ is obtained by taking the inertial and viscous effects to be of the same order of magnitude:⁵

$$\rho_2 k U_0 \omega_2 \sim \mu_2 \frac{\omega_2}{\delta^2}, \quad (6.47)$$

where $U_0 \sim (\tau_i/\mu_2)\delta$ is the speed at a distance δ from the interface. We then find

$$\delta = \left(\frac{k \mu_2^2}{\rho_2 \tau_i} \right)^{1/3}. \quad (6.48)$$

Repeating the analysis of the perturbed flow taking δ as the characteristic transverse scale, we find that the growth rate no longer varies as $(kh_1)^2$ but rather as $(kh_1)^{4/3}$; however, the prefactor is always proportional to the difference $(\mu_1 - \mu_2)$ (Charru and Hinch, 2000).

The qualitative result obtained for long wavelengths ($kh_2 \ll 1$) therefore remains valid for smaller wavelengths ($k\delta \ll 1$): a thin film is unstable if it is sheared by a less viscous fluid, and stable in the opposite case. As mentioned in the introduction to this chapter, this property is used by the oil industry to transport very viscous oils, where a water film is injected at the wall of the pipe (Figure 6.2).

6.3.4 Instability of a falling film revisited

We end this chapter with a comparison of the instabilities of a falling film and a sheared film. The analyses in both cases display on the one hand an initiation mechanism, and on the other an amplification mechanism. For the falling film the initiation mechanism resides in the continuity of the *shear* at the free surface, while for the sheared film it resides in the continuity of the *velocity* at the interface. These initiation mechanisms cause the development of purely viscous perturbations. In both cases it is then advection due to weak inertia that is responsible for amplifying the perturbations, directly for the falling film and in a more indirect manner via the interface stress $\tau_i^{(1)}$ for the sheared film.

⁵ Beyond δ the perturbations tend to zero in an irrotational layer of thickness k^{-1} . This potential layer corresponds to the “upper deck” of the triple-deck theory (Cousteix and Mauss, 2006).

6.4 Exercises

6.4.1 Critical slope for a falling film

- Derive the relations (6.1) defining the base flow. Find the thickness of a water film ($\mu = 10^{-3}$ Pa s) on a 1-m wide plane inclined at 10° for a flow rate of 1 l/min per meter of cross-section. What is this thickness for a film of oil of viscosity eight times higher, keeping the flow rate fixed? How does this thickness change when the slope is increased?
- Determine the critical slope beyond which a water film becomes unstable, for a flow rate of 1 l/min per meter of width.

6.4.2 Boundary conditions on a free interface

- Rederive the expression for the kinematic condition (6.6) using the principle of mass conservation in a control volume of thickness dx and bounded by the lower wall and the interface.
- Derive the linearized boundary conditions (6.13)–(6.14). Start by finding the two conditions (6.8) on the interface stresses, and then linearizing them. It is important, in particular, to carefully linearize the pressure at the interface using a Taylor series approach:

$$P(\eta) = \bar{P}(\eta) + p(\eta) = \bar{P}(0) + \eta \partial_y \bar{P}(0) + p(0) + \mathcal{O}(\eta^2).$$

6.4.3 Solution for long waves

- Derive the system of Stokes equations (6.17)–(6.18) starting from (6.11)–(6.13). Solve this system and obtain the solution (6.19).
- Carry out the algebra required to calculate the inertial correction and find the growth rate $\sigma = \alpha c_i$, where c_i is given by (6.20).

6.4.4 Stability using the depth-averaged equations

Consider the consistent depth-averaged equations (6.24) and (6.26) for the falling film.

- Show that these equations admit a base flow solution \bar{h} and \bar{U} for the film thickness and mean velocity, given by

$$\bar{U} = \frac{\rho g \bar{h}^2 \sin \theta}{3\mu}, \quad Q = \bar{U} \bar{h},$$

where Q is the imposed flow rate per unit width.

2. Taking \bar{h} and \bar{h}/\bar{U} as the length and time scales, show that the linearized mass and kinetic-energy equations for the dimensionless disturbances η and u are

$$\begin{aligned}\partial_t \eta + \partial_x \eta + \partial_x u &= 0, \\ \frac{3}{5} \partial_t \eta + \frac{6}{5} \partial_t u + \frac{27}{35} \partial_x \eta + \frac{81}{35} \partial_x u &= -\frac{\partial_x \eta}{\bar{F}r} + \frac{3}{\bar{R}e} (2\eta - u),\end{aligned}$$

where $\bar{R}e = \rho \bar{U} \bar{h} / \mu$ and $\bar{F}r = \bar{U}^2 / g \bar{h}$.

3. Introducing disturbances proportional to $e^{i\alpha(x-ct)}$, show that the dispersion relation is

$$\frac{6}{5}c^2 - \frac{102}{35}c + \frac{54}{35} = \frac{1}{\bar{F}r} + \frac{3}{i\alpha\bar{R}e}(c-3).$$

4. For $\alpha\bar{R}e$ small (as it must be here), expand the eigenvalue as $c = c^{(0)} + \alpha\bar{R}e c^{(1)}$ and show that one of the two roots is given by

$$c^{(0)} = 3, \quad c^{(1)} = \frac{i}{3} (\bar{F}r_c^{-1} - \bar{F}r^{-1}),$$

where $\bar{F}r_c = 5/18$ is the critical Froude number. Verify that this result corresponds to the same dimensional wave velocity and growth rate as those obtained from the Orr–Sommerfeld equations (i.e., $c = c^{(0)} + \alpha c^{(1)}$, where $c^{(0)}$ and $c^{(1)}$ are given by (6.19) and (6.20) with the interface velocity $U_0 = \frac{3}{2}\bar{U}$ as the velocity scale).

5. Show that the other root of the dispersion relation corresponds to a strongly damped mode.

7

Avalanches, ripples, and dunes

7.1 Introduction

In this chapter we present an introduction to dense granular flows and their stability by discussing two classes of phenomena: avalanches on an inclined plane, and particle transport on an erodible bed sheared by a fluid flow. These granular flows lead to the appearance of surface waves, called ripples or dunes depending on whether their wavelength is of a few centimeters or a few meters (the relevance of this common distinction will be discussed later on). Owing to the difficulty – both experimental and theoretical – of studying granular media, the mechanisms responsible for these waves remain poorly understood, and so the results presented in this chapter are definitely less well established than those in the preceding chapters.

Avalanches, ripples, and dunes present serious problems for human activities. Among natural phenomena, snow and mud avalanches are well known for their destructive nature; the displacement of a sand dune by the wind – the so-called aeolian dunes – while less dramatic, can cut communication links and threaten habitation and industrial installations. Subaqueous dunes perturb navigation in rivers and shallow seas such as the North Sea, while on river bottoms such dunes increase friction and raise the water level, thereby contributing to flooding. Granular flows are also omnipresent in industry: flow and transport of coal, construction materials (cement, sand, gravel), agricultural foodstuffs, pharmaceutical materials, and sand from oilfields are some examples. Instabilities occur in the conduits used to transport these materials, giving rise to dunes which perturb the flow and may form obstructions, causing serious damage to operating equipment.

When studying the situations mentioned above, the first problem to consider, before dealing with instabilities, is how to model a granular flow. This requires understanding the relation between the stresses and deformations of the granular medium. Depending on how it is prepared, a noncohesive granular medium

may behave like an elastic solid (for example, scree), or it may undergo plastic deformation (sand underfoot), or it may flow like a fluid (sand in an hour glass). The general behavior of a granular medium therefore admits no simple description, and so it is much more difficult to study than an elastic solid or a Newtonian fluid.¹ This is because, first of all, there is not a large separation between the scale of the observed phenomena (on the order of a meter or less) and the grain size (on the order of a millimeter or more), with the result that finite-size effects play a role and fluctuations remain important. Second, the interaction between the grains is complicated, much more so than that between molecules. It is dissipative owing to friction between grains, and it involves the grain shape and the packing geometry. This leads to both strongly nonlinear and threshold behavior, which can depend on the history of the medium. Therefore, there is no general statistical mechanics theory available for granular media, in contrast to simpler materials. A further difficulty is the interaction of the grains with the interstitial fluid, either a gas or a liquid: when this interaction is negligible, the granular medium is termed “dry.”

It was Coulomb who, at the end of the 18th century, first developed a model of a dry granular medium, introducing a relation of proportionality between the normal and tangential stresses at contact involving a friction coefficient. This simple law succeeds remarkably well in describing a number of static phenomena, but it fails to describe flows, at least in its elementary version where the friction coefficient is constant. Improvement of this law using the physics of granular media is at present the object of very active numerical, experimental, and theoretical research. The prospects of obtaining a general theory remain rather remote, but some real progress has been made (Aranson and Tsimring, 2006).

The following section is devoted to surface waves and avalanches. The third section deals with the modeling of granular transport on a bed sheared by a flow, including some recent concepts regarding relaxation phenomena. This is followed by a quick overview of aeolian and subaqueous ripples and dunes, from the viewpoint of dimensional analysis (Section 7.4). We then give a more detailed discussion of the formation of subaqueous ripples in continuous flow (Section 7.5) and in oscillating flow (Section 7.6). Finally, we conclude this chapter with an analysis of the formation of subaqueous dunes (Section 7.7).

7.2 Avalanches

When the slope of a granular pile exceeds a critical value of about 30° , the surface of the granular medium suddenly begins to move (GDR MiDi, 2004; Forterre and

¹ Cohesive effects of electrostatic or capillary origin, which are manifested for tiny grains typically smaller than $10\ \mu\text{m}$, will not be considered in this chapter.

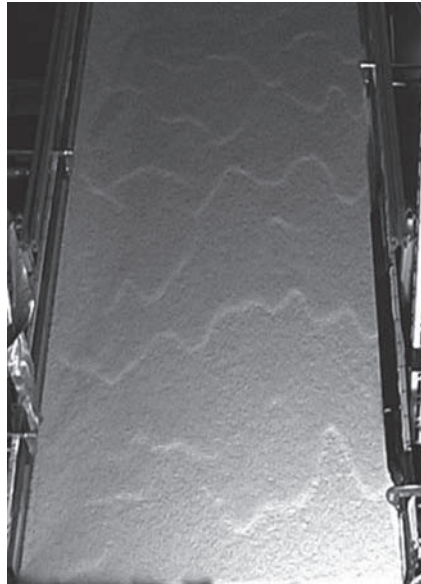


Figure 7.1 View from above of surface waves on a sand flow (grain diameter $d = 0.8$ mm, slope $\alpha = 34^\circ$, thickness $h = 4.6$ mm, flow width $W = 70$ cm) (Forterre and Pouliquen, 2003).

Pouliquen, 2008). This avalanche phenomenon can also arise following a physical modification of the medium, for example, a change in the grain cohesion (as in snow avalanches) or the interstitial water content (as in landslides).

Here we shall consider the special case of a granular flow on a rough inclined plane, where the thickness h is of a few tens of grain diameters. Surface waves appear, as shown in Figure 7.1. These waves have a triangular profile, a wavelength long compared to the thickness h , and an amplitude of order h . As shown by Forterre and Pouliquen (2003), whose work we report here, these waves correspond to an inertial instability very similar to the instability of a liquid film studied in the preceding chapter.

7.2.1 Particle flow on a rough inclined plane

The Saint-Venant equations

We consider a granular flow on a rough plane inclined at an angle α to the horizontal.² When the scale on which the flow varies in the longitudinal direction x is large compared to the layer thickness, a good description of the flow is given by the

² Here we use α rather than θ to denote this angle, reserving θ for the Shields number, to be consistent with the literature on granular media.

mass and momentum conservation equations integrated over the thickness of the layer, with some simplifying assumptions. These *Saint-Venant equations*, derived in the Appendix, govern the evolution of the depth-averaged speed $U(x, t)$ and the thickness $h(x, t)$. For plug flow (i.e., flow with uniform velocity in the direction normal to the plane), these equations become

$$\partial_t h + \partial_x(hU) = 0, \quad (7.1a)$$

$$\rho h \partial_t U + \rho h U \partial_x U = -\rho g h \cos \alpha \partial_x h - \tau + \rho g h \sin \alpha, \quad (7.1b)$$

where ρ is the density of the dense flow, which we assume to be uniform, and τ is the shear stress exerted by the bed on the flowing material. The rheology of the medium is not involved in the conservation equations (7.1), but it does enter into the modeling of the stress τ . This modeling is crucial because it governs the essentials of the stability properties. Inspired by the Coulomb laws for dry friction between two solids, we assume that this stress is proportional to the hydrostatic pressure, i.e.,

$$\tau = \mu_f \rho g h \cos \alpha, \quad (7.2)$$

where μ_f is a friction coefficient. The expression for this coefficient as a function of U and h , or, rather, as a function of the dimensionless parameters of the problem in the form of a constitutive law, corresponds to the desired modeling. Once the constitutive law is chosen, the Saint-Venant equations admit a base solution \bar{U} and \bar{h} defined by the two equations

$$\mu_f(\bar{U}, \bar{h}) = \tan \alpha, \quad Q = \bar{U} \bar{h}, \quad (7.3)$$

where Q is the imposed flow rate per unit width. We note that the significance of the first of the above equations is that the values of \bar{U} and \bar{h} are such that the friction coefficient is exactly $\tan \alpha$.

Constitutive laws for the friction coefficient

The easiest approach would be to choose the friction coefficient μ_f to be a constant, but this is not satisfactory. In fact, a constant friction coefficient would imply the existence of only a single slope $\alpha = \tan^{-1} \mu_f$ at which a stationary and uniform flow would be possible. However, experiments (see for example Pouliquen (1999)) show that such a flow exists for a range of slopes of several degrees about a typical value of 30° . Pouliquen (1999) therefore proposed a more elaborate constitutive law involving an important length scale: the residual thickness of the granular layer at which the grains stop moving when the upstream supply of material is cut off. This scale, denoted h_{stop} , is characteristic of the type of grain and decreases with

the slope α , as shown later in Figure 7.4. The relation between the speed and thickness of the granular layer is then well represented by an expression of the form

$$\frac{U}{\sqrt{gh}} = c_1 \frac{h}{h_{\text{stop}}(\alpha)}, \quad \mu_f(U, h) = \tan \alpha, \quad (7.4)$$

where c_1 is a coefficient whose value depends on the type of grain. The above two relations, together with an empirical rule $h_{\text{stop}}(\alpha)$, completely define a relation between U and h in terms of the parameter α and therefore, together with the relation $Q = Uh$, completely define the base solution.

We note that the case of an avalanche on an *erodible* bed, a typical example of which is a sand avalanche on the surface of a dune or a simple pile, can be described using Saint-Venant equations of the same type, by introducing an additional term describing grain exchange between the immobile substrate and the layer of mobile particles (Aradian *et al.*, 2002).

7.2.2 Linear stability

Linearizing the full nonlinear equations (7.1) about the base solution defined by (7.3) with the constitutive law (7.4) results in a set of equations governing small perturbations. Introducing normal modes proportional to $e^{ik(x-ct)}$ in the usual way and after some straightforward algebra, we find the dispersion relation

$$(c/\bar{U} - 1)^2 + \frac{ia}{k\bar{h}\text{Fr}}(c/\bar{U} - 1) - \frac{1}{\text{Fr}} \left(1 - \frac{ib}{k\bar{h}}\right) = 0, \quad (7.5)$$

where $\text{Fr} = \bar{U}^2/(g\bar{h} \cos \alpha)$ is the Froude number of the base flow and a and b are two coefficients coming from the perturbation of the constitutive law (7.4) defined as

$$a = \bar{U} \frac{\partial \mu_f}{\partial U}, \quad b = \bar{h} \frac{\partial \mu_f}{\partial h}. \quad (7.6)$$

Experiments show that the coefficient a is positive while b is negative, i.e., the friction coefficient increases with U and decreases with h .

For a given wave number k the dispersion relation (7.5) possesses two roots c_{\pm} . We note first of all that for constant friction coefficient the coefficients a and b vanish, and there is no instability. In this case, neutral perturbations propagate with speed

$$c_{\pm} = \bar{U} \pm \sqrt{g\bar{h} \cos \alpha} \quad (7.7)$$

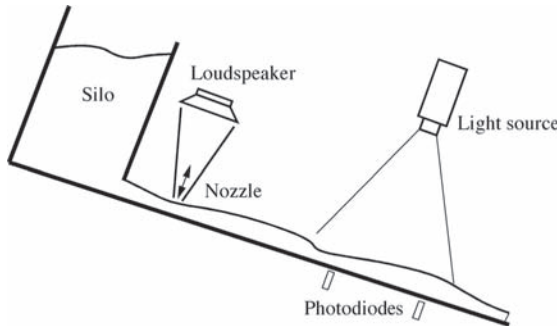


Figure 7.2 Schematic view of the experimental setup of Forterre and Pouliquen (2003).

as gravity waves in shallow water. For nonconstant friction coefficient, i.e., a and b nonzero, the instability criterion $c_i > 0$ for k real is found to be

$$\text{Fr} > \frac{a^2}{b^2}. \quad (7.8)$$

This criterion is independent of the wave number.³ For a medium with behavior described by (7.4) the ratio b/a can be calculated explicitly and we find $-b/a = 3/2$. There therefore exists a critical Froude number $\text{Fr}_c = (2/3)^2$ above which the avalanche is unstable to perturbations of all wavelengths. However, the validity of this conclusion is, in fact, restricted to long waves since the starting Saint-Venant equations hold only for small longitudinal gradients.

7.2.3 Experiments

The experiments of Forterre and Pouliquen (2003) use a silo which pours grains onto a rough inclined plane (Figure 7.2). Air jets produced by loudspeakers upstream force perturbations with a well-defined frequency but which contain many harmonics. The flow thickness is determined by means of light transmitted through the grain layer. The experimental procedure is quite similar to that used by Liu *et al.* (1993) for studying the stability of a falling liquid film (Chapter 6). For a given forcing frequency, measurement of the spatial variation of the thickness shows that the amplitude of the perturbation grows or falls exponentially with distance, and allows the wave speed and spatial growth rate to be determined.

It was found that the wave speed is independent of the frequency, i.e., the waves are not dispersive. An instability arises at forcing frequencies on the order of a

³ It is simple to obtain this criterion for long wavelengths, by expanding the roots of the dispersion relation (7.5) in a series for $k\bar{h} \ll 1$ with, for a complex number $z = z_r + iz_i = |z|e^{i\theta}$, $\sqrt{z} = \sqrt{|z|}e^{i\theta/2} \sim \sqrt{|z|}(1 + iz_i/2z_r)$ for $|z_i| \ll |z_r|$.

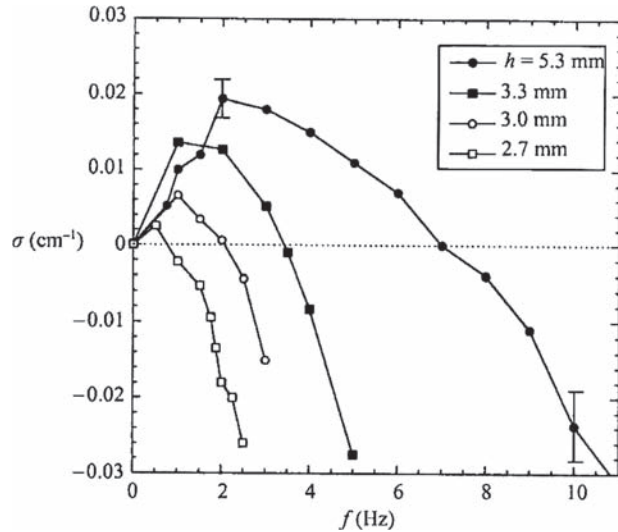


Figure 7.3 Spatial growth rate as a function of the forcing frequency for the angle $\alpha = 29^\circ$ and various layer thicknesses of glass beads; the Froude number varies from 0.26 to 1.04 (Forterre and Pouliquen, 2003).

Hertz (Figure 7.3), corresponding to long wavelengths ($kh \ll 1$), with a well-defined cutoff frequency. The unstable band vanishes when the thickness is less than some critical value. By varying the inclination angle it is possible to define the boundary in the $(\alpha, h/d)$ plane between stable and unstable regions shown in Figure 7.4. This boundary is described fairly well by a critical Froude number, equal to $Fr_c = 0.32 \pm 0.05$ for the glass beads used. This value compares reasonably well with the theoretical value (7.8), $Fr_c = (2/3)^2 \approx 0.44$.

In conclusion, the experiment shows that a granular flow on a rough inclined plane is unstable to long-wavelength perturbations beyond a critical Froude number. For glass beads this instability is described well by the Saint-Venant equations together with a constitutive law for the friction coefficient. However, the model slightly overestimates this critical number; the disagreement is undoubtedly partly associated with the use of the Saint-Venant equations which, in assuming self-similarity of the velocity profile (here plug flow), do not quantitatively account for advection of momentum.⁴ The other reason for the disagreement is the friction coefficient, the expression for which ($\mu_f = \mu_f(U, h)$) corresponds to uniform and stationary flow, yet is used in a dynamic situation. Moreover, the model predicts instability at all wave numbers, and so does not reproduce the stability seen at

⁴ The study of liquid films has revealed an analogous problem, see Chapter 6, end of Section 6.2.3.

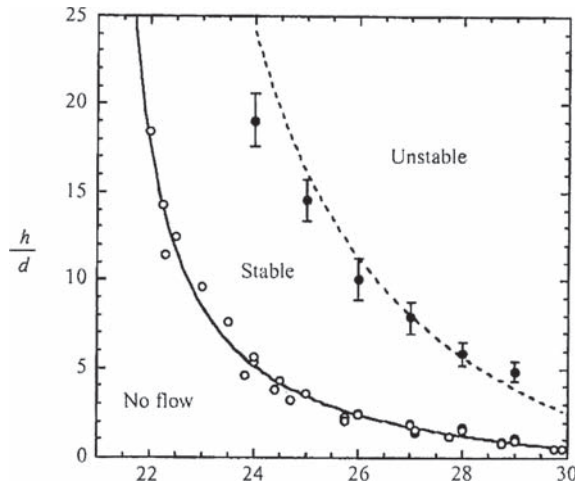


Figure 7.4 Stability diagram in the parameter space (α, h) for glass beads of diameter $d = 0.5$ mm: (\circ) h_{stop} , (\bullet) observed marginal stability, $(-$ $-$) theoretical prediction (Forterre and Pouliquen, 2003).

large wave numbers (high frequencies). This result is consistent with the fact that the Saint-Venant equations are valid for small gradients ($\partial_x h \ll 1$), and therefore cannot account for phenomena on the scale of the thickness h .

7.3 Sediment transport by a flow

Before studying the instabilities of a granular bed sheared by a flow, in this section we shall describe how sediment transport is modeled. First we present the classical modeling found in hydraulics texts such as that by Raudkivi (1998), then we describe more recent modeling involving relaxation phenomena.

7.3.1 Dimensional analysis

Let us consider a granular bed of particles with characteristic diameter d and density ρ_p , sheared by the flow of a fluid of density ρ and viscosity μ . The flux of transported particles is related to the shear stress τ exerted by the flow on the bed. The appropriate scale of this stress is obtained by assuming that the hydrodynamic force on a particle, say τd^2 , must be of the order of its “apparent weight” $mg' = (\rho_p - \rho)g\pi d^3/6$, which is the sum of its weight and the Archimedes force. The ratio of these two forces defines the *Shields number*:

$$\theta = \frac{\tau}{(\rho_p - \rho)gd}. \quad (7.9)$$

The reference stress $(\rho_p - \rho)gd$ is typically a few Pascals.

The Shields number can also be interpreted as a velocity ratio. In a turbulent shear flow with friction velocity $u_* = \sqrt{\tau/\rho}$ (Pope, 2000), the Shields number is seen to be the ratio of

$$u_*^2 = \frac{\tau}{\rho} \quad \text{and} \quad U_{\text{ref}}^2 = \frac{(\rho_p - \rho)gd}{\rho}.$$

The quantity u_* can be viewed as a characteristic fluid velocity at the particle scale and U_{ref} is a characteristic sedimentation velocity. In a viscous flow with shear rate γ near the bed⁵ the Shields number is the ratio of γd to $(\rho_p - \rho)gd^2/\mu$, the latter being the Stokes sedimentation velocity up to a numerical factor (Batchelor, 1967). Experiment shows that for $\theta \lesssim 0.4$ the mobile particles remain confined near the bed, where they form a *bedload* layer, while for $\theta \gtrsim 0.4$ they pass into *suspension* flow. We shall study only the bedload situation in this chapter.

Experiments show that for a particle to be set in motion a minimum stress is required that corresponds to a threshold Shields number θ_t between 0.03 and 0.2. This threshold depends on the Reynolds number

$$\text{Re}_p = \frac{\rho u d}{\mu}, \quad (7.10)$$

where u is a characteristic fluid speed at the particle scale, $u = \gamma d$ in viscous flow or $u = u_*$ in turbulent flow. The *Shields diagram* shown in Figure 7.5,

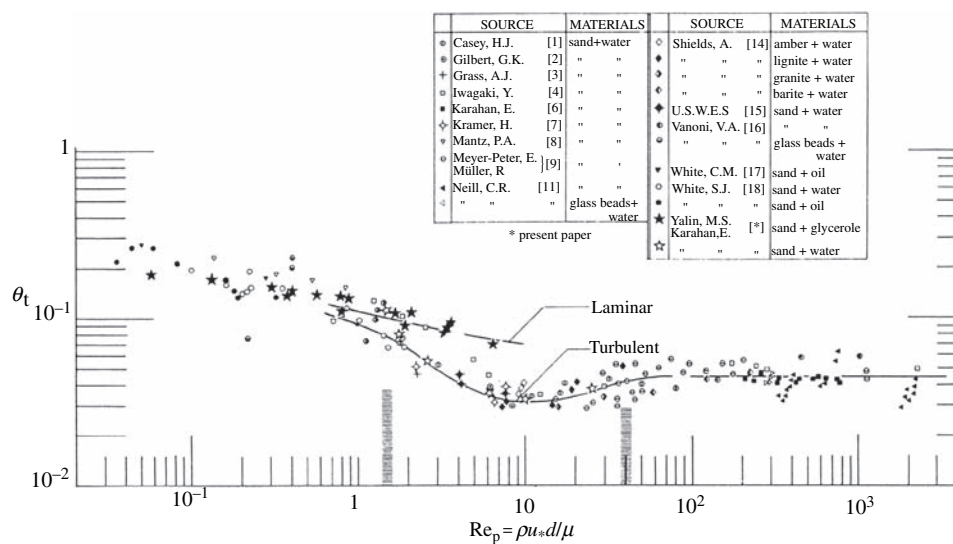


Figure 7.5 Shields diagram for incipient particle motion (Yalin, 1985).

⁵ The surface tension, also denoted γ , does not appear in this chapter, so there is no risk of confusion.

of empirical origin, gives the threshold Shields number θ_t as a function of the Reynolds number Re_p .

7.3.2 The speed of mobile particles

Beyond the threshold θ_t some particles begin to move on the bed surface. The mobile particles form a bedload layer whose thickness, on the order of a few particle diameters, increases with the shear. The average speed U_p of the particles results from an equilibrium between the force exerted by the flow and the resistance of the bed. In turbulent flow the hydrodynamic force can be written as

$$\frac{1}{2}C'_D \rho \frac{\pi d^2}{4} (u_{\text{eff}} - U_p)^2,$$

where C'_D is a drag coefficient and u_{eff} is an effective speed of the fluid at the height of a mobile particle. The resistance offered by the bed can be written as a Coulomb friction force

$$\mu_f mg',$$

where mg' is the apparent weight introduced above and μ_f is a “macroscopic” or “effective” friction coefficient. This coefficient includes not only the friction at points of particle–particle contact, but also the resistance of geometrical origin associated with the presence of neighboring particles. Setting $u_{\text{eff}} = \alpha u_*$, where α is a numerical coefficient of order unity, the equilibrium of a particle under the action of these two forces determines the particle speed (Bagnold, 1973):

$$\frac{U_p}{U_{\text{ref}}} = \alpha(\sqrt{\theta} - \sqrt{\theta_{\text{ref}}}), \quad U_{\text{ref}} = \sqrt{(\rho_p/\rho - 1)gd}, \quad \theta_{\text{ref}} = \frac{4\mu_f}{3\alpha^2 C'_D}. \quad (7.11)$$

Here U_{ref} is a characteristic sedimentation speed and θ_{ref} is a reference Shields number below the threshold value θ_t corresponding to zero particle speed.⁶ Turbulent flow experiments have confirmed the validity of this approach, with $\alpha \approx 5$ and $\theta_{\text{ref}} \approx 0.8\theta_t$ (Fernandez Luque and van Beek, 1973; Lajeunesse *et al.*, 2010). For viscous flow a similar analysis leads to a linear dependence of the velocity U_p on the Shields number (Charru *et al.*, 2007).

The above analysis does not give the friction coefficient itself, but only the ratio μ_f/C'_D , where C'_D , the particle drag coefficient near a rough wall, is not well known. The friction coefficient can be estimated from the experiments performed by Bagnold (1954) on the shearing of a suspension of neutrally buoyant particles in Couette flow between two cylinders. It was found in these experiments that the friction coefficient, defined as the ratio of the normal and tangential stresses between

⁶ The relation (7.11) can also be written as $(U_p - U_{\text{pt}})/U_s = \alpha(\sqrt{\theta} - \sqrt{\theta_t})$, where U_{pt} is the minimum particle speed at threshold.

the particles, depends on a modified particle Reynolds number called the *Bagnold number*, whose expression is not needed here.⁷ This coefficient decreases monotonically from $\mu_f = 0.75$ in the viscous regime to $\mu_f = 0.32$ in the inertial regime.

We conclude by noting that a more rigorous analysis would require measurements of the velocity profile inside the mobile layer or direct numerical simulations of the momentum equations. Such measurements have been performed for viscous flow, using a technique of matching the optical indices of the particles and the fluid (Mouilleron *et al.*, 2009), and reveal a parabolic velocity profile which is reasonably described by a model inspired by Bagnold (1956). Corresponding measurements have not yet been performed for turbulent flow.

Brigadier Ralph Alger Bagnold (1896–1990)



Born in Stoke-D Devonport, England, Ralph Alger Bagnold had a military career in the Royal Engineers and Royal Corps of Signals of the British Army, spending long periods in Egypt and Libya in particular during WWI. An adventurer of insatiable curiosity, he acquired great knowledge of deserts. After retiring from the army in 1935, he pursued his observations of sand transport by wind and water at the Hydraulics Laboratory of Imperial College in London. In 1941 he published his second book *The Physics of Blown Sand and Desert Dunes*, which profoundly influenced the development of the study of granular media. After he was remobilized in 1939 he

was given *carte blanche* to form a small army, the Long Range Desert Group, that operated in the Libyan desert, carrying out commando operations and observing the movements of the German Afrika Corps, exploring an immense, largely unknown territory, and making incursions into Chad (where he could have encountered Théodore Monod, a Frenchman as unconventional as he was). After WWII he returned to Imperial College, then moved to the United States where he worked in the U.S. Geological Survey. He published pioneering studies on sediment transport by rivers and oceans and on the physics of granular flow, works which have become standard references in the field. He became a

⁷ This Bagnold number is analogous to the inertial number I introduced by Forterre and Pouliquen (2008).

Fellow of the Royal Society in 1944 and received numerous other honors. He published his last paper at the age of 90 in the *Proceedings of the Royal Society of London*. A selection of 14 of his publications has been edited and published by the American Society of Civil Engineers under the title *The Physics of Sediment Transport by Wind and Water* (1988).

7.3.3 The number density of mobile particles

The second quantity involved in the particle flux is the surface density N of the mobile particles, i.e., the number of mobile particles per unit surface area of the bed. Close to threshold, a reasonable statement is that this density increases linearly with Shields number as

$$N d^2 = c_n(\theta - \theta_t), \quad (7.12)$$

where c_n is a coefficient. This expression can be obtained by the following argument due to Bagnold (1956). When the stress exerted by the fluid on the granular bed is larger than the threshold stress, the most exposed particles are set in motion. The underlying particles are then uncovered and are in turn subjected to the fluid stress. The problem thus arises of determining the mechanism limiting the “peeling off” of deeper and deeper particle layers, that is, the mechanism by which the density N becomes saturated. Bagnold advanced the following two ideas, which are illustrated in Figure 7.6:

- The stress τ exerted by the flow is transmitted to the bed partly by the fluid itself and partly by the mobile particles. Since the total stress must be constant for steady flow, in going toward the interior of the bed the contribution due to the particles grows while that due to the fluid falls.
- The base of the mobile layer corresponds to the depth at which the stress exerted by the fluid is reduced to the threshold stress τ_t : this is known as the “Bagnold conjecture.”

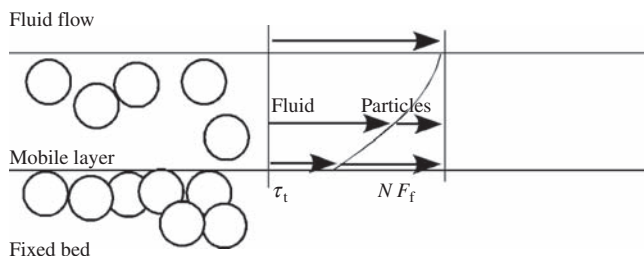


Figure 7.6 Schematic depiction of the Bagnold conjecture, according to which the fluid stress is reduced at the threshold τ_t on the fixed bed.

Assuming as before that the tangential force between the fixed bed and a mobile particle can be written as $\mu_f mg'$, we obtain, for N particles per unit surface area, $\tau - \tau_t = N \mu_f mg'$. The relation (7.12) then follows with the identification $c_n = 6/\pi \mu_f$.

According to the arguments by which it was derived, the relation (7.12) must be valid for viscous flow ($Re_p = \gamma d^2/v \lesssim 10$, $\tau = \mu \gamma$) as well as for turbulent flow ($Re_p = u_* d/v \gtrsim 3$, $\tau = \rho u_*^2$). Experiments show that it is well satisfied, with $c_n = 4.6$ for turbulent flow (Lajeunesse *et al.*, 2010), and the lower value $c_n = 0.47$ for viscous flow (Charru *et al.*, 2004). Note that $c_n < 2$ corresponds to values of μ_f larger than unity which lead us to doubt the Bagnold conjecture, at least near the threshold θ_t where the few grains in motion at the bed surface occupy only a tiny fraction of this surface. Another approach to this problem is discussed in a following section.

7.3.4 The particle flux

After finding N and U_p , we can obtain the particle flux $Q = N U_p$, i.e., the number of particles crossing a transverse cross-section of the flow per unit time. For turbulent flow it is given by

$$\frac{Q}{Q_{\text{ref}}} = \frac{\pi}{6} \alpha c_n (\sqrt{\theta} - \sqrt{\theta_{\text{ref}}}) (\theta - \theta_t), \quad Q_{\text{ref}} = \frac{U_{\text{ref}} d}{\pi d^3 / 6}. \quad (7.13)$$

This law, where the term $\sqrt{\theta_{\text{ref}}}$ is often omitted, agrees fairly well with experiments with the choice $\alpha c_n = 8-20$; however, the measurements show considerable scatter, especially near the threshold. Other empirical laws have been proposed which give similar results; one of the most widely used is that of Meyer-Peter and Muller, revised by Wong and Parker (2006):

$$\frac{Q}{Q_{\text{ref}}} = 3.97 (\theta - \theta_t)^{3/2}, \quad \theta_t = 0.047. \quad (7.14)$$

For viscous flow the linear laws for the velocity U_p and the density N lead to $Q/Q_{\text{ref}} \propto \theta(\theta - \theta_t)$ as long as the thickness of the mobile layer does not exceed two particle diameters, that is, for $\theta \lesssim 3\theta_t$ (Charru *et al.*, 2004; Mouilleron *et al.*, 2009). Beyond $\theta \approx 3\theta_t$, a model of viscous resuspension developed by Leighton and Acrivos (1986), which predicts $Q/Q_{\text{ref}} \propto \theta^3$, is likely to be more appropriate.

7.3.5 Particle relaxation effects

The previous analysis assumes implicitly that all particle transport properties are in local equilibrium with the fluid flow. This assumption is expected to fail when the fluid flow varies in space or in time and when some delay of the response of the particle transport is likely. A key quantity is the time scale or length scale associated with this delay, i.e., the relaxation scales of the particle motion. The equilibrium assumption – associated with an algebraic relation $Q(\tau)$ – is acceptable when the scale of the flow variation is long compared to that of the particle relaxation. Otherwise, time delays and relaxation processes may be of importance. This possibility will prove crucial in our later discussion of instabilities.

A model of inertial relaxation

An observation of Bagnold (1941, §13.6) clearly displays a relaxation of the particle flux: when a wind blowing on a rigid surface reaches an erodible bed, the particle flux, which is zero at the edge of the bed, grows over a distance L_{sat} on the order of a meter, and then saturates at a value Q_{sat} (Figure 7.7). The simplest equation accounting for this observation can be written as (Sauermann *et al.*, 2001; Andreotti *et al.*, 2002b)

$$L_{\text{sat}} \frac{\partial Q}{\partial x} = Q_{\text{sat}} - Q, \quad (7.15)$$

the solution of which is an exponential relaxation to Q_{sat} over the length L_{sat} .

Here, the physical origin of this delay is the inertia of the particles, and so the length scale L_{sat} is the characteristic acceleration length l_{acc} of a particle. This acceleration length can be obtained from the equilibrium between inertia and a drag force at large Reynolds number, giving the approximate dimensional balance

$$\rho_p d^3 u \frac{u}{l_{\text{acc}}} = \rho u^2 d^2,$$

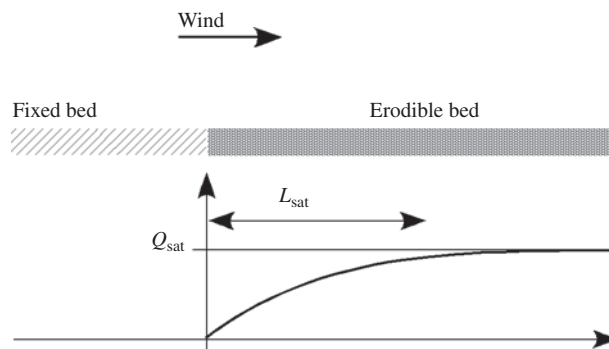


Figure 7.7 Illustration of the relaxation of a particle flux.

where u is the terminal velocity of the particle, equal to the wind velocity. We thus obtain $l_{\text{acc}} = (\rho_p/\rho) d$. Experiments using sand grains in air effectively show that

$$L_{\text{sat}} \approx 4 l_{\text{acc}} = 4 \frac{\rho_p}{\rho} d, \quad (7.16)$$

which is about 1.6 m for 0.2 mm grains in air. Equation (7.15) together with the acceleration length (7.16) is an essential element in the analysis of aeolian sand dunes, as will be discussed below. In water, the density of which is a thousand times higher than that of air, the acceleration length is of the order of the particle diameter. Viscosity and added mass effects complicate the hydrodynamics in this case, and the above analysis is certainly insufficient. The erosion–deposition model presented below suggests a more appropriate approach.

An erosion–deposition model

The dynamics of the particle flux can be described using an erosion–deposition model of particles at the surface of a sheared bed (Charru *et al.*, 2004). Here we shall consider the case of viscous flow (which is typical of the situations encountered in the oil industry, for example); for the turbulent case, see Lajeunesse *et al.* (2010). Let $N(x, t)$ be the number of mobile particles per unit surface area and $U_p(x, t)$ be their average velocity, so that the particle flux is $Q = N U_p$, as before. Let \dot{n}_e be the erosion rate, that is, the number of particles dislodged from the fixed bed by the flow, per unit time and unit surface area. In the same way, let \dot{n}_d be the particle deposition rate, i.e., the number of particles stopped in their trajectory by impact on the fixed bed. The conservation of the number of mobile particles in a slice of thickness dx and unit width, illustrated in Figure 7.8, is then written as

$$\frac{\partial N}{\partial t} = \dot{n}_e - \dot{n}_d - \frac{\partial Q}{\partial x}, \quad Q = N U_p. \quad (7.17)$$

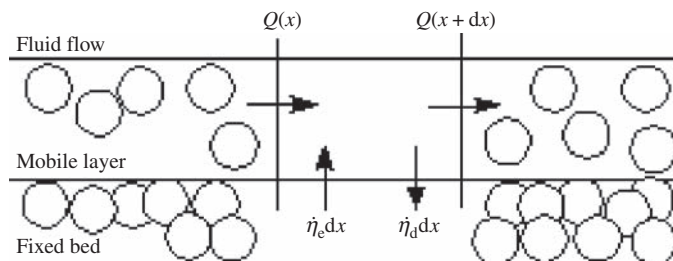


Figure 7.8 Schematic diagram of the particle flux balance in a slice of the mobile layer of length dx and unit width.

The solution of this equation for the density N requires the modeling of the erosion and deposition rates \dot{n}_e and \dot{n}_d , as well as the velocity U_p .

The deposition rate \dot{n}_d . The modeling of \dot{n}_d is based on the observation that the particles move intermittently, with periods of motion at average velocity U_p of typical duration t_d alternating with periods of rest. During the time t_d all the particles stop moving at least once on the average, and so the deposition rate can be written as

$$\dot{n}_d = \frac{N}{t_d}. \quad (7.18)$$

Deposition is a phenomenon controlled by gravity, and the time t_d can be assumed to be proportional to the sedimentation time d/U_s , where U_s is the sedimentation velocity. Therefore, t_d can be written as

$$\frac{1}{t_d} = c_d \frac{U_s}{d}, \quad (7.19)$$

where c_d is a deposition coefficient. For simplicity, in what follows we shall take for U_s the Stokes sedimentation velocity $(\rho_p - \rho)gd^2/18\mu$; other choices are to use the inertial velocity U_{ref} defined by (7.11) or the actual sedimentation velocity as determined by an empirical relation for the drag coefficient.

The erosion rate \dot{n}_e . When the mobile layer is thin, on the order of one or two particle diameters, the erosion rate \dot{n}_e depends only on the ability of the flow to dislodge a particle from a potential well of characteristic area d^2 . This rate can therefore be written as

$$\dot{n}_e = \frac{1}{t_e d^2}, \quad (7.20)$$

where t_e is a hydrodynamical time scale. For viscous flow this time scale is the inverse of the velocity gradient γ near the bed, from which we find

$$\frac{1}{t_e} = c_e (\gamma - \gamma_t),$$

where c_e is an erosion coefficient and γ_t is the velocity gradient at the motion threshold. Introducing the shear stresses $\tau = \mu\gamma$ and $\tau_t = \mu\gamma_t$, the above equation can be written in a way that is more useful for what follows:

$$\frac{1}{t_e} = \frac{1}{t_d} \frac{\tau - \tau_t}{\tau_{ref}}, \quad \tau_{ref} = \frac{c_d}{18c_e} (\rho_p - \rho)gd. \quad (7.21)$$

The particle speed U_p . In the case of viscous flow and small particle inertia, observation shows that the particle speed can be written as $U_p = c_u \gamma d$, where γd is a characteristic speed of the fluid near the bed and c_u is a numerical coefficient, or equivalently

$$\frac{U_p}{U_s} = 18 c_u \theta. \quad (7.22)$$

The values of the coefficients measured by Charru *et al.* (2004) are $c_d = 0.067$, $c_e = 0.0017$, and $c_u = 0.10$.

Equilibrium solution. The conservation equation (7.17) admits a stationary, uniform solution for the surface density of mobile particles corresponding to equality of the erosion and deposition rates (7.18) and (7.20). This solution can be identified with the saturated density

$$N_{\text{sat}} d^2 = \frac{t_d}{t_e} = 18 \frac{c_e}{c_d} (\theta - \theta_t). \quad (7.23)$$

Using the expression (7.22) for the particle velocity, for the particle flow rate we find

$$Q_{\text{sat}} = N_{\text{sat}} U_p = 18^2 \frac{c_u c_e}{c_d} \frac{U_s}{d^2} \theta (\theta - \theta_t). \quad (7.24)$$

The flux relaxation equation. We use the above models for the erosion rate (7.20) and the deposition rate (7.18), and assume that the particles have negligible inertia and move at the velocity (7.22). Then after multiplication by $U_p t_d$ the conservation equation (7.17) can be written in the form of the relaxation equation

$$L_{\text{sat}} \left(\frac{\partial N}{\partial t} + \frac{\partial Q}{\partial x} \right) = Q_{\text{sat}} - Q, \quad (7.25)$$

where the relaxation length here is defined as

$$L_{\text{sat}} = U_p t_d = \frac{1}{c_d} \frac{U_p}{U_s} d. \quad (7.26)$$

Finally, the analysis of erosion and deposition processes provides a relaxation length scale of the particle transport: this length is associated with the deposition of the particles and corresponds to the length traveled by a particle of velocity U_p during the sedimentation time t_d .

Note that the stationary version of Eq. (7.25) is the same as Eq. (7.15) introduced at the beginning of this section in the context of aeolian transport. However,

the physical phenomenon at the origin of the relaxation here is quite different: whereas earlier it was the inertia of the particles accelerated by the flow associated with the acceleration length (7.16), now it is the dynamics of the particle deposition.

7.4 Ripples and dunes: a preliminary dimensional analysis

Before embarking on a detailed analysis we give a brief overview of the structures observed on a granular bed sheared by a fluid flow. First we shall discuss ripples and dunes formed by the wind, and then ripples and dunes formed under water (or equivalently, any liquid).

7.4.1 Aeolian ripples and dunes

When the wind blows on a flat stretch of sand the transported grains form regular ripples about 10 cm long (Figure 7.9). The formation mechanism of these ripples appears to be related to the phenomenon of *saltation*, i.e., jumps of the sand grains that bounce off the bed, are accelerated by the wind, and then fall down again. This saltation motion enhances the momentum transfer from the wind to the bed, that is, it increases the friction. The simple model proposed by Bagnold (1941)

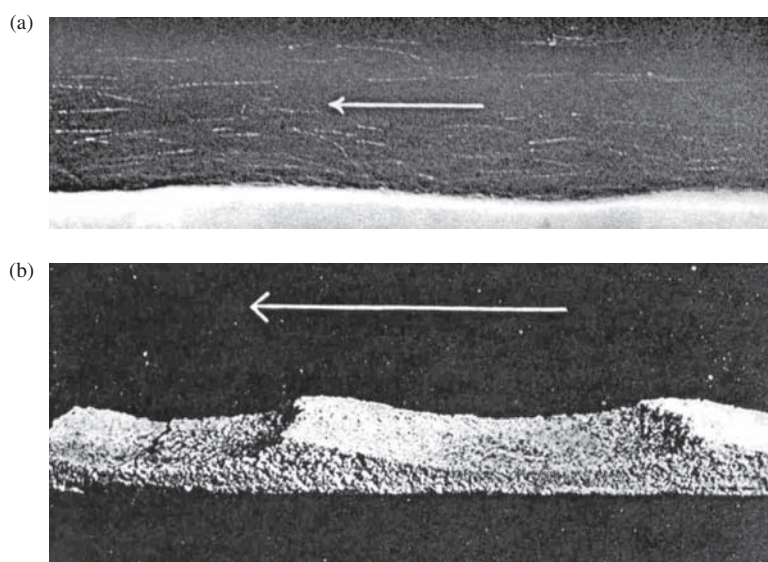


Figure 7.9 Sand ripples formed by the wind, from Bagnold (1941): (a) ripples undergoing formation (one can make out the jumping trajectories of the grains), (b) the final form.

relating the wavelength to the saltation length is not fully satisfactory, and no fully convincing model exists at present (Andreotti, 2004).

Sand structures much larger than ripples, on the scale of tens of meters, are also observed on the seashore and in deserts. The formation mechanism of these aeolian dunes is very different from that of ripples: it is hydrodynamic rather than granular (associated with jumping) in nature. There, a crucial role is played by the variation of the shear stress on the deformed surface of the bed, in particular, by the fact that the shear stress maximum does not coincide with the dune peak, but is located a bit upstream from it due to fluid inertia. For these aeolian dunes, relaxation processes related to particle inertia and the acceleration length (7.16) play an essential role in selecting the wavelength (Andreotti *et al.*, 2002a).

7.4.2 Subaqueous ripples and dunes

Structures similar to aeolian ripples and dunes are observed underwater: ripples on the scale of a centimeter, and dunes on the scale of a meter, as illustrated in Figures 7.10 and 7.11. However, the formation mechanisms of these subaqueous ripples and dunes are different from those of their aeolian cousins. One essential reason for this is the density ratio ρ_p/ρ : it is about 2000 in the aeolian case, and about 2 in the aqueous case. In the former the inertia of the air therefore plays a negligible role, while in the latter the inertia of the liquid strongly couples the motion of the fluid and the grains, and in general viscous effects are not negligible. This greatly complicates the analysis.

Subaqueous ripples are a manifestation of a hydrodynamical instability of the same type that produces aeolian dunes. The length scale of these ripples will be the

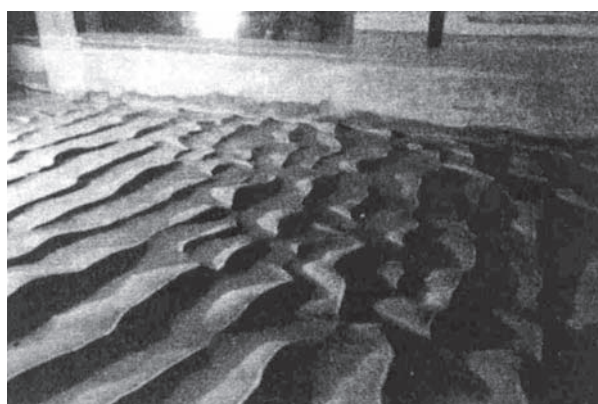


Figure 7.10 Sand ripples formed on a bed sheared by a weakly inclined water flow ($d = 0.12$ mm, flow height = 17.5 cm, average speed = 36 cm/s, friction velocity = 3.3 cm/s, slope = 0.007). From Raudkivi (1997) with permission from ASCE.

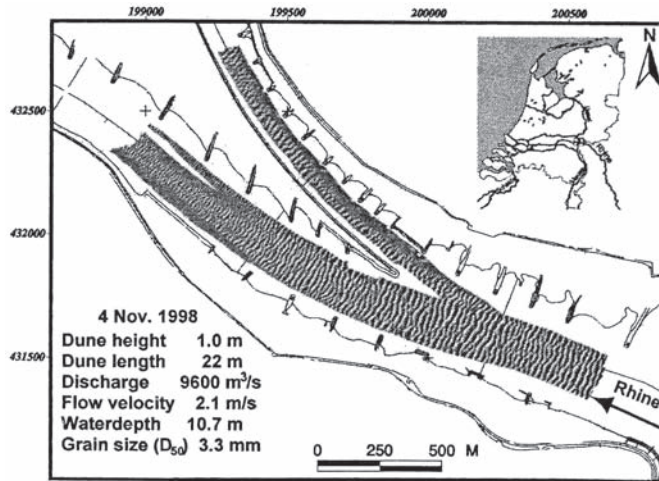


Figure 7.11 Dune field on the bed of the Rhine, observed by echo sounding (ASCE, 2002), with permission from ASCE.

deposition length (7.26) discussed in the preceding section, rather than the inertial length (7.16) which dominates for aeolian dunes.

Subaqueous dunes are structures whose wave number is related to the height h of the fluid and roughly satisfies the relation $kh \approx 1$. The origin of such dunes is not completely clear; at present there are two possible explanations. The first is that they correspond to a linear instability of a flat granular bed, where coupling to the free surface is involved. The second is that they result from a nonlinear coarsening process, where the smallest ripples catch up with the largest ones and merge with them.

The ripples and dunes discussed above are essentially two-dimensional. To complete our overview we should mention that three-dimensional structures are also observed, in particular, star dunes and barchan dunes. The latter take the form of a crescent and occur both in deserts (Bagnold 1941) and, at a much smaller scale, underwater (Mantz, 1978; Hersen *et al.*, 2002). We also mention the sand banks seen in shallow seas such as the North Sea, which have crests nearly aligned with the flow direction (Blondeaux, 2001). The rest of this chapter is devoted to developing an approach to analyzing ripples and dunes, limiting ourselves to two-dimensional and subaqueous structures.

7.5 Subaqueous ripples under a continuous flow

Observation shows that the characteristic evolution time of a sheared bed is in general large compared to all hydrodynamic time scales. This leads to an important

simplification of the analysis: the hydrodynamic field above a perturbed bed, and therefore the shear τ on the bed, can be calculated as if the bed were fixed. The problem to be solved is then quasi-static. In this section we shall first display the instability mechanism: owing to the fluid inertia, the phase of the shear on a sinusoidal bed is ahead of the phase of the bed deformation. Then we shall discuss the particle flux generated by the shear and the wavelength selection by the stabilizing effects of gravity and the deposition length.

7.5.1 Phase advance of the shear stress

The flow above a ripple

In turbulent flow, which is the dominant situation at geophysical scales, the calculation of the shear on the bed requires a model of turbulence and numerical solution (Richards, 1980; Sumer and Bakioglu, 1984), or a direct simulation of the Navier–Stokes equations. In order to remain within the analytic approach and display the essential mechanisms, here we shall consider the simpler case of viscous flow (which is of practical interest in certain industrial problems), where the velocity profile of the base flow remains linear up to a distance from the bed on the order of the ripple wavelength. This profile can then be written as $\bar{\gamma}y$, where $\bar{\gamma}$ is the shear rate. Using the Squire transformation for parallel flows (Chapter 4), for determining an instability criterion it is sufficient to consider two-dimensional perturbations. Here we present the dimensional analysis and give the result for the shear stress τ over an undulating bed, and refer the reader to Charru and Hinch (2000) for the complete calculation.

On a sinusoidal bed of wave form $\eta = \eta_0 \cos kx$ an essential scale is the penetration length l_v of perturbations of vorticity ω induced on the bed. This scale can be determined by considering the equilibrium between the longitudinal advection and the transverse diffusion of the vorticity perturbation:

$$\rho \bar{U} \frac{\partial \omega}{\partial x} = \mu \frac{\partial^2 \omega}{\partial y^2}.$$

In the asymptotic limit suitable for ripples, where this penetration length is small compared to the wavelength $2\pi/k$ and the flow depth, we can write $\bar{U} \sim \bar{\gamma} l_v$, $\partial_x \sim k$, and $\partial_y \sim 1/l_v$. The above equilibrium condition then defines the desired length:

$$l_v = \left(\frac{\mu}{\rho k \bar{\gamma}} \right)^{1/3}. \quad (7.27)$$

At the surface of the deformed bed, which is assumed fixed, the flow velocity must vanish. The velocity perturbation is therefore $u = -\bar{U}(\eta) \sim \gamma \eta$, and the shear perturbation is

$$\tau \sim \mu \frac{u}{l_v} \sim \bar{\tau} \frac{\eta_0}{l_v}.$$

The exact calculation of the shear perturbation over a small amplitude undulating bed gives a numerical prefactor of 1.06 and a phase advance of $\phi_\tau = \pi/6$, that is,

$$\tau = \tau_0 \cos(kx + \phi_\tau), \quad \tau_0 = 1.06 \bar{\tau} \frac{\eta_0}{l_v}, \quad \phi_\tau = \pi/6. \quad (7.28)$$

Since the phase advance ϕ_τ is positive, the maximum of the shear is located upstream of the ripple peak. This phase advance associated with the fluid inertia is a general result; it occurs in both laminar (Benjamin, 1959; Charru and Mouilleron-Arnould, 2002) and turbulent flows (Abrams and Hanratty, 1985; Hunt *et al.*, 1988).

Interpretation of the phase advance ϕ_τ

The phase advance ϕ_τ of the shear is due to fluid inertia, similar to that occurring at the perturbed interface between two sheared fluids discussed in Chapter 6. Let us recall the physical interpretation. In the absence of inertia the deformation of the bed gives rise to a velocity perturbation $u^{(0)} \sim -\bar{\gamma}\eta$ imposed by the no-slip condition (Figure 7.12a). This perturbation is in phase with the deformation η of

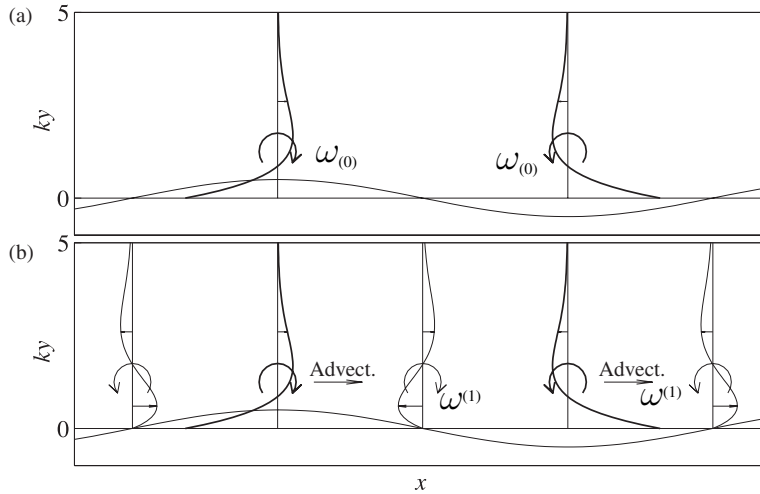


Figure 7.12 Longitudinal velocity perturbations induced by a sinusoidal deformation $\eta(x)$ of the bed and the associated vorticity, for viscous flow and $kl_v = 1$: (a) Stokes flow in phase with $\eta(x)$, (b) out-of-phase inertial correction.

the bed, as well as the associated vorticity perturbation $\omega^{(0)} \sim u^{(0)}/l_v$. The shear perturbation of the bed is also in phase with the bed deformation and generates a particle transport which displaces the ripple without amplifying it. The correction induced by weak inertial effects corresponds to advection of the vorticity perturbation $\omega^{(0)}$ by the base flow. This advection creates a component $\omega^{(1)} \sim \text{Re}_{\text{eff}}\omega^{(0)}$ out of phase with the bed deformation, where $\text{Re}_{\text{eff}} = \bar{\gamma}l_v^2/v$ is an effective Reynolds number. The velocity field $u^{(1)} \sim \omega^{(1)}l_v$ associated with $\omega^{(1)}$ must vanish on the bed, and corresponds to the out-of-phase profile sketched in Figure 7.12b. The shear $\tau^{(1)} \sim \mu u^{(1)}/l_v$ associated with this inertial correction therefore points from the troughs toward the peaks, hence reinforcing the advancement of the phase, resulting in instability.

7.5.2 Instability

Stability analyses of erodible beds have for a long time been based on algebraic particle transport laws of the type $Q = Q(\tau)$ established for stationary, uniform flow, such as the Meyer-Peter–Muller law (7.14). The inclusion of the relaxation of the particle flux in a spatially varying shear significantly modifies the results. Here we shall discuss the stability within the context of the erosion–deposition model presented in the preceding section, while restricting our analysis to viscous flow.

The particle flux

For stationary and uniform flow, the surface density \bar{N} of mobile particles and flux \bar{Q} correspond to the equilibrium solution (7.23) and (7.24) of the erosion–deposition model with the particle velocity (7.22). On a wavy bed with wave form $\eta = \eta_0 \cos kx$, the shear perturbation τ induces a perturbation u_p of the particle velocity given by

$$u_p = U'_p(\bar{\tau})\tau, \quad \text{where} \quad U'_p(\bar{\tau}) = \frac{\partial U_p}{\partial \tau}(\bar{\tau}). \quad (7.29)$$

The perturbation n of the surface density of mobile particles is the solution of the conservation equation (7.17), the linearized form of which is written as

$$0 = -nd^2 + \frac{\tau}{\tau_{\text{ref}}} - t_d d^2 \frac{\partial q}{\partial x}, \quad q = \bar{N} U'_p(\bar{\tau})\tau + \bar{U}_p n, \quad (7.30)$$

where q is the perturbation of the particle flux and for consistency with the quasi-static approximation for the flow we have neglected the time derivative.⁸ Seeking

⁸ An additional justification for this omission is that the term $\partial_t n$ is dominated by the propagation of the ripple at speed c , and not by its slow growth, so that $\partial_t n \approx -c \partial_x n$. Since $c \ll U_p$, we deduce that $\partial_t n$ is negligible compared to the term $\bar{U}_p \partial_x n$ on the right-hand side of (7.30).

a spatially periodic solution for n in the form

$$n = n_0 \cos(kx + \phi_\tau + \phi_n), \quad (7.31)$$

the quasi-steady solution of (7.30) is written as

$$n_0 d^2 = \frac{\tau_0}{\tau_{\text{ref}}} \sqrt{\frac{1 + (kl_d)^2 A^2}{1 + (kl_d)^2}}, \quad (7.32a)$$

$$\tan \phi_n = \frac{-kl_d}{(1+A)} 1 - (kl_d)^2 A \quad \text{with} \quad -\pi < \phi_n < 0, \quad (7.32b)$$

where the deposition length l_d and the constant A are defined as

$$l_d = \bar{U}_p t_d, \quad A = \frac{\bar{\tau} - \tau_t}{\bar{U}_p} U'_p(\bar{\tau}) = 1 - \frac{\theta_t}{\theta}. \quad (7.33)$$

It appears here that the phase of n , relative to the bed, is the sum of two contributions ϕ_τ and ϕ_n with quite different origins: the former, which is positive, arises from fluid inertia, while the latter, which is negative, arises from particle settling. We then find the perturbation of the particle flux

$$q = \frac{\tau_0 Q'(\bar{\tau})}{\sqrt{1 + (kl_d)^2}} \cos(kx + \phi_\tau + \phi_q), \quad (7.34a)$$

$$\tan \phi_q = -kl_d, \quad -\pi < \phi_q < 0, \quad (7.34b)$$

where $Q'(\bar{\tau})$ is the derivative of Q with respect to τ at $\tau = \bar{\tau}$. Since the phase ϕ_q is negative for all wave numbers, the maximum of the flux is located downstream from the maximum of the shear, consistent with the idea that the flux response to the spatial variation of the shear is delayed. Figure 7.13a shows that for $\phi_\tau = \pi/6$

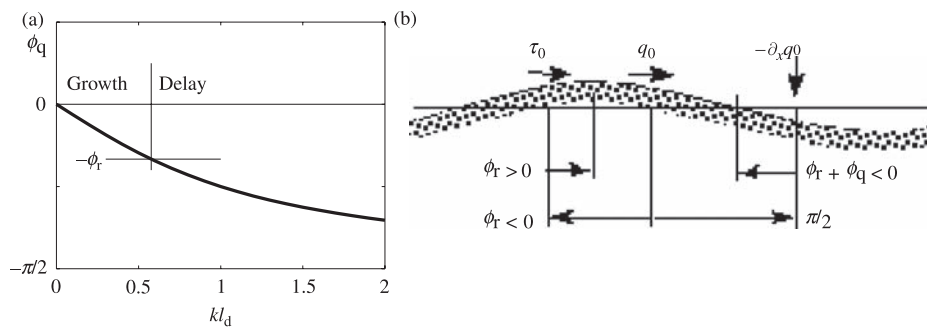


Figure 7.13 (a) Phase advance of the particle flux ϕ_q as a function of the wave number kl_d , (b) positions of the maxima of the shear, the particle flux, and the net deposition rate for $\phi_\tau + \phi_q < 0$ (large wave numbers).

(see Eq. (7.28)), small wave numbers correspond to $\phi_\tau + \phi_q > 0$ and so the particle flux is ahead of the bed deformation, while the opposite occurs for large wave numbers. The cutoff wave number k_{off} is such that $\phi_\tau + \phi_q = 0$, or

$$k_{\text{off}} l_d = \tan \phi_\tau. \quad (7.35)$$

Since the net deposition rate on a section of length dx and unit width is $Q(x) - Q(x+dx) = -\partial_x q dx$, the quasi-static evolution of the bed is governed by the mass conservation equation

$$\frac{\partial \eta}{\partial t} = -\frac{\pi d^3}{6C} \frac{\partial q}{\partial x} = \frac{\pi d^3}{6C} (\dot{n}_d - \dot{n}_e), \quad (7.36)$$

where $C \approx 0.6$ is the compactness of the bed (the volume fraction occupied by the particles). This evolution equation is closed using Eq. (7.34) for the particle flux. Figure 7.13b illustrates the case of large wave numbers for which $\phi_\tau + \phi_q < 0$. This case corresponds to net erosion of the peaks and deposition in the troughs, that is, damped perturbations. We note that if particle relaxation is neglected [$Q = Q(\tau)$], the particle flux is in phase with the shear ($l_d = 0$, $\phi_q = 0$) and all wave numbers are unstable (with $\phi_\tau > 0$).

The effect of gravity

On a bed of slope $\partial_x \eta$ the particle flux is affected by the component of gravity parallel to the slope. The corresponding force $(\rho_p - \rho)g \partial_x \eta$ per unit particle volume tends to shift the particles from the peaks toward the troughs and plays a stabilizing role. Assuming that the thickness of the mobile layer is approximately d , this force can be taken into account by replacing the shear stress τ by an “effective” stress defined as⁹

$$\tau_{\text{eff}} = \tau - c_g (\rho_p - \rho) g d \partial_x \eta, \quad (7.37)$$

where c_g is a numerical coefficient. Equivalently, the effect of gravity can be taken into account by an effective threshold for the start of the motion:

$$\tau_{t,\text{eff}} = \tau_t + c_g (\rho_p - \rho) g d \partial_x \eta = \tau_t (1 + (c_g / \theta_t) \partial_x \eta). \quad (7.38)$$

A slope also directly affects the threshold τ_t for the particles to start moving: the threshold is increased for a positive slope and decreased for a negative slope. In

⁹ The force per unit surface area due to gravity should grow with the thickness of the mobile layer and therefore with the Shields number. One method of taking this growth into account which is consistent with (7.12) is to multiply the correction of τ in (7.37) by $(\theta - \theta_t)/\theta_t$. The conclusions of the analysis are not fundamentally changed.

fact, this second effect of the slope can be assumed to be included in the coefficient c_g introduced above. This coefficient plays an essential role in the selection of the most amplified wavelength, but unfortunately its value remains uncertain; in general, it is chosen to lie between 0.1 and 0.4.

We can therefore consider that the density of mobile particles (7.32) and the flux (7.34) include the effect of gravity when τ_0 and ϕ_τ are replaced by the amplitude and the phase of the effective shear (7.37).

The speed and growth rate

The speed and the growth rate of the ripples are finally obtained from the mass conservation equation (7.36) with $\eta = \eta_0 e^{\sigma t} \cos k(x - ct)$. We find

$$c = \frac{\pi d^3}{6C} Q'(\bar{\tau}) \frac{\tau_0}{\eta_0} \cos \phi_q \cos(\phi_\tau + \phi_q), \quad (7.39a)$$

$$\sigma = \frac{\pi d^3}{6C} Q'(\bar{\tau}) \cos^2 \phi_q \left(\frac{k \tau_0}{\eta_0} \frac{\sin(\phi_\tau + \phi_q)}{\cos \phi_q} - c_g (\rho_p - \rho) g d k^2 \right). \quad (7.39b)$$

Let us make the following comments about these results:

- The above expressions for the speed and the growth rate are general; the precise nature of the flow – viscous or turbulent – is “encoded” in τ_0 and ϕ_τ , while that of the particle transport is encoded in $Q'(\bar{\tau})$ and ϕ_q .
- The equilibrium transport law $Q = Q(\tau)$ does not affect the stability or instability of the bed, but only the values of the speed and the growth rate.
- The particle relaxation introduced via the erosion–deposition model leads to the appearance of the deposition length l_d ; a purely algebraic transport law corresponds to $l_d = 0$.
- The stabilizing particle relaxation and gravity effects are weak at small wave numbers, where the destabilizing fluid inertia dominates, while they dominate at large wave numbers.

The general shape of the curve for the growth rate $\sigma(k)$ corresponds to that of a long-wavelength instability already encountered several times in preceding chapters. The unstable wave numbers lie below a cutoff k_{off} , the stable ones lie above it, and there exists a maximally amplified wave number k_{max} between $k = 0$ (neutral) and $k = k_{\text{off}}$. Figure 7.14 shows the behavior of $k_{\text{max}}d$ as a function of the Shields number for viscous shear (7.28) and the particle transport law (7.24). When the stabilizing mechanism due to gravity is the only one taken into account ($l_d = 0$), $k_{\text{max}}d$ varies as θ^2 (dashed lines, for two values of the sedimentation Reynolds number $\text{Re}_s = \rho U_s d / \mu$). Conversely, when the stabilizing mechanism of

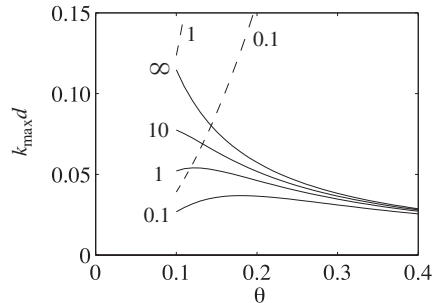


Figure 7.14 The most amplified wave number $k_{\max}d$ as a function of θ for viscous shear (7.28) and the transport law (7.24): (—) $Re_s = 0.1, 1, 10$, and ∞ (the last case corresponds to ignoring gravity), (---) the relaxation mechanism is ignored ($k_{\max}d \propto \theta^2$) for $Re_s = 0.1$ and 1. The other parameters are $\theta_t = 0.1$, $c_u/c_d = 1.5$, and $c_g = 0.17$. Reprinted with permission from Charru (2006). © 2006, American Institute of Physics.

erosion of the peaks is the only one taken into account (solid line for $Re_s = \infty$), $k_{\max}d$ decreases monotonically with θ . When both mechanisms are included (solid lines for $Re_s = 0.1, 1, 10$), $k_{\max}d$ varies only slightly: it decreases monotonically for $Re_s \gtrsim 1$, and increases and then decreases for $Re_s \lesssim 1$.

Finally, it appears that when gravity is the only stabilizing effect included (i.e., the relaxation of the particle flux is neglected), the most amplified wave number $k_{\max}d$ increases rapidly with the Shields number θ , as θ^2 . Conversely, when relaxation is included and gravity ignored, $k_{\max}d$ decreases as θ^{-1} . When both stabilizing effects are included, $k_{\max}d$ depends only weakly on θ ; near the threshold $\theta = \theta_t$ the two effects are of the same order of magnitude, while far from the threshold ($\theta \gtrsim 3\theta_t$) the effect of gravity becomes negligible.

7.5.3 Discussion

How do the predictions of the models described above compare with the observations? The easiest quantities to compare are the measured ripple lengths, which we expect to correspond to the most amplified wavelengths. Other possible quantities for comparison are the wave speeds and, although difficult to measure, the growth rates.

Ripple lengths have been measured in many studies; the main results are summarized in Figure 7.15, which presents the data collected by Yalin (1985). We see that the wavelength varies with at least two parameters: the Reynolds number at the particle scale, $Re_p = \rho u_* d / \mu$, and a number $\Xi = 18Re_s$, where $Re_s = \rho U_s d / \mu$ is the sedimentation Reynolds number (the Shields number is simply $\theta = Re_p^2 / \Xi$).

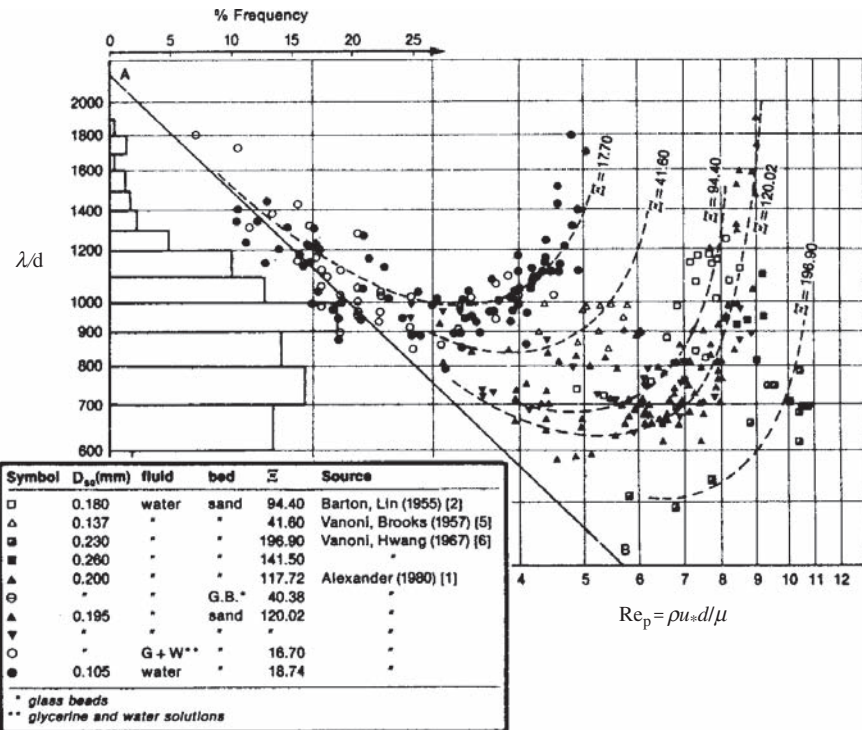


Figure 7.15 Measured lengths of “mature” ripples formed under continuous flow as a function of the Reynolds number Re_p for various numbers $\Xi = 18 Re_s$ (Yalin, 1985), with permission from ASCE.

In the viscous regime ($Re_p \lesssim 3$), the wavelength decreases, with the points clustering mostly near the line $\lambda/d = 2200 Re_p^{-1}$. In other words, the wavelength scales with the viscous length ν/u_* . For $Re_p \gtrsim 3$ the wavelength clearly also varies with Re_s : λ increases as Re_s decreases. However, these data are fairly scattered, and taking into account other measurements only adds to the confusion. Table 7.1 shows several correlations established from observations. These correlations vary widely and predict wavelengths differing by a factor of five or more; however, two general trends can be seen: the wavelength increases with the grain diameter and depends only weakly on the Shields number.

There are probably several reasons that the measurements show such scatter. The first is that ripples which have just begun forming (typically on a time scale of a few minutes) catch up to the larger ones and merge with them. This tends to increase the average length, as illustrated in Figure 7.16. This coalescence phenomenon occurs on a time scale comparable to that of the initial growth, and the measurements which have been made only rarely specify whether the reported lengths correspond to an initial length or the length of “mature” ripples. The data

Table 7.1. *Empirical correlations of lengths of ripples formed under steady flow of water or water-glycerine mixtures, on beds of glass or sand particles of diameter 0.1–0.8 mm, at short (λ_0), long (λ_∞), or undetermined (λ) times*

Reference	λ/d	Remarks
Yalin (1985)	$\lambda_\infty/d = 2200 \text{Re}_p^{-1}$	valid for $\text{Re}_p = u_*d/\nu < 3$
Yalin (1985)	$\lambda_\infty/d = \alpha f(\alpha \text{Re}_p)$	$f(\alpha \text{Re}_p)$ given by a curve
	$\alpha = 3.38 \Xi^{-0.25}$	$\Xi = (\rho_p/\rho - 1)gd^3/\nu^2$
Coleman and Melville (1996)	$\lambda_0/d = 316 \text{Re}_{pt}^{-0.2}$	$\text{Re}_{pt} = \text{Re}_p$ at threshold
Raudkivi (1997)	$\lambda = 150 d^{0.5}$ (mm)	
Coleman and Eling (2000)	$\lambda = 175 d^{0.75}$ (mm)	

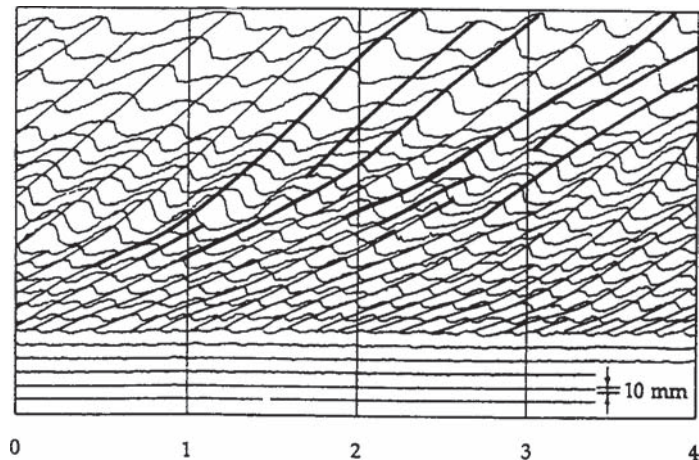


Figure 7.16 Profiles of a sand bed under a continuous flow of water from left to right taken at the initial time $t = 0$ (lower profile) and later at $t = 420$ s (upper profile). The longitudinal scale is in meters, $d = 0.83$ mm, $u_* = 59$ mm/s, and $U_s = 112$ mm/s (Coleman and Melville, 1994), with permission from ASCE.

in Figure 7.15 most likely correspond to mature ripples. Another reason is that the time scale of the ripple growth is not always large compared to the time for the flow to develop, so that the ripples grow in a nonstationary or spatially nonuniform flow. Finally, certain parameters are difficult to control or are poorly known, like the bed preparation or the polydispersity of the particle sizes. This situation is not favorable for checking model quantitative descriptions.

Taking into account the above-mentioned difficulties, the measurements of Coleman and Eling (2001) for sand grains in viscous oil appear the most reliable. Figure 7.17a compares these measurements at the most amplified wavelength

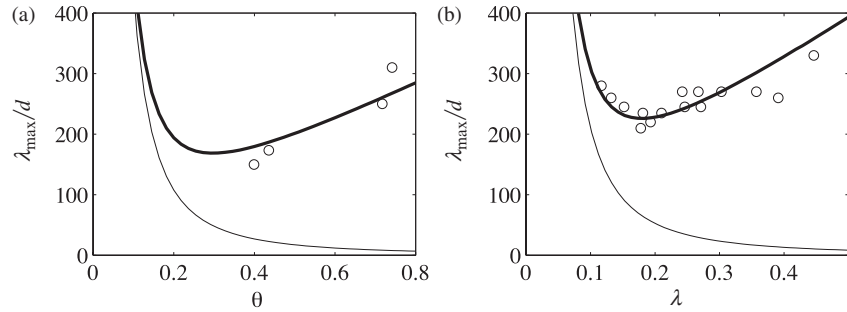


Figure 7.17 Ripple lengths measured (o) and predicted from λ_{\max}/d given by (7.39), with $\phi_q \neq 0$ (thick line) and $\phi_q = 0$ (thin line). (a) Viscous flow: (o) Coleman and Eling (2000) ($d = 0.30$ mm, $Re_s = 0.0034$, $\theta_t = 0.091$), model: $c_u/c_d = 0.9$, $c_g = 0.11$. (b) Turbulent flow: (o) Coleman and Melville (1996) ($d = 0.20$ mm, $Re_s = 7.76$, $\theta_t = 0.051$), model: $c_u/c_d = 2$, $c_g = 0.86$.

$\lambda_{\max} = 2\pi/k_{\max}$ obtained from (7.39) for viscous flow. We see that without the peak erosion mechanism (thin line) the wavelength is seriously underestimated and the falloff with θ is incorrect. When the erosion mechanism is included (thick line) and the two parameters are adjusted to values close to those found by Charru *et al.* (2004), the agreement is fairly good; in particular, the slow increase of λ with θ is reproduced well. Figure 7.17b compares measurements in turbulent flow to the same theoretical predictions, with similar conclusions: see Charru (2006) for details.

In conclusion, the stability analyses of a granular bed demonstrate the importance of relaxation phenomena for the flux of particles exposed to a variable shear. When these phenomena are ignored the predicted wavelengths are an order of magnitude lower than the measured ripple lengths. Taking relaxation into account very significantly improves the predictions, leading to the correct order of magnitude and the correct dependence on the Shields number. However, the debate is not yet over, in particular, regarding the three following points: the phase of the shear stress in turbulent flow, the specific role played by gravity, and weak dependences of the relaxation length on the dimensionless parameters.

7.6 Subaqueous ripples in oscillating flow

7.6.1 Introduction

The oscillatory motion of a liquid mass above a granular bed leads to the formation of ripples that are very similar to those observed under steady flow. The sand ripples one observes on a beach at low tide are an example. These ripples were formed when the beach was covered with water by the oscillations induced by the surface

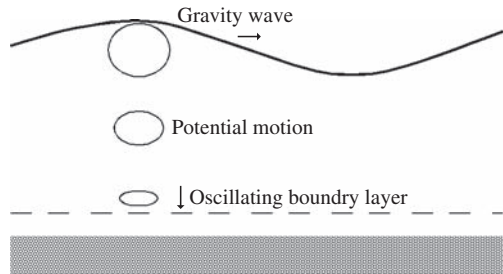


Figure 7.18 Oscillating boundary layer induced by a gravity wave in shallow water.

waves (Figure 7.18). The typical wavelength of the ripples is of order 10 cm, and their height is of order 1 cm. Similar structures are also observed on the continental shelf at water depths of two to three hundred meters, with a wavelength on the order of a meter. These ripples play an important role in attenuating the wave motion, essentially owing to viscous dissipation in the oscillating boundary layer and vortex detachment from their peaks. They also have an important effect on the particle transport induced by drift currents near the bed and therefore on geomorphology at large time scales (Nielsen, 1992). A remarkable observation is the sorting according to grain size induced by ripple formation: the smallest grains generally migrate toward the peaks while the larger ones remain in the troughs.

7.6.2 Observations

From de Candolle (1883) to Bagnold (1946)

Ripple formation was studied in the 19th century, in particular, by C. de Candolle and G. H. Darwin. A good description of these early observations is given by Ayrton (1910) and Bouasse (1924). The observations of Bagnold (1946) mark a decisive advance in three areas: the particle motion threshold, the ripple characteristics, and the growth of the friction associated with the ripples. These observations were made using a particle bed undergoing oscillatory motion of amplitude A and frequency ω inside a tank of water at rest. This situation, which is the opposite of the natural situation of fluid oscillating above a fixed bed, can be analyzed in the same way provided that the inertia force on the particles is small compared to the friction force, of order $\mu_f(\rho_p - \rho)gd^3$, where the coefficient μ_f is typically close to 0.1. The condition for the two situations to be equivalent is then written as $\rho A\omega^2 \ll \mu_f(\rho_p - \rho)g$.

Bagnold distinguishes two types of ripples: rolling grain ripples and vortex ripples. Right above the motion threshold the particles undergo a back-and-forth motion which is initially uniform. They then begin to align themselves along parallel transverse lines, as in the first photograph of Figure 7.19. The growth of these

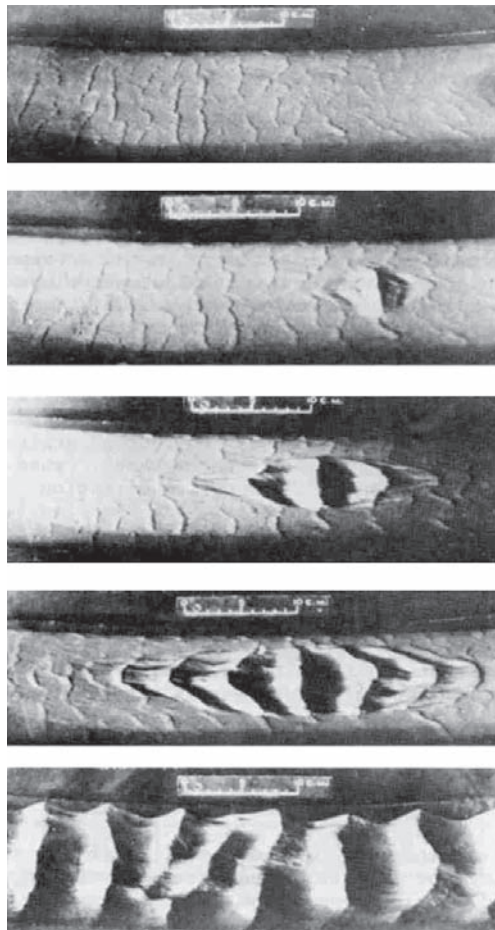


Figure 7.19 From top to bottom: rolling grain ripples and the development of a train of vortex ripples starting from a nucleation site (Bagnold, 1946).

rolling grain ripples leads to a decrease of the shear in the troughs and therefore a decrease of the particle motion: the growth stops when the shear in the troughs decreases below that required to maintain particle motion. An increase of the amplitude of the motion causes new particles to begin moving and therefore leads to an increase in the ripple height and adjustment of the wavelength by peak coalescence. When the oscillation speed exceeds about twice the threshold velocity a new flow regime arises: the flow detaches near the crests and vortices develop in the troughs which are sufficiently strong to extract particles there and carry them to the peaks. This phenomenon begins on the ripple which is initially the highest and then propagates on both sides of it, as shown in Figure 7.19. The amplitude of these *vortex ripples* grows rapidly, and their length adjusts itself such that the

vortex occupies the entire space between two peaks. On an extended bed several systems of vortex ripples can develop from several nucleation sites, thereby giving rise to irregular patterns. Experiments using various types of grain (steel, quartz, carbon) show that the natural length varies approximately as the square root of the grain diameter, and appears to be independent of the grain density. These vortex ripples can also develop on a flat bed and nucleated by an obstacle such as a pebble. We note that in terms of dynamical systems, this development starting from a “perturbation of sufficiently large amplitude” can be interpreted as corresponding to a subcritical bifurcation. Among the other observations of Bagnold, we mention the appearance, at small oscillation amplitude, of grain bridges connecting two adjacent crests, which lead to “brick patterns.”

More recent studies

The observations of Bagnold have been studied more thoroughly using various experimental setups: a wave flume (Faraci and Foti, 2001), an oscillating viscous Couette flow (Mouilleron *et al.*, 2001), and a particle bed oscillating in a fluid at rest in a rectilinear (Sleath, 1976) or annular channel (Scherer *et al.*, 1999; Stegner and Wesfreid, 1999; Rousseaux *et al.*, 2004).

For oscillation of the fluid with amplitude A and angular frequency ω , the thickness of the laminar Stokes layer is $\delta_\omega = \sqrt{2\nu/\omega}$, which is typically about a millimeter, and the speed just above this layer is $U_0 = \omega A$. Since the Reynolds number of the boundary layer, defined as

$$\text{Re}_\delta = \frac{\rho U_0 \delta_\omega}{\mu}, \quad (7.40)$$

is of the order of several hundred, the boundary layer is generally considered to be laminar. The stress can therefore be estimated as $\tau \sim \mu U_0 / \delta_\omega$, and the threshold for motion to begin is written as (Bagnold, 1946)

$$\frac{\nu^{1/2} \omega^{3/2} A}{(\rho_p/\rho - 1) g d} \approx 0.05.$$

The experiments of Scherer *et al.* (1999) have shown that the prediction $A \sim \omega^{-3/2}$ is well satisfied, but that the dependence on the diameter is $A \sim \sqrt{d}$ rather than $A \sim d$.

The wavelength of rolling grain ripples has been studied in wave flumes, in particular by Sleath (1976) in connection with a linear stability study. The lengths measured for three types of grain are given in Figure 7.20a. The length clearly grows with the oscillation amplitude and with the grain diameter, and the frequency dependence is weak and non-monotonic. The rolling grain ripples obtained by

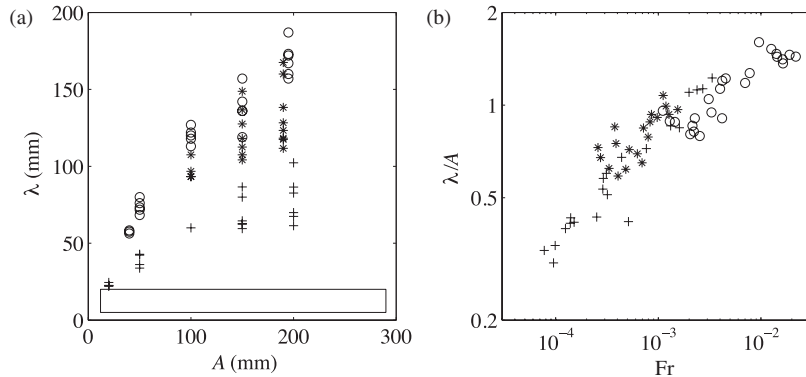


Figure 7.20 (a) Ripple lengths measured by Sleath (1976): (+) sand, $d = 0.40$ mm; (*) sand, $d = 1.14$ mm; (○) nylon, $d = 3$ mm. The rectangle shows the region occupied by the measurements of Rousseaux *et al.* (2004) (glass beads with $d = 65\mu\text{m}$ to $310\mu\text{m}$). (b) The same lengths plotted on a logarithmic graph (λ/A , Fr).

Rousseaux *et al.* (2004) for an annular configuration lie inside the rectangle shown in Figure 7.20a. These ripples are quite different from those of Sleath (1976): their length of about a centimeter is much smaller, and near threshold is independent of the oscillation amplitude. This study revealed the importance of the bed preparation.

The measurements of Sleath and others collected by Blondeaux (1990) are fairly closely grouped together when plotted on a logarithmic graph of λ/A as a function of the Froude number

$$Fr = \frac{\rho(\omega d)^2}{(\rho_p - \rho)gd}, \quad (7.41)$$

as shown in Figure 7.20b. However, this apparent grouping is dubious: it indicates that the wavelength varies as ω^2 , in contradiction with the observation mentioned above of a weak frequency dependence. This doubt is reinforced by noting on the figure the small arcs corresponding to variation of the oscillation frequency, which are not at all aligned with the general trend.

7.6.3 Steady streaming over a wavy bottom

When a fluid oscillates above an undulating surface, the fluid particles do not return exactly to their initial position after one period. There exists a mean stationary flow – or steady streaming – corresponding to recirculation cells. The photograph in Figure 7.21, taken from Kaneko and Honji (1979), gives an idea of this mean

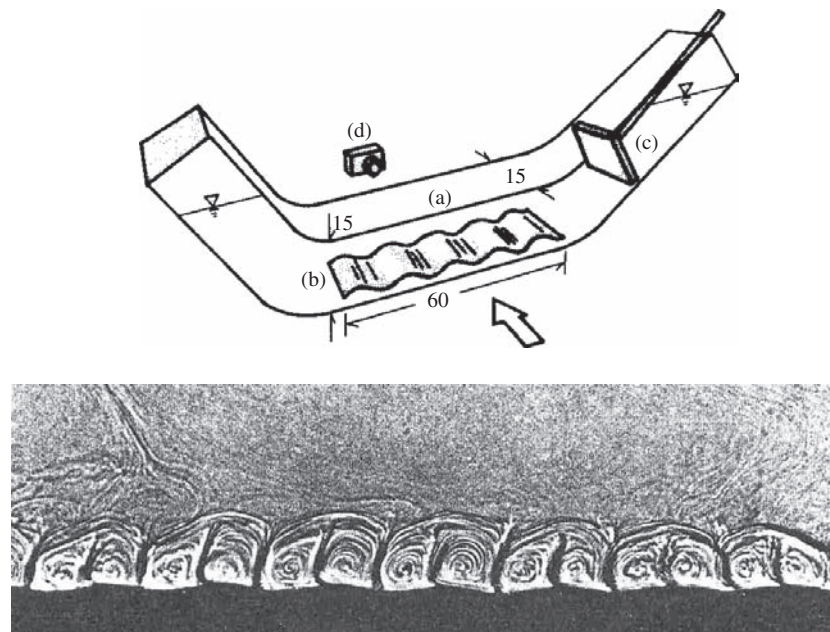


Figure 7.21 Oscillating flow above a wavy wall: schematic view of the experimental setup (top) and visualization of the mean flow (bottom) for $\eta_0 = 1.5$ mm, $\lambda = 40$ mm, $\nu = 1.01 \text{ cm}^2 \text{ s}^{-1}$, and $\delta_\omega = 5.5$ mm (Kaneko and Honji, 1979).

flow. The mean flow has been calculated by many authors using different approximations (Lyne, 1971; Sleath, 1976; Blondeaux, 1990; Larrieu *et al.*, 2009). Figure 7.22 gives two illustrations. Both the observations and the calculations show in particular that near the surface the velocity field points from the troughs toward the peaks.

The origin of the mean flow is identical to that of the phase shift of the shear stress in steady flow: it lies in the fluid inertia. For simplicity, let us consider a quasi-static viscous base flow $\bar{U}(y) = \bar{\gamma}y \sin \omega t$. The structure of the perturbations during the phase of the motion where the flow is to the right is illustrated in Figure 7.23a. This structure is identical to that presented in Figure 7.12b: the advection by the base flow of the vorticity perturbations $\omega^{(0)} \sim \bar{\gamma}\eta/l_v$ generated by the deformation of the bed induces an inertial correction $\omega^{(1)} \sim \text{Re}_{\text{eff}} \omega^{(0)}$ of these perturbations (recall that l_v is the penetration length of the vorticity perturbations and $\text{Re}_{\text{eff}} = \bar{\gamma}l_v^2/\nu$ is the effective Reynolds number). The signature of this inertial correction near the bed is a flow directed from the troughs toward the peaks associated with a shear $\tau^{(1)} \sim \mu\omega^{(1)}$. During the following half-period the base flow is reversed, as is the viscous correction $u^{(0)}$ (Figure 7.23b). On the other hand, the inertial correction $u^{(1)}$ does not change direction, nor does the associated

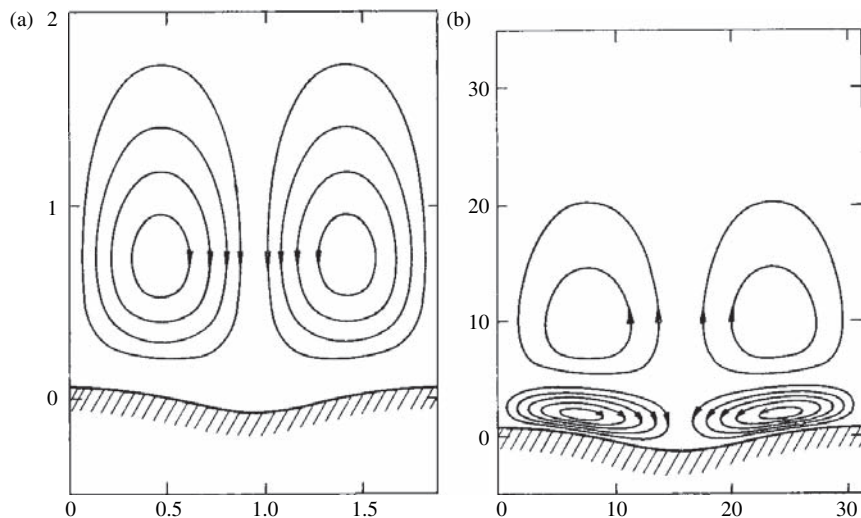


Figure 7.22 Calculated steady streaming induced by the oscillation of a fluid above an undulating bed (δ is the unit of length): (a) $\eta_0/\lambda = 0.03$ and $\lambda/\delta_\omega = 2$; (b) $\eta_0/\lambda = 0.03$ and $\lambda/\delta_\omega = 30$. Reprinted from Sleath (1976) by permission of the publisher (Taylor & Francis Group, <http://www.informaworld.com>).

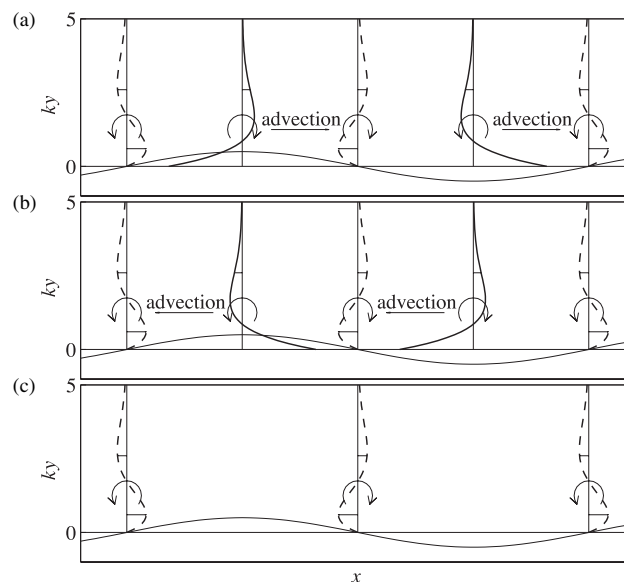


Figure 7.23 Oscillating flow of height H over a wavy bed: $u^{(0)}$ (—) and $u^{(0)}$ (— —). (a) Base flow toward the right; (b) base flow toward the left; (c) perturbation velocity averaged over one period. $kH = 10$ and $kl_v = 1$.

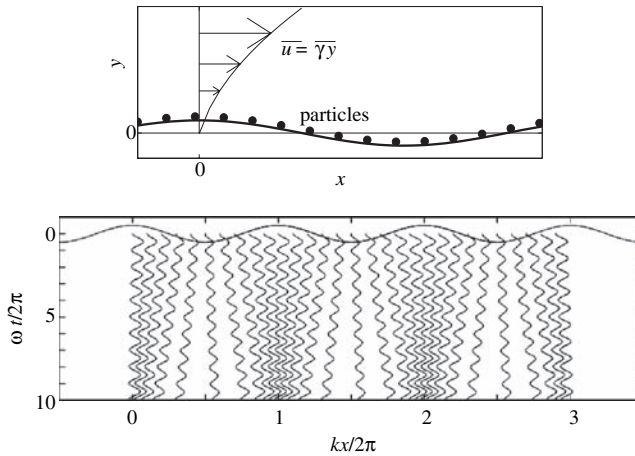


Figure 7.24 (a) Initial particle distribution on an undulating bed in an oscillating viscous flow. (b) Spatio-temporal diagram of the particle motion over time (Charru and Hinch, 2006).

correction $\tau^{(1)}$. The time average of the base velocity field $\bar{U}(y) \sim \sin \omega t$ is zero over a period, as is that of the viscous correction $u^{(0)} \sim \sin \omega t \cos kx$; however, the average of the inertial correction $u^{(1)} \sim \sin^2 \omega t \sin kx$ is not zero. The mean flow due to this inertial correction is a recirculation cell, directed toward the peaks near the bed (Figure 7.23c).

We note that the steady streaming above an undulating surface is analogous to particle transport in a tube when a stationary acoustic wave is present (for example, an organ pipe or a Kundt tube). The effect of a mean flow can be visualized by a fine powder deposited on the bottom: the powder accumulates at the nodes of vibration of the wave. In this problem, analyzed by Rayleigh (1894, vol. II, §352), it is the gradient of the wave amplitude which is responsible for the mean flow. This gradient plays the same role as the periodic deformation of the bed in our erosion problem (both break the translational invariance). For a more general discussion of streaming phenomena, see Batchelor (1967, §5.13) and Riley (2001).

7.6.4 Instability

The particle motion generated by the oscillation of the fluid is illustrated in Figure 7.24. Particles are distributed uniformly on a sinusoidal surface and are set in motion by an oscillating viscous flow (Figure 7.24a). The position of each particle is followed over time by integrating the particle velocity, assuming that it is proportional to the local shear. The spatio-temporal graph (Figure 7.24b) shows the principal oscillation and a mean drift toward the peaks causing particles to accumulate there. On an erodible bed this accumulation corresponds to amplification of the

initial perturbation of the bed. Particle movement toward the troughs is observed when the wavelength is large or the frequency is low.

As for a bed under steady flow, it is possible to take into account the relaxation of the particle flux associated with particle deposition in a shear field that now varies in time and in space (Charru and Hinch, 2006). It is found that this mechanism here plays a negligible role when the flight time of the particles is large compared to the oscillation period.

We now return to the ripples on a sand bed created by a surface gravity wave. The ripple growth has been calculated by Blondeaux (1990) by matching the potential flow due to the surface wave to that in the oscillating Stokes layer. This study (which ignores all relaxation effects for the particles) shows that instability is manifested at a finite wave number (it is therefore not a long-wave instability). The decay of long ripples is due to mean flow associated with the unsteadiness of the base flow, which is opposite and dominates that due to advection. The predictions for the most amplified wavelength are good (as far as can be judged given the scatter in the experimental data), but the scaling laws are not given.

In conclusion, an oscillating flow above an undulating bed gives rise to a steady streaming – a mean flow – toward the peaks. This streaming flow, due to the fluid inertia, leads to a phase shift of the shear stress relative to a deformation of the bed and can induce ripple formation. This mechanism, which is purely hydrodynamic, is identical to that discussed earlier for steady flow. Another, less well studied mechanism may also play an important role, i.e., the aggregation of particles which get trapped in the wakes of adjacent particles. This aggregation, described by Bagnold (1946) and by Sleath (1976), has been modeled by Andersen (2001).

7.7 Subaqueous dunes

7.7.1 Introduction

Subaqueous dunes, which were presented briefly in Section 7.4.2, are structures of long wavelength on the order of ten times the fluid depth and height which can reach half this depth. These structures develop on riverbeds (Figure 7.11) or at the bottom of shallow seas swept by tidal currents such as the English Channel or the North Sea (Blondeaux, 2001). They are also encountered, at a much smaller scale, in pipe flow of mixtures of liquid and particles.

A subaqueous dune differs from a ripple in that its formation involves a coupling between the erodible bed and the upper boundary of the flow (free surface or wall). Two scenarios have been proposed for this formation: it could result from an actual instability of the flat bed, or it could be the result of a coarsening process by successive coalescence of larger and larger ripples, the first stages of which are

shown in Figure 7.16. The first scenario involves linear stability studies like those of Richards (1980) and Colombini (2004). The second, which has hardly been studied at all, is essentially nonlinear. The most pertinent question about subaqueous dune formation therefore remains unanswered; here we shall only consider the first scenario, using the very elementary model described in the following section.

7.7.2 A simple model

Although the elementary model presented below fails to reproduce dune formation, it does have the advantage of permitting an analytic approach based on the Saint-Venant equations, as well as displaying important aspects of the problem. For a more comprehensive approach based on consistent depth-averaged equations, see Luchini and Charru (2010b).

The model

We consider the flow in the x -direction of a fluid layer of thickness $h(x, t)$, on an erodible bed defined by $h_b = h_b(x, t)$ of average slope $\alpha \ll 1$ relative to the horizontal. We assume that the scale of variation in the direction of the flow is large compared to the characteristic vertical length h . Therefore, the vertical pressure distribution is hydrostatic, and integration of the mass and longitudinal momentum conservation equations over the height gives the Saint-Venant equations for the height $h(x, t)$ and the average longitudinal velocity $U(x, t)$ (see the Appendix). With the approximation of uniform (plug) flow, these equations can be written as

$$\partial_t h + \partial_x(hU) = 0, \quad (7.42a)$$

$$\rho h \partial_t U + \rho h U \partial_x U = -\rho gh \partial_x(h_b + h) - \tau + \rho gh\alpha, \quad (7.42b)$$

where τ is the shear stress exerted by the bed. This stress can be written as

$$\tau = c_f \frac{\rho U^2}{2}, \quad (7.43)$$

where c_f is a friction coefficient which *a priori* depends on the dimensionless numbers of the problem, i.e., the Reynolds number and possibly the bed roughness.¹⁰ The modeling of this friction coefficient is crucial, as it essentially determines the stability results. In the present approach we shall assume it is constant, $c_f = 0.01$. Particles are assumed to be transported as bedload according to some law of the Meyer-Peter–Muller type (7.14),

$$Q = Q(\tau). \quad (7.44)$$

¹⁰ We note that this coefficient is defined differently from the coefficient (7.2) introduced in modeling avalanches.

The evolution of the bed height h_b is therefore related to the above flux Q by the mass conservation law:

$$\partial_t h_b + \partial_x Q = 0 \quad (7.45)$$

(where we have omitted the compactness C of the bed).

The base solution

Equations (7.42) to (7.45) have a stationary, uniform solution corresponding to equilibrium between the stress $\bar{\tau}$ exerted by the bed and the weight per unit area $\rho g \bar{h} \alpha$. For a given flow rate per unit width $(\bar{U}\bar{h})$ this solution can be written as

$$\bar{U}^3 = \frac{2\alpha g (\bar{U}\bar{h})}{c_f}, \quad (7.46a)$$

$$\bar{h}^3 = \frac{c_f (\bar{U}\bar{h})^2}{2\alpha g}, \quad (7.46b)$$

$$\bar{\tau} = \rho g \bar{h} \alpha, \quad (7.46c)$$

$$\bar{h}_b = 0, \quad (7.46d)$$

$$\bar{Q} = Q(\bar{\tau}). \quad (7.46e)$$

We see that for a given flow rate an increase of the friction coefficient decreases the speed and increases the height, as expected. For this base solution the Froude number $Fr = \bar{U}^2 / g \bar{h}$ is

$$Fr = \frac{2\alpha}{c_f}. \quad (7.47)$$

To establish magnitudes, for a river with flow rate of $(\bar{U}\bar{h}) = 1 \text{ m}^3/\text{s}$ per unit width, slope $\alpha = 10^{-3}$, and constant $c_f = 0.01$, the height and average speed are $\bar{h} = 0.80 \text{ m}$ and $\bar{U} = 1.25 \text{ m/s}$. This gives $Fr = 0.2$, which corresponds to subcritical flow, and $Re = \rho \bar{U} \bar{h} / \mu = 10^6$, so that the flow is turbulent as expected. The stress on the bed is 7.8 Pa, which for sand grains 0.3 mm in diameter corresponds to Shields number $\theta = 1.6$, which is well above the threshold. The Meyer-Peter–Muller law (7.14) then gives a particle flow rate per unit width of $\bar{Q} = 8.5 Q_{\text{ref}} = 0.17 \times 10^{-3} \text{ m}^2/\text{s}$.

7.7.3 Stability on a flat rigid bed

We first consider the case of a nonerodible flat bed ($h_b = 0, Q = 0$). Linearizing the equations for perturbations of the base flow (7.46) and introducing normal modes

proportional to $e^{ik(x-ct)}$, we obtain the dispersion relation

$$\left(\frac{c}{\bar{U}} - 1\right)^2 + \frac{ic_f}{k\bar{h}} \left(\frac{c}{\bar{U}} - \frac{3}{2}\right) - \frac{1}{Fr} = 0. \quad (7.48)$$

Introducing the dimensionless wave number $K = 2k\bar{h}/c_f$, the solutions of the dispersion relation are

$$\frac{c_{r\pm}}{\bar{U}} - 1 = \frac{i}{K} \left(-1 \pm \left(1 - \frac{K^2}{Fr} - iK \right)^{1/2} \right). \quad (7.49)$$

A Taylor series expansion for small K gives the following for the wave speed c_r and the temporal growth rate $\sigma = kc_i$:

$$\frac{c_{r\pm}}{\bar{U}} = 1 \pm \frac{1}{2}, \quad (7.50a)$$

$$\frac{\sigma_{\pm}}{\sigma_{\text{ref}}} = -1 \pm 1 \pm \frac{Fr - 4}{8} \frac{K^2}{Fr}, \quad (7.50b)$$

where $\sigma_{\text{ref}} = \frac{1}{2}c_f\bar{U}/\bar{h}$. These expressions show that long wavelengths are not dispersive, and that the fast mode ($c_+ > \bar{U}$) is unstable for $Fr > 4$, with a growth rate that scales as $(k\bar{h})^2$. Figure 7.25 shows the speed and growth rate for two Froude numbers $Fr = 1$ and $Fr = 8$. We see that the wave numbers are all stable for $Fr = 1$ and all unstable for $Fr = 8$. It can be verified directly using (7.49) that $Fr = 4$ corresponds to marginal stability of all wave numbers.

7.7.4 Stability on an erodible bed

Let us now consider an erodible bed. Repeating the calculations of the preceding section (see Exercise 7.8.3), we find that the dispersion relation for perturbations of the base flow (7.46) is given by

$$\left(\frac{c}{\bar{U}} - 1\right)^2 + \frac{ic_f}{k\bar{h}} \left(\frac{c}{\bar{U}} - \frac{3}{2}\right) - \frac{1}{Fr} - \frac{B}{Fr} \frac{c/\bar{U} - 1}{c/\bar{U}} = 0, \quad (7.51)$$

which is the same as (7.48) except for the last new term where B is defined as

$$B = \frac{Q'(\bar{\tau})\tau'(\bar{U})}{\bar{h}} > 0.$$

Multiplying this dispersion relation by c/\bar{U} , we obtain a cubic equation in c/\bar{U} (or $c/\bar{U} - 1$) which has three solutions. For $B = 0$ we recover the two eigenvalues

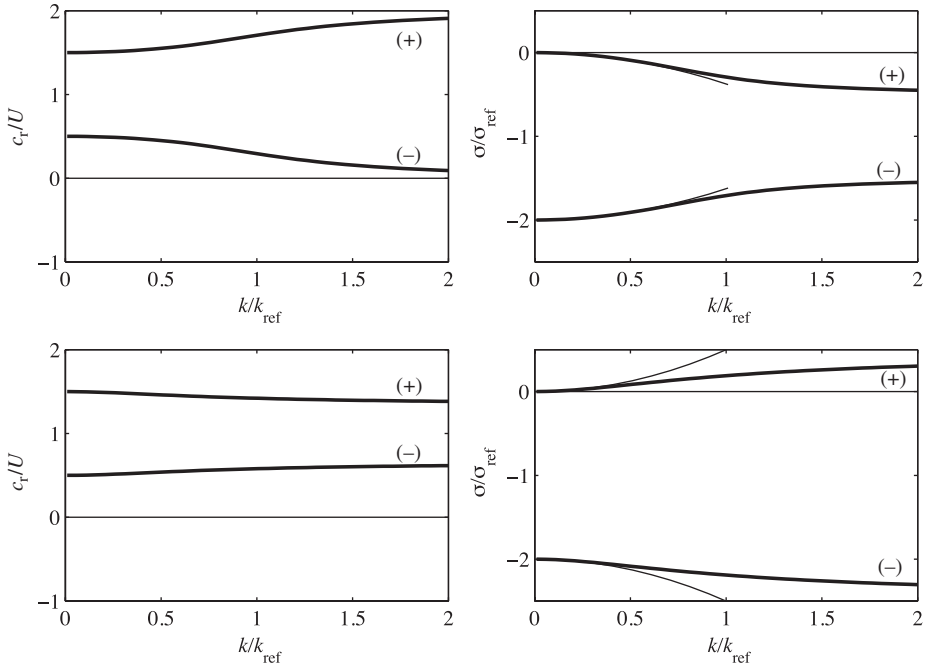


Figure 7.25 Wave speed (left) and growth rate (right) corresponding to the eigenvalues (7.49) of the problem with a nonerodible bed, for $\text{Fr} = 1$ (top) and $\text{Fr} = 8$ (bottom). Thin solid lines on the right: asymptotic series (7.50). $k/k_{\text{ref}} = K/\sqrt{\text{Fr}}$.

c_{\pm} corresponding to a rigid bed, given by (7.49), along with an additional zero eigenvalue $c_0 = 0$. For small but nonzero B , we can seek the corrections c'_{\pm} and c'_0 to these eigenvalues by linearizing the dispersion relation about c_{\pm} and c_0 . In the small wavenumber limit ($K \ll 1$) these corrections are

$$\frac{c'_0}{U} = -i \frac{B}{3} \frac{K}{\text{Fr}}, \quad \frac{c'_+}{U} = -i \frac{B}{6} \frac{K}{\text{Fr}}, \quad \frac{c'_-}{U} = +i \frac{B}{2} \frac{K}{\text{Fr}}.$$

These corrections are purely imaginary and therefore affect only the growth rates $\sigma = kc_i$, which become

$$\frac{\sigma_0}{\sigma_{\text{ref}}} = -\frac{B}{3} \frac{K^2}{\text{Fr}}, \tag{7.52a}$$

$$\frac{\sigma_+}{\sigma_{\text{ref}}} = \left(\frac{\text{Fr} - 4}{8} - \frac{B}{6} \right) \frac{K^2}{\text{Fr}}, \tag{7.52b}$$

$$\frac{\sigma_-}{\sigma_{\text{ref}}} = -2 - \left(\frac{\text{Fr} - 4}{8} - \frac{B}{2} \right) \frac{K^2}{\text{Fr}}. \tag{7.52c}$$

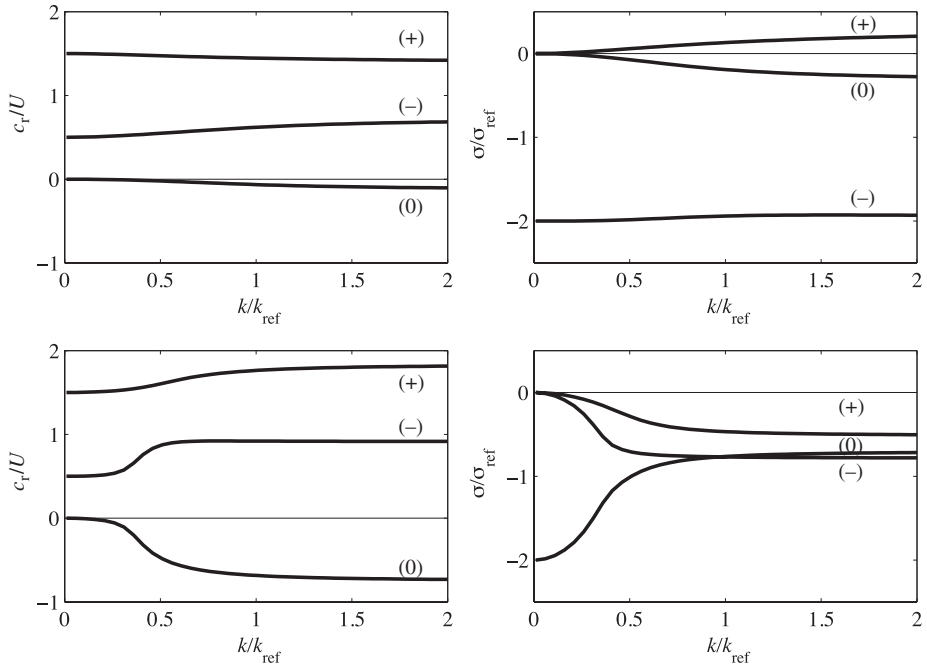


Figure 7.26 Wave speed c/\bar{U} (left) and growth rate $\sigma/\sigma_{\text{ref}} = kc_i/(g\alpha/U)$ (right) of the three eigenvalues of the problem with erodible bed for $B = 1$ (top) and $B = 10$ (bottom), with $\text{Fr} = 8$. The mode (0) is the mode introduced by the erodible bed. $k/k_{\text{ref}} = K/\sqrt{\text{Fr}}$.

The new mode associated with the erodible bed has negative growth rate and is therefore stable, and the surface-mode correction is negative for σ_+ and positive for σ_- . Since this latter mode σ_- is very stable, the correction, even though it is positive, cannot destabilize it.

The roots of the complete dispersion relation are sketched in Figure 7.26 for $B = 1$ and $B = 10$. These graphs confirm the stability analysis for small wave numbers, and also show that large wave numbers $K \gg 1$ behave in the same way.

The conclusion then is that the presence of an erodible bed introduces a new stable mode and does not destabilize the two surface modes. The introduction of the stabilizing effect of gravity through the effective shear stress (7.37), or a relaxation length between the shear and the particle flux, can only further stabilize the bed.

The failure of the model to reproduce the instability of an erodible bed can be attributed to two possible causes: (i) the hypothesis of self-similar flow, where the velocity distribution is uniform over the height, and (ii) the modeling of the friction. Hypothesis (i) may oversimplify the inertial effect giving rise to the instability, while the constant friction used here forces the perturbation of the shear

stress to be in phase with that of the velocity. However, our earlier study of ripples showed that a phase shift is in fact crucial. We can attempt to generate an instability by relaxing the hypothesis for the friction coefficient in various ways (see Exercise 7.8.4). However, these offer little hope of obtaining a good description of the instability mechanism, which has its origins in subtle phase shifts. Only consistent depth-averaged equations can properly account for this phase shift.

7.8 Exercises

7.8.1 Stability of an avalanche

Establish the dispersion relation (7.5) for perturbations of an avalanche flow over an inclined plane. Show that in the limit $Fr \ll 1$, all disturbances are damped. Find the critical Froude number $Fr_c = (a/b)^2$.

7.8.2 Stability of a river flow over a flat bed

Consider the problem studied in Section 7.7.3 of the stability of a flow above a nonerodible flat bed ($Q(\tau) = 0$). Use u , η , and τ to denote small perturbations of the velocity, the water depth, and the wall shear corresponding to the base flow (7.46). Linearize Eqs (7.42) and (7.43), introduce normal modes of the type

$$u = \frac{1}{2} \hat{u} e^{i(kx - \omega t)} + \text{c.c.}$$

in the usual fashion, and show that the amplitudes of the perturbations satisfy the homogeneous system

$$\begin{aligned} -i\omega \hat{\eta} + ik(\bar{U} \hat{\eta} + \bar{h} \hat{u}) &= 0, \\ -i\omega \rho \bar{h} \hat{u} + ik\rho \bar{h} \bar{U} \hat{u} &= -ik\rho g \bar{h} \hat{\eta} - \hat{\tau} + \rho g \alpha \hat{\eta}, \\ \hat{\tau} &= c_f \rho \bar{U} \hat{u}. \end{aligned}$$

Derive the dispersion relation (7.48).

7.8.3 Dunes: constant friction coefficient

Consider the case of an erodible bed studied in Section 7.7.4. Derive the linearized equations for small perturbations u , η_b , η , q , and τ of the base flow (7.46), introduce the normal modes, and show that the amplitudes of these normal modes

satisfy the homogeneous algebraic system

$$\begin{aligned} -i\omega \hat{\eta} + ik(\bar{U} \hat{\eta} + \bar{h} \hat{u}) &= 0, \\ -i\omega \rho \bar{h} \hat{u} + ik\rho \bar{h} \bar{U} \hat{u} &= -ik\rho g \bar{h} \cos \alpha (\hat{\eta}_b + \hat{\eta}) - \hat{\tau} + \rho g \sin \alpha \hat{\eta}, \\ \hat{\tau} &= c_f \rho \bar{U} \hat{u}, \\ \hat{q} &= Q'(\bar{\tau}) \hat{\tau}, \\ -i\omega \hat{\eta}_b + ik \hat{q} &= 0. \end{aligned}$$

Show that the dispersion relation is given by Eq. (7.48) with the additional term (7.51).

7.8.4 Dunes: nonconstant friction coefficient

Repeat the preceding exercise with a nonconstant friction coefficient given by:

1. the Blasius law $c_f = 0.316 \text{Re}^{-1/4}$, $\text{Re} = \rho U h / \mu$;
2. the Manning–Strickler law $c_f = 0.1 (z_0/h)^{1/3}$, where z_0 is the roughness scale of the bed and is of the order of the grain diameter.

8

Nonlinear dynamics of systems with few degrees of freedom

8.1 Introduction

According to the linear stability theory developed in the preceding chapters, a perturbation of a base flow can be expressed as a sum of eigenmodes, each uncoupled from the other and written as

$$u(\mathbf{x}, t) = \frac{1}{2} (A(t)f(\mathbf{x}) + A^*(t)f^*(\mathbf{x})). \quad (8.1)$$

Here $f(\mathbf{x})$ describes the spatial structure of the mode and $A(t)$ describes its time evolution, with the asterisk denoting complex conjugation. However, the predictions of the linear analysis, and indeed this representation, are valid only for perturbations of sufficiently small amplitude, when the nonlinearities of the problem are effectively negligible. The object of a *nonlinear stability* study is to predict what happens beyond the initial period of growth when nonlinear effects become important. Unfortunately, there is no general theory of nonlinear effects analogous to the linear stability theory, which exploits the linearity of the underlying mathematical problem. Various approaches have been developed, each permitting the study of certain classes of nonlinearities and/or classes of solutions. One of these approaches, known as *weakly nonlinear analysis*, is particularly important owing to its fairly general nature based on perturbation methods.

The basic idea of weakly nonlinear analysis is due to the Soviet physicist Lev Landau (1944) (see Landau and Lifshitz, 1987, §26). Landau first notes that for a linearized problem governed by constant coefficient equations, the (complex) amplitude $A(t)$ of an eigenmode grows exponentially as the solution of the differential equation

$$\frac{dA}{dt} = \sigma A, \quad (8.2)$$

where σ is the temporal growth rate. For small A this equation can be viewed as a Taylor series expansion of the growth rate dA/dt in powers of the amplitude, truncated at first order. Therefore, nonlinearities can be treated in a natural way by including higher-order terms, first quadratic A^2 , AA^* , A^{*2} , then cubic A^3 , A^2A^* , and so on. Analysis of the symmetries of the problem generally allows a large number of these terms to be eliminated. Let us consider the important case of a problem invariant under time translation, that is, invariant under change of t to $t_0 + t$ (arbitrary time origin t_0). Then, if $A \propto e^{i\sigma t}$ is a solution, any function translated by a phase ϕ of the form $A \propto e^{i(\sigma t+\phi)}$ must also be a solution.¹ The equation for A must therefore be invariant under rotations in the complex plane $A \rightarrow Ae^{i\phi}$. None of the quadratic or quartic terms satisfies this invariance, and the only cubic term satisfying it is $|A|^2 A$. Therefore, up to terms of fifth order the amplitude is governed by the nonlinear equation

$$\frac{dA}{dt} = \sigma A - \kappa |A|^2 A. \quad (8.3)$$

This equation, called the *Landau amplitude equation*, involves a new coefficient κ which, like σ and A , is *a priori* complex and is known as the *Landau coefficient*. As we will see, this coefficient can be determined by means of a perturbation expansion for small but finite amplitude instabilities.

In hydrodynamics the nonlinearity determining the Landau constant κ generally comes from the advective acceleration term, but it can also arise from the boundary conditions on a deformable interface, a nonlinear constitutive law, or a coupling to nonhydrodynamic phenomena such as thermal convection. The general method of finding the Landau coefficient is to seek the solution of the problem as a power series in the amplitude of the perturbation to the base solution. The pioneers of this “weakly nonlinear approach” were Gor’kov (1957) and Malkus and Veronis (1958) for thermal convection and Stuart (1958, 1960) and Watson (1960) for parallel shear flows.² It has been shown that the Rayleigh–Bénard instability is *supercritical*: for the marginal mode, the real part of κ is positive and the nonlinear cubic term saturates the instability (Koschmieder, 1993). The same occurs for another well-studied fundamental instability, the Couette–Taylor centrifugal instability (Chossat and Iooss, 1994). On the other hand, the instability of plane Poiseuille flow is *subcritical*: for the marginal mode ($k_c h = 1.02$ for $Re_c = 5772$; see Chapter 5) the real part of κ is negative and the instability is not saturated by the nonlinear cubic term. In such a case of a subcritical instability the Landau equation is of little help, and the calculation of the higher-order stabilizing terms

¹ The heuristic derivation presented here is made more precise later in this chapter and in Chapter 11.

² In hydrodynamics the Landau equation is sometimes more correctly called the Stuart–Landau equation, and the technique used to derive it, the Stuart–Watson expansion.

is nearly intractable. This is a limitation of the weakly nonlinear approach (Huerre and Rossi, 1998; Drazin, 2002; Drazin and Reid, 2004): it is most useful when small-norm solutions saturate to finite amplitude at long times.

Lev Davidovich Landau (1908–1968)



Lev Davidovich Landau was born in Baku, Azerbaijan, in the Russian Empire. He entered Baku State University at the age of 14 and then two years later moved to Leningrad State University. His first published paper at the age of 19 was on quantum theory. In 1929 and 1930 he traveled in Europe, working in particular at the Niels Bohr Institute for Theoretical Physics. He was known for his enthusiastic temperament and was regarded as the *enfant terrible* of physics. During 1932–1937 he was head of the Theoretical Department of the Ukrainian Physico-Technical

Institute at Kharkov. His scientific output was extraordinary: he published an original scientific paper every six weeks for two years on a great variety of subjects. He made Kharkov the center of theoretical physics in the USSR. In 1937 he left for Moscow to become head of the Theoretical Department of the Institute for Physical Problems of the Academy of Sciences of the USSR. He worked on atomic collisions, astrophysics, low-temperature physics, nuclear and atomic physics, thermodynamics, quantum electrodynamics, the kinetic theory of gases, quantum field theory, and plasma physics. Under suspicion of being a German spy, he was imprisoned for a year in 1938, but freed after Niels Bohr and Pyotr Kapitsa interceded on his behalf with Stalin, Kapitsa threatening to end his own scientific work. He was awarded the Nobel Prize in 1962 for his theory explaining the superfluid behavior of liquid helium. Landau wrote many books on physics, in particular the landmark 10-volume *Course of Theoretical Physics*, written with one of his students, E. M. Lifshitz, and published between 1930 and 1979. After a serious car accident in 1962 he spent six weeks in a coma. He recovered, but his intellectual activity was diminished. He belonged to many academies of science and received numerous awards including the Fritz London Memorial Prize and the Max Planck Medal.

In a hydrodynamics problem, even the simplest one, determining the coefficient κ requires detailed and difficult calculations which usually cannot be completed without resorting to numerical computation. Before discussing such problems,

it is instructive to consider simpler problems governed by ordinary differential equations, especially the classical nonlinear oscillators. The first part of this chapter is devoted to analysis of these oscillators, using the techniques of perturbation theory.³ With the help of the *method of multiple scales*, we show that the Landau equation can be obtained as a *solvability condition* of a differential equation. Two important canonical nonlinear effects can be studied that are also manifested qualitatively in the same way in more complicated hydrodynamics problems: the saturation of the amplitude for the van der Pol oscillator, and the shift of the frequency for the Duffing oscillator. In the second part of the chapter we return to spatio-temporal problems governed by partial differential equations. We show that when the spatial structure of the perturbation can be described by a small number of Fourier modes, its dynamics can be described by a system of coupled equations for the amplitudes of the modes which reduces to a single Landau equation near the instability threshold.

In this chapter we focus on the “good” behaviors, periodic or quasi-periodic, which generally arise near the threshold of a primary instability and are accessible to perturbation methods. Farther from the threshold, chaotic behavior occurs, whose analysis requires other techniques; see, for example, Bergé *et al.* (1987).

8.2 Nonlinear oscillators

We begin by analyzing the simple classical problem of a particle in a potential well, which we mentioned briefly in the first chapter. This example will be useful for introducing the idea of saturation of an instability. Then we turn to the study of nonlinear oscillators in order to gain a more general understanding of two major nonlinear effects. The first of these canonical effects is saturation of the exponential growth at a finite value of the amplitude; the van der Pol oscillator (1927) is the standard example of this. The second effect is the change of the oscillation frequency, illustrated by the Duffing oscillator (1918). Forced oscillators are then briefly considered.

8.2.1 A strongly dissipative oscillator in a double-well potential

Let us consider an oscillator described by a real amplitude $A(t)$ which evolves in a potential $V(A)$ assumed invariant under the reflection symmetry $A \rightarrow -A$ ($V(A)$ is therefore an even function). In addition, we assume that this oscillator is strongly dissipative, i.e., that the second-order “inertial” term d^2A/dt^2 is negligible compared to a “friction force” proportional to dA/dt . This oscillator is therefore

³ Here we present only a basic introduction to a very rich topic; for further information see, for example, Bogolioubov and Mitropolski (1962) or Glendinning (1994, chapter 7).

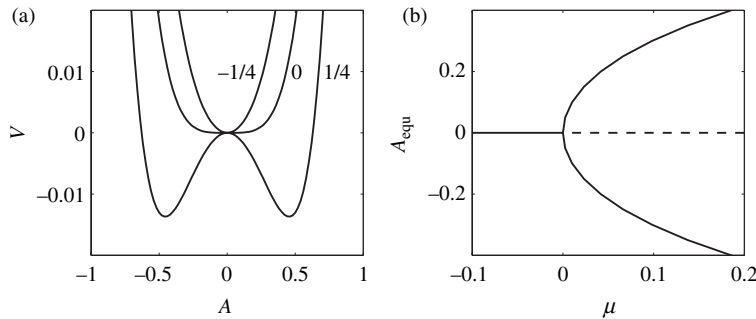


Figure 8.1 (a) The potential $V(A)$ for $\kappa = +1$, $\lambda = 0$, and $\mu = -1/4, 0, 1/4$; (b) the bifurcation diagram: stable (—) and unstable (---) equilibrium states.

governed by the real equation

$$\frac{dA}{dt} = -V'(A), \quad \text{with} \quad V'(A) = \mu A - \kappa A^3 - \lambda A^5 \quad (8.4)$$

up to higher-order terms. Here we recognize the Landau equation with an additional fifth-order term. We note that in thermodynamics this equation serves as a good model for studying the phase transitions of a pure substance whose thermodynamical state is described by the “order parameter” $A(t)$ (Callen, 1985).

First we consider the case of positive Landau constant (which can be set to unity, $\kappa = 1$, without loss of generality), and $\lambda = 0$. For $\mu < 0$ the potential possesses a single minimum (Figure 8.1a) and the system can only relax to $A_0 = 0$. For $\mu > 0$ the state $A_0 = 0$ becomes unstable ($V(0)$ is a local maximum) and the system bifurcates to one of the two potential wells $A_{\pm} \sim \pm\sqrt{\mu}$ for small μ . In the formalism of dynamical systems (Chapter 1), the system undergoes a supercritical pitchfork bifurcation at $\mu = 0$ corresponding to the bifurcation diagram of Figure 8.1b.

Now let us consider negative Landau constant, $\kappa = -1$, but with $\lambda = 1$. For $\mu > 0$ the cubic term is no longer stabilizing and it is the term of fifth degree that will saturate the instability. It is easily verified that (Figure 8.2a):

- for $\mu \leq -1/4$ the potential $V(A)$ possesses a single minimum;
- for $\mu > 0$ the potential $V(A)$ possesses two minima;
- in the range $-1/4, 0$ the potential $V(A)$ possesses three minima; these minima are equal for $\mu = -3/16$.

We then obtain the bifurcation diagram (Figure 8.2b), from which we see that:

- for μ increasing from $\mu < -1/4$ the system undergoes a subcritical pitchfork bifurcation at $\mu = 0$ and jumps from the branch $A = A_0 = 0$ to one of the stable branches $A = A_{\pm}$;

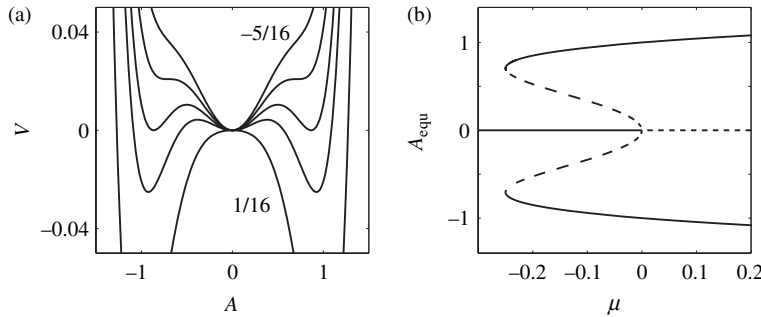


Figure 8.2 (a) The potential $V(A)$ for $\kappa = -1$, $\lambda = 1$, and $\mu = -5/16$, $-4/16$, $-3/16$, $-2/16$, and $1/16$; (b) the bifurcation diagram: stable (—) and unstable (---) equilibrium states.

- for μ decreasing the system moves along one of the stable branches $A = A_{\pm}$ until it undergoes a saddle-node bifurcation at $\mu = -1/4$ and returns to the branch $A = 0$;
- for $-1/4 < \mu < -3/16$ the state $A_0 = 0$ corresponds to an absolute minimum of the potential $V(A)$, while the states A_{\pm} correspond only to local minima $V(A_{\pm})$. The states A_{\pm} , which are less stable than A_0 , are called metastable; for $-3/16 < \mu < 0$ it is A_0 which is metastable.

Therefore, to each value of μ in the range $[-1/4, 0]$ there correspond several values of the saturated amplitude, with the selected amplitude depending on the initial conditions of the motion. A consequence is that the system exhibits *hysteresis*. Let us start with a stable equilibrium solution $A_0 = 0$ and $\mu < 0$; as μ is increased slowly, the equilibrium state follows the branch $A_0 = 0$ until $\mu = 0$ is reached. Then the solution jumps to one of the stable branches $A = A_{\pm}$ (depending on the sign of the perturbation). For μ now decreasing, the branch $A = A_{\pm}$ is followed until $\mu = -1/4$; the solution then jumps back to the original stable solution $A_0 = 0$. The system has executed a hysteresis loop.

8.2.2 The van der Pol oscillator: amplitude saturation

The van der Pol oscillator provides a simple example of supercritical Hopf bifurcation from a stable stationary state to an oscillatory state of finite amplitude. This is a dissipative oscillator with linear eigenfrequency ω_0 , where the dissipation depends nonlinearly on the amplitude:⁴

$$\frac{d^2u}{dt^2} - (2\epsilon\mu - u^2)\frac{du}{dt} + \omega_0^2 u = 0, \quad \mu = \mathcal{O}(1), \quad \epsilon \ll 1. \quad (8.5)$$

⁴ By changing the time scale from t to $t' = \omega_0 t$ it is possible to eliminate ω_0 from the problem, but here we prefer to retain this parameter explicitly.

We shall assume that the small parameter ϵ is fixed and that μ is the bifurcation parameter. It is easily verified⁵ that the solution $u = 0$ is linearly stable for $\mu < 0$ and unstable for $\mu > 0$, that the frequency of small oscillations is $\omega_0 + \mathcal{O}(\epsilon)$, and that the growth rate is $\epsilon\mu$, which is very small compared to ω_0 .

For $\mu > 0$, Eq. (8.5) shows that the term responsible for the instability vanishes for $u^2 = 2\epsilon\mu$, so that we expect saturation for an amplitude of order $\epsilon^{1/2}$. We therefore seek a solution of the form

$$u(t) = \epsilon^{1/2}\tilde{u}(t), \quad \tilde{u} = \mathcal{O}(1), \quad (8.6)$$

which leads to the following equation for $\tilde{u}(t)$:

$$\frac{d^2\tilde{u}}{dt^2} - \epsilon(2\mu - \tilde{u}^2)\frac{d\tilde{u}}{dt} + \omega_0^2\tilde{u} = 0, \quad \mu = \mathcal{O}(1), \quad \epsilon \ll 1.$$

Since the growth rate of the linear instability is of order ϵ , we expect nonlinear effects to appear after a time of order ϵ^{-1} , which is much larger than the oscillation period. We therefore seek an equation describing the slow variation of the amplitude of $\tilde{u}(t)$ using the *method of multiple scales* (Bender and Orszag, 1978; Hinch, 1991; Glendinning, 1994). We set

$$\tilde{u}(t) = \tilde{u}(\tau, T), \quad (8.7)$$

where $\tau = t$ is the “fast” time describing the phase variation and $T = \epsilon t$ is the “slow” time describing the amplitude variation. Saturation is therefore expected for $T = \mathcal{O}(1)$. Next we seek $\tilde{u}(\tau, T)$ as a series in powers of ϵ :

$$\tilde{u} = u_0 + \epsilon u_1 + \epsilon^2 u_2 + \dots \quad (8.8)$$

Using the rule for the derivative of a composite function,

$$\frac{d}{dt} = \frac{\partial}{\partial \tau} + \epsilon \frac{\partial}{\partial T},$$

substituting into the original equation and collecting terms of the same order in ϵ , we obtain the series of differential equations. At orders ϵ^0 and ϵ^1 these equations

⁵ Within the framework of the theory of dynamical systems (Chapter 1), the van der Pol equation can be written as a system of ordinary differential equations of first order in u and $v = du/dt$, whose solutions are represented by curves in the phase space (u, v) . The eigenvalues of the linearized system are complex conjugates of each other and the fixed point $(u, v) = (0, 0)$ is a focus. For $\mu < 0$ ($\mu > 0$) this focus is stable (unstable) and the phase portrait in its vicinity consists of convergent (divergent) spirals. For $\mu = 0$ the fixed point is a center, and the phase portrait of the linearized system consists of closed ellipses.

are respectively

$$Lu_0 = 0 \quad \text{with} \quad L = \frac{\partial^2}{\partial \tau^2} + \omega_0^2, \quad (8.9a)$$

$$Lu_1 = -2 \frac{\partial^2 u_0}{\partial \tau \partial T} + (2\mu - u_0^2) \frac{\partial u_0}{\partial \tau}. \quad (8.9b)$$

Each of the problems of this series is *linear*, homogeneous at order ϵ^0 , and inhomogeneous at higher orders with the nonhomogeneous terms determined by the solutions from the preceding orders.

At order ϵ^0 the general long-time periodic solution is

$$u_0 = \frac{1}{2} \left(A(T) e^{i\omega_0 \tau} + A(T)^* e^{-i\omega_0 \tau} \right). \quad (8.10)$$

We note that the integration constant A is an amplitude which depends on the slow time T , here treated as a parameter. At order ϵ^1 , Eq. (8.9b) is written as

$$Lu_1 = i\omega_0 (\mu A - \frac{dA}{dT}) e^{i\omega_0 \tau} - \frac{i\omega_0}{8} \left(|A|^2 A e^{i\omega_0 \tau} + A^3 e^{3i\omega_0 \tau} \right) + \text{c.c.}, \quad (8.11)$$

where c.c. denotes the complex conjugate. This equation can be interpreted as describing a harmonic oscillator forced by the term on the right-hand side. However, this forcing term contains resonant terms of frequency ω_0 (terms involving $e^{i\omega_0 \tau}$) leading to linear, unbounded growth of the amplitude of u_1 (see Exercise 1.6.1). (Within the context of celestial mechanics, where this type of analysis was first introduced by Poincaré, this growth and the terms responsible for it are termed “secular.”) Since we are seeking a bounded periodic solution, this secular growth must be excluded, which implies that the coefficient of the term $e^{i\omega_0 \tau}$ must vanish. The amplitude $A(T)$ must then satisfy the *solvability condition*

$$\frac{dA}{dT} = \mu A - \kappa |A|^2 A, \quad \kappa = \frac{1}{8}. \quad (8.12)$$

This is a Landau equation describing the evolution of the amplitude as a competition between a linear term and a cubic term. Setting $A = a(T)e^{i\phi(T)}$ where $a = |A|$, and separating the real and imaginary parts, we obtain separate equations for the modulus and phase of A :

$$\frac{da}{dT} = \mu a - \kappa a^3, \quad \frac{d\phi}{dT} = 0.$$

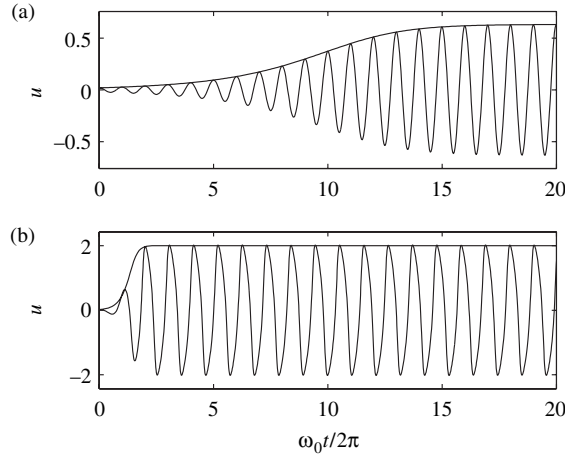


Figure 8.3 Response of the van der Pol oscillator (8.5) for the initial conditions $u(0) = 0.02$, $u'(0) = 0$: (a) $2\epsilon\mu = 0.1$, (b) $2\epsilon\mu = 1$. For the sake of clarity the asymptotic solution (8.14) is represented only by its amplitude (8.13), and the oscillating curve corresponds to the numerical solution.

For μ positive the solutions of these equations are

$$a = a_0 \left(\frac{\kappa}{\mu} a_0^2 + \left(1 - \frac{\kappa}{\mu} a_0^2\right) e^{-2\mu T} \right)^{-1/2}, \quad (8.13a)$$

$$\phi = \phi_0, \quad (8.13b)$$

from which we finally obtain the solution for $u(t)$:

$$u(t) = \epsilon^{1/2} a(t) \cos(\omega_0 t + \phi_0) + \mathcal{O}(\epsilon^{3/2}). \quad (8.14)$$

This result, which conforms to the initial conjecture $u(t) \sim \epsilon^{1/2}$, shows that the amplitude of the saturated oscillation is $2\sqrt{2\mu\epsilon}$ and its frequency is ω_0 , independent of the amplitude of the order to which we are working. Figure 8.3 compares the numerical solution of Eq. (8.5) to the asymptotic solution (8.14), represented only by its envelope $a(t)$, for two values of $2\mu\epsilon$. The agreement is excellent not only near threshold ($2\mu\epsilon = 0.1$, Figure 8.3a), but also relatively far from it ($2\mu\epsilon = 1$, Figure 8.3b). However, we see that for $2\mu\epsilon = 1$ the numerical solution is not quite sinusoidal, which corresponds to the presence of harmonics of the fundamental frequency $\omega_0/2\pi$. These harmonics do not exist in the asymptotic solution (8.14), but they can be determined by pursuing the calculations to higher order. Figure 8.4 shows the corresponding phase portraits for the numerical solution. Close to threshold ($2\epsilon\mu = 0.1$, left-hand portrait) the limit cycle is a circle, which corresponds to a sinusoidal response. Far from threshold ($2\epsilon\mu = 1$,

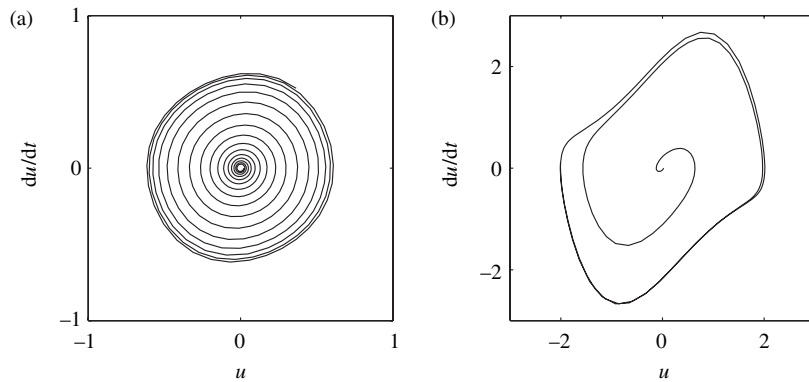


Figure 8.4 Phase portrait of the van der Pol oscillator (8.5) corresponding to the time evolutions of Figure 8.3 (numerical solution): (a) $2\epsilon\mu=0.1$, (b) $2\epsilon\mu=1$.

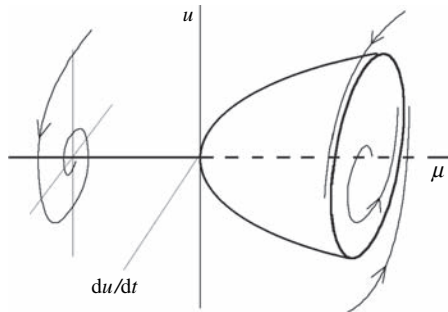


Figure 8.5 Diagram of the Hopf bifurcation occurring at $\mu=0$.

right-hand portrait) the limit cycle is deformed, corresponding to the presence of harmonics.

In conclusion, the stationary state $u=0$ of the van der Pol oscillator, stable for $\mu < 0$, becomes unstable for $\mu > 0$ via a supercritical Hopf bifurcation, with the amplitude of the saturated state growing as the square root of the bifurcation parameter μ (*cf.* Chapter 1). Figure 8.5 shows the corresponding bifurcation diagram.

8.2.3 The Duffing oscillator: the frequency correction

Let us now consider the Duffing oscillator, described by the equation

$$\frac{d^2u}{dt^2} + u + \epsilon u^3 = 0, \quad \mu = \mathcal{O}(1), \quad \epsilon \ll 1. \quad (8.15)$$

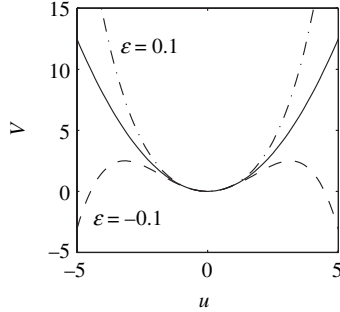


Figure 8.6 (a) The potential $V(u)$ for $\epsilon = -0.1$ ($--$), $\epsilon = 0$ ($-$), and $\epsilon = 0.1$ ($-\cdot-$).

This equation can also be written as

$$\frac{d^2u}{dt^2} = -V'(u), \quad V(u) = \frac{u^2}{2} + \epsilon \frac{u^4}{4},$$

which we recognize as the equation of motion of a mass with a single degree of freedom $u(t)$, subject to a force $F = -V'(u)$ deriving from a potential $V(u)$, with the scales chosen such that the mass and eigenfrequency of the oscillator are normalized to unity. For example, for a simple pendulum in a gravity field the degree of freedom is the angular position, and the restoring force $F = -\sin u$ may be approximated by $F = -u + u^3/6$ for small u , which corresponds to $\epsilon = -1/6$. The potential $V(u)$ is shown in Figure 8.6 for three values of the parameter ϵ .

The Duffing equation admits the first integral

$$H(u, v) = H_0, \quad \text{where} \quad H(u, v) = \frac{1}{2}v^2 + V(u) \quad (8.16)$$

with $v = du/dt$, which represents the constant mechanical energy of the oscillator. The energy curves $H(u, v) = \text{constant}$ define trajectories in the phase space (u, v) , which are ellipses centered on the fixed point $(0, 0)$.⁶ The corresponding periodic solution $u(t)$ can be found by a perturbation method leading to an amplitude equation.

We seek the solution in the form of a series in powers of ϵ

$$u(t) = u_0(t) + \epsilon u_1(t) + \dots,$$

and introduce a fast time $\tau = t$ and a slow time $T = \epsilon t$. We then have a hierarchy of linear equations, similar to the van der Pol oscillator. At orders ϵ^0 and ϵ^1 these

⁶ For $\epsilon < 0$ there exist two other fixed points $(\pm(-\epsilon)^{-1/2}, 0)$, which are saddles. These saddles are joined by two heteroclinic trajectories outside which the trajectories are unbounded.

equations are respectively

$$Lu_0 = 0 \quad \text{with} \quad L = \frac{\partial^2}{\partial \tau^2} + 1, \quad (8.17a)$$

$$Lu_1 = -2 \frac{\partial^2 u_0}{\partial \tau \partial T} - u_0^3. \quad (8.17b)$$

At order ϵ^0 the solution corresponds to harmonic oscillations, as for the van der Pol oscillator. At order ϵ^1 the equation to be solved is

$$Lu_1 = \left(-i \frac{dA}{dT} - \frac{3}{8} |A|^2 A \right) e^{i\tau} - \frac{1}{8} A^3 e^{3i\tau} + \text{c.c.}$$

This equation can be interpreted as that of a forced harmonic oscillator, whose response can be periodic only if the coefficient of the resonant forcing on the right-hand side is zero. Hence the solvability condition gives

$$\frac{dA}{dT} = \frac{3i}{8} |A|^2 A. \quad (8.18)$$

We therefore recover a Landau equation with no linear term (zero linear growth rate) and purely imaginary Landau coefficient of the cubic term, $\kappa = -3i/2$. Setting $A = a(T)e^{i\phi(T)}$ and separating the real and imaginary parts of this equation, we obtain

$$\frac{da}{dT} = 0, \quad \frac{d\phi}{dT} = \frac{3}{8} a^2. \quad (8.19)$$

The solutions of these equations are

$$a = a_0, \quad \phi = \frac{3}{8} a_0^2 T + \phi_0, \quad (8.20)$$

which leads to the expression for $u(t)$:

$$u(t) = a_0 \cos(\omega t + \phi_0) + \mathcal{O}(\epsilon), \quad \omega = 1 + \frac{3}{8} \epsilon a_0^2 + \mathcal{O}(\epsilon^2). \quad (8.21)$$

Therefore, the nonlinear term of the Duffing equation does not affect the oscillation amplitude but only the frequency, in contrast to the case of the van der Pol oscillator.⁷ The frequency correction of order ϵa_0^2 can be interpreted by treating

⁷ If we had defined the potential without a small parameter and looked for a small solution of order ϵ , we would have found the frequency correction $\frac{3}{8} \epsilon^2 a_0^2$, of order ϵ^2 . The difference arises solely from the different definition of the small parameter.

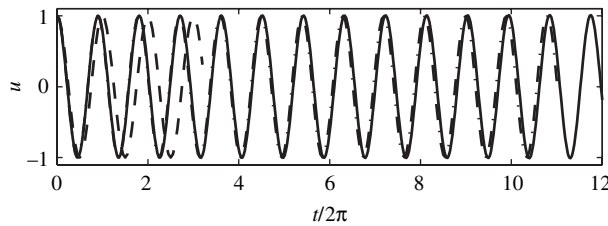


Figure 8.7 Response of the Duffing oscillator (8.15) for $\epsilon = 0.3$: (—) numerical solution, (---) solution at order ϵ^0 , (- · -) solution at order ϵ^1 (8.21).

the Duffing equation (8.15) as the equation for an oscillator subject to a restoring force

$$F = -(1 + \epsilon u^2)u \approx -(1 + \epsilon a_0^2)u.$$

This force corresponds to that of a nonlinear spring with stiffness $r = 1 + \epsilon a_0^2$ depending on the oscillation amplitude a_0 . The corresponding frequency is then $\omega = r^{1/2} \approx 1 + \frac{1}{2}\epsilon a_0^2$, which clearly depends on the amplitude following a law of the same type as (8.21).

Figure 8.7 presents a comparison of the solutions at orders ϵ^0 and ϵ^1 with the exact solution obtained numerically. As expected, we see that the order ϵ^0 solution is valid only for $t \ll 1/\epsilon$ and the order ϵ^1 one for $t \ll 1/\epsilon^2$, i.e., as long as the (uncalculated) phase correction remains small. For t of order $1/\epsilon^2$ the order ϵ^2 correction should be included, see Hinch (1991, §6.2). See Guckenheimer and Holmes (1983, §2.2) for a detailed study of the Duffing oscillator.

8.2.4 Forced oscillators

The forcing of a nonlinear oscillator leads to remarkable and unexpected phenomena. Here we give a brief discussion of a few of them for the two cases of the van der Pol oscillator and parametrically forced oscillators, leaving the calculations and the study of frequency locking phenomena as exercises. For more details the reader may consult one of the many expositions on the subject, for example those of Bender and Orszag (1978) and Glendinning (1984).

The forced van der Pol oscillator

We consider the van der Pol oscillator (8.5) subject to a forcing of frequency ω_f and amplitude F , described by the equation

$$\frac{d^2u}{dt^2} - (2\epsilon\mu - u^2)\frac{du}{dt} + \omega_0^2u = F \cos \omega_f t, \quad 0 < \epsilon \ll 1, \quad (8.22)$$

where ϵ is fixed and $\mu = \mathcal{O}(1)$ is the bifurcation parameter. In the absence of forcing ($F = 0$) we know that the equilibrium position $u = 0$ is linearly stable for $\mu < 0$ and unstable for $\mu > 0$, and the nonlinear evolution of the amplitude $A(T)$ is described by the Landau equation (8.12). For forcing of amplitude of order $\epsilon^{1/2}$, i.e., $F = \epsilon^{1/2} f$ where $f = \mathcal{O}(1)$, the solvability condition implies (see Exercise 8.5.2)

$$\frac{dA}{dT} = \xi A - \frac{1}{8}|A|^2 A, \quad \xi = \mu - \frac{1}{4} \left(\frac{f}{\omega_0^2 - \omega_f^2} \right)^2. \quad (8.23)$$

We again obtain a Landau equation, showing that the equilibrium position $u = 0$ is stable for $\xi < 0$ and unstable for $\xi > 0$, with supercritical bifurcation at $\xi = 0$ (the Landau constant is real and positive). We see that, for increasing μ , the forcing decreases ξ and therefore delays the onset of the instability; the delay is larger the closer the excitation frequency ω_f is to the eigenfrequency ω_0 of the oscillator.

For nearly resonant forcing ($\omega_f \approx \omega_0$), another interesting phenomenon arises: the *locking* of the oscillator frequency to that of the forcing. Let us consider the van der Pol oscillator (8.22) for a forcing of frequency $\omega_f = \omega_0 + \epsilon\Omega$ with $\Omega = \mathcal{O}(1)$ and small amplitude $F = \epsilon^{3/2} f$ with $f = \mathcal{O}(1)$. The solvability condition at order ϵ becomes (Exercise 8.5.3)

$$\frac{dA}{dT} = \mu A - \frac{1}{8}|A|^2 A - \frac{if}{2\omega_0} e^{i\Omega T}. \quad (8.24)$$

This equation appears to be a nonautonomous Landau equation (the right-hand side depends explicitly on the time T), but if we make the change of variable $B = Ae^{-i\Omega T}$ we obtain an autonomous equation. It can then be shown that if the frequency difference $\epsilon\Omega$ is sufficiently small, the response is indeed locked to the forcing frequency. However, if the difference is too large, the oscillator “hesitates” between ω_f and ω_0 and its dynamics is *quasi-periodic* (Glendinning, 1994, §7.9).

The parametrically forced oscillator

The parametrically forced oscillator is a simple model which displays an instability frequently encountered in physics: the subharmonic instability (Bergé *et al.*, 1987). The simplest illustration of this instability is a child on a swing: a vertical oscillation of the suspended mass, which is equivalent to modulation of gravity, destabilizes the static equilibrium of the swing at rest. The instability is manifested as a vertical oscillation of the child and swing at a frequency ω_0 that is approximately one half the forcing frequency ω_f . The corresponding model equation is the Mathieu equation:

$$\frac{d^2u}{dt^2} + 2\epsilon\mu \frac{du}{dt} + \omega_0^2(1 + \epsilon f \sin \omega_f t) \sin u = 0, \quad 0 < \epsilon \ll 1. \quad (8.25)$$

The resonances exhibited by this equation can clearly be seen by rewriting it in autonomous form as two coupled oscillators, with the linearization $\sin u \sim u$ for small u :

$$\begin{aligned} \frac{d^2u}{dt^2} + 2\epsilon\mu \frac{du}{dt} + \omega_0^2 u &= -vu, \\ \frac{d^2v}{dt^2} + \omega_f^2 v &= 0. \end{aligned}$$

The solution for v is simply that of a harmonic oscillator, $v \propto \sin \omega_f t$. It can now be seen that the solution $u = 0$ is unstable when the coupling term $-vu$ in the first equation is resonant, i.e., when the forcing frequency satisfies $\omega_0 = \omega_f - \omega_0$, or $\omega_f = 2\omega_0$. Other, weaker, resonances also appear for $\omega_0 = n\omega_f - \omega_0$.

An interesting situation is that of small damping and forcing of the same order of magnitude, $\mu = \mathcal{O}(1)$, $f = \mathcal{O}(1)$, and near-resonance, $\omega_f - 2\omega_0 = 2\epsilon\Omega$ with $\Omega = \mathcal{O}(1)$. Expanding the solution for $u(t)$ as a power series in $\epsilon^{1/2}$ (see Exercise 8.5.5), the solvability condition arising at order $\epsilon^{3/2}$ is found to be

$$\frac{dA}{dT} = -\mu A + \frac{\omega_0 f}{4} A^* e^{2i\Omega T} - \frac{i\omega_0}{16} |A|^2 A.$$

This amplitude equation is nonautonomous, but, as for the van der Pol forced oscillator, it is possible to make it autonomous with the change of variable $B = Ae^{-i\Omega T}$. For further analysis see Fauve (1998, §2.2) and Exercise 8.5.5.

The best known hydrodynamic phenomenon related to the parametrically forced oscillator is the instability of a fluid layer in a container subject to vertical vibrations. The planar free surface, destabilized by the vibrations, displays a pattern of hexagonal or square cells. This was demonstrated experimentally by Faraday (1831), and later analyzed by Rayleigh (1883b, 1883c). Benjamin and Ursell (1954) have shown that the dynamics of small perturbations of the interface is governed by the Mathieu equation (8.25). More recently, many studies have analyzed weakly nonlinear effects (Miles, 1984) and, for strong forcing, chaotic behavior; see the review of Miles and Henderson (1990).

8.3 Systems with few degrees of freedom

The van der Pol and Duffing oscillators have allowed us to understand the effect of the cubic term in the Landau equation on the amplitude and phase of an oscillation. Now let us consider a system with a larger but finite number of degrees of freedom. This situation is relevant to a system governed by an equation involving

partial derivatives with respect to time and space, where the smallest possible wave number is imposed by the finite size of the system or by a periodicity condition and where, at the other end of the wave number spectrum, a dissipative process at small scales limits the number of Fourier components.

8.3.1 A model equation

Let us consider the Kuramoto–Sivashinsky (KS) model equation:

$$\partial_t u + 2Vu\partial_x u + R\partial_{xx}u + S\partial_{xxxx}u = 0. \quad (8.26)$$

This equation describes, for example, the height of the free surface of a thin film falling down an inclined plane, the position of a flame front, or the concentration of chemical species in a reactive system (Cross and Hohenberg, 1993). For $S = 0$ it becomes the Burgers equation, an elementary model which describes competing advection and diffusion. For $S > 0$ (the most common case), the fourth-order term corresponds to a dissipative process at small scales, such as surface tension in the case of the falling film.⁸

The essential features of the dynamics of a system with a *small number of degrees of freedom* can be illustrated by seeking solutions of the KS equation whose spatial structure involves a finite number N of Fourier components:

$$u(x, t) = \frac{1}{2} \sum_{n=-N}^N A_n(t) e^{ink_1 x}, \quad \text{with} \quad A_{-n} = A_n^*. \quad (8.27)$$

Here the term “degree of freedom” refers to the complex amplitudes $A_n(t)$ of the Fourier components, and the term “small” means “finite” in principle and often “two or three” in practice. We shall see that study of the spatially periodic solutions of the KS equation displays the essential role played by the harmonics in the nonlinear evolution of an unstable fundamental mode, and allows interpretation of many results obtained experimentally and/or by numerical simulation.

8.3.2 The amplitude equations

Equation (8.26) admits the solution $u_0 = 0$. Linearizing the equation for perturbations of this base solution and seeking these perturbations in the form of normal modes proportional to $e^{\sigma t + i(\omega t - kx)}$, we obtain the dispersion relation

$$\sigma + i\omega = Rk^2 - Sk^4. \quad (8.28)$$

⁸ A slightly different equation, $\partial_t u - \sin u - R\partial_{xx}u = 0$, is studied in the same spirit by Drazin and Reid (2004, §50) and Drazin (2002, §5.2), while another, $\partial_t u + u\partial_x u = Ru - (\partial_{xx} + 1)^2 u$, is studied by Manneville (1990, chapter 5).

For real k the temporal growth rate is then $\sigma = Rk^2 - Sk^4$ and the frequency ω is zero. Therefore, for $R < 0$ the solution $u_0 = 0$ is stable ($\sigma < 0$ for all k), and for $R > 0$ it is unstable to perturbations of wave number below $k_c = \sqrt{R/S}$ (such a situation where the band of unstable wave numbers spans an interval including $k = 0$ is referred to as a long-wave instability).

For positive R the unstable perturbations therefore grow exponentially, and after a time of order σ^{-1} they reach amplitudes for which nonlinear effects can no longer be ignored. By choosing k_1^{-1} as the length scale and rescaling u and t to set S to unity, we can eliminate two parameters. Then, substituting the expansion (8.27) of $u(x, t)$ into (8.26) and isolating the exponential factors e^{inx} , we obtain the following system of differential equations for the amplitudes:

$$\frac{dA_n}{dt} = \sigma_n A_n + iV \sum_{p=-\infty}^{\infty} p A_p^* A_{n+p}, \quad (8.29a)$$

$$\sigma_n = Rn^2 - n^4, \quad \text{integer } n. \quad (8.29b)$$

This system of amplitude equations corresponds to an infinite number of modes with linear growth (decay) rates σ_n which are coupled quadratically. The equation of the $n = 0$ mode reduces to $dA_0/dt = 0$, which gives $A_0 = \text{constant}$; in what follows we shall assume that this constant, which is the spatial average of u , is zero.

8.3.3 Reduction of the dynamics near threshold

As R increases the instability first occurs for $R = 1$ and according to (8.29b) the first unstable mode is the fundamental, $n = 1$. Near the instability threshold, $R \gtrsim 1$, this is the only unstable mode, as the growth rates of higher harmonics ($n = 2, 3, \dots$) remain large and negative, as shown in Figure 8.8.

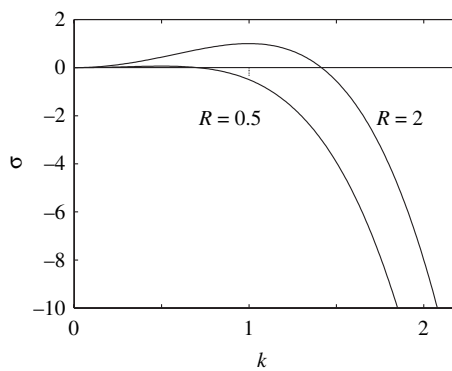


Figure 8.8 The growth rate (8.29b). The fundamental mode of wave number $k = n = 1$, stable for $R = 0.5$, is unstable for $R = 2$, while the $n = 2$ harmonic remains strongly stable.

Thus, for $R \gtrsim 1$, we expect the amplitude of the perturbation to remain small, of order $\epsilon \ll 1$, and to be dominated by the fundamental mode. Let us assume, to be confirmed later, that the amplitude of the n th harmonic is of order ϵ^n . Then, keeping the first three harmonics, the system (8.29) reduces to the dynamical system

$$\frac{dA_1}{dt} = \sigma_1 A_1 - iVA_1^* A_2 + \mathcal{O}(A_1^5), \quad (8.30a)$$

$$\frac{dA_2}{dt} = \sigma_2 A_2 - iVA_1^2 + \mathcal{O}(A_1^4), \quad (8.30b)$$

$$\frac{dA_3}{dt} = \sigma_3 A_3 - 3iVA_1 A_2 + \mathcal{O}(A_1^5). \quad (8.30c)$$

This dynamical system can be simplified further near threshold. Indeed, for $R \gtrsim 1$ only the fundamental mode A_1 is weakly unstable while the other modes are strongly damped, i.e.,

$$\sigma_1 > 0, \quad \sigma_n < 0 \quad \text{with} \quad |\sigma_n| \gg \sigma_1. \quad (8.31)$$

This means that following a very short initial transient during which the effects of initial conditions die out (due to the strong damping), the evolution of the higher modes will be driven by the forcing from the nonlinear coupling terms on the right-hand sides of (8.30b), (8.30c), etc. The time scale for the growth of the unstable mode, A_1 , is the inverse growth rate σ_1^{-1} . This is also the time scale for the evolution of the higher-order modes, so that the variation rate of all harmonics is, in order of magnitude,

$$\frac{dA_n}{dt} \sim \sigma_1 A_n. \quad (8.32)$$

Since $\sigma_1 \ll |\sigma_n|$ for $n \geq 2$, we deduce that the variation rate of the harmonics in (8.30b) and (8.30c), dA_2/dt and dA_3/dt , is much smaller than $\sigma_2 A_2$ and $\sigma_3 A_3$, respectively. Therefore, the amplitudes A_2 and A_3 are given by the quasi-static balance of the terms on the right-hand sides:

$$A_2 = \frac{iV}{\sigma_2} A_1^2 + \mathcal{O}(A_1^4), \quad (8.33a)$$

$$A_3 = \frac{3iV}{\sigma_3} A_1 A_2 + \mathcal{O}(A_1^5) \sim -\frac{3V^2}{\sigma_2 \sigma_3} A_1^3. \quad (8.33b)$$

We note that for $A_1 \sim \epsilon$ we do in fact have $A_n \sim \epsilon^n$, which conforms to the initial assumption. Substituting the above expression for A_2 into (8.30a), we find that the

dynamics of the fundamental is governed by the Landau equation:

$$\frac{dA_1}{dt} = \sigma_1 A_1 - \kappa |A_1|^2 A_1 + \mathcal{O}(A_1^5), \quad \kappa = -\frac{V^2}{\sigma_2}, \quad (8.34)$$

where the Landau constant κ is real and positive (because $\sigma_2 < 0$). Let us check the orders of magnitude. Letting $\epsilon^2 = R - 1$ be the distance from threshold, from (8.29) we have $\sigma_1 = \epsilon^2$, and the saturated amplitude for A_1 at long times is indeed of order ϵ . For times of order σ_1^{-1} all the terms of the Landau equation (8.34) are then of the same order, ϵ^3 .

Setting $A_n(t) = a_n(t)e^{i\phi_n(t)}$ and separating the real and imaginary parts, we obtain

$$\frac{da_1}{dt} = \sigma_1 a_1 - \kappa a_1^3, \quad \frac{d\phi_1}{dt} = 0. \quad (8.35)$$

We recognize the equation for a_1 as the normal form of the pitchfork bifurcation at $\sigma_1 = 0$ ($R = 1$), and that it is supercritical because κ is positive.

Therefore, near the instability threshold ($R = 1$) the weakly nonlinear dynamics of the fundamental mode is governed by a Landau equation. The dynamics of higher-order harmonics is “slaved” to that of the fundamental mode through Eqs (8.33a)–(8.33b); although these harmonics are linearly stable and strongly damped ($\sigma_n < 0$), they become finite via the weak nonlinear interaction with the fundamental mode; it is this coupling that forces the amplitude of the higher modes and “pumps” energy into them and out of the fundamental, thus leading to saturation of the instability.

The theory of dynamical systems allows the above process of reduction to the dynamics of the marginal mode to be made systematic; this systematization consists of projecting the equations of the perturbation onto a subspace of the space spanned by the amplitudes (the degrees of freedom), the so-called “central manifold.” This approach is developed in Chapter 11, as well as by Glendinning (1994), Manneville (1990, chapter 5), and Newell *et al.* (1993).

8.4 Illustration: instability of a sheared interface

The above general results are illustrated here with an experimental study of the instability of a sheared interface between two viscous fluids (Barthelet *et al.*, 1995). The experimental setup, shown schematically in Figure 8.9, consists of an annular channel of rectangular cross-section partially filled with a first liquid above which lies a second, less dense liquid (a water–glycerin mixture and a mineral oil). The channel is enclosed by an upper plate whose rotation drags the fluids, and the position of the interface is measured by conductance probes. The vertical velocity

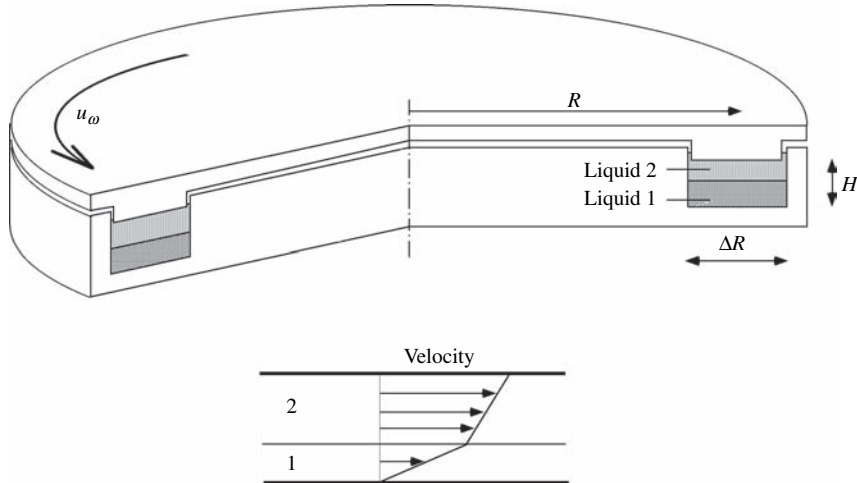


Figure 8.9 Schematic diagram of the experimental setup for studying the instability of the interface between two viscous liquids. The average diameter of the annular channel is $R = 40$ cm, $\Delta R = 4$ cm, $H = 2$ cm (from Barthelet *et al.* (1995), © Cambridge University Press, reproduced with permission).

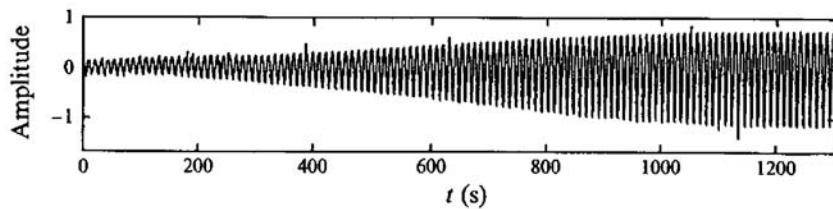


Figure 8.10 Temporal growth of the interface wave measured by the conductance probe for $U/U_c = 1.13$. The position of the interface is normalized by the saturated amplitude (from Barthelet *et al.* (1995), © Cambridge University Press, reproduced with permission).

profile is linear in the central part of the channel (plane Couette flow) as long as the centrifugal inertia effects remain weak (practically, as long as the Reynolds number is less than 100 for the aspect ratio of the experiment).

For low speeds U of the upper plate the interface remains planar (upper trace in Figure 8.11). Beyond a critical speed U_c of order 10 cm/s (the exact value depends on the fluid viscosities, densities, and heights) a wave appears at the interface, grows, and saturates at an amplitude A_{sat} , as illustrated in Figure 8.10. Its wavelength is equal to the channel perimeter and its period is about ten seconds. The profile of the saturated wave is seen more clearly in Figure 8.11 (the wave propagates as though it were “frozen,” i.e., it is a stationary wave in a rotating frame, so

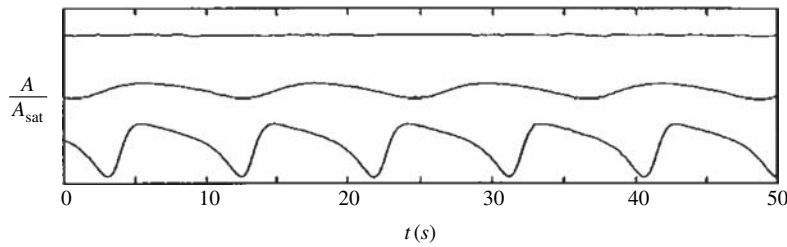


Figure 8.11 Time recording of the interface position $\eta(x_0, t)$ for three speeds U of the upper plate near the critical velocity U_c . From top to bottom: $U/U_c = 0.97$, $U/U_c = 1.06$, and $U/U_c = 1.33$ (from Barthelet *et al.* (1995), © Cambridge University Press, reproduced with permission).

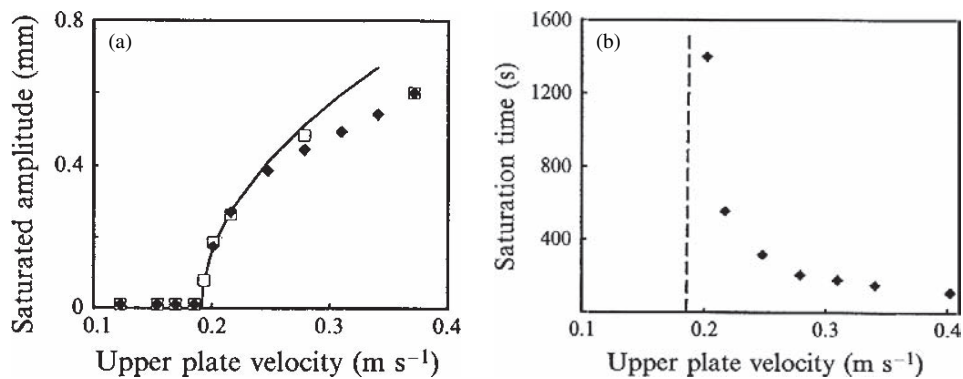


Figure 8.12 (a) Variation of the saturated amplitude A_{sat} of the interface wave for plate speeds U increasing (\blacklozenge) and decreasing (\square); (b) the saturation time (from Barthelet *et al.* (1995), © Cambridge University Press, reproduced with permission).

that a time trace gives the reversed spatial profile). This profile is nearly sinusoidal near the instability threshold (the middle trace), and then departs significantly from sinusoidal behavior farther from the threshold, with its front steeper than its tail (the lower trace).

Figure 8.12a shows the variation of the saturated amplitude of the wave, A_{sat} , with the speed U . The amplitude is zero below the critical speed U_c and then grows as the square root of the distance from the threshold, $\sqrt{U - U_c}$. The measurements made for decreasing speeds lie on those for increasing speeds, indicating that the phenomenon does not display hysteresis. The bifurcation is therefore supercritical. Figure 8.12b shows the evolution of the saturation time, i.e., the time needed to reach the saturated amplitude. We see that the saturation time is longer the closer the speed is to threshold, where it diverges (i.e. the growth rate vanishes).

Comparison with the weakly nonlinear theory presented in the preceding section requires isolating the time evolution of each spatial harmonic. This can be done by pass-band filtering about the frequency $n\omega_1^0$, where n is the mode number of the harmonic and ω_1^0 is the frequency of the fundamental mode in the initial phase of its growth (i.e., the mode with wavelength equal to the perimeter $L = 2\pi/k_1$ of the channel). These harmonics can be expressed as

$$\frac{1}{2} A_n(t) e^{in(k_1 x - \omega_1^0 t)} + \text{c.c.},$$

where $A_n(t) = |A_n(t)|e^{i\phi_n(t)}$ is the complex amplitude of the harmonic. Here we have subtracted from each amplitude $A_n(t)$ the fast evolution $n\omega_1^0 t$ of the phase corresponding to oscillation at frequency $n\omega_1^0$, and so these amplitudes contain only the slow variation $\phi_n(t)$. The modulus $|A_n(t)|$ and the slow phase $\phi_n(t)$ of each amplitude can then be obtained by a demodulation technique involving the Hilbert transform.

Figure 8.13 shows the time evolution of the moduli $|A_n(t)|$ and the slow phases $\phi_n(t)$ for the first three harmonics. Figure 8.13a, where the ordinate is on a

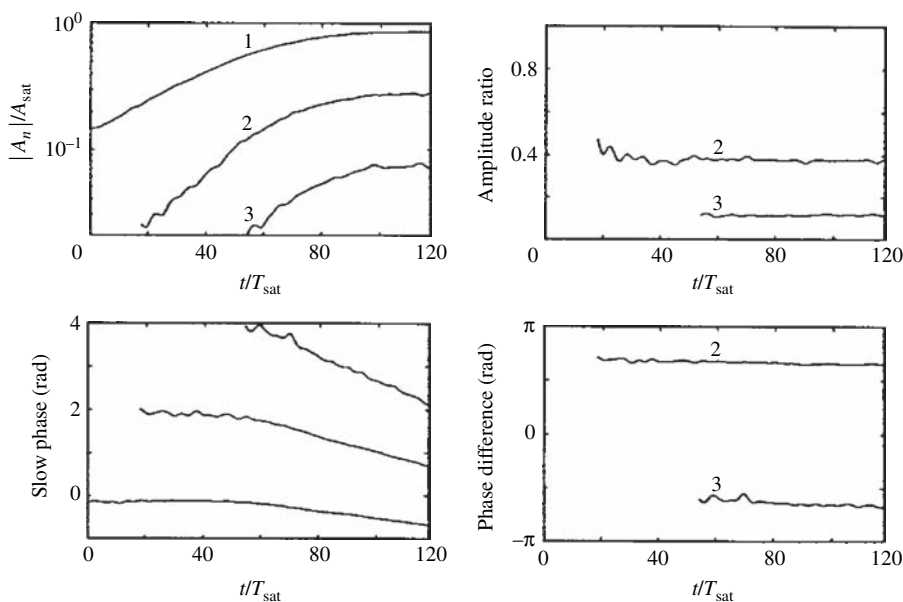


Figure 8.13 Time evolution of the amplitudes and slow phases of the first three harmonics A_1 , A_2 and A_3 (curves labeled 1, 2, 3) for $U/U_c = 1.13$; T_{sat} is the period of the saturated wave: (a) moduli normalized by the amplitude of the saturated wave; (b) ratios $|A_2|/|A_1|^2$ and $|A_3|/|A_1|^3$; (c) slow phases ϕ_1 , ϕ_2 , and ϕ_3 ; (d) slow phase differences $\phi_2 - 2\phi_1$ and $\phi_3 - 3\phi_1$ (from Barthelet *et al.* (1995), © Cambridge University Press, reproduced with permission).

logarithmic scale, displays the exponential growth followed by saturation of the fundamental mode of amplitude A_1 , with the corresponding evolutions for A_2 and A_3 . The theory developed in the preceding section is validated in the figures that follow. Figure 8.13b shows that the ratios $|A_2|/|A_1|^2$ and $|A_3|/|A_1|^3$ are indeed constant as predicted by Eqs (8.33a) and (8.33b). Figure 8.13c shows the time evolution of the slow phases; the phase ϕ_1 first appears to be constant, corresponding to the linear growth with frequency ω_1^0 ; then slowly decreases at a constant rate corresponding to a decrease of the frequency, of 0.2%. The slow phases of A_2 and A_3 evolve in the same way, with slopes that are respectively two and three times larger. Finally, Figure 8.10d shows the evolution of the phase differences $\phi_2 - 2\phi_1$ and $\phi_3 - 3\phi_1$. These differences are constant, which agrees well with the predictions of Eqs (8.33a) and (8.33b). In conclusion, the evolution of the modulus ratios and the phase differences of the complex amplitudes are well described by

$$A_2 \propto A_1^2, \quad A_3 \propto A_1^3,$$

that is, the linearly stable second and third harmonics have no dynamics of their own, but are slaved to the evolution of the linearly unstable fundamental mode. Such a behavior is observed up to $U/U_c \approx 1.6$; beyond, more complicated time evolutions arise.

8.5 Exercises

8.5.1 The van der Pol–Duffing oscillator

1. From Eq. (8.11) for u_1 , which frequencies can be expected in the spectrum of $u(t)$? How does the amplitude of a harmonic vary with its rank?
2. Show that if the term $\omega_0^2 u$ in the van der Pol equation is replaced by $\omega_0^2 \sin u$, a term involving A^2 appears in the equation for ϕ . Find the frequency of the saturated oscillations.

8.5.2 The van der Pol oscillator: restabilization

The forced van der Pol oscillator is governed by the equation

$$\frac{d^2u}{dt^2} - (2\epsilon\mu - u^2)\frac{du}{dt} + \omega_0^2 u = F \cos \omega_f t, \quad 0 < \epsilon \ll 1, \quad (8.36)$$

where $\mu = \mathcal{O}(1)$ is the bifurcation parameter. We consider that the forcing has amplitude $F = \epsilon^{1/2} f$ with $f = \mathcal{O}(1)$. Seeking a solution whose amplitude is of order $\epsilon^{1/2}$ by making the change of variable $u = \epsilon^{1/2} \tilde{u}$, $\tilde{u} = \mathcal{O}(1)$, we obtain the

following equation for \tilde{u} :

$$\frac{d^2\tilde{u}}{dt^2} + \omega_0^2\tilde{u} = \epsilon(2\mu - \tilde{u}^2)\frac{d\tilde{u}}{dt} + f \cos \omega_f t.$$

1. Use the multiple-scale method to show that at leading order the response is written as

$$u_0 = \frac{1}{2}A(T)e^{i\omega_0\tau} + \frac{f}{\omega_0^2 - \omega_f^2} \frac{e^{i\omega_f\tau}}{2} + \text{c.c.}$$

2. Show that at the next order the nonresonance condition is the Landau equation

$$\frac{dA}{dT} = \xi A - \frac{1}{8}|A|^2 A,$$

with

$$\xi = \mu - \frac{1}{4} \left(\frac{f}{\omega_0^2 - \omega_f^2} \right)^2.$$

What can be concluded about the effect of the forcing on the instability of the solution $u=0$? (Fauve, 1998, §2.3; Glendinning, 1994, §7.9).

8.5.3 The van der Pol oscillator: frequency locking

Consider the van der Pol oscillator (8.36) with nearly resonant forcing, of frequency $\omega_f = \omega_0 + \epsilon\Omega$ with $\Omega = \mathcal{O}(1)$, and small amplitude $F = \epsilon^{3/2}f$ with $f = \mathcal{O}(1)$.

1. Show that the nonresonance condition is written as

$$\frac{dA}{dT} = \mu A - \frac{1}{8}|A|^2 A - \frac{if}{2\omega_0} e^{i\Omega T}.$$

2. Show that by the change of variable $B = Ae^{-i\Omega T}$ it is possible to obtain an autonomous amplitude equation (with no explicit time dependence). Show that near resonance the frequency of the oscillator is locked to that of the forcing, and that otherwise the dynamics is quasi-periodic (Fauve, 1998, §2.3; Glendinning, 1994, §7.9).

8.5.4 The van der Pol oscillator subject to a constant forcing

Consider the van der Pol oscillator subject to a constant forcing described by the equation

$$\ddot{x} + \epsilon(x^2 - 1)\dot{x} + x = 1 + \mu, \quad \epsilon \gg 1, \quad (8.37)$$

where μ is a real parameter. For $\mu = -1$ the above equation corresponds to a relaxation oscillator, which has a stable limit cycle of amplitude close to 2. Here the problem is to determine how this limit cycle is created or destroyed when μ varies (Glendinning, 1994, §7.13).

1. Show that the above equation can be written as

$$\begin{aligned}\dot{x} &= y - \epsilon x \left(\frac{1}{3}x^2 - 1 \right), \\ \dot{y} &= -x + 1 + \mu,\end{aligned}$$

and that this dynamical system possesses a single fixed point which is stable for $\mu < -2$ and for $\mu > 0$. Which type of bifurcation probably appears at $\mu = -2$ and $\mu = 0$?

2. Study the bifurcation appearing at $\mu = 0$. Show that if the fixed point is moved to the origin by a translation of the coordinate axes, the dynamical system can be written as

$$\begin{aligned}\dot{u} &= v - \epsilon u \left(\mu(\mu+2) + (1+\mu)u + \frac{1}{3}u^2 \right), \\ \dot{v} &= -u.\end{aligned}$$

3. Show that the bifurcation is indeed a Hopf bifurcation, i.e., that the transversality condition $d\sigma_r/d\mu(\mu = 0) \neq 0$ is satisfied, where σ_r is the real part of the eigenvalue. Is the bifurcation supercritical or subcritical? Sketch the phase portrait. Find the frequency of the limit cycle and the law describing how its amplitude varies with μ .

8.5.5 The parametrically forced oscillator

Consider a forced oscillator governed by the Mathieu equation (8.25):

$$\frac{d^2u}{dt^2} + 2\epsilon\mu \frac{du}{dt} + \omega_0^2(1 + \epsilon f \sin \omega_f t) \sin u = 0, \quad \epsilon \ll 1.$$

We assume that the damping and the forcing are small and of the same order of magnitude: $\mu = \mathcal{O}(1)$, $f = \mathcal{O}(1)$ (Fauve, 1998, §2.2; Glendinning, 1994, §7.7–7.8).

1. Study the oscillator response near the resonance $\omega_f = 2\omega_0$ by seeking a solution of the form

$$u(t) = \epsilon^{1/2} \left(u_0(\tau, T) + \epsilon^{1/2} u_1(\tau, T) + \epsilon u_2(\tau, T) + \dots \right),$$

where $\tau = t$ is the fast variable describing the phase variations and $T = \epsilon t$ is the slow variable describing the amplitude variation (*cf.* the solution of the van der Pol equation). Show that for the first three orders $\epsilon^{1/2}$, ϵ^1 , and $\epsilon^{3/2}$ the series of differential equations to be solved is

$$\begin{aligned} Lu_0 &= 0 \quad \text{with } L = \frac{\partial^2}{\partial \tau^2} + 1, \\ Lu_1 &= 0, \\ Lu_2 &= -2 \frac{\partial^2 u_0}{\partial \tau \partial T} - 2\mu \frac{\partial u_0}{\partial \tau} - \omega_0^2 f u_0 \sin \omega_f t + \frac{1}{6} \omega_0^2 u_0^3. \end{aligned}$$

2. Show that at order $\epsilon^{3/2}$ the nonresonance condition (the condition for the right-hand side not to be resonant, i.e., the condition for u_2 to remain bounded over time) is written as

$$\frac{dA}{dT} = -\mu A + \frac{\omega_0 f}{4} A^* e^{2i\Omega T} - \frac{i\omega_0}{16} |A|^2 A,$$

where the distance from resonance is assumed to be small: $\omega_f - 2\omega_0 = 2\epsilon\Omega$ with $\Omega = \mathcal{O}(1)$. (As for the van der Pol oscillator, the solution at order ϵ^1 has the same form as that at order $\epsilon^{1/2}$ and does not enter at order $\epsilon^{3/2}$, and so without loss of generality we can set $u_1 = 0$.)

3. Show that by the change of variable $B = Ae^{-i\Omega T}$ it is possible to obtain an autonomous amplitude equation. Taking B to be the amplitude of the motion, what is the frequency of the oscillations of $u(t)$?
4. Study the linear stability of the rest state $B = 0$ by setting $B = X + iY$ and determining the system of two ordinary differential equations (ODE) with real coefficients satisfied by X and Y . Study the linear stability of the fixed point $(0, 0)$. Sketch the evolution of the two eigenvalues in the complex plane as the forcing increases. Determine the domains of stability and instability in the (Ω, f) plane. Show that the forced response is quasi-periodic in the stable domain and that there is frequency locking in the unstable domain. Additional problem: find the explicit expression for the response of an oscillator initially at rest ($u(0) = du/dt(0) = 0$) in the unstable case.
5. Study the nonlinear stability by setting $B = be^{i\phi}$ and finding the system of two ODE with real coefficients satisfied by b and ϕ . Show that the fixed points of this system (the stationary states for the amplitude B) correspond to

$$b_0 = 0,$$

$$\frac{\omega_0}{16} b_0^2 = -\Omega \pm \sqrt{F^2 - \mu^2} \text{ for } F = \frac{\omega_0 f}{4} \geq \mu.$$

Represent these stationary states in the (F^2, b_0^2) plane, distinguishing the cases $\Omega < 0$ and $\Omega > 0$. Setting $b = b_0 + b'$ and $\phi = \phi_0 + \phi'$ and linearizing the equations, determine the linear stability of the solutions $b_0 \neq 0$ (the stability of the solution $b_0 = 0$ has been studied in the preceding question).

6. Use the preceding results to derive the bifurcation diagrams of the parametrically forced oscillator in the (F^2, b_0^2) plane for $\Omega < 0$ and for $\Omega > 0$. In each case specify the nature of the bifurcation when the rest state $B = 0$ becomes unstable.

8.5.6 Weakly nonlinear dynamics of the KS–KdV equation

In this exercise we derive the Landau equation for the partial derivative equation

$$\partial_t u + c_0 \partial_x u + 2Vu \partial_x u + R \partial_{xx} u + M \partial_{xxx} u + S \partial_{xxxx} u = 0. \quad (8.38)$$

This equation is a combination of the Kuramoto–Sivashinsky equation (8.26) ($c_0 = M = 0$) and the Korteweg–de Vries equation ($R = S = 0$; see Chapter 9). It describes the propagation of nonlinear waves in a weakly dispersive medium.

1. Show that for k real (temporal stability) the dispersion relation is written as

$$\sigma(k) = Rk^2 - Sk^4, \quad \omega = c_0 k - Mk^3.$$

Discuss this equation (the instability condition, the wave speed of the normal modes).

2. Seek a nonlinear solution by means of a series similar to (8.27):

$$u(x, t) = \frac{1}{2} \sum_{n=-\infty}^{\infty} A_n(t) e^{in(k_1 x - \omega(k_1)t)}, \quad \text{with } k_1 = 1, \quad A_n = A_n^*$$

(setting $k_1 = 1$ amounts to defining the length scale and does not lead to loss of generality of the problem). Assuming that the amplitudes vary slowly, the above series is valid only when the frequency $\omega(k_n)$ of the n th harmonic is close to $n\omega(k_1)$, which corresponds to weakly dispersive waves, so that M must be small. Show that the system of amplitude equations is

$$\frac{dA_n}{dt} = (\sigma_n + in(n^2 - 1)M) A_n + iV \sum_{p=-\infty}^{\infty} p A_p^* A_{n+p},$$

where $\sigma_n = \sigma(n) = Rn^2 - Sn^4$.

3. Show that the above system, truncated after the first three harmonics A_1 , A_2 , and A_3 , is identical to the system (8.30a)–(8.30c) when σ_2 and σ_3 are respectively replaced by $(\sigma_2 + 6iM)$ and $(\sigma_3 + 24iM)$. Then show that near threshold

the system reduces to

$$\begin{aligned}\frac{dA_1}{dt} &= \sigma_1 A_1 - \kappa |A_1|^2 A_1 + \mathcal{O}(A_1^5), & \kappa &= -\frac{V^2}{\sigma_2 + 6iM}, \\ A_2 &= \frac{iV}{\sigma_2 + 6iM} A_1^2 + \mathcal{O}(A_1^4), \\ A_3 &\propto A_1^3 + \mathcal{O}(A_1^5).\end{aligned}$$

Setting $A_n(t) = a_n(t)e^{i\phi_n(t)}$ and separating the real and imaginary parts, show that

$$\begin{aligned}\frac{da_1}{dt} &= \sigma_1 a_1 - \kappa_r a_1^3, \\ \frac{d\phi_1}{dt} &= -\kappa_i a_1^2.\end{aligned}$$

4. How do these equations differ from those obtained starting from the Kuramoto–Sivashinsky equation? Find the explicit expression for $u(x, t)$ and determine the order of magnitude of the neglected terms.

9

Nonlinear dispersive waves

9.1 Introduction

When a fluid is locally perturbed by an impulse (for example, by an impact) or a periodic excitation (the vibration of a membrane, string, or mechanical blade), the perturbation may propagate from the source in the form of a wave. Examples include acoustic waves, surface waves, and internal waves in a stratified fluid (Lighthill, 1978). The solution of the linearized equations for small amplitude perturbations leads to a major result: the wave number k and frequency ω (or the wave speed $c = \omega/k$) are not independent, they are related by a dispersion relation. Since this relation is obtained from linearized equations, another major result is that dispersion does not depend on the amplitude of the perturbation. However, if the amplitude exceeds some level, new effects arise that the dispersion relation of linear theory obviously does not describe. To explain these new effects it is necessary to include nonlinear terms neglected in the linear study, i.e., to develop a theory of *nonlinear waves*. Such waves are also referred to as *finite-amplitude waves*, in contrast to the waves of infinitesimal amplitude considered in a linear analysis.

The objective of the present chapter is to give an elementary account of the theory of nonlinear waves. We will show (i) how nonlinear waves can be constructed by a perturbation method (essentially the multiple-scale method presented in the preceding chapter), and (ii) how the linear stability of these waves can be studied. This analysis is based on a great classic of hydrodynamics, the problem of gravity waves. Its analysis was initiated by G. G. Stokes (1847), who made a decisive advance in the field: a history of further developments in the field can be found in the articles by A. D. D. Craik (2004, 2005) and O. Darrigol (2003, 2005). Gravity waves have become a paradigm for nonlinear waves: the study of waves in elastic solids, optical or electromagnetic waves, and, more generally, waves propagating in weakly dissipative dispersive media is based on the

same ideas and uses the same analysis techniques (Whitham, 1974; Billingham and King, 2000). In this chapter we shall neglect dissipative effects, which we justify by considering the orders of magnitude: for a gravity wave of wavelength 100 m in deep water, the ratio of the inertial forces to the viscous forces is of order $\omega/vk^2 = \sqrt{gk}/vk^2 = 2 \times 10^8$. Dissipative effects will be reintroduced in the next chapter.

In the following section we present the nonlinear Stokes wave along with the experimental evidence for its instability (Benjamin and Feir, 1967). This instability can be interpreted in two different ways (thus highlighting two different aspects of the problem), namely in terms of *resonances* among Fourier modes, or in terms of the *modulation instability* of the envelope of a quasi-monochromatic wave. These two interpretations are presented in Sections 9.3 and 9.4. The ideas and calculational methods are illustrated by the model problem of masses coupled by springs, where the continuum limit is governed by a classical equation of field theory, the *Klein–Gordon equation*. This model problem has the advantage of containing all the essential physics (dispersion and nonlinearities), while requiring much less computing than typical hydrodynamics problems. In the final section of the chapter we return to the problem of resonances.

9.2 Instability of gravity waves

9.2.1 Stokes waves

Let us consider a gravity wave propagating on the surface of a deep fluid, where viscosity and surface tension effects are negligible. If we further assume the motion to be irrotational, the velocity field is governed by Laplace's equation for the velocity gradient. The condition of constant pressure at the interface then couples the velocity potential to the pressure and the wave height through Bernoulli's equation. For a wave of wave number k_0 , frequency ω_0 , small amplitude a_0 (more precisely, wave slope $k_0 a_0 \ll 1$), and large fluid depth h (more precisely, $k_0 h \gg 1$), solution of the linearized problem for small amplitude waves on deep water gives the dispersion relation (see Chapter 2, or Lighthill (1978)):

$$\omega_0^2 = gk_0. \quad (9.1)$$

However, observation shows that a gravity wave on the surface of the ocean, for example, differs from a sinusoidal wave: it displays sharper crests and flatter troughs. This implies that the wave profile contains harmonics and that these harmonics propagate at the same speed as the fundamental. However, this is forbidden by the expression (9.1), which means that nonlinear phenomena must be involved. Furthermore, observation shows that the relation (9.1) is not really accurate. We

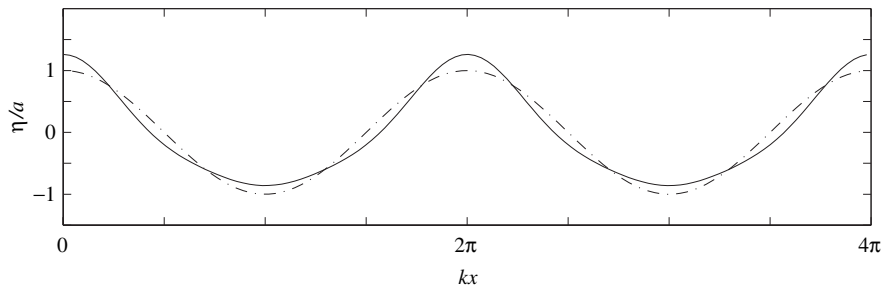


Figure 9.1 (—) Stokes wave (9.2) for $ka = 0.4$; (− · −) a sinusoidal wave.

are indebted to Stokes (1847) for resolving these issues. Using a series expansion in powers of the wave slope, the profile of the free surface $\eta(x, t)$ is found to be (Lamb, 1932, §250; Whitham, 1974, §13.13)

$$\frac{\eta(x, t)}{a_0} = \frac{k_0 a_0}{2} + \cos \theta + \frac{k_0 a_0}{2} \cos 2\theta + \frac{3(k_0 a_0)^2}{8} \cos 3\theta + \mathcal{O}[(k_0 a_0)^3], \quad (9.2)$$

where the phase θ and the frequency ω are defined as

$$\theta = k_0 x - \omega t, \quad \omega^2 = \omega_0^2 \{1 + k_0^2 a_0^2 + \mathcal{O}[(k_0 a_0)^4]\}.$$

The profile of this wave is shown in Figure 9.1, where we compare it to a sinusoidal wave. Its frequency ω is not quite equal to the frequency ω_0 of a wave of infinitesimal amplitude; to leading order it is given by

$$\frac{\omega}{\omega_0} = 1 + \frac{1}{2} k_0^2 a_0^2. \quad (9.3)$$

These results display two qualitatively new phenomena compared to the linear theory. The first is that a wave of finite amplitude can propagate without deformation, with the harmonics propagating at the same speed as the fundamental (which *a priori* is not at all obvious since linear waves are dispersive). The second is that the dispersion relation (9.3) involves the amplitude: the frequency of a wave of wave number k_0 , and therefore the wave speed $c_0 = \omega_0/k_0$, grows with the amplitude. Thus we have a wave of permanent form that exhibits both wave number dispersion and *amplitude dispersion*. In Exercise 9.6.2 we propose the calculation of a nonlinear wave similar to (9.2) using the Klein–Gordon equation.

George Gabriel Stokes (1819–1903)

George Gabriel Stokes was born in Skreen, County Sligo, Ireland, into a very religious Protestant family. His father was the minister of the parish of Skreen, and each of his three older brothers also became ministers. He studied in Dublin and later Bristol, where he was noticed for his talent in mathematics. In 1837 he entered Pembroke College at Cambridge, where he proved to be a brilliant student. His tutor William Hopkins advised him to undertake research in hydrodynamics. He was given a Fellowship by Pembroke College starting in 1841.

In 1845 he published a paper entitled *On the theories of the internal friction of fluids in motion*, where he derived the equations of motion of a viscous flow, and demonstrated their relationship to those of an elastic solid (in fact, these equations had been obtained earlier by Navier (1821) and then by Poisson and Saint-Venant (1843), who contributed the correct treatment of the viscous stresses, but those studies were not known in Cambridge). He did a number of studies in optics, on chromatic aberrations (1845), on diffraction (1849) (Cauchy also studied this problem), and on Fraunhofer lines in the solar spectrum (1854). He published a work of major importance on geodesy, *On the variation of gravity at the surface of the earth*, in 1849. He was appointed Lucasian Professor of Mathematics at Cambridge that same year and was elected to the Royal Society in 1851. He wrote a major work on the motion of a sphere in a viscous flow in 1851. In 1852 he named and explained the phenomenon of fluorescence using a molecular theory involving an elastic aether. He married in 1857, which required that he give up his Fellowship at Pembroke College, since at that time Fellows had to be single. His career then took a different turn, becoming more oriented towards experimental work and administration. He served as president of the Royal Society from 1885 until 1890, and of the Victoria Institute from 1886 until his death in 1903. He was awarded the Copley Medal by the Royal Society in 1893. Stokes's influence is summed up well by Parkinson: "... Stokes was a very important formative influence on subsequent generations of Cambridge men, including Maxwell. With Green, who in turn had influenced him, Stokes followed the work of the French, especially Lagrange, Laplace, Fourier, Poisson, and Cauchy. This is seen most clearly in his theoretical studies in optics and hydrodynamics; but it should also be noted that Stokes, even as an undergraduate, experimented incessantly."

Yet his interests and investigations extended beyond physics, for his knowledge of chemistry and botany was extensive, and often his work in optics drew him into those fields." Stokes' papers were published in five volumes, the first three edited by Stokes himself and the last two by Sir Joseph Larmor.

9.2.2 The Benjamin–Feir instability

The wave train produced by an oscillating paddle located at one end of a channel does not remain uniform as it propagates, but degenerates into a series of wave groups and eventually disintegrates, as seen in the photographs in Figure 9.2. This well-known phenomenon was for a long time thought to be caused by imperfections in the paddle motion, and attempts were made to minimize them by modifying the design. After trying in vain to correct the problem, Benjamin and Feir turned to theory and showed that the phenomenon in fact was not related to the paddle, but was the result of an intrinsic instability of the Stokes wave (Benjamin and Feir, 1967; Hunt, 2006). It was then realized that this instability is very general: it is an instability of a monochromatic dispersive wave, of wave number k_0 , to perturbations with nearby wave numbers $k_0 + \delta k$, now known as a *side-band instability* (Phillips, 1981). These perturbations, which are unavoidably

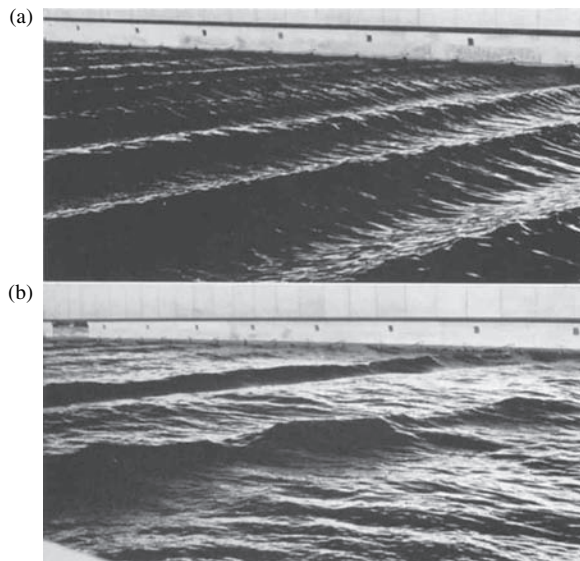


Figure 9.2 Photographs of a progressive wave train at two stations, illustrating disintegration due to instability: (a) view near the wave-maker; (b) view at 60 m farther from the wave-maker. Fundamental wavelength, 2.20 m. From Benjamin and Hasselman (1967).

present in any experiment, grow exponentially via a resonance mechanism when

$$\frac{\delta k^2}{k_0^2} < 8(k_0 a_0)^2, \quad (9.4)$$

that is, when their wave number lies in a narrow band about k_0 . Using the dispersion relation (9.1), the frequency of these perturbations is found to lie inside the narrow range $\omega_0(1 \pm \sqrt{2}k_0 a_0)$. The two most highly amplified perturbations are those with wave numbers $k_0(1 \pm 2k_0 a_0)$, and their growth rate is

$$\sigma_{\max} = \frac{\omega_0}{2}(k_0 a_0)^2. \quad (9.5)$$

We note that this maximum growth rate is equal to the nonlinear correction to the frequency, see (9.3).

The experiments performed by Lake *et al.* (1977) confirmed Benjamin's analysis, as shown in Figures 9.3, 9.4, and 9.5. Figure 9.3 shows time recordings of the interface position at various distances from the paddle; the amplification of the modulations is clearly seen. Figure 9.4 shows the corresponding amplitude spectra, which display the growth of wave numbers close to the fundamental. The growth of perturbations with frequency close to those of the harmonics is also clearly seen. Figure 9.5 compares the measurements by Lake *et al.* (1977) of the growth of the amplitude of the perturbation to the predictions of Benjamin and Feir (1967); the agreement is seen to be excellent.

As announced in the introduction, rather than presenting the hydrodynamical study of Benjamin and Feir, here we shall discuss a simpler model problem illustrating the general nature of the side-band instability of a dispersive nonlinear wave.

9.3 Instability due to resonant interactions

9.3.1 The model problem

The model equation used here to display the instability of a wave due to resonant interactions is the nonlinear Klein–Gordon equation:

$$\frac{\partial^2 u}{\partial t^2} - \frac{\partial^2 u}{\partial x^2} = -V'(u), \quad V(u) = \frac{u^2}{2} + \gamma u^4, \quad (9.6)$$

where $V'(u)$ is the derivative of the potential $V(u)$ and γ is a real parameter. This equation is a generalization of the classical equation for linear waves which

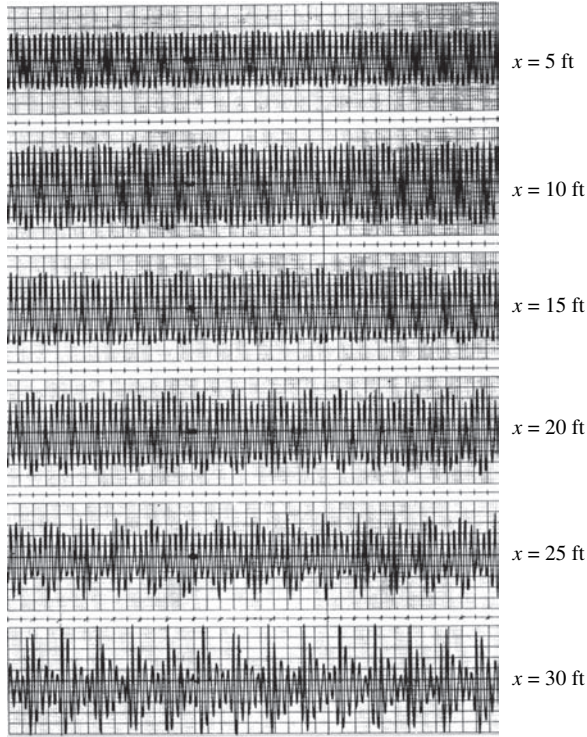


Figure 9.3 Time recording of a gravity wave in a channel measured at various distances x from the paddle, showing the growth of a modulation on an initially unmodulated wave train (Lake *et al.*, 1977).

is ubiquitous in physics (Whitham, 1974, §14; Fauve, 1998, §3; Dauxois and Peyrard, 2006, chapter 2)¹.

Equation (9.6) corresponds to a continuum modeling of a chain of elastically coupled pendulums (Duffing oscillators), as shown schematically in Figure 9.6. Each pendulum consists of a mass m at the end of a stem of length l which is articulated at its other end, with angular position measured by the angle u . Each mass oscillates in the gravity potential $-mgl \cos u$ and is coupled to its two nearest neighbors by a torsional spring with spring constant C . The equation of motion is then written as

$$ml^2 \frac{\partial^2 u}{\partial t^2} = -mgl \sin u + C(u_{n+1} - 2u_n + u_{n-1}). \quad (9.7)$$

¹ A similar equation possessing a quadratic nonlinearity, $\partial_{tt}u + \partial_{xx}u + \partial_{xxxx}u + u = u^2$, is discussed by Drazin and Reid (2004, §51.2).

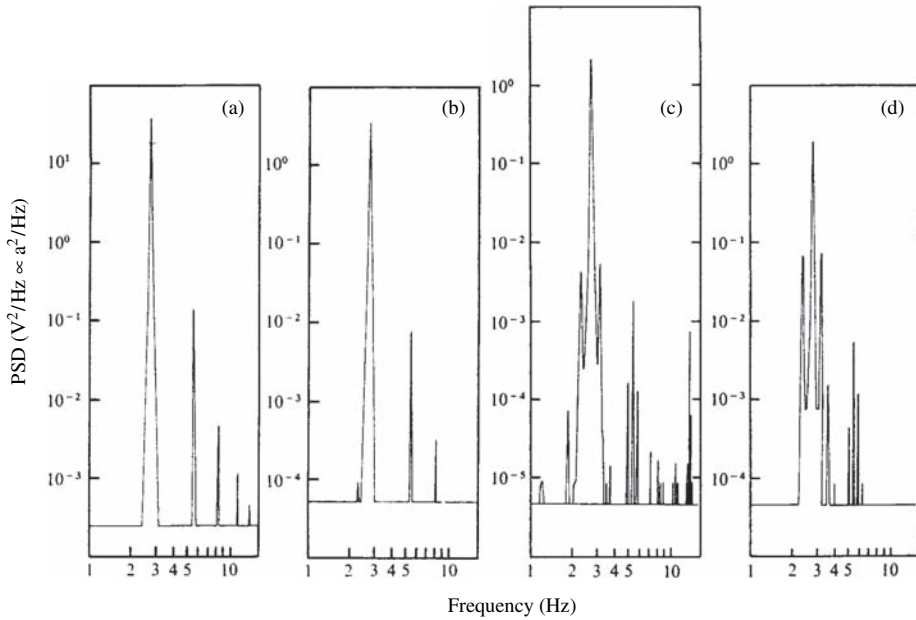


Figure 9.4 Power spectra (PSD = power spectral density) corresponding to the time recordings in Figure 9.3: (a) $x = 5$ ft, (b) $x = 10$ ft, (c) $x = 20$ ft, (d) $x = 30$ ft (Lake *et al.*, 1977).

In the limit where the wavelengths in question are large compared to the distance between two oscillators, (9.7) reduces to the equation $\partial_{tt}u - \partial_{xx}u = -\sin u$ (the sine-Gordon equation) after an appropriate choice of the time, mass, and length scales.² For small amplitudes the sine-Gordon equation corresponds to the Klein–Gordon equation (9.6) with $\gamma = -1/24$.

9.3.2 A nonlinear Klein–Gordon wave

The dispersion relation

Linearizing (9.6) about the base solution $u = 0$ and using the normal modes $u \propto e^{i(kx - \omega t)}$, we obtain the dispersion relation:

$$\omega^2 = 1 + k^2. \quad (9.8)$$

This relation shows that perturbations of infinitesimal amplitude propagate at a speed $c = \omega/k$ depending on the wave number, so that waves are dispersive.

² It is easy to recognize the nearest-neighbor interaction terms as being related to the centered finite difference approximation for $\partial_{xx}u$.

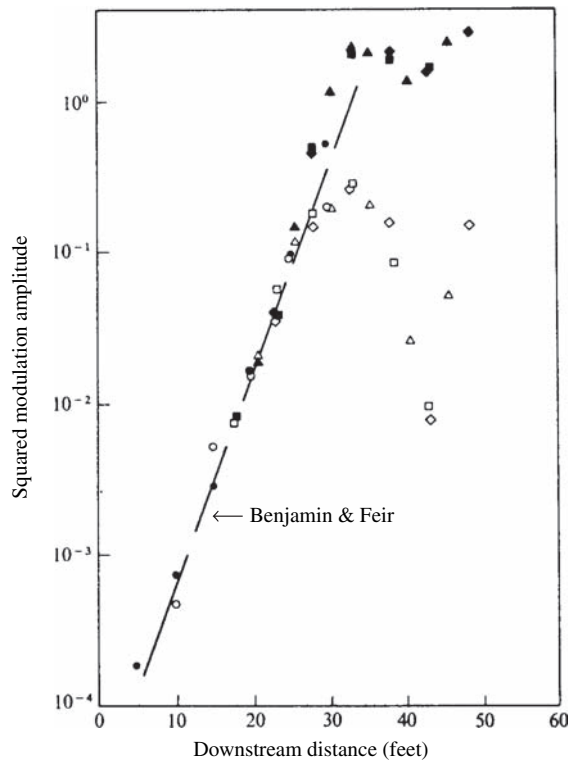


Figure 9.5 Spatial growth of the amplitude of perturbations with wave number close to the fundamental: comparison of the measurements made by Lake *et al.* (1977) to the predictions (9.5) of Benjamin and Feir (1967). Dark symbols: the perturbation $\omega_0 - \Delta\omega$, light symbols: the perturbation $\omega_0 + \Delta\omega$ ($f_0 = \omega_0/2\pi = 2.5$ Hz, $ka_0 = 0.16$).

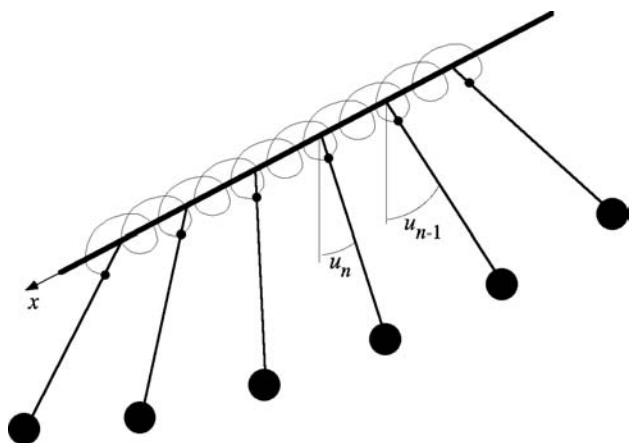


Figure 9.6 A chain of elastically coupled pendulums.

The amplitude equations

We seek a traveling wave solution³ propagating in the direction of increasing x ($c = \omega/k > 0$) in the form of a finite sum of Fourier components of small amplitude (Whitham, 1974, §15.6):

$$u(x, t) = \frac{1}{2} \sum_{n=-N}^N \epsilon \hat{u}_n(t) e^{ik_n x}, \quad (9.9)$$

with

$$k_{-n} = -k_n, \quad \hat{u}_{-n} = \hat{u}_n^* = \mathcal{O}(1), \quad \epsilon \ll 1.$$

Substituting this series into the Klein–Gordon equation (9.6), we obtain the following equation satisfied by each Fourier component:

$$\frac{d^2 \hat{u}_n}{dt^2} + \omega_n^2 \hat{u}_n = -\epsilon^2 \gamma \sum_{k_p+k_q+k_r=k_n} \hat{u}_p \hat{u}_q \hat{u}_r. \quad (9.10)$$

The right-hand side corresponds to the coupling among Fourier modes, and of course originates from the cubic nonlinearity of the initial equation. This coupling, of order ϵ^2 , is weak, and so for each Fourier mode we can expect a nonlinear solution close to the linear solution proportional to $e^{-i\omega_n t}$. We therefore seek $\hat{u}_n(t)$ in the form

$$\hat{u}_n(t) = A_n(t) e^{-i\omega_n t}, \quad (9.11)$$

with

$$A_{-n} = A_n^* = \mathcal{O}(1), \quad \omega_n = \sqrt{1+k_n^2} \quad \text{for } k_n > 0, \quad \omega_{-n} = -\omega_n,$$

where the time dependence of the amplitude allows nonlinear effects to be taken into account. Substituting (9.11) into (9.10), we obtain

$$\frac{d^2 A_n}{dt^2} - 2i\omega_n \frac{dA_n}{dt} = -\epsilon^2 \gamma \sum_{k_p+k_q+k_r=k_n} A_p A_q A_r e^{i(\omega_n - \omega_p - \omega_q - \omega_r)t}.$$

This equation shows that the time scale of the nonlinear interactions is of order ϵ^{-2} , which suggests that we introduce a slow time scale $T = \epsilon^2 t$ (the analogy with the analysis of the Duffing oscillator should be noted). The second derivative with

³ For solutions of the solitary-wave type see Whitham (1974, §17.10); Fauve (1998, §3.2); Dauxois and Peyrard (2006, chapter 2).

respect to time then appears as a negligible term of order ϵ^4 , and we obtain the amplitude equation for the n th mode:

$$\frac{dA_n}{dT} = -\frac{i\gamma}{2\omega_n} \sum_{k_p+k_q+k_r=k_n} A_p A_q A_r e^{i(\omega_n - \omega_p - \omega_q - \omega_r)T/\epsilon^2}. \quad (9.12)$$

This equation corresponds to an interaction among Fourier modes whose wave numbers satisfy the condition $k_p + k_q + k_r = k_n$. This interaction leads to remarkable solutions, in particular, when the argument of the exponential vanishes, that is, when the frequencies satisfy the *resonance condition*

$$\omega_p + \omega_q + \omega_r = \omega_n. \quad (9.13)$$

We note that owing to the dispersion relation (9.8), the quadruplets of waves which satisfy $k_p + k_q + k_r = k_n$, together with the above resonance equation, are very special.

A monochromatic nonlinear wave

Let us consider the simple and important case of the resonant interaction of a monochromatic wave of wave number k_0 with itself (self-interaction). The summation in (9.9) runs over the two wave numbers k_0 and $-k_0$. Among the 2^3 triads $(\pm k_0, \pm k_0, \pm k_0)$, only three satisfy the condition $k_p + k_q + k_r = k_0$ and the resonance condition (9.13), namely, $(k_0, k_0, -k_0)$, $(k_0, -k_0, k_0)$, and $(-k_0, k_0, k_0)$. The amplitude equation (9.12) for A_0 then reduces to

$$\frac{dA_0}{dT} = -i\beta A_0^2 A_0^*, \quad (9.14)$$

with

$$\beta = \frac{3\gamma}{2\omega_0}, \quad \omega_0 = \sqrt{1 + k_0^2}.$$

The solution of this equation is

$$A_0 = a_0 e^{-i\beta a_0^2 T}, \quad a_0 = \mathcal{O}(1) \text{ real}, \quad (9.15)$$

or, returning to the original angular variable $u(x, t)$,

$$u(x, t) = \epsilon a_0 \cos(k_0 x - \omega t) + \mathcal{O}(\epsilon^3), \quad (9.16a)$$

$$\omega = \omega_0 + \beta (\epsilon a_0)^2, \quad (9.16b)$$

which is valid for t of order ϵ^{-2} .

Therefore, the frequency and speed of the wave of finite amplitude (9.16) are modified by the self-interaction due to the cubic nonlinearity of the Klein–Gordon

equation, so that now they depend on the amplitude. We note that the frequency correction is exactly the same as that of a simple Duffing oscillator! Moreover, this correction is very similar to the result (9.2)–(9.3) obtained by Stokes for gravity waves. A more complete calculation including two harmonics is the subject of an exercise.

9.3.3 Instability of a monochromatic nonlinear wave

Instability of the Klein–Gordon wave (9.16)

Let us now consider the effect of a perturbation of the monochromatic wave (9.16) in the form of two waves with wave numbers $k_0 \pm \epsilon K$, $K = \mathcal{O}(1)$, close to k_0 , frequencies ω_{\pm} , and amplitudes $|A_{\pm}| \ll |A_0|$. Keeping only the dominant terms, the system (9.12) reduces to

$$\frac{dA_0}{dT} = -i\beta A_0^2 A_0^*, \quad \beta = \frac{3\gamma}{2\omega_0}, \quad \omega_0 = \sqrt{1+k_0^2}, \quad (9.17a)$$

$$\frac{dA_-}{dT} = -i\beta(2A_0 A_0^* A_- + A_0^2 A_+^* e^{i\Omega T}), \quad (9.17b)$$

$$\frac{dA_+}{dT} = -i\beta(2A_0 A_0^* A_+ + A_0^2 A_-^* e^{i\Omega T}), \quad (9.17c)$$

with

$$\Omega = \frac{1}{\epsilon^2}(\omega_+ + \omega_- - 2\omega_0) \approx \omega_0'' K^2 = \mathcal{O}(1), \quad \omega_0'' = \frac{\partial^2 \omega}{\partial k^2}(k_0) = \omega_0^{-3}.$$

Equation (9.17a), which is identical to (9.14), describes the self-interaction, and its solution is given by (9.15) (the effect of the perturbations on A_0 is of higher order). Equations (9.17b) and (9.17c) describe the evolution of the perturbation: the first term on the right-hand sides corresponds to the exact resonance $\omega_{\pm} = \omega_0 - \omega_0 + \omega_{\pm}$ and the second to a near-resonance. Substituting the solution (9.15) into (9.17b) and (9.17c), we find

$$\frac{dA_-}{dT} = -i\beta a_0^2 \left(2A_- + A_+^* e^{i(\Omega - 2\beta a_0^2)T} \right), \quad (9.18a)$$

$$\frac{dA_+}{dT} = -i\beta a_0^2 \left(2A_+ + A_-^* e^{i(\Omega - 2\beta a_0^2)T} \right). \quad (9.18b)$$

Replacing (9.18b) by its complex conjugate, we obtain a linear system in A_- and A_+^* which is nonautonomous (it depends explicitly on time). This system can be made autonomous by the change of variable $B_{\pm} = A_{\pm} e^{i\rho T}$ corresponding to a rotation in the complex plane, and by substitution we easily find that we require $\rho = \beta a_0^2 - \Omega/2$. The resulting system is an eigenvalue problem which has solutions

of the form $B \sim e^{\sigma T}$ provided that σ is an eigenvalue, i.e., that it satisfies the characteristic polynomial

$$\sigma^2 + \beta\omega_0''a_0^2 K^2 + \frac{\omega_0''^2}{4} K^4 = 0, \quad (9.19)$$

where we have used $\Omega = \omega_0''K^2$. If $\beta\omega_0''$ is positive, the roots of this polynomial are purely imaginary, and the nonlinear wave (9.16) is linearly stable. If $\beta\omega_0''$ is negative, the roots are real and of opposite sign for K below a cutoff wave number

$$K_{\text{off}} = 2a_0 \sqrt{-\frac{\beta}{\omega_0'}} \quad (9.20)$$

and are given by

$$\sigma_{\pm} = \pm\sigma_{\text{ref}} \sqrt{\frac{K^2}{K_{\text{off}}^2} - \frac{K^4}{K_{\text{off}}^4}}, \quad \sigma_{\text{ref}} = 2|\beta|a_0^2. \quad (9.21)$$

The perturbation associated with σ_+ grows and therefore the nonlinear wave (9.16) is linearly unstable.

Finally, a necessary condition for instability is

$$\beta\omega_0'' < 0. \quad (9.22)$$

When this condition is satisfied, the wave is unstable to side-band perturbations of wave numbers $k = k_0 \pm \epsilon K$ with $K < K_{\text{off}}$.

Figure 9.7a shows the variation of $\sigma^2/\sigma_{\text{ref}}^2$ with K^2/K_{off}^2 in the two cases $\beta\omega_0'' < 0$ (unstable) and $\beta\omega_0'' > 0$ (stable). Figure 9.7b shows the normalized growth rates $\sigma_r/\sigma_{\text{ref}}$ and $\sigma_{-r}/\sigma_{\text{ref}}$ of the two modes as functions of $|K|/K_{\text{off}}$ for the

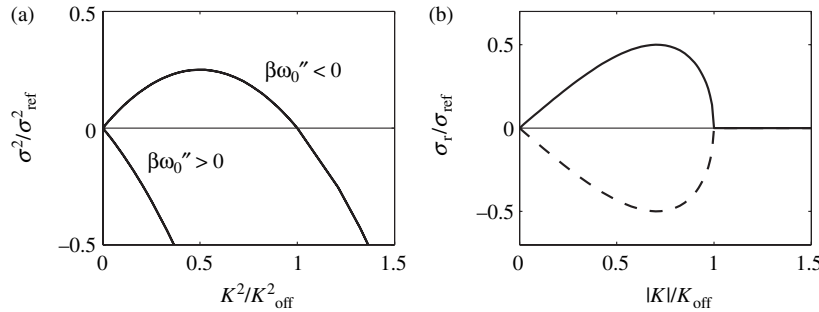


Figure 9.7 (a) The normalized squared eigenvalue corresponding to the dispersion relation (9.19) as a function of K^2/K_{off}^2 ; (b) for $\beta\omega_0'' < 0$, the normalized growth rates of the two modes as functions of $|K|/K_{\text{off}}$: (—) σ_{+r} , (--) σ_{-r} .

unstable case. Using (9.21) it is easily verified that the two most amplified wave numbers are

$$k_{\max} = k_0 \pm \frac{1}{\sqrt{2}} \epsilon K_{\text{off}}. \quad (9.23)$$

The Klein–Gordon wave, for which $\omega''_0 = \omega_0^{-3}$ and $\beta = 3\gamma/2\omega_0$, is therefore stable if γ is positive and unstable otherwise. Thus, a chain of pendulums (for which $\gamma = -1/24$) is unstable.

The Stokes wave instability revisited

The instability condition (9.22) established for the Klein–Gordon wave (9.16) is actually general: it is valid for any dispersive nonlinear wave, with ω''_0 given by the dispersion relation for waves of infinitesimal amplitude and β the coefficient of the nonlinear correction $\beta(\epsilon a_0)^2$ to the frequency. For example, for a gravity wave we obtain from the dispersion relation (9.3) for finite-amplitude waves found by Stokes:

$$\omega''_0 = -\frac{\omega_0}{4k_0^2}, \quad \beta = \frac{1}{2}\omega_0 k_0^2.$$

The instability condition (9.22) is then written as

$$(\epsilon K)^2 < 8k_0^4(\epsilon a_0)^2.$$

We recover the identical instability condition (9.4) obtained by Benjamin and Feir (1967) in their solution of the hydrodynamical problem! This is no accident, as the instability results from a competition between the linear dispersion and the nonlinearity, the effect of the latter being contained entirely in the nonlinear correction of the wave frequency.

9.4 Instability to modulations

The Benjamin–Feir instability of a nonlinear wave, interpreted above in terms of resonant interactions, can also be interpreted as an instability to long-wavelength modulations (Benney and Newell, 1967; Stuart and DiPrima, 1978). This interpretation results from an analysis of the equation governing the envelope of a quasi-monochromatic *wave packet*, the nonlinear Schrödinger equation. First we study the general evolution, linear followed by nonlinear, of such a wave packet, and then we give an illustration based on the chain of oscillators described above.

9.4.1 Linear dynamics of a wave packet: envelope equation

Let us resume our study of the propagation and dispersion of a wave packet begun in Chapter 3 with the ultimate goal of including nonlinear effects. We consider a wave represented by the Fourier integral

$$u(x, t) = \frac{1}{2} \int_{-\infty}^{+\infty} \hat{u}(k) e^{i(kx - \omega t)} dk, \quad (9.24)$$

where $\omega = \omega(k)$ is a real branch of the dispersion relation corresponding to propagation in the direction of increasing x , so that $\omega(-k) = -\omega(k)$ (for example, for a gravity wave in deep water $\omega = +\sqrt{gk}$ for $k > 0$ and $\omega = -\sqrt{-gk}$ for $k < 0$). Since $u(x, t)$ is real, we must have $\hat{u}^*(k) = \hat{u}(-k)$, and the above integral can also be written as

$$u(x, t) = \frac{1}{2} \int_0^{+\infty} \hat{u}(k) e^{i(kx - \omega(k)t)} dk + \text{c.c.} \quad (9.25)$$

Let us now assume that $u(x, t)$ is a wave packet of width δk centered on the wave number k_0 , i.e., that the complex amplitudes $\hat{u}(k)$ are nonzero only in a narrow band centered on k_0 (Lighthill, 1978, §3.7; Whitham, 1974, §17.7). Isolating the dominant monochromatic wave, the packet can be written as

$$u(x, t) = \frac{1}{2} A(x, t) e^{i(k_0 x - \omega_0 t)} + \text{c.c.}, \quad (9.26)$$

where $\omega_0 = \omega(k_0)$ and the *envelope* $A(x, t)$ of the wave packet is defined as

$$A(x, t) = \int_0^{+\infty} \hat{u}(k) e^{i(k - k_0)x - i(\omega(k) - \omega_0)t} dk. \quad (9.27)$$

Since the amplitudes $\hat{u}(k)$ are zero outside a distance δk from k_0 , the integration can be restricted to this range, with the frequency $\omega(k)$ given by a Taylor series expansion about k_0 . Truncating it at second order, we have

$$\omega - \omega_0 = c_g(k - k_0) + \frac{\omega''_0}{2}(k - k_0)^2,$$

where the group velocity c_g and the coefficient ω''_0 are given by

$$c_g = \frac{\partial \omega}{\partial k}(k_0), \quad \omega''_0 = \frac{\partial^2 \omega}{\partial k^2}(k_0).$$

Substituting this series into (9.27), we recognize it as the general solution (a continuous sum of Fourier modes) of the *envelope equation*

$$i \partial_t A = -i c_g \partial_x A + \alpha \partial_{xx} A, \quad \alpha = \frac{1}{2} \omega''_0. \quad (9.28)$$

This linear equation therefore gives a generic description of the linear evolution of the envelope $A(x, t)$ of a dispersive wave packet centered on k_0 . This packet propagates at the group velocity c_g and, since the dispersion causes different wave numbers to propagate at slightly different speeds, the width of the packet grows linearly in time while its amplitude decreases as $1/\sqrt{t}$.

9.4.2 Nonlinear dynamics: the nonlinear Schrödinger equation

What sort of influences do nonlinear effects have on the dispersion of a wave packet? To answer this question we can seek the dominant nonlinear term to be added to the envelope equation (9.28). The form of this term can be deduced from symmetry arguments (Fauve, 1998). Let us assume that the problem is invariant under translations $x \rightarrow x + \xi$ and $t \rightarrow t + \tau$, as in the coupled pendulum problem studied earlier. Then if A is the solution of the amplitude equation, $Ae^{i\phi}$ corresponding to a wave with phase shifted by ϕ must also be a solution. The equation must therefore be invariant under the transformation $A \rightarrow Ae^{i\phi}$, and the term of lowest degree possessing this property, which dominates for small $u(x, t)$, is $|A|^2 A$. In a reference frame undergoing translation at the group velocity c_g , the envelope equation is therefore *the nonlinear Schrödinger equation*:

$$i \partial_t A = \alpha \partial_{xx} A - \beta |A|^2 A. \quad (9.29)$$

Moreover, if the problem is invariant under reflections $x \rightarrow -x$ and $t \rightarrow -t$ (again like the coupled pendulum problem), the coefficient β must be real. Then in view of these symmetries, if $u(x, t)$ is a solution, $u(-x, -t)$ must also be one (the two reflections being applied simultaneously in order to preserve the propagation direction of the wave). Therefore, if $A(x, t)$ is a solution of (9.29), $A^*(-x, -t)$ must also be a solution owing to (9.26). The Schrödinger equation (9.29) must therefore be invariant under the transformations $x \rightarrow -x$, $t \rightarrow -t$, and $A \rightarrow A^*$, and so it is written as

$$-i \partial_t A^* = \alpha \partial_{xx} A^* - \beta |A|^2 A^*.$$

Taking the complex conjugate of this equation, we obtain (9.29) with β^* instead of β . We therefore have $\beta^* = \beta$, from which we see that β is real. However, symmetry arguments do not allow us to determine the coefficient β , and in particular its sign, on which the wave stability depends. This coefficient is determined below in the simple case of the nonlinear Klein–Gordon equation.

We note that the Schrödinger equation possesses the same cubic nonlinearity as the Landau equation, and that in place of the amplification term σA it involves a diffusion term $\alpha \partial_{xx} A$ (up to a factor of i).

The nonlinear Schrödinger equation (9.29) (often abbreviated as NLS) arises in many areas of physics (electric circuits, fiber optics, plasmas) and biology (DNA dynamics) (Dauxois and Peyrard, 2006, chapter 3). In hydrodynamics this equation was first obtained by Benney and Newell (1967) in describing the weakly nonlinear dynamics of slow modulations of gravity waves in deep water. These authors actually studied a slightly more general problem including modulations in the transverse spatial direction y .

9.4.3 Stability of a quasi-monochromatic wave

The nonlinear Schrödinger equation (9.29) admits the spatially uniform solution

$$A_0 = a_0 e^{i(\Omega t + \Phi)}, \quad a_0 = |A_0| \text{ real}, \quad \Omega = \beta a_0^2, \quad (9.30)$$

which corresponds to the unmodulated traveling wave

$$u(x, t) = a_0 \cos(k_0 x - \omega t + \Phi), \quad \omega = \omega_0 + \beta a_0^2, \quad (9.31)$$

where Φ is an undetermined phase associated with the translational invariance of the original problem. This solution shows that the nonlinear Schrödinger equation describes a remarkable phenomenon: a cubic nonlinearity can counteract the linear dispersion so as to support a wave which propagates without deformation. This result, which Stokes obtained in the special case of gravity waves, is therefore very general, and is valid for all dispersive waves of finite amplitude described generically (for the same symmetries) by the Schrödinger equation. We note that this equation also admits localized solutions which we shall not discuss here (Fauve, 1998; Dauxois and Peyrard, 2006, chapter 3).

We can study the stability of this wave by perturbing the solution A_0 as

$$A(x, t) = (a_0 + a(x, t)) e^{i(\Omega t + \Phi + \varphi(x, t))} \quad (9.32)$$

and substituting this expression into Eq. (9.29). After linearizing and separating the real and imaginary parts, we obtain

$$\frac{\partial a}{\partial t} = \alpha a_0 \frac{\partial^2 \varphi}{\partial x^2}, \quad (9.33a)$$

$$\frac{\partial \varphi}{\partial t} = 2\beta a_0 a - \frac{\alpha}{a_0} \frac{\partial^2 a}{\partial x^2}. \quad (9.33b)$$

This linear system with constant coefficients admits solutions of the form $e^{\sigma t - ipx}$ if its determinant vanishes, that is, if p and σ satisfy the dispersion relation

$$\sigma^2 + 2\alpha\beta a_0^2 p^2 + \alpha^2 p^4 = 0. \quad (9.34)$$

This dispersion relation is very similar to the relation (9.19) obtained for resonant interactions. If α and β have the same sign ($\alpha\beta > 0$), the roots σ_{\pm} of this equation are imaginary and the growth rate σ_r is zero; the traveling wave is then stable, because the nonlinearity counteracts the dispersion. In the opposite case ($\alpha\beta < 0$) the roots are purely imaginary for $p^2 > p_{\text{off}}^2$, where $p_{\text{off}} = -2\beta/\alpha a_0^2$ is a cutoff wave number, and they are real and of opposite sign for $p^2 < p_{\text{off}}^2$:

$$\sigma_{\pm} = \pm \sigma_{\text{ref}} \sqrt{\frac{p^2}{p_{\text{off}}^2} \left(1 - \frac{p^2}{p_{\text{off}}^2}\right)}, \quad \sigma_{\text{ref}} = 2|\beta|a_0^2. \quad (9.35)$$

The positive root corresponds to an instability of the nonlinear wave to long-wavelength perturbations of its envelope. This instability is manifested as the growth of a modulation of the wave train, similar to that shown in Figure 9.3.

Figure 9.8a, which is identical to Figure 9.7a, shows $\sigma^2/\sigma_{\text{ref}}^2$ as a function of p^2/p_{off}^2 in the stable and unstable cases. Figure 9.8b, which is very similar to Figure 9.7b (it displays negative values of p), shows the normalized growth rates of two modes, $\sigma_{-r}/\sigma_{\text{ref}}$ and $\sigma_{+r}/\sigma_{\text{ref}}$, as functions of the normalized wave number p/p_{off} . Using (9.34) it is easily verified that the two most amplified wave numbers are

$$p_{\max} = \pm \frac{1}{\sqrt{2}} p_{\text{off}}. \quad (9.36)$$

The strong resemblance of this discussion to the earlier one of resonant interactions is due to the fact that the dispersion relations (9.19) and (9.34) are identical if we identify K in (9.19) with p in (9.34), and the coefficient β of the cubic

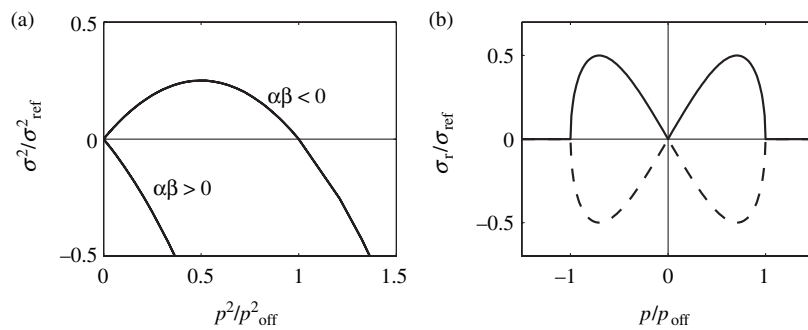


Figure 9.8 (a) The normalized squared eigenvalue corresponding to the dispersion relation (9.34) as a function of p^2/p_{off}^2 ; (b) for $\alpha\beta < 0$, the normalized growth rates of the two modes as functions of p/p_{off} : (—) σ_{+r} , (--) σ_{-r} . The similarity with Figure 9.7 should be noted.

nonlinearity in (9.14) with that in the Schrödinger equation (9.29) (while noting that $\alpha = \omega_0''/2$). This identification will become more clear in the following section, where we derive the Schrödinger equation for the Klein–Gordon wave. The situation can finally be summarized as follows:

- the dynamics of a dispersive wave of finite amplitude is generically governed by the nonlinear Schrödinger equation;
- when the dispersion and the nonlinearity cooperate ($\alpha\beta < 0$) the wave is unstable to long-wavelength modulations; conversely, when the steepening due to nonlinearity is balanced by dispersion ($\alpha\beta > 0$), the wave is stable;
- this instability is identical to the side-band instability due to resonant interaction with nearby wave numbers discovered by Benjamin and Feir.

9.4.4 Interpretation in terms of phase instability

Let us very briefly show how the Benjamin–Feir instability can be interpreted in terms of phase dynamics. Differentiating the equation for the phase perturbation (9.33b) with respect to time and substituting the equation for the amplitude perturbation (9.33a), we obtain the *phase equation*

$$\partial_{tt}\varphi - 2\alpha\beta a_0^2 \partial_{xx}\varphi + \alpha^2 \partial_{xxxx}\varphi = 0.$$

This equation is a classical wave equation plus a fourth-order term which admits traveling wave solutions of the form $\varphi = \varphi(x \pm ct)$ provided that $c^2 = 2\alpha\beta a_0^2$ is positive. It therefore appears that the instability condition $\alpha\beta < 0$ corresponds to an imaginary propagation velocity of the phase perturbations. We refer the reader to Manneville (1990) for a more general presentation of phase instabilities.

9.4.5 Derivation of the NLS equation for the Klein–Gordon wave

For the chain of oscillators shown in Figure 9.6 modeled by the Klein–Gordon equation (9.6), the coefficients of the linear terms in the Schrödinger equation are known from the dispersion relation (9.8):

$$c_g(k_0) = \omega'_0 = \frac{k_0}{\omega_0}, \quad \alpha = \frac{\omega''_0}{2} = \frac{1}{2\omega_0^3}.$$

Here the goal is to determine the dominant nonlinear term in the envelope equation, which can be done using the multiple-scale method. Let $\epsilon = \delta k/k_0 \ll 1$ be the relative width of the wave packet. In a reference frame moving at the group velocity c_g , two Fourier modes with wave numbers differing by δk have speeds whose

relative difference $\delta c/c$ is of order $\delta k/k_0$. This dispersion gives rise to a difference on the order of a wavelength in the distance traveled over a time of order $(k_0\delta c)^{-1} = (\epsilon\omega_0)^{-1}$, after a distance traveled of order $c/k_0\delta c = (\epsilon k_0)^{-1}$. These dispersive effects are therefore manifested at long times of order $T_1 = \epsilon t = \mathcal{O}(1)$ and over large distances of order $X = \epsilon x = \mathcal{O}(1)$. On the other hand, nonlinear effects are manifested only at even longer times of order $T_2 = \epsilon^2 t$. We therefore set

$$u(x, t) = u(x, t, X, T_1, T_2) \quad (9.37)$$

and seek u as a series in powers of ϵ :

$$u = \epsilon u_1 + \epsilon^2 u_2 + \dots \quad (9.38)$$

The calculations present no particular difficulty, so we omit the details. At order ϵ we find the following solution propagating in the positive x direction:

$$u_1 = \frac{1}{2} A(X, T_1, T_2) e^{i(k_0 x - \omega_0 t)} + \text{c.c.}, \quad (9.39)$$

where $\omega_0 = \omega(k_0)$ is given by the dispersion relation. At order ϵ^2 the solvability condition is written as

$$\frac{\partial A}{\partial T_1} = -c_g \frac{\partial A}{\partial X}, \quad c_g = c_g(k_0) = \frac{k_0}{\omega_0}, \quad (9.40)$$

the solution of which is

$$A(X, T_1, T_2) = A(X - c_g T_1, T_2). \quad (9.41)$$

The interpretation of this result is that at the order we are studying the wave envelope propagates at the group velocity without deformation.

At order ϵ^3 the solvability condition gives the nonlinear Schrödinger equation:

$$i \frac{\partial A}{\partial T_2} = \alpha \frac{\partial^2 A}{\partial X^2} - \beta |A|^2 A, \quad \alpha = \frac{\omega_0''}{2} = \frac{1}{2\omega_0^3}, \quad \beta = \frac{3\gamma}{2\omega_0}. \quad (9.42)$$

This equation is identical to the nonlinear Schrödinger equation (9.29) up to the definition of the length and time scales, and the coefficient β is the same as in (9.14). This equation has the solution (9.30) corresponding to the nonlinear wave (9.16). In view of the stability results obtained in Section 9.4.3, we can conclude that the nonlinear wave solution of the Klein–Gordon equation (9.6) is unstable for $\alpha\beta$ negative, as for the chain of pendulums. These conclusions are of course identical to those obtained from the analysis in terms of resonant interactions.

9.5 Resonances revisited

The Benjamin–Feir instability of a gravity wave to nearby wave numbers – or side-band instability – is a special case of instabilities resulting from a resonant interaction among certain wave numbers. We conclude this chapter by discussing a resonance related to a quadratic nonlinearity.⁴

Let us consider a quadratically nonlinear problem with a solution $u(x, t)$ given by the Fourier sum

$$u(x, t) = \sum_{j=-\infty}^{\infty} A_j e^{i(k_j x - \omega(k_j)t)}, \quad A_j = A(k_j). \quad (9.43)$$

In the equation for the amplitude A_n (which we need not write) the quadratic nonlinearity leads to the appearance of a sum

$$\sum_{k_p+k_q=k_n} A_p A_q e^{i(\omega_n - \omega_p - \omega_q)t} \quad (9.44)$$

analogous to that in Eq. (9.12). If the triad of numbers satisfying $k_p + k_q = k_n$ is such that the frequencies obey the condition

$$\omega_n = \omega_p + \omega_q, \quad (9.45)$$

it is said that the triad is resonant. Such a resonance does not necessarily imply the appearance of an instability, but greatly favors it.

The resonance condition (9.45) can be satisfied for gravity–capillary waves. For such waves, the dispersion relation is given by

$$\omega^2 = gk + \frac{\gamma k^3}{\rho},$$

where ρ is the fluid density and γ is the surface tension. It can be verified that triads such that $k_3 = k_1 + k_2$ are resonant if the ratio $r = k_2/k_1$ obeys the relation (McGoldrick, 1965; Craik, 1985, chapter 5)

$$\Gamma = \frac{(1+r^2) + (1+r)(1+7r+r^2)^{1/2}}{r(9+14r+9r^2)},$$

where $\Gamma = \gamma k_1^2 / 2\rho g$. This equation can be arranged as a cubic polynomial in r with coefficients depending on Γ . A simple solution for $\Gamma = 1/4$ (corresponding to a wavelength $\lambda_1 = 2.4$ cm in water) is $r = 1$, which corresponds to the triad

$$k_1 = k_2 = -k_3/2.$$

⁴ A simple illustration of resonances with quadratic nonlinearity is treated in detail by Drazin and Reid (2004, §51), for a double pendulum.

Therefore, a gravity–capillary wave can be unstable owing to interaction with itself and with a wave of half its wave number. This resonance is termed *subharmonic*. As another example, such triad resonances can also arise in stratified fluids between two surface waves and an internal wave. Note that if the waves can propagate in more than one spatial direction, the condition on the wave numbers $k_p + k_q = k_n$ becomes a condition on the wave vectors:

$$\mathbf{k}_n + \mathbf{k}_p + \mathbf{k}_q = \mathbf{0},$$

and the resonance condition is then less restrictive. Higher dimensionality is therefore more favorable to the appearance of resonances.

For gravity waves the dispersion relation forbids any triad resonances. Therefore, for waves of small slope $\epsilon = ka$, no resonant interaction can appear at order ϵ^2 . Resonant interactions arise first at the following order ϵ^3 , among quadruplets. In particular, the interaction of the wave numbers

$$k, \quad k, \quad -k(1+\epsilon), \quad -k(1-\epsilon),$$

with the respective frequencies

$$\omega, \quad \omega, \quad -\omega(1 + \frac{1}{2}\epsilon), \quad -\omega(1 - \frac{1}{2}\epsilon),$$

corresponds to the Benjamin–Feir instability. A deeper understanding of this subject, due most notably to the work by Phillips and Benney in the early 1960s, can be gained from the reviews by Phillips (1981), Hammack and Henderson (1993), and Dias and Kharif (1999).

9.6 Exercises

9.6.1 A nonlinear wave including two harmonics (1)

Consider a wave $u(x, t)$ governed by the Klein–Gordon equation (9.6), of small amplitude of order ϵ , composed of a fundamental harmonic k_1 of amplitude ϵA_1 and the second harmonic $k_2 = 2k_1$ of amplitude ϵA_2 .

1. The summation in (9.9) runs over the four wave numbers $\pm k_1$ and $\pm k_2$. Show that out of the 4^3 possible cubic products of wave numbers, there are only nine triads (k_p, k_q, k_r) satisfying $k_1 = k_p + k_q + k_r$. Show that they are all resonant, and that the same is true for triads satisfying $k_2 = k_p + k_q + k_r$. Derive the system

of amplitude equations

$$\frac{dA_1}{dT} = -i\beta A_1^2 A_1^* - 2i\beta A_2 A_2^* A_1, \quad (9.46a)$$

$$\frac{dA_2}{dT} = -i\beta A_2^2 A_2^* - 2i\beta A_1 A_1^* A_2, \quad (9.46b)$$

with

$$\beta = \frac{3\gamma}{2\omega_{10}}, \quad \omega_{10} = \sqrt{1 + k_1^2}.$$

2. Verify that this system has no nonzero solution that is independent of time.
3. Find a solution for $|A_2| \sim \epsilon |A_1|$ and derive the expression for $u(x, t)$ (Craik, 1985, p. 177):

$$u(x, t) = \epsilon a_1 \cos \theta + \epsilon^2 a_2 \cos(2\theta - k_2(c_1 - c_2)t) + \mathcal{O}(\epsilon^3),$$

with

$$\theta = k_1 x - \omega_1 t, \quad \omega_1 = \omega_{10} + \beta \epsilon^2 a_1^2, \quad c_j = \omega_j / k_j, \quad a_j = \mathcal{O}(1), \quad j = 1, 2.$$

Is the nonlinear frequency correction affected by the second harmonic? What condition must the dispersion relation satisfy for the wave to propagate without deformation? Can this condition be satisfied here?

4. A solution of the system of differential equations (9.46) can be found for amplitudes of the same order of magnitude, $|A_2| \sim |A_1| \sim \epsilon$, by separating the modulus and the phase; the conclusions remain unchanged. It is also possible to rework this exercise using the wave numbers k_1 and $k_3 = 3k_1$. Are the conclusions unchanged in this case?

9.6.2 A nonlinear wave including two harmonics (2)

As shown by the preceding exercise, assuming that the amplitudes vary slowly can lead only to a small correction of order ϵ^2 to the frequency and speed of the Fourier modes. It is therefore impossible to construct a Stokes wave including harmonics which propagates without deformation, except in the special case of a subharmonic resonance where the harmonics have the same speed.⁵ The present exercise shows how to construct a nonlinear wave by “locking in” the speeds of the harmonics at the start.

⁵ Such a resonance occurs, for example, in Kelvin–Helmholtz gravity–capillary waves for the triad $(k, k, k/2)$; see Exercise 4.5.1, as well as Nayfeh and Saric (1972) and Craik (1985, §§14,19).

1. We seek a nonlinear solution of the Klein–Gordon equation (9.6) in the “naive” form

$$u = \epsilon u_1(\theta) + \epsilon^3 u_3(3\theta) + \dots, \quad \theta = kx - \omega(k)t,$$

where $\omega(k)$ is a branch of solutions of the dispersion relation. Show that the system of equations obtained is

$$Lu_1 = 0, \tag{9.47a}$$

$$Lu_3 = -4\gamma u_1^3, \tag{9.47b}$$

where the operator L is defined by $L = (\omega^2 - k^2)\partial_{\theta\theta} + 1$. Show that the solution at order ϵ^3 leads to the appearance of a secular (unbounded) term proportional to $\theta e^{i\theta}$. (This is the same problem as that encountered in the naive solution of the Duffing oscillator; see Chapter 8.)

2. The difficulty encountered above, namely, the appearance of a secular term, is due to the fact that we are seeking a nonlinear wave with frequency given by a linear dispersion relation. To resolve the difficulty we relax the wave frequency by setting $\omega = \omega_0 + \epsilon^2 \omega_2 + \dots$, which introduces an unknown correction ω_2 . Show that the system of equations to be solved is now

$$Lu_1 = 0, \tag{9.48a}$$

$$Lu_3 = -4\gamma u_1^3 - 2\omega_0 \omega_2 \frac{\partial^2 u_1}{\partial \theta^2}. \tag{9.48b}$$

3. Show that the solution at order ϵ is

$$u_1 = \frac{1}{2} A_1 e^{i\theta} + \text{c.c.}, \quad \theta = kx - \omega_0 t,$$

and that the solvability condition at order ϵ^3 implies that

$$\omega_2 = \frac{3\gamma}{2\omega_0} a^2, \quad a = |A_1|.$$

Show that the solution is given by

$$u(x, t) = \epsilon a \cos \theta + \frac{\gamma}{8} (\epsilon a)^3 \cos 3\theta + \mathcal{O}(\epsilon^5), \quad \omega = \omega_0 + \frac{3\gamma}{2\omega_0} (\epsilon a)^2.$$

We note that the frequency correction obtained is identical to the correction (9.16b) found for a monochromatic wave by solving the amplitude equations (9.12), and also to the correction (9.42) found by calculating the cubic term in the Schrödinger equation for the envelope of a wave packet.

9.6.3 A nonlinear Korteweg–de Vries wave

Consider the Korteweg–de Vries equation (Boussinesq, 1871; Korteweg and de Vries, 1895; Miles, 1981), which governs the dynamics of gravity waves of wavelength long compared to the depth h ($kh \ll 1$) (Whitham, 1974, §13.12–13):

$$\partial_t \eta + c_0 \left(1 + \frac{3}{2} \frac{\eta}{h} \right) \partial_x \eta + \gamma \partial_{xxx} \eta = 0, \quad (9.49)$$

with

$$c_0 = \sqrt{gh}, \quad \gamma = \frac{1}{6} c_0 h^2$$

(the Stokes calculation (1847) corresponds to the opposite limit $kh \gg 1$). For a wave of amplitude a and wave number k , the nonlinear term is of order $c_0/h \eta \partial_x \eta \sim c_0 kh(a/h)^2$ and the dispersion is of order $c_0 h^2 \partial_{xxx} \eta \sim c_0 h^3 k^3 a/h$. When the two effects are of the same order of magnitude, that is, $a/h \sim k^2 h^2$, the above equation admits localized solutions of the solitary wave type. The waves of finite amplitude we are seeking here can be obtained by an expansion in powers of $\epsilon = a/h$ with $a/h \ll k^2 h^2$.

Following the same method as in the preceding exercise, we therefore seek a solution of the form

$$\frac{\eta}{h} = \epsilon \eta_1(\theta) + \epsilon^2 \eta_2(2\theta) + \dots$$

with

$$\theta = kx - \omega t, \quad \omega = \omega_0 + \epsilon \omega_1 + \epsilon^2 \omega_2 + \dots, \quad \omega_0 = c_0 k - \gamma k^3.$$

(The first nonlinear correction is of order ϵ^2 because the nonlinearity in the equation is quadratic.)

1. Show that there is no resonance at order ϵ^2 , so that we can set $\omega_1 = 0$, and show that the nonresonance (or solvability) condition at order ϵ^3 is written as

$$\omega_2 = \frac{3c_0^2}{32\gamma k}.$$

2. Obtain the solution

$$\frac{\eta}{h} = \epsilon \cos \theta + \frac{3\epsilon^2}{4k^2 h^2} \cos 2\theta + \frac{27\epsilon^3}{64k^4 h^4} \cos 3\theta + \dots \quad (9.50)$$

with

$$\omega = \omega_0 + \frac{9\epsilon^2}{16k^2 h^2}.$$

10

Nonlinear dynamics of dissipative systems

10.1 Introduction

As we have discussed in earlier chapters, a dissipative physical system in a uniform, stationary state can become linearly unstable when a control parameter R exceeds a critical value R_c . This occurs, for example, in the instability of a fluid layer heated from below governed by the Rayleigh number, or in the instability of plane Poiseuille flow governed by the Reynolds number. The instability can be manifested as the appearance of a stationary, spatially periodic structure (Rayleigh–Bénard convection rolls, for example), or as a growing traveling wave (Tollmien–Schlichting waves). This type of situation was studied in Chapter 8 for spatially confined systems, or systems with imposed periodicity, where the dynamics can be reduced to a system of differential equations for the amplitudes of a few spatial harmonics. When the physical system is *spatially extended*, that is, when its size is large compared to the wavelength of the periodic structure, the wave number spectrum tends to become continuous, and spatial modulations of the amplitudes can arise. The appropriate formalism for describing these modulations is that of *envelope equations*.

In the present chapter we shall present this formalism and study the conditions for saturation of the primary instability arising at $R = R_c$, as well as for secondary instabilities which arise when the bifurcation parameter exceeds a second threshold. First we study the case where the periodic structure is stationary, that is, where the eigenvalue of the linearized system crossing the imaginary axis at threshold $R = R_c$ is *real*, i.e., the bifurcation is of the saddle–node or pitchfork type for a system possessing the reflection symmetry $x \rightarrow -x$. The corresponding envelope equation is the Ginzburg–Landau equation with *real* coefficients. The secondary instability that typically arises in this situation is the Eckhaus instability, as encountered prototypically in Rayleigh–Bénard convection and Couette–Taylor flow between two coaxial cylinders. We then present the case

of waves corresponding to a Hopf bifurcation (complex-conjugate eigenvalues). The corresponding envelope equation is the Ginzburg–Landau equation with *complex* coefficients. Here we recover the Benjamin–Feir instability introduced in the previous chapter, and briefly discuss Tollmien–Schlichting waves again. The final section is devoted to the case where, owing to a particular symmetry, the wave number $k=0$ is neutral; accordingly, the dynamics of the mode of finite wave number k_c , which is marginal at threshold $R=R_c$, is strongly influenced by coupling to nearly neutral long-wavelength perturbations.

10.2 Weakly nonlinear dynamics

10.2.1 Linear evolution of a wave packet

Let us consider the case where, for a critical value R_c of a bifurcation parameter R , an instability of finite wave number k_c and zero speed and group velocity ($\omega=\partial\omega/\partial k=0$ at $k=k_c$) appears, corresponding to an absolute instability. For $r=R/R_c$ near $r_c=1$, that is, for

$$\epsilon^2=r-r_c \ll 1, \quad (10.1)$$

the growth rate $\sigma(k, r)$ near k_c has the shape shown in Figure 10.1a: for $r < r_c$, it is negative for all wave numbers, and for $r > r_c$ there exists a band of unstable wave numbers centered on r_c , of width of order ϵ with growth rate of order ϵ^2 .

Let us expand this growth rate in a Taylor series near the critical point (k_c, r_c) :

$$\sigma(k, r) = \sigma(k_c, r_c) + \frac{\partial\sigma}{\partial k}(k - k_c) + \frac{\partial\sigma}{\partial r}(r - r_c) + \frac{1}{2} \frac{\partial^2\sigma}{\partial k^2}(k - k_c)^2 + \dots, \quad (10.2)$$

where the derivatives are evaluated at the critical point (k_c, r_c) . We shall see below that the omitted quadratic terms, proportional to $(r - r_c)^2$ and $(k - k_c)(r - r_c)$, are smaller in order of magnitude than the term $(k - k_c)^2$ that we have kept. In fact, two terms in the above Taylor expansion are zero: the growth rate $\sigma(k_c, r_c)$, and the term $\partial\sigma/\partial k$ since the curve $\sigma(k)$ is tangent to the k -axis for $r = r_c$. The above equation then reduces to

$$\tau_c \sigma(k, r) = (r - r_c) - \xi_c^2 (k - k_c)^2 + \dots, \quad (10.3)$$

where τ_c and ξ_c are characteristic time and length scales defined as

$$\frac{1}{\tau_c} = \frac{\partial\sigma}{\partial r}, \quad \frac{\xi_c^2}{\tau_c} = -\frac{1}{2} \frac{\partial^2\sigma}{\partial k^2}.$$

In the (k, r) plane the marginal stability curve, defined as $\sigma(k, r) = 0$, is then given by the parabola

$$r - r_c = \xi_c^2 (k - k_c)^2$$

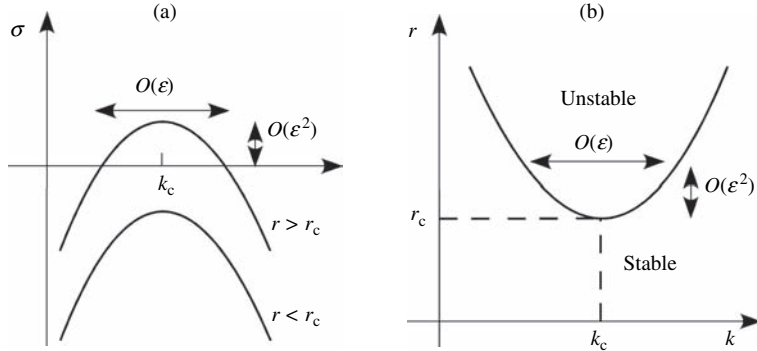


Figure 10.1 (a) The growth rate $\sigma(k)$ below and above threshold $r = r_c$; (b) the marginal stability parabola $\sigma = 0$.

and shown in Figure 10.1b. For $r > r_c$ and for a given $\epsilon^2 = r - r_c$, the wave numbers inside the parabola are unstable and form a band whose width is of order ϵk_c . The terms omitted in (10.3) can therefore be seen to be at least of order ϵ^3 .

Now let us consider a perturbation of the base state, represented as in the preceding chapter by a Fourier integral

$$u(x, t) = \frac{1}{2} \int_0^{+\infty} \hat{u}(k) e^{ikx + \sigma(k)t} dk + \text{c.c.} \quad (10.4)$$

The perturbation can then be written as

$$u(x, t) = \frac{1}{2} \mathcal{A}(x, t) e^{ik_c x} + \text{c.c.}, \quad (10.5)$$

where the envelope $\mathcal{A}(x, t)$ of the wave packet is defined as

$$\mathcal{A}(x, t) = \int_0^{+\infty} \hat{u}(k) e^{i(k - k_c)x + \sigma(k)t} dk. \quad (10.6)$$

This integral is dominated by wave numbers near k_c (the other modes are strongly damped), wherein $\sigma(k)$ can be replaced by the Taylor series (10.3). We then recognize (10.6) as the general solution of the envelope equation

$$\tau_c \partial_t \mathcal{A} = (r - r_c) \mathcal{A} + \xi_c^2 \partial_{xx} \mathcal{A}. \quad (10.7)$$

This equation describes the linear evolution of the envelope of a wave packet near the marginal stability. The first term on the right-hand side corresponds to exponential amplification of the envelope, and the second to broadening – or diffusion – of the envelope. The length ξ_c is seen to be the characteristic length for diffusion during the time τ_c . This equation, which has real coefficients, looks similar to the equation governing the envelope of a dispersive wave packet found (by the same method) in the preceding chapter. Actually it differs considerably, as it contains an amplification term, and the term involving the spatial derivative describes diffusion rather than dispersion of the wave packet.

10.2.2 Weakly nonlinear effects: the Ginzburg–Landau equation

As for the dispersive waves in the preceding chapter, we can introduce into (10.7) the dominant nonlinear term using symmetry arguments. For a system invariant under time and space translations, the equation must be invariant under rotations of \mathcal{A} in the complex plane, and so the dominant term must be a cubic term of the form $|\mathcal{A}|^2\mathcal{A}$ (see the preceding chapter). The envelope equation (10.7) then becomes

$$\tau_c \partial_t \mathcal{A} = (r - r_c)\mathcal{A} + \xi_c^2 \partial_{xx} \mathcal{A} - \kappa |\mathcal{A}|^2 \mathcal{A}, \quad (10.8)$$

where the Landau coefficient κ must be real. This equation, usually called the *Ginzburg–Landau equation*, therefore governs the weakly nonlinear dynamics of the envelope of a wave packet near marginal stability. It generalizes the Landau equation (with real coefficients) by allowing spatial modulations of the envelope. The first calculation of the Landau coefficient for a problem related to hydrodynamics is due to Newell and Whitehead (1969), and Segel (1969), for Rayleigh–Bénard convection.

Here we shall consider the case $\kappa > 0$, where the nonlinear term counteracts the exponential growth, giving rise to a supercritical bifurcation. To begin, we find time, space and amplitude scales for which the various terms in Eq. (10.8) have the same order of magnitude, that is, the scales for which

$$\tau_c \partial_t \sim (r - r_c) \sim \xi_c^2 \partial_{xx} \sim \kappa |\mathcal{A}|^2.$$

For $r > r_c$ the instability appears on a time scale of the order of the inverse growth rate, $\tau_c/(r - r_c)$. Next, spatial modulations can be expected to arise on a distance of the order of the inverse width of the wave packet, $\xi_c/\sqrt{r - r_c}$. Finally, for the nonlinear term to have the same magnitude as the other two, the amplitude of the

envelope must be of order $\epsilon = \sqrt{r - r_c}$. The desired scales are therefore

$$T = \epsilon^2 \frac{t}{\tau_c} = \mathcal{O}(1), \quad (10.9a)$$

$$X = \epsilon \frac{x}{\xi_c} = \mathcal{O}(1), \quad (10.9b)$$

$$A = \frac{\sqrt{\kappa}}{\epsilon} \mathcal{A} = \mathcal{O}(1). \quad (10.9c)$$

With these scales the Ginzburg–Landau equation can be written in normalized form as

$$\partial_T A = A + \partial_{XX} A - |A|^2 A. \quad (10.10)$$

We note that this equation has the advantage of being independent of any parameters, but at the price of a change of scale which depends on the distance to threshold via the small parameter $\epsilon = \sqrt{r - r_c}$: indeed, the scales even diverge at threshold. To avoid this divergence it is sometimes preferable to introduce a change of scale which is *independent* of the distance to threshold, by writing this distance as $r - r_c = \mu \epsilon^2$, where $\epsilon \ll 1$ is a *fixed*, formal small parameter and $\mu = \mathcal{O}(1)$ is a measure of the distance to threshold. The Ginzburg–Landau equation is then written in a form involving the bifurcation parameter μ :

$$\partial_T A = \mu A + \partial_{XX} A - |A|^2 A. \quad (10.11)$$

Various generalizations of Eq. (10.8) exist accounting for, e.g., the existence of a slow drift of the primary pattern, or modulations in two spatial directions. One example is

$$\tau_c \partial_T \mathcal{A} = (r - r_c) \mathcal{A} + \xi_c^2 \left(\partial_X - \frac{i}{2k_c} \partial_{YY} \right)^2 \mathcal{A} - \kappa |\mathcal{A}|^2 \mathcal{A}, \quad (10.12)$$

where the transverse coordinate Y is defined analogously to X , which accounts for secondary instabilities of a stationary pattern of parallel rolls with wavenumber k_c (Newell and Whitehead, 1969; Segel, 1969). Predictions of this equation have been tested successfully in experiments by Wesfreid *et al.* (1978).

10.2.3 Example of the derivation of the Ginzburg–Landau equation

As an example, we derive in this section the Ginzburg–Landau equation from a model equation of the Rayleigh–Bénard convection, the Swift–Hohenberg equation (Swift and Hohenberg, 1977). The one-dimensional version of this

equation is¹

$$\tau_c \partial_t u = (r - r_c)u - \xi^4 (\partial_x^2 + k_c^2)^2 u - \gamma u \partial_x u. \quad (10.13)$$

The linear part comes from the Boussinesq equations, while the nonlinear part models advection in a heuristic manner. The base state $u_0 = 0$, which is linearly stable for $r < r_c$, undergoes a bifurcation for $r = r_c$ with respect to the marginal mode of wave number k_c . Near threshold, the growth rate is given by the dispersion relation

$$\tau_c \sigma = (r - r_c) - \xi^4 (k^2 - k_c^2)^2,$$

the graph of which is shown in Figure 10.1. Close to threshold ($\epsilon^2 = r - r_c \ll 1$), the width of the band of unstable wave numbers is $2\epsilon/k_c \xi^2$ and the growth rate is of order ϵ^2 . Therefore, the relevant time and space variables for describing slow variations of the amplitude are

$$T = \epsilon^2 t, \quad X = \epsilon x.$$

Here we shall sketch only the main steps of the calculation, leaving the details to Exercise 10.7.1. Seeking the solution in the form of an expansion

$$u(x, t) = \epsilon u_1(x, X, T) + \epsilon^2 u_2(x, X, T) + \dots,$$

the order- ϵ solution can be written as

$$u_1 = \frac{1}{2} A_1(X, T) e^{ik_c x} + \text{c.c.},$$

where $A_1(X, T)$ is the slowly varying envelope of the wave packet centered on k_c . The quadratic nonlinearity gives rise at order ϵ^2 to a harmonic of wave number $2k_c$ which interacts with the fundamental at order ϵ^3 , and this interaction is resonant ($k_c = 2k_c - k_c$). The solvability condition then gives the Ginzburg–Landau equation:

$$\tau_c \partial_T A_1 = A_1 + \xi_c^2 \partial_{XX} A_1 - \kappa |A_1|^2 A_1, \quad \xi_c^2 = 4\xi^4 k_c^2, \quad \kappa = \frac{\gamma^2}{9\xi_c^2}.$$

The normalized Ginzburg–Landau equation (10.10) is then obtained by choosing τ_c and ξ_c for the time and length scales, and $\kappa^{-1/2}$ for the amplitude scale.

¹ Manneville (1990, chapter 8) discusses a more general version of the Swift–Hohenberg equation which includes transverse diffusion and allows a description of modulations in both directions in the horizontal plane.

10.3 Saturation of the primary instability

For $\kappa > 0$ the normalized Ginzburg–Landau equation (10.10) possesses a continuous family of uniform, stationary solutions defined as

$$A_0 = a_0 e^{i(q_0 X + \Phi)}, \quad a_0 = \sqrt{1 - q_0^2}, \quad (10.14)$$

where q_0 is a parameter lying between -1 and 1 and Φ is an undetermined phase. Returning to the initial variables, these solutions correspond to a periodic pattern

$$U_0(x) = u_0 \cos(k_0 x + \Phi) \quad (10.15)$$

of amplitude u_0 and wave number k_0 defined as

$$u_0 = \sqrt{r - r_c} \sqrt{\frac{1 - q_0^2}{\kappa}}, \quad k_0 = k_c + \epsilon q_0 / \xi_c.$$

That the phase Φ is undetermined is a result of the assumed translational invariance, that is, if $u(x, t)$ is a solution, then $v(x, t) = u(x + \Phi, t)$ is also one. The amplitude, which is proportional to the square root of the distance from threshold $\epsilon = \sqrt{r - r_c}$, is seen to be a maximum at $k_0 = k_c$ ($q_0 = 0$), to decrease as the wave number moves away from k_c , and then to vanish for $k_0 = k_c \pm \epsilon / \xi_c$ ($q_0 = \pm 1$), that is, on the marginal stability parabola.

We note that the Ginzburg–Landau equation, like the nonlinear Schrödinger equation, admits other remarkable spatially localized solutions, which we shall not discuss here (Fauve, 1998; Dauxois and Peyrard, 2006).

10.4 The Eckhaus secondary instability

10.4.1 The instability criterion

Are the stationary solutions (10.15) of the Ginzburg–Landau equation (10.10) stable? To answer this question, we perturb the amplitude a_0 and the phase Φ of this solution as

$$\begin{aligned} \sqrt{\frac{\kappa}{r - r_c}} U(x, t) &= [a_0 + \tilde{a}(X, T)] \cos[kx + \Phi + \varphi(X, T)] \\ &= \frac{1}{2} A(X, T) e^{i(k_c x + \Phi)} + \text{c.c.} \end{aligned}$$

with

$$A(X, T) = [a_0 + \tilde{a}(X, T)] e^{i[q_0 X + \varphi(X, T)]}.$$

Substituting the perturbed amplitude $A(X, T)$ into (10.10), linearizing about $(\tilde{a}, \varphi) = (0, 0)$, and separating the real and imaginary parts, we obtain

$$\partial_T \tilde{a} = -2a_0^2 \tilde{a} + \partial_{XX} \tilde{a} - 2a_0 q_0 \partial_X \varphi, \quad (10.16a)$$

$$\partial_T \varphi = -\frac{2q_0}{a_0} \partial_X \tilde{a} + \partial_{XX} \varphi. \quad (10.16b)$$

We first note that for spatially *uniform* perturbations, i.e., perturbations of zero wave number, this system reduces to

$$\begin{pmatrix} \dot{a} \\ \dot{\varphi} \end{pmatrix} = \begin{pmatrix} -2a_0^2 & 0 \\ 0 & 0 \end{pmatrix} \begin{pmatrix} a \\ \varphi \end{pmatrix}. \quad (10.17)$$

This expression displays two decoupled modes: a stable *amplitude mode* and a neutral *phase mode*. In light of the discussion of active and slaved modes in the case of systems with a small number of degrees of freedom (Chapter 8), this suggests that the phase mode governs the weakly nonlinear dynamics while the amplitude mode is slaved to it. The phase mode is neutral for $k=0$ owing to the translational invariance. We shall return to this subject in the following section.

Since the differential system (10.16) is linear, homogeneous, and has constant coefficients, it admits solutions of the form $e^{ipX+\sigma T}$ if the determinant of the associated algebraic system vanishes. We then derive the dispersion relation

$$(\sigma + 2a_0^2 + p^2)(\sigma + p^2) - 4q_0^2 p^2 = 0,$$

which has the roots

$$\sigma_{\pm} = -(a_0^2 + p^2) \pm \sqrt{a_0^4 + 4q_0^2 p^2}. \quad (10.18)$$

The root σ_- is always negative and for small p is written as

$$\sigma_- = -2a_0^2 + \mathcal{O}(p^2). \quad (10.19)$$

This root therefore corresponds to the amplitude mode. The other root σ_+ corresponds to the phase mode; it is always negative for p large but can be positive for p small. In the latter case it is given by

$$\sigma_+ = -\frac{1 - 3q_0^2}{1 - q_0^2} p^2 + \mathcal{O}(p^4). \quad (10.20)$$

Since $|q_0| < 1$, σ_+ is positive for

$$q_0^2 > \frac{1}{3}, \quad \text{or} \quad \xi_c^2 (k_0 - k_c)^2 > \frac{r - r_c}{3}. \quad (10.21)$$

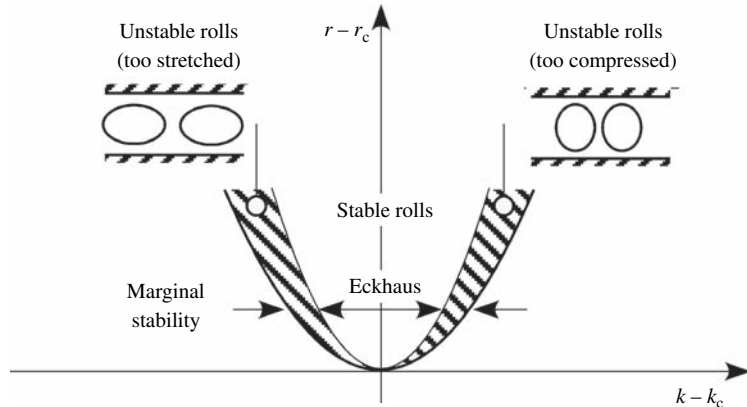


Figure 10.2 The marginal stability parabola ($\sigma = 0$) and the Eckhaus parabola in the $(k - k_c, r - r_c)$ plane. For a given $r > r_c$ a convection roll for which the wave number is located between the two parabolae is unstable.

The condition $q_0^2 = 1/3$ defines a parabola in the (k, r) plane inside the marginal stability parabola $r - r_c = \xi_c^2(k_0 - k_c)^2$, as shown in Figure 10.2. Inside the inner parabola σ_+ is negative and so the periodic structure (10.15) is stable, while between the two parabolae, this structure is unstable to long-wavelength perturbations (Eckhaus, 1965).

Therefore, a pattern of convection rolls is linearly stable if $q_0^2 < 1/3$, that is, if the wave number k is close enough to k_c . Otherwise, the pattern is too compressed or too stretched, and is linearly unstable. It can be shown that this secondary bifurcation is subcritical, that is, that the dominant nonlinear term does not saturate the instability (Fauve, 1998). The perturbation is amplified in a ‘‘catastrophic’’ fashion, which leads to the disappearance of a roll or to the nucleation of a new one, and to the relaxation of the pattern to a new uniform wave number closer to k_c . If this new wave number lies inside the Eckhaus parabola, the structure does not change further; otherwise, a new disappearance and/or nucleation can occur.

10.4.2 Interpretation in terms of phase dynamics

The preceding analysis has shown that when a periodic pattern is subjected to a long-wavelength perturbation ($p \ll 1$), the modulus of the perturbation amplitude relaxes over a time much shorter than the phase:

$$|\sigma_-| \sim |-2a_0^2| \gg |\sigma_+| \sim |p^2|.$$

This result suggests that we seek a *phase equation* decoupled from the modulus of the slaved amplitude. We can do this by starting from the system (10.16) governing the dynamics of the perturbations, or by returning to the original Ginzburg–Landau

equation (10.10) and separating the evolutions of the modulus and the phase of the envelope by introducing $A = ae^{i\phi}$. Choosing the second option, we obtain the coupled equations

$$\partial_T a = \left(1 - (\partial_X \phi)^2\right) a + \partial_{XX} a - a^3, \quad (10.22a)$$

$$a \partial_T \phi = a \partial_{XX} \phi + 2 \partial_X a \partial_X \phi. \quad (10.22b)$$

Rather than dealing with the actual phase ϕ , which increases (or decreases) spatially monotonically, it is convenient to introduce the *gradient* of the phase

$$q(X, T) = \partial_X \phi, \quad (10.23)$$

which measures the *local* correction of the wave number k_c to the pattern [$kx = k_c x + qX = (k_c + \epsilon q)x$]. Then, after differentiating (10.22b) with respect to X , the above system of equations becomes

$$\partial_T a = (1 - q^2)a + \partial_{XX} a - a^3, \quad (10.24a)$$

$$\partial_T q = \partial_X \left(\partial_X q + \frac{2q}{a} \partial_X a \right). \quad (10.24b)$$

This system admits a continuous family of stationary, uniform solutions

$$a_0 = \sqrt{1 - q_0^2}, \quad |q_0| < 1,$$

parametrized by the phase gradient q_0 . These solutions naturally correspond to the pattern described by (10.14) and (10.15). When one of these solutions is perturbed, the relaxation time of the perturbed amplitude a is much shorter than that of the phase gradient q , so that a remains nearly in equilibrium with q , i.e., it is given by $a^2 = 1 - q^2$ (a is said to follow q “adiabatically” or to be “slaved” to q). We then find that $\partial_X a = (-q/a)\partial_X q$. Inserting this expression into (10.24b), we obtain

$$\partial_T q = \partial_X (D(q) \partial_X q), \quad D(q) = \frac{1 - 3q^2}{1 - q^2}. \quad (10.25)$$

This is a nonlinear diffusion equation involving a diffusivity $D(q)$. Linearizing the equation for small perturbations $\delta q = q - q_0$, we find

$$\partial_T \delta q = D(q_0) \partial_{XX} \delta q. \quad (10.26)$$

For $q_0^2 < 1/3$ the diffusivity $D(q_0)$ is positive and the wave number q relaxes to equilibrium q_0 ; otherwise, the diffusivity $D(q_0)$ is negative and the local wave number diverges. We therefore arrive at the Eckhaus instability criterion (10.21) from the point of view of phase dynamics.

A weakly nonlinear expansion of the phase equation near the Eckhaus instability leads to an equation of the Kuramoto–Sivashinsky type, in which the nonlinear term is such that the bifurcation is *subcritical*, as mentioned above (Kuramoto, 1984; Fauve, 1998, §6). The idea of phase dynamics, introduced by Pomeau and Manneville (1979), has proved to be very fruitful. Beyond the weakly nonlinear regime, it led to the introduction of the concept of “phase turbulence” to analyze chaotic behaviors (Manneville, 1990, chapter 10).

10.4.3 Some experimental illustrations

Two physical systems corresponding to the above situation have been studied extensively: the Rayleigh–Bénard convection between two horizontal plates and the Couette–Taylor flow between two cylinders. A review is given in the books of Koschmieder (1993) and Chossat and Iooss (1994). These studies reveal generic types of behavior that must occur in any system possessing the same symmetries, that is, in any system invariant under the reflectional and translational symmetries.

In the case of Rayleigh–Bénard convection, the observed spatial patterns depend on the shape and size of the box, on the type of wall (whether it imposes a temperature or a thermal flux), and on the Prandtl number $\text{Pr} = \nu/\kappa$, where ν and κ are the kinematic viscosity and thermal diffusivity of the fluid. These patterns can be aligned rolls, or two-dimensional rectangular or hexagonal structures (Manneville, 1990, chapter 4). In the case of rolls, the Eckhaus secondary instability is manifested as a local compression (stretching) of the initial pattern, which typically leads to the disappearance (appearance) of rolls and the relaxation of the system to a larger (smaller) wavelength. Figure 10.3 illustrates a particular manifestation of the Eckhaus instability, the *cross-roll* instability (Busse and Whitehead, 1971). The initial pattern is imposed by a thermal impression technique, which consists of gently heating the fluid just below the critical Rayleigh number Ra_c using a lamp shining through a grill. The illuminated regions are warmer than the ones in the shadow of the grill, and a forced convection motion arises. Upon passing through Ra_c and suppressing the forcing, the initial rolls (top left panel) are unstable because they are too compressed; a system of rolls with a larger wavelength and orthogonal to the original ones develops and tends to replace them, as seen in the bottom right panel.

Another variant of the Eckhaus instability is the zigzag instability, illustrated in Figure 10.4. Here the initial rolls, shown in the top left panel, are too stretched, and the appearance of the zigzags (bottom right panel) is an economical way of locally reducing the wavelength via small perturbations, that is, without the need to create new rolls.

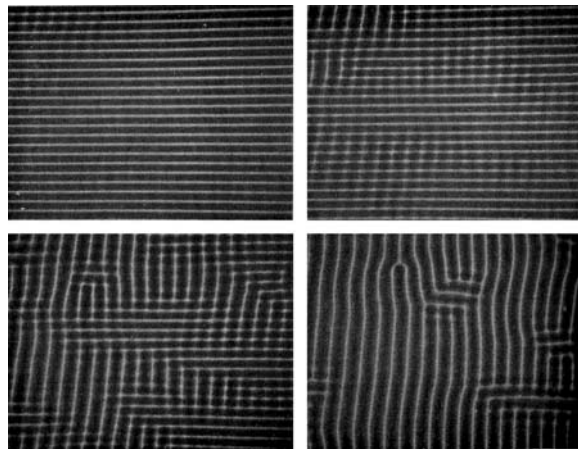


Figure 10.3 Cross-roll instability of Rayleigh–Bénard rolls in a silicone oil between two plates of spacing $d = 5$ mm, for Rayleigh number $\text{Ra} = 3000$. Time intervals between the panels are 10, 7, and 35 min (from left to right and top to bottom). Note that the final wavelength is larger than the initial wavelength of $\lambda = 1.64d$ (Busse and Whitehead, 1971).

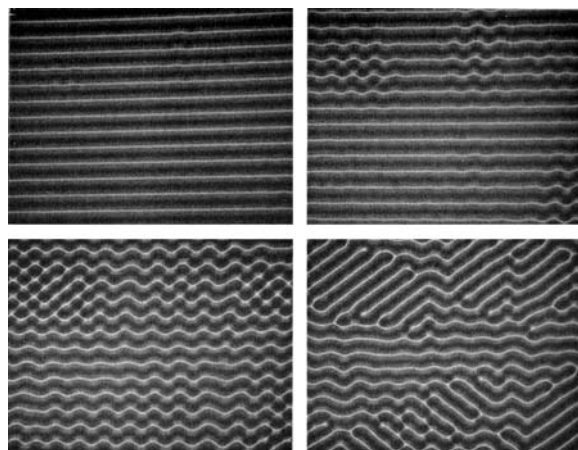


Figure 10.4 Zigzag instability of Rayleigh–Bénard convection rolls in a silicone oil between two plates of spacing $d = 5$ mm, for Rayleigh number $\text{Ra} = 3600$. Time intervals between the panels are 19, 36, and 72 min (from left to right and top to bottom). Here the final wavelength is smaller than the initial wavelength of $\lambda = 2.8d$ (Busse and Whitehead, 1971).

In the case of Couette–Taylor flow, the rolls due to the supercritical primary bifurcation become unstable beyond a second critical velocity (Chapter 4). This instability is manifested by an azimuthal undulation of the rolls, as illustrated in Figure 10.5. The flow appears stationary when observed in a rotating reference frame and may be interpreted as the result of the zigzag instability for this system.

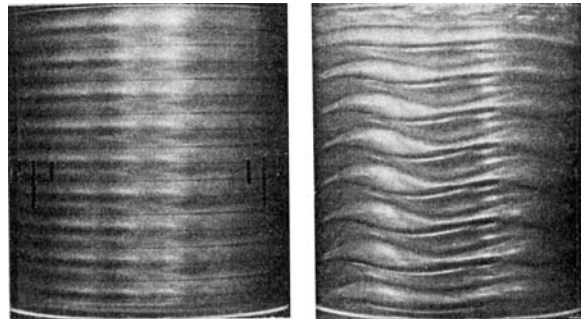


Figure 10.5 Couette–Taylor straight rolls (left) and undulating rolls due to a secondary instability (right) (Fenstermacher *et al.*, 1979).

For a more general discussion and a classification of secondary instabilities of periodic patterns based on symmetries, see Coullet and Iooss (1990).

10.5 Instability of a traveling wave

The above theory gives a good description of the saturation of *stationary* primary instabilities and the appearance of secondary instabilities in the case of Rayleigh–Bénard convection or Couette–Taylor flow. More generally, this theory describes the weakly nonlinear dynamics of systems possessing translational invariance $x \rightarrow x + \Phi$ and reflection symmetry $x \rightarrow -x$. From a slightly different viewpoint, this description owes its success to the fact that the primary instability is *absolute* and supercritical.

In general, *flows* do not possess the reflectional symmetry (Couette–Taylor flow is an exception, because it curls back on itself). Primary instabilities are then manifested as waves which propagate with nonzero speed; a typical example is that of Tollmien–Schlichting waves that develop in a shear flow near a wall (Chapter 5). Here the weakly nonlinear analysis must be modified in order to take into account the fact that the eigenvalue of the marginal mode is complex, corresponding to a Hopf bifurcation.

10.5.1 Evolution of a wave packet

The envelope equation of a packet of traveling waves near the instability threshold, and propagating with positive velocity (say), can be obtained as in the preceding section. Let $r = R/R_c$ be the normalized bifurcation parameter and k_c and ω_c be the wave number and frequency of the marginal mode. At threshold the eigenvalue $s = \sigma + i\omega$ crosses the imaginary axis ($\sigma = 0$ and $\omega = \omega_c$), and near threshold the

frequency ω and the growth rate σ are given by their Taylor series expansions:

$$\omega = \omega_c + c_g(k - k_c) + \frac{\omega_c''}{2}(k - k_c)^2 + \dots, \quad (10.27a)$$

$$\tau_c \sigma = (r - r_c) - \xi_c^2(k - k_c)^2 + \dots, \quad (10.27b)$$

where, in addition to the notation introduced earlier, the group velocity c_g and the coefficient ω_c'' are defined as

$$c_g = \frac{\partial \omega}{\partial k}(k_c), \quad \omega_c'' = \frac{\partial^2 \omega}{\partial k^2}(k_c).$$

Introducing the envelope $\mathcal{A}(x, t)$ of the wave packet $u(x, t)$ as

$$u(x, t) = \frac{1}{2}\mathcal{A}(x, t)e^{i(k_c x - \omega_c t)} + \text{c.c.} \quad (10.28)$$

and reasoning as above, from the inverse Fourier transform of the dispersion relation (10.27) we derive the linear evolution equation of the envelope:

$$\tau_c(\partial_t \mathcal{A} + c_g \partial_x \mathcal{A}) = (r - r_c)\mathcal{A} + (\xi_c^2 + \frac{i\tau_c \omega_c''}{2})\partial_{xx} \mathcal{A}. \quad (10.29)$$

Proceeding to the weakly nonlinear regime, the form of the dominant nonlinearity can be determined as before by symmetry arguments. For a problem invariant under time and space translations, any solution shifted by a phase is still a solution, and so the envelope equation must be invariant under the transformation $\mathcal{A} \rightarrow \mathcal{A}e^{i\phi}$. We then see that the dominant nonlinearity is $|\mathcal{A}|^2 \mathcal{A}$. Thus, the weakly nonlinear dynamics of the wave packet is governed by the *Ginzburg–Landau equation with complex coefficients* (or CGL equation for short):

$$\tau_c(\partial_t \mathcal{A} + c_g \partial_x \mathcal{A}) = (r - r_c)\mathcal{A} + (\xi_c^2 + \frac{i\tau_c \omega_c''}{2})\partial_{xx} \mathcal{A} - \kappa |\mathcal{A}|^2 \mathcal{A}, \quad (10.30)$$

where the Landau constant $\kappa = \kappa_r + i\kappa_i$ is *a priori* complex. This equation differs from the Ginzburg–Landau equation (10.8) by (i) the term describing propagation at the group velocity, and (ii) the complex coefficients of the diffusive and nonlinear terms. Assuming that the bifurcation is supercritical ($\kappa_r > 0$), the rescaling (10.9) leads to the following normalized equation in a reference frame moving at the group velocity [$X = \epsilon(x - c_g t)/\xi_c$]:

$$\partial_T A = A + (1 + i c_1) \partial_{XX} A - (1 + i c_2) |A|^2 A, \quad (10.31)$$

with

$$c_1 = \frac{\tau_c \omega_c''}{2\xi_c^2}, \quad c_2 = \frac{\kappa_i}{\kappa_r}.$$

As we shall see, solutions and their stability are governed by the parameters c_1 and c_2 .

10.5.2 A nonlinear wave

The complex Ginzburg–Landau equation (10.31) admits the family of solutions

$$A_0(X, T) = a_0 e^{i(q_0 X - \Omega T + \Phi)}, \quad (10.32a)$$

$$a_0 = \sqrt{1 - q_0^2}, \quad (10.32b)$$

$$\Omega = c_2 + (c_1 - c_2)q_0^2, \quad (10.32c)$$

parametrized by q_0 spanning the interval $[-1, 1]$, where Φ is an undetermined phase reflecting the translational invariance of the problem. These solutions correspond to traveling waves

$$U_0(x, t) = u_0 \cos(k_0 x - \omega_0 t + \Phi), \quad (10.33)$$

with amplitude, wave number, and frequency given by

$$u_0 = \sqrt{r - r_c} \sqrt{\frac{1 - q_0^2}{\kappa}}, \quad (10.34a)$$

$$k_0 = k_c + \frac{q_0 \sqrt{r - r_c}}{\xi_c}, \quad (10.34b)$$

$$\omega_0 = \omega_\ell + \frac{1}{\tau_c} \kappa_i u_0^2 \quad \text{with} \quad \omega_\ell = \omega_c + c_g(k_0 - k_c) + \frac{\omega_c''}{2}(k_0 - k_c)^2. \quad (10.34c)$$

The frequency is therefore the sum of the frequency ω_ℓ of waves of infinitesimal amplitude (where the subscript ℓ refers to the result (10.27a) of the linear analysis) and a finite-amplitude correction proportional to κ_i . We note that the amplitude and wave number are identical to those of the solutions (10.15) of the Ginzburg–Landau equation with *real* coefficients, and that the frequency correction is identical to the Stokes correction of a dispersive wave introduced in Chapter 9.

Like the Ginzburg–Landau equation with real coefficients and the nonlinear Schrödinger equation, the complex Ginzburg–Landau equation admits localized solutions (Cross and Hohenberg, 1993; Fauve, 1998) which we do not discuss here.

10.5.3 The Benjamin–Feir–Eckhaus instability

The stability analysis of the nonlinear wave (10.33) goes along the same lines as that of the stationary pattern (10.15) governed by the real Ginzburg–Landau

equation. Perturbing the amplitude and phase of the envelope (10.32) as

$$A(X, T) = [a_0 + \tilde{a}(X, T)] e^{i[q_0 X - \Omega T + \Phi + \varphi(X, T)]},$$

substituting this expression into the CGL equation, and linearizing for small disturbances, we obtain a system similar to (10.16). The dispersion relation is then obtained by expressing the solution in the form of normal modes. As before, this analysis reveals a strongly damped amplitude mode as well as a weakly damped or amplified phase mode in the limit of perturbations with zero wave number (related to the translational invariance). The instability criterion emerges clearly when we study the equation for the phase perturbation $\varphi(X, T)$. In the long-wavelength limit this equation is a diffusion equation with diffusion coefficient (Kuramoto, 1984; Janiaud *et al.*, 1992)

$$D(q_0) = 1 + c_1 c_2 - \frac{2q_0^2(1 + c_2^2)}{1 - q_0^2}. \quad (10.35)$$

From this expression we deduce the following results, which are summarized in Figure 10.6 showing the various cases in the (c_1, c_2) plane:

- For $1 + c_1 c_2 > 0$, i.e., between the two branches of the hyperbola $1 + c_1 c_2 = 0$ shown in Figure 10.6, there exist stable waves of finite amplitude among all

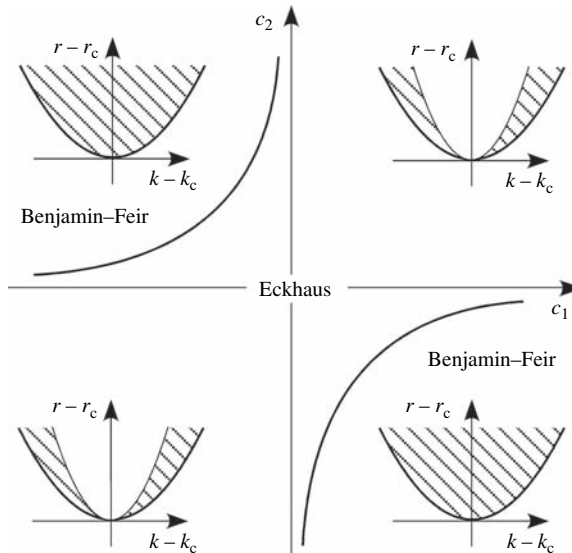


Figure 10.6 Domain where unstable waves exist (shaded region) in the $(k - k_c, r - r_c)$ plane, depending on whether the point (c_1, c_2) is outside or inside the hyperbola of Lange and Newell.

the waves existing for $r - r_c > \xi_c^2(k - k_c)^2$ (i.e., inside the marginal stability parabola) such that the parameter q_0 satisfies the condition

$$q_0^2 < \frac{1 + c_1 c_2}{2(1 + c_2^2) + 1 + c_1 c_2}. \quad (10.36)$$

For $c_1 = c_2 = 0$ we recover the Eckhaus criterion (10.21) (since the CGL equation then has real coefficients). For nonzero c_1 and c_2 the width of the band of stable wave numbers depends on c_1 and c_2 , and vanishes on the hyperbola.

- For $1 + c_1 c_2 < 0$, i.e., outside the two branches of the hyperbola $1 + c_1 c_2 = 0$, the diffusion coefficient is negative for all q_0 lying between -1 and $+1$, and none of the finite-amplitude waves (10.15) is stable (Lange and Newell, 1974). For large $c_2 = -c_1$ the coefficients of the diffusive and nonlinear terms of the CGL equation are essentially imaginary, and the CGL equation degenerates into a nonlinear Schrödinger equation: the wave instability therefore corresponds to the Benjamin–Feir instability discussed in the preceding chapter.

Therefore, the Eckhaus and Benjamin–Feir instabilities are unified in the formalism of envelope equations. This kinship of the two instabilities was noticed by Stuart and DiPrima (1978), who showed, by perturbing a finite-amplitude wave by a sum of two nearby wave numbers, that the Eckhaus instability can be interpreted in terms of resonant interactions, as in the Benjamin–Feir instability. (In the Eckhaus case there is only the resonance condition on the wave numbers; the resonance condition on the frequencies is degenerate as all the frequencies are zero.)

10.5.4 Tollmien–Schlichting waves and the transition to turbulence

With the above results on the stability of nonlinear traveling waves in mind, we now return to the problem of the stability of parallel flows $\bar{U}(y)$. As discussed in Chapter 5, plane Poiseuille flow is linearly unstable beyond the critical Reynolds number $Re_c = 5772$ with marginal wave number $k_c h = 1.02$. Stewartson and Stuart (1971) have shown that near this threshold the weakly nonlinear dynamics are effectively governed by the Ginzburg–Landau equation (10.30), with negative real part of the Landau coefficient: the Hopf bifurcation is subcritical. The cubic nonlinearity does not saturate the primary instability, but instead further amplifies the perturbation (Drazin, 2002, §5.2 and §8.9).

The search for finite-amplitude bifurcated branches requires numerical computation. These computations show that there exists a *nonlinear neutral surface* in the (Re, kh, E) parameter space, where E is the disturbance energy of the wave (see references in Bayly *et al.* (1988)). Two sections of this surface are shown

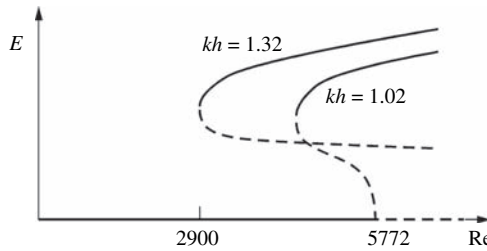


Figure 10.7 Bifurcation diagram for plane Poiseuille flow for two-dimensional perturbations with energy E , for $k_c h = 1.02$ and 1.32 ; (—), stable branches; (---), unstable branches.

in Figure 10.7 for fixed wave numbers. The section for the critical wave number $k_c h = 1.02$ shows the branch of unstable waves which arises from the subcritical Hopf bifurcation, and merges with a stable branch at a Reynolds number approximately equal to 4600 (the merging corresponding to a saddle-node bifurcation). The second section is for wave number $kh = 1.32$: although this wave number is linearly unstable for any Reynolds number, there exist two branches of finite amplitude waves, one unstable and the other stable, which merge for $Re_g \approx 2900$. Below this Reynolds number the flow is globally stable, that is, it relaxes to Poiseuille flow for initial two-dimensional perturbations of arbitrary amplitude (Chapter 3). More general solutions, such as three-dimensional waves, are however found to exist for Reynolds number even below Re_g (Ehrenstein and Koch, 1991; Huerre and Rossi, 1998).

In spite of the subcritical nature of the bifurcation, secondary instabilities of forced Tollmien–Schlichting waves have been observed before the transition to turbulence. For example, in the case of boundary layer flow, Klebanoff *et al.* (1962) observed that beyond a certain distance downstream a spanwise (along the z -direction) undulation of the wave crests with a well-defined wavelength λ_z appears. Two successive crests are typically out of phase by $\lambda_z/4$ and form an alternating “ Λ ” pattern. These observations stimulated further analysis, which revealed two secondary instability mechanisms of two-dimensional waves: an elliptical mechanism and a subharmonic mechanism (see the reviews by Bayly *et al.* (1988); Herbert (1988); Huerre and Rossi (1998, §8); and Kerswell (2002)). Both of these instabilities are inviscid and therefore develop over a time of the order of the inverse of the velocity gradient, $\bar{U}'(y)$, which is much shorter than the time scale of the primary (viscous) instability, which in turn is why they can be observed.

However, the diagram in Figure 10.7, along with the observations briefly summarized above regarding secondary instabilities, are not at all the last word on the stability of Poiseuille flow or boundary layer flow. Importantly, as discussed in

Chapter 5, the perturbations remain two-dimensional only in very well-controlled experiments and for velocity fluctuations which are initially very weak. When these conditions are not met the flow is unstable for Reynolds numbers below the critical value, both for Poiseuille flow and for boundary layer flow. The instability is manifested not as a Tollmien–Schlichting wave but as a three-dimensional structure of longitudinal streaks which evolves rapidly to turbulence. It is likely that three phenomena play an important role:

- the convective nature of the instability, by which any noise can be amplified without the selection of a particular eigenmode;
- the transient growth of certain linear superpositions of stable eigenmodes (linear mechanism);
- nonlinear effects (here due to advection), without which any perturbation would die out over the long term.

The nonlinear effects cause a rapid transition to turbulence. This transition is manifested as *intermittency*, an alteration between laminar phases and turbulent bursts, a phenomenon studied in particular by Wygnanski and Champagne (1973) for Poiseuille flow in a tube. The persistence of turbulent bursts in a linearly stable flow is the subject of current theoretical, numerical, and experimental research, with the nature of the initial perturbations likely to play a crucial role. We refer the reader to the excellent review of Kerswell (2005) for further discussion.

10.6 Coupling to a field at large scales

10.6.1 Galilean invariance and conservation laws

The above analysis of finite-amplitude waves needs to be modified when the wave number $k_0 = 0$ is neutral. The growth rate in this case has the shape shown in Figure 10.8. Long-wavelength ($k \ll k_c$) perturbations, which are hardly damped at

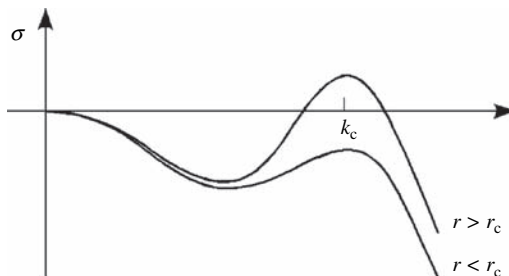


Figure 10.8 Sketch of the growth rate $\sigma(k)$ below and above the threshold of a finite-wave number instability, when $k_0 = 0$ is neutral and small wave numbers are weakly stable.

all, can easily be excited by a linearly unstable mode of finite wave number k_c . The coupling of the two modes then leads to new dynamics.

This situation arises, in particular, when the problem satisfies *Galilean invariance*, that is, invariance under the transformation

$$y = x - Vt, \quad v = u - V. \quad (10.37)$$

As an example, let us consider the model equation

$$\partial_t u = Lu - u \partial_x u, \quad L = \partial_x^2 + 2r \partial_x^4 + \partial_x^6. \quad (10.38)$$

We note first of all that this equation is translationally invariant: if $u(x, t)$ is a solution, it is easily checked that the function $v(x, t) = u(x - \phi, t)$, corresponding to $u(x, t)$ translated by a phase ϕ , is also a solution. As discussed in Section 10.4, this translational invariance is associated with a neutral phase mode. Equation (10.38) also satisfies Galilean invariance; indeed, under the Galilean transformation $y = x - Vt$ it becomes

$$\partial_t u = \partial_y^2 u + 2r \partial_y^4 u + \partial_y^6 u - (u - V) \partial_y u,$$

and it can be verified that the transformation $v = u - V$ restores Eq. (10.37).²

In hydrodynamics, Galilean invariance is generally broken by the no-slip condition at the walls, but it can survive in certain cases, for example, in Rayleigh–Bénard convection with free boundaries. It is also possible to have approximate Galilean invariance, for example, in Rayleigh–Bénard convection with fixed boundaries but small Prandtl number (which for low viscosity results in thin velocity boundary layers on the upper and lower walls). Far from the lateral walls, a slow horizontal flow at large scales has almost no dissipation, which corresponds to nearly neutral perturbations of very small wave number (Siggia and Zippelius, 1981).

The situation of neutral zero wave number is also encountered when the evolution equation can be written in the form of a conservation law:

$$\partial_t U + \partial_x [f(U, \partial_x U, \dots)] = 0, \quad (10.39)$$

where the function f is a sum of products of U and its derivatives. A perturbation $\hat{u} e^{i(kx - \omega t)} + \text{c.c.}$ of a stationary, uniform solution U_0 of this equation satisfies the dispersion relation

$$-i\omega + ik f'(U_0) + \mathcal{O}(k^2) = 0, \quad (10.40)$$

² As a counter-example, it can be checked that the Swift–Hohenberg equation (10.13) is not Galilean-invariant.

which clearly shows that the $k=0$ mode is neutral. This is the case in thermohaline convection, where $U(x, t)$ is the salt concentration field (Riecke, 1992). Another example is a flow of finite depth with a free surface.³ In this case the field $U(x, t)$ represents the thickness of the fluid layer, $f(U, \partial_x U, \dots)$ is the horizontal flow rate, and the mass conservation is expressed by a law of the type (10.39) (Renardy and Renardy, 1993).

10.6.2 Coupled evolution equations

Let us consider a perturbation of a stationary, uniform base flow near the marginal stability $r = r_c$ in the form of the sum

$$u(x, t) = \frac{1}{2} \mathcal{A}(x, t) e^{i(k_c x - \omega_c t)} + \text{c.c.} + \mathcal{B}(x, t). \quad (10.41)$$

Here $\mathcal{A}(x, t)$ is the complex envelope of a wave packet centered on the finite wave number k_c and $\mathcal{B}(x, t)$ represents the (real) long-wavelength perturbation, which is nearly neutral.

Neglecting for the moment the coupling between \mathcal{A} and \mathcal{B} , the weakly nonlinear evolution of the envelope \mathcal{A} is, as before, governed by the complex Ginzburg–Landau equation (10.30). The linear evolution equation of the mode \mathcal{B} is obtained from a Taylor series expansion of the dispersion relation about $k_0 = 0$, or

$$\partial_t \mathcal{B} = -c_0 \partial_x \mathcal{B} + \frac{\xi_0^2}{\tau_c} \partial_{xx} \mathcal{B}, \quad (10.42)$$

where the speed c_0 and the diffusion length ξ_0 of the $k_0 = 0$ mode are defined as

$$c_0 = \frac{\partial \omega}{\partial k}, \quad \frac{\xi_0^2}{\tau_c} = -\frac{1}{2} \frac{\partial^2 \sigma}{\partial k^2},$$

with the derivatives evaluated at the critical point ($r_c = 1, k_0 = 0$). The diffusion coefficient ξ_0^2/τ_c is positive for linearly stable, long-wavelength waves corresponding to Figure 10.8.

The determination of the dominant coupling terms depends on the choice of the relative order of magnitude of \mathcal{A} and \mathcal{B} . Since experiment shows that \mathcal{B} is small

³ We note that the weakly nonlinear stability of a liquid film falling down an inclined plane is not described by this analysis. In fact, the linear analysis shows that the instability does not arise on a mode of isolated finite wave number, but instead occurs on an unstable band extending from $k = 0$ to the cutoff wave number (long-wave instability); see Chapter 6 and also Ruyer-Quil and Manneville (2000) and Chang (1994). The analysis of Benney (1966), which considers the interaction of a harmonic k_0 with the average flow ($k = 0$) and the second harmonic $2k_0$, leads to a CGL equation, but this analysis is incomplete as it ignores the continuous nature of the spectrum of unstable wave numbers.

compared to $|\mathcal{A}|$, we can take

$$\mathcal{B} \sim \epsilon \mathcal{A} \sim \epsilon^2.$$

The dominant coupling terms satisfying translational invariance are then \mathcal{AB} in the equation for \mathcal{A} , and $\partial_x |\mathcal{A}|^2$ in the equation for \mathcal{B} (since the latter term is larger by at least one order of magnitude compared to nonlinear terms involving only \mathcal{B}). Finally, the change of scale (10.9) leads, in a reference frame moving at the group velocity $c_g(k_c)$, to the following system of coupled equations:

$$\partial_T A = A + (1 + ic_1) \partial_{XX} A - (1 + ic_2) |A|^2 A + (1 + ic_3) AB, \quad (10.43a)$$

$$\partial_T B = \frac{\epsilon^{-1} \tau_c}{\xi_c} (c_g - c_0) \partial_X B + \frac{\xi_0^2}{\xi_c^2} \partial_{XX} B + \epsilon^{-1} \gamma \partial_X |A|^2, \quad (10.43b)$$

where the mode \mathcal{B} has been scaled such that the coefficient of the coupling term \mathcal{AB} is normalized to $1 + ic_3$. This equation describes, for example, the evolution of the interface between two layers of viscous fluids in Couette–Poiseuille flow: the coefficients for this case have been calculated by Renardy and Renardy (1993).

Therefore, all the terms in the equation for A are of the same order of magnitude (ϵ^3), but this is not the case in the equation for B . If the coefficients $\tau_c(c_g - c_0)/\xi_c$ and γ are of order unity, Eq. (10.43b) becomes degenerate and can be integrated to give

$$B = \frac{\xi_c \gamma}{\tau_c (c_g - c_0)} |A|^2.$$

The mode B is therefore slaved to A and does not bring in anything qualitatively new. However, the situation is changed if the difference $c_g - c_0$ and the coupling coefficient γ are small, of order ϵ : in this case the four terms of Eq. (10.43b) are then all of the same order of magnitude. It is this situation that we shall study below.

We note that in the case of a *stationary* bifurcation ($\omega_c = 0$), a similar system of amplitude equations which also possesses reflection symmetry $x \rightarrow -x$ has been studied by Coullet and Fauve (1985).

10.6.3 Wave stability

The system (10.43) admits the family of solutions $B_0 = 0$ and A_0 given by Eq. (10.32), which corresponds to the finite-amplitude waves (10.33). The stability of these waves has been studied by Barthelet and Charru (1998), and here we only quote the main results. For spatially *uniform* perturbations, i.e., perturbations with

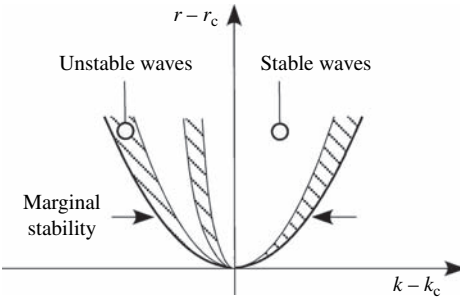


Figure 10.9 Marginal stability parabola in the $(k - k_c, r - r_c)$ plane and the parabolae bounding the regions where stable and unstable waves exist (white and hatched regions, respectively).

zero wave number, the system of equations for the perturbations reduces to

$$\begin{pmatrix} \dot{a} \\ \dot{\varphi} \\ \dot{b} \end{pmatrix} = \begin{pmatrix} -2a_0^2 & 0 & 1 \\ -2a_0 c_1 & 0 & c_3 \\ 0 & 0 & 0 \end{pmatrix} \begin{pmatrix} a \\ \varphi \\ b \end{pmatrix}, \quad (10.44)$$

which has the eigenvalues

$$s_1 = -2a_0^2, \quad s_2 = 0, \quad s_3 = 0.$$

We recover the stable amplitude mode and the two neutral modes corresponding to the two invariances, translational and Galilean (we note that this matrix can be diagonalized by a change of variables for A and B corresponding to a rotation in the complex plane). For spatially *periodic* rather than uniform perturbations, it can be shown from the dispersion relation that there are stable waves inside the marginal stability parabola in the (k, r) plane, i.e. in the lenticular regions bounded by arcs of parabolae, as shown in Figure 10.9. These arcs are not symmetric about the $k = k_c$ axis, which is consistent with the absence of reflection symmetry. Finally, the coupling to a long-wavelength mode has the effect of breaking the Eckhaus parabola (10.21) into several arcs.

10.6.4 An experimental illustration

The results of this analysis can be illustrated by observations of the secondary instability of waves at the interface between two superposed sheared liquids (Charru and Barthelet, 1999). The experiment, already described in Chapter 8, consists of an annular channel of perimeter L with a rotating upper plate which sets the fluids in motion. For certain viscosity ratios a wave of wavelength $2\pi/k$ on the centimeter scale appears at the interface above a critical speed U_c of the

plate, corresponding to supercritical bifurcation, and propagates at a speed ω/k close to the interface speed.

When the upper plate velocity is increased by small increments, the saturated amplitude $|A|$ of the wave grows as $\sqrt{U - U_c}$, with about 30 wavelengths along the perimeter of the channel. However, when the speed becomes too high (typically $U \approx 1.1 U_c$), a pinch arises in the wave envelope, which ends with the disappearance of one wavelength and subsequent relaxation of the train to a longer wavelength. This phenomenon is illustrated in Figure 10.10 where open (black) symbols represent stable (unstable) wave trains; it can repeat several times (so that several wavelengths vanish) before the new equilibrium is reached. The reverse process of nucleation of a new wavelength occurs when the speed is decreased. This nucleation–coalescence process displays hysteresis. It can be shown in Figure 10.10 that the stable wave trains (open symbols) lie in between two parabolae (dashed lines) which can be interpreted as the boundaries between the stable and unstable parabolic regions shown in Figure 10.9.

Figure 10.11 shows the process by which two wavelengths disappear. On the left is the time evolution of the interface profile, where the length of a line corresponds to the time, equal to 4.02 s, for a wave crest to travel the whole perimeter, so that it essentially gives a (reversed) spatial image of the wave train in the annular channel. The disappearance of the first wavelength can be seen between lines 10 and 11 ($t \approx 140$ s), and then the second between lines 23 and 24 ($t \approx 190$ s). On the right we show the corresponding evolutions of the amplitude $|A|$ and the frequency f of the mode k (obtained by demodulation using the Hilbert transform), and of the long-wavelength mode B (obtained by low-pass filtering). The growth of the

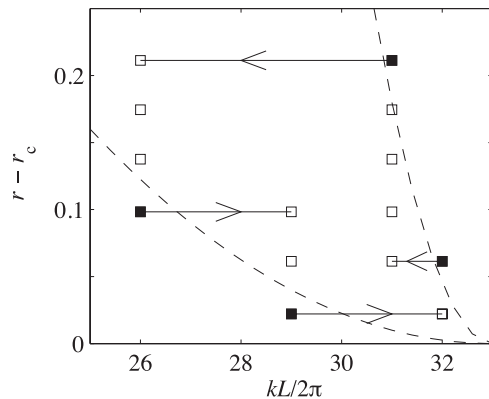


Figure 10.10 The wave number $kL/2\pi$ as a function of the distance from threshold $r - r_c = (U - U_c)/U_c$ for viscosity ratio $\mu_2/\mu_1 = 1.55$. (□) stable wave train; (■) unstable wave train; (—), parabolae bounding the stable domain. From Charru and Barthelet (1999).

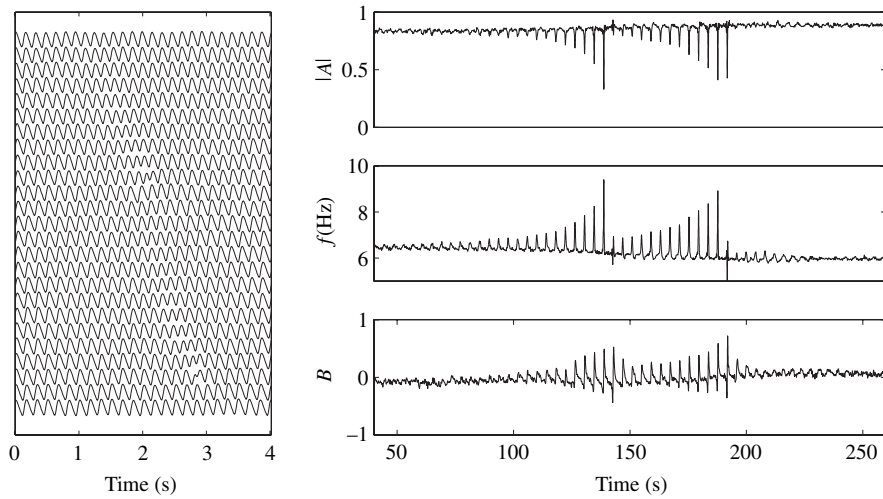


Figure 10.11 Left: time evolution of the interface (from left to right and top to bottom); the length of a line corresponds to the time (4.02 s) to travel the perimeter of the channel at the phase velocity. Right: the time evolutions $|A|(t)$, $f(t)$, and $B(t)$. From Charru and Barthelet (1999).

defect is associated with (i) a decrease of the amplitude $|A|$, (ii) an increase of the frequency f (local compression of the wave number), and (iii) a local variation of the average position B of the interface. The first relaxation is immediately followed by the growth of a second defect, and the second coalescence allows the wave to finally reach equilibrium. We note that since two wavelengths have disappeared, the frequency has decreased slightly from 6.5 to 6.0 Hz.

10.7 Exercises

10.7.1 Derivation of the GL equation for the Swift–Hohenberg model

We want to obtain the Ginzburg–Landau equation (i.e., compute the Landau coefficient) governing the slow dynamics of the envelope of straight convection rolls, close to the critical Rayleigh number, using a simplified model based on the Boussinesq approximation, the Swift–Hohenberg equation (Swift and Hohenberg, 1977; Manneville, 1990, chapter 8):

$$\tau_c \partial_t u = \mu u - \xi^4 (\partial_x^2 + k_c^2)^2 u - \gamma u \partial_x u.$$

1. Show that the dispersion relation of small perturbations $\hat{u} e^{ikx+\sigma t}$ of the base solution $u=0$ is

$$\tau_c \sigma = \mu - \xi^4 (k^2 - k_c^2)^2.$$

Show that $u = 0$ is unstable for $\mu > 0$, and that the marginal mode has wave number k_c . Sketch the behavior of the growth rate $\sigma(k)$ near k_c for $\mu \lesssim 0$ and $\mu \gtrsim 0$.

2. Show that at a distance $\mu = \epsilon^2$ from threshold, where ϵ is a small parameter, the width of the band of unstable wave numbers is $2\epsilon/k_c\xi^2$, and the growth rate is of order ϵ^2 . Show that the time and spatial scales of the slow variations of the amplitude are

$$T = \epsilon^2 t, \quad X = \epsilon x, \quad X_2 = \epsilon^2 x.$$

3. Seeking a solution in the form of an expansion

$$u(x, t) = \epsilon u_1(x, X, X_2, T) + \epsilon^2 u_2(x, X, X_2, T) + \dots,$$

show that the successive derivatives are given by

$$\begin{aligned} \partial_t u &= \epsilon^3 \partial_T u_1 + \mathcal{O}(\epsilon^4), \\ \partial_x u &= \epsilon \partial_X u_1 + \epsilon^2 (\partial_x u_2 + \partial_X u_1) + \epsilon^3 (\partial_x u_3 + \partial_X u_2 + \partial_{X_2} u_1) + \mathcal{O}(\epsilon^4), \\ \partial_x^2 u &= \epsilon \partial_X^2 u_1 + \epsilon^2 (\partial_x^2 u_2 + 2\partial_x \partial_X u_1) + \\ &\quad \epsilon^3 (\partial_x^2 u_3 + 2\partial_x \partial_X u_2 + 2\partial_x \partial_{X_2} u_1 + \partial_X^2 u_1) + \mathcal{O}(\epsilon^4), \\ \partial_x^3 u &= \epsilon \partial_X^3 u_1 + \epsilon^2 (\partial_X^3 u_2 + 3\partial_x^2 \partial_X u_1) + \\ &\quad \epsilon^3 (\partial_X^3 u_3 + 3\partial_x^2 \partial_X u_2 + 3\partial_x \partial_X^2 u_1 + 3\partial_x^2 \partial_{X_2} u_1) + \mathcal{O}(\epsilon^4), \\ \partial_x^4 u &= \epsilon \partial_X^4 u_1 + \epsilon^2 (\partial_X^4 u_2 + 4\partial_x^3 \partial_X u_1) + \\ &\quad \epsilon^3 (\partial_X^4 u_3 + 4\partial_x^3 \partial_X u_2 + 6\partial_x^2 \partial_X^2 u_1 + 4\partial_x^3 \partial_{X_2} u_1) + \mathcal{O}(\epsilon^4), \\ u \partial_x u &= \epsilon^2 u_1 \partial_X u_1 + \epsilon^3 (u_2 \partial_X u_1 + u_1 \partial_X u_2 + u_1 \partial_{X_2} u_1) + \mathcal{O}(\epsilon^4). \end{aligned}$$

4. Show that the sequence of linear problems to be solved at orders ϵ , ϵ^2 , and ϵ^3 is

$$\begin{aligned} Lu_1 &= 0, \quad L = -\xi^4 (\partial_x^2 + k_c^2)^2, \\ Lu_2 &= \xi^4 (4\partial_X^3 u_1 + 4k_c^2 \partial_X u_1) + \gamma u_1 \partial_X u_1, \\ Lu_3 &= \tau_c \partial_T u_1 - u_1 + \xi^4 (4\partial_X^3 u_1 + 4k_c^2 \partial_X u_1) u_2 + \\ &\quad + \xi^4 (4\partial_X^3 u_2 + 6\partial_X^2 \partial_X u_1 + 4k_c^2 \partial_X u_2 + 2k_c^2 \partial_X^2 u_1) u_1 + \\ &\quad \gamma (u_2 \partial_X u_1 + u_1 \partial_X u_2 + u_1 \partial_{X_2} u_1). \end{aligned}$$

5. Show that at order ϵ the solution is

$$u_1 = \frac{1}{2} A_1(X, X_2, T) e^{ik_c x} + \text{c.c.},$$

where $A_1(X, X_2, T)$ is the slowly varying envelope of the wave packet centered on k_c .

6. Show that at order ϵ^2 the right-hand side reduces to the nonresonant term

$$\frac{ik_c\gamma}{4} A_1^2 e^{2ik_c x} + \text{c.c.},$$

and that the solution is

$$u_2 = \frac{1}{2} A_2(X, X_2, T) e^{ik_c x} + \frac{1}{2} B_2(X, X_2, T) e^{2ik_c x} + \text{c.c.},$$

where the first term corresponds to the general solution of the homogeneous equation, and the second is the particular solution:

$$B_2 = -\frac{i\gamma}{18\xi^4 k_c^3} A_1^2.$$

7. Show that at order ϵ^3 the right-hand side is a sum of exponentials $e^{ink_c x}$ with $n = 0, \pm 1, \pm 2, \pm 3$, and that, in particular, the resonant terms are

$$\frac{1}{2} (\tau_c \partial_T - 1) A_1 - 2\xi^4 k_c^2 \partial_X^2 A_1 + \frac{ik_c\gamma}{4} B_2 A_1^*,$$

along with their complex conjugates (the two terms proportional to $\partial_{X_2} A_1$ cancel each other out).

8. Show that the nonresonance (or solvability) condition, also known as the Fredholm alternative, corresponds to the Ginzburg–Landau equation

$$\tau_c \partial_T A_1 = A_1 + \xi_c^2 \partial_{XX} A_1 - \kappa |A_1|^2 A_1, \quad \xi_c^2 = 4\xi^4 k_c^2, \quad \kappa = \frac{\gamma^2}{9\xi_c^2}.$$

10.7.2 Translational invariance and Galilean invariance

Consider the three evolution equations

$$\begin{aligned} \partial_t u &= Lu - u \partial_x u, & L &= \mu - (\partial_x^2 + 1)^2, \\ \partial_t u &= Lu - u^3, & L &= \partial_x^2 + 2\mu \partial_x^4 + \partial_x^6, \\ \partial_t u &= Lu - u \partial_x u, & L &= \partial_x^2 + 2\mu \partial_x^4 + \partial_x^6. \end{aligned}$$

1. Show that each of these equations satisfies translational invariance, that is, if $u(x, t)$ is a solution, then $v(x, t) = u(x - \phi, t)$ is also one.
2. Show that only the last equation satisfies Galilean invariance, that is, if $u(x, t)$ is a solution, then $v(x, t) = u(x - Vt, t) - V$ is also one.

11

Dynamical systems and bifurcations

11.1 Introduction

A useful mathematical framework for studying linear and nonlinear stability is the theory of *ordinary differential equations* (ODEs), also known as the theory of dynamical systems when the focus is on geometric and qualitative representations of the ideas and solutions. An informal presentation of this theory was given in Chapter 1. The goal of this chapter is to give a more systematic account of it from a mathematical point of view. In particular, we shall show how to reduce the number of degrees of freedom of a problem to obtain the “normal forms” of elementary bifurcations referred to often in the previous chapters.

In spite of its restrictive nature relative to the theory of partial differential equations, the theory of dynamical systems has revealed the extraordinary richness and complexity of the types of behavior that can arise when nonlinear effects play a role. This theory originated in the work of Henri Poincaré, in particular, in his book *Méthodes nouvelles de la mécanique céleste*. Poincaré’s ideas were further developed during the first half of the twentieth century by the Russian school of mathematics (Kolmogorov, Arnold). The discovery that a system with a small number of degrees of freedom can display unpredictable, chaotic behavior then led to a great deal of research in this area beginning in the 1960s. Qualitatively new concepts such as deterministic chaos and sensitivity to the initial conditions were introduced, and these have significantly modified our understanding of deterministic models and their use in the description of natural phenomena.

This chapter is organized as follows. First we present the ideas of phase space, generalized flow in the phase space, and an attractor (Section 11.2), which will allow us to carry out linear stability studies within a geometric framework (Section 11.3). Next we discuss the behavior of nonlinear systems through the study of invariant manifolds and normal forms (Section 11.4). After discussing structural stability, genericity, and transversality (Section 11.5), we embark on the study

of systems with parameters and of local bifurcations of codimension 1 and 2 (Section 11.6).

The essential points that we develop are the following. First we study the linear stability of a fixed point. Then we discuss the idea of the projection of the dynamics of a system with a large number of degrees of freedom on a “surface” of low dimension, the center manifold. This is the most technical part of the chapter. Finally, we study the elementary bifurcations of codimension 1 and 2 of a fixed point.

Extensions to the study of chaos can be found in the classical studies of Bergé *et al.* (1987) and Schuster and Wolfram (2005). The subject is treated from a more mathematical viewpoint by Glendinning (1994) and in the more advanced book of Guckenheimer and Holmes (1986). For an approach based on symmetries, see the reviews of Crawford (1991) and Crawford and Knobloch (1991).

11.2 Phase space and attractors

11.2.1 Flow generated by a vector field and orbits in phase space

Let us consider a physical system whose state is entirely determined by n independent, real, scalar quantities $x_i(t)$, $i = 1, \dots, n$, called the degrees of freedom of the system. Then the state of the system at a given instant can be represented by a point in phase space $V \subset \mathbb{R}^n$ whose coordinates are the $x_i(t)$. Certain conditions can be used to restrict the $x_i(t)$ to only a part of \mathbb{R} , or rather the $x_i(t)$ can be defined only *modulo* some relation (the angles, for example). Therefore, V is often only a part of \mathbb{R}^n , or a quotient subspace (a cylinder, sphere, torus, etc.). We shall assume that it is possible to define a global coordinate system on V , that is, that V is a manifold (Arnold, 1973, chapter 5).

The evolution equations of the system can be written very generally as a system of ordinary differential equations:

$$\frac{d\mathbf{x}}{dt} = \mathbf{X}(\mu, \mathbf{x}, t), \quad (11.1)$$

where $\mathbf{x} = (x_1, \dots, x_n)$ is the state vector, t is the time, $\mu \in \mathbb{R}^m$ designates the m parameters of the problem, and \mathbf{X} defines a vector field on V . Equations (11.1) show that the evolution of the system depends only on the current state of the system and not, for example, on its history.

When the field \mathbf{X} does not explicitly depend on the time, the system is termed autonomous; otherwise, it is termed nonautonomous. We note that a nonautonomous system can always be transformed into a higher-dimensional autonomous system by introducing a new degree of freedom $\theta = t$ satisfying the equation $d\theta/dt = 1$.

Example 11.1 The forced van der Pol oscillator, governed by the equation

$$\ddot{x} + \alpha(x^2 - 1)\dot{x} + x = \cos \omega t,$$

can be written in the autonomous form as

$$\dot{x} = y - \alpha(x^3/3 - x), \quad \dot{y} = -x + \cos \omega \theta, \quad \dot{\theta} = 1.$$

The dependence of \mathbf{X} on parameters will be discussed only at the end of the chapter, and so for now we omit it. For an autonomous system, Eqs (11.1) are then rewritten as

$$\frac{d\mathbf{x}}{dt} = \mathbf{X}(\mathbf{x}). \quad (11.2)$$

Geometrically, such a system can be interpreted in two ways: in terms of a *flow* at fixed t , or in terms of the *trajectory* of a point representing the time evolution of the physical system. These interpretations, defined in detail below, are analogous to the Eulerian and Lagrangian points of view in fluid mechanics.

- Under the action of the field \mathbf{X} , a part V_1 of the manifold V will be transported after a time t toward another part $\phi_t(V_1)$ of \mathbb{R}^n . The flow generated by the vector field \mathbf{X} is defined as the map $\phi_t: V \rightarrow \mathbb{R}^n$ responsible for this transport, Figure 11.1a. (In particular, this idea of a flow will allow us to define the *invariant submanifolds* of V .) The flow ϕ_t and the vector field \mathbf{X} are related as

$$\frac{d}{dt} (\phi_t(\mathbf{x}))_{t=\tau} = \mathbf{X}(\phi_\tau(\mathbf{x})).$$

- A solution $\mathbf{x}(t)$ of (11.2) associated with an initial condition $\mathbf{x}(0) = \mathbf{x}_0$ can be represented by a curve in the phase space V , Figure 11.1b. This curve is also

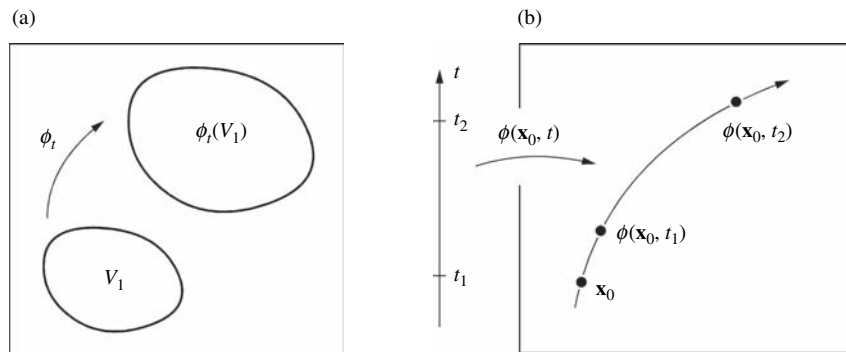


Figure 11.1 (a) Image made by the flow ϕ_t of a part V_1 of V ; (b) integral curve or trajectory of the differential system, associated with a particular initial condition.

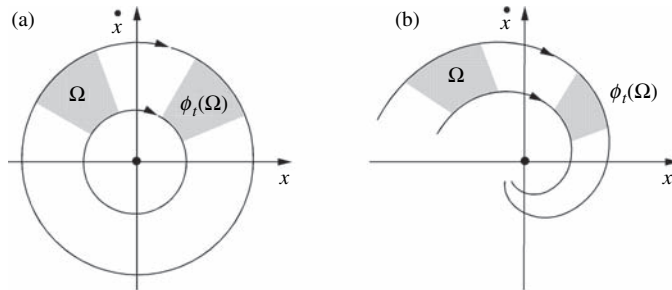


Figure 11.2 Phase portrait of the pendulum in the phase space (x, \dot{x}) : (a) nondissipative pendulum: area conservation; (b) damped pendulum: area contraction.

called the integral curve, the orbit, or the trajectory. In other words, a trajectory is the image made by the flow ϕ_t of a time interval $]t_1, t_2[$, with the flow viewed as a function of t for fixed $\mathbf{x} = \mathbf{x}_0$:

$$\phi(\mathbf{x}_0, t):]t_1, t_2[\rightarrow \mathbb{R}^n.$$

It can be shown that if the vector field \mathbf{X} is continuously differentiable, then Eq. (11.2) associated with an initial condition $\mathbf{x}(t_0) = \mathbf{x}_0$ admits a unique solution (at least “locally”, i.e., in a neighborhood of $t = t_0$), and that this solution has a regular dependence on the initial condition.

A major step in studying a differential system such as (11.2) is the determination of the topological structure of the ensemble of its solutions. This structure can be represented by a sketch of typical trajectories, which is called the *phase portrait* of the differential system. Some trajectories for a particular problem are shown in Figure 11.2.

11.2.2 Dissipative and conservative systems, and attractors

The simplest types of behavior of a physical system are either stationary or periodic states. A stationary state corresponds by definition to $d\mathbf{x}/dt = 0$, and is represented in the phase space by a fixed point of the differential system. A fixed point coincides with a singular point of the vector field \mathbf{X} given by $\mathbf{X}(\mathbf{x}) = 0$. Periodic behavior is represented in the phase space by a closed orbit. In general, it is more difficult to determine periodic orbits than fixed points.

Example 11.2 Let us consider a damped linear pendulum of eigenfrequency ω_0 and damping coefficient $\beta \geq 0$ (where we can take $\omega_0 = 1$ without loss of generality by rescaling the time). The displacement x of the pendulum obeys the momentum

balance (Newton's second law):

$$\ddot{x} + \beta \dot{x} + x = 0.$$

This second-order differential equation can be written as a system of two first-order equations:

$$\begin{aligned}\dot{x} &= y, \\ \dot{y} &= -x - \beta y,\end{aligned}$$

for which the only fixed point in the phase space (x, \dot{x}) is the origin $(0, 0)$. The trajectory determined by any initial condition is a spiral converging to this fixed point. In the case of a nondissipative pendulum ($\beta = 0$), the origin is the only fixed point as before, and the trajectories are circles centered at the origin. These two cases are shown in Figure 11.2.

Example 11.3 Let us consider a nonlinear oscillator described in polar coordinates by the dynamical system

$$\begin{aligned}\dot{r} &= r(1 - r^2), \\ \dot{\theta} &= 1.\end{aligned}$$

This system admits a fixed point at the origin $r = 0$, and a periodic orbit, defined by the circle $r = 1$ for which $\dot{r} = 0$, with period 2π . For $r > 1$, we get $\dot{r} < 0$, while for $0 < r < 1$, we get $\dot{r} > 0$. The origin is therefore an unstable fixed point, and the periodic orbit is stable. In the phase space, a trajectory coming from any point (except the origin) converges toward the circle $r = 1$.

The essential difference between dissipative and nondissipative (sometimes improperly called “conservative”) systems amounts to the following property in the phase space: the flow generated by the vector field of a nondissipative system preserves volume, while for a dissipative system it contracts or expands an initial volume. The expansion or contraction is measured by the divergence of the vector field. The “compressibility” of dissipative flows is illustrated in Figure 11.2b for the pendulum discussed above, for which it can be shown that $\text{div}\mathbf{X} = -\beta$.

The fixed points and limit circle discussed in the previous examples represent asymptotic behaviors of the system: they are typical examples of *attractors* of dissipative systems. The ensemble of initial conditions from which the system evolves toward a given attractor is called the *basin of attraction* of the attractor. In a two-dimensional phase space it can be shown that the only possible attractors are fixed points and periodic orbits. In higher dimensions other attractors can exist: tori representing periodic or quasi-periodic behavior with several frequencies, or “strange

attractors” representing chaotic behavior. A strange attractor is characterized by its fractal structure and by the fact that the trajectories coming from two neighboring points diverge exponentially (while remaining on the attractor). This latter phenomenon is very important and is referred to as sensitivity to, or exponential dependence on, the initial conditions. It makes the physical system unpredictable beyond a certain time, which is called the predictability horizon, because the initial conditions can never be known exactly (Lighthill, 1986; Bergé *et al.*, 1987; Schuster and Wolfram, 2005). A classic example of a system exhibiting chaotic behavior is the Lorenz system, which we describe briefly.

Example 11.4 Starting from the equations for momentum and energy conservation, Lorenz (1963) proposed the following greatly simplified system for describing the motion in atmospheric convection:

$$\begin{aligned}\dot{x} &= -\sigma x + \sigma y, \\ \dot{y} &= -xz + rx - y, \\ \dot{z} &= xy - bz,\end{aligned}$$

where σ , r , and b are positive constants. The classical approach is to fix the constants $\sigma = 10$ and $b = 8/3$ and study the solutions for varying r . For $r < 1$ the origin is the only fixed point and the only attractor. For $r = 1$ the origin becomes unstable and two other fixed points appear, which are stable as long as $r < 24.74$. For $r > 24.74$ a strange attractor appears. For more details, see the study of the thermal convection in a ring in Chapter 1.

11.2.3 Poincaré sections

The study of periodic orbits can to some extent be reduced to that of fixed points, by resorting to the idea of *first return map* in a *Poincaré section*. This idea is essentially a geometrical interpretation of the Floquet theory of differential equations with periodic coefficients (Glendinning, 1994). Let us consider a three-dimensional phase space and a periodic orbit with period T of a flow ϕ_t (Figure 11.3). We represent a local section of this orbit by a surface segment Σ , and denote their intersection by \mathbf{p} .

The first return map F of an open neighborhood $U \subset \Sigma$ in Σ is defined as

$$F(\mathbf{q}) = \phi_\tau(\mathbf{q}), \quad (11.3)$$

where τ is the time needed for the point $\mathbf{q} \in U$ to return to Σ under the action of the flow. The time τ in general depends on the point \mathbf{q} , with $\tau \rightarrow T$ for $\mathbf{q} \rightarrow \mathbf{p}$ on Σ . The point \mathbf{p} is therefore a fixed point of the map F , and the stability of the

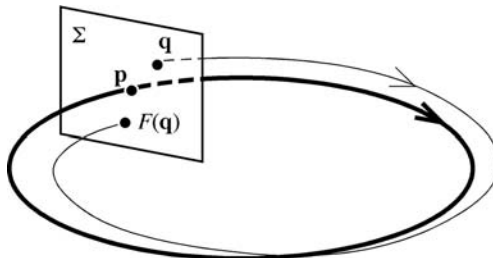


Figure 11.3 Poincaré section Σ of a periodic orbit. The intersection point \mathbf{p} is a fixed point of the first return map F ; the image of a point \mathbf{q} on Σ is $F(\mathbf{q})$.

orbit under the action of the flow ϕ_t is manifestly related to the stability of the fixed point \mathbf{p} for the map F . We note, however, that the definition of the first return map involves the flow ϕ_t , and therefore the study of the stability of an orbit in general requires that the solutions of the differential system be known! Fortunately, averaging techniques may shortcut the detailed knowledge of these solutions.

The study of first return maps is interesting beyond the subject of Poincaré sections. In fact, many physical systems are modeled not by differential equations, but by nonlinear recursion relations, maps, or “discrete dynamical systems” of the type

$$\mathbf{x}_{n+1} = \mathbf{F}(\mathbf{x}_n), \quad (11.4)$$

where \mathbf{F} is a continuously differentiable map. For such discrete systems there is a theory analogous to that of differential systems, but we shall not discuss it here. The logistic map is a simple example of such a recursion relation.

Example 11.5 The logistic map is defined as

$$x_{n+1} = \lambda x_n(1 - x_n), \quad x \in [0, 1], \quad \lambda > 0.$$

This map possesses a rich variety of surprising phenomena, ranging, for increasing parameter λ , from a simple fixed point $F(x) = x$ for $\lambda < 0.75$, to periodic dynamics $F^m(x) = x$ (the map F iterated m times), and then to chaotic dynamics for $\lambda > 0.89$ (Feigenbaum, 1978; Tresser and Coullet, 1978). The same sequence of behaviors is found for all functions F possessing a quadratic extremum, and so the logistic map is of general interest.

The Hénon attractor, which is another classical example of a strange attractor, is studied in Exercise 11.7.1.

Jules Henri Poincaré (1854–1912)

Jules Henri Poincaré was born in Nancy, France into an upper-middle-class Lorraine family. (He was a first cousin of Raymond Poincaré, president of the French Republic from 1913 to 1920.) He graduated from the Ecole Polytechnique in 1875 and then from the Ecole des Mines. He received his doctorate in mathematics from the University of Paris in 1879, with Charles Hermite as his thesis advisor. He taught in Caen and then in Paris, where in 1881 he was appointed to a chair of mathematical physics and probability at the Sorbonne, as well as to a chair at the Ecole

Polytechnique. He is considered the founder of algebraic topology and the theory of analytic functions of several complex variables, and he made major contributions to number theory. He developed a novel method of characterizing the solution of differential equations based on geometrical intuition: in the words of I. Ekeland, he was the “*most penetrating critic of quantitative methods, and the main precursor of qualitative methods.*” He dominated the mathematics of his time. He won the prize in a mathematical competition (1889) organized by Oscar II, King of Sweden and Norway, by showing that the solution of the three-body problem can only be expressed in terms of divergent series; a consequence is that the stability of the solar system at long times cannot be proved. His books *Méthodes nouvelles de la mécanique céleste*, in three volumes published between 1892 and 1899, and *Leçons de mécanique céleste* (1905) are major works which form the basis of the theory of dynamical systems and chaos. His work came very close to the theory of special relativity of Albert Einstein. He was elected to the Académie des Sciences in 1887, and as its president in 1906. He was the only member elected in each of the five sections of Geometry, Mechanics, Physics, Geography, and Navigation. In 1908 he was elected to the Académie Française. He wrote many books on the history and philosophy of science, examining in particular the relations between reason and intuition, and the psychology of scientific discoveries: *La Science et l’Hypothèse* (1901), *La Valeur de la Science* (1905), and *Science et Méthode* (1908). “*La pensée n’est qu’un éclair entre deux longues nuits, mais c’est un éclair qui est tout.*” (Thought is only a flash between two long nights, but this flash is everything.)

11.3 Linear stability

The natural first step in analyzing the local phase portrait near a fixed point is to linearize the vector field: this is the principle on which a linear stability study is based. We therefore consider the differential system (11.2) linearized at a fixed point \mathbf{a} , with $\mathbf{L} = D\mathbf{X}(\mathbf{a})$ being the linearized operator of the field \mathbf{X} calculated at \mathbf{a} . For n degrees of freedom, the matrix form of \mathbf{L} (also denoted as \mathbf{L}) is the Jacobian matrix of \mathbf{X} calculated at the point \mathbf{a} , and its elements are $\partial_{x_j} X_i(\mathbf{a})$, $i, j = 1, \dots, n$.

11.3.1 Solution of the linearized system

The unique solution of the linearized system associated with an initial condition $\mathbf{x}(0) = \mathbf{x}_0$ is written as (Arnold, 1973; Glendinning, 1994)

$$\mathbf{x}(t) = e^{t\mathbf{L}} \mathbf{x}_0, \quad (11.5)$$

where the exponential of the matrix is defined by the series

$$e^{t\mathbf{L}} = \sum_{n=0}^{\infty} \frac{t^n}{n} \mathbf{L}^n. \quad (11.6)$$

Using this definition, it can be verified that if the matrix \mathbf{L} has one of the forms

$$\begin{pmatrix} \lambda_1 & 0 \\ 0 & \lambda_2 \end{pmatrix}, \quad \begin{pmatrix} \sigma & \omega \\ -\omega & \sigma \end{pmatrix}, \quad \text{or} \quad \begin{pmatrix} \lambda & 1 \\ 0 & \lambda \end{pmatrix}, \quad (11.7)$$

then the exponential $e^{t\mathbf{L}}$ is respectively (see Exercise 11.7.2)

$$\begin{pmatrix} e^{\lambda_1 t} & 0 \\ 0 & e^{\lambda_2 t} \end{pmatrix}, \quad e^{\sigma t} \begin{pmatrix} \cos \omega t & -\sin \omega t \\ \sin \omega t & \cos \omega t \end{pmatrix}, \quad \text{or} \quad e^{\lambda t} \begin{pmatrix} 1 & t \\ 0 & 1 \end{pmatrix}. \quad (11.8)$$

The first case corresponds to two real eigenvalues, the second to a pair of complex-conjugate eigenvalues, and the third to a double eigenvalue associated with an eigen-subspace of dimension one.

In general, the exponential of a matrix is actually calculated using the Jordan form \mathbf{J} of the matrix \mathbf{L} , composed of blocks of the above type. Let \mathbf{P} be the matrix whose columns are the eigenvectors of \mathbf{L} . This matrix may involve generalized eigenvectors when the dimension of the eigenspace spanned by the eigenvectors associated with an eigenvalue is smaller than the multiplicity of the eigenvalue. Then the Jordan form of \mathbf{L} is $\mathbf{J} = \mathbf{P}^{-1} \mathbf{L} \mathbf{P}$ and the exponential $e^{t\mathbf{L}}$ is written as

$$e^{t\mathbf{L}} = \mathbf{P} e^{t\mathbf{J}} \mathbf{P}^{-1}. \quad (11.9)$$

Calculation of the solution of some differential systems using the exponential of a matrix is proposed in Exercise 11.7.3.

11.3.2 Invariant subspaces

The matrix $e^{t\mathbf{L}} = D\phi_t(\mathbf{a})$ defines a linear flow, an endomorphism of the vector space E tangent to V at \mathbf{a} , generated by the linear vector field \mathbf{Lx} . In an eigenbasis the differential equations associated with each of the eigenvalues are decoupled and can be integrated separately. It follows that any eigenspace of \mathbf{L} is invariant under the flow $D\phi_t(\mathbf{a})$. For example, let us consider the eigenspace generated by a real simple eigenvalue λ_j . The differential equation associated with λ_j is written as $dx_j/dt = \lambda_j x_j$, and for any initial condition $(0, \dots, x_0, \dots, 0)$ on the eigenspace we have $\mathbf{x}(t) = (0, \dots, x_0 e^{\lambda_j t}, \dots, 0)$, so that the eigenspace associated with λ_j is invariant under the flow. Similarly, a two-dimensional eigenspace associated with a pair of complex-conjugate eigenvalues is invariant, as is an eigenspace of dimension m associated with an eigenvalue of multiplicity m .

We can therefore partition the space E into three subspaces E^s , E^u , and E^c , respectively generated by the eigenvectors associated with eigenvalues having negative, positive, and zero real part, with each invariant under the flow $e^{t\mathbf{L}}$. These subspaces E^s , E^u , and E^c are respectively called the stable eigenspace (in the sense that the flow pulls the points of E^s toward the fixed point), the unstable eigenspace, and the center eigenspace, as shown schematically in two dimensions in Figure 11.4.

11.3.3 Types of fixed point

The type of fixed point depends on the eigenvalues of the matrix \mathbf{L} , i.e., the roots of the characteristic polynomial. In two dimensions the type of a fixed point depends only on the trace and determinant of \mathbf{L} , as discussed in the first chapter, Section 1.2.2, and summarized in Figure 1.2. In more than two dimensions we find the same types of fixed point:

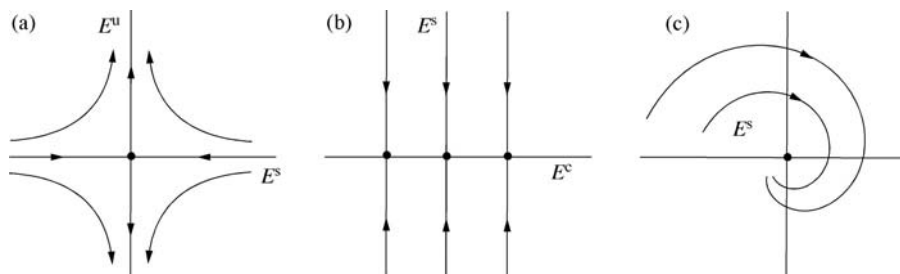


Figure 11.4 Examples of invariant subspaces and the corresponding phase portraits: (a) $\lambda_1 < 0$ and $\lambda_2 > 0$; (b) $\lambda_1 = 0$ and $\lambda_2 < 0$; (c) $\lambda_{1,2} = \sigma \pm i\omega$, $\sigma < 0$.

- When the roots are all real but some positive and others negative, the fixed point is called a *saddle*. A saddle is repulsive (unstable), except for the very special initial conditions lying on the stable eigenspace.
- When the roots are all real and of the same sign, the fixed point is called a *node*; it is attractive (stable) if the roots are negative and repulsive (unstable) otherwise.
- When the roots are complex, the fixed point is called a *focus*, and it is attractive (stable) if the real parts are all negative and repulsive (unstable) otherwise.
- When the roots are purely imaginary the fixed point is a *center*.

If the real part of each of the eigenvalues is nonzero, the fixed point is termed hyperbolic;¹ otherwise the fixed point is termed nonhyperbolic (there exists an eigenvalue whose real part is zero).

11.3.4 “Resemblance” of nonlinear and linearized fields

Once the local phase portrait of the system linearized about a fixed point is obtained, the question arises of how much the linearized system “resembles” the initial nonlinear system. Intuitively, we can say that two fields resemble each other if each trajectory of one can be put into correspondence with a trajectory of the other. More precisely, we say that two fields \mathbf{X}_1 and \mathbf{X}_2 are orbitally (or topologically) equivalent if there exists a homeomorphism \mathbf{h} (if the map \mathbf{h} and its inverse exist and are continuous) which transforms each trajectory of \mathbf{X}_1 into a trajectory of \mathbf{X}_2 while conserving the direction of the motion. It can then be shown that a field \mathbf{X} which is continuously differentiable on a manifold V and its version \mathbf{L} , linearized at a fixed point \mathbf{a} , are topologically equivalent if all the eigenvalues of \mathbf{L} have nonzero real part, i.e., if the fixed point is *hyperbolic* (the Hartman–Grobman theorem).

An important consequence of the Hartman–Grobman theorem is that if the fixed point \mathbf{a} is hyperbolic, the linearization procedure can be used to find the topological type of the fixed point (node, focus, saddle, etc.) and to sketch the shape of the phase portrait in its vicinity. If \mathbf{a} is not hyperbolic, the linearization does not give any information about the stability of the fixed point, which is determined by terms of higher degree. Only by taking into account these higher-degree terms in \mathbf{X} is it possible to get an idea of the phase portrait, which will take us back to the subject of nonlinear stability.

Example 11.6 Let us consider the vector field given by

$$\mathbf{X}(x, y) = [y + x\phi(x^2 + y^2), -x + y\phi(x^2 + y^2)], \quad (11.10)$$

¹ Note that for nondissipative (conservative) systems, fixed points are either saddles or centers, so that hyperbolic points and saddles are the same, and centers are also called elliptic points.

where ϕ is a function such that $\phi(0) = 0$. The linearized field is $\mathbf{L}(x, y) = (y, -x)$, and it possesses two purely imaginary eigenvalues. The fixed point is therefore not hyperbolic, and the trajectories of \mathbf{L} are circles centered at the origin. The phase portrait of \mathbf{X} , on the other hand, actually depends on the choice of the function ϕ . Let us change to polar coordinates (r, θ) . The trajectories are then defined by the equation $dr/d\theta = r\phi(r^2)$. For any value of r which makes ϕ vanish, the circle of radius r is a trajectory of \mathbf{X} . If, for example, the function ϕ vanishes for the two values a and b of the radius r and is positive between a and b , then any trajectory starting from a point of the ring located between $r = a$ and $r = b$ will tend towards the outer circle of radius b . There are therefore at least as many nonorbitally equivalent phase portraits as there are ways of choosing the zeros of the function ϕ !

We note that the resemblance defined above involves only the topological properties of the trajectories and not the law of motion (for example, the period of a closed orbit). It is possible to define a stronger resemblance between the field \mathbf{X} and its linearized version \mathbf{L} which preserves the law of motion along the trajectories; this requires that the transport homeomorphism \mathbf{h} be differentiable (i.e., that it be a diffeomorphism). The resemblance will be the stronger the higher the differentiability class of \mathbf{h} . However, this differentiability gives rise to *nonresonance conditions* between the eigenvalues of \mathbf{L} (the Sternberg theorem).

Example 11.7 Let us consider the vector field given by

$$\mathbf{X}(x, y) = (2x + y^2, y). \quad (11.11)$$

The field linearized at the origin is $\mathbf{L}(x, y) = (2x, y)$, and the flows generated by \mathbf{L} and \mathbf{X} are respectively

$$\phi_t^{\mathbf{L}}(x, y) = (xe^{2t}, ye^t), \quad \phi_t^{\mathbf{X}}(x, y) = [(x + ty^2)e^{2t}, ye^t]. \quad (11.12)$$

These flows look similar and it can be shown that they are topologically equivalent, but the map which permits the trajectories of one to be transformed into those of the other is of class C^1 at most. Indeed, let us try to construct two functions $f(x, y)$ and $g(x, y)$ with nonzero Jacobian at the origin and with

$$\phi_t^{\mathbf{L}}[f(x, y), g(x, y)] = [f(\phi_t^{\mathbf{X}}(x, y)), g(\phi_t^{\mathbf{X}}(x, y))]. \quad (11.13)$$

For our particular case this gives

$$e^{2t} f(x, y) = f[(x + ty^2)e^{2t}, ye^t]. \quad (11.14)$$

However, it can be verified by differentiating twice with respect to y that as soon as f is of class C^2 , this latter relation, even for a single nonzero value of t , implies that the two partial derivatives of f at 0 are zero.

11.4 Invariant manifolds and normal forms

By studying the linear stability of a fixed point it is possible to sketch the phase portrait near the fixed point if the latter is hyperbolic, i.e., if all the eigenvalues have nonzero real part. When the fixed point is not hyperbolic, the linear stability study is insufficient and nonlinearities must be taken into account. We therefore need to generalize the idea of an invariant tangent subspace to that of an invariant submanifold (or simply invariant manifold). This will reveal the essential role played by the center manifold, on which we shall attempt to simplify the vector field by calculating its normal form. We stress the fact that the methods introduced here are applicable only locally, i.e., in the neighborhood of a fixed point or of a periodic orbit.

11.4.1 Stable and unstable manifolds of a hyperbolic fixed point

We have already introduced the subspaces E^s and E^u , which are invariant under the linearized flow. The idea of an invariant subspace can be generalized to nonlinear flows, at least locally in a neighborhood U of a fixed point \mathbf{a} , and the stable and unstable manifolds V^s and V^u can be defined. This is the stable manifold theorem, which states that for any hyperbolic fixed point \mathbf{a} of a differential system there exist a stable manifold and an unstable manifold, respectively defined as

$$V^s(\mathbf{a}) = \{\mathbf{x} \in U \mid \phi_t(\mathbf{x}) \rightarrow \mathbf{a} \text{ for } t \rightarrow \infty \text{ and } \phi_t(\mathbf{x}) \in U \forall t \geq 0\}, \quad (11.15)$$

$$V^u(\mathbf{a}) = \{\mathbf{x} \in U \mid \phi_t(\mathbf{x}) \rightarrow \mathbf{a} \text{ for } t \rightarrow -\infty \text{ and } \phi_t(\mathbf{x}) \in U \forall t \leq 0\}, \quad (11.16)$$

of the same dimension as E^s and E^u , and tangent to E^s and E^u at the point \mathbf{a} (Figure 11.5). These manifolds are unique and as regular as the field \mathbf{X} .

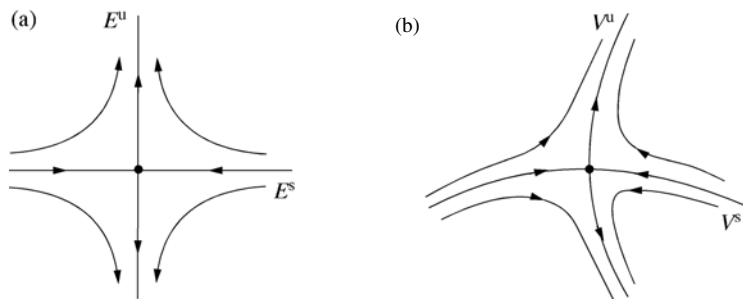


Figure 11.5 (a) Invariant tangent subspaces E^s and E^u ; (b) invariant manifolds V^s and V^u .

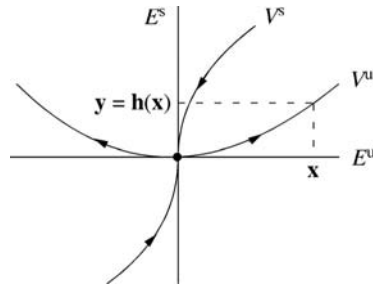


Figure 11.6 Stable and unstable eigenspaces and the corresponding manifolds of a hyperbolic fixed point.

These manifolds can be represented by the graph of a function (Figure 11.6) in the following manner. Let us assume that the differential system, here denoted as $\dot{\mathbf{z}} = \mathbf{Z}(\mathbf{z})$, is written in the Jordan form. We set $\mathbf{z} = \mathbf{x} + \mathbf{y}$ with $\mathbf{x} \in E^u$, $\mathbf{y} \in E^s$. Let \mathbf{L}_+ (\mathbf{L}_-) be the restriction of \mathbf{L} to E^u (E^s). The system can then be written as

$$\frac{d\mathbf{x}}{dt} = \mathbf{L}_+ \mathbf{x} + \mathbf{X}(\mathbf{x}, \mathbf{y}), \quad (11.17)$$

$$\frac{d\mathbf{y}}{dt} = \mathbf{L}_- \mathbf{y} + \mathbf{Y}(\mathbf{x}, \mathbf{y}). \quad (11.18)$$

Let us find the unstable manifold V^u . Since V^u is tangent to E^u at \mathbf{a} , it can be described locally as

$$V^u = \{(\mathbf{x}, \mathbf{y}) | \mathbf{y} = \mathbf{h}(\mathbf{x}), \quad \mathbf{h}(\mathbf{a}) = \mathbf{0} \text{ and } D\mathbf{h}(\mathbf{a}) = \mathbf{0}\}, \quad (11.19)$$

where \mathbf{h} is a map from E^u in E^s . This map can be determined from the following two expressions for $\dot{\mathbf{y}}$ on the unstable manifold [where $\mathbf{y} = \mathbf{h}(\mathbf{x})$]:

$$\frac{d\mathbf{y}}{dt} = \mathbf{L}_- \mathbf{h}(\mathbf{x}) + \mathbf{Y}(\mathbf{x}, \mathbf{h}(\mathbf{x})), \quad (11.20)$$

$$\frac{d\mathbf{y}}{dt} = D\mathbf{h}(\mathbf{x}) \dot{\mathbf{x}} = D\mathbf{h}(\mathbf{x}) [\mathbf{L}_+ \mathbf{x} + \mathbf{X}(\mathbf{x}, \mathbf{h}(\mathbf{x}))]. \quad (11.21)$$

Equating these two expressions for $\dot{\mathbf{y}}$ leads to a partial differential equation for $\mathbf{h}(\mathbf{x})$ which can be successively calculate the coefficients of the Taylor series expansion of \mathbf{h} at the fixed point \mathbf{a} . We note that the first nonzero terms of this series are of degree at least two.

Example 11.8 Let us determine the stable and unstable manifolds of the system

$$\dot{x} = x + X(x, y), \quad X(x, y) = 0,$$

$$\dot{y} = -y + Y(x, y), \quad Y(x, y) = ax^2.$$

The only fixed point of this system is the origin, the eigenvalues of the linearized system are 1 and -1 , and the associated eigenspaces are respectively the x -axis and the y -axis. We seek the unstable manifold in the form $y = h(x)$. Setting the two expressions for \dot{y} on the unstable manifold,

$$\begin{aligned}\dot{y} &= -y + Y(x, h(x)), \\ \dot{y} &= h'(x)\dot{x} = h'(x)[x + X(x, h(x))],\end{aligned}$$

equal to each other, and seeking $h(x)$ in the form of a polynomial series $h(x) = \sum_i h_i x^i$, we obtain

$$-\sum_i h_i x^i + ax^2 = \sum_i i h_i x^i,$$

from which we find $h_2 = a/3$ and $h_i = 0$ for $i \geq 3$. The unstable manifold is then defined by $y(x) = ax^3/3$.

Some other calculations of stable and unstable manifolds are proposed in Exercises 11.7.4 and 11.7.5.

11.4.2 The center manifold

In the case of a nonhyperbolic fixed point \mathbf{a} it is tempting to generalize the preceding definitions and introduce, in addition to the stable and unstable manifolds, the *center manifold* tangent to the center subspace at the point \mathbf{a} . It can be proved that such a center manifold V^c exists and has the same dimension as E^c : this is the center manifold theorem. However, two technical difficulties arise which were not present in the stable manifold theorem: (i) V^c is not necessarily unique, and (ii) if \mathbf{X} belongs to the class C^r , then V^c belongs only to the class C^{r-1} (see Guckenheimer and Holmes, 1983, p. 124). However, these two details are unimportant for our purposes.

The determination of the center manifold via a function $\mathbf{y} = \mathbf{h}(\mathbf{x})$ is done exactly as for the stable and unstable manifolds. In the important case of marginal stability, where all the eigenvalues have negative real part except a few whose real part is zero, it is sufficient to rewrite Eqs (11.17)–(11.21) replacing \mathbf{L}_+ , V^u , and E^u by \mathbf{L}_0 , V^c , and E^c . The function $\mathbf{h}(\mathbf{x})$ is then the solution of the partial differential equation

$$\mathbf{L}_- \mathbf{h}(\mathbf{x}) + \mathbf{Y}(\mathbf{x}, \mathbf{h}(\mathbf{x})) = D\mathbf{h}(\mathbf{x}) [\mathbf{L}_0 \mathbf{x} + \mathbf{X}(\mathbf{x}, \mathbf{h}(\mathbf{x}))], \quad (11.22)$$

which can be solved by seeking $\mathbf{h}(\mathbf{x})$ in the form of a Taylor series.

Example 11.9 We consider the differential system (Guckenheimer and Holmes, 1983, p. 132)

$$\begin{aligned}\dot{u} &= v, \\ \dot{v} &= -v + \alpha u^2 + \beta uv.\end{aligned}$$

The origin is the only fixed point, and the eigenvalues of the linearized system are 0 and -1 . Making a change of variable using the matrix whose columns are the eigenvectors

$$\begin{pmatrix} u \\ v \end{pmatrix} = \begin{pmatrix} 1 & 1 \\ 0 & -1 \end{pmatrix} \begin{pmatrix} x \\ y \end{pmatrix},$$

the system can be written in the standard form where the linear part is in the Jordan form (which here is diagonal):

$$\begin{pmatrix} \dot{x} \\ \dot{y} \end{pmatrix} = \begin{pmatrix} 0 & 0 \\ 0 & -1 \end{pmatrix} \begin{pmatrix} x \\ y \end{pmatrix} + \begin{pmatrix} -1 \\ 0 \end{pmatrix} (\alpha(x+y)^2 - \beta y(x+y)).$$

Since E^c and E^s have dimension one, the map $y = h(x)$ is a real-valued function and Eq. (11.22) becomes

$$\begin{aligned}h'(x) \left(\alpha(x+h(x))^2 - \beta h(x)(x+h(x)) \right) &= -h(x) - \alpha(x+h(x))^2 \\ &\quad - \beta \left(xh(x) + h^2(x) \right)\end{aligned}$$

with

$$h(0) = h'(0) = 0.$$

The coefficients a, b, \dots can be determined by substituting the expansion $h(x) = ax^2 + bx^3 + \dots$ into this equation. This gives

$$h(x) = -\alpha x^2 + \alpha(4\alpha - \beta)x^3 + \mathcal{O}(x^4).$$

In this case of marginal stability, any initial state always relaxes to the center manifold. The dynamics of the system on this manifold is therefore very important, because it represents the asymptotic behavior of the system. It is governed by Eqs (11.17)–(11.18) with \mathbf{L}_+ replaced by \mathbf{L}_0 and $\mathbf{y} = \mathbf{h}(\mathbf{x})$. Since the center manifold is tangent to the center eigenspace E^c , a good approximation of the asymptotic dynamics is given by its projection onto E^c :

$$\frac{d\mathbf{x}}{dt} = \mathbf{L}_0 \mathbf{x} + \mathbf{X}(\mathbf{x}, \mathbf{h}(\mathbf{x})). \tag{11.23}$$

Example 11.10 Continuing with the above example, a good approximation of the dynamics on the center manifold is

$$\dot{x} = \alpha x^2 + \alpha(\beta - 2\alpha)x^3 + \mathcal{O}(x^4).$$

We note that at second order we can obtain the same result without calculating the center manifold, by inserting into Eq. (11.23) the approximation $h(x) = 0 + \mathcal{O}(x^2)$, which is called the tangent space approximation.

In Exercise 11.7.6 we propose the calculation of a center manifold.

11.4.3 The normal form of a vector field

Calculating the normal form of a vector field involves finding a coordinate transformation that simplifies the expression for this vector field as much as possible. To motivate the existence of such a transformation, let us consider a linear vector field. It can easily be imagined that a nonlinear transformation can transform this linear field into a nonlinear field. The nonlinearities that arise in this case are only complications due to the use of a coordinate system poorly adapted to the problem. Conversely, one can ask if, for a given nonlinear field, some of the nonlinearities – perhaps all of them – might not be due to the use of a less than optimal choice of coordinate system.

We are going to show that in fact it is possible to find a “natural” curvilinear coordinate system in which the dynamical system is simpler to study. This is the normal form theorem. Moreover, such a coordinate system may reveal properties of the system, in particular, symmetry properties, that were hidden in the original formulation. However, it appears that some nonlinearities are resistant to any coordinate transformation and cannot be eliminated. Such irreducible nonlinearities are termed *resonant* and are important from the viewpoint of the system dynamics. For example, the differential system

$$\dot{x} = 2x + y^2, \quad \dot{y} = y \tag{11.24}$$

cannot be written as

$$\dot{u} = 2u, \quad \dot{v} = v \tag{11.25}$$

in any local coordinate system (u, v) , because the nonlinearity y^2 is resonant.

Let us therefore consider a differential system defined by a regular vector field on a manifold V of dimension n . The origin is assumed to be a fixed point near which the field can be expanded in a Taylor series:

$$\frac{d\mathbf{x}}{dt} = \mathbf{X}(\mathbf{x}) = \mathbf{L}\mathbf{x} + \mathbf{X}_2(\mathbf{x}) + \dots + \mathbf{X}_N(\mathbf{x}) + \mathcal{O}(|\mathbf{x}|^{N+1}). \tag{11.26}$$

Here $\mathbf{L} = D\mathbf{X}(\mathbf{0})$ is the Jacobian operator of \mathbf{X} , assumed to be diagonal, and \mathbf{X}_r is the vector function whose components X_{ri} , $i = 1, \dots, n$, contain the terms of degree $r \geq 2$. Defining

$$M_r = \{\mathbf{m} = (m_1, m_2, \dots, m_n) \in \mathbb{N}^n \quad \text{with} \quad \sum m_j = r\},$$

$\mathbf{X}_r(\mathbf{x})$ can be written as

$$\mathbf{X}_r(\mathbf{x}) = \sum_{\mathbf{m} \in M_r} \mathbf{X}_{\mathbf{m}} \mathbf{x}^{\mathbf{m}} \quad \text{with} \quad \mathbf{x}^{\mathbf{m}} = x_1^{m_1} x_2^{m_2} \dots x_n^{m_n}, \quad (11.27)$$

where the $\mathbf{X}_{\mathbf{m}}$ are vectors whose n components represent the coefficients of monomials of degree r . For example, in two dimensions, $M_1 = \{(1, 0), (0, 1)\}$, $M_2 = \{(2, 0), (1, 1), (0, 2)\}$, and \mathbf{X}_2 is written as

$$\mathbf{X}_2 = \mathbf{X}_{(2,0)} x^2 + \mathbf{X}_{(1,1)} xy + \mathbf{X}_{(0,2)} y^2. \quad (11.28)$$

The calculation of the normal form of the field $\mathbf{X}(\mathbf{x})$ consists of constructing a sequence of coordinate transformations preserving the linear part \mathbf{L} of the field (called “near-identity” transformations) which allow the elimination of as many nonlinear terms of higher and higher order as possible. Let us consider a differential system of the form

$$\frac{d\mathbf{x}}{dt} = \mathbf{L}\mathbf{x} + \mathbf{X}_r(\mathbf{x}) + \mathcal{O}(|\mathbf{x}|^{r+1}), \quad r \geq 2, \quad (11.29)$$

and seek a coordinate transformation of the form

$$\mathbf{y} = \mathbf{x} + \phi_r(\mathbf{x}), \quad r \geq 2, \quad (11.30)$$

where ϕ_r contains only terms of degree r , which allows the system (11.29) to be expressed in the new coordinates as

$$\frac{d\mathbf{y}}{dt} = \mathbf{L}\mathbf{y} + \mathcal{O}(|\mathbf{y}|^{r+1}), \quad r \geq 2. \quad (11.31)$$

If this transformation exists, it is therefore possible by repeating the operation to successively eliminate all the nonlinear terms.

Let us show the reasoning for the components of the differential system. The i th component of the transformation (11.30) is

$$y_i = x_i + \sum_{\mathbf{m} \in M_r} \phi_{\mathbf{m},i} \mathbf{x}^{\mathbf{m}}, \quad (11.32)$$

the inverse of which is written as

$$x_i = y_i - \sum_{\mathbf{m} \in M_r} \phi_{\mathbf{m},i} \mathbf{y}^{\mathbf{m}} + \mathcal{O}(|\mathbf{y}|^{r+1}) \quad (11.33)$$

(the correctness of this inversion can be found by using an example in one dimension and a polynomial of second degree: $y = x + ax^2$). The system can be written in the form (11.31) by first differentiating (11.32) with respect to the time:

$$\dot{y}_i = \dot{x}_i + \sum_{\mathbf{m} \in M_r} \phi_{\mathbf{m},i} \frac{d\mathbf{x}^{\mathbf{m}}}{dt}. \quad (11.34)$$

Successively using (11.29) and then (11.33) with $\mathbf{x}^{\mathbf{m}} = \mathbf{y}^{\mathbf{m}} + \mathcal{O}(|\mathbf{y}|^{r+1})$, \dot{x}_i can be written as

$$\begin{aligned} \dot{x}_i &= \lambda_i x_i + \sum_{\mathbf{m} \in M_r} X_{\mathbf{m},i} \mathbf{x}^{\mathbf{m}} \\ &= \lambda_i y_i - \lambda_i \sum_{\mathbf{m} \in M_r} \phi_{\mathbf{m},i} \mathbf{y}^{\mathbf{m}} + \sum_{\mathbf{m} \in M_r} X_{\mathbf{m},i} \mathbf{y}^{\mathbf{m}} + \mathcal{O}(|\mathbf{y}|^{r+1}). \end{aligned} \quad (11.35)$$

On the other hand, defining $(\mathbf{m}, \lambda) = \sum_{k=1,n} m_k \lambda_k$, the derivative of $\mathbf{x}^{\mathbf{m}}$ can be written as

$$\begin{aligned} \frac{d\mathbf{x}^{\mathbf{m}}}{dt} &= \sum_{k=1,n} \frac{\dot{x}_k}{x_k} m_k \mathbf{x}^{\mathbf{m}} \\ &= (\mathbf{m}, \lambda) \mathbf{x}^{\mathbf{m}} + \mathcal{O}(|\mathbf{x}|^{r+1}) \\ &= (\mathbf{m}, \lambda) \mathbf{y}^{\mathbf{m}} + \mathcal{O}(|\mathbf{y}|^{r+1}). \end{aligned} \quad (11.36)$$

Substituting (11.35) and (11.36) into (11.34), we obtain an approximation of the dynamical system in the transformed coordinates:

$$\dot{y}_i = \lambda_i y_i + \sum_{\mathbf{m} \in M_r} (X_{\mathbf{m},i} - [\lambda_i - (\mathbf{m}, \lambda)] \phi_{\mathbf{m},i}) \mathbf{y}^{\mathbf{m}} + \mathcal{O}(|\mathbf{y}|^{r+1}). \quad (11.37)$$

We therefore see that if for all $\mathbf{m} \in M_r$ the conditions

$$\lambda_i - (\mathbf{m}, \lambda) \neq 0 \quad (11.38)$$

are satisfied, then it is possible to choose the $\phi_{\mathbf{m},i}$ so as to cancel the terms of order r . These conditions are called the *nonresonance conditions at order r* of the eigenvalues. The desired coordinate transformation is then written explicitly as

$$\phi_{\mathbf{m},i} = \frac{X_{\mathbf{m},i}}{\lambda_i - (\mathbf{m}, \lambda)}. \quad (11.39)$$

If for a particular $\mathbf{m} \in M_r$ the nonresonance condition is not satisfied, the corresponding monomial is termed *resonant* and cannot be eliminated. We note that

whether or not a nonlinear term is resonant depends only on the eigenvalues and therefore on the linear terms. Let us make a few observations:

1. The right-hand side of Eq. (11.37) contains, aside from the linear term $\lambda_i y_i$, only terms of degree r or higher. In particular, if $\mathbf{X}_2, \dots, \mathbf{X}_{r-1}$ are zero before the transformation, they are always zero after it.
2. It can be verified that the resonant terms appearing at order r are not modified by later transformations to eliminate the terms of order higher than r . On the contrary, the nonlinearities of order higher than r are in general modified.
3. The preceding discussion rests on the hypothesis that the fixed point is hyperbolic and that \mathbf{L} is diagonal. The arguments can be generalized to the nonhyperbolic case and nondiagonal \mathbf{L} ; see Guckenheimer and Holmes (1983, §3.3) and Elphick *et al.* (1987) for a more formal and general presentation.

Therefore, we now possess two fundamental tools for studying a system of differential equations:

- The center manifold theorem, which allows us to focus on the asymptotic behavior of the system on the center manifold of low dimension (in practice, projection of the dynamics on the center subspace is usually sufficient).
- The normal-form theorem, which allows the differential system to be expressed more simply on the center manifold by the introduction of a suitable coordinate system.

Exercises 11.7.7 and 11.7.8 propose resonance and normal-form calculations.

11.5 Structural stability and genericity

11.5.1 The basic problem

The question we tackle here which will lead us to the study of bifurcations is: for a given system, what happens as one of the system parameters varies? Does the phase portrait remain qualitatively the same, or does it undergo profound changes such as modification of the type or even disappearance of a fixed point?

Another essential question from the physical point of view is the following: is the system of equations sufficiently “robust” to not only describe the observed phenomena but also to make reliable predictions? Would some physical effect, neglected in the modeling and whose inclusion would lead to a system of “similar” equations, completely change the nature of the solutions? In other words, is the system of equations both sufficiently general and its predictions sufficiently “robust” to small changes to it? What happens if it is “perturbed” by the addition of a small term?

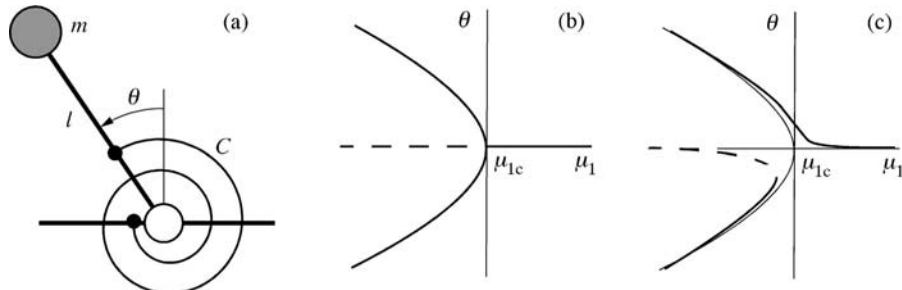


Figure 11.7 (a) The physical system and the bifurcation diagrams for (b) $\mu_2 = 0$, (c) $\mu_2 \neq 0$. (—) stable equilibrium branches; (--) unstable equilibrium branches.

As an illustration, let us consider the oscillator already discussed in the first chapter: a rod which pivots at its base and undergoes displacements in a vertical plane (Figure 11.7). The rod is subject to gravity and to a restoring force due to two identical springs. The classical modeling of the system leads to the following equation of motion for suitably chosen time and length scales:

$$\ddot{\theta} = \sin \theta - \mu_1 \theta. \quad (11.40)$$

We note that this oscillator possesses the reflection symmetry $\theta \rightarrow -\theta$. When the spring stiffness μ_1 is sufficiently large, the vertical position $\theta = 0$ is the only equilibrium position and it is stable. If the stiffness is smaller than a critical value $\mu_{1c} = 1$, the vertical position becomes unstable and two stable equilibrium positions appear which are symmetric with respect to the vertical. The equilibrium positions, and their stable or unstable nature, are represented as in Figure 11.7b as a function of the stiffness. The differential system corresponding to $\mu_1 = \mu_{1c}$ is therefore very special, because there exist values of μ_1 arbitrarily close to μ_{1c} for which the oscillator possesses two fixed points and for which the phase portrait in the $(\theta, \dot{\theta})$ plane is topologically different. The differential system with $\mu_1 = \mu_{1c}$ is termed *structurally unstable*. The critical value $\mu_1 = \mu_{1c}$ of the stiffness corresponds to a *bifurcation*, an idea which is developed in the following section, and Figure 11.7b is called the *bifurcation diagram* of the oscillator. Note that the idea of structural stability introduced here is quite different, and must be carefully distinguished, from the stability of a fixed point or periodic orbit discussed previously: the latter is stability of a solution of a particular differential system, while the former is stability of the differential system itself.

In the model just discussed, the physical system possesses the symmetry $\theta \rightarrow -\theta$. Let us now take into account the possibility of an asymmetry in the spring stiffness, or a deviation from the horizontal of the plane in which the springs are attached. Such a situation gives rise to a second parameter μ_2 , which we assume

to be small. The modeling equation becomes

$$\ddot{\theta} = \sin \theta - \mu_1 \theta + \mu_2. \quad (11.41)$$

The symmetry $\theta \rightarrow -\theta$ is now broken. It can be checked that the bifurcation diagram is that represented in Figure 11.7c, which is qualitatively different from that of Figure 11.7b. For example, for μ_1 slightly less than μ_{1c} there is only a single equilibrium position. In the parameter plane (μ_1, μ_2) the locus of points corresponding to the bifurcation can be represented by a curve. The model including μ_2 now correctly represents the physical system no matter what its “hidden” imperfections are, and so this model is said to be *generic*.

As a second example, let us consider the Descartes laws of reflection of a light ray on a planar mirror. These laws are found to be consistent with experiment – away from the critical angle – in spite of the inevitable defects in the planarity of the mirror and in the homogeneity of its reflection properties. Here, the assumption that the mirror is perfectly planar is fine, in contrast to the symmetry hypothesis of the preceding example. Small imperfections of the mirror can be neglected: the Descartes laws can also be said to be generic.

11.5.2 Definitions

Let us recall the two questions posed in the introduction to this section:

- Does a vector field subject to small perturbations, induced for example by the variation of a parameter, resemble the initial field (structural stability)?
- Is a field chosen at random representative of the ensemble of fields to which it belongs (genericity)?

Now we need to make the ideas of structural stability and genericity more precise. These ideas are in fact related to an old problem in geometry, that of the “general position,” which is formalized by introducing the mathematical concepts of an open set and a dense set. Let us explain this by means of a simple example.

We consider the set of triplets of lines in a plane, supplied with a suitable topology allowing the “distance between two triplets” to be defined precisely. On the one hand, any deformation of a triangle, provided it is small, remains a triangle: the set of triplets forming a triangle is open in the set of triplets of lines in the plane. On the other hand, a triplet of lines “almost always” forms a triangle. Here “almost always” means that triplets not forming a triangle are rare, and that there always exists an arbitrarily small deformation which transforms such a triplet into a triplet forming a triangle. The set of triplets forming a triangle is said to be dense within the set of triplets of lines in the plane.

Now that we have recalled the ideas of open and dense sets, we can state the definitions of a *structurally stable field* and a *generic field*.

Definition 11.11 Let $E^1(V)$ be the vector space of vector fields of class C^1 on a compact manifold V (for example, the closed and bounded subsets of \mathbb{R}^n). A vector field \mathbf{X} of $E^1(V)$ is termed *structurally stable* if there exists an open set Ω of $E^1(V)$ containing \mathbf{X} such that any element of Ω is orbitally equivalent to \mathbf{X} (that is, if for any element \mathbf{X}' of Ω there exists a homeomorphism \mathbf{h} which transforms any trajectory of \mathbf{X}' into a trajectory of \mathbf{X}).

Definition 11.12 A property of a vector field is termed *generic* if it holds for any arbitrarily chosen field, i.e., if the ensemble of fields satisfying it forms a dense subset in $E^1(V)$.

The fundamental question that naturally arises is whether or not a randomly chosen generic field is structurally stable (invariant under small deformations), as would seem plausible. More precisely, how does one determine which fields are structurally stable and which are generic, and how does one define the relations, in particular the *inclusion relations*, between these two ensembles of fields? The problem is a purely mathematical one, and its solution lies outside the scope of this text. We simply state without proof that the classification is complete in two dimensions, but only a few results are available for higher dimensions. Here we shall present only the results which we shall need for our later discussion.

11.5.3 Structural stability conditions

A first necessary condition: hyperbolicity

One of the essential results is that a necessary condition for a vector field to be structurally stable is that all its fixed points and periodic orbits be hyperbolic. This result can be easily understood from the example of the undamped oscillator, whose eigenvalues are purely imaginary: the periodic orbits are all disrupted by even a tiny dissipation. Unfortunately, hyperbolicity is not a sufficient condition for structural stability. More precisely, hyperbolicity is a sufficient condition for *local* structural stability, i.e., in the neighborhood of a fixed point or a hyperbolic periodic orbit, but it is not a sufficient condition for *global* structural stability, at the scale of the whole phase portrait. Let us consider, for example, a phase portrait containing a *homoclinic orbit*, that is, a trajectory which has a loop at a fixed point (Figure 11.9). This homoclinic orbit can be structurally unstable with respect to any variation of a parameter (the loop gets cut) without the phase portrait in the neighborhood of the fixed point being qualitatively changed.

A second necessary condition: transversality

In addition to the hyperbolicity of fixed points and periodic orbits, another necessary condition for structural stability concerns the relative positions of the stable and unstable manifolds of fixed points and periodic orbits, more precisely, their transversality. The concept of the transversality of two manifolds, defined below, formalizes the idea of “general position.” The definitions below make use of the notion of *codimension* of a subspace, which is the complement of its dimension (in a space of dimension n , the codimension of a subspace of dimension p is $n - p$).

Definition 11.13 Two subspaces E_1 and E_2 of a vector space E are termed *transverse* if one of the following conditions is satisfied (these conditions are equivalent in any finite dimension):

- $E_1 + E_2 = E$;
- $\text{codim}(E_1 \cap E_2) = \text{codim}E_1 + \text{codim}E_2$;
- $\dim(E_1 \cap E_2) = \dim E_1 + \dim E_2 - \dim E$.

More generally, two submanifolds V_1 and V_2 of a manifold V are transverse if, at any point where they intersect, their tangent subspaces are transverse. If $\dim V_1 + \dim V_2 < \dim V$, V_1 and V_2 will be termed transverse if they do not intersect (this is the case of two curves ($\dim V_1 = \dim V_2 = 1$) in a space of three dimensions).

By making a few sketches (Figure 11.8), we can deduce that with these definitions the concept of transversality is invariant under small deformations of the manifolds in question, and that a transverse intersection corresponds to the general position of two manifolds.

Let us now consider the stable and unstable manifolds of fixed points and periodic orbits. Stable (unstable) manifolds can never intersect each other, because if they did, a point of their intersection would evolve to (from) two different futures

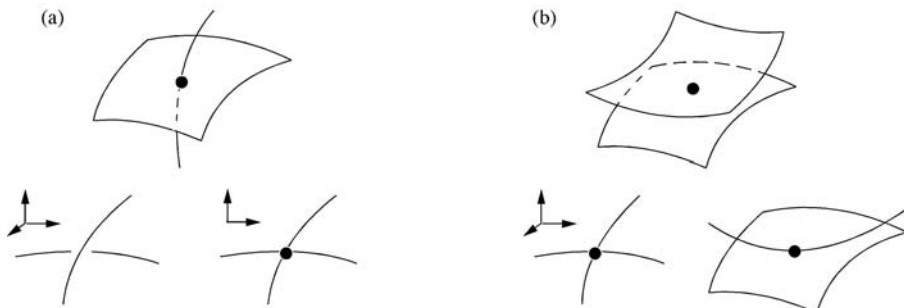


Figure 11.8 (a) Three examples of transverse intersections; (b) three examples of nontransverse intersections.

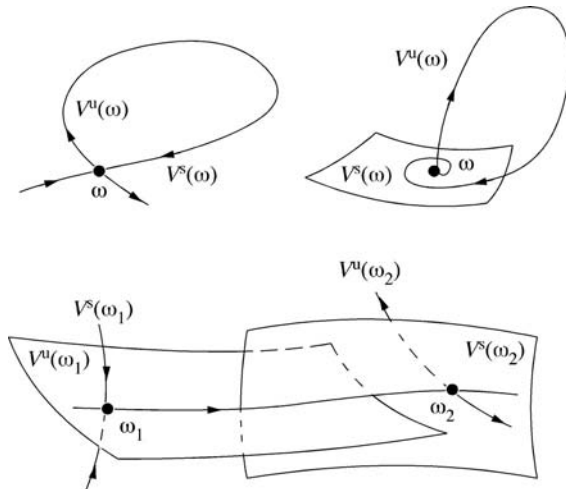


Figure 11.9 Top: two homoclinic orbits for a fixed point, which are structurally unstable. Bottom: a heteroclinic orbit between two fixed points, which is structurally stable.

(pasts). On the other hand, a stable manifold $V^s(\omega_1)$ can intersect an unstable manifold $V^u(\omega_2)$, where ω_1 and ω_2 are fixed points or periodic orbits (Figure 11.9). It can also be shown that a necessary (but still not sufficient!) condition for structural stability is that the stable and unstable manifolds intersect transversely (fields satisfying this condition are called Kupka–Smale fields).

This last result allows us, in particular, to easily show that a field whose phase portrait possesses a homoclinic orbit (Figure 11.9) for a fixed point can never be structurally stable. Actually, let ω_1 and ω_2 be two fixed points or periodic orbits, assumed to be hyperbolic. We assume that the manifolds $V^s(\omega_1)$ and $V^u(\omega_2)$ are transverse, and that their intersection, denoted I , is nonempty and does not reduce to ω_1 if $\omega_1 = \omega_2$. We then have $\dim I > 0$. Using n to denote the dimension of the manifold V , we have

- by transversality: $\dim V^s(\omega_1) + \dim V^u(\omega_2) = n + \dim I$,
- by hyperbolicity: $\dim V^s(\omega_j) + \dim V^u(\omega_j) = n + \dim \omega_j$, $j = 1, 2$.

Then, for example, we can deduce that $\dim I = \dim V^s(\omega_1) - \dim V^s(\omega_2) + \dim \omega_2$. Now, if ω_1 and ω_2 are the same fixed point, this relation leads to $\dim I = 0$, contradicting the hypothesis $\dim I > 0$. Therefore, the intersection of the stable and unstable manifolds of ω_1 can only be nontransverse (a homoclinic orbit), and the corresponding field is then not structurally stable. See Exercise 11.7.9 for another example of this type of reasoning.

Necessary and sufficient conditions

By imposing additional restrictions on the vector fields it is possible to obtain classes of structurally stable fields. Particular examples are gradient fields (such as $\mathbf{X}(\mathbf{x}) = \nabla U(\mathbf{x})$) and Morse–Smale fields (Guckenheimer and Holmes, 1983, §1.7).

In two dimensions the situation is easier and it can be shown (the Peixoto theorem) that in a planar phase space, the Kupka–Smale fields (which satisfy hyperbolicity and transversality of the stable and unstable manifolds) are structurally stable and generic (the Peixoto theorem is in fact a bit more general, and applies to the case of nonplanar phase spaces such as tori).

11.6 Bifurcations

11.6.1 Introduction

The behavior of any physical system generally depends on a number of parameters. The response of the system to variations in these parameters is usually regular, but there may exist particular parameter values for which the system suddenly adopts a qualitatively different behavior. Such a change of behavior is called a *bifurcation*. In the example of the pendulum discussed in the preceding section, the passage from one to two equilibrium positions was a bifurcation. The hydrodynamical instabilities discussed in previous chapters also correspond to bifurcations. For example, the transition between the conductive and convective regimes in the Rayleigh–Bénard problem is a bifurcation governed by the Rayleigh number.

A continuous increase of a parameter generally leads to a cascade of such transitions, with the observed behavior becoming more and more complex or disordered. For many physical systems an initial stable stationary state is followed by periodic behavior, which becomes unstable in turn, giving rise to phenomena such as period-doubling, intermittency, quasi-periodicity, and perhaps ultimately unpredictable, chaotic behavior. The fact that the same cascade of transitions or bifurcations occurs for mechanical, electrical, and chemical systems suggests that these bifurcations are universal in a certain sense, which has greatly stimulated their study.

11.6.2 Definition of a bifurcation

How can a bifurcation be defined precisely? Let us consider a differential system on a manifold V , depending on a parameter μ ($\mu \in \mathbb{R}^m$ if there are m parameters):

$$\frac{d\mathbf{x}}{dt} = \mathbf{X}(\mathbf{x}, \mu). \quad (11.42)$$

A natural definition of a bifurcation might be the following. We can say that the vector field $\mathbf{X}(\mathbf{x}, \mu)$ undergoes a bifurcation for the value $\mu = \mu_c$ of the parameter if, at this value, the field is not structurally stable. This definition corresponds well to the intuitive idea of a bifurcation: on either side of μ_c the solutions are qualitatively different, corresponding to qualitatively different behaviors of the physical system. However, some peculiarities with this definition may arise in dimensions higher than two, where, as already noted, structurally stable fields do not form a dense set. It is therefore possible to find generic families of vector fields in which no element is structurally stable: for such a family, all the parameter values will be bifurcation values! To avoid this inconvenience and to ensure that the bifurcation values are isolated, we restrict the preceding definition as follows:

Definition 11.14 The family $\mathbf{X}(\mathbf{x}, \mu)$ of vector fields is said to present a *bifurcation* for the parameter value μ_c if the field $\mathbf{X}(\mathbf{x}, \mu_c)$ is not of the Kupka–Smale type, that is,

- if one of the fixed points or one of the periodic orbits loses its hyperbolicity (a local accident which leads to the definition of a local bifurcation); or
- if one stable manifold and one unstable manifold no longer intersect transversely (an accident which globally affects the phase portrait, corresponding to a global bifurcation).

11.6.3 Codimension of a bifurcation

In general, a model – in this context a system of ordinary differential equations – involves several parameters. A bifurcation condition then amounts to a relation between these various parameters:

$$f(\mu_1, \dots, \mu_m) = 0. \quad (11.43)$$

Geometrically, this relation defines a hypersurface Σ in the parameter space \mathbb{R}^m of dimension $m - 1$: thus Σ can be said to have codimension one. Therefore, in moving along a curve Γ of \mathbb{R}^m of dimension one, in general one will intersect the hypersurface Σ (Figure 11.10). At the cost of changing the reference frame, it is sufficient to vary a single parameter to reach the bifurcation. Such a bifurcation will be referred to as a bifurcation of codimension one.

If the bifurcation condition involves two relations of the type (11.43), the bifurcation points will be located on the intersection of the two corresponding hypersurfaces Σ_1 and Σ_2 . To reach this intersection of dimension $m - 2$, or codimension 2, the two parameters must be varied independently. Such a bifurcation will be referred to as a bifurcation of codimension two. Bifurcations of higher codimension are defined analogously.

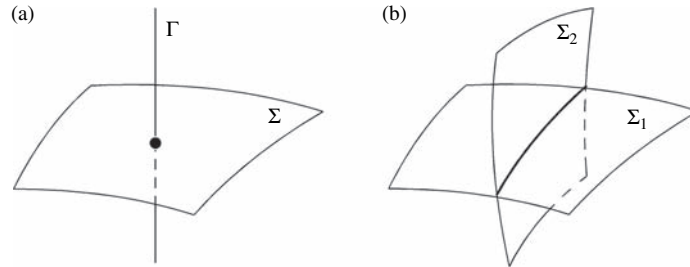


Figure 11.10 (a) A bifurcation of codimension 1: the variation of a single parameter on Γ is sufficient to reach the bifurcation locus Σ ; (b) a bifurcation of codimension two: two parameters must be varied (on a manifold Γ which is not shown) in order to reach the bifurcation locus $\Sigma_1 \cap \Sigma_2$.

However, in order for this characterization of the codimension of a bifurcation to be useful, the vector field must be generic. Let us imagine that a symmetry hypothesis, or a perturbation method terminated at too low an order, masks a parameter, say μ_{m+1} . Then the “apparent” parameter space is only the hyperplane $\mu_{m+1} = 0$ of the complete space, whose dimension is $m + 1$. Therefore, $\mu_{m+1} = 0$ is an auxiliary condition for the bifurcation to appear. Its real codimension will then be one unit higher than its apparent codimension.

Of course, bifurcations of codimension 1 are the simplest ones and it can be shown that they necessarily correspond to one of the following situations:

1. A saddle-node bifurcation. The field \mathbf{X} linearized at the fixed point possesses 0 as an eigenvalue of multiplicity 1, while all the other eigenvalues have nonzero real part. In an eigenbasis, the matrix \mathbf{L}_0 of the restriction of the linearized field to the center manifold is written as

$$\mathbf{L}_0 = (0).$$

2. A Hopf bifurcation. The field \mathbf{X} linearized at the fixed point possesses a pair of purely imaginary eigenvalues $\pm i\omega$ of multiplicity 1, while all the other eigenvalues have nonzero real part. The matrix \mathbf{L}_0 is written as

$$\mathbf{L}_0 = \begin{pmatrix} 0 & -\omega \\ \omega & 0 \end{pmatrix}.$$

3. Bifurcations of a periodic orbit (also called a limit cycle for a dissipative system). The study of these bifurcations involves study of the first return map in a Poincaré section of this orbit. A bifurcation occurs when one of the eigenvalues

of this map departs from the unit circle in the complex plane: successive iterations then take one farther and farther from the orbit. Depending on whether the eigenvalue crosses the unit circle at $1, -1$, or $\sigma \pm i\omega$, the bifurcation is respectively called a *saddle-node bifurcation*, a *period-doubling bifurcation*, or a *Hopf bifurcation*. The difficulty here is determining the first return map in the neighborhood of the orbit.

4. Global bifurcations. One of the orbits of \mathbf{X} is a nontransverse intersection of a stable manifold and an unstable manifold. If the two manifolds come from the same fixed point or periodic orbit, the bifurcation is termed homoclinic, otherwise it is heteroclinic.

The study of bifurcations of codimension two leads to an analogous list of bifurcation conditions. Limiting our discussion to local bifurcations of fixed points, the Jordan form of the restriction of the linearized field to the center manifold is one of the three following types:

5. Double-zero eigenvalue, nondiagonalizable:

$$\mathbf{L}_0 = \begin{pmatrix} 0 & 1 \\ 0 & 0 \end{pmatrix}.$$

6. A simple zero plus a pair of imaginary complex conjugates: \mathbf{L}_0 is composed of two blocks of the types in cases (1) and (2) above.
7. Two different pairs of imaginary complex conjugates: \mathbf{L}_0 is composed of two blocks of the type in case (2).

A detailed study of the bifurcations listed above can be found in Iooss and Joseph (1990). Here we limit ourselves to cases 1, 2, and 5. The general form of the system of differential equations for these bifurcations can be determined by using the transversality conditions, but we shall seek them instead in the form of Taylor series, which are less elegant but more straightforward.

11.6.4 The saddle-node bifurcation

The saddle-node bifurcation corresponds to the case where a fixed point \mathbf{a} loses its hyperbolicity at a value μ_c of a parameter μ for which zero is the single eigenvalue of the field linearized at the point \mathbf{a} . Once the center manifold has been determined, a good approximation of the dynamics on this manifold is given by its projection on the center subspace of dimension one:

$$\frac{dx}{dt} = X(x, \mu). \quad (11.44)$$

In order to study the system for x and μ close to a and μ_c , it is convenient to change to the usual system without a parameter by enlarging the phase space (here reduced to the center manifold) to include the parameter μ . In this enlarged phase space the system becomes

$$\frac{dx}{dt} = X(x, \mu), \quad \frac{d\mu}{dt} = 0. \quad (11.45)$$

The fixed points of the vector field thus defined are given by $X(x, \mu) = 0$, the equation which defines the “equilibrium manifold” in the (x, μ) plane. By means of translation along the x and μ axes it is always possible to shift the bifurcation to $x = 0$ for $\mu = 0$. For $\mu = 0$ the origin $x = 0$ is a fixed point and the linearized X has zero eigenvalue, so that X must satisfy

$$X(0, 0) = 0, \quad X_x(0, 0) = 0. \quad (11.46)$$

The general form of the field X near $(0, 0)$ is then

$$\frac{dx}{dt} = X_\mu \mu + \frac{1}{2}(X_{xx}x^2 + 2X_{\mu x}\mu x + X_{\mu\mu}\mu^2) + \mathcal{O}(3), \quad (11.47)$$

where X_μ designates the derivative of X with respect to μ calculated at $(0, 0)$, with similar notation for the other derivatives, and where $\mathcal{O}(3)$ stands for the neglected cubic terms.

The general saddle-node bifurcation

The fixed points of (11.47) are given by $X(x, \mu) = 0$. The solution $x = -X_\mu / X_{\mu x} + \mathcal{O}(\mu)$, obtained by keeping only terms of order 1 in x , is itself of order 1, and therefore is not admissible because it is not in the neighborhood of $x = 0$. Let us assume that X_{xx} and X_μ are nonzero. We shall study only the case $X_\mu > 0$ and $X_{xx} < 0$, to which the other cases can be brought by redefining x or μ . To second order, the branches of fixed points near the bifurcation point are therefore given by

$$x = \pm \sqrt{\frac{-2X_\mu\mu}{X_{xx}}} + \mathcal{O}(\mu). \quad (11.48)$$

We note that the conditions of nonzero X_{xx} and X_μ can be interpreted in terms of transversality conditions: the form of the field X near $(0, 0)$ is “general” if the surface $X(x, \mu)$ intersects the (x, μ) plane in a manner invariant under small perturbations, i.e., if the intersection is transverse. The condition $X_\mu \neq 0$ is the condition that X is not tangent to the (x, μ) plane, and the condition $X_{xx} \neq 0$ is the condition of nonzero curvature.

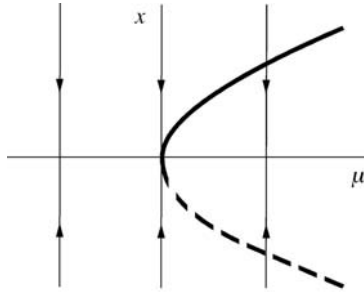


Figure 11.11 Diagram of the saddle–node bifurcation.

For $\mu < 0$ no fixed point exists, while for $\mu > 0$ there is a pair of fixed points. A linear stability analysis immediately shows that the branch of positive solutions is stable and the other branch is unstable. The corresponding bifurcation diagram is shown in Figure 11.11. The name “saddle–node” comes from the fact that if we imagine having an additional hyperbolic dimension, assumed to be stable, the bifurcation appears when the stable node and the unstable saddle merge.

We end by noting that at the price of redefining x and μ , we can arrange that $X_\mu = 1$ and $X_{xx} = -1$, and so the normalized vector field for which a saddle–node bifurcation occurs is

$$X(x, \mu) = \mu - x^2. \quad (11.49)$$

This is the normal form of the saddle–node bifurcation.

The transcritical bifurcation

The transcritical bifurcation is a variant of the saddle–node bifurcation and arises in the many systems admitting a stationary solution for all values of the parameter μ . This condition is satisfied if, in addition to the conditions (11.46), the field X satisfies

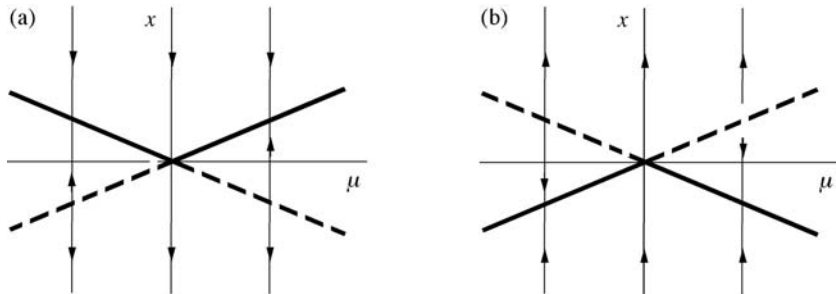
$$X_\mu(0, 0) = 0. \quad (11.50)$$

Accordingly, the general form of the field X near $(0, 0)$ is then

$$\frac{dx}{dt} = \frac{1}{2}(X_{xx}x^2 + 2X_{\mu x}\mu x + X_{\mu\mu}\mu^2) + \mathcal{O}(3), \quad (11.51)$$

and the branches of fixed points near the bifurcation point are given by

$$x = \frac{-X_{\mu x} \pm \sqrt{X_{\mu x}^2 - X_{xx}X_{\mu\mu}}}{X_{xx}}\mu + \mathcal{O}(\mu^2), \quad (11.52)$$

Figure 11.12 Diagram of the transcritical bifurcation: (a) $X_{xx} < 0$, (b) $X_{xx} > 0$.

provided the discriminant is positive (if it is negative the fixed point $(0, 0)$ is isolated and terms of higher degree must be considered). These two branches intersect transversely at the point $(0, 0)$. Study of the stability of the fixed points leads to the conclusion that the upper branches are stable and the lower ones unstable if $X_{xx} < 0$, with these stability properties being reversed for $X_{xx} > 0$ (Figure 11.12). The term “transcritical” emphasizes the “stability exchange” of the two fixed points at the bifurcation.

By means of a change of variable such that $x = 0$ is the stationary solution for all values of the parameter μ , the vector field can be reduced to the following normal form satisfying the conditions (11.46) and (11.50):

$$X(x, \mu) = \mu x - x^2. \quad (11.53)$$

The pitchfork bifurcation

This bifurcation is again a variant of the saddle-node bifurcation, corresponding to the case where the field does not possess a term quadratic in x . It arises, in particular, in systems possessing reflection symmetry (invariance of the equations under the transformation $x \rightarrow -x$). The general form of the field X in the neighborhood of a pitchfork bifurcation is then

$$\frac{dx}{dt} = \frac{1}{2}(2X_{\mu x}\mu x + X_{\mu\mu}\mu^2) + \frac{1}{3!}(X_{xxx}x^3 + 3X_{\mu\mu x}\mu^2 x + X_{\mu\mu\mu}\mu^3) + \mathcal{O}(4). \quad (11.54)$$

Earlier, the branches of fixed points $x(\mu)$ corresponded to asymptotic series in powers of $\sqrt{\mu}$ for the saddle-node bifurcation, and in powers of μ for the transcritical bifurcation. Now each of these two series leads to a branch of fixed points. The first corresponds to the balance between the terms proportional to μx and x^3 (all the others being of higher order), and the second to the balance between

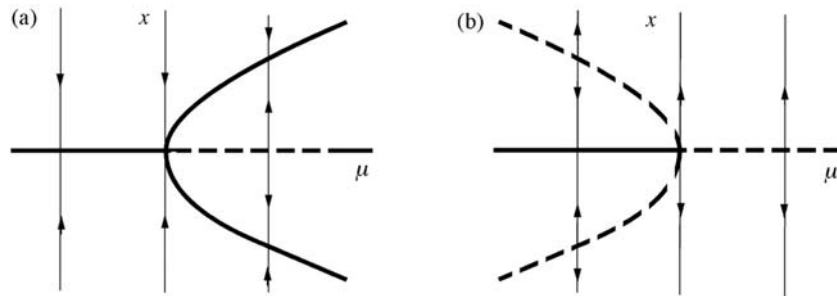


Figure 11.13 Diagram of the pitchfork bifurcation: (a) supercritical, (b) subcritical.

the terms proportional to μx and μ^2 (all the others being of higher order). These branches of solutions are given by

$$x = \pm \sqrt{\frac{-6X_{\mu x}\mu}{X_{xxx}}} + \mathcal{O}(\mu), \quad (11.55)$$

$$x = \frac{-X_{\mu\mu}}{2X_{\mu x}}\mu + \mathcal{O}(\mu^2), \quad (11.56)$$

where the first branch exists only for $\mu > 0$ or $\mu < 0$, depending on whether $X_{xxx}X_{\mu x} < 0$ or $X_{xxx}X_{\mu x} > 0$. The stability of the fixed points on these branches, which is easily studied, is shown in Figure 11.13. We see from this diagram why the bifurcation is called a “pitchfork.” For $X_{xxx} < 0$ the cubic nonlinearity saturates the instability of the fixed point $x = \mathcal{O}(\mu)$ for $\mu > 0$, and the bifurcation is termed supercritical. On the contrary, for $X_{xxx} > 0$ the nonlinearity amplifies the instability and the bifurcation is termed subcritical.

By means of a translation taking the stationary solution to $x = 0$ for all values of the parameter μ , we obtain the normal form of the pitchfork bifurcation, which satisfies the conditions (11.46) as well as the symmetry condition $x \rightarrow -x$:

$$X(x, \mu) = \mu x - \delta x^3, \quad (11.57)$$

the bifurcation being supercritical or subcritical depending on whether $\delta = 1$ or $\delta = -1$.

As an illustration of the above calculations, the determination of the normal form of the Lorenz equations is proposed in Exercise 11.7.10, and the determination of the corresponding bifurcation diagrams in Exercises 11.7.11 and 11.7.12.

11.6.5 The Hopf bifurcation

The Hopf bifurcation corresponds to the case where a fixed point \mathbf{a} loses its hyperbolicity for a value μ_c of a parameter μ at which the field linearized at the point \mathbf{a} admits a pair of purely imaginary eigenvalues $\pm i\omega_0$ of multiplicity one. Let us assume that we have shifted the bifurcation to the origin ($\mathbf{a} = \mathbf{0}$) for $\mu_c = 0$. The center subspace is then of dimension two, and the projection onto this subspace of the dynamics on the center manifold is

$$\begin{aligned}\dot{x} &= -\omega_0 y + \text{nonlinear terms}, \\ \dot{y} &= \omega_0 x + \text{nonlinear terms}.\end{aligned}$$

For μ near 0 the eigenvalues are $\lambda(\mu) = \sigma(\mu) \pm i\omega(\mu)$ with $\sigma(0) = 0$ and $\omega(0) = \omega_0$, or, keeping only the first two orders of the Taylor series,

$$\lambda(\mu) = \sigma_1 \mu \pm i(\omega_0 + \omega_1 \mu) + \mathcal{O}(|\mu|^2). \quad (11.58)$$

Setting $z = x + iy$ and using the relations $x = (z + z^*)/2$ and $y = (z - z^*)/2i$, it is convenient to condense the above two equations into a single one, with the center subspace now being C :

$$\dot{z} = Z(z, \mu_c = 0) = i\omega_0 z + \text{nonlinear terms}. \quad (11.59)$$

Always for the sake of convenience, we can without loss of generality assume that the origin is a fixed point for any value of μ close to 0, or $Z(0, \mu) = 0$. In fact, since the map $z \rightarrow i\omega_0 z$ is invertible, the equation $Z(z, \mu) = 0$ giving the fixed points has, for μ close to 0, a unique solution $z = z(\mu)$ close to $z(0) = 0$ (this is the implicit function theorem). Then, for any μ close to 0, it is possible to move the fixed point to the origin by a translation $z \rightarrow z - z(\mu)$.

Finally, the condition for the bifurcation to be generic is that the two eigenvalues intersect the imaginary axis transversely for $\mu = 0$, or

$$\sigma_1 \neq 0 \quad \text{with} \quad \sigma_1 = \frac{d\sigma}{d\mu}(\mu = 0). \quad (11.60)$$

The eigenvalues $\lambda(0)$ and $\lambda^*(0)$ are resonant at orders $2n + 1$ for any integer n , because $i\omega_0 = (n + 1)i\omega_0 + n(-i\omega_0)$, and so the resonant monomials are all of the type $z^{n+1}z^{*n} = z|z|^{2n}$. The normal form $Z(z)$ of the vector field is therefore (the Hopf theorem)

$$Z(z, \mu) = \lambda(\mu)z - \kappa(\mu)|z|^2z + \mathcal{O}(|z|^5). \quad (11.61)$$

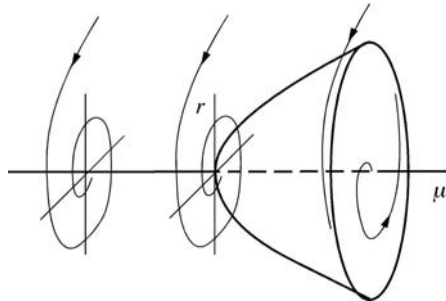


Figure 11.14 Diagram of a supercritical Hopf bifurcation.

Passing to polar coordinates (r, θ) and setting $\kappa(0) = \kappa_r + i\kappa_i$, Eq. (11.59) becomes

$$\dot{r} = \sigma_1 \mu r - \kappa_r r^3 + \mathcal{O}(|r|^5), \quad (11.62a)$$

$$\dot{\theta} = \omega_0 + \omega_1 \mu - \kappa_i r^2 + \mathcal{O}(|r|^4). \quad (11.62b)$$

We recognize here the Landau equation encountered in Chapter 8, with $\kappa(0)$ being the Landau coefficient. For $\kappa_r > 0$, the bifurcation therefore gives rise to the appearance for $\mu > 0$ of stable periodic orbits of radius $\sqrt{\sigma_1 \mu / \kappa_r}$, corresponding to supercritical bifurcation. For $\kappa_r < 0$, these periodic orbits appear for $\mu < 0$ and are unstable, corresponding to subcritical bifurcation. The corresponding phase portraits are shown in Figure 11.14.

When studying a particular system that *a priori* involves quadratic nonlinearities, the main difficulty is calculating the normal form, i.e., removing the quadratic nonlinearities and determining the Landau coefficient κ . Determinations of some Hopf bifurcations are proposed in Exercises 11.7.13 and 11.7.14.

11.6.6 An example of a bifurcation of codimension two

The problem considered here corresponds to a physical situation discussed in Chapter 6, that of the stability of a film flowing down an inclined plane. Analysis of this problem reveals the existence of a bifurcation of codimension two corresponding to a double-zero eigenvalue whose associated eigenspace has only a single dimension (Pumir *et al.*, 1983). The Jordan form of the linearized field is then

$$\mathbf{L}_0 = \begin{pmatrix} 0 & 1 \\ 0 & 0 \end{pmatrix},$$

for which the normal form is, up to homotheties on x_1 , x_2 , and t ,

$$\mathbf{X}(x_1, x_2) = (x_2, -x_1^2 - \delta x_1 x_2) + \mathcal{O}(|\mathbf{x}|^2), \quad \delta = \pm 1. \quad (11.63)$$

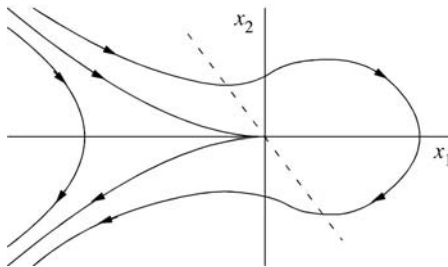


Figure 11.15 Phase portrait of (11.64) for $\mu = \nu = 0$. $(--)$, $dx_2/dx_1 = 0$.

Here we shall study only the case $\delta = +1$. This field is structurally unstable (the fixed point $(0, 0)$ is not hyperbolic), and it can be shown that the following family of two-parameter fields is generic, that is, it contains all possible perturbations of the field given in Eq. (11.63):

$$\mathbf{X}(x_1, x_2) = (x_2, \mu + \nu x_2 - x_1^2 - x_1 x_2). \quad (11.64)$$

For $\mu < 0$ there is no fixed point. For $\mu = 0$ the origin is the only fixed point. For $\mu > 0$ the two fixed points are $(\pm\sqrt{\mu}, 0)$. We shall describe the two cases $\mu = 0$ and $\mu > 0$.

For $\mu = 0$ the problem linearized at the origin has the eigenvalues 0 and ν . For $\nu = 0$ we easily find the phase portrait shown in Figure 11.15. For $\nu \neq 0$, $\mu = 0$ corresponds to a saddle-node bifurcation, with the transverse part being stable for $\nu < 0$ and unstable for $\nu > 0$.

Let us now turn to the case $\mu > 0$. Using the results obtained above, we see that the fixed point $\mathbf{a}_1 = (-\sqrt{\mu}, 0)$ is a saddle. The type of the point $\mathbf{a}_2 = (\sqrt{\mu}, 0)$ depends on the relative values of ν and $\sqrt{\mu}$:

- for $\nu < \sqrt{\mu}$, \mathbf{a}_2 is hyperbolic and attractive;
 - for $\nu > \sqrt{\mu}$, \mathbf{a}_2 is hyperbolic and repulsive;
 - for $\nu = \sqrt{\mu}$, the eigenvalues are $\pm i\sqrt{2}\mu^{1/4}$, corresponding to a Hopf bifurcation.
- It can be shown that the periodic orbit (or limit cycle) appears for $\nu < \sqrt{\mu}$ and that it is repulsive.

Now we can sketch the phase portraits corresponding to different regions of the (μ, ν) parameter space (Figure 11.16). Is this phase portrait complete? Let us fix μ to be positive and allow ν to vary. For ν less than $\sqrt{\mu}$, the point \mathbf{a}_2 is encircled by a repulsive periodic orbit which cordons off the separatrices of the saddle, while for $\nu < 0$ one of the separatrices arrives at \mathbf{a}_2 . It appears to be impossible to pass continuously from one situation to the other without a global bifurcation arising somewhere between them (with the fixed points remaining hyperbolic).

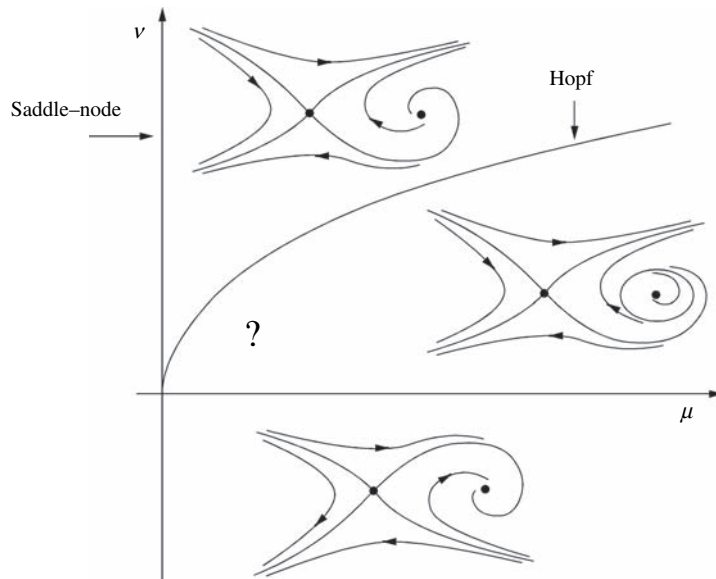


Figure 11.16 Sketches of phase portraits in different domains of the parameter space.

This problem can be solved by a “blowing-up” technique, as follows. We magnify what happens in the region in question by means of the change of variable

$$\mu = \epsilon^4, \quad v = \epsilon^2 \alpha, \quad x_1 = \epsilon^2 y_1, \quad x_2 = \epsilon^3 y_2, \quad \epsilon \geq 0, \quad (11.65)$$

and replace t by ϵt . The system (11.64) becomes

$$\mathbf{X}(y_1, y_2) = [y_2, 1 - y_1^2 - \epsilon(\alpha y_2 - y_1 y_2)], \quad (11.66)$$

with the fixed points $\mathbf{a}_1 = (-1, 0)$ and $\mathbf{a}_2 = (1, 0)$. We note that the parameter transformation is a bijective mapping of the half-plane $\mu > 0$ onto the half-plane $\epsilon > 0$, but that it transforms the point $(\mu, v) = (0, 0)$ into the entire line $\epsilon = 0$.

The essential consequence of this transformation is that the field (11.66) becomes the sum of a nondissipative (“conservative”) part and a dissipative (“nonconservative”) perturbation. In fact, for $\epsilon = 0$ the field (11.66) can be written as

$$\mathbf{X}_0(y_1, y_2) = \left(\frac{\partial H}{\partial y_2}, -\frac{\partial H}{\partial y_1} \right), \quad (11.67)$$

where the Hamiltonian $H(y_1, y_2)$ is defined as

$$H(y_1, y_2) = \frac{y_2^2}{2} - y_1 + \frac{y_1^3}{3}. \quad (11.68)$$

The phase portrait of the conservative system (11.67) can be sketched using the fact that the trajectories are the curves $H(y_1, y_2) = \text{const}$. Actually, along a trajectory,

$$\begin{aligned}\frac{dH}{dt} &= \frac{\partial H}{\partial y_1} \frac{\partial y_1}{\partial t} + \frac{\partial H}{\partial y_2} \frac{\partial y_2}{\partial t} \\ &= \frac{\partial H}{\partial y_1} \frac{\partial H}{\partial y_2} + \frac{\partial H}{\partial y_2} \left(-\frac{\partial H}{\partial y_1} \right) \\ &= 0.\end{aligned}$$

This phase portrait is shown in Figure 11.17. It displays a continuous family of periodic orbits $H(y_1, y_2) = \text{const}$. about \mathbf{a}_2 , which eventually coincide with a homoclinic orbit Γ_0 coming from \mathbf{a}_1 , which corresponds to $H(y_1, y_2) = 2/3$.

What happens to this homoclinic orbit Γ_0 when the dissipative field in (11.66) is taken into account? This problem can be solved by the so-called Melnikov method. For sufficiently small ϵ we can assume that the two separatrices of the saddle, Γ^u and Γ^s , remain close to Γ_0 and therefore intersect the axis $y_2 = 0$ transversely at two points \mathbf{p}^u and \mathbf{p}^s close to \mathbf{p} (Figure 11.18). The complete field \mathbf{X} possesses

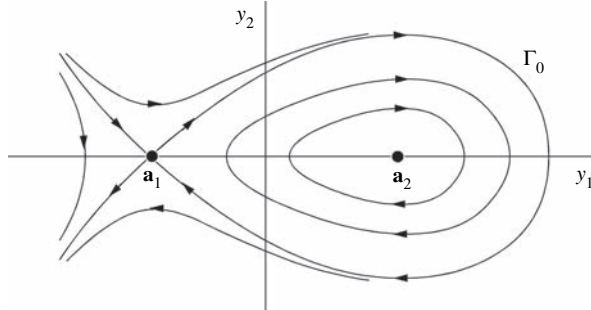


Figure 11.17 Phase portrait of the conservative system (11.67).

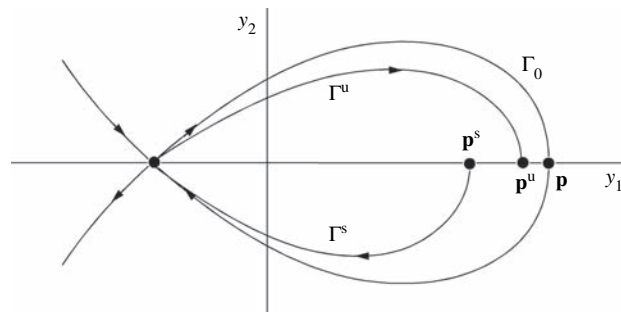


Figure 11.18 Illustration of the Melnikov method.

a homoclinic orbit Γ if it is possible to solve $H(\mathbf{p}^u) = H(\mathbf{p}^s)$, which necessarily implies that $\mathbf{p}^u = \mathbf{p}^s$. The variation of the Hamiltonian between \mathbf{p}^s and \mathbf{a}_1 along the trajectory Γ^s is

$$H(\mathbf{a}_1) - H(\mathbf{p}^s) = \int_{\Gamma^s} \frac{\partial H}{\partial t} dt = \epsilon \int_0^\infty y_2^2(t)[\alpha - y_1(t)]dt. \quad (11.69)$$

From this equation and the analogous equation for the unstable separatrix, we deduce that along the desired homoclinic orbit Γ , which corresponds to $H(\mathbf{p}^u) = H(\mathbf{p}^s)$, we have

$$M(\alpha, \epsilon) = H(\mathbf{p}^s) - H(\mathbf{p}^u) = 0$$

where

$$M(\alpha, \epsilon) = \epsilon \int_{-\infty}^\infty y_2^2(t)[\alpha - y_1(t)]dt. \quad (11.70)$$

Since the homoclinic orbit Γ is unknown this integral cannot be calculated directly, but it can be estimated as

$$M(\alpha, \epsilon) = \epsilon M(\alpha, 0) + \mathcal{O}(\epsilon^2), \quad (11.71)$$

where $M(\alpha, 0)$ represents the integral along the homoclinic orbit Γ_0 of the conservative field, which is close to Γ . The Melnikov integral $M(\alpha, 0)$ has the form $\alpha M_1 - M_0$, and its calculation gives $\alpha = 5/7$. Then, invoking the implicit function theorem, there must exist a function $\alpha(\epsilon)$ with $\alpha(0) = 5/7$ such that for sufficiently small ϵ the saddle \mathbf{a}_1 of the field \mathbf{X} possesses a homoclinic separatrix for $\alpha = \alpha(\epsilon)$, and only in this case.

Returning to the original coordinates, we have shown that there exists a homoclinic orbit along a curve of the (μ, v) plane which is the osculating curve at the origin at the half-parabola $v = 5\sqrt{\mu}/7$ (Figure 11.19). The study of this bifurcation of codimension two is therefore complete.

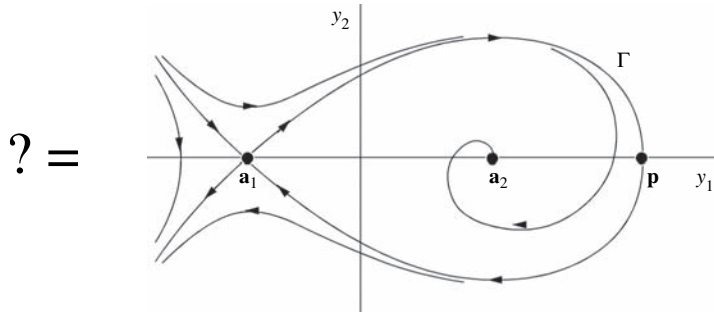


Figure 11.19 Figure 11.16 is completed by this phase portrait displaying a homoclinic orbit along the parabola $v = 5\sqrt{\mu}/7$.

11.7 Exercises

11.7.1 The Hénon attractor

The Hénon attractor is a classical example of a strange attractor corresponding to the mapping

$$\begin{aligned}x_{n+1} &= y_n + 1 - \alpha x_n^2, \\y_{n+1} &= \beta x_n(1 - x_n).\end{aligned}$$

The usual values of the parameters are $\alpha = 1.4$ and $\beta = 0.3$.

1. Use graphics software to visualize the successive iterations of an initial condition somewhere in the square $-1 < x < 1$, $-1 < y < 1$. Try out several different initial conditions.
2. Visualize the first few iterations of a set of points located on the unit circle centered at the origin.
3. Check that the distance between two points initially very close together (10^{-6}) grows exponentially (sensitivity to the initial conditions) until this distance is of the order of the attractor size.
4. Starting from an initial condition, calculate and visualize 10^5 iterations (or more if possible). By successively zooming in, observe the self-similarity of the attractor, which attests to its fractal nature (Bergé *et al.*, 1987, §6.3).

11.7.2 Exponential of a matrix

Check that the matrices (11.8) are indeed the exponentials of the matrices (11.7) (for the second matrix, decompose into its symmetric and antisymmetric parts S and A , and use the property $e^{t(S+A)} = e^{tS}e^{tA}$).

11.7.3 Integration of linear differential systems

Show that the general solution of the differential systems defined by the matrices

$$\begin{pmatrix} -2 & 1 \\ 0 & 2 \end{pmatrix}, \quad \begin{pmatrix} 2 & 1 \\ -2 & 0 \end{pmatrix}, \quad \begin{pmatrix} 5 & -3 \\ 3 & -1 \end{pmatrix}$$

are given by

$$\begin{aligned}\begin{pmatrix} ae^{-2t} + b(e^{2t} - e^{-2t})/4 \\ be^{2t} \end{pmatrix}, \quad e^t \begin{pmatrix} a \cos t + (a+b) \sin t \\ b \cos t - (2a+b) \sin t \end{pmatrix}, \\ e^{2t} \begin{pmatrix} a + 3(a-b)t \\ b + 3(a-b)t \end{pmatrix}.\end{aligned}$$

11.7.4 The phase portrait

Show that the stable manifold of the example given in Section 11.4.1 is the axis Oy . Sketch the phase portrait for $a = 1$ (noting that $\dot{y} = 0$ on the parabola $y = x^2$).

11.7.5 Stable and unstable manifolds

Determine the stable and unstable manifolds, to third order, for the following systems:

$$\begin{aligned}\dot{x} &= -3x + 2y^2 + xy, & \dot{y} &= -y + 3y^2 + x^2y - 4x^3; \\ \dot{x} &= -2x - 3y - x^2, & \dot{y} &= x + 2y + xy - 3y^3.\end{aligned}$$

In each case find the equation of motion on the unstable manifold to second order.

11.7.6 The center manifold

Determine the center manifold and the dynamics on this manifold for the system

$$\begin{aligned}\dot{x} &= xy, \\ \dot{y} &= -y + \alpha x^2.\end{aligned}$$

Can this dynamics be determined here by the tangent-space approximation $h(x) = 0 + \mathcal{O}(x^2)$? Sketch the phase portrait about the origin. Solution in Guckenheimer and Holmes (1983, p. 133).

11.7.7 Resonances of eigenvalues

Consider a differential system of dimension two whose linear part has the eigenvalues λ_1 and λ_2 . If $\lambda_1 = 2$ and $\lambda_2 = -1$, the system is resonant of order 4, because $\lambda_1 = 2\lambda_1 + 2\lambda_2$ (or $\lambda_2 = \lambda_1 + 3\lambda_2$). From this example, determine whether the eigenvalues below are resonant. If they are, what is the order of the resonance?

- $\lambda_1 = 1, \lambda_2 = -1$;
- $\lambda_1 = 3, \lambda_2 = -1$;
- $\lambda_1 = 1, \lambda_2 = 2$;
- $\lambda_1 = \alpha, \lambda_2 = \alpha, \alpha > 0$;
- $\lambda_1 = \alpha, \lambda_2 = -\alpha, \alpha > 0$.

11.7.8 The normal form

Show that the normal form of the differential system

$$\begin{aligned}\dot{x} &= x + o(x, y), \\ \dot{y} &= -y + o(x, y)\end{aligned}$$

is written as

$$\begin{aligned}\dot{x} &= x + \alpha x^2 y + \mathcal{O}(5), \\ \dot{y} &= -y + \beta x y^2 + \mathcal{O}(5).\end{aligned}$$

11.7.9 Structural stability of a heteroclinic orbit

Using arguments similar to those at the end of Section 11.5.3, show that a heteroclinic orbit joining two saddles is structurally unstable in two dimensions, but may be structurally stable in higher dimensions. What can be said about a heteroclinic orbit joining a saddle and a node?

11.7.10 The normal form of the Lorenz equations

Calculate the normal form of the Lorenz equations

$$\begin{aligned}\dot{x} &= -\sigma x + \sigma y, \\ \dot{y} &= -xz + rx - y, \\ \dot{z} &= xy - bz\end{aligned}$$

near the fixed point $(0, 0, 0)$ which becomes nonhyperbolic for $r = 1$, with $\sigma = 10$ and $b = 8/3$. Show that $r = 1$ corresponds to a saddle-node bifurcation.

11.7.11 Bifurcation diagram (1)

Determine the bifurcation diagram of the differential system

$$\dot{x} = x(x^2 - \mu)(x^2 + \mu^2 - 1).$$

11.7.12 Bifurcation diagram (2)

Determine the bifurcation diagram of the differential system

$$\dot{x} = 4x \left[(x - 1)^2 - \mu - 1 \right].$$

The solution is given in Figure 11.20.

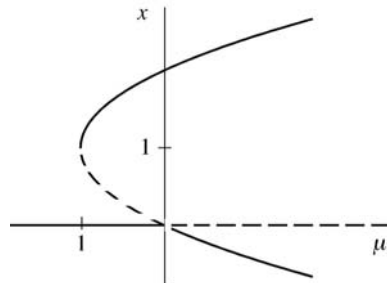


Figure 11.20 Bifurcation diagram corresponding to the solution of Exercise 11.7.12.

11.7.13 Hopf bifurcation

Determine the Hopf bifurcations of the system

$$\begin{aligned}\dot{x} &= x - \omega y - x(x^2 + y^2), \\ \dot{y} &= \omega x + y - y(x^2 + y^2) - \mu.\end{aligned}$$

11.7.14 Hopf bifurcation of the Lorenz system

Show that the two fixed points symmetric about the origin in the Lorenz system become nonhyperbolic for some r in the range [24, 25], and that the bifurcation is a subcritical Hopf bifurcation (this rather lengthy computational exercise requires calculation of the normal form near the fixed point in order to explicitly determine the Landau coefficient κ of the cubic term).

Appendix A: The Saint-Venant equations

In this appendix we shall derive a system of depth-averaged conservation equations, the classic *Saint-Venant equations* (de Saint-Venant, 1871), which give a good description of the dynamics of a fluid flow when the spatial scale λ of the variations in the longitudinal direction x is large compared to the flow depth or thickness, h . These equations do not explicitly involve the nature of the flowing medium, and so they are valid, under certain conditions stated explicitly below, for a fluid flow either laminar or turbulent, as well as for a granular flow. The equations can be obtained by two equivalent methods: by depth-averaging the local conservation equations in the transverse direction, or by writing down the conservation laws for a control volume corresponding to a slice of fluid of thickness dx . Here we shall use the latter method.

A.1 Outflow from a slice of fluid

Let us consider a flow in the x -direction, inclined at an angle θ relative to the horizontal, between a bed located at $y = y_b(x, t)$, where y is the transverse direction, and a free surface at $y = (y_b + h)(x, t)$, where h is the local flow depth (Figure A.1).

We define the control volume as the slice of fluid between the two planes at x and $x + dx$. At any point on the boundary of the control volume, let \mathbf{n} be the exterior normal, \mathbf{u} the fluid velocity and \mathbf{w} the speed of the boundary. The outflow of a scalar quantity ϕ across the surface A of the slice is

$$\int_A \phi (\mathbf{u} - \mathbf{w}) \cdot \mathbf{n} dA.$$

Since the speed \mathbf{w} is zero on the planes at x and $x + dx$, while the normal velocities $\mathbf{u} \cdot \mathbf{n}$ and $\mathbf{w} \cdot \mathbf{n}$ are equal on the bed as well as on the free surface (the kinematic condition is equivalent to the condition that these surfaces are impermeable), the

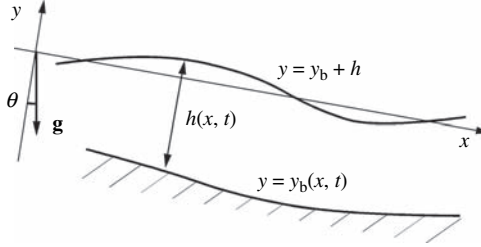


Figure A.1 Sketch of the flow.

net outflow can be written as

$$\int_{y_b(x+dx)}^{(y_b+h)(x+dx)} (\phi u)(x+dx, y) dy - \int_{y_b(x)}^{(y_b+h)(x)} (\phi u)(x, y) dy.$$

We introduce the depth-averaged longitudinal speed U

$$U(x, t) = \frac{1}{h(x, t)} \int_{y_b(x, t)}^{(y_b+h)(x, t)} u(x, y, t) dy, \quad (\text{A.1})$$

and the velocity-weighted average Φ of the quantity ϕ :

$$\Phi(x, t) = \frac{1}{(hU)(x, t)} \int_{y_b(x)}^{(y_b+h)(x)} (\phi u)(x, y) dy. \quad (\text{A.2})$$

Here ϕ may be, e.g., the fluid density, one component of the momentum, or the kinetic energy. The outflow of ϕ can then be written as

$$\int_A \phi (\mathbf{u} - \mathbf{w}) \cdot \mathbf{n} dA = (h\Phi U)(x+dx) - (h\Phi U)(x) = \frac{\partial(h\Phi U)}{\partial x} dx. \quad (\text{A.3})$$

A.2 Mass conservation

During an infinitesimal time dt , the variation of the mass in the slice of thickness dx is, for incompressible flow,

$$dx \int_{y_b(t+dt)}^{(y_b+h)(t+dt)} \rho dy - dx \int_{y_b(t)}^{(y_b+h)(t)} \rho dy = \rho \frac{\partial h}{\partial t} dt dx.$$

On the other hand, from (A.3) with $\phi = \rho$, the net mass entering the slice during dt is

$$dt \int_{y_b(x)}^{(y_b+h)(x)} \rho u(x, y) dy - dt \int_{y_b(x+dx)}^{(y_b+h)(x+dx)} \rho u(x+dx, y) dy = -\rho \frac{\partial(hU)}{\partial x} dx dt.$$

Mass conservation implies that the variation of the mass is equal to the net mass entering the slice, or

$$\frac{\partial h}{\partial t} + \frac{\partial(hU)}{\partial x} = 0. \quad (\text{A.4})$$

A.3 Momentum conservation

Since the longitudinal and transverse velocities, u and v , are such that $v \sim (h/\lambda)u$ owing to incompressibility, the hypothesis of slow variation in the x -direction, or $\lambda \gg h$, implies that v is small compared to u . Therefore, it is possible to neglect the inertia and the viscous stresses in the transverse momentum equation (Batchelor, 1967, §5.7). The pressure distribution is then hydrostatic in the vertical:

$$p(x, y, t) = p_a + \rho g \cos \theta (y_b(x, t) + h(x, t) - y), \quad (\text{A.5})$$

where p_a is the pressure, assumed to be uniform, above the free surface.

The variation of the longitudinal momentum in the control volume during the time dt is

$$dx \int_{y_b(t+dt)}^{(y_b+h)(t+dt)} \rho u(x, y, t+dt) dy - dx \int_{y_b(t)}^{(y_b+h)(t)} \rho u(x, y, t) dy = \rho \frac{\partial(hU)}{\partial t} dt dx.$$

The momentum entering this volume during the same time is obtained from (A.3) with $\phi = \rho u$, which gives

$$dt \int_{y_b(x)}^{(y_b+h)(x)} (\rho u^2)(x, y) dy - dt \int_{y_b(x+dx)}^{(y_b+h)(x+dx)} (\rho u^2)(x+dx, y) dy = \\ - \rho \frac{\partial(c_{u^2} h U^2)}{\partial x} dx dt,$$

where the *shape factor*

$$c_{u^2}(x, t) = \frac{1}{U^2 h} \int_{y_b(x,t)}^{(y_b+h)(x,t)} u^2(x, y, t) dy \quad (\text{A.6})$$

corresponds to $\Phi = \rho c_{u^2} U$ in (A.3). This coefficient depends on the velocity profile, which is generally unknown. A simplification is commonly made here, which consists of assuming a particular velocity profile. In particular:

- $c_{u^2} = 1$ for a uniform velocity profile $u(y) = U$, which, however crude, is a widely used approximation for turbulent flows at large Reynolds number.
- $c_{u^2} = 4/3$ for the linear velocity profile $u(y) = \gamma y$ of sheared films or certain granular flows (Rajchenbach, 2000).

- $c_{u^2} = 5/4$ for the Bagnold velocity profile $u(y) \sim y^{3/2}$ of a granular flow (Bagnold, 1956).
- $c_{u^2} = 6/5$ for the semi-parabolic profile corresponding to a falling viscous film $u(y) = U_{\max}(y/h)(2 - y/h)$, where $U_{\max} = \frac{3}{2}U$ is the speed of the free surface.

In any case, we see that the shape factor does not vary much and is a constant of order unity. If the relaxation time of the flow over the flow depth is short compared to the other time scales, the velocity profile is nearly fully developed, and the coefficient c_{u^2} can be considered as constant, with error of the order of the small gradient parameter h/λ .

Taking into account the hydrostatic pressure distribution (A.5), and neglecting terms of order $(h/\lambda)^2$, the longitudinal momentum flux associated with the pressure forces is

$$\begin{aligned} & \int_{y_b(x)}^{(y_b+h)(x)} p(x, y) dy - \int_{y_b(x+dx)}^{(y_b+h)(x+dx)} p(x+dx, y) dy + \\ & + p_a(x, y_b + h) dx \partial_x (y_b + h) \\ & - p(x, y_b) dx \partial_x y_b = dx \rho g h \cos \theta \partial_x (y_b + h) \end{aligned}$$

(the pressure p_a vanishes upon integration). The momentum flux associated with the viscous stresses is nonzero only on the bed (when the normal viscous stresses can be neglected) and equal to $-\tau dx$ per unit time, where τ is the tangential stress exerted by the fluid on the bed. Finally, the flux associated with gravity is $\rho g h \sin \theta dx$.

Therefore, assuming constant shape factor c_{u^2} , the final form of the depth-averaged momentum equation is

$$\frac{\partial(Uh)}{\partial t} + c_{u^2} \frac{\partial(U^2h)}{\partial x} = -gh \cos \theta \frac{\partial(y_b + h)}{\partial x} - \frac{\tau}{\rho} + gh \sin \theta. \quad (\text{A.7})$$

This equation, together with the mass conservation equation (A.4), constitutes the Saint-Venant equations. For turbulent flow, the additional approximation $c_{u^2} = 1$ allows a further simplification of the left-hand side: using mass conservation (A.4), the above equation becomes

$$h \frac{\partial U}{\partial t} + Uh \frac{\partial U}{\partial x} = -gh \cos \theta \frac{\partial(y_b + h)}{\partial x} - \frac{\tau}{\rho} + gh \sin \theta. \quad (\text{A.8})$$

A.4 Modeling the wall friction

The Saint-Venant equations involve the unknown wall shear, which must be modeled, that is, expressed as a function of the averages U and h , in order to result in

a closed set of equations. This is where we encounter the second major difficulty (after the problem of the shape factor) in accurately representing the physics of the problem. Here we shall give the classical closure relations for three types of flow: a viscous film, a flow at large Reynolds number, and a granular flow.

- For a viscous film, the hypothesis of a fully developed profile, that is, a parabolic profile ($c_{u^2} = 6/5$ uniform) leads to

$$\tau = \mu \frac{\partial u}{\partial y}(y_b) = \mu \frac{2U_{\max}}{h} = \mu \frac{3U}{h} = \frac{3\mu}{Q} U^2, \quad (\text{A.9})$$

where $Q = Uh$ is the flow volume per unit width.

- For flows at large Reynolds number, the shear is classically related to the speed U by a friction coefficient c_f defined as

$$\tau = c_f \frac{\rho U^2}{2}. \quad (\text{A.10})$$

This friction coefficient depends on the Reynolds number $\text{Re} = \rho Uh/\mu$ and the dimensionless bed roughness z_0/h . For turbulent flow on smooth walls, a relation often used in hydraulics is the empirical Blasius relation (Pope, 2000):

$$c_f = 0.316 \text{Re}^{-1/4}, \quad (\text{A.11})$$

while for rough walls, a widely used expression is that of Manning–Strickler:

$$c_f = 0.1 \left(\frac{z_0}{h} \right)^{1/3}. \quad (\text{A.12})$$

More complex relations involving both Re and z_0/h , or the logarithmic velocity profile, are also available.

- For a dry granular flow the shear can be related to the normal stress ρgh by a Coulomb friction coefficient μ_f :

$$\tau = \mu_f \rho gh. \quad (\text{A.13})$$

This coefficient can be assumed to be constant (Savage and Hutter, 1989), or related to the speed and thickness of the flow by a phenomenological relation $\mu_f = \mu_f(U, h)$ (Pouliquen, 1999).

A.5 Consistent depth-averaged equations

Finally, it must be stressed that the Saint-Venant equations are not a consistent approximation of the Navier–Stokes equations, in the sense that they do not account correctly for first-order corrections in the small parameter h/λ . Thus, the

use of these equations for stability calculations is questionable, at least when seeking quantitative predictions. A consistent set of depth-averaged equations based not on the momentum equation but on the kinetic energy equation has been developed recently (Luchini and Charru, 2010a, 2010b). These give the correct quantitative predictions of stability.

References

- Abramowitz, M. and Stegun, I. A. (1964) *Handbook of Mathematical Functions with Formulas, Graphs, and Mathematical Tables*. New York: Dover.
- Abrams, J. and Hanratty, T. J. (1985) Relaxation effects observed for turbulent flow over a wavy surface. *J. Fluid Mech.* **151**, 443–55.
- Acheson, D. J. (1990) *Elementary Fluid Dynamics*. Oxford: Clarendon Press.
- Andersen, K. H. (2001) A particle model of rolling grain ripples under waves. *Phys. Fluids* **13**(1), 58–64.
- Andreotti, B. (2004) A two species model for aeolian sand transport. *J. Fluid Mech.* **510**, 47–70.
- Andreotti, B., Claudin, P. and Douady, S. (2002a) Selection of dune shapes and velocities. Part 1: dynamics of sand, wind and barchans. *Eur. Phys. J. B* **28**, 321–39.
- Andreotti, B., Claudin, P. and Douady, S. (2002b) Selection of dune shapes and velocities. Part 2: a two-dimensional modelling. *Eur. Phys. J. B* **28**, 341–52.
- Anshus, B. E. and Goren, S. L. (1966) A method of getting approximate solutions of the Orr–Sommerfeld equation for flow on a vertical wall. *AIChE J.* **12**, 1004–8.
- Aradian, A., Raphael, É. and de Gennes, P. G. (2002) Surface flows of granular materials: a short introduction to some recent models. *C.R. Physique* **3**(2), 187–96.
- Aranson, I. S. and Tsimring, L. S. (2006) Patterns and collective behavior in granular media: Theoretical concepts. *Rev. Mod. Phys.* **78**, 641–92.
- Arnal, D. (1994) Predictions based on linear theory. AGARD Rep. 793. ONERA.
- Arnold, V. I. (1973) *Ordinary Differential Equations*. Cambridge, MA: MIT Press.
- ASCE Task Committee on Flow and Transport over Dunes (2002) Flow and transport over dunes. *J. Hydr. Engrg.* **128**(8), 726–8.
- Ayrton, H. (1910) The origin and growth of ripple-mark. *Proc. R. Soc. Lond. A* **84**, 285–310.
- Bagnold, R. A. (1941) *The Physics of Blown Sand and Desert Dunes*. London: Chapman & Hall.
- Bagnold, R. A. (1946) Motion of waves in shallow water. interaction between waves and sand bottoms. *Proc. R. Soc. Lond. A* **187**, 1–18.
- Bagnold, R. A. (1954) Experiments on a gravity-free dispersion of large solid spheres in a Newtonian fluid under shear, *Proc. R. Soc. Lond. A* **225**, 49–63.
- Bagnold, R. A. (1956) The flow of cohesionless grains in fluids. *Phil. Trans. R. Soc. Lond. A* **249**, 235–97.
- Bagnold, R. A. (1973) The nature of saltation and of ‘bed-load’ transport in water. *Proc. R. Soc. Lond. A* **332**, 473–504.

- Baines, P. G., Majumdar, S. and Mitsudera, H. (1996) The mechanics of the Tollmien–Schlichting wave. *J. Fluid Mech.* **312**, 107–24.
- Barthelet, P. and Charru, F. (1998) Benjamin–Feir and Eckhaus instabilities with Galilean invariance: the case of interfacial waves in viscous shear flows. *Eur. J. Mech. B* **17**(1), 1–18.
- Barthelet, P., Charru, F. and Fabre, J. (1995) Experimental study of interfacial long waves in a two-layer shear flow. *J. Fluid Mech.* **303**, 23–53.
- Batchelor, G. K. (1967) *An Introduction to Fluid Dynamics*. Cambridge: Cambridge University Press.
- Bayly, B. J., Orszag, S. A. and Herbert, T. (1988) Instability mechanisms in shear-flow transition. *Annu. Rev. Fluid Mech.* **20**, 359–91.
- Bénard, H. (1900) Les tourbillons cellulaires dans une nappe liquide. *Revue Gén. Sci. Pures Appl.* **11**, 1261–71, 1309–28.
- Bender, C. M. and Orszag, S. A. (1978) *Advanced Mathematical Methods for Scientists and Engineers*. New York: McGraw-Hill.
- Benjamin, T. B. (1957) Wave formation in laminar flow down an inclined plane. *J. Fluid Mech.* **2**, 554–74.
- Benjamin, T. B. (1959) Shearing flow over a wavy boundary. *J. Fluid Mech.* **6**, 161–205.
- Benjamin, T. B. and Feir, J. E. (1967) The disintegration of wave trains on deep water. *J. Fluid Mech.* **27**, 417–30.
- Benjamin, T. B. and Hasselmann, K. (1967) Instability of periodic wavetrains in nonlinear dispersive systems. *Proc. R. Soc. Lond. A* **299**(1456), 59–76.
- Benjamin, T. B. and Ursell, F. (1954) The stability of the plane free surface of liquid in vertical periodic motion. *Proc. R. Soc. Lond. A* **225**, 505–15.
- Benney, D. J. (1966) Long waves on liquid films. *J. Math. Phys.* **45**, 150–55.
- Benney, D. J. and Newell, A. C. (1967) The propagation of non-linear wave envelopes. *J. Math. Phys.* **46**, 133–45.
- Bergé, P., Pomeau, Y. and Vidal, C. (1987) *Order Within Chaos: Towards a Deterministic Approach to Turbulence*. New York: John Wiley & Sons.
- Betchov, R. and Szewczyk, A. (1963) Stability of a shear layer between parallel streams. *Phys. Fluids* **6**, 1391–6.
- Billingham, J. and King, A. C. (2000) *Wave Motion*. Cambridge: Cambridge University Press.
- Binney, J. and Tremaine, S. (1988) *Galactic Dynamics*. Princeton, NJ: Princeton University Press.
- Blondeaux, P. (1990) Sand ripples under sea waves. Part 1. Ripple formation. *J. Fluid Mech.* **218**, 1–17.
- Blondeaux, P. (2001) Mechanics of coastal forms. *Annu. Rev. Fluid Mech.* **33**, 339–70.
- Bogolioubov, N. and Mitropolski, I. (1962) *Les méthodes asymptotiques en théorie des oscillations non linéaires*. Paris: Gauthier-Villars.
- Bottaro, A. and Luchini, P. (1999) Görtler vortices: are they amenable to local eigenvalue analysis. *Eur. J. Mech. B/Fluids* **18**(1), 47–65.
- Bouasse, H. (1924) Houle, rides, seiches et marées. In *Bibliothèque scientifique de l'ingénieur et du physicien*. Paris: Delagrave.
- Boussinesq, J. (1871) Théorie de l'intumescence liquide, appelée onde solitaire ou de translation, se propageant dans un canal rectangulaire. *C. R. Acad. Sci. Paris* **72**, 755–9.
- Busse, F. and Whitehead, J. A. (1971) Instabilities of convection rolls in a high Prandtl number fluid. *J. Fluid Mech.* **47**, 305–20.
- Butler, K. M. and Farrell, B. F. (1992) Three-dimensional optimal perturbations in viscous shear flow. *Phys. Fluids A* **4**(8), 1637–50.

- Callen, H. B. (1985) *Thermodynamics and an Introduction to Thermostatistics*. New York: John Wiley & Sons.
- Canuto, C., Hussaini, M. Y., Quarteroni, A. and Zang, T. A. (1988) *Spectral Methods in Fluid Dynamics*. New York: Springer-Verlag.
- Case, K. M. (1960) Stability of inviscid plane Couette flow. *Phys. Fluids* **3**, 143–8.
- Chandrasekhar, S. (1961) *Hydrodynamic and Hydromagnetic Stability*. New York: Dover.
- Chang, H.-C. (1994) Wave evolution on a falling film. *Annu. Rev. Fluid Mech.* **26**, 103–36.
- Charru, F. (1997) A simple mechanical system mimicking phase transitions in a one-dimensional medium. *Eur. J. Phys.* **18**, 417–24.
- Charru, F. (2006) Selection of the ripple length on a granular bed sheared by a liquid flow. *Phys. Fluids* **18**, 121508.
- Charru, F. and Barthelet, P. (1999) Secondary instabilities of interfacial waves due to coupling with a long wave mode in a two-layer Couette flow. *Physica D* **125**, 311–24.
- Charru, F. and Hinch, E. J. (2000) ‘Phase diagram’ of interfacial instabilities in a two-layer Couette flow and mechanism for the long-wave instability. *J. Fluid Mech.* **414**, 195–223.
- Charru, F. and Hinch, E. J. (2006) Ripple formation on a particle bed sheared by a viscous liquid. Part 2. Oscillating flow. *J. Fluid Mech.* **550**, 123–37.
- Charru, F., Larrieu, E., Dupont, J.-B. and Zenit, R. (2007) Motion of a particle near a rough wall in a viscous shear flow. *J. Fluid Mech.* **570**, 431–53.
- Charru, F., Mouilleron, H. and Eiff, O. (2004) Erosion and deposition of particles on a bed sheared by a viscous flow. *J. Fluid Mech.* **519**, 55–80.
- Charru, F. and Mouilleron-Arnould, H. (2002) Instability of a bed of particles sheared by a viscous flow. *J. Fluid Mech.* **452**, 303–23.
- Chavanis, P. H. (2002) Gravitational instability of finite isothermal spheres. *Astron. Astrophys.* **381**, 340–56.
- Chomaz, J.-M. (2005) Global instabilities in spatially developing flows: non-normality and nonlinearity. *Annu. Rev. Fluid Mech.* **37**, 357–92.
- Chossat, P. and Iooss, G. (1994) *The Couette–Taylor Problem*. Applied Mathematics Series, Vol. 102. New York: Springer-Verlag.
- Clanet, C. and Searby, G. (1998) First experimental study of the Darrieus–Landau instability. *Phys. Rev. Lett.* **80**, 3867–70.
- Coleman, S. E. and Eling, B. (2000) Sand wavelets in laminar open-channel flows. *J. Hydraul. Res.* **38**(5), 331–8.
- Coleman, S. E. and Melville, B. W. (1994) Bed-form development. *J. Hydr. Engrg.* **120**(4), 544–60.
- Coleman, S. E. and Melville, B. W. (1996) Initiation of bed forms on a flat sand bed. *J. Hydr. Engrg.* **122**(6), 301–10.
- Colombini, M. (2004) Revisiting the linear theory of sand dune formation. *J. Fluid Mech.* **502**, 1–16.
- Couder, Y. (2000) Viscous fingering as an archetype for growth patterns. In *Perspectives in Fluid Mechanics, a Collective Introduction to Current Research* (ed. G. K. Batchelor). Paris: Lavoisier.
- Couette, M. (1890) Études sur le frottement des liquides. *Ann. Chim. Phys.* **21**(6), 433–510.
- Coullet, P. and Fauve, S. (1985) Propagative phase dynamics for systems with Galilean invariance. *Phys. Rev. Lett.* **55**, 2857–9.
- Coullet, P. and Iooss, G. (1990) Instabilities of one-dimensional cellular patterns. *Phys. Rev. Lett.* **64**(8), 866–9.
- Cousteix, J. and Mauss, J. (2006) *Analyse asymptotique et couche limite*. Mathématiques & Applications, Vol. 56. Berlin: Springer-Verlag.

- Craik, A. D. D. (1985) *Wave Interactions and Fluid Flows*. Cambridge: Cambridge University Press.
- Craik, A. D. D. (2004) The origins of water wave theory. *Annu. Rev. Fluid Mech.* **36**, 1–28.
- Craik, A. D. D. (2005) George Gabriel Stokes on water wave theory. *Annu. Rev. Fluid Mech.* **37**, 23–42.
- Crawford, J. D. (1991) Introduction to bifurcation theory. *Rev. Mod. Phys.* **63**(4), 991–1037.
- Crawford, J. D. and Knobloch, E. (1991) Symmetry and symmetry-breaking bifurcations in fluid mechanics. *Annu. Rev. Fluid Mech.* **23**, 341–87.
- Cross, M. C. and Hohenberg, P. C. (1993) Pattern formation outside of equilibrium. *Rev. Mod. Phys.* **65**(3), 851–1113.
- Darrieus, G. (1938) Propagation d'un front de flamme: essai de théorie des vitesses anormales de déflagration par développement spontané de la turbulence. Travail non publié présenté à La Technique Moderne, Paris.
- Darrigol, O. (2003) The spirited horse, the engineer, and the mathematician: water waves in nineteenth-century hydrodynamics. *Arch. Hist. Exact Sci.* **58**, 21–95.
- Darrigol, O. (2005) *Worlds of Flow – A history of hydrodynamics from the Bernoullis to Prandtl*. Oxford: Oxford University Press.
- Dauxois, T. and Peyrard, M. (2006) *Physis of Solitons*. Cambridge: Cambridge University Press.
- Denn, M. M. (2001) Extrusion instabilities and wall slip. *Annu. Rev. Fluid Mech.* **33**, 265–87.
- Dias, F. and Kharif, C. (1999) Nonlinear gravity and capillary-gravity waves. *Annu. Rev. Fluid Mech.* **31**, 301–46.
- Donnelly, R. J. and Glaberson, W. (1966) Experiments on the capillary instability of a liquid jet. *Proc. R. Soc. Lond. A* **290**, 547–56.
- Drazin, P. G. (2002) *Introduction to Hydrodynamic Stability*. Cambridge: Cambridge University Press.
- Drazin, P. G. and Reid, W. H. (2004) *Hydrodynamic Stability*, 2nd edn. Cambridge: Cambridge University Press.
- Duffing, G. (1918) *Erzwungene Schwingungen bei Veränderlicher Eigenfrequenz*. Braunschweig: F. Veiweg u. Sohn.
- van Dyke, M. (1982) *An Album of Fluid Motion*. California: Parabolic Press.
- Eckhaus, W. (1965) *Studies in Non-linear Stability Theory*. Springer Tracts in Natural Philosophy 6. Berlin: Springer-Verlag.
- Eggers, J. (1997) Nonlinear dynamics and breakup of free-surface flows. *Rev. Mod. Phys.* **69**(3), 865–929.
- Ehrenstein, U. and Koch, W. (1991) Three-dimensional wavelike equilibrium states in plane Poiseuille flow. *J. Fluid Mech.* **228**, 111–48.
- Ellingsen, T. and Palm, E. (1975) Stability of linear flow. *Phys. Fluids* **18**, 487–8.
- Elphick, C., Tirapegui, E., Brachet, M. E., Coullet, P. and Iooss, G. (1987) A simple global characterization for normal forms of singular vector fields. *Physica* **29D**, 95–127.
- Faraci, C. and Foti, E. (2001) Evolution of small scale regular patterns generated by waves propagating over a sandy bottom. *Phys. Fluids* **13**(6), 1624–34.
- Faraday, M. (1831) On a peculiar class of acoustic figures, and on certain forms assumed by groups of particles upon vibrating elastic surfaces. *Phil. Trans. R. Soc. Lond.* **121**, 299–340.
- Farrell, B. F. (1988) Optimal excitation of perturbations in viscous shear flows. *Phys. Fluids* **31**(8), 2093–102.

- Fasel, H. and Konzelmann, U. (1990) Non-parallel stability of a flat plate boundary layer using the complete Navier–Stokes equations. *J. Fluid Mech.* **221**, 311–47.
- Fauve, S. (1998) Pattern forming instabilities. In *Hydrodynamics and Nonlinear Instabilities* (eds. C. Godrèche and P. Manneville), pp. 387–492. Cambridge: Cambridge University Press.
- Feigenbaum, M. J. (1978) Quantitative universality for a class of nonlinear transformations. *J. Stat. Phys.* **19**, 1–25.
- Fenstermacher, P. R., Swinney, H. L. and Gollub, J. (1979) Dynamical instabilities and the transition to chaotic Taylor vortex flow. *J. Fluid Mech.* **94**, 103–28.
- Fermigier, M., Limat, L., Wesfreid, J. E., Boudinet, P., Petitjean, M., Quilliet, C. and Valet, T. (1990) Gravitational and magnetic instabilities of thin fluid layers. *Phys. Fluids A* **2**(9), 1518.
- Fermigier, M., Limat, L., Wesfreid, J. E., Boudinet, P. and Quilliet, C. (1992) Two-dimensional patterns in Rayleigh–Taylor instability of a thin layer. *J. Fluid Mech.* **236**, 349–83.
- Fernandez Luque, R. and van Beek, R. (1976) Erosion and transport of bedload sediment. *J. Hydraul. Res.* **14**(2), 127–44.
- Fjørtoft, R. (1950) Application of integral theorems in deriving criteria of stability for laminar flows for the baroclinic circular vortex. *Geofys. Publ., Oslo* **17**(6), 1–52.
- Floryan, J. M. (1991) On the Görtler instability of boundary layers. *Prog. Aerospace Sci.* **28**, 235–71.
- Floryan, J. M., Davis, S. H. and Kelly, R. E. (1987) Instabilities of a liquid film flowing down a slightly inclined plane. *Phys. Fluids* **30**, 983–9.
- Forsterre, Y. (2006) Kapiza waves as a test for three-dimensional granular flow rheology. *J. Fluid Mech.* **563**, 123–32.
- Forsterre, Y. and Pouliquen, O. (2003) Long-surface-wave instability in dense granular flows. *J. Fluid Mech.* **486**, 21–50.
- Forsterre, Y. and Pouliquen, O. (2008) Flows of dense granular media. *Annu. Rev. Fluid Mech.* **40**, 1–24.
- Gaster, M. (1962) A note on the relation between temporally-increasing and spatially-increasing disturbances in hydrodynamic stability. *J. Fluid Mech.* **14**, 222–4.
- Gaster, M. (1974) On the effects of boundary-layer growth on flow stability. *J. Fluid Mech.* **66**, 465–80.
- Gaster, M., Kit, E. and Wygnanski, I. (1985) Large-scale structures in a forced turbulent mixing layer. *J. Fluid Mech.* **150**, 23–39.
- GDR MiDi (2004) On dense granular flows. *Eur. Phys. J. E* **14**(4), 341–65.
- de Gennes, P. G. and Badoz, J. (1994) *Les objets fragiles*. Paris: Plon.
- Glendinning, P. (1994) *Stability, Instability and Chaos: an introduction to the theory of nonlinear differential equations*. Cambridge: Cambridge University Press.
- Gor'kov, L. P. (1957) Stationary convection in a plane liquid layer near the critical heat transfer point. *Zh. Eksp. Teor. Fiz.* **33**, 402–7 (English transl. in *Sov. Phys. J.E.T.P.* (1958), vol. 6, pp. 311–15).
- Guckenheimer, J. and Holmes, P. (1983) *Nonlinear Oscillations, Dynamical Systems, and Bifurcations of Vector Fields*. New York: Springer-Verlag.
- Guyon, E., Hulin, J. P. and Petit, L. (2001) *Physical Hydrodynamics*, 1st edn. Oxford: Oxford University Press.
- Hammack, J. L. and Henderson, D. M. (1993) Resonant interactions among surface water waves. *Annu. Rev. Fluid Mech.* **25**, 55–97.
- Hanratty, T. J. (1983) Interfacial instabilities caused by air flow over a thin liquid film. In *Waves on Fluid Interfaces* (ed. R. Meyer), pp. 221–59. New York: Academic Press.

- Heisenberg, W. (1924) Über stabilität und turbulenz von flüssigkeitsstromen. *Ann. Phys.* **74**, 577–627.
- von Helmholtz, H. (1868) On discontinuous movements of fluids. *Phil. Mag.* **36**, 337–46.
- Herbert, T. (1988) Secondary instability of boundary layers. *Annu. Rev. Fluid Mech.* **20**, 487–526.
- Hersen, P., Douady, S. and Andreotti, B. (2002) Relevant lengthscale of Barchan dunes. *Phys. Rev. Lett.* **89**, 264–301.
- Hesla, T. I., Pranckh, F. R. and Preziosi, L. (1986) Squire's theorem for two stratified fluids. *Phys. Fluids* **29**(9), 2808–11.
- Hickox, C. E. (1971) Instability due to viscosity and density stratification in axisymmetric pipe flow. *Phys. Fluids* **14**(2), 251–62.
- Hinch, E. J. (1984) A note on the mechanism of the instability at the interface between two shearing fluids. *J. Fluid Mech.* **144**, 463–5.
- Hinch, E. J. (1991) *Perturbation Methods*. Cambridge: Cambridge University Press.
- Hinch, E. J., Harris, O. J. and Rallison, J. M. (1992) The instability mechanism for two elastic liquids being co-extruded. *J. Non-Newtonian Fluid Mech.* **43**, 311–24.
- Hof, B., van Doorn, C. W. H., Westerweel, J., Nieuwstadt, F. T. M., Faisst, H., Eckhardt, B., et al. (2004) Experimental observation of nonlinear traveling waves in turbulent pipe flow. *Science* **305**, 1594–98.
- Homsy, G. (1987) Viscous fingering in porous media. *Annu. Rev. Fluid Mech.* **19**, 271–311.
- Hooper, A. P. and Boyd, W. G. C. (1983) Shear-flow instability at the interface between two viscous fluids. *J. Fluid Mech.* **128**, 507–28.
- Hooper, A. P. and Boyd, W. G. C. (1987) Shear flow instability due to a wall and a viscosity difference at the interface. *J. Fluid Mech.* **179**, 201–25.
- Hopf, E. (1942) Abzweigung einer periodischen lösung von einer stationären lösung eines differentialsystems. *Ber. Verh. Sächs. Akad. Wiss. Leipzig. Math.-phys. Kl.* **94**, 1–22 (English transl. in *The Hopf Bifurcation and its Applications* (1976), pp. 163–93, eds J. E. Marsden and M. McCracken. New York : Springer-Verlag).
- Howard, L. N. (1961) Note on a paper of John W. Miles. *J. Fluid Mech.* **10**, 509–12.
- Huerre, P. and Monkewitz, P. A. (1985) Absolute and convective instabilities in free shear layers. *J. Fluid Mech.* **159**, 151–68.
- Huerre, P. and Monkewitz, P. A. (1990) Local and global instabilities in spatially developing flows. *Annu. Rev. Fluid Mech.* **22**, 473–537.
- Huerre, P. and Rossi, M. (1998) Hydrodynamic instabilities in open flows. In *Hydrodynamics and Nonlinear Instabilities* (eds C. Godrèche and P. Manneville), pp. 81–294. Cambridge: Cambridge University Press.
- Hunt, J. C. R. (2006) Nonlinear and wave theory contributions of T. Brooke Benjamin. *Annu. Rev. Fluid Mech.* **38**, 1–25.
- Hunt, J. C. R., Leibovich, S. and Richards, K. J. (1988) Turbulent shear flows over low hills. *Q. J. R. Meteorol. Soc.* **114**, 1435–70.
- Huppert, H. E. and Turner, J. S. (1981) Double-diffusive convection. *J. Fluid Mech.* **106**, 299–329.
- Iooss, G. and Adelmeyer, M. (1999) *Topics in Bifurcation Theory*, 2nd edn. Advanced Series in Nonlinear Dynamics 3. Singapore: World Scientific.
- Iooss, G. and Joseph, D. D. (1990) *Elementary Stability and Bifurcation Theory*, 2nd edn. New York: Springer-Verlag.
- Janiaud, B., Pumir, A., Bensimon, D., Croquette, V., Richter, H. and Kramer, L. (1992) The Eckhaus instability for travelling waves. *Physica D* **55**, 269–86.
- Jeans, J. H. (1902) The stability of a spherical nebula. *Phil. Trans. R. Soc. Lond. A* **199**, 1–53.

- Jeffreys, H. (1928) Some cases of instability in fluid motion. *Proc. R. Soc. Lond. A* **118**, 195–208.
- Jordinson, R. (1970) The flat plate boundary layer. Part 1. Numerical integration of the Orr–Sommerfeld equations. *J. Fluid Mech.* **43**, 801–11.
- Joseph, D. D., Bai, R., Chen, K. P. and Renardy, Y. Y. (1997) Core-annular flows. *Annu. Rev. Fluid Mech.* **29**, 65–90.
- Joulin, G. and Vidal, P. (1998) An introduction to the instability of flames, shocks and detonations. In *Hydrodynamics and Nonlinear Instabilities* (eds C. Godrèche and P. Manneville), pp. 493–673. Cambridge: Cambridge University Press.
- Kaneko, A. and Honji, H. (1979) Double structures of steady streaming in the oscillatory viscous flow over a wavy wall. *J. Fluid Mech.* **93**(4), 727–36.
- Kapitza, P. L. (1948) Wave flow of thin layers of a viscous liquid. *Zh. Eksp. Teor. Fiz.* **18**, 3–28 (English transl. in *Collected Papers of P.L. Kapitza*, ed. D. Ter Haar, Pergamon, 1965).
- Kapitza, P. L. and Kapitza, S. P. (1949) Wave flow of thin layers of a viscous liquid. *Zh. Eksp. Teor. Fiz.* **19**, 105–120 (English transl. in *Collected Papers of P.L. Kapitza*, ed. D. Ter Haar, Pergamon, 1965, pp. 690–709).
- von Kármán, T. (1934) Some aspects of the turbulence problem. In *Proceedings of the 4th International Congress for Applied Mechanics, Cambridge, England*, pp. 54–91.
- Kelvin, L. (1871) Hydrokinetic solutions and observations. *Phil. Mag.* **42**, 362–77.
- Kerswell, R. R. (2002) Elliptical instability. *Annu. Rev. Fluid Mech.* **34**, 83–113.
- Kerswell, R. R. (2005) Recent progress in understanding the transition to turbulence in a pipe. *Nonlinearity* **18**, 17–44.
- Klebanoff, P. S., Tidstrom, K. D. and Sargent, L. M. (1962) The three-dimensional nature of boundary-layer transition. *J. Fluid Mech.* **12**, 1–34.
- Korteweg, D. J. and de Vries, G. (1895) On the change of form of long waves advancing in a rectangular channel, and on a new type of long stationary waves. *Phil. Mag.* **39**(5), 422–43.
- Koschmieder, E. L. (1993) *Bénard Cells and Taylor Vortices*. Cambridge: Cambridge University Press.
- Kuramoto, Y. (1984) Phase dynamics of weakly unstable periodic structures. *Prog. Theor. Phys.* **71**, 1182–96.
- Lagréé, P.-Y. (2003) A triple deck model of ripple formation and evolution. *Phys. Fluids* **15**(8), 2355–68.
- Lajeunesse, E., Molverti, L. and Charru, F. (2010) Bedload transport in turbulent flow at the grain scale: experiments and modeling. *J. Geophys. Res.* **115**, F04001.
- Lake, B. M., Yuen, H. C., Rungaldier, H. and Ferguson, W. E. (1977) Nonlinear deep-water waves: theory and experiment. Part 2. Evolution of a continuous wave train. *J. Fluid Mech.* **83**, 49–74.
- Lamb, H. (1932) *Hydrodynamics*, 6th edn. Cambridge: Cambridge University Press.
- Landahl, M. T. (1980) A note on an algebraic instability in inviscid parallel shear flows. *J. Fluid Mech.* **98**, 243–51.
- Landau, L. (1944) On the problem of turbulence. *C. R. Acad. Sci. U.R.S.S.* **44**, 311–14.
- Landau, L. and Lifshitz, E. (1976) *Mechanics*, 3rd edn. Oxford: Butterworth-Heinemann.
- Landau, L. and Lifshitz, E. (1987) *Fluid Mechanics*, 2nd edn. Oxford: Butterworth-Heinemann.
- Lange, C. G. and Newell, A. C. (1974) A stability criterion for envelope equations. *SIAM J. Appl. Math.* **27**, 441–56.
- Larrieu, E., Hinch, E. J. and Charru, F. (2009) Lagrangian drift near a wavy boundary in a viscous oscillating flow. *J. Fluid Mech.* **630**, 391–411.

- Leighton, D. and Acrivos, A. (1986) Viscous resuspension. *Chem. Engng Sci.* **41**(6), 1377–84.
- Lighthill, J. (1978) *Waves in Fluids*. Cambridge: Cambridge University Press.
- Lighthill, J. (1986) The recently recognized failure of predictability in Newtonian dynamics. *Proc. R. Soc. Lond. A* **407**, 35–50.
- Lin, C. C. (1955) *The Theory of Hydrodynamic Stability*. Cambridge: Cambridge University Press.
- Linz, S. J. (1995) A simple non-linear system: the oscillator with quadratic friction. *Eur. J. Phys.* **16**, 67–72.
- Liu, J., Paul, J. D. and Gollub, J. P. (1993) Measurements of the primary instabilities of film flows. *J. Fluid Mech.* **250**, 69–101.
- Longair, M. S. (2006) *The Cosmic Century: A History of Astrophysics and Cosmology*. Cambridge: Cambridge University Press.
- Lorenz, E. N. (1963) Deterministic non-periodic flow. *J. Atmos. Sci.* **20**, 130–41.
- Luchini, P. (2000) Reynolds-number-independent instability of the boundary layer over a flat surface: optimal perturbations. *J. Fluid Mech.* **404**, 289–309.
- Luchini, P. and Bottaro, A. (1998) Görtler vortices: a backward-in-time approach to the receptivity problem. *J. Fluid Mech.* **363**, 1–23.
- Luchini, P. and Charru, F. (2010a) Consistent section-averaged equations of quasi-one-dimensional laminar flow. *J. Fluid Mech.* **656**, 337–41.
- Luchini, P. and Charru, F. (2010b) The phase lead of shear stress in shallow-water flow over a perturbed bottom. *J. Fluid Mech.* **665**, 516–39.
- Lyne, W. H. (1971) Unsteady viscous flow over a wavy wall. *J. Fluid Mech.* **50**, 33–48.
- Mack, L. M. (1976) A numerical study of the eigenvalue spectrum of the Blasius boundary layer. *J. Fluid Mech.* **73**, 497–570.
- Malkus, W. V. R. and Veronis, G. (1958) Finite amplitude cellular convection. *J. Fluid Mech.* **4**, 225–60.
- Manneville, P. (1990) *Dissipative Structures and Weak Turbulence*. New York: Academic Press.
- Mantz, P. A. (1978) Bedforms produced by fine, cohesionless, granular and flakey sediments under subcritical water flows. *Sedimentology* **25**, 83–103.
- Marangoni, C. G. M. (1871) Über die ausbreitung der tropfen einer flüssigkeit auf der oberfläche einer anderen. *Ann. Phys. Chem.* **143**, 337–54.
- McGoldrick, L. F. (1965) Resonant interactions among capillary-gravity waves. *J. Fluid Mech.* **21**, 305–31.
- Michalke, A. (1964) On the inviscid instability of the hyperbolic-tangent velocity profile. *J. Fluid Mech.* **19**, 543–56.
- Miles, J. W. (1957) On the generation of surface waves by shear flows. *J. Fluid Mech.* **3**, 185–204.
- Miles, J. W. (1960) The hydrodynamic stability of a thin film of liquid in uniform shearing motion. *J. Fluid Mech.* **8**, 593–610.
- Miles, J. W. (1981) The Korteweg-de Vries equation: a historical survey. *J. Fluid Mech.* **106**, 131–47.
- Miles, J. W. (1984) Nonlinear Faraday resonance. *J. Fluid Mech.* **146**, 285–302.
- Miles, J. W. and Henderson, D. M. (1990) Parametrically forced surface waves. *Annu. Rev. Fluid Mech.* **22**, 143–65.
- Milne-Thompson, L. M. (1968) *Theoretical Hydrodynamics*, 5th edn. London: MacMillan (reprinted by Dover, 1996).
- Mouilleron, H., Charru, F. and Eiff, O. (2009) Inside the moving layer of a sheared granular bed. *J. Fluid Mech.* **628**, 229–39.

- Mouilleron-Arnould, H., Charru, F. and Eiff, O. (2001) Experimental study of ripple growth in a granular bed sheared by an oscillating viscous fluid. 4th International Conference on Multiphase Flows (New-Orleans, USA).
- Nayfeh, A. H. and Saric, W. S. (1972) Nonlinear waves in a Kelvin–Helmholtz flow. *J. Fluid Mech.* **55**, 311–27.
- Newell, A. C., Passot, T. and Lega, J. (1993) Order parameter equations for patterns. *Annu. Rev. Fluid Mech.* **25**, 399–453.
- Newell, A. C. and Whitehead, J. A. (1969) Finite bandwidth, finite amplitude convection. *J. Fluid Mech.* **38**, 279–304.
- Nielsen, P. (1992) *Coastal Bottom Boundary Layers and Sediment Transport*. Singapore: World Scientific.
- Nishioka, M., Iida, S. and Ichikawa, Y. (1975) An experimental investigation of the stability of plane Poiseuille flow. *J. Fluid Mech.* **72**, 731–51.
- Orr, W. M. (1907) The stability or instability of the steady motions of a perfect liquid and of a viscous liquid. *Proc. R. Irish Acad. A* **27**, 9–68, 69–138.
- Orszag, S. A. (1971) Accurate solution of the Orr–Sommerfeld stability equation. *J. Fluid Mech.* **50**, 689–703.
- Pearson, J. R. A. (1958) On convection cells induced by surface tension. *J. Fluid Mech.* **4**, 489–500.
- Phillips, O. M. (1981) Wave interactions – the evolution of an idea. *J. Fluid Mech.* **106**, 215–27.
- Plateau, J. (1857) Recherches expérimentales et théoriques sur les figures d'équilibre d'une masse liquide sans pesanteur. *Ann. Chim. Phys.* **50**, 97–124.
- Plateau, J. (1873) *Statique expérimentale et théorique des liquides soumis aux seules forces moléculaires*. Paris: Gauthier-Villars.
- van der Pol, B. (1927) Forced oscillations in a circuit with nonlinear resistance (receptance with reactive triode). *London, Edinburgh and Dublin Phil. Mag.* **3**, 65–80.
- Pomeau, Y. and Manneville, P. (1979) Stability and fluctuations of a spatially periodic convective flow. *J. Physique-Lettres* **40**, 609–12.
- Pope, S. B. (2000) *Turbulent Flows*. Cambridge: Cambridge University Press.
- Pouliquen, O. (1999) Scaling laws in granular flows down rough inclined planes. *Phys. Fluids* **11**, 542–8.
- Prandtl, L. (1921) Bemerkungen über die entstehung der turbulenz. *Z. Angew. Math. Mech.* **1**, 431–6.
- Probstein, R. F. (2003) *Physicochemical Hydrodynamics. An Introduction*, 2nd edn. New York: John Wiley & Sons.
- Pumir, A., Manneville, P. and Pomeau, Y. (1983) On solitary waves running down an inclined plane. *J. Fluid Mech.* **135**, 27–50.
- Quéré, D. (1999) Fluid coating on a fiber. *Annu. Rev. Fluid Mech.* **31**, 347–84.
- Rabaud, M., Michalland, S. and Couder, Y. (1990) Dynamical regimes of directional viscous fingering: spatiotemporal chaos and wave propagation. *Phys. Rev. Lett.* **64**(2), 184–7.
- Rajchenbach, J. (2000) Granular flows. *Adv. Phys.* **49**, 229–56.
- Raudkivi, A. J. (1997) Ripples on stream bed. *J. Hydr. Engrg.* **123**(1), 58–64.
- Raudkivi, A. J. (1998) *Loose Boundary Hydraulics*. Rotterdam: A.A. Balkema.
- Rayleigh, L. (1879) On the instability of jets. *Proc. Lond. Math. Soc.* **10**, 4–13.
- Rayleigh, L. (1880) On the stability, or instability, of certain fluid motions. *Proc. Lond. Math. Soc.* **11**, 57–70.
- Rayleigh, L. (1883a) Investigation of the character of the equilibrium of an incompressible heavy fluid of variable density. *Proc. Lond. Math. Soc.* **14**, 170–77.
- Rayleigh, L. (1883b) On maintained vibrations. *Phil. Mag.* **15**, 229–35.

- Rayleigh, L. (1883c) On the crispations of fluid resting on a vibrating support. *Phil. Mag.* **16**, 50–58.
- Rayleigh, L. (1892) On the instability of a cylinder of viscous liquid under capillary force. *Phil. Mag.* **34**, 145–54.
- Rayleigh, L. (1894) *The Theory of Sound*, 2nd edn. London: MacMillan (reprinted by Dover, 1945).
- Rayleigh, L. (1916a) On the convection currents in a horizontal layer of fluid, when the higher temperature is on the under side. *Phil. Mag.* **32**, 529–46.
- Rayleigh, L. (1916b) On the dynamics of revolving fluids. *Proc. R. Soc. Lond. A* **93**, 148–54.
- Reed, H. L., Saric, W. S. and Arnal, D. (1996) Linear stability theory applied to boundary layers. *Annu. Rev. Fluid Mech.* **28**, 389–428.
- Renardy, M. and Renardy, Y. (1993) Derivation of amplitude equations and analysis of sideband instabilities in two-layer flows. *Phys. Fluids A* **5**(11), 2738–62.
- Renardy, Y. (1985) Instability at the interface between two shearing fluids in a channel. *Phys. Fluids* **28**, 3441–3.
- Reynolds, O. (1883) An experimental investigation of the circumstances which determine whether the motion of water shall be direct or sinuous, and of the law of resistance in parallel channels. *Phil. Trans. R. Soc. Lond.* **174**, 935–82.
- Richards, K. J. (1980) The formation of ripples and dunes on an erodible bed. *J. Fluid Mech.* **99**(3), 597–618.
- Riecke, H. (1992) Self-trapping of traveling wave pulses in binary mixture convection. *Phys. Rev. Lett.* **68**, 301–4.
- Riley, N. (2001) Steady streaming. *Annu. Rev. Fluid Mech.* **33**, 43–65.
- Rocard, Y. (1967) *Thermodynamique*, 2nd edn. Paris: Masson.
- Romanov, V. A. (1973) Stability of plane-parallel Couette flow. *Funktional Anal. i Prilozhen* **7** (2), 62–73 (English transl. in *Functional Analysis and Its Applications*, vol. 7, pp. 137–46).
- Ross, J. A., Barnes, F. H., Burns, J. G. and Ross, M. A. S. (1970) The flat plate boundary layer. Part 3. Comparison of theory with experiments. *J. Fluid Mech.* **43**, 819–32.
- Rousseaux, G., Stegner, A. and Wesfreid, J. E. (2004) Wavelength selection of rolling-grain ripples in the laboratory. *Phys. Rev. E* **69**, 031307.
- Ruschak, K. J. (1985) Coating flows. *Annu. Rev. Fluid Mech.* **17**, 65–89.
- Ruyer-Quil, C. and Manneville, P. (2000) Improved modeling of flows down inclined planes. *Eur. Phys. J. B* **15**, 357–69.
- Saffman, P. G. and Taylor, G. I. (1958) The penetration of a fluid into a porous medium or Hele-Shaw cell containing a more viscous fluid. *Proc. R. Soc. Lond. A* **245**, 312–29.
- de Saint-Venant, A. J. C. B. (1871) Théorie du mouvement non-permanent des eaux, avec application aux crues des rivières et à l'introduction des marées dans leur lit. *C. R. Acad. Sci. Paris* **73**, 147–54, 237–40.
- Sauermann, G., Kroy, K. and Herrmann, H. J. (2001) Continuum saltation model for sand dunes. *Phys. Rev. E* **64**(3), 031305.
- Savage, S. B. and Hutter, K. (1989) The motion of a finite mass of granular material down a rough incline. *J. Fluid Mech.* **199**, 177–215.
- Savart, F. (1833) Mémoire sur la constitution des veines liquides lancées par des orifices circulaires en minces parois. *Ann. Chim. Phys.* **53**, 337–86, clichés dans le volume 54.
- Schatz, M. F. and Neitzel, G. P. (2001) Experiments on thermocapillary instabilities. *Annu. Rev. Fluid Mech.* **33**, 93–127.
- Scherer, M. A., Melo, F. and Marder, M. (1999) Sand ripples in an oscillating annular sand–water cell. *Phys. Fluids* **11**(1), 58–67.

- Schlichting, H. (1933) Zur entstehung der turbulenz bei der plattenströmung. *Nachr. Ges. Wiss. Göttingen, Math.-Phys. Kl.* pp. 181–208.
- Schluter, A., Lortz, D. and Busse, F. (1965) On the stability of steady finite amplitude convection. *J. Fluid Mech.* **23**, 129–44.
- Schmid, P. J. and Henningson, D. S. (2001) *Stability and Transition in Shear Flows*. New York: Springer-Verlag.
- Schubauer, G. B. and Skramstad, H. K. (1947) Laminar boundary-layer oscillations and transition on a flat plate. *J. Res. Nat. Bur. Stand.* **38**, 251–92.
- Schuster, H. G. and Wolfram, J. (2005) *Deterministic Chaos, an Introduction*. Berlin: Wiley-VCH.
- Segel, L. A. (1969) Distant sidewalls cause slow amplitude modulation of cellular convection. *J. Fluid Mech.* **38**, 203–24.
- Shkadov, V. Y. (1967) Wave flow regimes of a thin layer of a viscous fluid under the action of gravity. *Izv. Akad. Nauk SSSR, Mekh. Zhidk. i Gaza* **1**, 43–51 (English transl. in *Fluid Dynamics* (1970), vol. 2, pp. 29–34, Faraday Press, New York).
- Siggia, E. D. and Zippelius, A. (1981) Pattern selection in Rayleigh–Bénard convection near threshold. *Phys. Rev. Lett.* **47**, 835–8.
- Sleath, J. F. A. (1976) On rolling-grain ripples. *J. Hydraul. Res.* **14**, 69–81.
- Smith, M. K. (1990) The mechanism for the long-wave instability in thin liquid films. *J. Fluid Mech.* **217**, 469–85.
- Sommerfeld, A. (1908) Ein beitrag zur hydrodynamischen erklaerung der turbulenten fluessigkeitsbewegungen. In *Atti del 4 Congresso Internazionale dei Matematici, Ser. I*, vol. 3, pp. 116–24. Rome.
- Squire, H. B. (1933) On the stability of three-dimensional disturbances of viscous flow between parallel walls. *Proc. R. Soc. Lond. A* **142**, 621–8.
- Stegner, A. and Wesfreid, J. E. (1999) Dynamical evolution of sand ripples under water. *Phys. Rev. E* **60**, 3487–90.
- Stewartson, K. and Stuart, J. T. (1971) A nonlinear instability theory for a wave system in plane Poiseuille flow. *J. Fluid Mech.* **48**, 529–45.
- Stokes, G. G. (1847) On the theory of oscillatory waves. *Camb. Trans.* **8**, 441–73 (Papers 1, 197–229).
- Stuart, J. T. (1958) On the nonlinear mechanics of hydrodynamic stability. *J. Fluid Mech.* **4**, 1–21.
- Stuart, J. T. (1960) On the nonlinear mechanics of wave disturbances in stable and unstable parallel flows, Part 1. The basic behavior in plane Poiseuille flow. *J. Fluid Mech.* **9**, 353–70.
- Stuart, J. T. (1963) Hydrodynamic stability. In *Laminar Boundary Layers* (ed. L. Rosenhead), Chap. 9. Oxford: Oxford University Press.
- Stuart, J. T. and Di Prima, R. C. (1978) The Eckhaus and Benjamin–Feir resonance mechanisms. *Proc. R. Soc. Lond. A* **362**, 27–41.
- Sumer, B. M. and Bakioglu, M. (1984) On the formation of ripples on an erodible bed. *J. Fluid Mech.* **144**, 177–90.
- Swift, J. and Hohenberg, P. C. (1977) Hydrodynamic fluctuations at the convective instability. *Phys. Rev. A* **15**, 319–28.
- Taylor, G. I. (1923) Stability of a viscous liquid contained between two rotating cylinders. *Phil. Trans. R. Soc. Lond. A* **223**, 289–343.
- Taylor, G. I. (1950) The instability of liquid surfaces when accelerated in a direction perpendicular to their planes. I. *Proc. R. Soc. Lond. A* **201**, 192–6.
- Taylor, G. I. and Michael, D. H. (1973) On making holes in a sheet of fluid. *J. Fluid Mech.* **58**, 625–39.

- Thorpe, S. A. (1969) Experiments on the instability of stratified shear flows: immiscible fluids. *J. Fluid Mech.* **39**, 25–48.
- Thorpe, S. A. (1971) Experiments on the instability of stratified shear flows: miscible fluids. *J. Fluid Mech.* **46**(2), 299–319.
- Tollmien, W. (1929) Über der entstehung der turbulenz. *Nachr. Ges. Wiss. Göttingen, Math.-Phys. Kl.* pp. 21–44.
- Trefethen, L. N., Trefethen, A. E., Reddy, S. C. and Driscoll, T. A. (1993) Hydrodynamic stability without eigenvalues. *Science* **261**, 578–84.
- Tresser, C. and Coullet, P. (1978) Iterations of endomorphisms and renormalization group. *Comptes Rendus Acad. Sci. Paris* **287A** (7), 577–80.
- Tritton, D. J. (1988) *Physical Fluid Dynamics*. Oxford: Clarendon Press.
- de Vega, H. J., Sanchez, N. and Combes, F. (1996) Self-gravity as an explanation of the fractal structure of the interstellar medium. *Nature* **383**, 56–8.
- Villermaux, E. (1998) On the role of viscosity in shear instabilities. *Phys. Fluids* **10**, 368–73.
- Vittori, G. and Blondeaux, P. (1990) Sand ripples under sea waves. Part 2. Finite-amplitude development. *J. Fluid Mech.* **218**, 19–39.
- Watson, J. (1960) On the nonlinear mechanics of wave disturbances in stable and unstable parallel flows, Part 2. The development of a solution for plane Poiseuille and for plane Couette flow. *J. Fluid Mech.* **9**, 371–89.
- Welander, P. (1967) On the oscillatory instability of a differentially heated fluid loop. *J. Fluid Mech.* **29**, 17–30.
- Werlé, H. (1980) Transition and separation: visualizations in the ONERA water tunnel. *La Rech. Aérospatiale, Bi-monthly Bull.* (5), 35–49.
- Wesfreid, J. E., Pomeau, Y., Dubois, M., Normand, C. and Bergé, P. (1978) Critical effects in Rayleigh–Bénard convection. *J. Physique* **39**(7), 725–31.
- Whitham, G. B. (1974) *Linear and Nonlinear Waves*. New York: John Wiley & Sons.
- Williamson, C. H. K. (1996) Vortex dynamics in the cylinder wake. *Annu. Rev. Fluid Mech.* **28**, 477–539.
- Wong, M. and Parker, G. (2006) Reanalysis and correction of bed-load relation of Meyer-Peter and Müller using their own database. *J. Hydr. Engrg.* **132**(11), 1159–68.
- Wygnanski, I. J. and Champagne, F. H. (1973) On transition in a pipe. Part 1. The origin of puffs and slugs and the flow in a turbulent slug. *J. Fluid Mech.* **59**, 281–335.
- Yalin, M. S. (1985) On the determination of ripple geometry. *J. Hydr. Engrg.* **111**, 1148–55.
- Yih, C. S. (1963) Stability of liquid flow down an inclined plane. *Phys. Fluids* **6**, 321–34.
- Yih, C. S. (1967) Instability due to viscous stratification. *J. Fluid Mech.* **27**, 337–52.

Index

- acoustic wave, 44–7, 237
adjoint operator, 35
amplitude equation, 247, 256, 261, 269, 271, 272, 283, 284, 289, 296, 297, 320
nonautonomous, 260
area contraction, 330
asymptotic expansion
 long-wave, 179
 short-wave, 181
attractor, 326, 330
 basin, 2, 93, 330
 fractal, 365
 Hénon, 332, 365
 strange, 331
avalanche, 38, 202–8
 angle, 202
- Bénard–Marangoni thermocapillary instability, xx, 76–8
Bagnold’s conjecture, 212
Bagnold, Ralph Alger, 211
Benjamin–Feir instability, 278–9, 300
 –Eckhaus, 313
 experiment, 279
- bifurcation, 6–12, 44, 327, 346, 351–64
 codimension, 327, 352–4
 generic, 11
 global, 352, 354, 361
 heteroclinic, 354
 homoclinic, 354
 Hopf, 12, 27, 29, 101, 255, 270, 300, 311, 353, 359–60, 368
 local, 352
 of a periodic orbit, 353
 of codimension two, 360–4
 period-doubling, 354
 pitchfork, 9–12, 23, 26, 250, 264, 299, 357
 saddle-node, 7–9, 14, 15, 20, 23, 251, 299, 353–8
 subcritical, 158, 233, 307, 309, 315
 supercritical, 302
 transcritical, 12, 356
- bifurcation diagram, 8, 14, 250, 272, 346, 367
 Hopf, 360
 pitchfork, 358
 saddle-node, 356
 transcritical, 357
- boundary layer instability, xix, xx, 101, 102, 143, 162–9, 193
 nonparallel effect, 164–8
 secondary instability, 316
 turbulent streaks, xx
- Boussinesq approximation, 24, 28, 73, 304
Brunt–Väisälä frequency, 29
bubble of gas and vapor, 16–20
- Cauchy conditions, 99
central manifold, 264
Chandrasekhar, Subrahmanyam, 52
characteristic polynomial, 4
Chebyshev polynomials, 151, 181
colloidal suspension, 20–3
consistent depth-averaged equations, 183, 239, 373
convection
 in a ring, 23–7
 thermal, xx
 thermohaline, 27, 319
- Couette plane flow stability, 113, 162, 169
Couette–Taylor instability, xix, xx, 126–34, 169, 247
 Rayleigh criterion, 130, 136
 secondary instability, 310
- Coulomb laws, 202, 204, 210
coupling between finite k and zero k , 317–23
critical layer, 111, 150, 153
- Darrieus–Landau instability, 85
Dean vortices, 127, 169
degree of freedom, 1, 327
deterministic chaos, 26, 69, 249, 260, 326
dewetting instability, xx
- dispersion
 of a wave packet, 88–92, 102, 289
 dispersion relation, 43–6, 50, 51, 109, 149
 nonlinear, 276

- Duffing oscillator, 249, 255–8, 285
coupled oscillators, 280
- dune
aeolian, 201, 218
barchan, 220
subaqueous, 201, 219, 238
- dynamical system, 2, 326
autonomous, 1
discrete, 332
nonautonomous, 36, 327
- Eckhaus instability, 299, 305–11
zigzag, 309
- effective mass, 55
- eigenfunction
boundary layer, 164
falling film, 179, 181, 193
plane Poiseuille flow, 156
- eigenmode, 46, 51
- eigenspace, 335
- eigenvalue, 4, 334
continuous spectrum, 111, 113
discrete spectrum, 155
- eigenvector, 4, 5, 31, 334
generalized, 334
nonorthogonality, 30, 33
- envelope equation, 288–93, 299, 312
- erosion, 215–8
- exponential of a matrix, 334, 365
- Faraday instability, xxi, 260
- Faraday, Michael, 21
- ferrofluid instability, xxi
- fixed point, 327, 329, 330, 334, 335
definition, 3
focus, 5, 336
hyperbolic, 5, 336
in two dimensions, 4–5
linear stability, 2–5
node, 4, 336
nonhyperbolic, 6
saddle, 4, 336
- Fjørtoft theorem, 114
- Floquet theory, 331
- fluid
elastic, 173
miscible, 173
- Fredholm alternative, 325
- frequency
cutoff, 188, 207
locking, 259, 269, 271
nonlinear correction, 257
- friction coefficient, 202, 204, 210, 239, 373
Blasius, 245, 373
Manning–Strickler, 245, 373
- friction velocity, 209
- Froude number (critical), 180, 206, 207, 241, 244
- Görtler vortices, 127, 169
- Gaster relation, 101, 191
- genericity, 345–51
- Ginzburg–Landau equation, 98, 302–4
complex coefficients, 312
localized solution, 305, 313
- granular ripples, 201
aeolian, 218
oscillating flow, 230–8
rolling, 231
subaqueous, 219, 221–30
vortex, 231
- gravitational potential, 49
- gravity wave, 103, 206, 238
- gravity–capillary wave, xx, 54, 60
- Green function, 94
- group velocity, 90, 91, 98–100, 102, 289
- growth rate
maximum, 191
spatial, 100, 101, 190, 206
temporal, 96, 99, 101, 102
- Hamiltonian, 362
- Hartman–Grobman theorem, 336
- Helmholtz, Hermann L. F. von, 121
- Hilbert transform, 267, 322
- Howard’s semicircle theorem, 115
- hysteresis, 8, 251
- implicit function theorem, 359, 364
- impulse response, 94, 99, 192
- initial-value problem, 96
- instability
at small Reynolds number, 171
absolute, 95, 98–101, 300, 311
centrifugal, 107
convective, 94, 98–102, 155, 181, 192, 317
elliptical, 316
long-wave, 61, 123, 125, 174, 178–81, 262, 319
secondary, 309
subharmonic, 316
three-dimensional, 160
- interface
dynamic condition, 58, 176
instability, 178
kinematic condition, 58, 176
- intermittency, 317
- internal wave, 135
- invariance
Galilean, 95, 317–9, 325
reflectional, 10, 60, 249, 289, 309, 311, 320, 346,
357
rotational, 129
translational, 45, 50, 129, 237, 247, 289, 302, 306,
309, 311–3, 318, 325
- Jeans gravitational instability, 44–53
- jet, xxi, 104, 124
- Kapitza, Pyotr Leonidovich, 174, 186
- Kelvin (Lord), William Thomson, 120
- Kelvin–Helmholtz instability, xx, 104, 117–26
absolute instability, 124
nonparallel effects, 126

- on a viscous film, 137
- with a wall, 135
- with gravity and capillarity, 134
- Klein–Gordon
 - amplitude equation, 283
 - equation, 275, 279, 281–7
 - nonlinear wave, 284, 297
- Korteweg–de Vries equation, 272, 298
- Kuramoto–Sivashinsky equation, 261, 272, 309
- Landau equation, 247, 264, 289, 302, 360
- Landau, Lev Davidovich, 248
- Laplace–Young law, 13, 17
- limit cycle, 12, 254, 270, 353, 361
- linearization, 50
- liquid film
 - annular, 171
 - falling, 174–92, 203
 - sheared, 171, 193, 264
- Lorenz
 - equations, 23, 26, 331, 368
 - normal form, 367
- manifold, 327
 - center, 327, 340, 366
 - invariant, 326, 338–45, 366
- map
 - first return, 331, 332, 353
 - Hénon, 365
 - logistic, 332
- Mathieu equation, 259, 270
- matrix
 - exponential, 334
 - Jacobian, 3, 334
 - Jordan, 5, 31, 334, 341, 354, 360
- Melnikov (perturbation method), 363
- metastability, 129, 251
- mixing layer, xx, 100, 104, 116–26
- mode
 - amplitude, 306
 - global, 95
 - normal, 43, 44, 46
 - phase, 306, 318
 - slave, 74, 79, 133, 264, 306, 307, 320
- modulation, 275
 - instability, 287
- multimedia fluid mechanics, xix
- multiple scales method, 249, 252, 274
- non-normality of an operator, 30–6, 160
- normal form
 - of an ODE, 326, 342, 367
 - of the Hopf bifurcation, 12, 359
 - of the pitchfork bifurcation, 10, 30, 358
 - of the saddle-node bifurcation, 9, 356
 - of the transcritical bifurcation, 357
- nucleation–coalescence of a wave, 322
- optimal excitation of an unstable mode, 33–6, 41–2
- orbit
 - heteroclinic, 350, 367
- homoclinic, 348, 350, 363, 364
- periodic, 329–31, 350, 360
- order parameter, 39, 250
- ordinary differential equation, 1, 326, 327
- Orr–Sommerfeld equation, 148–51, 177, 193
 - asymptotic solution, 150
 - numerical solution, 150
- oscillating boundary layer, 233, 238
- oscillating flow, 202, 230–8
- oscillator
 - coupled, 280
 - dissipative, 249
 - forced harmonic, 36
 - harmonic, 1
 - nonlinear, 249–60
 - parametrically forced, 259, 270–2
 - quasi-periodic, 37, 271
 - relaxation, 270
- particle transport, 208–18
 - Meyer–Peter–Muller law, 213, 239
- perturbation
 - isentropic, 50
 - of finite amplitude, 10
 - of infinitesimal amplitude, 10
 - optimal, 32, 41, 161, 168
 - rotational, 56, 119
- phase
 - dynamics, 307, 309
 - equation, 308, 314
 - gradient, 308
 - instability, 292
 - turbulence, 309
- phase portrait, 2, 3, 31, 32, 254, 329, 334–8, 345, 346, 348, 350, 352, 360–4, 366
- phase space, 2, 4, 326, 327
 - enlarged, 355
- phase transition
 - first-order, 39
 - second-order, 39
- Poincaré section, 331–2, 353
- Poincaré, Jules Henri, 326, 333
- Poiseuille flow instability
 - annular flow, 193, 194
 - pipe flow, xix, 100, 140, 162, 194, 317
 - plane flow, 100, 154–62, 168, 194, 247, 315
- potential, 3, 22, 38, 39
 - chemical, 19
 - double-well, 37
 - electrostatic, 22
 - extremum, 3
 - grand, 19
 - gravitational, 49
 - mechanical, 7, 9
 - thermodynamical, 15, 19, 20, 39
- predictability horizon, 331
- printer’s instability, 85
- quasi-periodicity, 259, 269, 330
- quasistatic (boundary condition), 137, 221, 225

- Rayleigh
 equation, 110
 inflection point theorem, 113
- Rayleigh, John William Strutt, Lord, 75
- Rayleigh–Bénard instability, xx, 68–74, 132–4, 247
 boundary conditions, 73
 free boundaries, 318
 Landau coefficient, 302
 mechanism, 71
 secondary instability, 309
- Rayleigh–Plateau capillary instability, xx, xxi, 64–8, 82
- Rayleigh–Taylor instability, xx, 53–64, 176
 between walls, 80
 of a viscous film, xx, 81
 of an evaporating liquid, xxi
 turbulent, xxi
- relaxation phenomena, 202, 208, 214–8, 223, 227, 230
 in oscillating flow, 238
 acceleration length, 219
 deposition length, 220
- residue theorem, 97
- resonance, 37
 among Fourier modes, 275, 284, 294
 among side-band modes, 279–87, 291
 linear, 154, 170
 near-resonance, 285
 of eigenvalues, 337, 344, 366
 quadruplet, 295
 self-interaction, 284
 subharmonic, 295
 triad, 294
- resonant nonlinearity, 342
- Reynolds
 experiment, 140
 stress, 152
- Reynolds number
 critical, 187
 effective, 195, 223, 235
- Reynolds, Osborne, 142
- Reynolds–Orr equation, 152
- Richtmeyer–Meshkov instability, xxi
- Saffman–Taylor instability, 83
- Saint-Venant equations, 182, 203–6, 239–45, 369–74
- saturation
 of the amplitude, 249, 251–5, 264–6
 time, 266
- Schrödinger equation, 289–93
 localized solution, 290
 nonlinear wave, 290
- second law of thermodynamics, 19
- sensitivity to initial conditions, 326, 331, 365
- Shields
 diagram, 209
 number, 208
- side-band instability, 278
- soap film, xx, xxi, 12–15
- solvability condition, 249, 253, 257, 293, 297, 298, 304, 325
- Squire
 theorem, 110, 146–8, 162, 176
 theorem with a deformable interface, 148
 transformation, 109, 146
- stability
 asymptotic, 4, 92
 global, 93, 316
 in the Lyapunov sense, 92
 linear, 94, 96
 marginal, 180
 mechanical, 18
 metastability, 8, 17, 40
 neutral, 5
 nonlinear, 6, 336
 spatial, 124, 149
 structural, 326, 345–52, 367
 temporal, 51, 149
 thermodynamical, 19
- stability diagram, 180, 181
- stationary phase, method of, 89, 99
- steady streaming, 234–8
- Stokes
 flow, 185, 196
 wave, 275–6, 287
- Stokes, George Gabriel, 277
- subharmonic instability, 259
- Swift–Hohenberg equation, 303, 318, 323
- symmetry breaking, 10, 44, 346
- system
 confined, 299
 extended, 299
- Taylor, Geoffrey Ingram, 15
- Tollmien–Schlichting wave, xx, 145, 174, 193, 299, 300, 311
 forced, 156, 162
 linear resonance, 170
 mechanism, 151–4
 nonlinear wave, 315
- transient growth, 1, 30–3, 41–2, 158, 168, 317
- transversality, 270, 349–50, 355
- triple deck theory, 198
- turbulence (transition to), 104, 127, 128, 141–3, 158, 162, 163, 317
- van der Pol oscillator, 249, 251–5
 forced, 258, 268
- van der Waals forces, 22
- velocity
 group, 99, 180, 191, 312
 phase, 51
- video resources, xix–xxi
- viscous fingering, xx, xxi, 83
- viscous resuspension, 213
- vorticity
 Helmholtz equation, 56, 110, 119, 196
 penetration depth, 198, 221, 235
- wake, xix–xxi, 101, 105, 124

- wave
 - dispersive, 88
 - gravity, 103, 206, 238, 274, 290
 - gravity–capillary, 54, 60, 294
 - internal, 135
 - nonlinear, 274, 311
 - oblique, 167
- solitary, 174, 187
- soliton, 298
- stationary acoustic, 237
- Stokes, 313
- wave packet, 88, 102, 288–9, 300, 302, 311–3
- weakly nonlinear analysis, 246

